Reference
Only

Ref label

41 0627386 9

ProQuest Number: 10183551

All rights reserved

INFORMATION TO ALL USERS
The quality of this reproduction is dependent upon the quality of the copy submitted.

In the unlikely event that the author did not send a complete manuscript
and there are missing pages, these will be noted. Also, if material had to be removed,
a note will indicate the deletion.



ProQuest 10183551

Published by ProQuest LLC (2017). Copyright of the Dissertation is held by the Author.

All rights reserved.
This work is protected against unauthorized copying under Title 17, United States Code
Microform Edition © ProQuest LLC.

ProQuest LLC.
789 East Eisenhower Parkway
P.O. Box 1346
Ann Arbor, MI 48106 – 1346

10345562

THE NOTTINGHAM TRENT UNIVERSITY LIS

Short Loan

Ref

M. Phil/CP/00 CHO

Characterisation of Surfaces and Surface Breaking Defects Using Magnetic NDE Methods.

Al-Amin R. Choudhury

A thesis submitted in partial fulfilment of the requirements of The Nottingham Trent University for the degree of Master of Philosophy

December 2000

"Perhaps even these things, one day, will be pleasing to remember."

-Publius Vergilius Maro (70-19 bc), Aenid

ABSTRACT

The Barkhausen phenomenon is reviewed in relation to current knowledge, and the direction of modern research is discussed. Acoustic Barkhausen Emission (ABE) and Electromagnetic Barkhausen Emission (EBE) from ferromagnetic specimens has been studied. Test samples were magnetised using a silicon iron yoke electromagnet and a triangular magnetising frequency of 0.1Hz. A coil transducer of 2000 turns and a piezoelectric transducer were used as the sensors for EBE and ABE respectively.

Initially, finite element analysis of the magnetising field spread through a test sample was studied. A central region of uniform intensity of magnetisation was found, from where consistent EBE signals were detected. The relationship between the Barkhausen signals and sample volume was studied. The signals were analysed and distinct relationships were found for the ABE and EBE signals, for a range of sample volumes. Utilising the fundamental differences between the ABE and EBE, the effect of surface modifications on nickel, generated by machining, has been examined. The Barkhausen signals indicated a relationship between these modifications and time of EBE peak.

The effect of an idealised surface breaking defect on the Barkhausen emission (BE) is considered. Differing EBE sensors and two different magnetising yokes and their effect on the detected ABE and EBE signals from the slotted steel specimen have been studied. EBE envelopes were found to split due to the presence of the slot and a range of Barkhausen signal parameters (time of peak, signal energy and signal amplitude) were used to indicate the slot location. Optimum combination of experimental variables would allow the detection of surface breaking cracks. The BE from a tight surface breaking fatigue crack, was also studied. Barkhausen envelopes were found to be similar from points across the specimen surface. The analysed BE parameters were found to yield useful information about the crack location and surrounding material.

Barkhausen emission from EN-43A steel specimens, plain, welded and containing a low-cycle fatigue crack within the weld, were studied. The effect of these material changes on the BE envelopes was found to be significant. The effects of machining the surface of each specimen, using electrical and mechanical machining, were also studied. Different

machining processes yielded significantly different EBE signals and as a result envelope parameters were found to change. Time of peak was found to occur earlier over the crack affected region, where an increase in the energy was also noted. Mechanisms for the generation of the differing ABE and EBE results are discussed.

The effect of crack depth reduction by machining away the specimen thickness has been examined. The different machining techniques, used to reduce the crack depth, had significant effects on the Barkhausen emission. Barkhausen response from mechanically machined surfaces failed to exhibited any noticeable trend with decreasing crack depth. Electrical machining generated a consistently reproducible surface texture and as a result, the effect of reducing crack depth was found to have a measurable influence on the EBE envelope parameters. Possible applications of the Barkhausen technique and the reported results are also considered.

CONTENTS

		Page
Abstract		ii
Contents		iv
	PART 1	
1.	**INTRODUCTION TO MAGNETISM AND THE BARKHAUSEN PHENOMENON.**	2
1.1.	INTRODUCTION TO MAGNETISM.	4
1.1.1.	Ferromagnetism.	5
1.1.2.	Magnetic Domains.	6
1.1.3.	Domain Patterns and Domain Walls.	7
1.2.	THE BARKHAUSEN EFFECT.	10
1.2.1.	Barkhausen Signals and Sensors.	12
1.2.2.	Barkhausen Emission and Material Microstructure.	14
1.2.3.	Barkhausen Emission and Grain Size.	14
1.2.4.	Barkhausen Emission and Precipitates.	16
1.2.5.	Barkhausen Emission and Stress.	17
1.2.6.	Barkhausen Emission and Dislocation.	18
1.3.	MAGNETIC TESTING.	21
1.3.1.	Barkhausen Emission and Applications.	23
1.4.	CURRENT RESEARCH AND AIMS OF THIS WORK.	27
1.4.1.	Current Research.	27
1.4.2.	Aims of the Research.	29
1.5.	APPARATUS AND EXPERIMENTAL SYSTEM USED IN THIS RESEARCH.	30
1.5.1.	Experimental System.	30
1.5.2.	Magnetising System.	31
1.5.3.	ABE Sensors and Signal Amplification.	31
1.5.4.	EBE Sensor and Signal Amplification.	32
1.5.5.	Signal Recording.	33
1.5.6.	Sensor Attachment and Barkhausen Signals.	34

2. BARKHAUSEN EMISSION -MATERIAL VOLUME AND SURFACE EFFECTS. 35

2.1. FINITE ELEMENT MODELLING. 37
2.1.1. Introduction to Finite Element Analysis. 37
2.1.2. Finite Element Modelling of the Barkhausen Magnetisation System. 40
2.1.2.1. *Results of FE modelling.* 42
2.1.3. Finite Element Modelling of Different Specimen Thicknesses. 46
2.1.3.1. *Modelling differing thicknesses of nickel specimen.* 46
2.1.3.2. *Results from modelling different nickel specimen thicknesses.* 46
2.1.4. Finite Element Modelling of a Slot in a Barkhausen Test Specimen. 53
2.1.4.1. *Modelling of a slot within a test specimen.* 53
2.1.4.2. *Results from FE modelling of a slotted specimen.* 53

2.2. SPECIMEN MAGNETISATION AND BARKHAUSEN ENVELOPES. 59
2.2.1. Effect of Sensor Position on the Barkhausen Envelope. 59
2.2.2. Barkhausen Envelope Parameters. 60
2.2.3. Barkhausen Results from the Surface of the Nickel Specimen. 61

2.3. EFFECT OF SPECIMEN VOLUME ON THE BARKHAUSEN SIGNALS ENVELOPES. 64
2.3.1. Experimental Detail. 64
2.3.2. Results and Data Analysis. 65

2.4. INVESTIGATION OF THE EFFECTS OF MACHINING ON THE SURFACE AND BULK PROPERTIES OF A TEST MATERIAL, USING BARKHAUSEN EMISSION TO MONITOR SURFACE CONDITION. 69
2.4.1. Experimental Procedure. 70
2.4.2. Results and Analysis of the Barkhausen Emissions from the 'As-Machined', Annealed and Surface Machined Nickel Specimen. 71
2.4.3. Discussion of the Barkhausen Emission Results. 76
2.4.3.1. *Discussion of EBE results from the different states of the nickel specimen.* 76
2.4.3.2. *Discussion of ABE results from the different states of the nickel specimen.* 80

3. BARKHAUSEN EMISSION AROUND SURFACE BREAKING DEFECTS. 83

3.1. BARKHAUSEN EMISSION FROM A SPECIMEN CONTAINING A SLOT. 85
- 3.1.1. Experimental Detail and Specimen Labelling. 85
- 3.1.2. Barkhausen Emission Results from the Slotted Specimen. 88
  - 3.1.2.1. *EBE results detected from the steel slot specimen using a pencil probe.* 88
  - 3.1.2.2. *ABE results detected from the steel slot specimen.* 93

3.2. BARKHAUSEN EMISSION FROM A SLOTTED SPECIMEN DETECTED USING A LARGE COIL SENSOR. 97
- 3.2.1. Experimental Detail and Specimen Surface Labelling. 97
- 3.2.2. The EBE Results from the Slotted Specimen Detected Using the Large Coil Transducer. 98

3.3. BARKHAUSEN EMISSION FROM THE SLOTTED SPECIMEN MAGNETISED USING A HAND HELD 'Y6' ELECTROMAGNET. 102
- 3.3.1. Experimental Detail and Specimen Surface Labelling. 102
- 3.3.2. EBE Results from the Slot Specimen Magnetised using Hand Held Yoke. 102

3.4. BARKHAUSEN EMISSION AROUND A FATIGUE CRACKED STEEL SPECIMEN. 107
- 3.4.1. Experimental Detail and Specimen Surface Labelling. 107
- 3.4.2. Barkhausen Emission Results from the Fatigue Cracked Steel Specimen. 110
  - 3.4.2.1. *EBE results from the fatigue cracked steel specimen.* 110
  - 3.4.2.2. *ABE results from the fatigue cracked steel specimen.* 117

PART 2

4. BARKHAUSEN EMISSION FROM PLAIN, WELDED AND CRACKED WELD SPECIMENS OF EN-43A STEEL. 121

4.1. EXPERIMENTAL DETAIL. 123
- 4.1.1. Specimen Details. 123
- 4.1.2. Experimentation and Specimen Labelling. 125
- 4.1.3. TIG Welding and Fatigue Crack Generation. 126
- 4.1.4. Machining of the Steel Specimens. 128
  - 4.1.4.1. *Surface planing of the steel specimens.* 128
  - 4.1.4.2. *Surface machining using Electro-Discharge Machining (EDM).* 130
  - 4.1.4.3. *EDM machined specimens.* 132

4.2. RESULTS AND ANALYSIS OF BARKHAUSEN EMISSION FROM PARENT METAL, WELDED STEEL, CRACKED WELD STEEL AND MACHINED SPECIMENS. 133

4.2.1. Results from the Plain Steel Specimen. 133

4.2.1.1. *EBE Results from the plain steel specimen (3P).* 133

4.2.1.2. *ABE results from the plain steel specimen (3P).* 139

4.2.2. Results from the Welded Steel Specimen. 143

4.2.2.1. *EBE results from the welded steel specimen (2P).* 143

4.2.2.2. *ABE results from the welded steel specimen (2P).* 149

4.2.3. Results from the Cracked Weld Specimens. 153

4.2.3.1. *The EBE results from cracked weld specimen (21B).* 153

4.2.3.2. *The ABE results from cracked weld specimen (21B).* 159

4.2.3.3. *The EBE results from the cracked weld specimen (21A).* 162

4.2.3.4. *The ABE results from the cracked weld specimen (21A).* 168

4.2.4. Barkhausen Results Following Surface Machining of the Steel Specimens. 172

4.2.4.1. *The EBE results after planing and EDM machining of the plain steel specimen (3P).* 172

4.2.4.2. *The EBE results after planing and EDM machining of the welded steel specimen (2P).* 176

4.2.4.3. *The EBE results from the cracked weld specimen surface (22B) after EDM machining.* 179

4.2.4.4. *The EBE results from the surface of the cracked weld specimen (22A) after surface planing.* 184

4.3. MAGNETIC LEAKAGE FIELD MEASUREMENTS. 189

4.3.1. GMR Sensors. 189

4.3.2. Experimental System using the GMR Sensor. 192

4.3.2.1. *Specimen magnetisation.* 193

4.3.3. Results the from GMR Sensor. 194

4.3.3.1. *Leakage field from the plain steel specimen (3P).* 194

4.3.3.2. *Leakage field from the welded steel specimen (2P).* 194

4.3.3.3. *Leakage field from the cracked weld specimens (21B and 21A).* 195

4.3.3.4. *Leakage field from the machined cracked weld specimen surfaces (22A and 22B).* 198

4.4. DISCUSSION OF BARKHAUSEN EMISSION FROM PLAIN, WELDED AND CRACKED WELD SPECIMENS OF EN-43A STEEL. 204

4.4.1. The Plain Steel Specimen. 204

4.4.1.1. *The EBE signal envelopes from the plain steel specimen (3P).* 205

4.4.1.2. *The ABE signal envelopes from the plain steel specimen (3P).* 206

4.4.2. The TIG Welded Steel Specimen. 209

4.4.2.1. *Microstructure due to welding.* 209

4.4.2.2. *Mechanical properties of weld metal.* 210

4.4.2.3. *Residual stress due to welding.* 212
4.4.2.4. *Leakage field and the effect of material hardness.* 214
4.4.2.5. *Original 'as-received' surface finish.* 215
4.4.2.6. *The EBE envelope shape from the welded steel specimen (2P).* 216
4.4.2.7. *The ABE envelopes from the welded steel specimen (2P).* 222
4.4.3. The Cracked Weld Steel Specimens. 225
4.4.3.1. *The EBE results from both the cracked weld specimens (21B and 21A).* 225
4.4.3.2. *The ABE results from both the cracked weld specimens (21B and 21A).* 232
4.4.4. The Effect of Surface Machining the Steel Specimens. 238
4.4.4.1. *The effect on EBE of machining the plain steel specimen surface (3P).* 238
4.4.4.2. *The effect on EBE of machining the welded steel specimen surface (2P).* 242
4.4.4.3. *The effect on EBE of machining the cracked weld specimens' surfaces (22B and 22A).* 246

5. REDUCTION OF THE CRACK DEPTH BY MACHINING AND THE EFFECT ON BARKHAUSEN EMISSION. 254

5.1 EXPERIMENTAL AND SPECIMEN DETAILS. 256
5.1.1. Specimen Labelling Using the BE Sensor. 259

5.2. RESULTS AND ANALYSIS OF BARKHAUSEN EMISSION FROM THE CRACKED WELD SPECIMENS. 261
5.2.1. Crack Depth Reduction by Planing of the Cracked Weld Specimen. 261
5.2.1.1. *EBE Results from the planed cracked weld specimen 21A for different thicknesses.* 261
5.2.1.2. *ABE Results from the planed cracked weld specimen 21A for different thicknesses.* 277
5.2.2. Crack Depth Reduction by EDM machining of the Cracked Weld Specimen. 282
5.2.2.1. *EBE Results from the EDM machined cracked weld specimen 21B for different thicknesses.* 282
5.2.2.2. *ABE Results from the EDM machined cracked weld specimen 21B for different thicknesses.* 294

5.3. MAGNETIC LEAKAGE FIELD FROM THE MACHINED CRACKED WELD STEEL SPECIMENS' SURFACES. 299
5.3.1. Magnetic Leakage Field Patterns from the Planed Cracked Weld Specimen's Surfaces. 299
5.3.2. Magnetic Leakage Field Patterns from the EDM Machined Cracked Weld Specimens Surfaces. 304

5.4. DISCUSSION OF THE BARKHAUSEN EMISSION RESULTS FROM THE VARIOUS MACHINED SURFACES. 312
5.4.1. EBE Signal Envelopes from the Machined Cracked Weld Specimens. 312
5.4.2. ABE Signal Envelopes from the Machined Cracked Weld Specimens. 334

PART 3

6. CONCLUSION. 349
6.1. FUTURE WORK. 358

Acknowledgements 359
References 360
Appendix 371

PART 1

Initial Study of Barkhausen Emission from Ferromagnetic Materials.

CHAPTER 1

INTRODUCTION TO MAGNETISM AND THE BARKHAUSEN PHENOMENON

1. INTRODUCTION TO MAGNETISM AND THE BARKHAUSEN PHENOMENON.

Barkhausen emission is probably the least utilised non-destructive testing technique around today. Since its discovery in 1919 by Barkhausen very little work on the phenomena was carried out and only in the last three decades has this trend changed. Barkhausen emission is now known to be superior as a non-destructive evaluation (NDE) technique, compared to the more established magnetic NDE methods.

The most common magnetic non-destructive testing relies on the detection of magnetic permeability change within a test material. This yields little direct information about the intrinsic properties of the test material. However, Barkhausen emission depends on the magnetisation process occurring in a material and, therefore, reflects more directly the way a material reacts to a changing field. Clear understanding of Barkhausen emission is expected to provide information about the stress state, as well as, microstructure; composition, grain size, second phase precipitates, inclusions dislocation content and changes within these properties. Barkhausen emission was originally detected from a piece of iron which was subjected to a changing magnetic field. An encircling coil around the iron specimen detected the Barkhausen pulses, which were amplified and observed via loud speakers. The audible "clicks" were caused by the dynamic changes of the

magnetic field within the iron specimen. To understand the processes that were taking place within this specimen certain aspects of magnetism must be understood.

1.1. INTRODUCTION TO MAGNETISM.

An important concept in magnetism is the magnetic field, **H**. When a field is generated in a volume of space there is an energy gradient and a change in energy of that volume. This particular energy is able to apply a force on a moving electron and thus can be detected by the acceleration of that electron. Definition of magnetic field strength **H** (Am^{-1}) is explained in terms of the current passing through a unit length of a conductor. A current of 1 A passing through a straight 1 m length of conductor generates a tangential field strength of $1/4\pi$ Am^{-1} at a radial distance of 1 m. This gives the Biot-Savart law.

$$\delta H = \frac{1}{4\pi r^2} i\delta l \times \underline{u} \qquad (1.1)$$

Where i is the current flowing in the wire. δH is the magnetic field at a distance r. r is the radial distance from the current carrying wire. $\underline{u}$ is a unit vector along the radial direction and δl is the length of conductor.

The response of a material to an applied magnetic field is known as its magnetic induction **B**. It is measured in units of Tesla (Vsm^{-2}). An induction of 1 Tesla generates a force of 1 Newton, per metre length of a conductor carrying a current of 1 ampere perpendicular to the direction of induction. With the smoothly increasing magnetic field (**H**) on a magnetic material, the change in its induction (**B**) is discontinuous. This discontinuous change gives rise to the Barkhausen emission. Also, the response of a magnetic material to an applied field in not linear and the expression for a magnetic field acting upon a substance is given by:

$$\boldsymbol{B} = \mu_o(\boldsymbol{H} + \boldsymbol{M}) \qquad (1.2)$$

Where μ_o is the permeability of free space and has the units of $VsA^{-1}m^{-1}$, also known as Henries/metre (Hm^{-1}). μ_o has a value of $4\pi \times 10^{-7}$ Hm^{-1}. $\boldsymbol{M}$, known as the magnetisation, is defined as the magnetic moments, $\underline{m}$, per unit volume of solid, V.

$$\boldsymbol{M} = (\underline{m}/V) \qquad (1.3)$$

It is the alignment of the magnetic moments which results in the magnetisation of a volume of solid. In the case where there is no external electric current present to generate an external magnetic field, then $\boldsymbol{B} = \mu_o \boldsymbol{M}$. **Figure 1.1.1** shows the magnetic field patterns around a bar magnet.

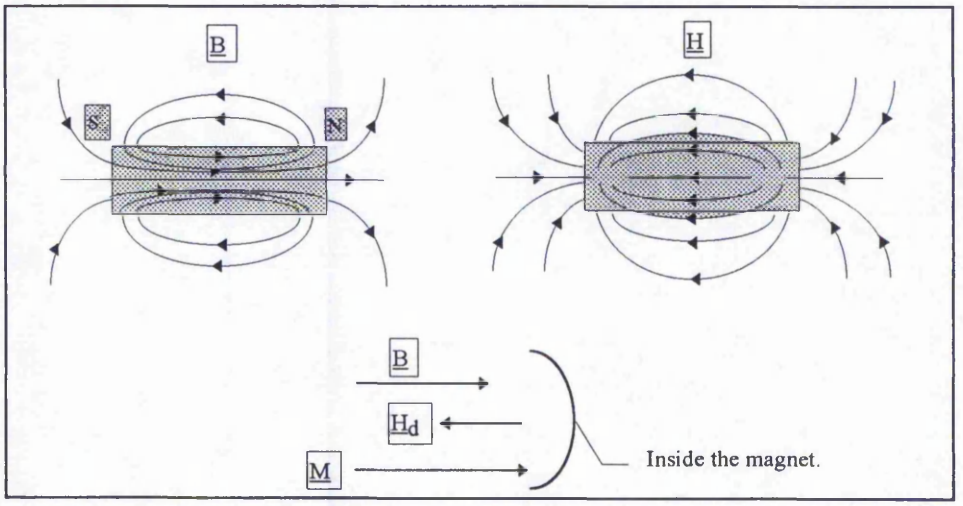


Figure 1.1.1 Magnetic induction **B** and magnetic field **H** patterns inside and outside of a bar magnet.

1.1.1. Ferromagnetism.

There are several classes of magnetic behaviour, the most common of which are diamagnetism and paramagnetism. The most widely recognised magnetic materials are

the ferromagnetic solids. They are so named because they show a similar response to iron. These materials include cobalt, nickel and iron along with several rare earth metals and their compounds. The susceptibility, of these materials, is positive and much greater than 1, typically $\chi \approx 50$ to 10000. Magnetic saturation can be achieved with relatively small applied fields. In ferromagnets neither χ nor μ have a constant value. Both permeability and susceptibility in ferromagnets are strongly affected by the magnetic field, $\boldsymbol{H}$, as well as the sample and its magnetic history.

Ferromagnets lose their ferromagnetic characteristics once they have reached and passed the Curie Temperature, (T_c). Above this temperature ferromagnets behave like paramagnets. The Curie temperature for nickel is 358°C, iron is 770°C and for cobalt 1130°C. At the Curie temperature the permeability drops suddenly and the coercivity and remanence become zero. The reason for ferromagnets behaving like this is due to their microscopic structure. A ferromagnet has regions within itself where all the electron spins align parallel. These regions are known as magnetic domains and the existence of domains explains why small fields are capable of magnetising the sample.

1.1.2. Magnetic Domains.

The origin of the atomic magnetic moments was first suggested by Ampere. He suggested that they were due to 'electrical currents continuously circulating within atoms'. This was remarkable as he postulated the existence of the electron approximately 70 years before J. J. Thompson discovered the electron and at a time when it was not know if charge separation existed within an atom or even if atoms really existed. Ferromagnets below the Curie temperature exist with regions of magnetic saturation separated by domain walls. These regions of magnetic saturation are know as domains. In these domains large numbers of atomic moments (around 10^{12} to 10^{15}) align parallel. The reasons for magnetic moments lying in the same direction, are that they provide the lowest energy condition as shown by Weiss **[1][2]**. The idea of the existence of domains in ferromagnets was suggested by Weiss in 1907. Evidence confirming the existence of

magnetic domains was provided by the Barkhausen effect **[3]**. This effect showed that movement of domain walls caused discontinuous changes, of magnetic induction within a ferromagnet, which were detected using a search coil. The Bitter Technique **[4]** provided direct observational proof of the existence of domains. Fine magnetic particles suspended in a fluid and applied on a treated ferromagnetic surface were used to visually detect the domain walls.

1.1.3. Domain Patterns and Domain Walls.

Ferromagnets have a tendency to group into small areas of magnetically ordered regions called magnetic domains. These domains are a consequence of a ferromagnetic material trying to minimise its magnetostatic energy, which arises due to the magnetic moments lying in the same direction. Lowering of the magnetostatic energy of the material can be achieved by flux closure. As long as the magnetostatic energy decrease is greater than energy required to form a magnetic domain, then a multi-domain specimen will exist. **Figure 1.1.2** shows how domains arise which result in reduced magnetostatic energy.

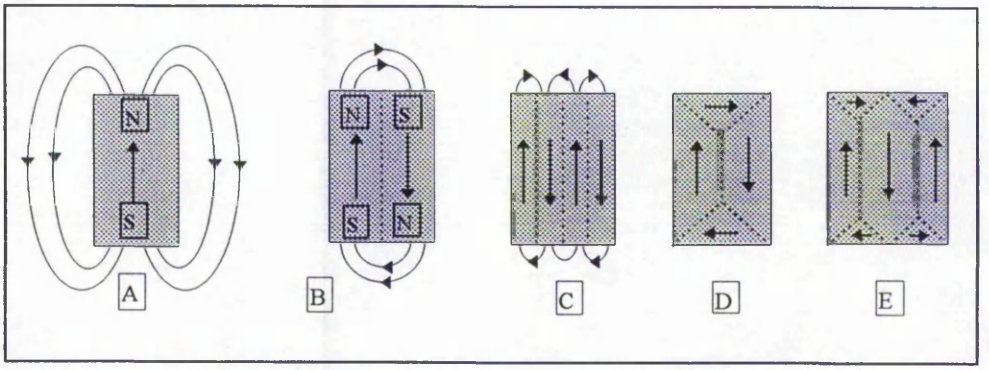


Figure 1.1.2 Picture of magnetic domains and domain wall patterns. Pictures 'A' to 'E' shows a lowering of the energy state within a ferromagnetic solid.

The energy per unit volume of a dipole magnetisation, $\boldsymbol{M}$, in a magnetic field, $\boldsymbol{H}$, is given by:

$$E = -\mu_o \int H \cdot dM \qquad (1.4)$$

When the single domain particle is subjected to its own demagnetising field, $\boldsymbol{H_d}$, which is generated by $\boldsymbol{M}$. Then $\boldsymbol{H_d}$=-$\boldsymbol{N_d}$ $\boldsymbol{M}$, where $\boldsymbol{N_d}$ is the demagnetising factor. Therefore, the energy can now be written as:

$$E = -\mu_o N_d \int M \cdot dM \qquad (1.5)$$

Solving the integral:

$$E = \frac{\mu_o}{2} N_d M^2 \qquad (1.6)$$

The magnetostatic energy of a single domain specimen is given by **equation 1.6**. Multi-domain specimen energy calculations are more complex, as the size and number of the domains need to be taken into consideration, along with domain wall energy.

As mentioned earlier, domain structures minimise the overall energy of the system. As well as magnetostatic energy and domain wall energy, there are other contributors to the overall energy of the system. In magnetic materials there are directions along which it is easier to magnetise the material. For that reason these are called 'easy directions' and are dependent on material crystallography. For instance, the directions of easy magnetisation in nickel are [111] [$\bar{1}$11] [1$\bar{1}$1] and [11$\bar{1}$], whereas, in iron, the easy directions of magnetisation are [100] [010] and [001] **[1]**. If magnetisation is not along the easy direction, there will be an additional contribution to the overall energy of the system (anisotropy energy). Magnetostriction can also contribute to the total energy of the system. This is because a change in magnetisation can cause a change in the physical dimensions of the material leading to stress anisotropy within the material. The work done against the stress caused by the magnetostriction gives a contribution to the domain energy in the form of magnetoelastic energy.

Figure 1.1.2 shows the differing states of magnetisation and magnetic domain wall patterns, which are explained below.

A) Shows a single domain specimen with a very large magnetostatic energy and there are no domain walls and the magnetisation is in the easy direction.

B) To reduce the very large magnetostatic energy the specimen has split into two domains. This has lowered the magnetostatic energy and has introduced a 180° domain wall.

C) The number of domains have increased and the magnetostatic energy has been reduced further. The domains still lie in the easy direction.

D) This shows a sample with no magnetostatic energy as the domains are closed. This, however, is not energetically favourable as the large 90° closure domains increase the magnetoelastic energy significantly.

E) This specimen shows a situation where the magnetostatic energy is zero and has a minimum magnetoelastic energy since the closure domains are small.

The central domain walls are 180° walls. In each case this refers to the angle of change of magnetisation in crossing the domain boundary. For this reason, the closure domain walls are 90° walls. A perfect condition is achieved, when there is a balance between magnetoelastic energy and domain wall energy. The closure domains occur more often in materials with a cubic crystal structure than those with hexagonal crystal structure. Nickel (FCC) and iron (BCC at room temperature) both show cubic crystal structures whereas cobalt has a hexagonal crystal structure.

1.2. THE BARKHAUSEN EFFECT.

Barkhausen emission (BE) is caused by the discontinuous motion of magnetic domain walls. A multidomain material placed within an increasing magnetic field is forced to realign its magnetic moments along the direction of the external field. This occurs at the expense of the less favourably orientated magnetic moments within the material. The external magnetic field forces the domain walls to sweep across, expanding the volume of the favourably orientated domains. At higher fields the magnetic moments of the domains rotate in order to lie in the direction of the magnetising field. At lower fields, in real magnetic materials, domain walls do not move smoothly. As the domain wall crosses obstacles in its path, its smooth movement is disrupted. It is pinned by these obstacles. Only when the field increases and overcomes the pinning energy will the domain wall break away. This gives step-like changes in the magnetisation of the specimen. These transient magnetic field changes are detected by a pick-up coil as changes in potential. This has been termed Electromagnetic Barkhausen Emission (EBE). Due to the nature of these emissions, eddy current dampening causes an exponential decay of the signals, thus, restricting the depths from which the signals are detected.

There is another form of Barkhausen emission termed Acoustic Barkhausen Emission (ABE). Though it was not discovered along with EBE or by Barkhausen it is still associated with BE, mainly because of the fact it occurs in ferromagnetic materials, whilst they are being magnetised around the hysteresis loop. ABE was first reported by Lord **[5]** in 1975. It is believed that Acoustic Barkhausen Emission arises from the effect of magnetostriction. Magnetostriction is a phenomena where the shape of the ferromagnetic specimen changes during magnetisation. The physical changes in shape $\delta l/l$, where l is a dimension, is small (approximately 10^{-5} to 10^{-6}).

Magnetostriction originates from the interaction between atomic magnetic moments. When the distance between adjacent atomic magnetic moments is variable, the interaction energy is expressed as:

$$w(r,\cos\phi) = g(r) + l(r)(\cos^2\phi - \tfrac{1}{3}) + q(r)(\cos^4\phi - \tfrac{6}{7}\cos^2\phi + \tfrac{3}{35}) + \ldots \quad (1.7)$$

Where (r) is the interatomic distance shown in **figure 1.1.3**. The first term is the exchange interaction term and is independent of direction of magnetisation and, thus, does not contribute to the usual magnetostriction. The second term is the dipole-dipole interaction term and is a function of (r). Upon the application of a magnetic field the crystal lattice will deform since the distance of the bond length will change. This gives rise to magnetostriction. The higher terms do affect magnetostriction but are neglected as their influence is small in comparison **[1]**. Thus a multidomain specimen will be strained in its direction of magnetisation. Depending on the sign of the interaction force the strain will be positive or negative. As a consequence, when the ferromagnetic material is magnetised, its domain walls move in the direction which aids the magnetisation of the specimen. This will cause a change in the magnetostrictive strain in that region, giving rise to the emission of elastic waves. Since the strain is unchanged on the reversal of the magnetisation direction, 180° domain wall motion is considered not to give rise to any ABE **[6]**.

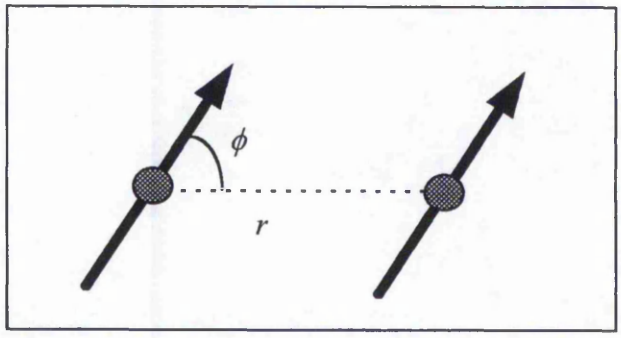


Figure 1.1.3 Magnetic dipole pair.

It is also reported that ABE signals could be caused by rotation of magnetisation vector at high **B** fields. At low B fields, ABE is caused by the domain wall motion **[7]**. Guyot and Caragan **[8][9]** have indicated, in their work on ferrites, that ABE is due to domain nucleation and annihilation. The have also reported that the total Barkhausen acoustic activity is proportional to the hysteresis losses and use this to imply a common origin in domain wall creation and annihilation.

Today Barkhausen Emission is studied by several research laboratories around the world. As a consequence of this a varied nomeculture has sprung into existence. Barkhausen Emission (BE) is referred to as Magneto-Barkhausen Emission (MBE), Electromagnetic Barkhausen Emission (EBE), Barkhausen Noise (BN) and a multitude of combinations arising from these titles. Throughout this work Barkhausen Emission, as discovered by Barkhausen, is referred to as Electromagnetic Barkhausen Emission (EBE). This is to distinguish it from the Acoustic Barkhausen Emission (ABE). ABE also has a variety of names assigned to it, such as Magneto-Acoustic Barkhausen Emission (MAE), Acoustic Barkhausen Noise (ABN) as well as Barkhausen Acoustic Noise (BAN).

1.2.1. Barkhausen Signals and Sensors.

The EBE signal is mainly generated due to impulsive 180° domain wall motion from one pinning site to another. There have been a number of EBE sensors used in the past and these have taken a variety of different shapes, but all have used multi-turn copper wire pick-up coils in one form or an other.

An early design for an EBE sensor was composed of two coils wound in opposite directions. The axis of the coils lay in the direction of magnetisation. Each coil was of 7500 turn, 13mm in length and possessed a 4 mm internal diameter **[10]**. The specimens placed within this sensor had to be less than this diameter. Other workers have used three dimensional Barkhausen measuring systems **[11]** and have found that the results showed that a greater amount of EBE noise was picked up at 90° to the magnetising field. The design consisted of five search coils, one to pick up the z-components of the Barkhausen pulse and two pairs of coils for the x and y-components. A surface mounting pick-up coil transducer was designed by Saynajakangas **[12]**. The sensor detects the transients in the magnetic potential, which occurs on the surface of a specimen, under the action of an impulsively changing magnetic field. A coil of 2000 turns, with a high frequency ferrite

core was used. This transducer was mounted at 90° to the magnetising field. A similar design of EBE sensor has been used for the work reported here.

High resolution EBE measurements were carried out by Atherton **[13]** and Buque **[14]** using a small magnetic disk read head. The read head was obtained from a computer disk drive. The dimensions of the read head were 4.2 mm long and 3 mm high, with the section of ferrite being 0.2 mm by 0.3 mm in thickness and width. This detector proved useful for detecting EBE signals from a small region on a specimen around a defect. It is very important to ensure that a good contact between the transducer and specimen surface is achieved, since the EBE signals are received from the material depth of approximately 1 mm, depending on the measurement system's band-width **[15]**.

Acoustic Barkhausen Emission (ABE) are elastic stress waves generated during magnetisation of a ferromagnetic sample. They are associated with localised magnetostrictive changes within the material. Lord **[5]** in 1975 detected the signal with a 175kHz piezoelectric probe attached to the surface of the sample. ABE can be detected by physically attaching the piezoelectric material to the surface of the sample **[16]** or the piezoelectric material can be mounted inside a transducer which can then be mounted on a specimen. This makes the transducer a practical NDT detector. Commercially produced transducers are widely available, which makes the transducer more practical. Placing the transducer onto the surface of the test specimen does mean that the contact between the transducer and the specimen must be a good one. For this, a couplant such as silicone grease or gel is used. The effect of the transducer and couplant thickness has been studied by Hill **[17]**. It was noted that the couplant had a significant effect and care must be taken to ensure that the transducer, couplant layer and specimen interface is kept constant or to a minimum value.

ABE signals are thought to be produced by impulsive changes in the localised magnetostrictive strain caused by non-180° domain wall motion. For iron, this wall is the 90° degree domain wall and for nickel is the 79° and the 109° degree domain wall. These magnetostrictive deformations are affected by the magnetostrictive properties of the material, and are stronger in nickel, as it has a much higher magnetostriction coefficient

compared to iron **[1][2]**. ABE is generated throughout the volume of the test specimen and due to the low ultrasonic attenuation, the ABE signal contains information about magnetostrictive deformation in the bulk material.

1.2.2. Barkhausen Emission and Material Microstructure.

Microstructure causes variation in the inherent magnetic characteristics of a material and thus is one of the most important features affecting its magnetic properties. Results indicate that the Barkhausen emission is a practical tool responding to changes in microstructure. The method has been applied for measuring microstructural parameters such as grain size, texture, precipitate, pearlite morphology and deformation **[18]**.

1.2.3. Barkhausen Emission and Grain Size.

Barkhausen emission occurs at around the point of coercivity, where the ratio of the change of magnetic flux density to change in field is at a maximum. It has been found that coercivity, H_C, and grain size have an inverse relationship **[19]**. This has been found to be valid for pure iron, low carbon steel and alloy steel. Microstructure, especially grain size, affects the coercivity of the material and this in turn affects the Barkhausen signal.

Early work by Tiitto, Sundstorm and Rastogi **[18][19][20]** found that the average amplitude of the EBE signal is affected by the grain size. Tiitto found that grain size of a recrystallised steel sheet with or without temper rolling strongly influences the EBE signals. It was claimed that the amplitude of the EBE signal directly reflected the grain size of the sample being studied. Experimental results yielded a grain size dependence relationship of the form :

$$M_{EBE} = A \ln D + B \qquad (1.8)$$

Where A and B are constants, D is the grain size and M_{EBE} is the amplitude of the EBE signal.

Ranjan **[20]** found the 'rms' voltage of the EBE signal increased with grain size in decarburised steel. Work on sheet steel showed that the EBE signal depended on the frequency of magnetisation, levels of magnetisation, thickness of the steel sheet and tensile stress. The carbon content affects both the grain size within the sheet steel, as well as, the EBE signal through domain wall pinning. When magnetisation was at saturation level, EBE peak height decreased with grain size and when magnetisation was below saturation it increased **[21]**. Ranjan **[22]** found an inverse relationship between both ABE and EBE signal amplitude and grain size, for nickel; explaining this in terms of the density of the domain walls and the mean free path of domain wall motion. Both types of Barkhausen signals were shown to increase with grain size in decarburised steel **[20][22]**. This was related to the presence of precipitates and grain boundary segregation which act as nucleating point for domains.

Hill et al. **[23]** showed the position of the EBE peak and, thus, the magnetising field at which domain wall motion occurred, correlated with grain size in an inverse manner as did the relationship between 'rms' ABE signal and grain size. With increased heat treatment the EBE envelopes reduced in amplitude and spread out over a greater field range. The position of the EBE peak is also a parameter closely related to coercivity which clearly indicates that the increase in grain size occurs whilst a reduction in dislocation density is taking place.

1.2.4. Barkhausen Emission and Precipitates.

Tiitto **[24]** studied the effect of carbide precipitates, in 0.014% carbon steel, on the Barkhausen effect. It was shown that the initial precipitate of Fe_xC carbide caused the increase in the average amplitude of the EBE signal. This effect disappeared at about 10% carbon depletion from solid solution, as the effect of these precipitates on the domain wall became merged with its neighbouring precipitates, thus reducing the local stress field. For Fe_3C the average particle distance is long enough for domain wall pinning. The maximum effect on the EBE is observed around the final stages of the precipitation. This is in agreement with coercive field measurements.

ABE has been studied in terms of the effects of precipitates and hardness on the Barkhausen signal using steel specimens, which had been quenched and tempered. ABE peak heights increased rapidly for specimens tempered between 400°C and 600°C, when needle like Fe_3C formed **[25]**. In the same region EBE signals only increased slightly. EBE showed greater sensitivity to the epsilon carbides which appear in tempering range from 100°C to 200°C. In indicating the effects of Fe_3C carbide precipitates on heating, the ABE signals provided a clearer trend than the EBE signals.

Raj et al. **[26][27]** found it was possible to establish the point at which precipitates, formed in stress relieved, annealed 9Cr-1Mo steel, dissolved with ageing. With ageing , the strengthening phase M_2X ('X' denoting the combined presence of carbon and nitrogen) dissolves. It was demonstrated that the dissolution of this phase affects those parameters which relate to the domain activities around the knee region of the hysteresis loop, such as peak height voltage of the ABE and the width of the EBE signal envelope.

1.2.5. Barkhausen Emission and Stress.

It is well known that stress is a significant factor affecting magnetisation of ferromagnetic materials **[28]** and causes complications when it comes to interpreting the Barkhausen signals.

Work by Pasley **[29]** showed distinct variations in EBE signal amplitude with applied and residual stress. As the sample stress increased, the peak EBE amplitude for steel was found to increase, while in compression it was found to decrease. For the particular steel studied the sensitivity of the system was found to be greatest for low stress levels. Karjalainen et al. **[30]** looked at the effect of cyclic stressing on mild steel and its effect on the root mean square (rms) value of the EBE signal. They found that saturation took place at low stress and the rms EBE increased promptly during Luders straining at the yield strength. It was also found that the residual stress from the unloaded specimen could be detected using rms EBE signals. Changes occurring under cyclic load were much more complex and could simply not be related to the applied load. Ruuskanen and Kettunen **[31]** demonstrated that the median Barkhausen pulse amplitude, M, could be used to assess applied stress amplitude and determine whether the stress level was above or below the fatigue limit in polycrystalline iron. Fatigue cycles of $\approx 10^7$ were studied. Below the fatigue limit they found the M value to increase slowly and saturate at certain levels. Above the fatigue limit, the M value decreased. Therefore, the fatigue limit was taken to be the point at which M does not decrease, (for 10^7 stress cycles).

Work by Krause et al. **[32]** has shown that for steel, the Barkhausen signal energy increased for tensile and decreased for compressive stresses. It was also found that the application of tensile stress altered the magnetic easy direction in steel and was thought to be caused by the relative increase of the 180° domain walls **[33]**. Elastic deformation modifies the energetically favourable domain wall configuration **[34][35]**, and plastic deformation produces region of high dislocation densities which may act as domain wall pinning sites. Using a high resolution EBE sensor, stress concentration around a defect

have been successfully detected **[36]**. It was found that the EBE signal energy increased as the stress concentration around the defect increased.

A range of studies by the United Kingdom Atomic Energy Authority at Harwell studied the effects of stress on the Barkhausen effect **[37][38]**. The effect of tensile stress on materials with positive magnetostriction (iron, steel and Incoloy) was found to produce an increase in the central EBE signal. The effect was not the same for nickel, which has a negative magnetostriction. Nickel showed a decrease in EBE activity with increasing stress. ABE signals for the positive magnetostriction materials exhibited a decrease in central dip amplitude. On application of stress the materials which exhibited the greatest increase in the EBE showed the least reduction in the central dip amplitude and vice versa. It was also found that for nickel, the ABE signal's central region decreased on the application of stress but, here the decrease in activity was directly related with the increase in stress. Experimental work shows that increasing the levels of tension in a sample tends to reduce the amplitude of ABE that it can produce. It was found by Makar **[39]**, in low field regions the magnetostriction and, therefore, the closure domains have completely disappeared by the time a stress of 88 MPa is reached. This would suggest that above a material specific maximum stress the ABE will not change with further increases in stress, limiting the use of the technique as a method of stress monitoring. This is because ABE signals are highly sensitive to the presence of internal stresses within a ferromagnetic material, since stress alters the magnetocrystalline anisotropy energy, which results in a change in the relative number of 180° domain and non-180° domain walls. As the 180° domain wall motions do not contribute to the ABE, the amplitude of the emissions and the total number of emissions will not change with stress.

1.2.6. Barkhausen Emission and Dislocation.

Barkhausen signals are affected by dislocations present within test materials. This is a consequence of the dislocations interacting with domain walls. Scherpereels **[40]** calculations indicated that dislocations in iron interact more strongly with 180° domain

walls, than with the 90° domain walls. The difference in 180° domain wall interaction was found to be an order of magnitude greater than for the 90° domain walls. For iron, dislocations tend to impede the motion of 180° walls more effectively than for the 90° walls. In nickel dislocations tend to impede the motion on the non-180° domain walls. EBE signals correlate with fatigue damage, residual stress and plastic deformation with dislocations playing an important role. They also affect the magnetic properties of ferromagnetic materials by pinning their domain walls. An exact correlation of the effect of dislocations on ABE and EBE is difficult to obtain since dislocations are present in varying densities and morphologies. For example, in heat treated steels, dislocations are important, as large dislocation densities are found in quenched materials. The dislocation morphology changes on ageing of such materials. It is, therefore, difficult to have dislocations without having other microstructural features, such as second phase precipitates, grain boundaries etc.

Work by Buttle et al. **[41]** on an annealed and strained bar of pure iron, on successive heat treatments, showed the difficulty which is faced when trying to isolate the effects of dislocations on Barkhausen effects. It was found that the EBE peak reduced in height whereas the ABE actually got larger after heat treatment at 550°C. This was interpreted as stress relief being caused by the straightening of the dislocations. This would tend to increase the ABE more than the EBE, since 90° domain walls are more sensitive to stress than the 180° domain walls in iron. Therefore, the reduction in the dislocations would reduce both ABE and EBE, but this may be accompanied by reduction in stress which would be expected to increase ABE again. Thompson **[42]** showed, through work on nickel, that dislocation density clearly affected Barkhausen measurements. ABE signals are mainly due to sudden changes in local magnetostrictive strains associated with the irreversible translation on non- 180° domain walls. From the results it was concluded that the dislocations interacted more strongly with non-180° domain walls than with 180° domain walls. This is in support of Scherpereels's deduction.

EBE occurs around the coercive point. It is believed that dislocation activity is the main factor changing the magnetic properties of ferromagnetic materials under fatigue, as opposed to other microstructural features and internal stresses **[43]**. This implies the

dislocation density, with its effect on coercivity, would have a very significant effect on the Barkhausen emission.

1.3. MAGNETIC TESTING.

Magnetic Non-Destructive Testing (NDT) methods, on a volume basis, are the most widely used NDT technique **[44]**. This is not surprising, as more iron and steel are produced each year than any other metals **[45]**. Therefore, economically iron and steel must be considered as two of the most important industrial materials. The different magnetic based NDT methods used include; magnetic particle inspection, magnetic hysteresis measurements, magnetic flux leakage, electromagnetic Barkhausen emission and acoustic Barkhausen emission.

Magnetic hysteresis is inherent in the materials and is exhibited by all ferromagnetic materials **[46]**. The hysteresis loop (a plot of magnetic induction, **B**, against a changing magnetic field, **H**,) is the most common way to represent the bulk magnetic properties of a magnetic material. The hysteresis parameters used to quantify a magnetic material are permeability, remanence, coercivity and hysteresis loss. Permeability, μ, of a material is given by:

$$\mu = (B/H) \qquad (1.9)$$

As **B** and **M** are not usually a linear function of **H**, it should be noted that permeability (and susceptibility) will not be a constant. In systeme internationale (SI) units, the term 'relative permeability' is used. The relative permeability of a medium, μ_r, is given by:

$$\mu_r = (\mu/\mu_o) \qquad (1.10)$$

The relative permeability of free space is 1. The relative permeability is closely related to susceptibility, χ, ($\chi = M/H$) and the following identity is always true, $\mu_r = \chi + 1$. Remanence is the value of either the remaining induction ($\mathbf{B_R}$) or magnetisation ($\mathbf{M_R}$) when the applied saturating field has been removed. On the application of a reverse field from saturation the magnetic induction (**B**) can be reduced to zero. The field strength strength required to achive this, is known as the coercivity ($\mathbf{H_c}$) and is strongly

dependent on the condition of the sample. Factors such as heat treatment, deformation and microstructural composition influence the coercivity value. Hysteresis loss (W_h) is the measure of the energy loss, when a ferromagnetic material is taken through a cycle of magnetisation. The energy loss is calculated from the enclosed area within a full hysteresis loop ($W_h = \oint HdB$). This energy loss is due to the combined effects of hysteresis, induced eddy currents and factors affecting domain wall motion. These magnetic parameters are sensitive to factors such as stress, strain **[47]**, grain size, heat treatment and the presence of second phase precipitates. Similar variations apply to the Barkhausen effect and this is to be expected as Barkhausen emission arises during the magnetisation of a material around the hysteresis loop.

Magnetic Flux Leakage (MFL) consists of magnetising a test specimen and measuring the leakage field at the surface. MFL occurs when magnetic flux flows through a region of the material or defect with a lower permeability e.g. from pipe steel into the air within a crack. The leakage field is the greatest when the change in the permeability of the material is the greatest. Defects such as inclusions, cracks, sub-surface cracks, stress locations and welds are all detectable using MFL. The measurement of the flux leakage is carried out using a magnetometer, such as a Hall probe or induction coil. This method is capable of measuring surface and subsurface flaws on the outer diameter of a steel tube. Magnetic flux leakage has been used for not only detecting flaws but also for their characterisation. Using MFL the determination of crack size was carried out by Steinberg et al. **[48]**. MFL technique is used successfully for inservice inspection in the oil and gas industry.

Work by Krause et al. **[49][50]** showed that the change in MFL which arose due to an applied stress corresponded well with EBE signal energy ratio. EBE signal energy provided information on both the magnetic easy-axis direction of the material and its magnetic anisotropy variation with stress. Also, MFL signals from a blind hole defect in steel, was reported to increase linearly with increasing applied tensile surface stress. For compressive stresses the leakage field was reported to decrease or not exist at all. The relationship between compressive stresses and changes in magnetic anisotropy of steel may explain this.

MFL measurements from mechanical and electrochemically milled pits were carried out by Mandel et al. **[51][52]**. Steel pipes under differing circumferential and bending stresses were studied. It was reported that the relationship between the MFL and pit depth was non-linear. The greater leakage field was detected from the deeper defects as the amount of material through which the flux can travel is less, therefore, resulting in greater flux leakage. The effect of circumferential stress decreased the flux leakage and a greater sensitivity to stress was obtained at low magnetisation levels. Also the influence of stress on MFL increased as the pit depth increased.

MFL is the basis of a more widely used technique called Magnetic Particle Inspection (MPI). This method relies on the flux leakage caused by the changes in permeability as a result of the presence of a surface or near surface flaw **[53]**. The difference between MFL and MPI arises, in that for MPI fine magnetic particles are applied on the magnetised specimen. The leakage field attracts the magnet particles and concentrates their presence at the defect. This allows the visual detection of the defect. As a consequence this method is more qualitative than quantitative and is subject to the inspector's interpretation. In recent years it has been possible to automate the MPI technique **[54]** in an attempt to achieve a reproducible 'calibrated' procedure. This method, under controlled conditions, can be carried out using fluorescent and ultraviolet inks: this increases the probability of detection of the flux leakage.

1.3.1. Barkhausen Emission and Applications.

The Barkhausen effect has been used to study a variety of defects and phenomena which occur in ferromagnetic engineering materials. These defects can be analysed with other established techniques but Barkhausen emission can provide additional information.

Atherton et al. **[13]**, with the use of a high resolution magnetic read head sensor, showed it was possible to detect slots which were cut into steel specimens. It was found that the

EBE signal energy was at a minimum on and around the slot. The presence of the slot reduced magnetisation concentration at the surface, in the vicinity of the slots and through-cuts and, therefore, reduced the EBE signals. Using EBE, manufactured fatigue cracks have been imaged by Negley et al. **[55]**. The technique involved scanning the EBE probe across the surface of the specimen and producing a contour map of the rms EBE signal peaks. These contour maps clearly show the regions of stress concentration and it was claimed the determination of the location of cracks, and regions of fatigue and stress throughout a material, was possible.

The detection of surface stress in materials is becoming increasingly important in failure analysis **[56]**. The effect of machining the surfaces of engineering materials can play an important role in determining the fatigue lifetime of that material. Work by Parakka et al. **[57][58]** detected and assessed surface damage caused by limiting the coolant flow whilst machining a specimen. Surface damage such as rehardening and temper burns as well as tensile residual stresses and cracking or microcracking **[59]** can occur due to machining. Barkhausen effect was shown to correspond to thermal damage within the work piece and they concluded by showing the technique to be a viable tool in assessing surface damage in production. Gauthier et al. **[60]** carried out measurement of actual residual stress in a structural steel beam. Initially a calibration was carried out involving EBE signal energy measurements on a representative section of sample material using known applied stresses. It was reported that the technique was capable of measuring surfaces stresses (to an accuracy of ±25 MPa).

Surface alteration, in order to improve service life, is carried out in many engineering situations. Shot peening is used to improve fatigue strength by introducing residual compressive stresses in certain engineering components, such as landing gears. Work carried out by Sipahi **[61]** showed that the changes resulting from shot peening, were clearly detected using EBE signals. Electromagnetic Barkhausen emission was used in the analysis of texture, residual stress, measurements of creep and fatigue damage. Barkhausen emission is also capable of the characterisation of plastically deformed microstructure and non-destructive evaluation of partially damaged or fractured engineering components. Ng et al. **[62][63][64]** noted that upon the rupture of a nickel

bar the EBE signal was intensified and the ABE signal was suppressed. Results from a steel specimen were interpreted using EBE peak ratio and were found to show that after fracture the peak ratio was small. ABE peak ratio, on the other hand, showed an increase as a result of fracture.

Barkhausen emission was also used in an attempt to characterise fracture toughness in steel **[65]**. High strength steel samples, which were tempered around 300-400°C, showed characteristic tempered martensitic embrittlement. It was found that, in this case, EBE was more sensitive than ABE at detecting this embrittlement and its causes. The findings suggest the usefulness of the EBE peak signal measurements for characterising tempered martensite embrittlement. Tomita et al. **[66]** and other workers **[30][31]** have used Barkhausen emission for the estimation of fatigue damage and also attempted to predict the residual life of the sample. It was noted by Tomita et al. that when the applied stress range was above the fatigue limit, " the ratio of EBE peak voltage of stress level 'S' to 0 MPa at the N^{th} cycle varied clearly with loading cycles". It was commented that this could be used to predict the residual life. Barkhausen emission has also been used for the detection of hydrogen-induced stress corrosion cracking **[67]**. In an experiment on steel with martensitic microstructure, the EBE signal amplitude was found to peak before fracture failure. This could provide some early warning prior to catastrophic damage.

Lo et al. **[68]** conducted Barkhausen measurements on a cyclically fatigued specimen of 0.1 wt% C steel. Results showed that the EBE signal rapidly increased in the initial stages of the fatiguing process and before failure (in the last 10% - 25% of fatigue life). The rapid increase in the EBE activity was accounted for by reasoning that; "as the cracks grew into the sample more closure domains formed at surface of discontinuity. This increased the total area of domain walls and hence, the number of EBE jumps, giving rise to a large V_{BE}". V_{BE} being the EBE signal amplitude. Work on thermal shock fatiguing, in an 8 mm diameter high temperature steel, was carried out by Ginsztler **[69]**. A reciprocal trend in the Barkhausen emission to the cyclically fatigued specimen was reported. Initially, the Barkhausen emission continuously decreased until 2000 heating cycles were achieved from where it stabilised. This decrease in EBE activity was attributed to the thermal fatiguing which generated increased dislocation density within

the material. This was supported by the observation of the increased coercivity of the specimen.

Material used in high pressure vessels subjected to radiation, is know to suffer from embrittlement. Electromagnetic Barkhausen emission has also been applied to this problem. Normally, Charpy and tensile tests are used to establish the level of embrittlement in a material. Embrittlement is dependent on such parameters as precipitate size and concentration as well as dislocation density. Barkhausen emission may provide a way in which embrittlement in pressure vessels may be detected cost-effectively and in situ. Work by Buttel et. al. **[41]** on irradiated iron-copper alloy produced small changes in Barkhausen emission, though with sufficient sensitivity for useful characterisation of radiation effects. It was found that the irradiation caused significant strengthening with a hardness increase. This effect caused by the defect clusters and or copper precipitates increased pinning of the 180° domain walls and as a result an increase in the EBE signal was noted. There was little change observed in the ABE signals. Individual EBE events became smaller, indicating enhancement of pinning density with irradiation. Sipahi et. al. **[70]** found that as a consequence of irradiating a sample, its pinning concentration was increased, which resulted in a decrease in the Barkhausen emission. Blaszkiewicz **[71]** reviewed other papers and found that, in general, this decreasing EBE trend was supported. In a recent paper published by Park et al. **[72]**, reactor pressure vessel steel, irradiated by neutrons at 70°C, showed a decrease in the amplitude of the Barkhausen emission. It was also reported that a linear relationship exists between hardness and Barkhausen emission. As change in hardness is a well known effect of radiation damaged materials it was, therefore, suggested that degradation of mechanical properties by neutron irradiation can be evaluated by the measurement of EBE signal amplitude and energy.

1.4. CURRENT RESEARCH AND AIMS OF THIS WORK.

1.4.1. Current Research.

Barkhausen emission has been studied intensively for several decades. Attempts have been made at isolating the effects of individual microstructural phenomena, such as dislocation densities, precipitates, voids, inclusion, grain size and differing phases, so that their effects on the Barkhausen signal could be calibrated. Isolation of individual phenomenas has proved to be very difficult to achieve in practice, yet advances have been made in understanding the effects of these microstructural properties. In the literature published over the past two years it is evident that research groups around the world are concentrating their efforts in two distinct areas: macrostructural stress and microstructure. Work by groups in America and Canada have recently focused on applying the Barkhausen technique for the evaluation of gas and oil pipeline and as a consequence, the main focus of their work has led to the evaluation of macrostructural stresses experienced by these pipes due to loading **[51][52][73][60]**. Work studying the effect of magnetic flux leakage and EBE signals from pipeline steel with drilled or electrochemically milled defects were studied. It was reported that for positive magnetostrictive steel the application of tensile stress increased the 180° domain wall population in the direction of stress and enhanced the EBE signal. EBE was used to indicate the stress concentration near pits of various depths. Recent work **[74]** has involved measuring EBE from pits and defects which have been created under the presence and absence of an applied stress. EBE was used to measure stress distribution around these defects. It was found that the effect of applied stress during pit erosion was less than that when the same stress was applied during subsequent measurements. Also the effect of surface machining steels was evaluated by Gupta et. al. **[58][59]** at the centre for grinding research and development in the USA. It was reported that under harsh machining conditions, where increased damage is likely, the EBE signal amplitude decreased.

Work by the late Jackubovics **[16][75]** at Oxford University, England, has shown the feasibility of using ABE in conjunction with EBE in the assessment of microstructure, in particular, interlamella spacing in sphereodised steel. Lo and Scruby **[76]** in a recent publication have used EBE and ABE in the assessment of volume fraction of ferrite in ferritic/ pearlitic steels. In the low field region EBE activity decreased, whereas, ABE activity increased with increasing ferritic content. Monitoring the low field region of the Barkhausen emissions may indicate the volume fraction of ferrite within a ferritic/ pearlitic steel.

At the Indira Gandi Centre for Atomic Research in India, studies evaluating the microstructure of welds in Cr-Mo steels and the effect of post weld heat treatment, have been carried out. Recent work by Moorthy et al. **[27]** has involved studying the effect of tempered microstructure in ferritic steel using EBE. These studies have shown the possibility of using high resolution EBE as a microstructural analysis technique. In a paper by Rodriguez **[77]** it was reported that amongst other more established inspection techniques Barkhausen emission was used to assess stress relief in weld joints found in Cr-Mo steel sheet tube weld joints in pressurised heavy water reactors. Post weld heat treatment of weld joints was assessed using the EBE peak height, which increased with the reduction of residual stress and dislocation density. Assessment of carburisation depth in surface hardened steels have also been examined using EBE **[78]**. The different stages of tensile deformation in low carbon and Co-Mo steels has been assessed using EBE **[79]**. In particular, the technique can be used to accurately identify the beginning of 'microplastic yielding' and 'macro-yielding' which is not possible from stress-train curves. It was reported that the decrease in the EBE peak height and the merging of a double peaked envelope signifies each of these states respectively.

EBE measurements carried out by Jeong et al. at the Korean Atomic Energy Research Institute investigated the effect of microstructural changes in pressure vessels. The reported changes were simulated by a series of heat treatment processes **[80]**. Work on radiation damaged steel **[81][82]** examined the recovery characteristics of neutron irradiated steel. With increasing exposure to radiation, the ABE energy, as well as, EBE energy were found to decrease. However, EBE was found to be sensitive to the early

part of the irradiation process, whereas, ABE was more sensitive at higher irradiation levels.

1.4.2. Aims of the Research.

The work in this thesis begins by considering the origins of the Barkhausen emission and with the aid of finite element analysis, the magnetic field distribution in the specimens. Several short studies were carried out on pure nickel specimens which were expected to reveal the effects of magnetisation and specimen condition on BE. Work involving idealised surface breaking defects was also be examined. The BE technique is expected to provide an insight into the likelihood of effectively detecting such flaws. A fatigue cracked steel specimen has been examined using BE in an attempt to locate the position of the crack and assess the condition of the surrounding material. Following the literature review it is evident that current research groups are studying the microstructure of welds using BE while others are concentrating their efforts on the effects of simulated defects in steel. This study hopes to further the understanding of the combined effects of both of these effects on the Barkhausen phenomena. The main aim of this work relates to an in-depth study of the effect of the presence of welds and low-cycle flexural fatigue cracks within the weld in steel specimens. The aim is to yield further understanding of the effect of the uncracked and cracked welds in terms of the Barkhausen response. Results will be compared to those from plain steel and perfect weld specimens. Two types of surface machining techniques and their effects on the specimen's BE response are also examined. The effect of reducing the crack depth by machining and the effect on the Barkhausen signal, along with the flux leakage from a weld's surface breaking crack, will also be considered. It is hoped that this study will further the understanding of the effects of welds and their defects on Barkhausen emission and assess the feasibility of the technique as an effective NDT method.

1.5. APPARATUS AND EXPERIMENTAL SYSTEM USED IN THIS RESEARCH.

1.5.1. Experimental System.

The block diagram (**figure 1.5.1**) shows the apparatus used to detect and measure the Barkhausen emission reported in this work. When differences in the experimental system occur, they are noted in the relevant sections.

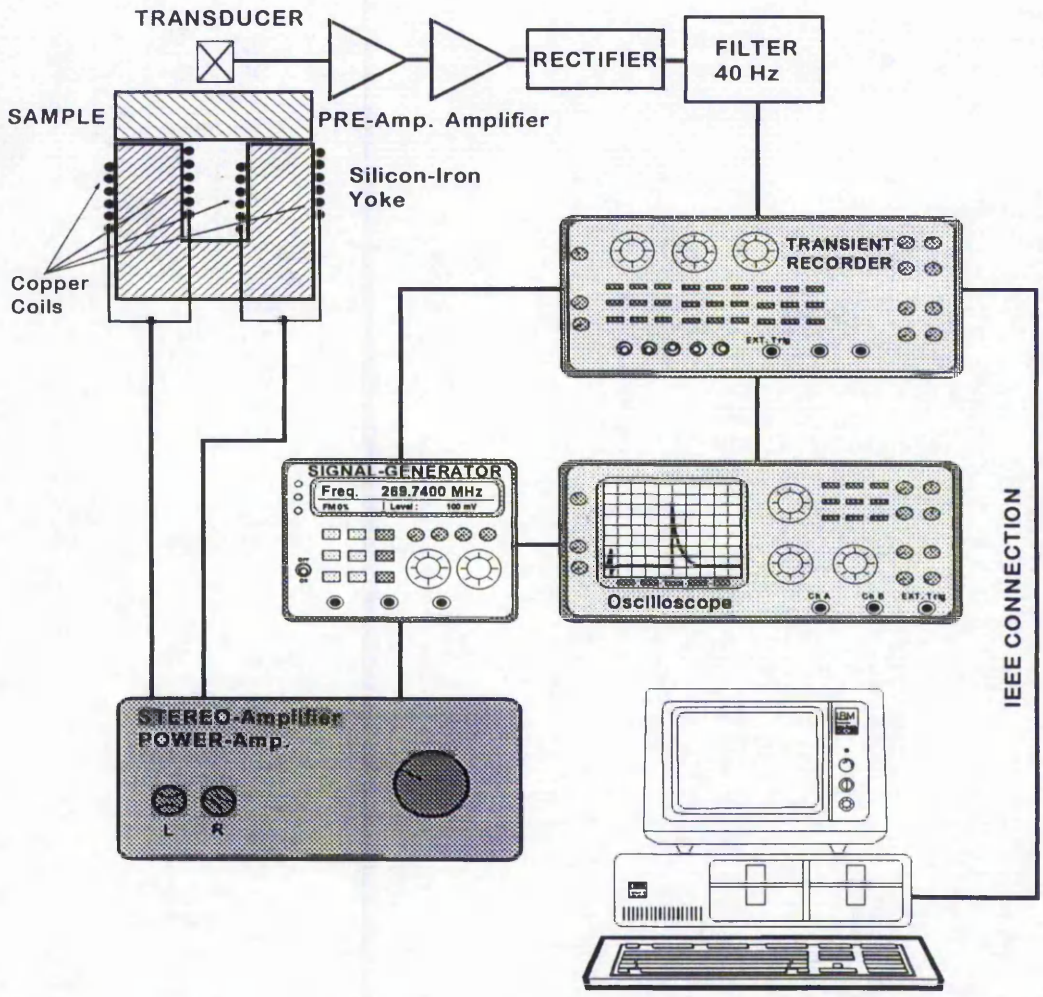


Figure 1.5.1 Experimental apparatus used in the detection of acoustic and electromagnetic Barkhausen emission from ferromagnetic specimens. The 40Hz filter is a low pass filter.

1.5.2. Magnetising System.

An electromagnet was used for magnetising the ferromagnetic test samples. A 'U' shaped core was used, consisting of laminated sheets of silicon iron, known as 'Scotsil 330'. This electromagnet was produced by Griffin and George Ltd., England. Two copper field coils, each with 1200 turns, were placed on the arms of the 'U' shaped silicon-iron core. The field coils have a measured resistance of approximately 9Ω each. The coils were magnetised using a 0.1 Hz triangular wave form produced by a signal generator. The 0.1 Hz signal from the generator was amplified by a power amplifier and used to drive the electromagnetic yoke. The function generator was a Wavetek Model 164 sweep generator, produced in San-Diego, California, USA. The frequency range of the generator was 30μHz to 30Mhz. The power amplifier is made by Amcron (model DC-300A, series II). A maximum current of 2.5 A was driven through the coils at a frequency of 0.1 Hz. During magnetisation of a ferromagnetic material, one magnetic transition can induce neighbouring domains to change their magnetisation direction within a very short time interval. This has been called a correlation domain and is detected as one unresolved transition by the EBE sensor. The magnetising frequency of 0.1Hz was found to be the lowest practical frequency, where the effect of correlation domain is minimised. Between the specimen and magnetising yoke a nonmagnetic spacer was used to minimise the transmission of any acoustic emission produced by the silicon-iron yoke.

1.5.3. ABE Sensors and Signal Amplification.

The magnetised samples generated ABE signals which were detected using a piezoelectric transducer. The ABE transducer had a diameter of **23 mm** and was surface mounted on the sample being studied. The resonant frequency of the transducer was 175kHz, and was made by Acoustic Emission technology (AET). A custom built clamp

was used to hold the transducer in place. Aluminium was utilised in the construction of the clamp because of it's non-magnetic properties. The ABE transducer was attached to the surface of the test sample using acoustic couplant gel. This gel was used to provide an improved contact between the sample surface and the ABE sensor. As the pressure on the sensor was increased, the couplant film reduced in thickness. This minimised any effect of couplant thickness on signal amplitude (Hill et al. **[17]**).

The gain of the acoustic Barkhausen signal pre-amplifier was 60dB and the band-pass frequency range was between 100kHz and 300kHz. The output from this amplifier was passed through a second amplifier giving a further amplification of ×400 **{52 dB}** for the ABE signal. Both the amplifiers were driven by a ±15v DC power supply made by Farnell.

1.5.4. EBE Sensor and Signal Amplification.

During this work the EBE signal was detected using two different coil sensors. The first sensor was a 450 turn, 42 swg copper wire, wound around a ferrite core and encased in a shielded case. The measured resistance of the coil was approximately 21Ω. The diameter of the copper coil was **26 mm** and the sensor was surface mounting. The ferrite core needed to complete a magnetic circuit for the flux changes to be measured. This design was based on a sensor designed and used by Saynajakangas **[83]**.

A Hocking pencil probe, consisting of a coil around a ferrite core, was used as the second EBE sensor. The Hocking pencil probe sensor provided a good spatial resolution and was used in the latter part of this study. This pencil probe had an inductance of **1.5mH** and a resistance of 12Ω. The EBE signal was passed through a similar series of amplifiers to the ABE signals. The pre-amplifiers bandwidth was 7kHz to 250kHz, with an amplification of **60 dB**. Further amplification of ×100 **{40dB}** was provided by the second amplifier. These two amplifiers were also powered by the ±15v, Farnell DC power supply.

The ABE and EBE signals at this stage were rectified and then passed through a low-pass filter to smooth the signal envelopes. A cut-off frequency of 40Hz was set using a Krohn-Hite filter, model 3202. The amplitude of the Barkhausen pulses were then recorded as a signal envelope. Further information on the experimental system is available in a Ph.D. thesis by J. W. Mackersie **[84]**.

1.5.5. Signal Recording.

Once the Barkhausen signal had passed through the low-pass 40Hz filter, the signal envelope was recorded using a transient recorder. The transient recorder, model DL 910, was produced by Data Lab Ltd., Micham, Surrey, England. The digital recorder was designed to capture single shot or low repetition events and represent them for continuous display on an oscilloscope. The transient recorder was set to capture data produced within a specific pre-set time window. The trigger for recording was set at 1.89 seconds after the peak of the 0.1 Hz triangular wave form. The trigger was activated automatically and the recorder commenced storing 4096 points at a sampling rate of 0.5×10^{-3} seconds per sample. This produced a sampling window of 2.048 seconds duration. This window was positioned within a time frame to include the region of the coercive field, where the maximum Barkhausen activity existed. This region of activity can be located where the rate of change of the hysteresis slope is the greatest, i.e. $d\underline{B}/d\underline{H}$ is at a maximum. The transient recorder was connected to the oscilloscope and the rectified Barkhausen signal envelope was monitored for each experimental run.

The stored signal envelope in the transient recorder was then transferred to an personal computer, connected by IEEE 488 protocol. This signal data could then be transferred, using a floppy disc, to another computer where the data could be analysed. Of the 4096 points used for recording the signal, only a tenth of that number were stored on disk. A total of 410 points were found to be sufficient to reproduce the signal envelope without losing envelope resolution.

1.5.6. Sensor Attachment and Barkhausen Signals.

Early experiments showed that the Barkhausen signal envelope was affected by sensor mounting. Originally all work done used a sensor that was held in place using a weight. It was found that in situations where the weight was not distributed evenly across the sensor, signal integrity was compromised and anomalous peaks could occasionally be found on the signal. This problem was resolved using a clamp, made from aluminium. Much work has been reported where Barkhausen signal amplitude has been taken as an indicator of the physical properties of the material being examined, yet, there has been no discussion of the way in which sensors have been attached to the sample except in situations where they were glued to the surface.

It has been found that by using a clamp to hold the sensor in position signal envelope shape and size are more reproducible. A constant, reproducible, evenly distributed pressure, applied to the EBE sensor but especially ABE sensor, ensured that the signal envelopes were dependent on the sample characteristics and not on the sensor mounting.

END *of* CHAPTER

CHAPTER 2

BARKHAUSEN EMISSION-MATERIAL VOLUME AND SURFACE EFFECTS

2. BARKHAUSEN EMISSION- MATERIAL VOLUME AND SURFACE EFFECTS.

Barkhausen emission (BE) is sensitive to a range of variables and care must be taken when measurement is attempted using this technique. Material specimen characteristics such as microstructure, composition, stress state, defects size and distribution as well as the magnetisation and detection systems are all known to affect Barkhausen emission. If meaningful comparisons between results are to be made, then the generating and detection systems must remain constant. Also, a thorough understanding of the effects of magnetisation and detection systems on the Barkhausen emission still need to be achieved.

In this chapter Finite Element (FE) modelling of the magnetic field is reported for different sized specimens and a slot specimen. It is expected that modelling will allow a better understanding of the effect of specimen geometry on BE signals. Along with the FE modelling, a range of experiments were carried out on a series of 'Nickel 200' specimens using the standard Barkhausen apparatus described in chapter 1. The changing BE signal envelopes from across the surface of a specimen are described. The effect of changing specimen size on the EBE and ABE is also examined. This is expected to provide some insight into the nature of the two different Barkhausen emissions. Finally,

the effects of specimen surface modifications and the resulting change in the surface structure of the specimen, on both the EBE and ABE, are examined using magnetically soft nickel. It is expected that modelling combined with the experimental work will allow a better understanding of the BE signals from differing sized specimens.

2.1. FINITE ELEMENT MODELLING OF MAGNETIC FIELDS.

Computer based finite element analysis of the magnetisation system was carried out. This was expected to provide a better understanding of the magnetisation process for the ferromagnetic specimen under investigation. Different specimen thicknesses of the same material were modelled in order to gain an understanding of the magnetic field spreading throughout the different sized specimens. The presence of a slot (idealised surface breaking crack) within the specimen and its effect on the magnetic field spread is also analysed. It is expected this will allow a better interpretation of the BE signals from plain and cracked specimens.

2.1.1. Introduction to Finite Element Analysis.

Computer based finite element (FE) analysis is used to model real life engineering or scientific problems. The obvious advantages of modelling, using finite element analysis, are the time and cost savings that can be made; for example, by reducing the need for the building and testing of numerous prototypes. It must be realised that many real engineering problems do not provide closed-form mathematical solution and FE analysis provides a convenient way of obtaining approximate solutions. An example of finite element analysis might be its use in the field of structural engineering, to predict the stresses and strains experienced when a structure is subjected to a force loading. Finite element software is, not only, capable of looking at structural problems, but also, at

thermal, mechanical, vibrational and magnetic problems. The "ANSYS" FE software used in this work is produced by Swanson Analysis Systems Inc., Houston, USA.

The name 'finite element' indicates the basic concept of the method, which is the transformation of a scientific or engineering system with an infinite number of unknowns (the response in every location in the system) into one that has a finite number of unknowns related to each other. The unknowns are the responses to applied actions. These are called the 'Degrees of Freedom'. For example, for magnetic problems, the 'Action' is the current segment and the type of 'Degrees of Freedom' is the magnetic potential. The 'Actions' and 'Degrees of Freedom' are related by a set of basic equations. The purpose of finite element analysis is to determine the solutions to these equations across the entire system. The simplest form of the equation is:

$$[k]\{d\}=\{A\} \qquad (2.1)$$

Where {d} is the 'degrees of freedom' and {A} is the 'action' vector. [k] is the matrix relating {d} to {A} and known as the coefficient matrix. In general [k] & {A} are known and {d} is an unknown. In order to solve the basic equation across an entire system, it must be modelled by discreet interconnected elements. When [k] is determined for each element, all of the individual [k] matrices are assembled together to form the set of simultaneous equations, [k] {d}={A}. Response values, for every degree of freedom across the entire system, are the solutions to these simultaneous equations.

When modelling, the appropriate element type is selected depending on the type of FE analysis required, (2D through to 3D). Every element has at least one node that lies along its boundary. Nodes connect elements together and are the location of the all-important 'degrees of freedom'. The element interconnects 'degrees of freedom' and determines the response to the 'applied actions'. The perturbation is passed on between elements by the shared common nodes.

The ANSYS software used in this work ran in three stages; pre-processing, solution and post processing. The pre-processing stage included the input data encompassing,

geometry, material properties, loading and design. The solution stage set up and solved the simultaneous equations to calculate the unknowns and the post processing (/Post1) stage organised the results in a tabulated or graphical form for ease of understanding. The mode /Post1 was used for viewing results data at a specific time during the hysteresis cycle. /Post26 was used only for transient analyses. A specific element could be viewed with results displayed for the whole transient analysis time period.

2.1.2. Finite Element Modelling of the Barkhausen Magnetisation System.

When a ferromagnetic material is taken around the hysteresis loop, Barkhausen noise is generated when $d\underline{B}/d\underline{H}$ is a maximum. The way in which the magnetic field is distributed throughout a sample would be expected to affect the Barkhausen signals. This is because BE should be influenced by the strength and rate of magnetisation, angle of the magnetisation vector relative to the sensor position, etc. FE modelling of the Barkhausen magnetisation system was carried out in order to provide information about the way in which magnetic field spreads throughout the sample.

ANSYS version 5.0 FE software was used and a two dimensional FE model of the magnetising system was created, shown in **figure 2.1.1**. Dimensions used in the FE model were taken from the experimental system. A nickel specimen, 100 mm in length and 26 mm in thickness was modelled using a 2D model. The silicon-iron yoke height and width were the same (100 mm in length) and each yoke leg was 26 mm in width. The edge of the coils in the model were positioned 2.5 mm from the yoke's edges. Within the experimental system an air gap, of approximately 0.5 mm in width was created between the nickel bar and the magnetic yoke. The air gap resulted from a non-magnetic spacer used between the nickel specimen and the yoke. This spacer eliminated the detection of any unwanted acoustic noise generated within the silicon-iron yoke and by the test specimen and yoke interface rubbing together. The effect of these spacers can been seen in the field measurements from the nickel specimens surface **(figure 2.1.3)**. The ANSYS model was created using material properties for the materials used in the experimental system. **B** and **H** data were obtained for the Scotsil electromagnetic yoke from Griffin and George Ltd. and are quoted in **appendix 1a**.

During the Barkhausen experimental tests, samples were subjected to a triangular magnetic excitation. For the FE model to incorporate this dynamic magnetic field loading, a transient model was created **(appendix 2a)**. This involved ramping up the current from 0 amps to a maximum value of 2.5 amps, then down to -2.5 amps and then back up to 0 amps over a time of 10 seconds **(figure 2.1.2)**.

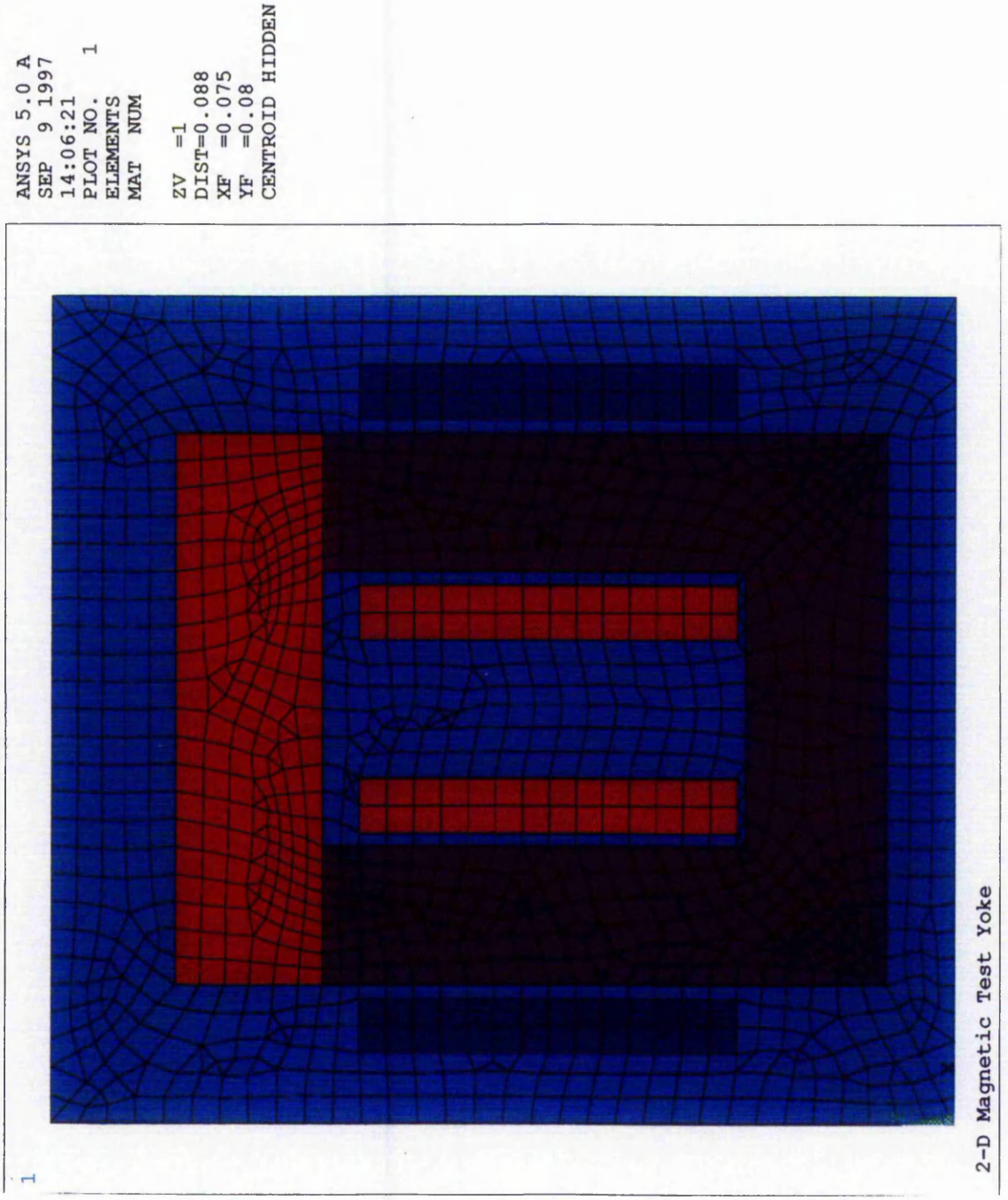


Figure 2.1.1 The ANSYS FE model of the Barkhausen experimental system showing the electromagnetic yoke (purple), coils (dark blue and pink), nickel specimen (red) and the surrounding region is air (blue).

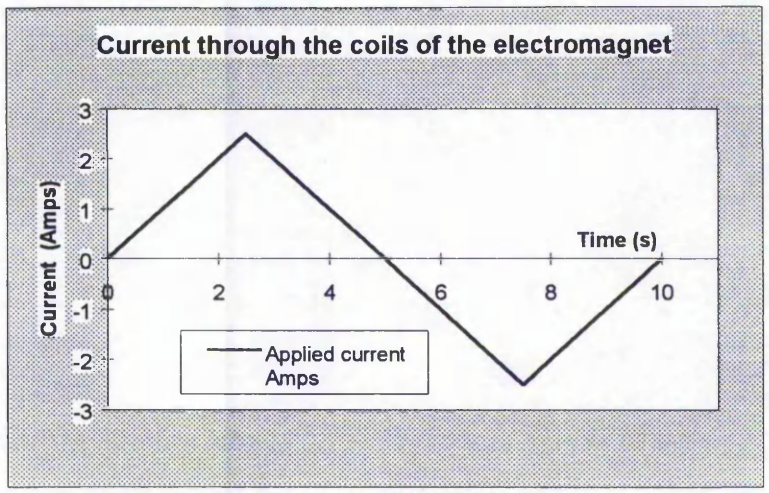


Figure 2.1.2 The transient FE loading cycle (frequency of 0.1 Hz) used for the electric current through each of the magnetising field coils.

2.1.2.1. *Results of FE modelling.*

Each of the ANSYS models generated data describing the changing values of the magnetic flux, **B**, and the magnetic field, **H**, across the entire system. Before the FE model was accepted as providing reliable information, the validity of the FE model was confirmed by comparing the FE model results with actual experimental results. To do this magnetic flux density **B**, parallel to the top surface of the nickel specimen was measured. The measurements were recorded at the maximum and minimum points on the triangular magnetising wave (**figure 2.1.2**), when magnetic saturation of the nickel specimen occurred. The measurements were taken by positioning a Hall probe on the surface of the nickel specimen. The Hall probe was calibrated using a standard permanent magnet with measurements taken using a Gaussmeter (model 912), manufactured by Dowty RFL Industries Inc. Due to the design of the Hall probe, the Hall element was approximately 2 mm from the surface of the nickel specimen. Care was taken to minimise contact time between the Hall probe and nickel specimen to prevent unwanted heating of the Hall element, if the test sample became hot during testing.

The experimental data was obtained by measuring the two vector components of the **B** field, **Bx** and **By**, using the Hall probe and Gauss meter. **Bx** is the magnetic field parallel to the nickel surface and **By** is the magnetic flux perpendicular to the nickel surface. Measurements were recorded every centimetre across the surface of the nickel sample. Surface values of **B** were extracted from the magnetic model to determine the degree of agreement between experiment and modelling. Disagreement would suggest the need to adjust the values for the magnetic material properties. Modelling the air gap enabled the influence of this experimental variable to be determined. **Figure 2.1.3** shows the ANSYS results for **Bx** and **By** data on the nickel surface, for the 'Air-Gap' and 'No Air-Gap' models. As expected, the air gap reduced the magnetic flux density on the nickel surface.

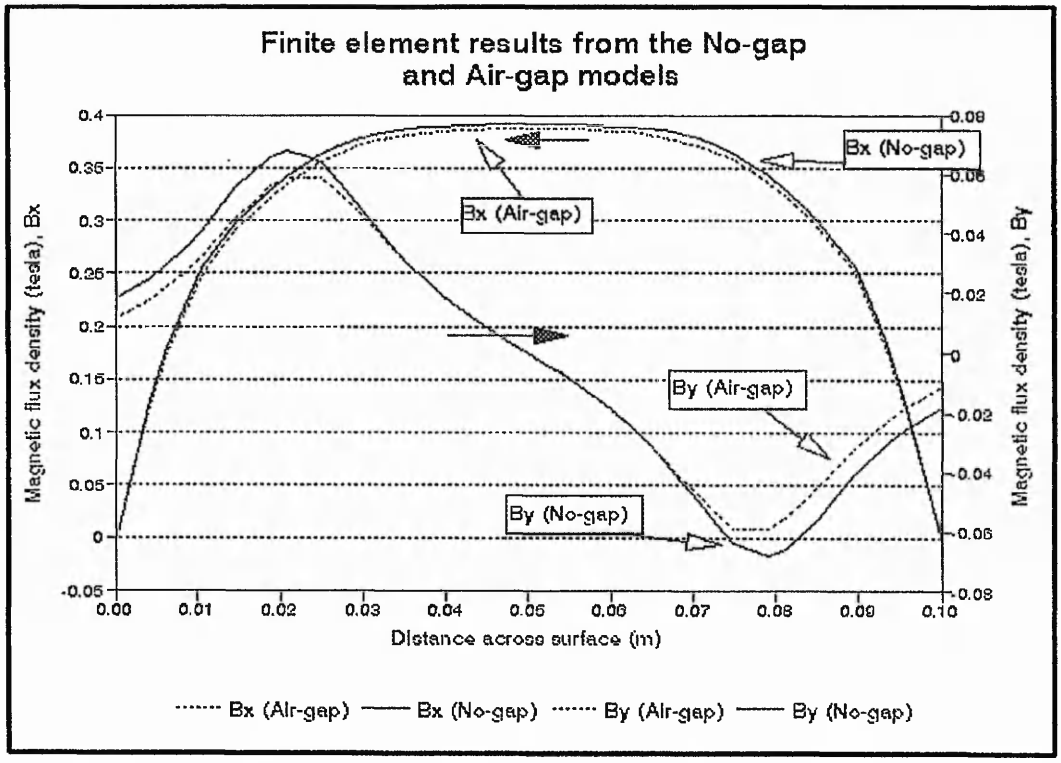


Figure 2.1.3 ANSYS FE model data of magnetic flux density (**B**) on the surface of the nickel sample at saturation on the maximum peak of the triangular wave form.

The **Bx** component from the FE model was found to be a maximum across the central 40 mm region of the specimen, with a value of **0.38 T**. It is clear that for the ANSYS generated data, the **By** field component was significantly smaller in magnitude compared to the **Bx** field component. For example, the **By** and **Bx** data from the Air-Gap model,

around the 25 mm from either end of the specimen, was recorded at a maximum value of **0.059 T and 0.355 T** respectively. The experimental results obtained from the Barkhausen experimental system are shown in **Figure 2.1.4**. The experimental data seemed to disagree with this view. **Figure 2.1.4** shows that the **Bx** and **By** component data were of similar magnitude, both lying within a field range of **0 to 0.1 T**. The experimental data and the ANSYS model generated results for the **By** component on the surface of the specimen, which appeared to have a similar magnitude.

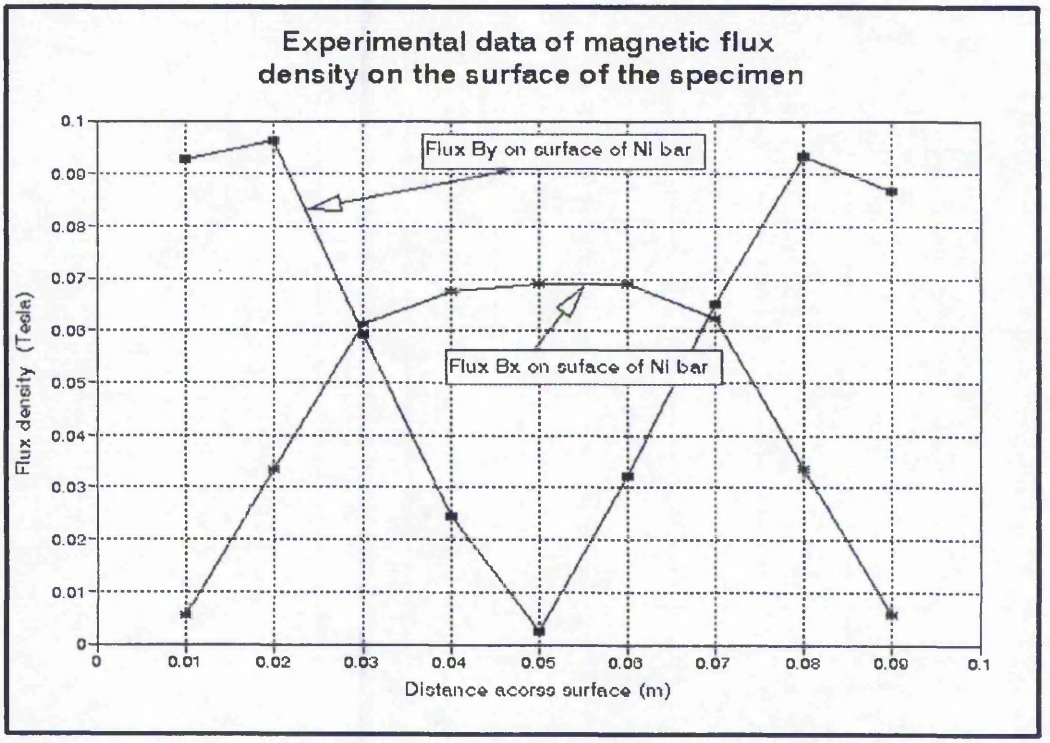


Figure 2.1.4 Experimental data for the magnetic flux density (**B**) across the surface of the nickel sample at saturation on the maximum peak of the triangular wave form.

The width of the silicon iron magnetic yoke's contact with the nickel bar was approximately 25 mm. This contact zone has a very strong magnetic field component in the Y-direction also evident on the surface. Reorientation of the field caused **By** to drop sharply around the centre of the nickel bar. Also, the ANSYS data for the **Bx** component was much larger in magnitude in comparison with the experimental data (**figures 2.1.3**

and **2.1.4**). On the central region of the specimen the ANSYS and experimental results for the **Bx** component were found to be **0.386 T** and **0.069 T** respectively. The Hall probe design may account for this difference. The ANSYS data was taken directly from the surface of the nickel specimen, whereas, for the experimental measurements, the edge and centre of the Hall element was 1.5 mm and 2.5 mm respectively off the surface of the specimen. The magnitude of the averaged **Bx** component at the edge regions of the specimen was very weak (**0.0057 T**), in comparison to the **By** component (**0.0899T**). The **Bx** component only increased close to the centre position of the nickel sample.

2.1.3. Finite Element Modelling of Different Specimen Thicknesses.

2.1.3.1. *Modelling differing thicknesses of nickel specimen.*

Following the success of the initial FE model, a series of new models were executed. Each model incorporated a nickel specimen of differing thickness. Five such models were run in transient mode, with nickel thicknesses varying from 26 mm to 5 mm. All other variables in the models were constant; (dimensions, node points and current through coil, etc.). The 26mm, 20mm, 15mm, 10mm and 5mm thick nickel samples were modelled using the same mesh size. For the thinnest 5 mm nickel model the mesh size proved inadequate, resulting in the magnetic field and the flux density spread being distorted. This was resolved by decreasing the mesh size from 5 mm to 3 mm for the nickel block. The air gap also had the mesh size decreased from 2 mm to 1 mm. This was necessary to match the air gap and nickel nodes more evenly. All six models were run in transient mode.

2.1.3.2. *Results from modelling different nickel specimen thicknesses.*

The net magnetic field and flux density, $\mathbf{B_{SUM}}$ **and** $\mathbf{H_{SUM}}$, on the surface of the nickel sample is shown in **figure 2.1.5 and 2.1.6**. The data presented in **figure 2.1.5 and 2.1.6** is from a time of 5.41 seconds into the magnetisation cycle; a time at which the electromagnetic Barkhausen peak is known to occur. The FE model indicated that the strongest magnetic field on the **26 mm** specimen thickness was achieved on the central portion of the nickel bar with values of **H=13.5 kAm^{-1}** and **B=0.0639 T**. On 25 mm from the edge of the specimen the field and flux density were measured as **H=9618 Am^{-1} and B=0.0599 T**, (see **table 2.1.1)**. As the nickel sample thickness decreased more flux leaked from the system, since the nickel block magnetic reluctance increased for thinner samples. Magnetic reluctance *'R'* is governed by the dimensions of length *'L'* and area *'A'* of a specimen ($R = L/\mu A$), where μ is the magnetic permeability of the material.

Therefore, as the thickness (cross sectional area '*A*') of the specimen was reduced the reluctance increased. This is analogous to increasing the resistance in an electrical circuit **[1]**. As a result, on the 5 mm thick FE modelled specimen values of **H** and **B** were **15.5 kAm^{-1}** and **0.0658 T**, recorded from the central (50 mm) regions (**table 2.1.1**). At 25 mm from the edge of the specimen, the magnetic measurements increased to **18.7 kAm^{-1}** and **0.0685 T**. All of this data is summarised in **table 2.1.1**.

The 5mm thick sample clearly demonstrated the importance of the mesh size and how the results could be distorted if incorrect mesh size was used. The model with a 5 mm nickel mesh size produced flux density values which appeared to fluctuate across the surface of the nickel sample (**figure 2.1.5**). The finer nickel mesh (mesh size 3mm) showed a steady variation of magnetic flux density across the central region of the nickel specimen.

ANSYS modelled specimen thickness.	Magnetic measurements from the 25 mm position on the FE specimen surface		Magnetic measurements from the 50 mm position on the FE specimen surface	
	Flux B_{SUM} (T)	Field H_{SUM} (Am^{-1})	Flux B_{SUM} (T)	Field H_{SUM} (Am^{-1})
26 mm	0.0599	9618	0.0639	13537
20 mm	0.0623	12310	0.0649	14604
15 mm	0.0644	14634	0.0653	14995
10 mm	0.0657	16043	0.0655	15192
5 mm	0.0685	18711	0.0658	15511

Table 2.1.1 ANSYS modelled data from differing specimen thicknesses. The magnetic flux and field values from two positions on the surface of the specimen. Data taken from **figures 2.1.5** and **2.1.6**.

The magnetisation of the whole specimen did not appear uniform, as seen in **figure 2.1.7**, which shows the 26 mm thick specimen magnetisation at 5.41 seconds into the magnetisation cycle. At around this time the maximum Barkhausen activity was recorded

for certain nickel and steel specimens. The FE model (**figure 2.1.7**) clearly showed that different regions within the specimen experienced differing intensities of magnetisation. The central region of the nickel specimen can be seen to be magnetised to field intensity of ≈**16.7 kAm^{-1}**, while the edge regions have a value of ≈**4 kAm^{-1}**. The spread of the magnetising field within the specimen exhibits a very high magnetisation at the contact position between the edge corner of the yoke's leg and specimen (≈**29 kAm^{-1}**). The transition between the high (central) and the low (edge) magnetisation regions indicates that the specimen, at a time =5.41 seconds, is under non-uniform magnetisation. This difference in the magnetisation between the edge and central portion of the specimen, at a given time, is expected to have an effect on the BE signals.

The magnetisation of the 5 mm thick specimen at 5.41 seconds into the magnetisation cycle is shown in **Figure 2.1.8**. In this thin specimen the field intensity was similar to the 26 mm thick specimen (**figure 2.1.7**). The central 50 mm region of the specimen was uniformly magnetised to a value of **16.7 kAm^{-1}**, while 20 mm regions at the ends of the specimen were magnetised to a intensity of **4.8 kAm^{-1}**. As the thickness of the specimen decreased the transitional region separating the high and low magnetisation regions became smaller (**figure 2.1.8**) and a more rapid decrease in the field was observed. The increased reluctance of the specimen led to the increased leakage field on the surface of the thin specimen (**figure 2.1.6**).

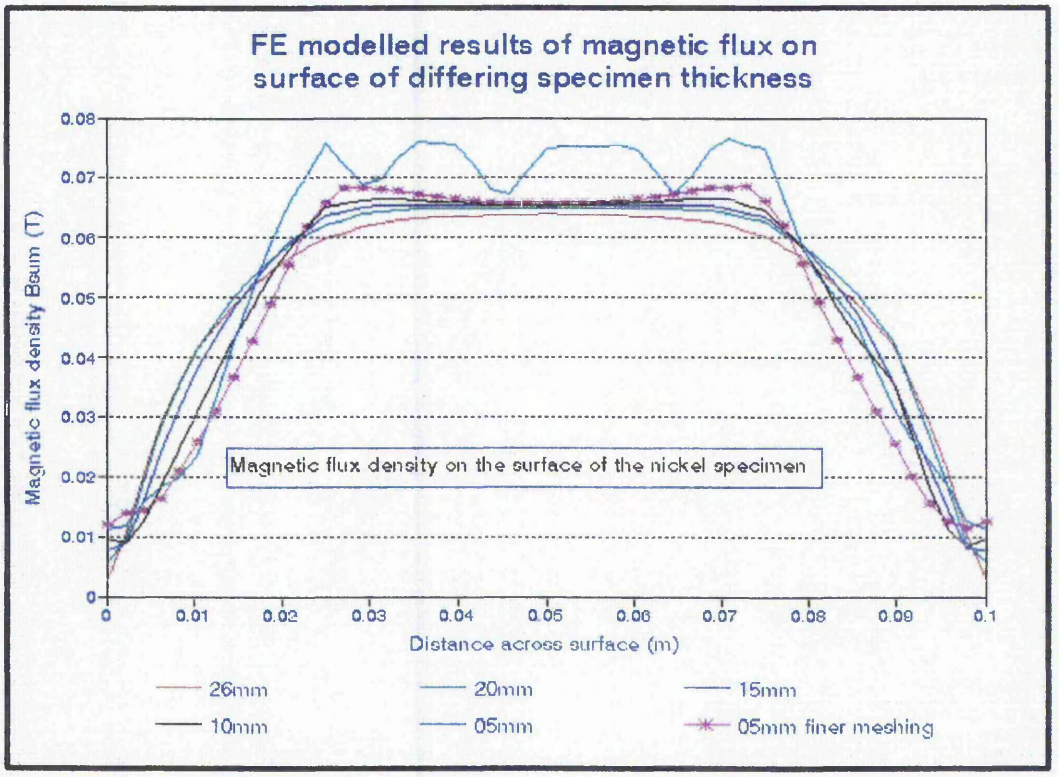


Figure 2.1.5 Magnetic flux density on the surface of the nickel specimen for 26 mm, 20 mm, 15 mm 10 mm and 5 mm thicknesses. The flux density values for the sample thicknesses of 5mm were modelled using different element sizes. Results from 5.41 seconds into the magnetising cycle. Unit of magnetic flux density is Tesla (T).

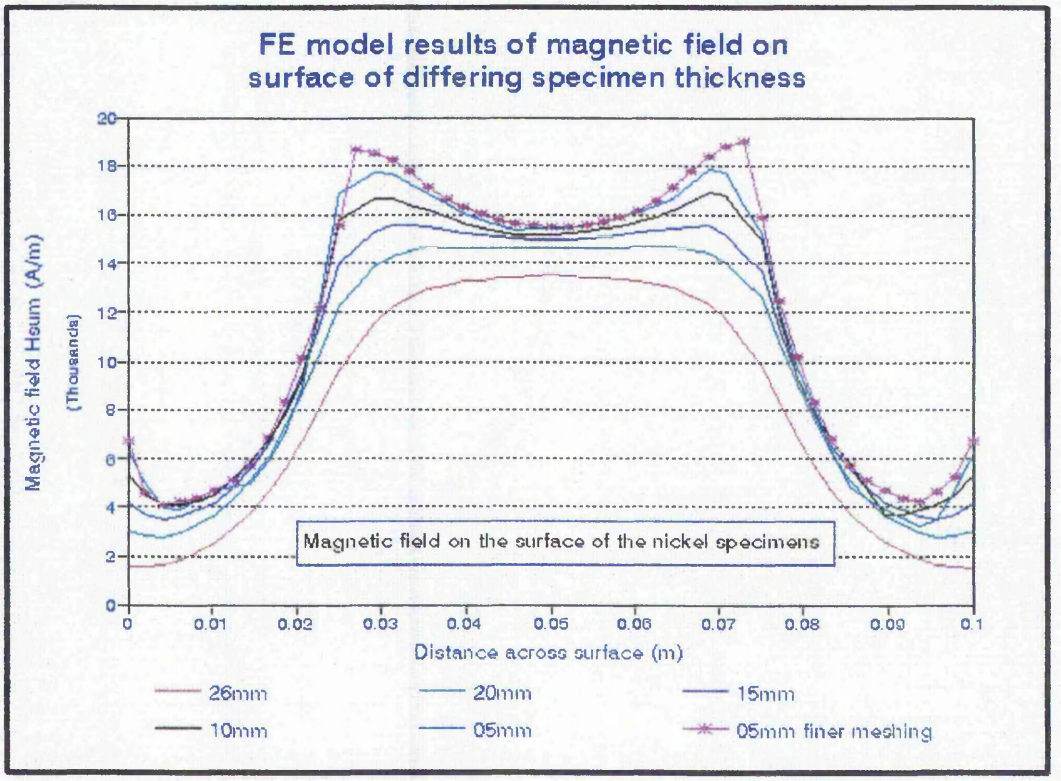


Figure 2.1.6 Magnetic field on the surface of the nickel specimen for 26 mm, 20 mm, 15 mm 10 mm and 5 mm thicknesses. The field values for the sample thicknesses of 5mm were modelled using different element sizes. Results from 5.41 seconds into the magnetising cycle. Unit of magnetic field is Am^{-1}.

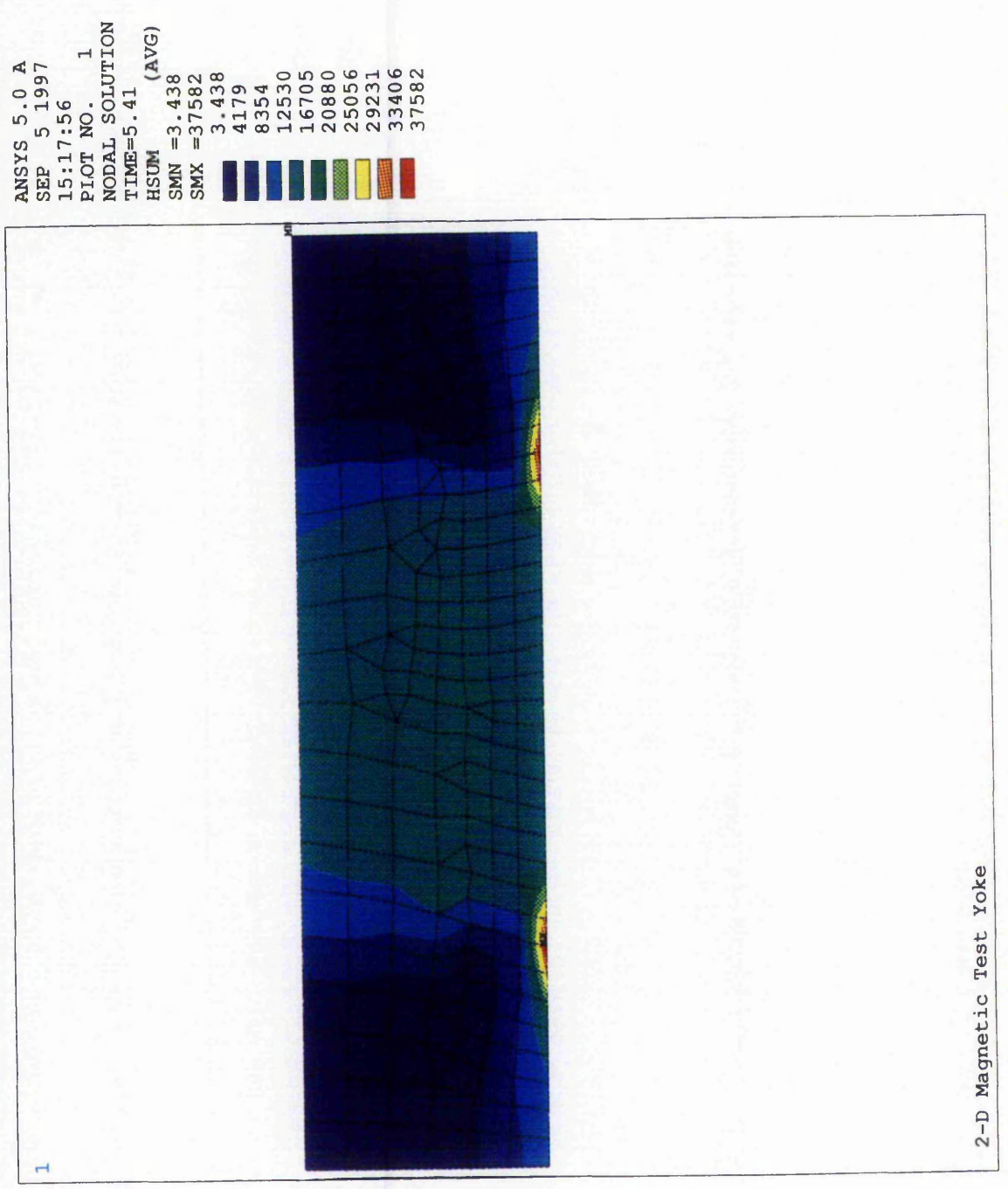


Figure 2.1.7 FE modelled magnetic field (**H**) within the 26 mm thick nickel specimen at a time of 5.41 seconds into the magnetising cycle.

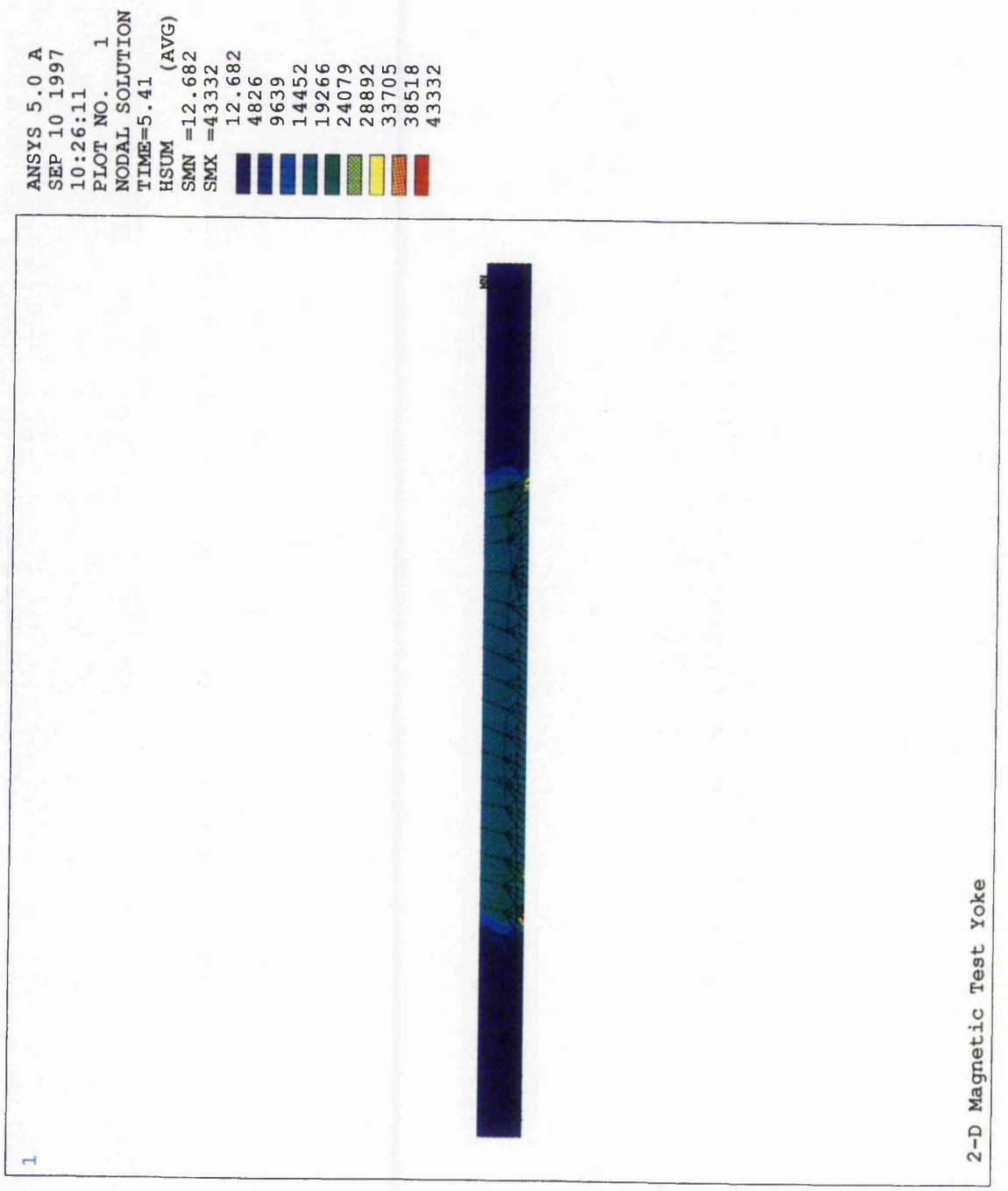


Figure 2.1.8 FE modelled magnetic field (**H**) within the 5 mm thick nickel specimen at a time of 5.41 seconds into the magnetising cycle.

2.1.4. Finite Element Modelling of a Slot in a Barkhausen Test Specimen.

2.1.4.1. *Modelling of a slot within a test specimen.*

To investigate the effect of a slot on the magnetic field distribution, a new ANSYS model similar to that used in **section 2.1.3** for a specimen thickness of 15 mm was created. The ANSYS model data is displayed in **appendix 2b**. The region in and around the centre of the nickel sample was modelled differently, as three new regions within the sample area were created. A thin slot was introduced, 0.3 mm in width and 7 mm in length, filled with air. A 20 mm× 20 mm region immediately surrounding the new slot was redesigned using a finer mesh. This dense mesh spreads throughout this region, which included air as well as the metal. The finer mesh provided a better transition from the very fine meshing of the slot through to relatively coarse meshing of the surrounding area. Meshing size ranged from 0.1 mm for the air-slot to 5 mm for air surrounding the model, away from the slot. The data for the magnetic material used in this analysis was provided by British Gas plc. and applied to a mild steel specimen with serial number OLI-95D (**appendix 1b**). A transient analysis on the new model provided results which showed how the flux density and magnetic field varied on the surface of the sample when crossing the slot.

2.1.4.2. *Results from FE modelling of a slotted steel specimen.*

Magnetisation in magnetic materials arises due to alignments of small atomic magnetic dipoles. When a slot is created in a material, new surfaces are exposed. These surfaces can be viewed as free dipoles, as the surfaces have no immediate adjacent dipoles for field cancellation.

Figure 2.1.9 shows the **Bx** and **By** field patterns on the surface of the slot sample arising due to these free poles. **Figure 2.1.10** shows the **Hx** and **Hy** field patterns on the surface

of the slot sample. The FE slot-model showed that the presence of the slot in the sample had a significant effect on the field patterns. Field patterns from the surface of a standard sample without a slot **(figure 2.1.3)** showed **Bx** to be uniform **(0.385 T)** around the central region of the magnetised sample. The results from the surface of the slot **(figure 2.1.9)** showed the **Bx** field increased to a maximum value of **1.597 T** at the central position due to the increased magnetic reluctance at the slot. The **By** field was found to be zero on the central position of the slot as a result of the leakage field changing direction. The total **B** field ($\mathbf{B_{SUM}}$) followed a similar pattern to the **Bx** field with the difference being a small dip at the central region of the slot. This was a consequence of the **By** field pattern. The FE model of the slot and surrounding region (approximately 12 mm^2) is shown in **figure 2.1.11**. A vector plot of the **H** field shows the way in which the magnetic field diverted around the slot. The dimension of the slot is 0.3 mm wide by 7 mm deep. **Figure 2.1.12** and **2.1.13** show the ANSYS modelled slot's top and bottom region, exhibiting the magnetic flux pattern as a vector plot.

Leakage fields are observed from both slots and cracks. Fatigue cracks generate a field pattern which is 'more compact' and detected across a smaller surface region compared to the field pattern from the slot **[85]**. Inclusions near the surface of the sample may also generate similar leakage field patterns, though the patterns have been reported to be broader and more 'spread out' over a larger surface region in comparison with a tight crack. The spread of the leakage field increases with the inclusion depth. These leakage patterns can and are used in non-destructive flaw detection. Using flux meters, leakage fields can be detected from various defects which cause a change in the permeability of the specimen, such as surface and subsurface cracks, pores and inclusions. Detection methods such as magnetic particle inspection (MPI) are also based on this phenomenon **[53]**. Instead of a flux meter, magnetic ink (fine magnetic particles suspended in a solvent) is sprayed onto a specimen's surface. The leakage field attracts the particles and the crack or defect is revealed **[86]**. This is, however, a very subjective detection method.

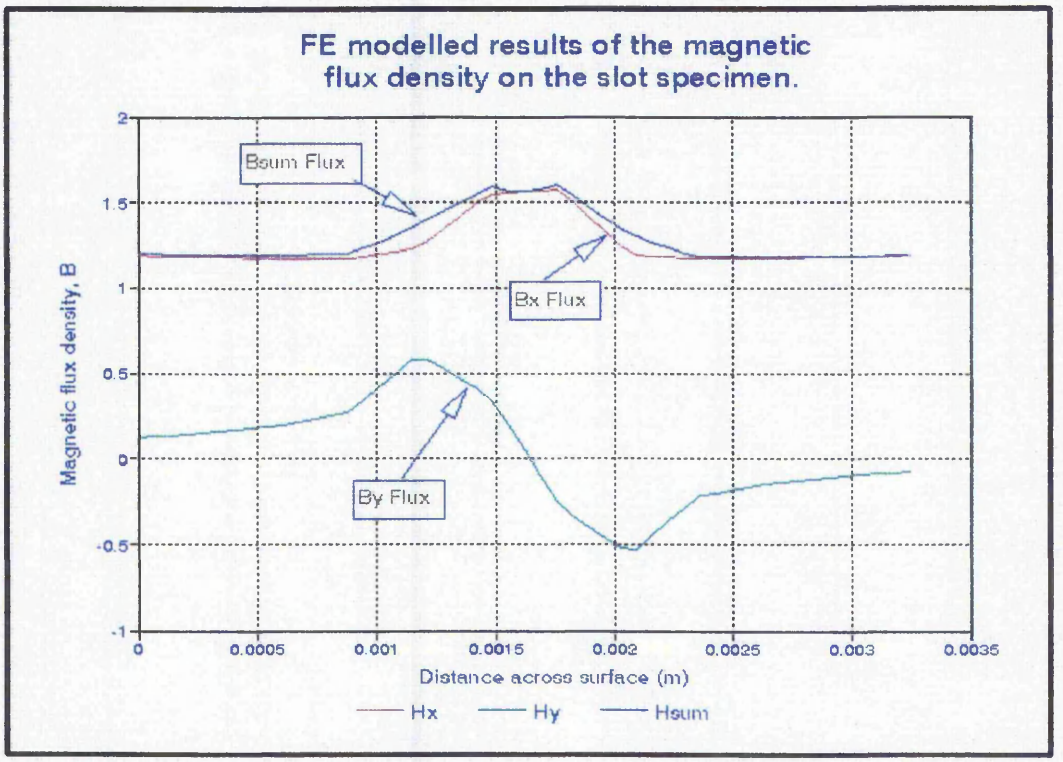


Figure 2.1.9 Magnetic flux leakage from the surface of the slot sample. The central region of the slot is located at 0.0016 m. The units of magnetic flux leakage (**B**) is Tesla (T).

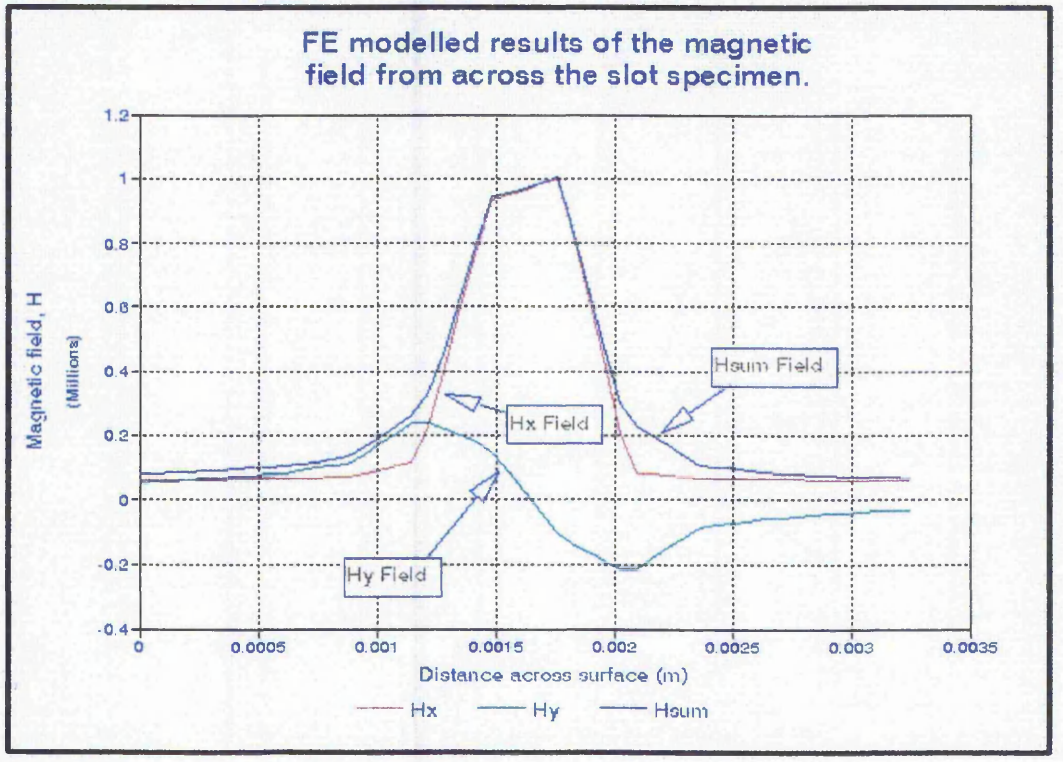


Figure 2.1.10 Magnetic leakage field from the surface of the slot specimen. The slot position is located at 0.0016 m and the units of magnetic leakage field (**H**) are Am^{-1}.

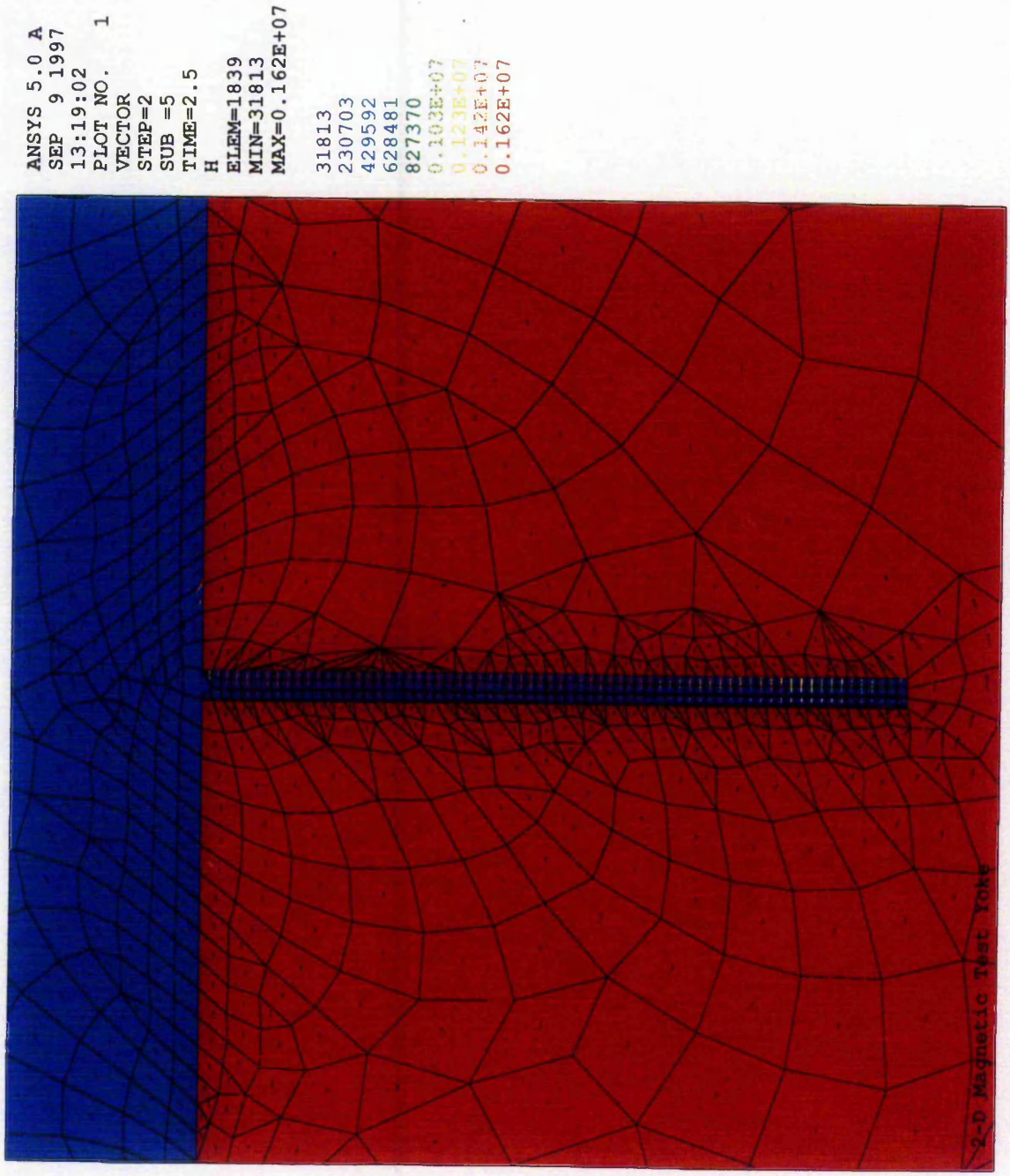


Figure 2.1.11 The magnetic field (**H**) vector plot on the slot in the steel sample OLI-95D.

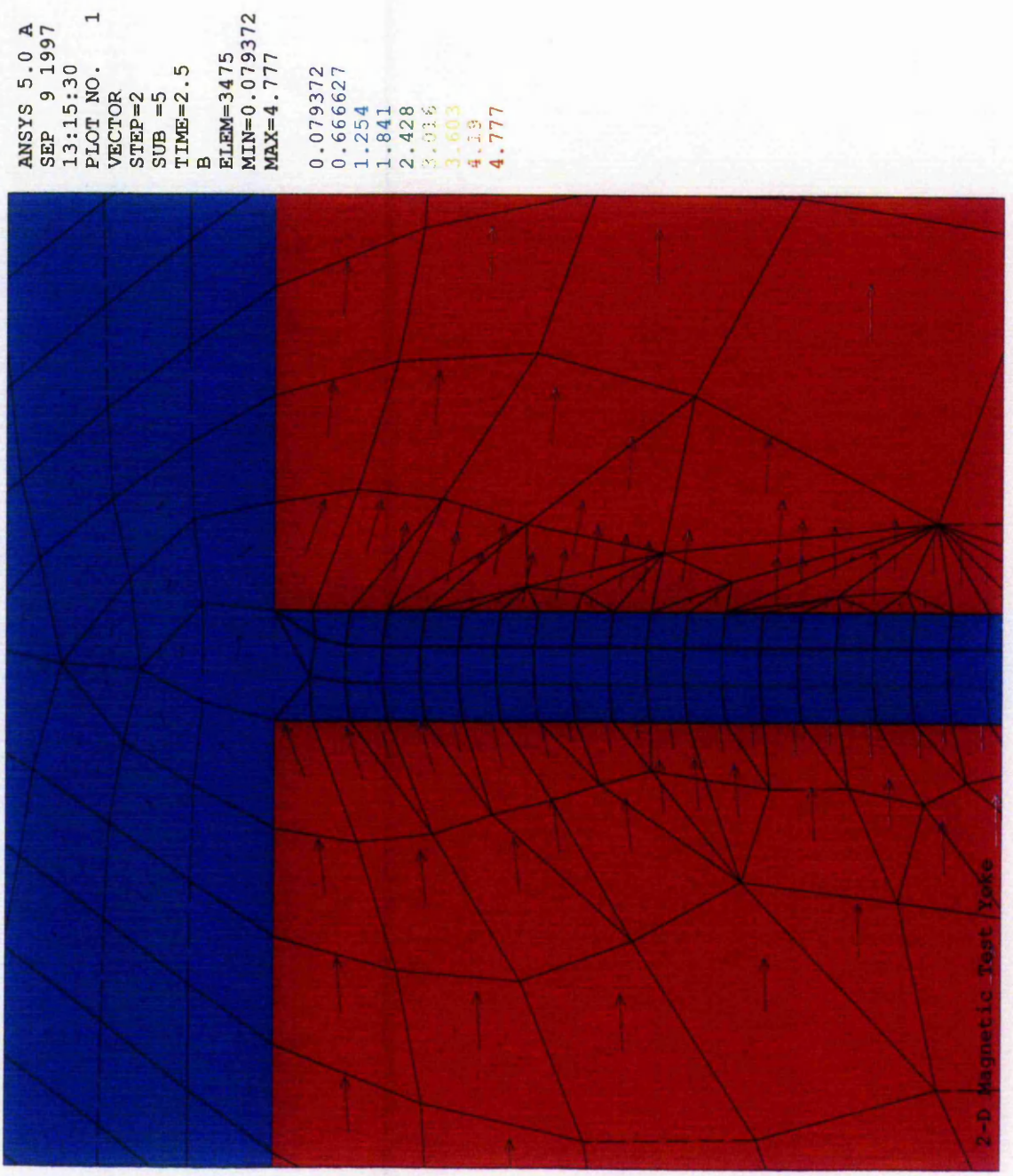


Figure 2.1.12 The **B** field vector plot on the top region of the slot in the steel sample OLI-95D.

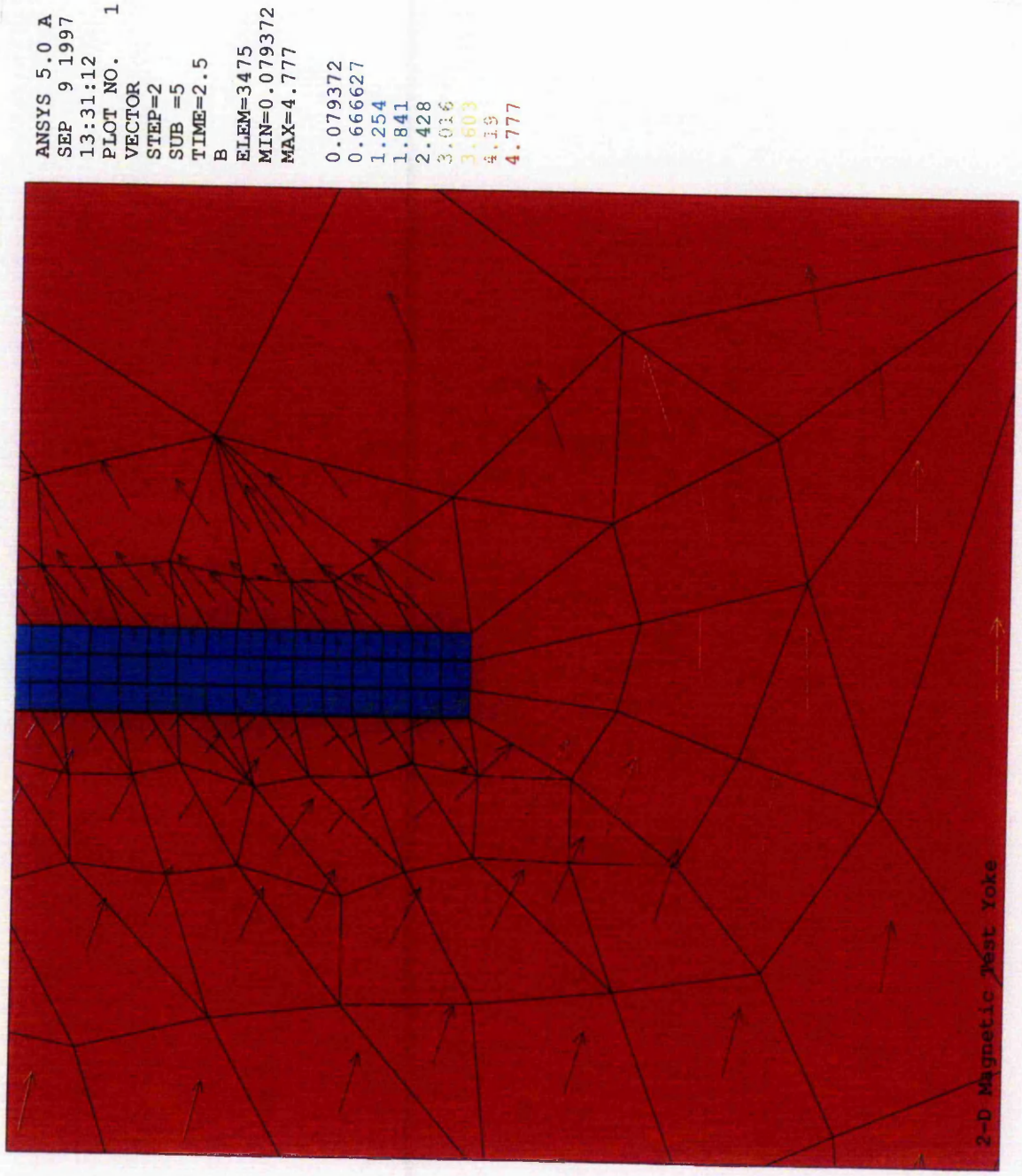


Figure 2.1.13 The **B** field vector plot of the lower region of the slot in the steel sample OLI-95D.

2.2. SPECIMEN MAGNETISATION AND BARKHAUSEN ENVELOPES.

The effect of EBE sensor position in relation to the magnetised specimen is considered in this section. Initial work involved studying the EBE signal envelope, trying to understand how they were generated and what influenced their shape and size. The change in the Barkhausen signal shape was studied for various positions of the sensor, along the surface of a polycrystalline nickel specimen. Experiments were carried out on a 'Nickel 200' specimens using the standard Barkhausen apparatus described in **chapter 1**. The large 26 mm diameter copper coil, ferrite core transducer was used for these experiments.

2.2.1. Effect of Sensor Position on the Barkhausen Envelope.

A cold rolled 'Nickel 200' bar was machined down to form a specimen with dimensions 100 mm × 30 mm× 26 mm. The surface of the 'as-machined' nickel sample (serial number 'Ni200/ 1') was subdivided into five locations; one position at the centre of the specimen and two on either side. Position 'C' was located at the centre, at a distance of 50mm from either ends of the specimen. Positions 'B' and 'D' were a located 15 mm either side the central position 'C'. Positions 'A' and 'E' were located 20 mm from the edges of the nickel specimen. Position 'A' and 'B' were mirror reflection of 'D' and 'E' about the central position 'C', as shown in **figure 2.2.1**. The metallurgical composition of 'Nickel 200' specimen is provided in **table 2.2.1**. The polycrystalline nickel specimen was uniform in composition.

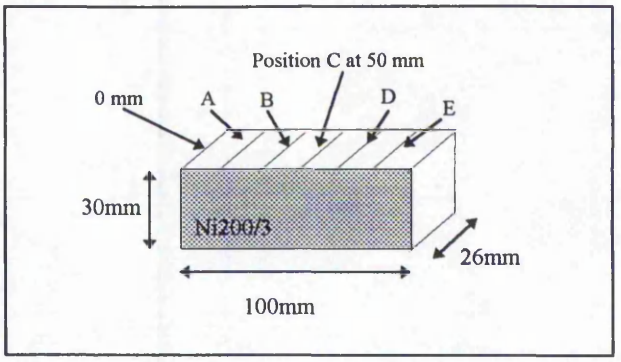


Figure 2.2.1 Diagram of 'nickel 200' sample showing the labelling on the specimen surface.

Ni	Fe	Co	C	Si	Cu	Mn	Mg	Ti	S
99.64	0.011	0.062	0.058	0.01	<0.005	0.078	<0.005	<0.005	0.002

Table 2.2.1 'Nickel 200' material composition. Weight %. (Manufacture's information).

2.2.2. Barkhausen Envelope Parameters.

Barkhausen measurements were recorded across the surface of the nickel specimen. The Barkhausen signals were analysed in terms of their envelope magnitude and time. The time within the recording window at which the maximum Barkhausen envelope peak point occurred was referred to as the 'time of peak', (T_P). The 'time of peak' was not fixed on a given peak in a multi-peaked BE envelope. If a different peak on the Barkhausen signal produced the largest amplitude, then the T_P value changed in accordance with the envelope's new peak position. The maximum Barkhausen signal amplitude was referred to as the 'Maximum signal voltage' (V_{MAX}) and is the magnitude of the highest peak on the BE envelope. V_{MAX} is measured in voltage.

2.2.3. Barkhausen Results from the Surface of the Nickel Specimen.

Figure 2.2.2 shows the EBE signal envelopes from the five locations on the nickel specimen. Over a number of experiments, Barkhausen measurements showed that the EBE signal peak was the greatest at the central region of the nickel specimen (location 'C'). **Table 2.2.2** shows that the Barkhausen signal envelopes from either side of the central location 'C' were slightly smaller in magnitude. This suggested that the material microstructure was not uniform throughout the surface of the specimen or that the Barkhausen signal envelope, being detected by the sensor, was different for differing regions. This was perhaps due to the magnetic field declining at the specimen's edges. For each reading across the surface of the specimen the EBE signal's 'T_P' occurred at a time around 0.85 seconds on the envelope, (see **table 2.2.2)**. However, a very slight shift in the T_P value was recorded on the EBE envelope from the central positions.

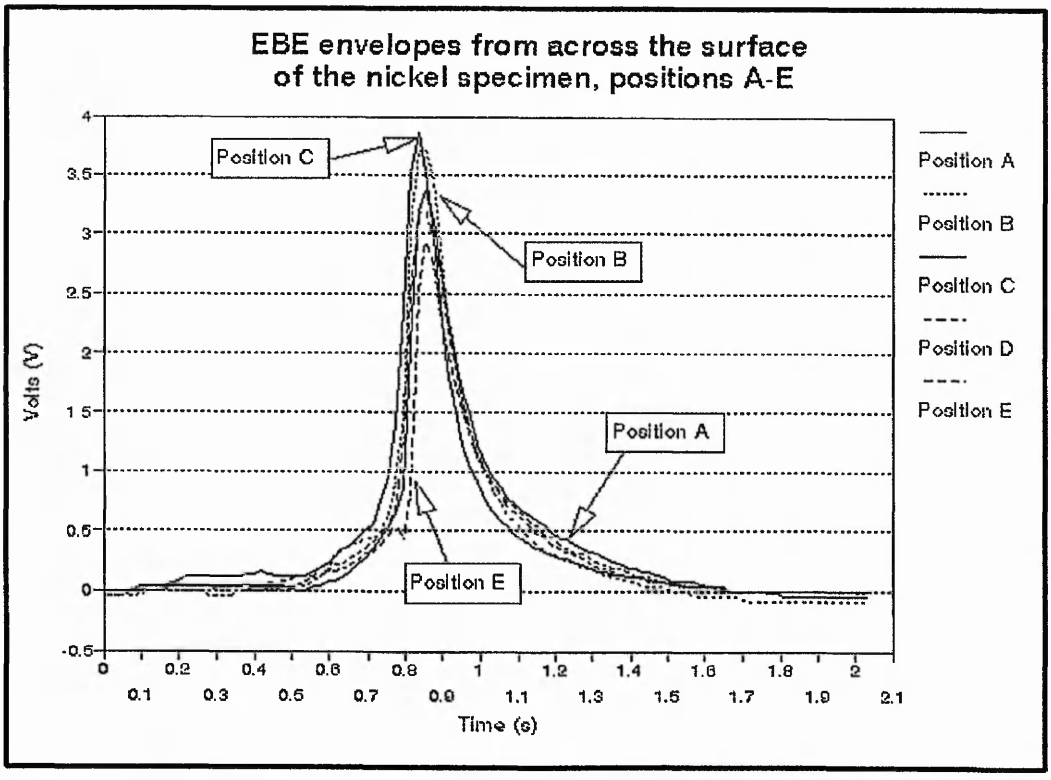


Figure 2.2.2 EBE signal envelopes from the surface of the nickel specimen. The graph shows the signal amplitudes varying relative to sensor position.

So, it can be said that the shape, height and width varied as the sensor traversed across the surface of the magnetised specimen. The EBE envelopes were asymmetrical in shape across the surface of the specimen. This will be discussed in **section 2.4**.

Location on the nickel specimen's surface.	Time of Peak. T_P (s)	Maximum signal voltage. V_{MAX} (V)	FE modelled magnetic flux Bx. (Tesla)
Position A (20 mm)	0.86 ±0.01	3.36 ±0.02	0.334
Position B (35 mm)	0.86	3.72	0.381
Position C (50 mm)	0.84	3.85	0.387
Position D (65 mm)	0.86	3.23	0.379
Position E (80 mm)	0.86	2.96	0.323

Table 2.2.2 The EBE envelope parameters from across the surface of the nickel specimen. EBE data taken from **figure 2.2.2**. FE modelled magnetic flux (**Bx**) on the surface of the specimen nickel. FE modelled data from **figure 2.1.3**.

The EBE sensor coil detects small changes in magnetisation, created as a consequence of the domain wall motion within the specimen. Tiitto **[87][24]** indicated that EBE sensors with a coil axis at right angle to the magnetising field detected the largest Barkhausen signals. Therefore, the central location would be expected to provide the largest EBE signal as the magnetic flux component (**Bx**) at the central location (at 90° to the sensor) was the greatest. This was also supported by the ANSYS data in **section 2.1.2**.

Asymmetrical 'V_{MAX}' values were detected from across the surface of the specimen. **Figure 2.2.3** shows the EBE envelopes V_{MAX} parameter in relation to the FE modelled magnetic flux component **Bx** on the surface of a nickel specimen. The match between the magnetic flux **Bx** is not expected to be exact as material characteristics have a strong influence on the EBE signal generation. The similarity between the V_{MAX} parameter and the magnetic flux from the surface of the nickel specimen (in **figure 2.2.3**) can be better

understood by noting the direction of the magnetisation vector with respect to the EBE sensor. The detected EBE peak height is influenced by the magnetisation intensity or direction of the magnetisation vector with respect to the sensor **[36]** as well as variables such as microstructure, composition, stress and dislocations.

This is similar to the magnetic easy direct of the material being at 90° to the sensor, which is known to generate larger EBE envelopes.

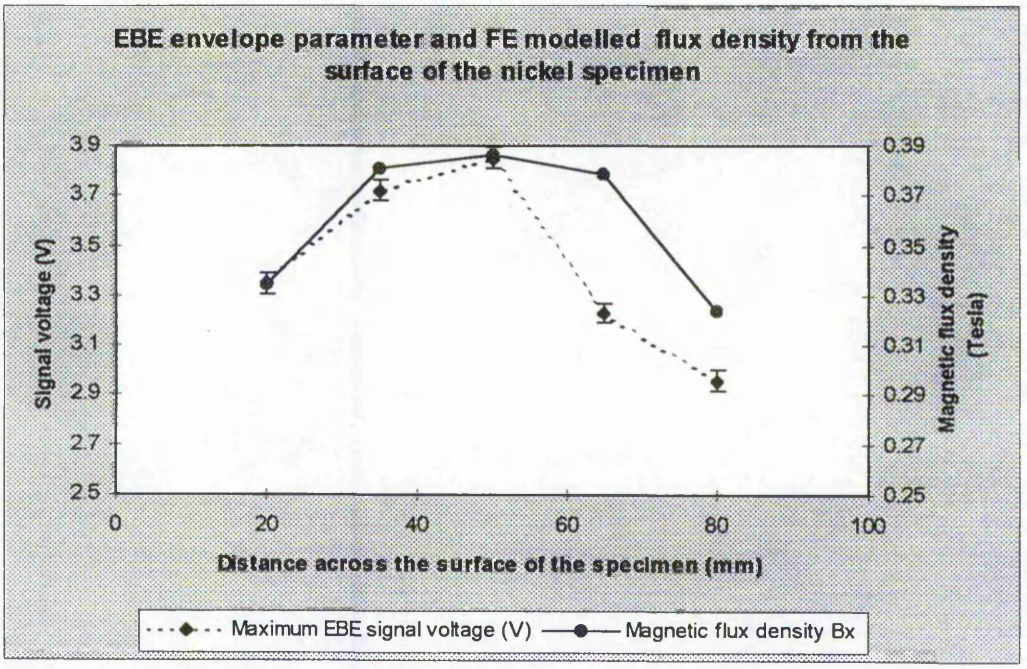


Figure 2.2.3 Magnetic flux density component (**Bx**) on the surface of the FE modelled nickel specimen and the experimental results of the EBE envelopes' V_{MAX} parameter from the surface of the nickel specimen. Both sets of measurements show a similar trend.

2.3. EFFECT OF SPECIMEN VOLUME ON THE BARKHAUSEN SIGNAL ENVELOPES.

The relationship between the volume of a specimen and its effect on the Barkhausen signal is considered in this section. Knowing the effect of specimen size on the ABE will allow better interpretation of data and also provide a better understanding of the origins of the Barkhausen noise.

2.3.1. Experimental Detail.

A 'Nickel 200' block of initial specimen length 100 mm, width 30 mm and a thickness of 20 mm was annealed in a furnace. The annealing temperature used was 840°C for 8 hours in a nitrogen atmosphere, after which it was allowed to furnace cool. This high temperature ensured that homogenous recrystallisation occurred. A cylindrical electrical furnace capable of reaching temperatures of 1100°C and above was used. A ceramic tube made by Thermal Syndicate Ltd., Wallsend, England, was placed in the furnace. The tube is described as an "Aluminous Porcelain 525", of length 830 mm and internal diameter 38.5 mm and tube wall thickness of 4.5 mm. The metal specimen to be annealed was placed on a steel tray and both were inserted into the aluminous cylinder. The cylinder, in turn, was placed inside the furnace, ensuring that the metal specimen was in the hottest region of the furnace. One end of the ceramic cylinder was attached to a nitrogen supply, with the other end connected to an exhaust tube which allowed the nitrogen to flow out. The atmosphere inside the aluminous cylinder was achieved by having nitrogen gas continuously flowing over the nickel block during the heating and cooling process. The flow rate of the nitrogen gas was approximately 1.5 litres per minute. Annealing was carried out on the nickel specimen in an attempt to homogenise and remove internal stresses.

Barkhausen measurements were then carried out on the nickel specimen. Both EBE and ABE measurements were conducted using the experimental system described in **chapter 1**. The specimen was then reduced in thickness by machining and then annealed again to remove any surface stresses, thermal shock effects and dislocations, which may have resulted from the machining process **[57]**. After further annealing, ABE and EBE measurements were recorded on the central region of the nickel specimen. Subsequent surface machining, annealing and Barkhausen measurements were carried out for a further six different specimen thicknessess.

2.3.2. Results and Data Analysis.

The Barkhausen signal envelopes from the seven different annealed specimen thicknesses were recorded. The ABE and EBE signal envelope peak amplitude was determined and a relationship between peak amplitude and specimen volume was not evident. As an alternative to peak height, the Barkhausen signal was also analysed in terms of the area under each envelope. The signal area, '*A*', was the area between the Barkhausen envelope and a predetermined baseline for the signal envelope. The signal area was calculated using the trapezium rule. Each signal envelope was split into 100 intervals separated by the sampling time between each voltage point.

$$A = \sum_{n=1}^{N=100} \left(\frac{1}{2}(x_n + x_{n+1}) \times \Delta t\right) \qquad (2.2)$$

A = area under Barkhausen envelope. x_n = voltage at point 'n'. x_{n+1} = voltage at point 'n+1'. Δt = time between points 'n' and 'n+1'.

Sample Thickness (mm)	EBE signal envelope area. (Vs)	ABE signal envelope area. (Vs)
19.93	0.093 ±0.008	0.167 ±0.008
18.05	0.102	0.200
15.31	0.089	0.178
11.98	0.042	0.131
8.00	0.095	0.092
6.00	0.079	0.099
4.00	0.089	0.084
2.00	0.104	0.072

Table 2.3.1 Variation of the area under the Barkhausen envelopes when changing the thickness of the nickel specimen. Unit for Barkhausen signal area is Vs.

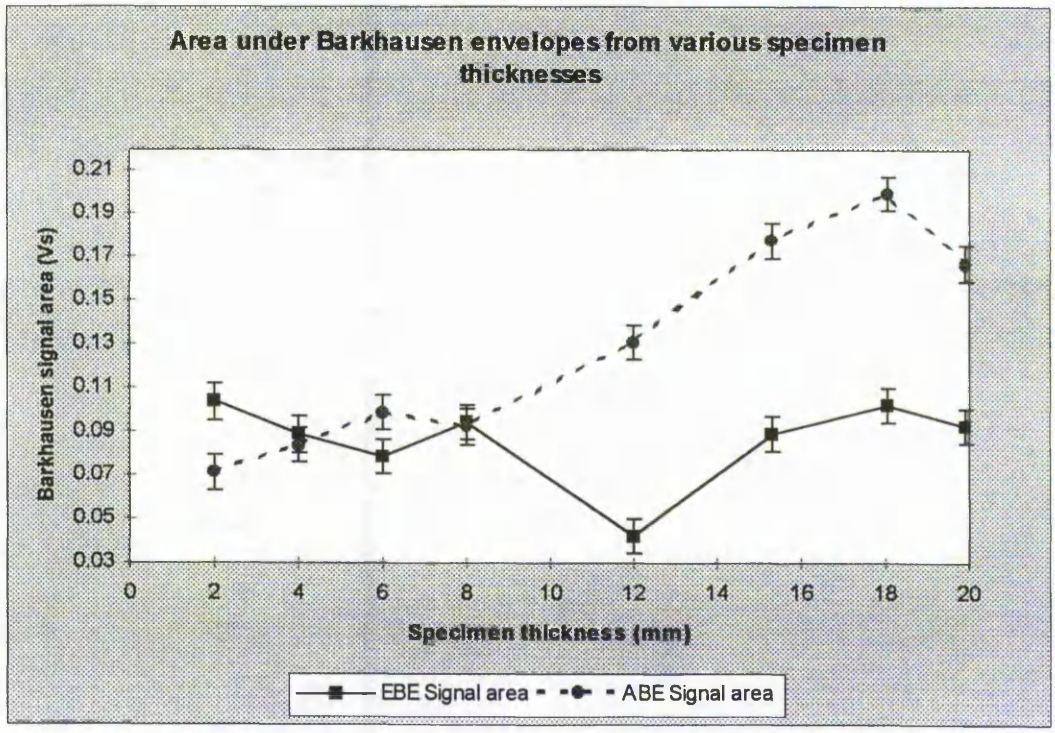


Figure 2.3.1 The area under the Barkhausen envelopes plotted against the varying annealed nickel specimen's thickness.

Figure 2.3.1 shows the relationship between the Barkhausen envelope area plotted against the specimen thickness. As the specimen thickness was reduced, the area under the ABE signal envelope decreased. This relationship was to be expected since ABE signals are generated when non-180° domain walls break-away from their pinning sites and cause stress waves as a result of magnetostrictive volume changes. This leads to the conclusion that in a large volume there are likely to be more pinning sites and, therefore, closure domains and, thus, more sites generating acoustic signals.

The EBE signals showed little variation in envelope area with specimen thickness. The EBE signal from the 12 mm specimen was thought to be affected by specimen variability. It may have been caused by machining of the sample's surface and as a consequence, the contact between the EBE transducer and the sample surface was imperfect. Apart from this divergent result, the rest of the EBE data indicated a relationship where signal area was not affected by specimen volume.

The gradual reduction in specimen volume (specimen thickness) would also lead to an increase in the flux density in the nickel bar due to an increased reluctance. It may be expected that, with the decrease in specimen thickness, the increased flux density (reported in **section 2.1** and also shown in **figure 2.3.2**) would aid an increase in the magnitude of the EBE signal. An increase in the EBE signal magnitude would have a direct affect on the signal area. The increased magnitude of magnetic flux (**Bx**) did not seem to be large enough to have a significant effect on the EBE results from the annealed nickel specimen. **Figure 2.3.2** show the FE modelled magnetic flux density data on the central region of the surface layer for specimen of differing thicknesses. The EBE signals are thought to be generated when magnetic domain walls break from their pinning sites. EBE signals are a surface effect and are limited to the surface by eddy current dampening, which causes attenuation of the signal at an exponential rate with depth **[1][2]**. The constancy of the EBE signal area with variation of specimen volume supports this view.

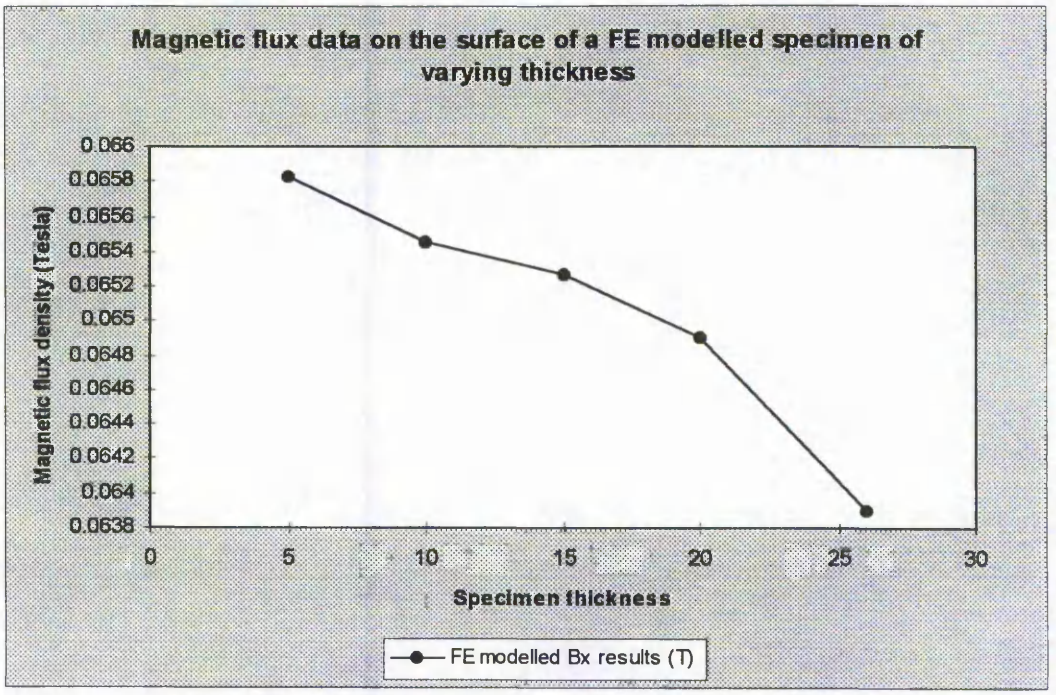


Figure 2.3.2 FE modelled magnetic flux density results on the centre of the specimen surface for differing thicknesses. Results show that the magnetic flux density increased as the specimen thickness was reduced.

2.4. INVESTIGATION INTO THE EFFECTS OF SURFACE MACHINING A TEST MATERIAL, USING BARKHAUSEN EMISSION TO MONITOR SURFACE CONDITION.

Knowing the origins and differences between the types of Barkhausen Emission (BE), it is possible to suggest utilising the differences to study the varying microstructural, stress and magnetic property differences between the surface and bulk of a material. It may also be possible to differentiate magnetic properties between the surface and the bulk and, therefore, assess surface damage of a material due to machining. The effect of machining a high purity nickel specimen, using BE, is studied in this section. The changes in microstructure and stress state are known to affect the BE. This makes Barkhausen emission an ideal candidate for analysing the effects of machining. A high purity nickel specimen is expected to have a reduced range of pinning sites compared with a steel or other complex alloys. This is expected to allow easier interpretation of the BE data.

Barkhausen signals (ABE and EBE) were both measured and are considered in this part of the work. As discussed before, the EBE signal is thought to be generated from the surface region of the test material. The use of the signal is limited to surface studies due to the eddy current damping which attenuates the signal. This means that the EBE signal is potentially useful as a surface analysis technique. The Acoustic Barkhausen signal is generated throughout the bulk of the material. In the case of nickel, the ABE envelopes often appeared double peaked. Both types of Barkhausen Emissions (BE) are accredited to certain types of domain wall motion. In the case of nickel, the 71° and 109° domain walls are the source of the ABE signals. The 180° domain walls do not contribute at all to the ABE signal, only to the EBE signals **[6]**.

2.4.1. Experimental Procedure.

A 'Nickel 200' specimen (sample number Ni200/3), with dimensions of 100 mm × 25mm × 20 mm was used. Positioning the nickel specimen on the electromagnet, Barkhausen signal measurements were recorded using the standard Barkhausen system with the large wound coil sensor. The Barkhausen measurements were repeated six times in order to obtain an averaged signal envelope. This confirmed the reproducibility of the Barkhausen envelopes. The Barkhausen measurements were repeated on three different locations. All three locations on the sample's surface were within the region of uniform field which was deduced from the ANSYS FE model, **section 2.1**. The three positions were labelled A, B and C. Position 'B' was on the central part of the nickel bar, 50 mm from either edge of the specimen. Position 'A' and 'C' were 10 mm on either side of the position 'B' (**figure 2.4.1**). On the three different locations, both the acoustic signals (ABE) and electromagnetic signal (EBE) were measured from the raw 'as-machined' nickel specimen.

This nickel block was then heat treated at 840°C for eight hours and allowed to furnace cool. This high temperature ensured that homogenous recrystallisation occurred. The annealing process is described in detail in **section 2.3.2**. After annealing, the nickel block appeared slightly tarnished with a small region at one end of the specimen having a fine residue; this was easily wiped off. The tarnished region of the specimen appeared to be dappled in appearance. Barkhausen signal measurements were then taken on the same three locations as for the raw 'as-machined' nickel surface.

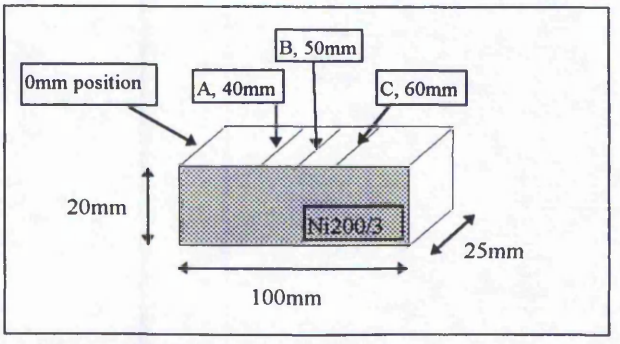


Figure 2.4.1 Nickel specimen (Ni200/3) dimensions and location of positions A, B and C.

The nickel specimen's top surface was then ground and polished, to give a reduced sample thickness of 19.5 mm, in order to generate surface disruptions. This treatment caused the surface of the specimen to become different from the annealed bulk material. The grinding process causes changes in the microstructure leading to increased density of dislocations, thermal shock and localised residual surface stresses **[57][59]**. These surface disruptions will be collectively referred to as 'surface stresses' throughout the rest of this section. Using the Barkhausen measurement system as before, EBE measurements were carried out. ABE signals were also measured and both were repeated several times on the three different locations. The ABE measurements recorded from the machined surface effectively acted as an experimental control. This showed that no new major internal stresses were generated by the surface grinding and polishing process.

2.4.2. Results and Analysis of the Barkhausen Emissions from the 'As-Machined', Annealed and Surface Machined Nickel Specimen.

The Barkhausen signals were analysed in terms of their envelopes, which were quantified using three different parameters: (i) the 'time of maximum peak' (T_P), (ii) the 'maximum signal voltage' (V_{MAX}) and (iii) the signal energy. The 'T_P' and 'V_{MAX}' values are discussed in **section 2.2.2**. The Barkhausen signal energy was calculated by splitting the area under the envelope into 408 thin strips, each strip 0.00501 seconds wide. The area below this envelope was calculated using the trapezium rule to evaluate $\int V^2 dt$ **[88][13]**.

The Barkhausen signal envelopes from the raw 'as-machined', annealed and machined surfaces of the nickel specimens are now considered. **Figures 2.4.2** and **2.4.3** show Barkhausen signals from the raw 'as-machined' nickel surface. The EBE and ABE signals from the three positions, labelled A, B and C, were all similar in shape and magnitude. The EBE envelopes possessed a single peak, which occurred at

approximately 0.84 seconds into the recording window. The magnitude of the signals were approximately 1.85 V. The ABE envelopes were all similar in magnitude and time of peak. The width of the envelopes were greater compared to the EBE signals. The ABE envelopes rise was at the start of the recording window, whereas the EBE envelopes began to rise after 0.4 seconds into the recording window. Repeated measurements from each of the three positions found all the Barkhausen envelopes to be reproducible.

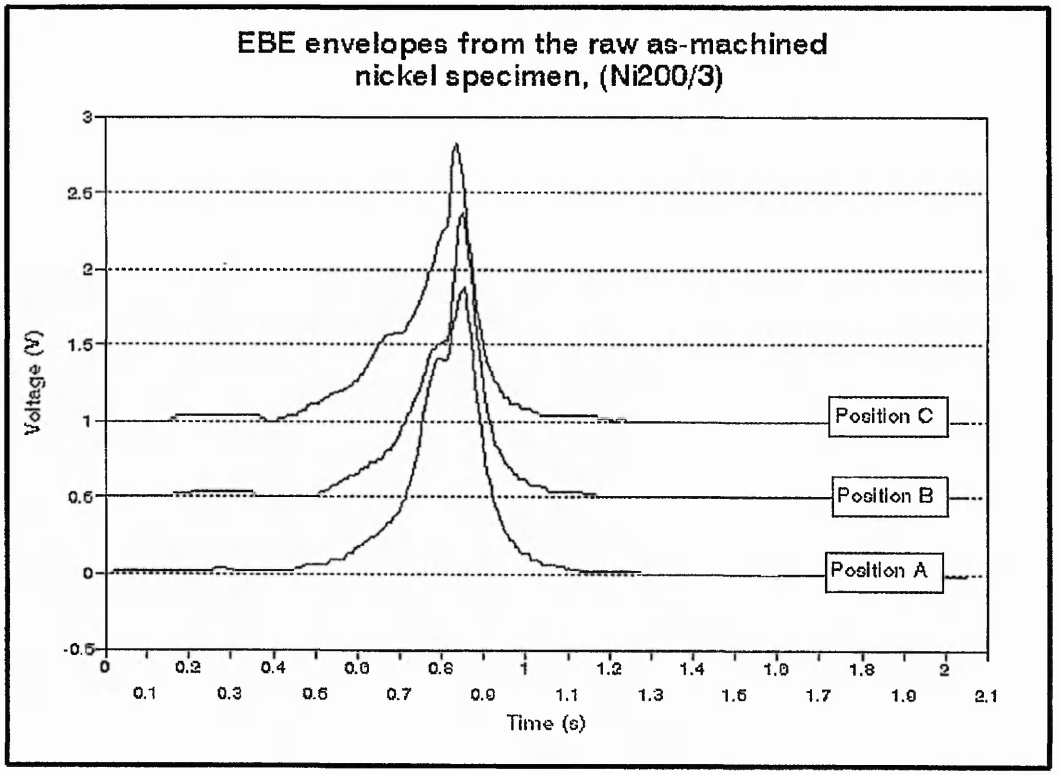


Figure 2.4.2 EBE signal envelopes from the three different locations on the raw 'as-machined' nickel specimen.

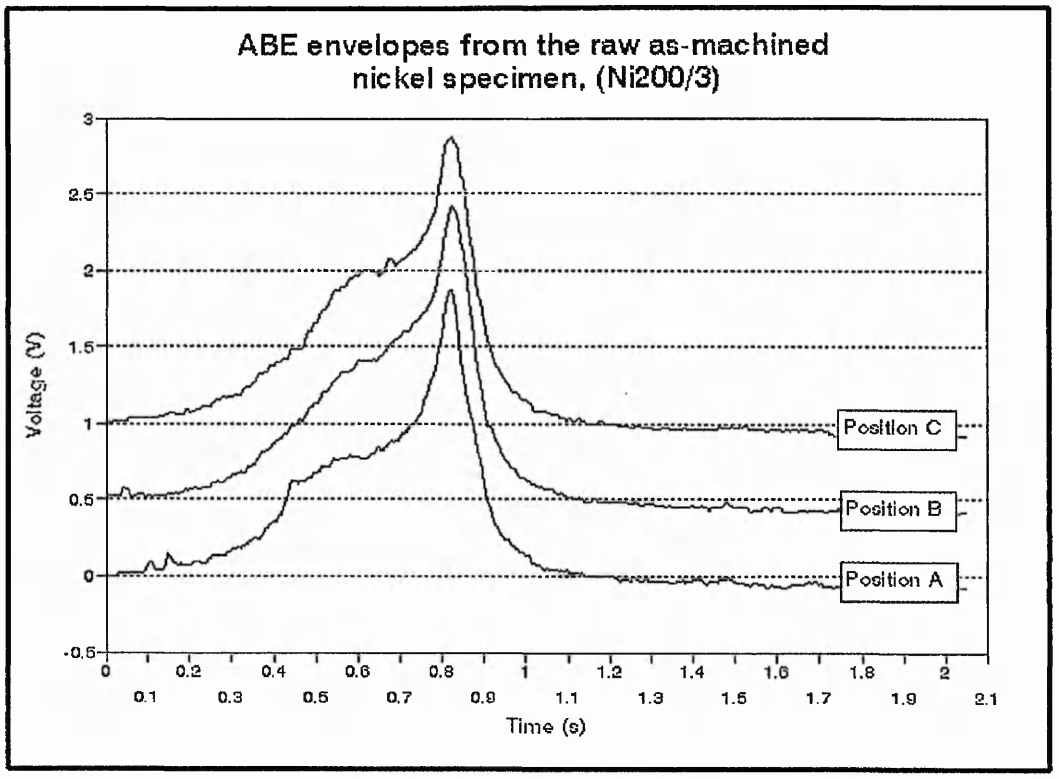


Figure 2.4.3 ABE signal envelopes from the three different locations on the raw 'as-machined' nickel specimen.

After annealing the nickel specimen in a nitrogen atmosphere, Barkhausen measurements were repeated on positions A, B and C. The results are shown in **figures 2.4.4** and **2.4.5**. The EBE signals from the annealed nickel specimen changed shape compared to the raw 'as-machined' specimen. The EBE envelopes from the annealed surface displayed three peaks; two small peaks on either side of a large central peak. The central EBE peak occurred at a time of 0.54 seconds with the two smaller peaks occurring at 0.31 and 0.84 seconds respectively. After annealing the ABE envelopes appeared double peaked; with a small first peak and a large second peak. The first peak occurred at 0.46 seconds whereas the second peak occurred at 0.80 seconds, which was very close to the maximum ABE peak from the raw 'as-machined' surface. Both the ABE and EBE envelopes began at the start of the recording window. The annealed nickel EBE envelope's rise started earlier in the recording window compared to the original EBE envelope from the raw 'as-machined' surface.

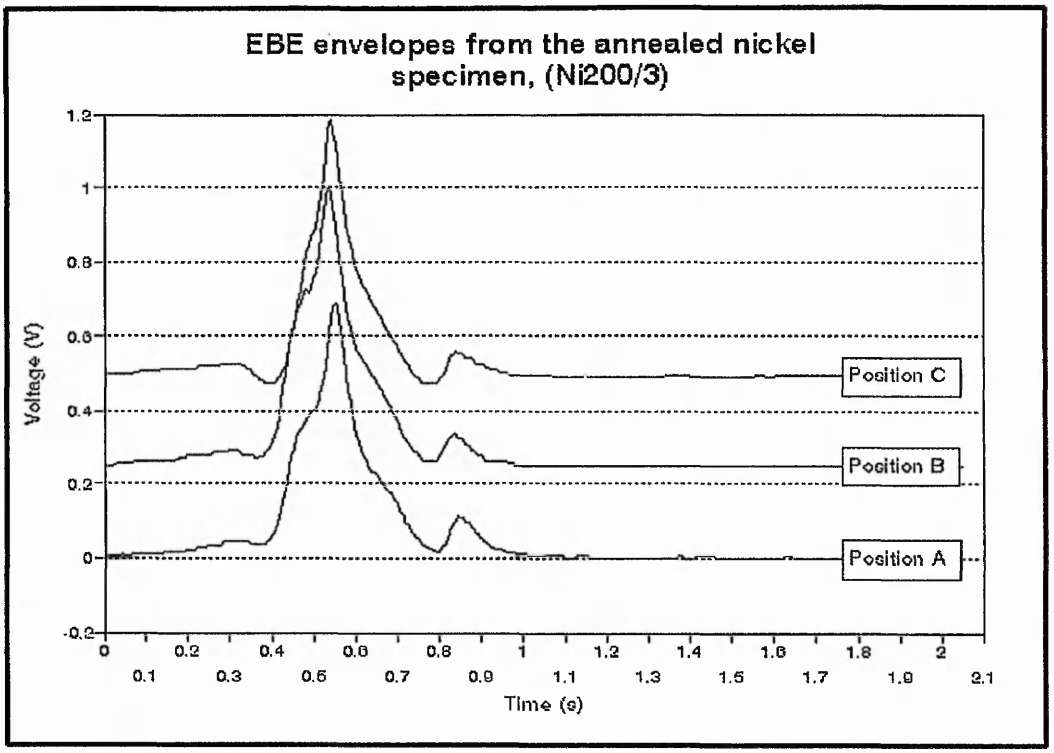


Figure 2.4.4 EBE signal envelopes for differing positions on the annealed nickel specimen.

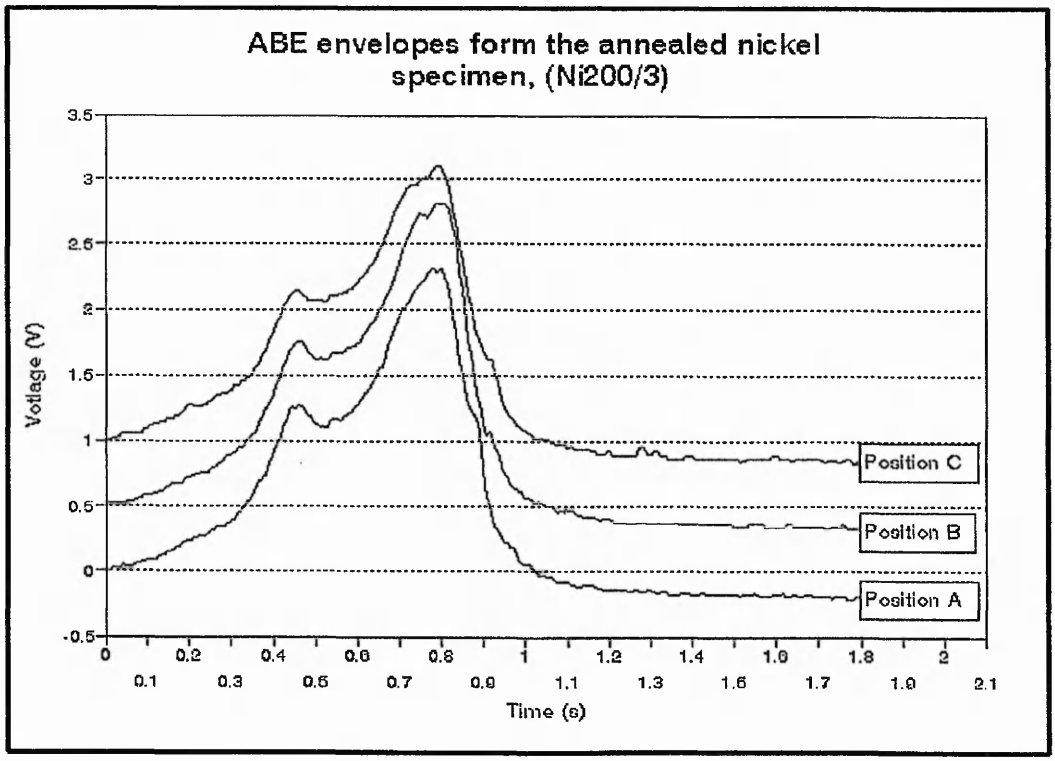


Figure 2.4.5 ABE signal envelopes for differing locations on the annealed nickel specimen.

Once the Barkhausen measurements were completed on the annealed nickel surface, it was then carefully ground and polished to give a revised average specimen thickness of 19.5mm. As before, EBE and ABE signal measurements were taken on all the predetermined positions. All the EBE envelopes on the machined surface (**figure 2.4.6**) appeared similar in shape, though for position 'C' the average signal was slightly smaller. This may have been due to uneven grinding and polishing, which would have led to differing surface disruption characteristics at different regions on the samples surface. The ground and polished surface generated two peaked EBE envelopes; a small peak at around 0.46 seconds and a much larger peak at 0.78 seconds. The time of the large second peak tended towards the original raw 'as-machined' surface's T_P value. The EBE envelope started after 0.3 seconds into the recording window. As expected the ABE envelopes from the machined surface (**figure 2.4.7**) appeared unchanged when compared to the annealed specimen, which is displayed in **figure 2.4.5**. This is because the surface machining did not affect the bulk of the nickel specimen.

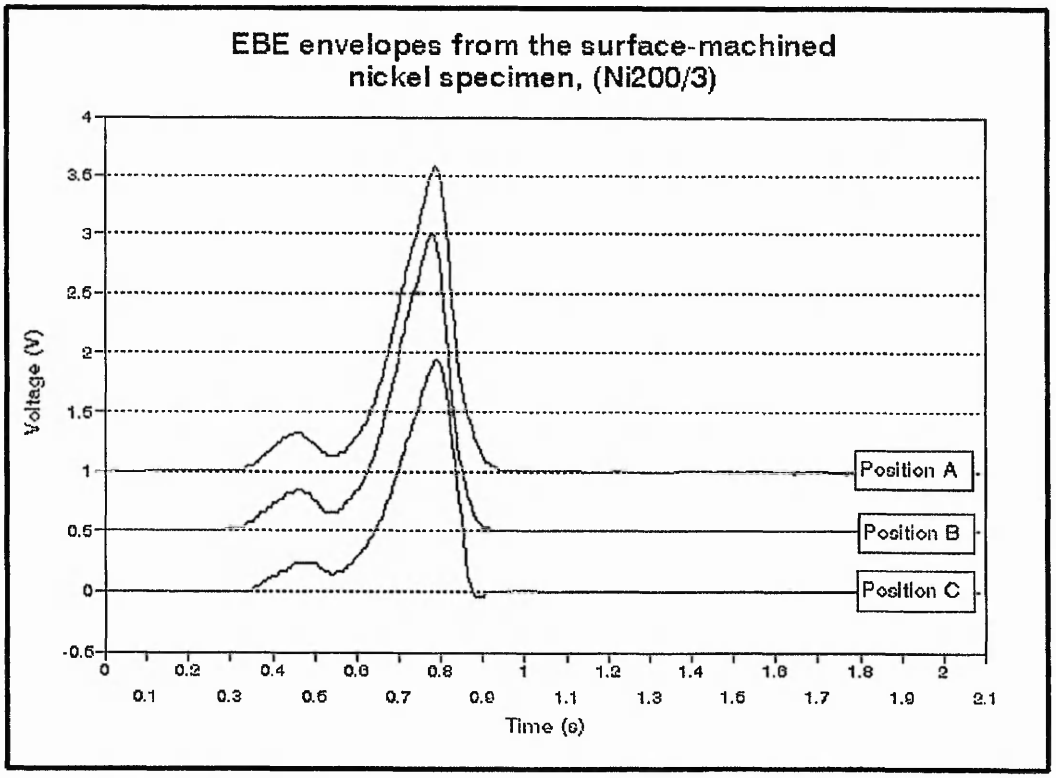


Figure 2.4.6 EBE signal envelopes from different positions on the annealed and then 'surface machined' nickel specimen.

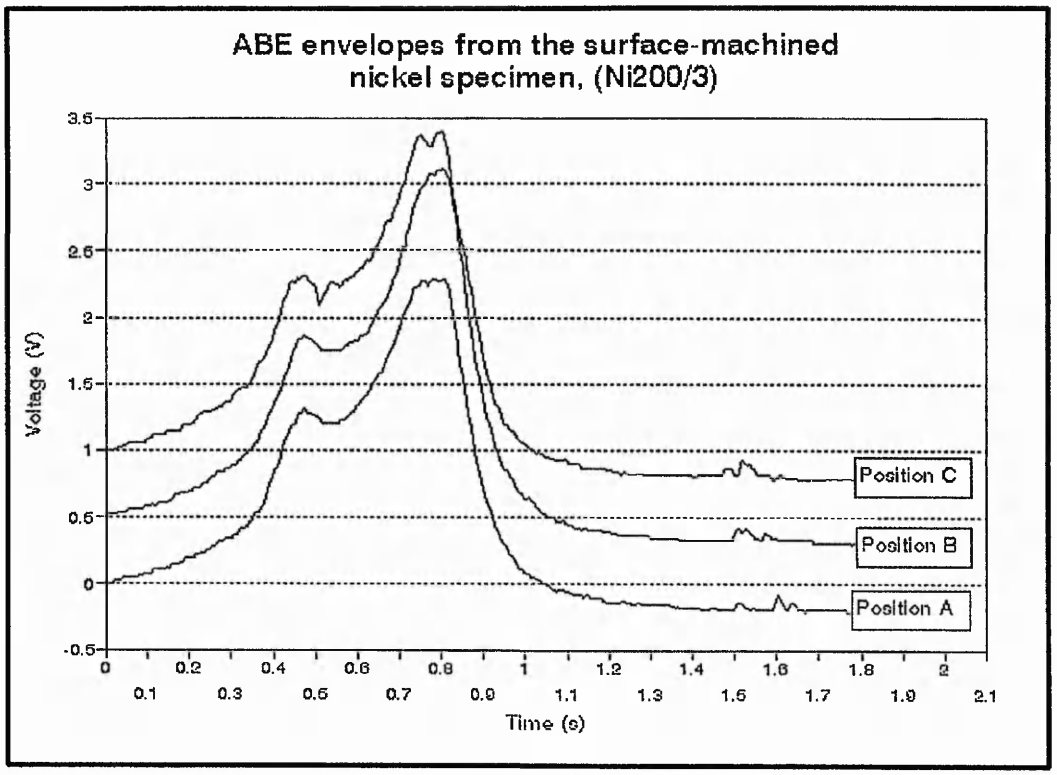


Figure 2.4.7 ABE signal envelopes from different positions on the annealed and then 'surface machined' nickel specimen.

2.4.3. Discussion of the Barkhausen Emission Results.

2.4.3.1. *Discussion of EBE results from the different states of the nickel specimen.*

The EBE envelopes from the three different states of the nickel specimen all exhibited a major single peak, but the 'surface-machined' and annealed surfaces also exhibited smaller secondary and tertiary peaks. The EBE envelopes from the nickel specimen surface's three differing states are shown in **figures 2.4.2, 2.4.4** and **2.4.6**. Considering the data in **table 2.4.1**, taken from these envelopes, the time of the maximum signal peak (T_P) changed from 0.84 seconds for raw 'as-machined' surface to 0.54 seconds for annealed nickel surface. The shape of the EBE signal envelope also changed due to annealing. The EBE signal for the annealed nickel specimen appeared not as a single peak, which was found on the raw 'as-machined' surface, but with two smaller signals on

either side of the large central peak. The annealed surface's EBE envelopes, shown in **figure 2.4.4**, were smaller in magnitude compared with the raw 'as-machined' surface. The annealed surface's envelope gave a maximum signal voltage (V_{MAX}) of approximately 0.7 V, whereas, on the raw 'as-machined' surfaces, the V_{MAX} value was 1.85 V -a voltage value of 2.5 times that of the annealed specimen. This was supposed to be because the annealed specimen had less dislocations and stress anomalies (due to the heat treatment). Dislocations normally oppose domain wall motion and help generate noise by inhibiting smooth change in the **B** field. The high temperature annealing process is expected to increase the nickel grain size and allow the magnetic domain walls to move more freely. Domain wall movement, due to an applied **H** field, was less impeded resulting in a smaller EBE signal amplitude.

The 'surface machined' nickel specimen clearly showed two peaks on the EBE envelopes, the second peak being larger than the first peak. The time of the maximum peak was at 0.78 seconds, which was tending towards the original raw 'as-machined' surface's T_P value. The averaged maximum EBE signal voltage (V_{MAX}) from the machined surface also increased to a value of 2.34 V. This included the EBE envelopes from location 'C' which appeared slightly smaller than the envelopes from locations 'A' and 'B'. The surface machining of the annealed specimen had increased the maximum signal voltage by 3.3 times. The double peaked form of the EBE envelope can be explained as being caused by domain nucleation and motion. In a magnetically saturated pure nickel specimen the reversal of the magnetisation direction would, firstly, nucleate new magnetic domains at the grain boundaries **[2]**. This domain nucleation, when it takes the form of 180° domain wall movement, is thought to generate the first small peak. The second and largest peak is most probably caused by the domain walls breaking away from pinning sites such as grain boundaries that are present within the microstructure.

The EBE signal energy of each of the Barkhausen envelopes is shown in **table 2.4.1**. The raw 'as-machined' surface of the nickel specimen exhibited a signal energy value of 0.298 V^2s. On annealing of the specimen, the signal envelope decreased in size. This reduced the energy to a value to 0.043 V^2s, a decrease of 6.5 times. The residual surface stresses, dislocations and other pinning sites on the 'as-machined' specimen surface

helped generate the initial larger EBE signals. When the annealed surface was re-machined and polished the EBE signal energy became a maximum at a value of $0.568V^2s$. This was nearly twice the signal energy detect from the raw 'as-machined' surface and thirteen times the signal energy from the annealed surface. The grinding and polishing caused large signal energy increases in the EBE envelopes.

Specimen condition.	Time of maximum EBE peak. T_P (s)	Maximum EBE signal voltage. V_{MAX} (V)	EBE Signal energy. (V^2s)
Raw 'as-machined'	0.84 ± 0.01	1.85 ± 0.02	0.298 ± 0.03
Annealed	0.543 ± 0.008	0.70 ± 0.03	0.043 ± 0.008
Surface machined	0.788 ± 0.005	2.34 ± 0.2	0.568 ± 0.1

Table 2.4.1 EBE signal envelope parameters for all three states of the nickel 200 specimen; original raw 'as-machined', annealed and surface machined. The parameter values are averaged for the three location on each of the nickel surfaces.

The **table 2.4.1** shows how shifts in the maximum EBE peak was caused by variations in material property. The raw 'as-machined' surface had a maximum peak at around 0.84 seconds. This was reduced to 0.54 seconds with the crystallographic growth and removal of residual stresses by annealing. On surface machining, the signal amplitude showed an increase and the time of the maximum peak now moved to 0.78 seconds. It is known that the magnetic coercivity of a material (H_c value) is affected by heat treatment, deformation, stress and most of all by dislocations **[2][89]**. It is also known that H_c occurs at a point where the rate of change of **B** versus **H** field is the greatest. This region on the hysteresis curve is where domain wall motion is responsible for the magnetisation reversal and where Barkhausen signals are generated in an annealed nickel specimen **[23]**. The EBE peak and ABE trough have been reported by Hill et al **[90]**. to occur at the point of coercivity for a annealed nickel specimen. This indicated that the late occurrence of maximum EBE peak was a consequence of the residual stress and dislocation density resulting from surface machining of the nickel specimen. This would

signify a change in the coercivity of the surface material. The change in peak position may be a useful tool when carrying out damage assessment due to machining. The later the 'time of peak' the more dislocations and residual stresses are present in the surface layer of the nickel specimen.

The shape of the EBE envelopes also changed for the three different states of the nickel specimen. If the largest peak from each EBE envelope is considered, then a simple observation can be made: it is clear that the shape of the largest peak, in each envelope, is affected by the specimen's surface condition. EBE envelopes form the annealed surface appeared more symmetrical when compared with the envelopes from the machined surface. In an attempt to quantify surface condition from each of the three surface states, the largest peak in the EBE envelope was isolated. The time of the EBE envelope's maximum peak point was then used as a dividing line and the signal energy of the largest peak about this point was calculated. Results from the central position 'B' are displayed in **table 2.4.2**.

(1.) Surface condition of the nickel specimen. [Location 'B']	(2.) The EBE energy of the maximum EBE peak. (V^2s)	(3.) EBE energy from the first half of the main EBE peak. (V^2s)	(4.) Signal energy percentage before the maximum peak time on the main EBE peak.
Raw 'as-machined'	0.266 ± 0.002	0.176 ± 0.002	66 %
Annealed	0.0514 ± 0.002	0.0309 ± 0.002	60 %
Surface machined	0.626 ± 0.02	0.465 ± 0.02	74 %

Table 2.4.2 EBE signal energy from the three different states of the nickel specimen. Column 2: Signal energy of the main peak of the EBE envelopes. Column 3: Signal energy of the first half of the main EBE peak. Column 4 displays the energy of the first half of the maximum EBE peak (column 3) in terms of the total EBE energy of the maximum peak (column 2), expressed as a percentage.

Results displayed in column 4 (of **table 2.4.2**) show the signal energy from the first half of the large EBE peak as a percentage of the total signal energy from that peak. It appeared that the annealed specimen generated a large EBE signal peak which was more symmetrical about the maximum point, i.e. 60% of signal energy was generated before the peak point of the EBE envelope. This, however, changed for the 'surface stressed' state, where an average of 74% signal energy was generated before the maximum peak point. A signal energy value of 67% was found to have been generated before the peak point on the raw 'as-machined' surface. This indicated that reduced stress and pinning concentrations on the surface of the nickel specimen led to the largest peak (in the EBE envelope) being more symmetrical, in terms of signal energy, about the maximum peak point.

2.4.3.2. *Discussion of ABE results from the different states of the nickel specimen.*

ABE envelopes from the raw 'as-machined' surface appeared as broad signals with a single peak envelope (**figure 2.4.3**). The width of the ABE envelope from the raw 'as-machined' specimen was similar to the width of the ABE envelope from the annealed specimen. The annealed nickel specimen was expected to possess a relatively stress free homogeneous microstructure and a reduced pinning density. As a result the ABE envelopes appeared double peaked with the first peak smaller than the second (**figure 2.4.5**). The averaged maximum signal voltage for the ABE envelopes increased from 1.89 V to 2.24 V upon annealing of the raw 'as-machined' specimen.

As seen in **figure 2.4.7**, the ABE envelope detected from the machined surface of the annealed specimen changed very little in size and shape with this surface treatment. This confirmed that the surface machining and polishing did not generate any adverse conditions within the annealed bulk of the nickel specimen. **Table 2.4.3** shows that the ABE signal energy from the raw 'as-machined' state was smaller than the energy from the annealed and 'surface machined' states of the specimen. The signal energy for the annealed and 'surface machined' states of the specimen were very similar. This was

because both states of the nickel specimen essentially had a stress free bulk and identical bulk microstructure. The careful surface modifications by grinding and polishing for the final condition of the sample had only affected a thin surface layer, which in relative comparison was not very significant to the overall ABE from the bulk material. Comparing **figures 2.4.2** and **2.4.3** show that EBE and ABE envelope's 'T_P' values occurred at similar times, around 0.82 s to 0.84 s. This was attributed to the difference in stress and pinning concentrations between surface and bulk of the material in its raw 'as-machined' state. Induced stress and defect differences between the bulk and surface gave similar results. **Figures 2.4.6** and **2.4.7** demonstrate this.

Specimen condition.	Time of maximum ABE peak. T_P (s)	Maximum ABE signal voltage. V_{MAX} (V)	ABE Signal energy. (V^2s)
Raw 'as-machined'	0.821 ± 0.005	1.89 ± 0.05	0.55 ± 0.03
Annealed	0.798 ± 0.005	2.25 ± 0.05	1.29 ± 0.06
Surface machined	0.798 ± 0.006	2.44 ± 0.15	1.43 ± 0.1

Table 2.4.3 ABE signal envelope parameters for all three states of the 'nickel 200' specimen; (i) raw 'as-machined', (ii) annealed and (iii) surface machined.

This ABE envelope shape could be attributed to the higher concentration of domain pinning sites in the raw 'as-machined' nickel specimen. The annealing process reduced the number of pinning sites, grain boundaries, dislocations and stress anomalies. These pinning sites restrict domain wall movement, which in turn, restrict the volume over which there is a change of strain due to domain wall motion. Less dislocations and pinning sites lead to a larger impulsive magnetostrictive change, thus helping to produce the larger ABE signal. ABE amplitude would be expected to be proportional to the magnitude of the magnetostrictive strain. It has been argued by Beal et al. **[91]** that the ABE signal's amplitude is proportional to the volume over which there is a change of strain due to domain wall motion and, hence, to the domain size. The annealing helped

develop larger domains and, therefore, the larger domain wall movements would also help generate larger ABE signals.

In the ABE from the annealed specimen (**figure 2.4.5**), there was a definite trough in the envelope which was not present on the raw 'as-machined' envelopes. ABE signals are generated by sudden changes in magnetostrictive strain due to domain wall motion. It has been argued that since two domains magnetised in the opposite directions separated by a 180° domain wall are strained identically, the movement of the 180° walls does not give rise to ABE signals **[6]**. As the annealed nickel specimen's surface and bulk microstructure were homogenous with respect to domain wall pinning sites, comparing the EBE and ABE envelopes (**figures 2.4.4** and **2.4.5**), it could be seen that the ABE trough coincided with the EBE envelope peak. This gives further credence to the fact that 180° domain walls are acoustically inactive but electromagnetically active.

The shape of the ABE signal envelope for the annealed nickel appeared double peaked with the first peak smaller than the second. The shape and the width of the signal envelope could possibly be attributed to the fact that the nickel specimen, at any moment in time, was not being uniformly magnetised. This was shown by the FE magnetic field modelling (**section 2.2**). The ABE was generated, throughout the volume of the specimen, due to the motion of the non-180° domain walls. Depending on the pinning strength, different domain walls will have different critical field values at different times for domain wall break-away. As the applied field on the domain walls increased, they began to breakaway from their pinning sites. A range of applied magnetic field values will be required to overcome the differing domain wall pinning site energies, which will also appear at different times. As the specimen is not uniformly magnetised at any given moment, this could suggest a mechanism for ABE envelope broadening.

END *of* CHAPTER

CHAPTER 3

BARKHAUSEN EMISSION AROUND SURFACE BREAKING DEFECTS

3. BARKHAUSEN EMISSION AROUND SURFACE BREAKING DEFECTS.

Common ferromagnetic engineering materials are generally classed as ductile materials and due to certain manufacturing techniques or under prolonged and excessive service conditions cracks and defects may result. In order to achieve an understanding of the effects of such defects on the Barkhausen emission a series of experiments using an idealised crack were carried out. A surface breaking cracked specimen was simulated using a slotted specimen and the effect of this on the Barkhausen emission (BE) is considered in this section. Initially, both Acoustic and Electromagnetic Barkhausen emission from the slotted specimen were characterised and explained in terms of the sample history. As well as the direct effect of the slot, the Barkhausen emission was detected using different sized probes. The differing spatial resolution provided by the probes and their effect on the EBE envelope is commented on. Two different magnetising systems were also used and the resulting magnetisation rates on the BE are assessed in order to gain a greater understanding of the processes involved. Finally, a fatigue cracked steel specimen was studied using both EBE and ABE. The effect of the presence of the crack within the steel specimen on the Barkhausen emission is examined and discussed.

3.1. BARKHAUSEN EMISSION FROM A SPECIMEN CONTAINING A SLOT.

Barkhausen emission from a steel specimen containing a slot was considered in this section. It was expected that the slotted specimen would provide an insight into the effect of a surface breaking crack on Barkhausen Emission (BE). A low carbon steel specimen was supplied by British Gas Plc., (serial number OLI-95D).

3.1.1. Experimental Detail and Specimen Labelling.

A steel specimen (serial number OLI 95D) had a slot cut into its surface. The specimen dimensions were 125 mm long by 30 mm wide with a depth of 10 mm, (**figure 3.1.1**). A slot, with a depth of approximately 7 mm, was located on the central position of the specimen. The slot width was approximately 0.25 mm and it crossed the entire width of the steel specimen. An Electrical Discharge Machine (EDM) wire cutter was used to create the slot. The slot was filled with a polymer resin to prevent corrosion. The slotted steel specimen was cut to size from a longer specimen. The specimen serial number was stamped on one side of the slot and this side was referred to as the right hand side of the specimen. The surface of the slotted specimen was marked with positions where Barkhausen measurements could be taken. These positions were located along the central axis and drawn on the specimen surface (**figure 3.1.2**).

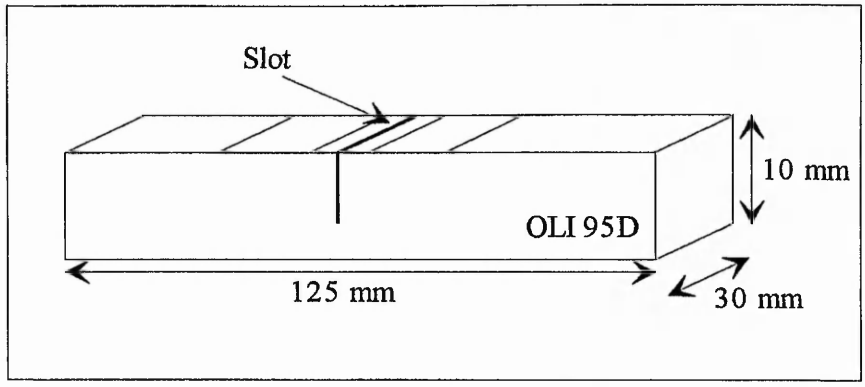


Figure 3.1.1 The dimensions of the mild steel slotted specimen (OLI-95D).

The standard Griffin & George Barkhausen magnetising yoke, discussed in **chapter 1**, was used. The magnetising frequency remained at 0.1Hz for this work. The sensor used for the EBE measurements was an "eddy current" pencil probe produced by Hocking NDT Ltd. This sensor provided a small contact point on the surface of the specimen. The probe consisted of a coil wound around a ferrite core of inductance 1.5mH. This was sufficient to provide clear Barkhausen signal envelopes, having a similar shape to those from the large coil EBE transducer, but with the added advantage of allowing higher spatial resolution for measurements.

Barkhausen measurements were taken either side of the slot. EBE measurements using the Hocking pencil probe sensor were recorded from ten different locations on the surface of the steel slotted specimen, as shown in **figure 3.1.2**. Measurements were recorded at a distances of 20 mm to 2.5 mm on either side of the slot. The direction left of the slot is referred to as the negative direction and each position was assigned a label, ranging from 'A' (-20 mm) through to 'J' (+20 mm).

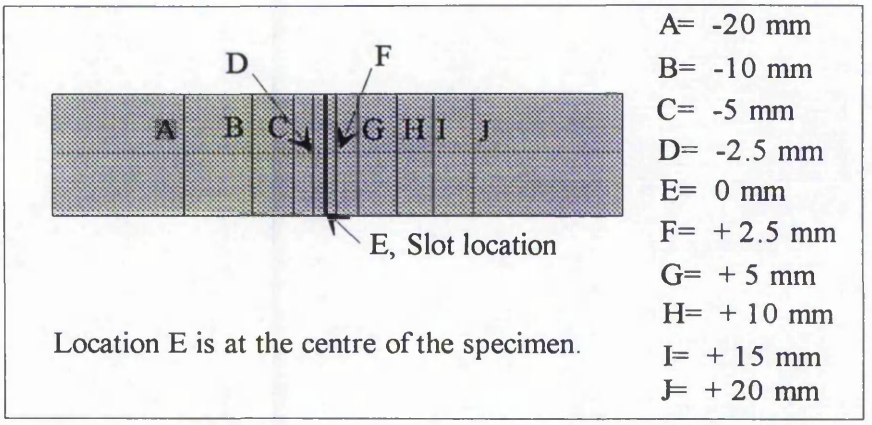


Figure 3.1.2 Positions for EBE measurement detected using the Hocking pencil probe from the steel slotted specimen (OLI-95D).

Acoustic Barkhausen Emission (ABE) measurements were also conducted on the slotted specimen. The 175 kHz piezoelectric transducer, 23 mm in diameter, was used to detect the ABE signals. The surface of the specimen was divided into seven positions, labelled A to G and are shown in **figure 3.1.3**. The ABE positions were different to the EBE positions. The furthest measurements were recorded at a distance of 20 mm on either side of the slot. The nearest measurements to the slot were taken 5 mm on either side. Distances from the slot refer to the centre of the ABE sensor.

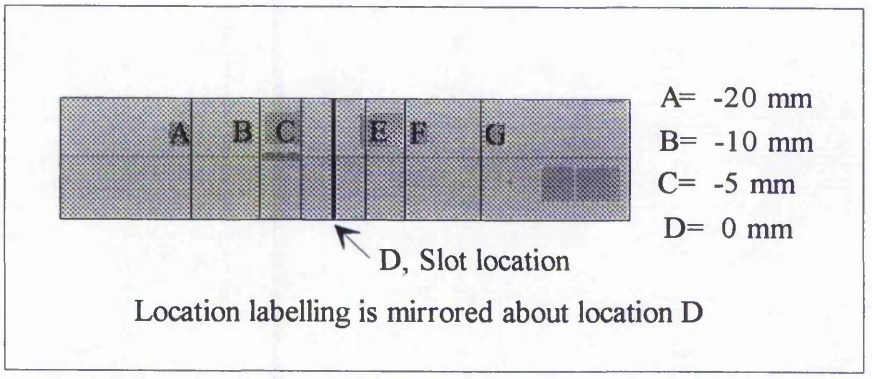


Figure 3.1.3 Steel slotted specimen's (OLI-95D) surface labelling for the ABE measurements using the 175kHz piezoelectric transducer.

3.1.2. Barkhausen Emission Results from the Slotted Specimen.

3.1.2.1. *EBE results detected from the steel slotted specimen using a pencil probe.*

The EBE envelopes detected using the pencil probe are shown in **figures 3.1.4** and **3.1.5**. The Barkhausen signal envelope changed shape as the sensor approached the slot from location 'A' on the specimen. On location 'A' (-20 mm from the slot) the EBE envelope appeared as a single peak, with a dome shaped top. The EBE envelopes began to split into two peaks as the probe approached the slot. Directly on the slot, the signal envelope possessed two distinct peaks, with the first peak larger than the second. Traversing toward location 'J,' away from the slot, the double peaked envelopes were found to gradually recombine into a single peak **(figure 3.1.5)**. On locations 'F' to 'J' on the specimen the EBE envelopes also possessed a larger amplitude. The EBE envelopes detected from close to the slot exhibited the double peaked effect. The width of the signal envelopes did not change throughout the experiment. The central region of the EBE envelope decreased in magnitude as the probe approached the slot and this was observed on both sides of the slot.

The EBE signals from the different locations across the surface of the steel slotted specimens exhibited differently shaped envelopes, as shown in **figures 3.1.4** and **3.1.5**. Each of the three different Barkhausen envelope parameters, T_P, V_{MAX} and signal energy, (as discussed in **chapter 2**) are now considered. **Figure 3.1.6** shows the 'time of peak' (T_P) and 'maximum signal voltage' (V_{MAX}) for each EBE envelope from across the surface of the specimen. As the slot was approached the EBE signals T_P value occurred earlier, as a result of the envelope splitting. On location 'A' the T_P value was recorded at **0.71 s** on the envelope, while the T_P from location 'F' (+2.5 mm from the slot) was recorded at **0.56 s**; the earliest peak for all the detected EBE envelopes. On the slot itself the time of maximum peak occurred at **0.57 s**; very close to the earliest T_P value. The splitting of the EBE envelope is known to occur in the presence of a strong demagnetising field, which arises due to the presence of a slot **[92]**.

The EBE envelopes' 'maximum signal voltage' (V_{MAX}) decreased from **0.51 V** on location 'A' down to **0.43 V** on location 'C', as seen in **figure 3.1.6**. On location 'D' (-2.5 mm from the slot) the V_{MAX} began to increase in magnitude. Directly above the slot the V_{MAX} was recorded at **0.60 V**. Moving past the slot, on to the right hand side of the specimen, the V_{MAX} amplitude continued to increase to a maximum on location 'G' and 'H'. The maximum signal voltage was constant for both these locations at a value of **0.70 V**. Further measurements showed that the EBE envelopes amplitude (V_{MAX}) decreased as the probe was moved further away from the slot.

The signal energy parameter was also extracted from the detected EBE envelopes and is summarised in **figure 3.1.7**. Signal energy analysis showed an energy minimum of **0.035 V^2s** very close to the slot, on location 'D'. The signal energy was found to reach a maximum (**0.095 V^2s**) at location 'H'. It was also noted that the signal energies from location 'A' to 'D' were smaller in magnitude compared to locations 'F' to 'J' and the overall trend was very similar to the V_{MAX} profile shown in **figure 3.1.6**. Generally, the EBE signal energy on the right hand side of the slot was larger compared to the signal energies obtained from the left hand side.

The splitting of the single peaked EBE envelope into the double peaked form was caused by the presence of the slot and the demagnetisation field on the slot edges **[92]**. The demagnetising field has been shown to tilt the magnetic hysteresis loop of the specimen, reducing the gradient of the near linear region of the hysteresis. This leads to the double peaked EBE envelope. Also, due to the high temperatures involved in EDM machining, the immediate region on either side of the slot is expected to have been stress relieved. This is expected to aid early generation of the EBE peak. Due to the size of the slot the EBE envelope splitting is mainly caused by the demagnetising field.

The slot acts as a extra reluctance in the magnetic circuit created by the specimen and the magnetisation system. This increased reluctance causes magnetic flux leakage to occur. The resulting change in the direction of the magnetisation vector around the slot created the differences in the magnitude of the EBE envelopes size. On top of the slot the flux

leakage was the greatest. The rounded design of the pencil probe tip diverts flux into the transducer. This increases the size of the Barkhausen signal **[13]**.

At manufacture, the slotted specimen was originally cut and then broken off from a longer specimen. This breaking process produced a lip on the left hand edge indicating that the slotted specimen had undergone severe straining. The strained left side of the specimen, (location 'A' through to 'D'), explained the late EBE signal's T_P value. On the right hand side of the specimen the signal energies were larger than the left. This was probably due to the specimen having uneven material property and residual stress resulting from the straining process. It is know that highly stressed steels exhibit low EBE amplitudes. This may explain why the signals on the left hand side of the slot had a lower amplitudes as well as low signal energy profiles (**figures 3.1.6** and **3.17**).

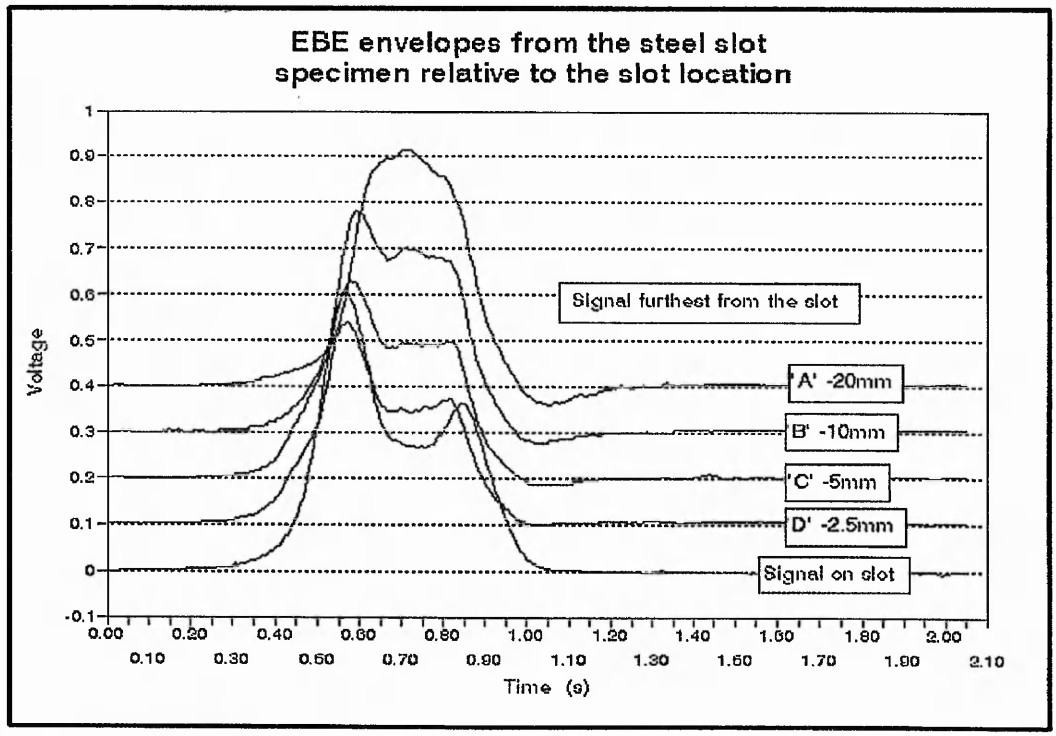


Figure 3.1.4 EBE envelopes detected using a pencil probe sensor, moving towards the slot from the left hand side (position A to E).

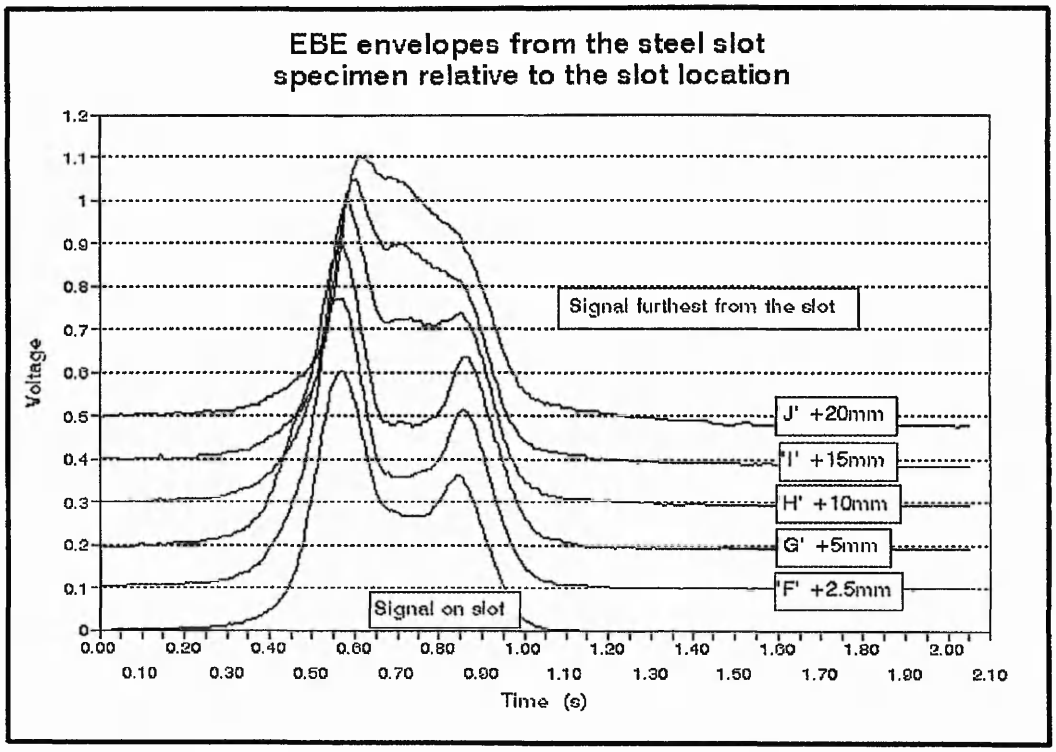


Figure 3.1.5 EBE envelopes detected using a pencil probe sensor, moving away from the slot. (position E to J).

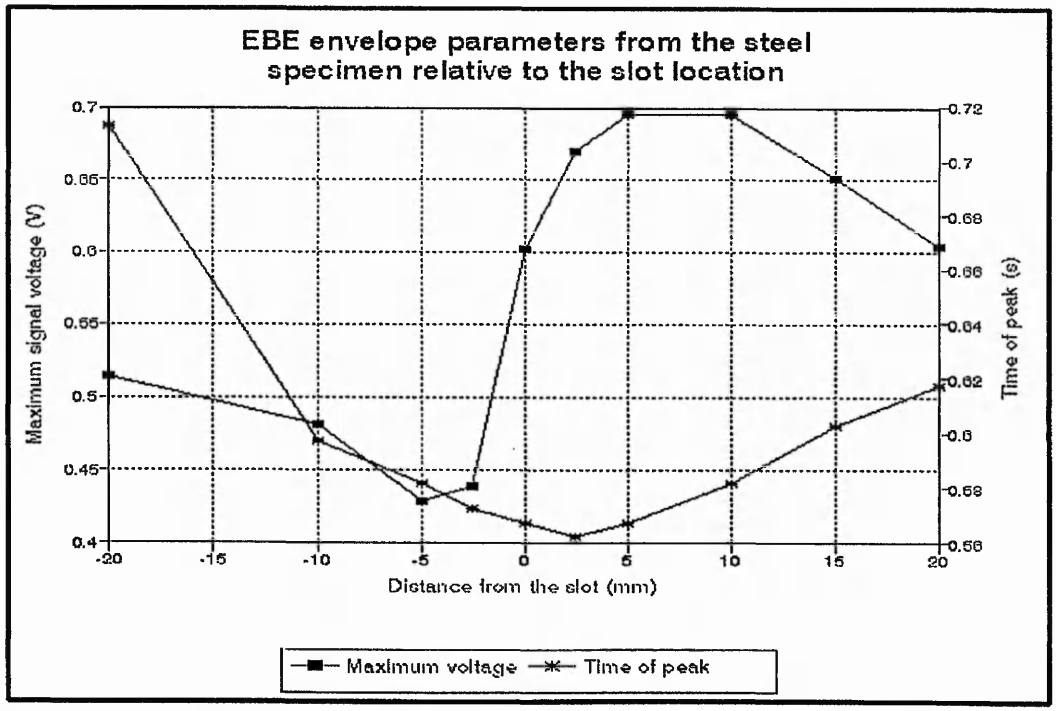


Figure 3.1.6 Maximum signal voltage (V_{MAX}) and time of maximum signal peak (T_P) with respect to the slot location.

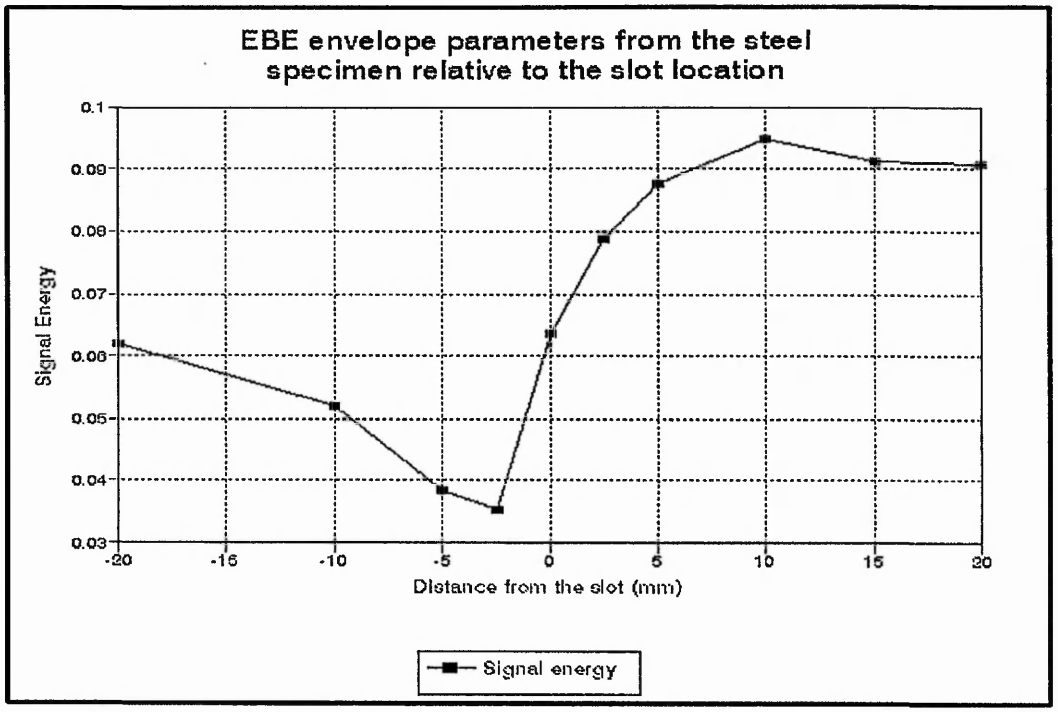


Figure 3.1.7 EBE signal energy (units V^2s) from the EBE envelopes detected from across the surface of the steel slotted specimen.

3.1.2.2. *ABE results detected from the steel slotted specimen.*

ABE is a volume effect (**chapter 2.3**) and, as such, is not expected to be sensitive to the presence of a small defect, such as a fine crack. However, if the crack is of a significant size then it is possible that the detected ABE will be affected by its presence due to the screening off of part of the specimen volume. The modified reluctance and demagnetising field resulting from a large crack may also affect the ABE envelope shape. Also, ABE is known to be sensitive to stress and it may provide a useful indication of the stressed regions (generated by the presence of a crack) within the surrounding bulk material. In this section the effect on the ABE of an idealised crack is studied. A slot was used to represent an idealised crack and these results are expected to aid interpretation of ABE data from a real crack.

ABE measurements were carried out on the slotted specimen with particular emphasis on the region around the slot. The ABE envelopes are shown in **figure 3.1.8** and **figure 3.1.9**. The detected ABE envelopes were all of a double peaked form; the first peak was small and the second peak larger. As the transducer was brought closer to the slot the magnitude of the ABE envelopes became larger. Location 'E' (+5 mm on the right hand side of the slot) exhibited an unusually large signal in comparison with the rest of the envelopes from the specimen. Repeated measurements found this large envelope to be reproducible. The ABE envelope detected on location 'C' was found to be the largest on the left hand side of the specimen. The envelope from location 'C' was considerably smaller than the envelope from location 'E'.

The ABE envelope V_{MAX} parameter appeared to increase as the slot was approached from both sides (**figure 3.1.10**). Locations on either side of the slot showed the highest signal voltage at **1.58 V** and **2.20 V**, compared to that obtained from the slot (**1.54V**). Location 'E' (+5 mm from the slot) in comparison with the other envelopes, exhibited an unusually large signal voltage (**2.20 V**). The ABE envelopes' T_P value was found to be relatively constant and did not vary as the transducer's position changed. The ABE envelopes' signal energies are plotted for various transducer positions in **figure 3.1.10**.

The trend shown by the V_{MAX} signal amplitude was found to be reflected in the signal energy profile of the specimen. The very large signal energy located next to the slot (on position 'E'), was only detected on one side and was found to be a material phenomenon. Generally, the ABE signal energy increased as the transducer approached the slot, (**figure 3.1.10**). The reason for this increase may have been due to the creation of the slot, which is known to have changed the metallurgical characteristics of the surrounding material.

A changed stress state may result from different thermally affected regions within the specimen, thus, creating differing ABE signal energy. The immediate region surrounding the slot would be thermally stress relieved, as EDM machining was used to create the slot. EDM works by melting and vaporising the metal at very high temperature **[93]** and is discussed in greater depth in **chapter 4**. ABE signals are generated as the domain walls move by sudden discontinuous jumps. This causes sudden changes in the magnetostrictive strain, which in turn generates acoustic waves. It is expected that the EDM machining would affect both sides of the slot equally. Therefore, the thermally affected regions on either side of the slot was expected to be under a relaxed stress state (stress relieved), which is known to encourage the observed large ABE signals. However, the -5 mm position exhibited a lower signal energy value compared to the +5mm position, as shown in **figure 3.1.10**. This observation may be explained by considering the specimen history. After the creation of the slot the left side of the OLI-95D specimen was partially cut and then broken off from a longer specimen, this is expected to have added residual stress around location 'C', thus suppressing the detected ABE envelope compared to location 'E'.

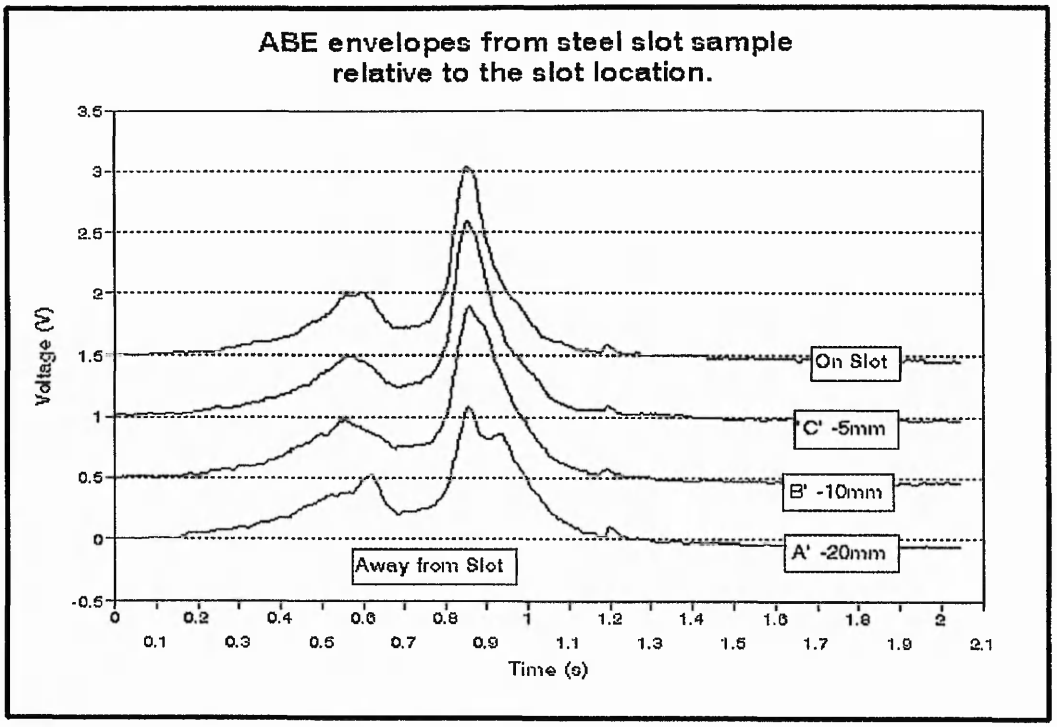


Figure 3.1.8 ABE signal envelopes detected from the steel slotted specimen (OLI 95D), locations 'A' to 'D'.

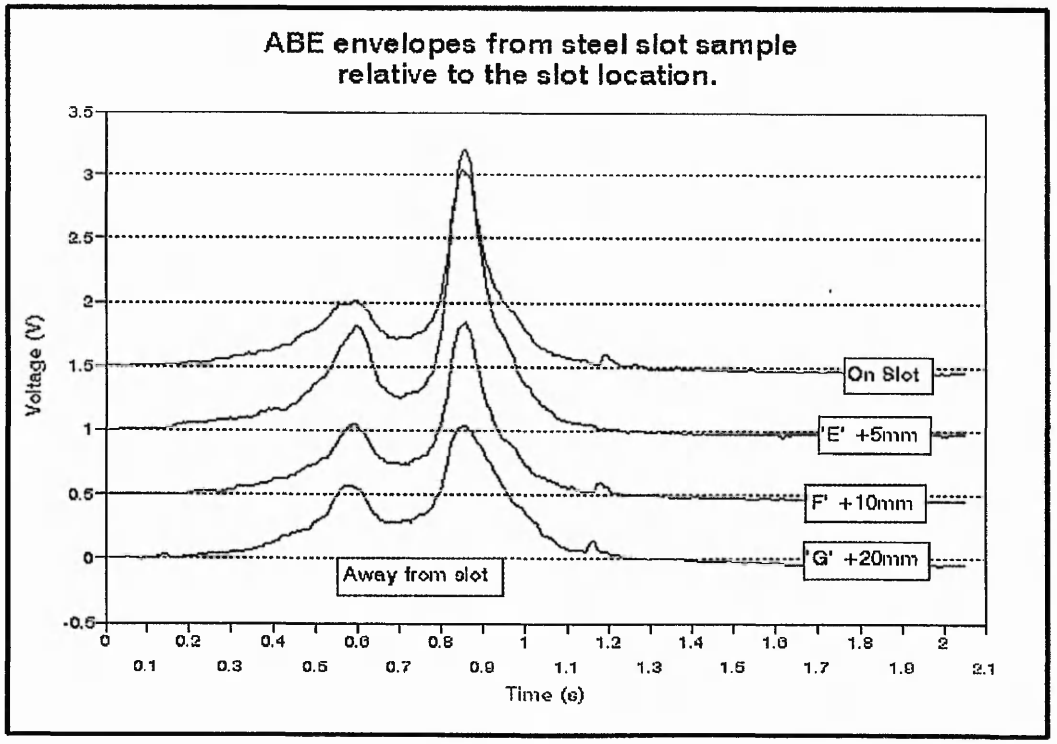


Figure 3.1.9 ABE signal envelopes detected from the steel slotted specimen (OLI 95D), locations 'D' to 'G'.

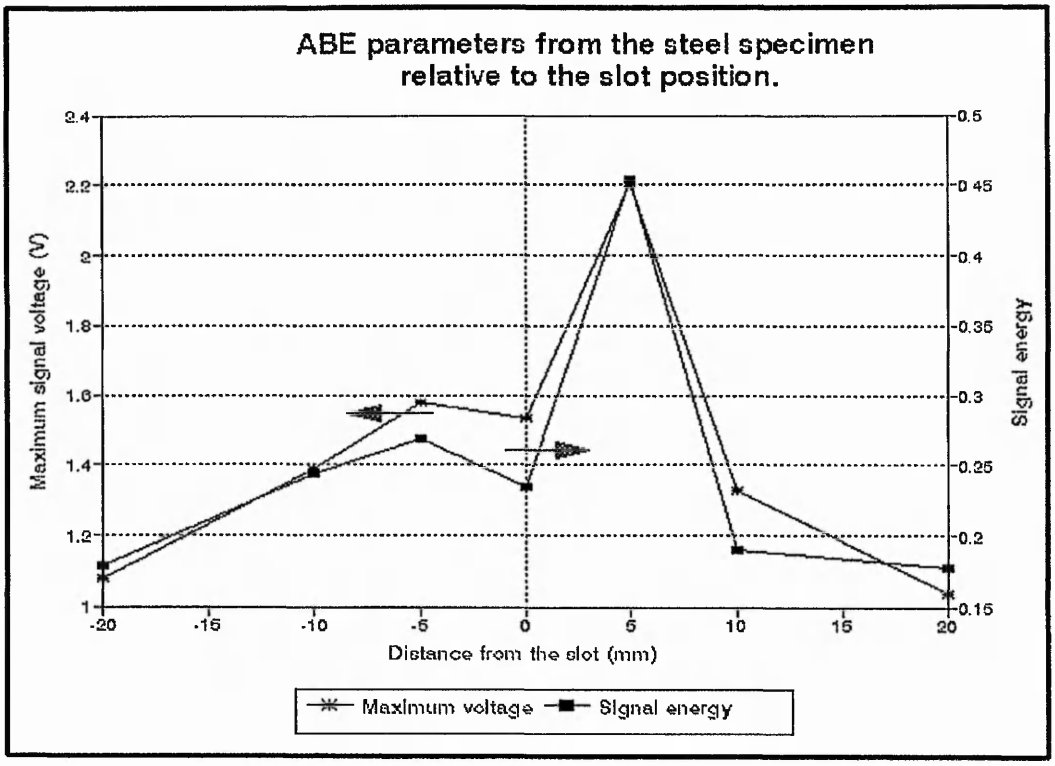


Figure 3.1.10 ABE 'maximum signal voltage' (V) and signal energy (V^2s) from different locations relative to the steel slot position.

Generally, the effect of a slot (idealised surface crack) has shown that EBE signals are sensitive to, and can be used for the detection of, surface breaking defects. Using a high resolution (small) sensor, EBE envelopes were shown to gradually split into double peaked envelopes, as the defect was approached. The 'time of peak' was a good indicator of the slot location. This was due to the demagnetising effect caused by the presence of the slot, which resulted in the envelope splitting. Although the ABE envelopes were not expected to directly locate the slot, they, however, showed that the region around the slot possessed a raised signal energy which was different from the rest of the specimen. ABE, under certain conditions, may also be used as an indicator of the location of the slot.

3.2. BARKHAUSEN EMISSION FROM A SLOTTED SPECIMEN DETECTED USING A LARGE COIL SENSOR.

3.2.1. Experimental Detail and Specimen Surface Labelling.

Using the large coil EBE transducer, the surface of the steel slotted specimen was studied further. The BE signals using the large coil transducer, as compared to the pencil probe (**section 3.1**), were expected to provide an improved understanding of the effect of transducer size, and hopefully, to indicate which might be the more suitable transducer.

The large coil transducer, with a soft ferrite core, described in the **chapter 1**, was used to detect EBE signals from the steel slotted specimen OLI-95D. The coil transducer covered a larger inspection area compared to the pencil probe, and thus, spatial resolution was reduced. EBE measurements were taken at various positions across the surface of the specimen, passing over the slot itself. Five separate locations on the specimen's surface were studied; the slot and 10 mm and 15 mm in either direction from the slot. These five locations were also labelled from 'A' through to 'E' and are shown in **figure 3.2.1**.

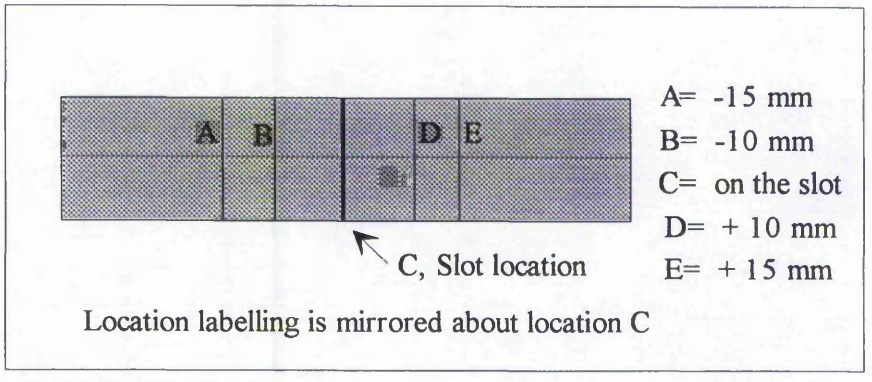


Figure 3.2.1 Surface labelling on the steel slotted specimen (OLI-95D) for the EBE measurements using the large coil transducer.

3.2.2. The EBE Results from the Slotted Specimen Detected Using the Large Coil Transducer.

The EBE signal envelopes obtained using the large coil transducer are shown in **figure 3.2.2**. The large coil transducer produced larger EBE envelopes, which were very similar in shape compared to the pencil probe sensor. An EBE envelope increase in magnitude was expected, since the large transducer had a greater number of coil turns compared with the pencil probe and it also covered a larger inspection area. As the slot was approached from position 'A', the EBE envelopes showed gradual change from a single dome shaped peak, into a complex three peaked plateaued envelope on top of the slot. Once past the slot, the EBE envelopes began to change back into a single peak. These envelopes mirror the results in **figures 3.1.4** and **3.1.5**, obtained using the pencil probe sensor.

The width of the plateau on the signal from above the slot (location 'C') may be a direct indicator of the slot width. Work by Bhattacharya **[92]** showed that the demagnetising field, due to a through slot, caused the EBE envelope to split. With a greater slot gap, the signal splitting was found to increase. Therefore, this raises the possibility that with a higher spatial resolution sensor, it may be possible to determine the width of a surface breaking stress crack.

The EBE envelope V_{MAX} profile **(figure 3.2.3)** exhibited a similar pattern to that observed using the pencil probe, **(figure 3.1.6)**. The maximum signal voltages from locations 'A' **(2.66 V)** and 'B' **(2.13 V)** were smaller compared to the V_{MAX} from positions 'D' **(3.58 V)** and 'E' **(3.36 V)**. Similar to the results obtained in **section 3.1.2** the left side of the slotted specimen exhibited a lower maximum signal voltages compared to the right hand side. A relative comparison of amplitudes showed that signals from location 'A' and location 'B' were 97% and 78% of the signal amplitude from the slot. This, however, changes to 132% and 124% for location 'D' and 'E'.

For the sensor positioned on the slot, the time of peak (T_P) was shown to occur earliest at **0.53 s** on the envelope (see **figure 3.2.3**). This was due to the splitting of the EBE envelope and was as previously observed in **section 3.1.2**. Using the large coil transducer, the T_P parameter from the EBE envelopes might be used to detect the slot position.

EBE signal energies from across the surface of the slotted specimen exhibited an energy minimum on the left side of the slot. **Figure 3.2.4** shows that the variation of EBE signal energy with position is similar to that for V_{MAX}. Since the large coil transducer covered a greater area of the slotted specimen and had a larger number of turns, a larger signal was recorded for a given flux change; for example, the crack location exhibited a signal energy value of **1.25 V^2s**, while on the same location the pencil probe detected n energy value of **0.064 V^2s**. The magnitude of these recorded EBE envelopes can be seen (in **figure 3.1.4** and **figure 3.2.2**) to change significantly from a given location depending on the probe size. The EBE energy profile recorded a minimum on the left side of the specimen and this result was also found using the pencil probe sensor. A large coil transducer may be useful for quickly detecting the approximate location of a slot type surface breaking defect, with the higher resolution probe providing a more localised Barkhausen defect detection.

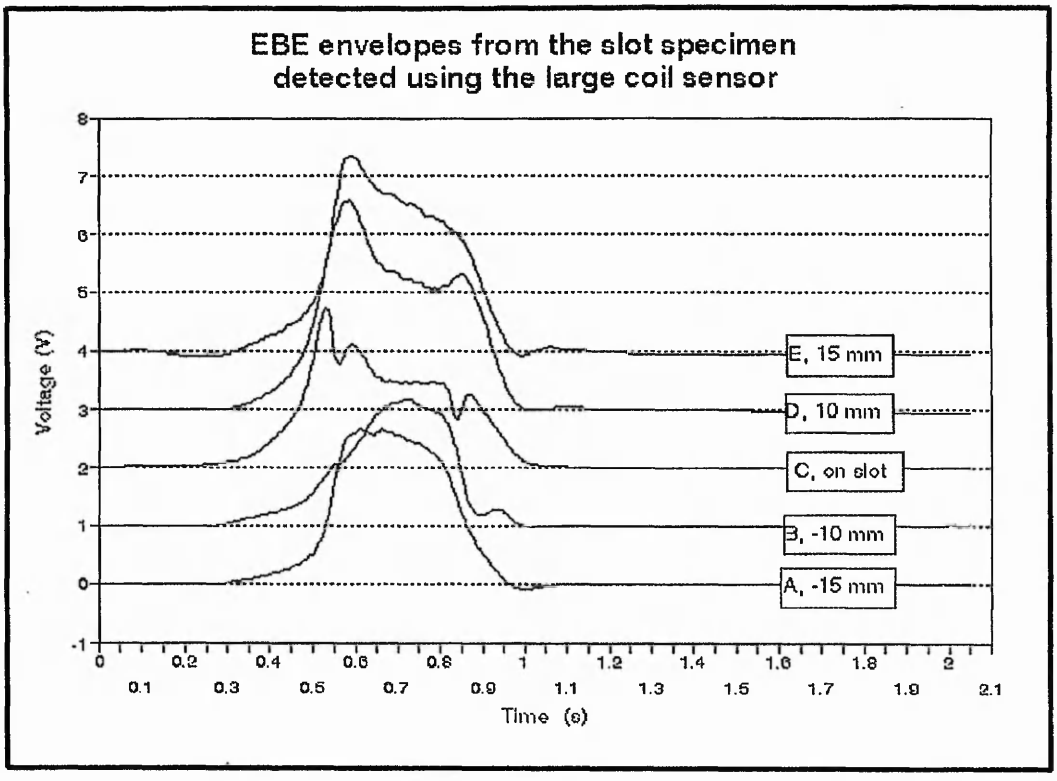


Figure 3.2.2 EBE signal envelopes detected, using the large wound coil transducer, from across the surface of the steel slotted specimen (OLI-95D).

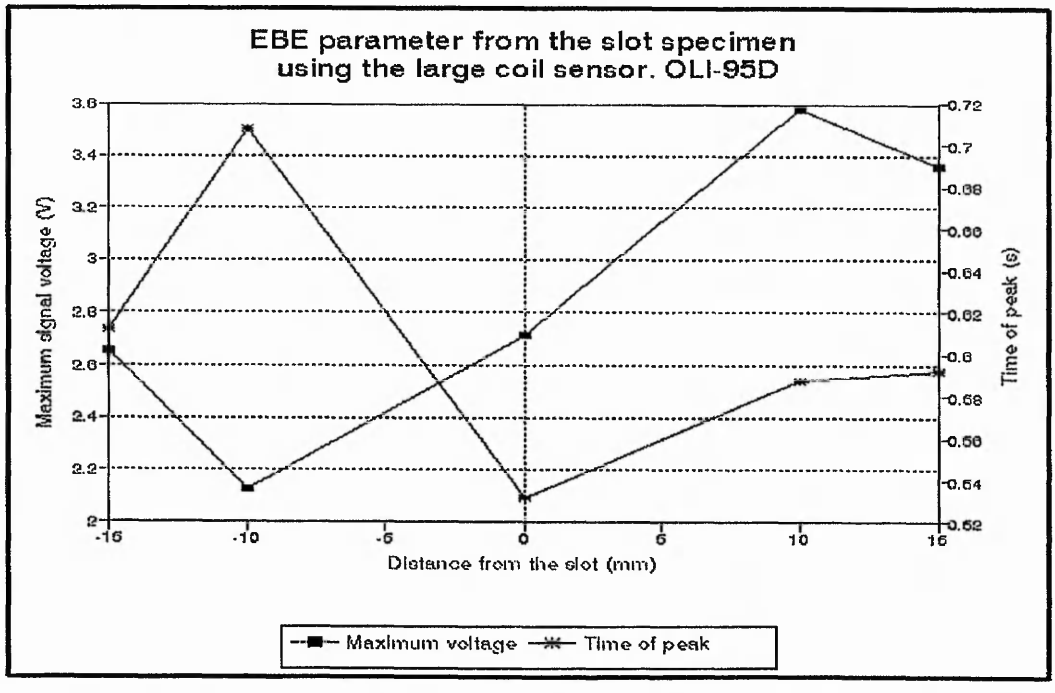


Figure 3.2.3 Maximum signal voltage (V_{MAX}) and the time of peak (T_P) with respect to the steel specimen slot location (specimen OLI-95D).

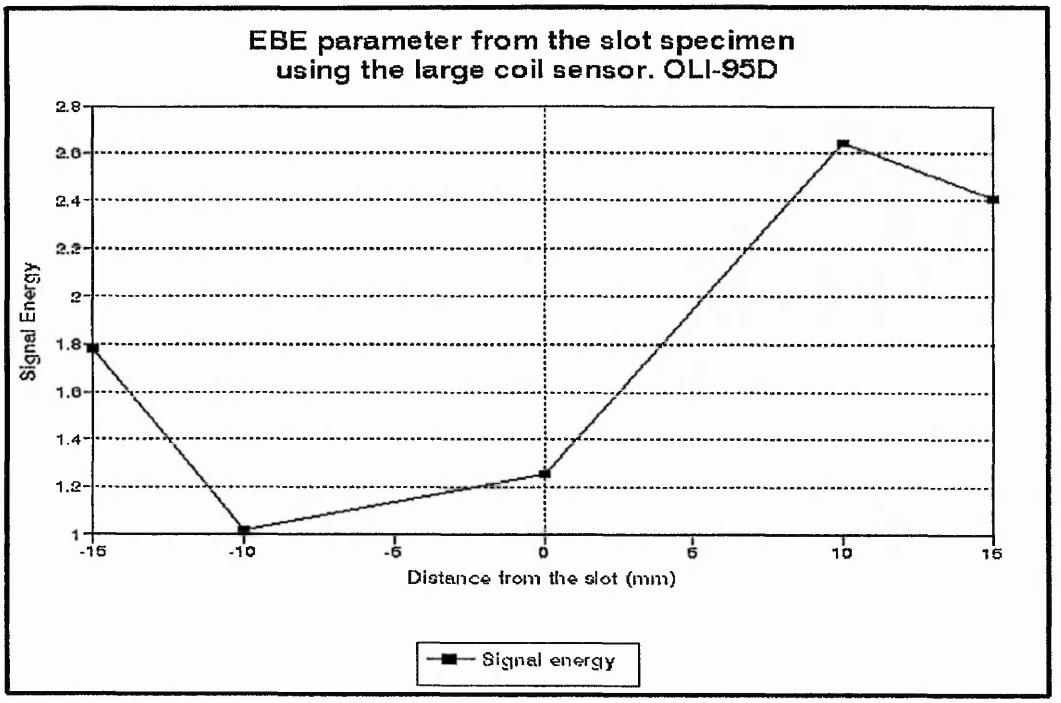


Figure 3.2.4 EBE signal energy (units V^2s) from across the OLI-95D steel slotted specimen surface.

3.3. BARKHAUSEN EMISSION FROM THE SLOTTED SPECIMEN MAGNETISED USING A HAND HELD 'Y6' ELECTROMAGNET.

3.3.1. Experimental Detail and Specimen Surface Labelling.

Using a hand held Magnaflux magnetic yoke, model 'Y6', the experiments discussed in **section 3.2** were repeated using the large coil EBE sensor. The 'Y6' electromagnet is designed for on-site magnetic non-destructive testing of ferromagnetic structures. A maximum current of 2.5A was passed through the 'Y6' electromagnet. This was exactly the same current as used with the Griffin and George electromagnet. The 'Y6' yoke produced a lower magnetising field, which in turn created a lower magnetisation level within the specimen. No attempts were made to measure the magnetic field generated by this electromagnet. The effect of a lower magnetising field in the slotted specimen is studied in this section. It was found that the pencil probe as well as the ABE transducer were both unable to measure the Barkhausen signals using the Y6 yoke. This was due to the lower rate of change of magnetic field, which generated a lower amplitude Barkhausen noise signal. The large coil transducer, however, was able to detect the Barkhausen envelopes from the steel slotted specimen (OLI-95D) without the need for greater signal amplification. The steel slotted specimen's surface was labelled in exactly the same way as discussed in the **section 3.2**. Five separate locations on the specimen's surface were studied; the slot itself, 10 mm and 15 mm in either direction from the slot (**figure 3.2.1**).

3.3.2. EBE Results from the Slotted Specimen Magnetised using Hand Held Yoke.

The EBE data detected from the predetermined positions on the slotted specimen's surface is shown in **figure 3.3.1** and summarised in **figure 3.3.2** and **figure 3.3.3**. The Barkhausen envelopes detected from these position appeared in two forms only; either a broad single peak or a double peak (see **figure 3.3.1**). The lower magnetisation rate

removed the finer details from the EBE signal. Unlike measurements taken with the standard Griffin and George magnetising system, the double peaked envelope was only found directly on top of the slot. All the other EBE envelopes detected from the various locations remained very similar in shape. This was very different from the EBE envelopes discussed in **section 3.2** and these differences are discussed below.

The width of the EBE envelopes greatly increased compared to the envelopes obtained using the Griffin and George magnetising yoke. The EBE envelopes generated using the 'Y6' yoke had a signal duration which lasted for approximately **1.7 s**. Using the original magnetising system, the EBE signal duration lasted for approximately **1.0 s** for both the pencil probe and large coil transducer. This showed that magnetising rate significantly affected the Barkhausen envelopes and similar observation have also been reported by Tiitto **[87][24][83]**.

The V_{MAX} values detected from across this specimen also changed, depending on the magnetisation system. With the hand-held 'Y6' electromagnet experimental arrangement, the maximum EBE envelope was detected from the slot location with a value of **1.36 V** (**figure 3.3.2**). This was a consequence of the signal splitting. The maximum signal voltage peaks, from the 5 different locations, varied over a **0.23 V** range. Measurements carried out on the slotted specimen (OLI 95D), using the large coil sensor, but differing magnetising system (higher rate of change of magnetising field) provided EBE envelopes which varied in amplitudes by **1.46 V**, (**figure 3.2.3**). The T_P value alone was able to distinguish between EBE envelopes away from the slot and on the slot. This was due to the signal splitting effect, which in turn caused the maximum peak height to occur earlier.

Figure 3.3.3 shows the signal energies from different positions on the slotted specimens surface. As the sensor was moved across the specimen, left to right, signal energies decreased on approach to the slot. Beyond the slot, the signal energies increased slightly and then dipped again. The overall energy profile shown in **figure 3.3.3** is unlike the energy profiles detected using the pencil probe and large coil sensor (**section 3.1** and **3.2**).

The lower magnetisation rate achieved using the hand-held yoke resulted in the loss of fine detail on the EBE envelope. **Section 3.1** and **3.2** have shown that the two different sizes of EBE sensors detected very similar envelopes from across the slotted specimen's surface. The higher magnetisation rate (achieved using the Griffin and George yoke) generated EBE envelopes which varied depending on the location where the measurements were taken. The hand-held yoke's lower magnetisation rate, combined with the large EBE transducer provided a means of detecting just the slot, and avoiding all other minor signal fine structure. The signal splitting effect, caused by the demagnetising field, may be used in detecting surface defects. This effect could, possibly, be used to locate a surface crack, though successful detection would depend up on:

1. The spatial resolution of the sensor (sensor size).
2. Defect size, in terms of surface opening and depth of the defect.
3. Magnetising field magnitude and magnetisation frequency.

If the optimum combination of magnetisation rate, magnetisation intensity (dependent on specimen size, geometry and composition) and probe size (dependent on defect type, size and location) were utilised then it may be possible to detect, locate and perhaps estimate the size of a surface crack using the EBE.

Using a large coil EBE sensor, results showed that spatial resolution was compromised. This, combined with a lower magnetising field rate produced more difficulty when conducting EBE measurements. An optimum combination of magnetising field rate and probe size meant that open surface defects could be located. Therefore, it can be concluded that, in theory, a combination of both ABE and EBE can be successfully used to determine the position of a surface defect, such as an open surface crack.

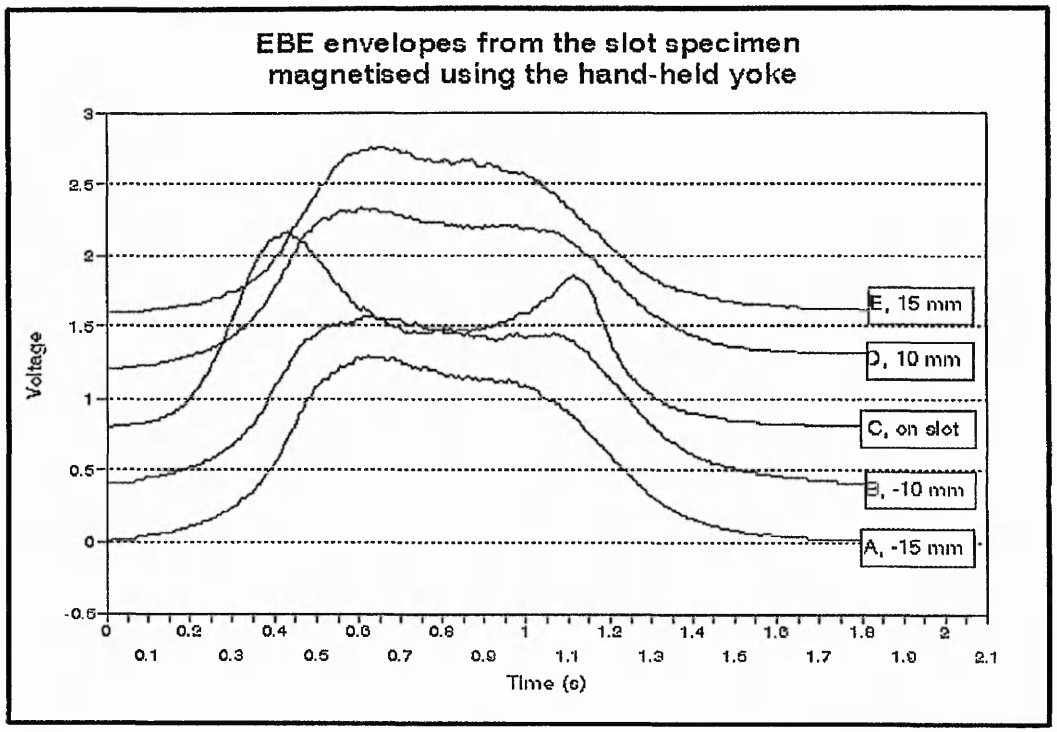


Figure 3.3.1 EBE signal envelopes generated by magnetising the steel slotted specimen using the Y6 hand-held electromagnet. The signal envelopes were detected from across the surface of the slotted specimen using the large wound coil transducer.

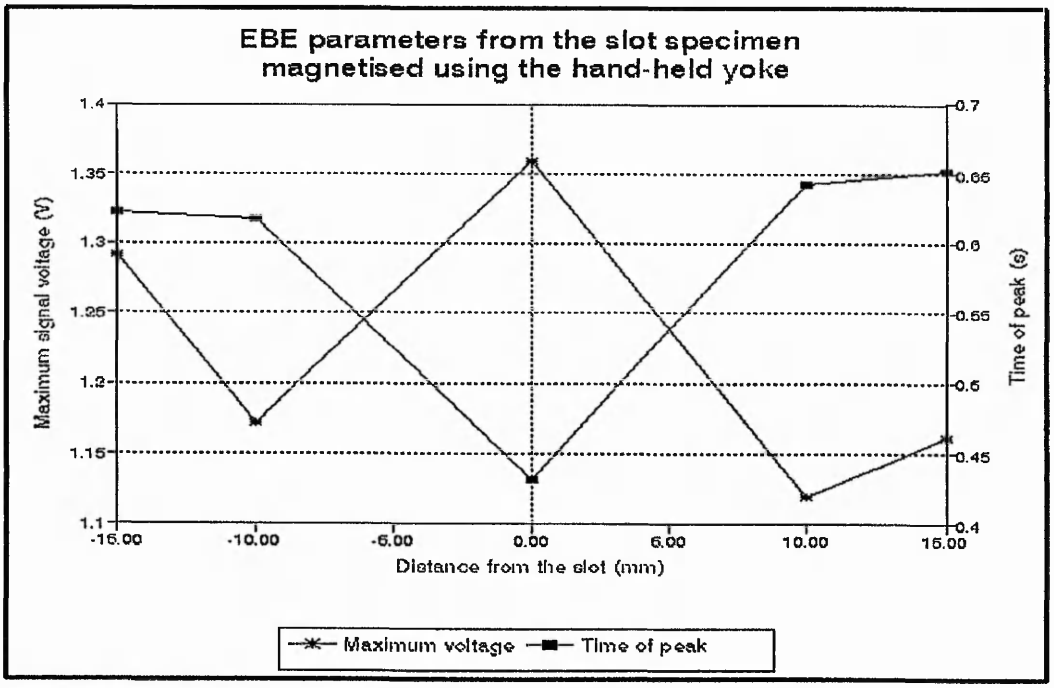


Figure 3.3.2 'Maximum signal voltage' (V_{MAX}) and 'time of peak' (T_P) with respect to the steel specimens slot location. Magnetisation of the specimen was carried out using the Y6 hand-held electromagnet.

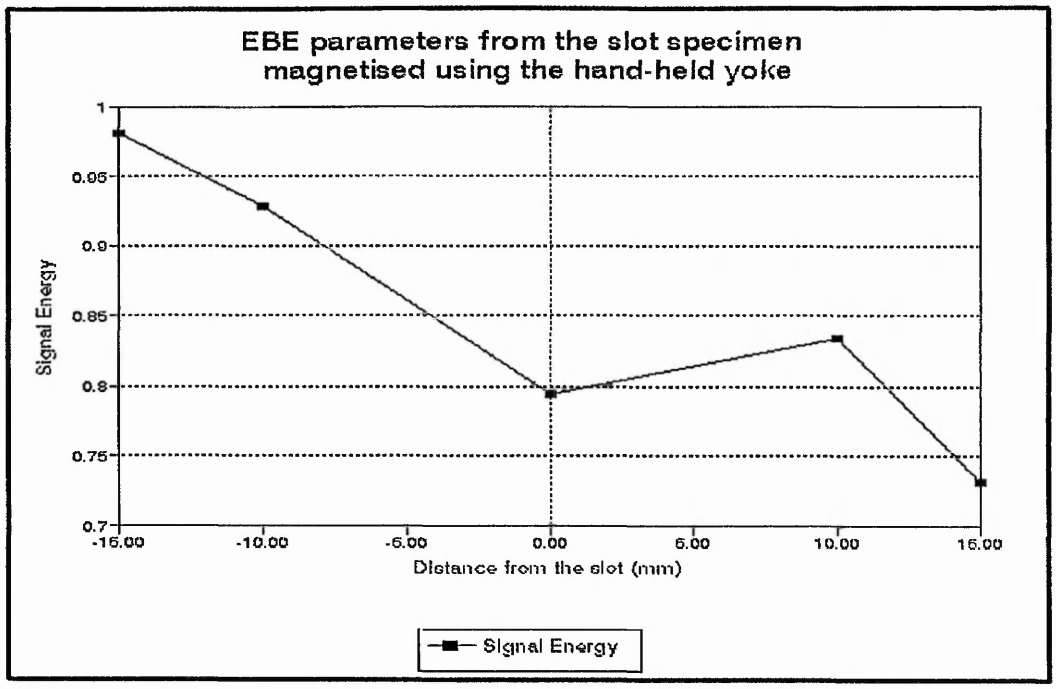


Figure 3.3.3 EBE signal energy (units V^2s) relative to the steel specimens (OLI-95D) slot location. Magnetisation of the specimen was carried out using the Y6 hand-held electromagnet.

3.4. BARKHAUSEN EMISSION AROUND A FATIGUE CRACKED STEEL SPECIMEN.

3.4.1. Experimental Detail and Specimen Surface Labelling.

In this section the effect on Barkhausen emission of a surface breaking fatigue crack in a 50D steel specimen is considered. A notched steel 'dog bone' specimen was fatigued until a crack was generated. The notch was further machined away leaving the crack mouth open on the surface. The specimen was then cut and machined into a bar measuring 250 mm and 30 mm by 15 mm. The specimen was provided by British Gas Research, Loughborough, and labelled OLI-95F. The specimen possessed a polished surface and the crack was not visible to the naked eye. Viewed under an optical microscope the crack became visible and measured approximately 5 μm in width. Measured at the side edge of the specimen, the depth of the crack was found to be 3mm to 4 mm from the surface of the specimen, although it may not be of constant depth across the specimen.

Barkhausen emission measurements were carried out on the surface of the cracked specimen. The pencil probe sensor was used for this section of work as it provided a greater spatial resolution. The crack was situated at the central position on the surface, 125 mm from either side of the specimen. The magnetising field and the traversing probe direction were both at 90° to the crack length on the specimen surface. The central 40 mm region on the specimen's surface was subdivided into 2 mm spacing. Each position was labelled from 'A' through to 'U'. The crack was located on position 'K' at the centre of the specimen. For details of the measurement configuration see **figure 3.4.1**.

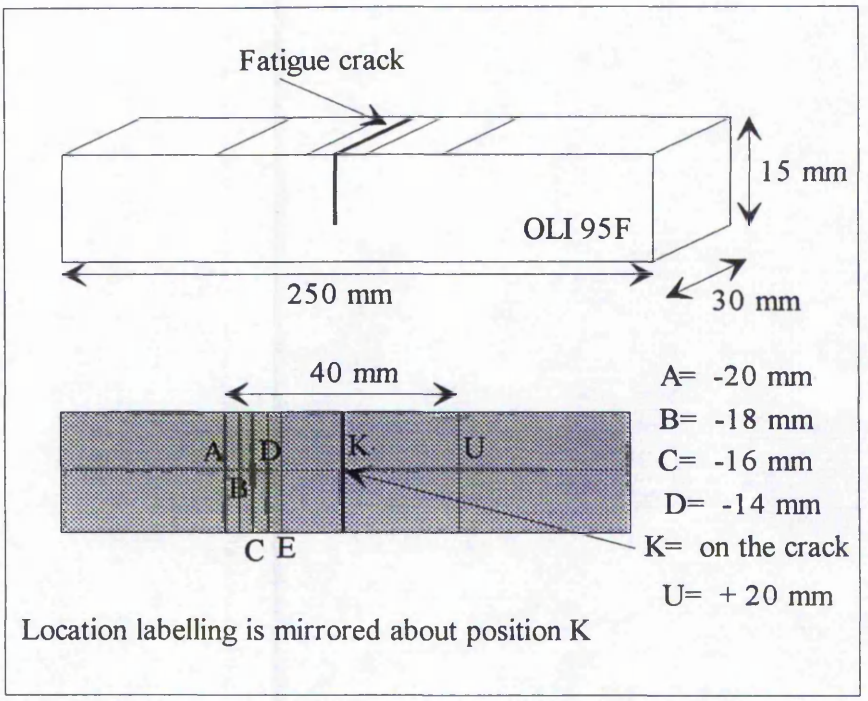


Figure 3.4.1 Fatigue crack specimen dimensions and location labelling across its surface. Specimen number OLI-95F, produced by British Gas Research. Positions 'A' to 'U' (not all shown).

Cyclic straining of a ferromagnetic metal results in increased dislocation density. Initially the dislocation networks grow rapidly but with increasing number of cycles the dislocation growth slows until a maximum is reached. This causes the hardness of the material to increase. At stress amplitudes lower than the fatigue limit, the dislocation content increases to form dense dislocation tangles called veins, distributed homogeneously over the structure **[31]**.

On cyclic straining above a given applied strain (10^{-3}), large scale motion of edge and screw dislocations culminate in the formation of dislocation cell structure. Cyclic hardening as well as changes in the shape of the crystal are observed due to asymmetric slip of screw dislocations in tension and compression. In low carbon steels under cyclic fatigue, slip bands are found **[94]**.

Fatigue cracking is strongly affected by the applied stress levels, slip characteristics and the extent of near tip plasticity of the material. In ductile materials, cyclic crack growth is caused by intense deformation in slip bands near the crack tip. When the crack and the zone of plastic deformation surrounding the crack tip are confined within a few grain diameters, crack growth occurs predominantly by single shear, in the direction of the primary slip system **[94]**. At higher stress intensity ranges, the plastic zone at the crack tip encompasses many grains. The crack growth process then involves simultaneous or alternating flow along two slip systems. **Figure 3.4.2** shows a small fatigue crack within the plastic zone resulting from the notch.

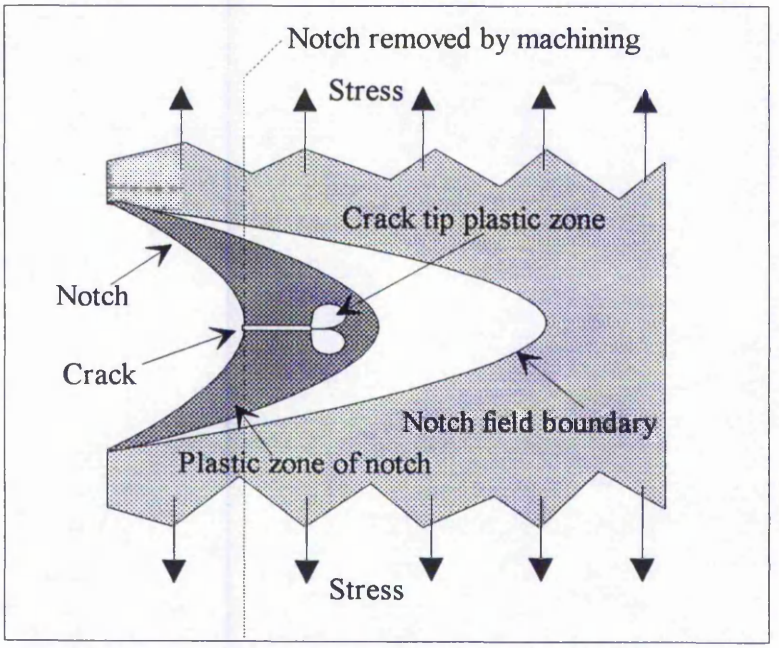


Figure 3.4.2 Cross section of a fatigued specimen showing a schematic close-up of the notch and expected fatigue crack and the specimen respective plastic zones.

3.4.2. Barkhausen Emission Results from the Fatigue Cracked Steel Specimen.

3.4.2.1. *EBE results from the fatigue cracked steel specimen.*

Repeated Barkhausen measurements were made across the designated surface of the fatigued specimen. From a given location the EBE envelopes, detected using the pencil probe, were very reproducible. **Figure 3.4.3** shows the Barkhausen envelopes from a given location and its averaged signal envelope. The repeated measurement of Barkhausen signals are shown, doubled in size, to highlight the reproducibility of the envelopes. Initially the EBE envelope started to increase gently, then at a time of 0.4 seconds the signals began to rapidly increase in magnitude. This rapid increase slowed down at a time of 0.5 seconds into the envelope. After 0.6 seconds the signal began to increase again to a maximum, at around 0.8 seconds. After the maximum signal amplitude, the envelope steadily decreased to zero. The EBE envelopes from across the surface of the specimen generally appear similar. The EBE envelopes from across the surface of the fatigued steel specimen are shown in **figures 3.4.4** to **3.4.7**. The different positions all exhibited envelopes containing a single peak. The EBE envelope splitting phenomenon found on the slotted specimen in **section 3.1** was not evident on the fatigue cracked specimen. This was mainly due to two reasons; firstly, the tight nature of the fatigue crack and secondly, due to the gradual change in magnetic permeability between the fatigue crack and the parent steel specimen. This gradual change is due to the plastically deformed region surrounding the fatigue crack itself. Bhattacharya **[92]** showed that as the slot width increased, the splitting effect observed in the EBE envelope also increased. Therefore, a very tight fatigue crack is not expected to cause the EBE signal to split into a double peaked envelope. The reasons for EBE envelope splitting are considered in detail in **chapter 4**. The presence of the crack, however, did shift the signal peak to an earlier time in the envelope. The summarised EBE data is shown in **figure 3.4.8**.

The time of peak (T_P) for the EBE envelopes clearly showed a significant change over the fatigue crack region. The envelope peak, around the fatigue crack region, occurred at

0.65 seconds (±0.01 s) on the envelope. Away from the central fatigue crack region, location 'A' and 'U', the T_P occurs earlier at a time of approximately **0.74 seconds**.

The maximum signal voltage (V_{MAX}) from across the studied surface of the fatigue cracked specimen, is also displayed in **figure 3.4.8**. For locations 'A' to 'G' and 'P' to 'U' the V_{MAX} values remained relatively constant, between **0.46 V** and **0.43 V** (±0.01 V) respectively. Between location 'H' and 'O' the V_{MAX} values changed rapidly. A large V_{MAX} with a value of **0.57 V** was recorded on location 'I', on the left side of the crack. On the right hand side of the crack, on location 'M', a large V_{MAX} value of **0.65 V** was detected. Locations on and immediately adjacent to the crack generated a V_{MAX} value of approximately **0.49 V**. The crack location displayed a V_{MAX} value of **0.48 V**.

The signal energy parameter displayed a similar pattern to the V_{MAX} parameter, (**figure 3.4.8**). Locations furthest away from the crack exhibited different signal energy levels compared to locations close to the crack. Locations 'A' to 'F' and 'Q' to 'U' exhibited an average signal energy of **0.054 V^2s** and **0.047 V^2s** (±0.001 V^2s) respectively. Moving away from the edge regions, approaching the crack, the EBE signal energy rapidly increased. Equidistant on either side of the crack the signal energy exhibited a maximum at positions 'I' (**0.067 V^2s**) and 'M' (**0.061 V^2s**). From these maximum signal energy locations the crack was located on a signal energy minimum. The crack on location 'K', displayed an EBE signal energy of **0.054 V^2s**. The data suggests that the presence of the fatigue crack generated a region of material immediately surrounding the crack with differing properties to the rest of the surface.

A reference specimen of the steel material was unavailable so relative comparison between the fatigued and unfatigued specimens was not carried out. This limited the interpretation of the Barkhausen signals, although, clearly, data was available away from the crack for the sample tested. The EBE signals from the fatigue cracked steel specimen clearly indicated a change in the magnitude of the signal energy around the location of the crack. Either side of the crack (located on position 'K') the symmetry present within the signal energy profile indicated that the creation of the crack had changed the specimen metallurgical microstructure. Cyclic fatiguing is known to alter the dislocation

density within a material **[94]** and the magnetic properties of a specimen are heavily influenced by the dislocation networks **[2]**. Work by Raj **[95]** on steel has shown that EBE envelopes change significantly depending on the thermal histories of the specimens. Small grain size and a very high dislocation network found in quenched specimens exhibit small EBE signals. In his work specimens aged for very long periods showed increased EBE activity, while specimens that were heat treated for an intermediate period of time exhibited the maximum EBE signals. The maximum EBE activity is detected from specimens which have an optimum density and distribution of pinning sites.

The presence of the notch generated a plastic zone, where the stress concentration was very high and, as a result, dislocation density increased **(figure 3.4.2)**. The altered material characteristics of the plastic zone were probably the reason for the T_P value occurring earlier on the EBE envelope, this is shown in **figure 3.4.8**. Also an increased EBE maximum signal voltage as well as signal energy was detected around this region. The presence of the increased pinning sites resulting within the plastics zone would aid the increase of both these parameters.

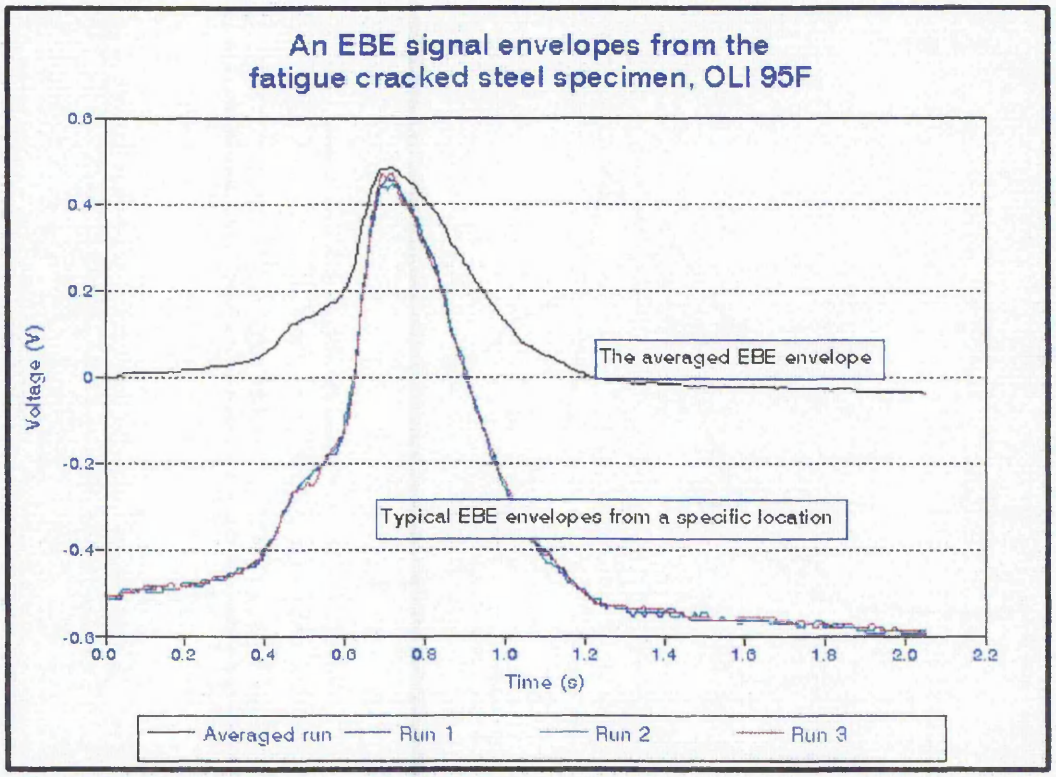


Figure 3.4.3 EBE envelopes detected using a pencil probe sensor from a given location on the surface of the fatigue crack on the steel specimen (OLI-95F). The detected EBE envelopes are seen (double in size) to be very reproducible (position 'A'). The error bars calculated for the EBE envelopes from a given location are T_P =±0.01 s, V_{MAX} =±0.005 V and Signal energy =±0.001 V^2s.

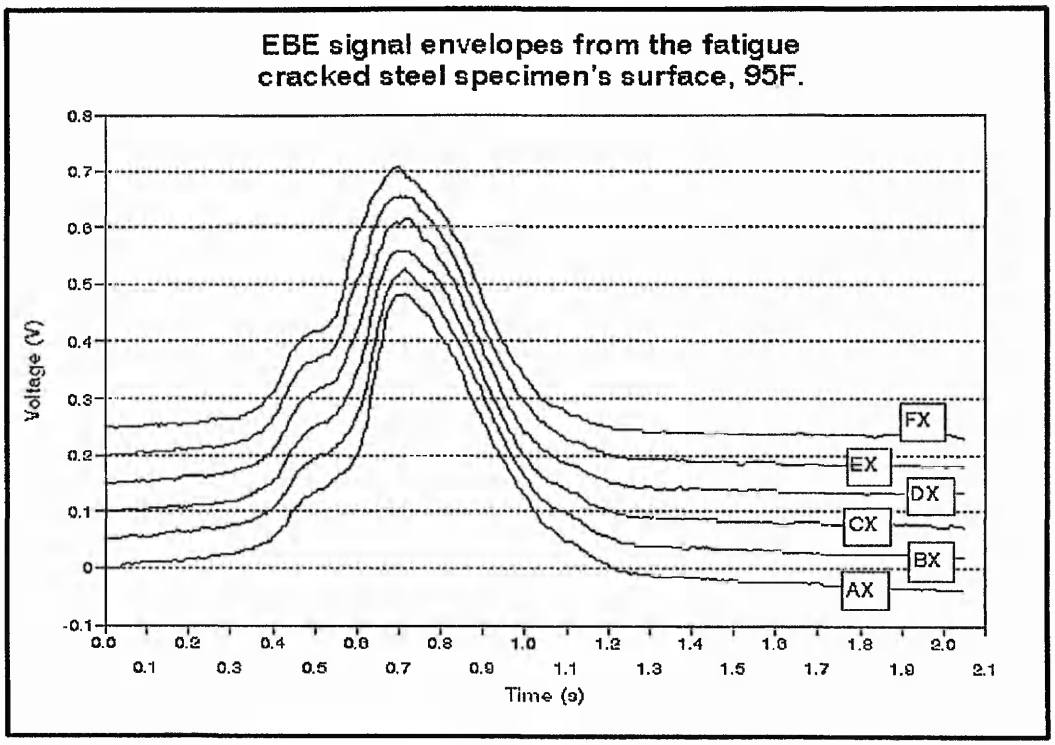


Figure 3.4.4 EBE envelopes detected using a pencil probe sensor, moving towards the fatigue crack on the steel specimen OLI-95F from the left hand side (positions 'A' to 'F').

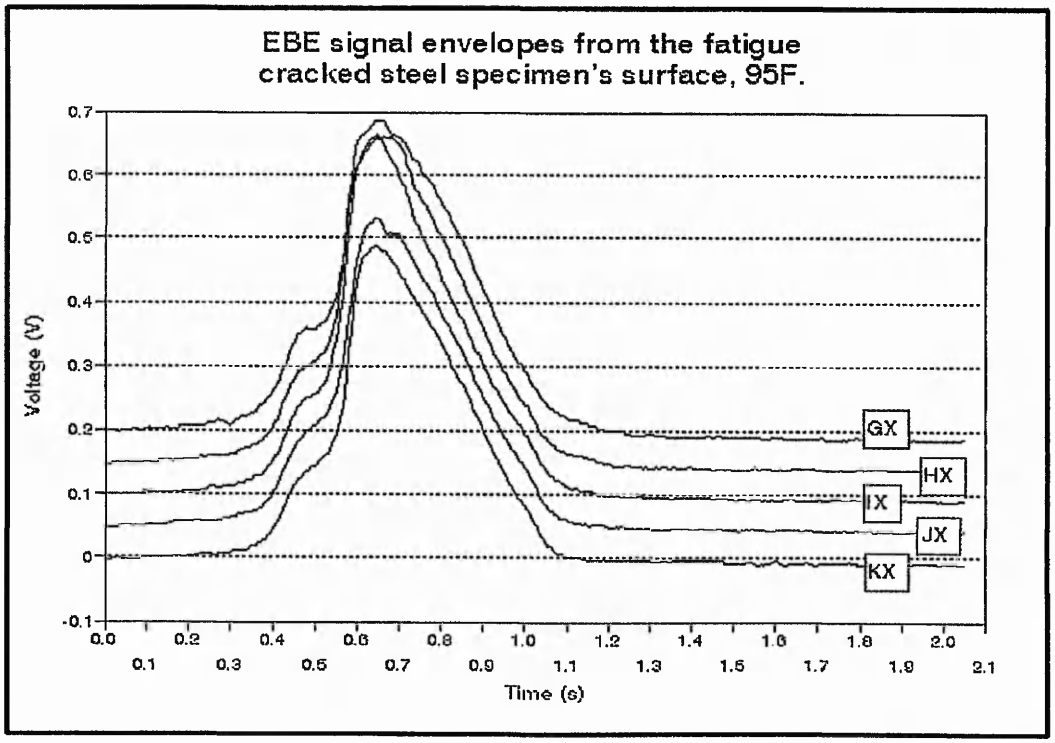


Figure 3.4.5 EBE envelopes detected using a pencil probe sensor, moving towards the fatigue crack on the steel specimen OLI-95F from the left hand side (positions 'G' to 'K').

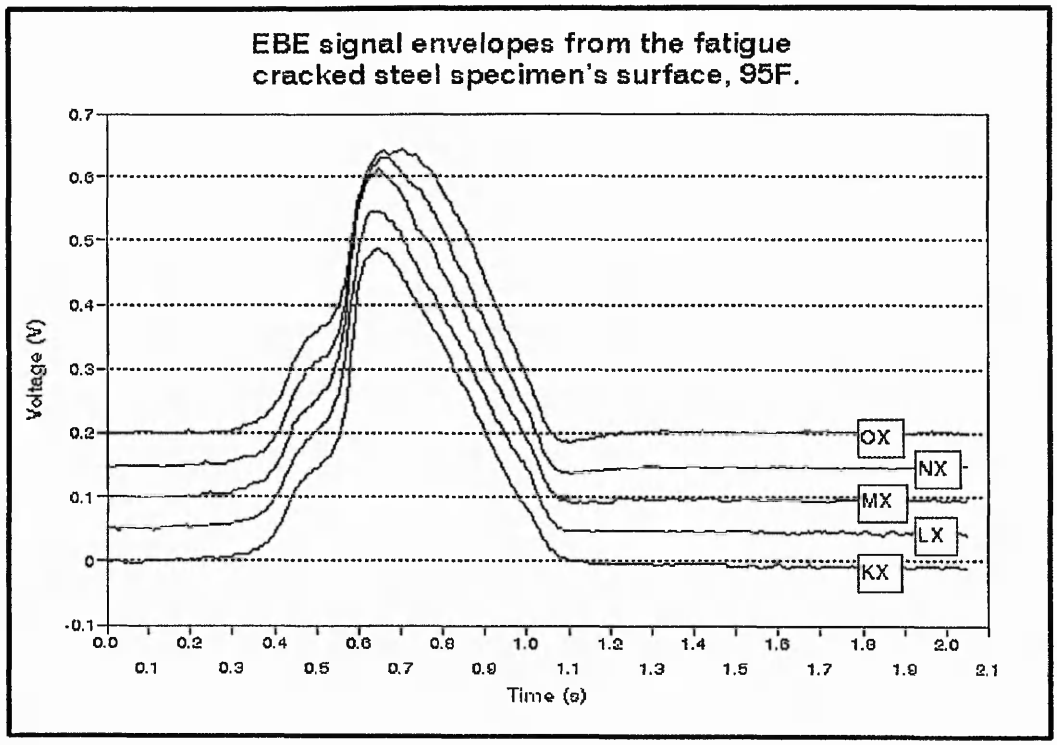


Figure 3.4.6 EBE envelopes detected using a pencil probe sensor, moving away from the fatigue crack on the steel specimen OLI-95F from the left hand side (positions 'K' to 'O').

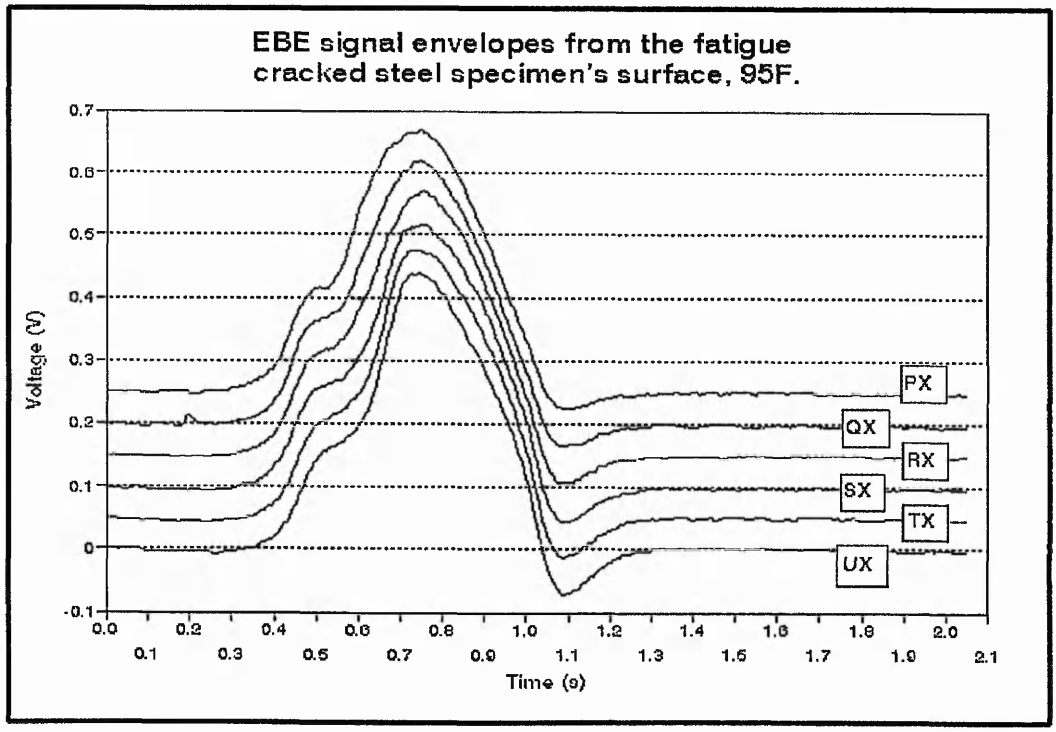


Figure 3.4.7 EBE envelopes detected using a pencil probe sensor, moving away from the fatigue crack on the steel specimen OLI-95F from the left hand side (positions P to U).

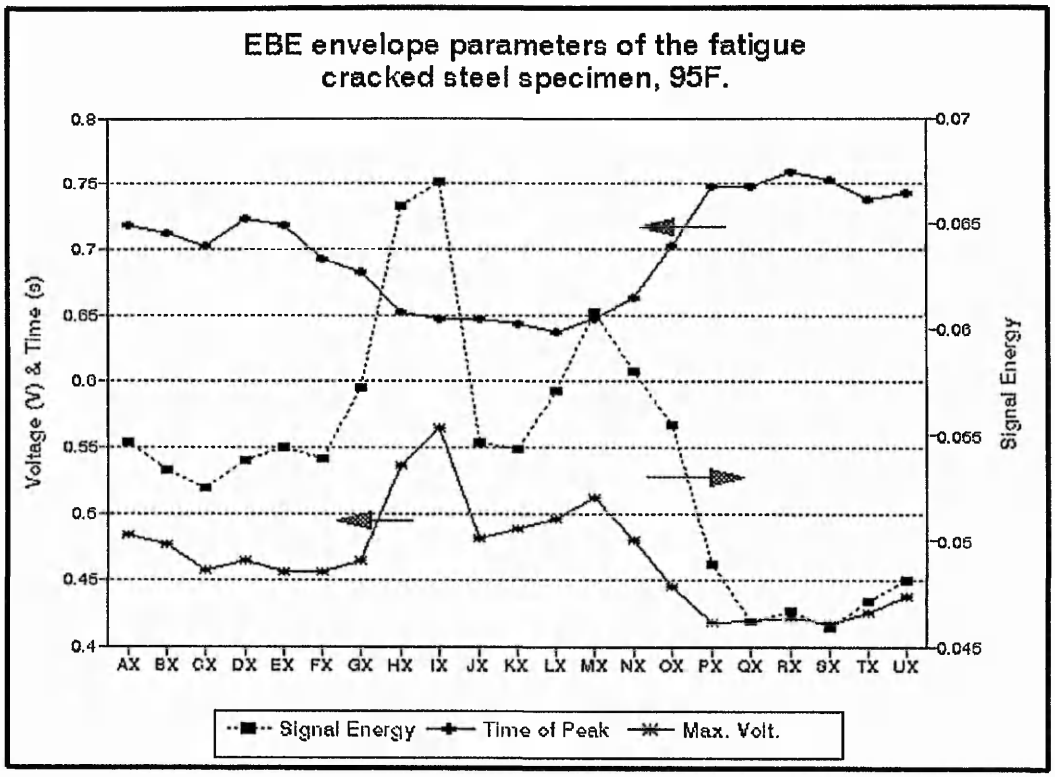


Figure 3.4.8 EBE signal envelopes parameters from the fatigue cracked steel specimen OLI-95F. The 'time of peak' (T_P), 'maximum signal voltage' (V_{MAX}) and signal energy are displayed for the positions across the studied surface of the specimen.

3.4.2.2. *ABE results from the fatigue cracked steel specimen.*

The ABE measurements were recorded from across the fatigue cracked specimen. The locations marked for the EBE measurement were also utilised for the ABE measurements. The ABE measurements were taken on location 'A', 'C', 'E', and so forth, up to location 'M'; every 4 mm starting from 'A' through to 'M', covering half of the studied cracked specimen's region.

The detected ABE envelopes are displayed in **figure 3.4.9**. The ABE envelope appeared essentially double peaked, the first peak being smaller than the second. The ABE signals possessed spikes on the central region of the envelope and occasionally a larger spike was recorded at the base of the large second peak. The cause of the spikes is not clear and their effect on the measured parameters must be considered when assessing any specimen. The large spike on the ABE envelope was always smaller in magnitude compared to the large second peak and, therefore, did not affect the T_P values. However, the spike did affect the V_{MAX} and signal energy parameters.

The Barkhausen envelope parameters showed a T_P value around **1.184 s** on the envelope and are summarised in **figure 3.4.10**. The maximum signal voltage (V_{MAX}) for the majority of the locations on the specimen were around **1.3 V** to **1.4 V** in magnitude. The V_{MAX} value detected on location 'C' was larger than the surrounding signal voltages at a value of **1.75 V**. This was due to the presence of the spike on the ABE envelope, (**figure 3.4.9**). The signal energy profile from the cracked specimen displayed a similar trend to the V_{MAX} profile. The presence of the unpredictable spikes on the central region of the envelope caused the variability in the signal energy value. Along with the envelope from location 'C', location 'I' also exhibited a similarly large signal energy parameter with a value of **0.299 V^2s**.

The cause of the spike is unclear and is the reason for the changes within the ABE envelope parameters. As expected the presence of the tight fatigue crack within the volume of the specimen did not show any clear effect on the ABE envelope parameters.

The ABE, being a volume effect, was not expected to be affected by the presence of a small crack. Averaged ABE envelope parameters from the fatigue cracked steel specimen were found to fluctuate significantly. The average signal energy was recorded at a value of **0.241 V^2s ±0.058 V^2s (±24%)**. The averaged maximum signal voltage **1.371V ±0.379 V (±27%)**. The averaged 'time of peak' **1.184 s ±0.027 s (±2.3%)**. For a given 50D steel containing a fatigue crack the these values may possibly be taken as average measurements, providing specimen size, magnetisation and detection systems are kept constant.

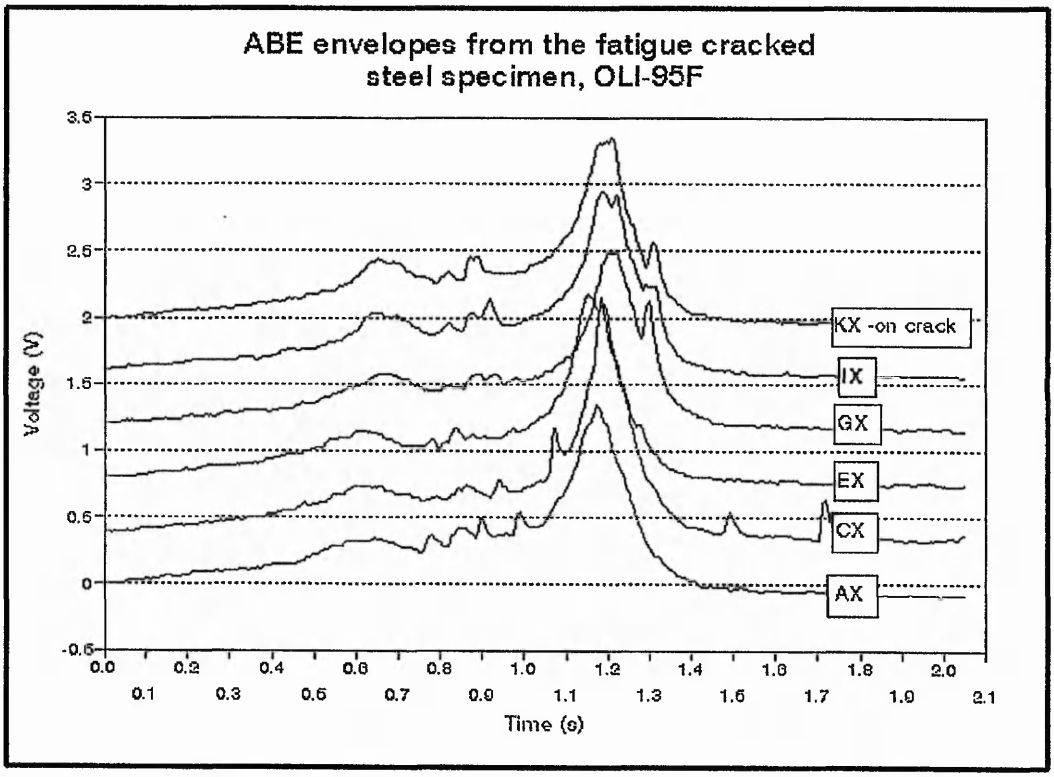


Figure 3.4.9 ABE envelopes detected using a 175 kHz piezoelectric transducer, moving towards the fatigue crack on the steel specimen OLI-95F from the left hand side (positions 'A' to 'K').

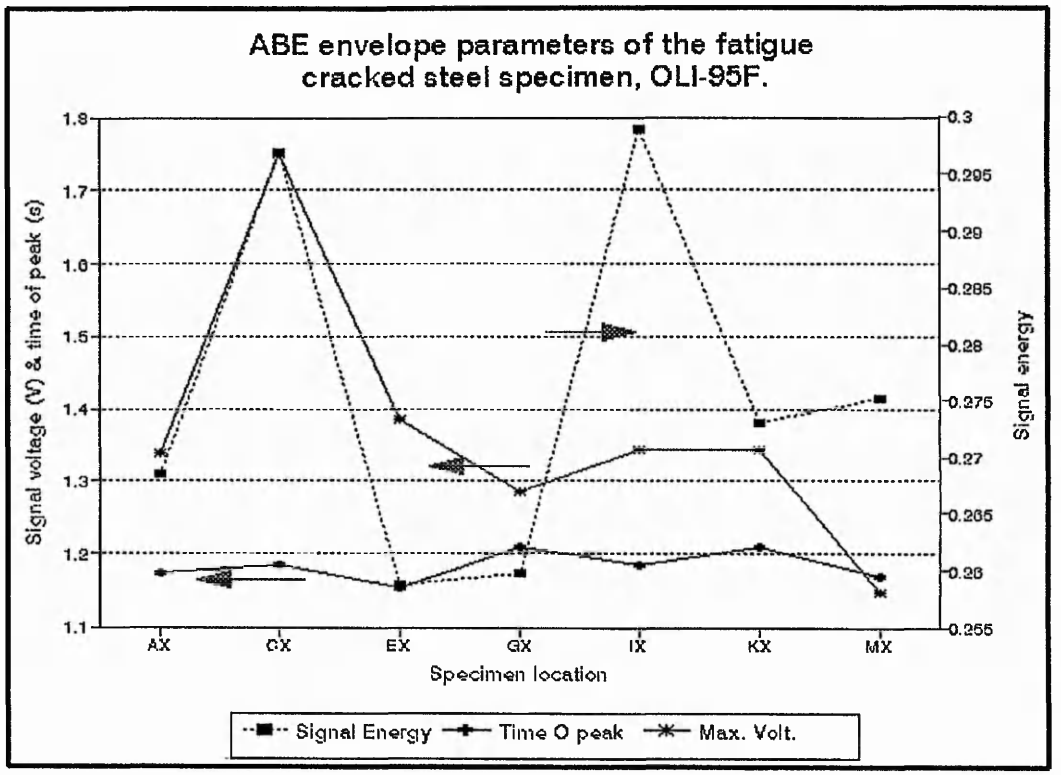


Figure 3.4.10 ABE signal envelopes parameters from the fatigue cracked steel specimen OLI-95F. The 'time of peak' (T_P), 'maximum signal voltage' (V_{MAX}) and 'signal energy' (units V^2s) are displayed for the positions across the studied surface of the specimen (positions 'A' to 'M').

END *of* CHAPTER

PART 2

Barkhausen Emission from EN-43A Steel.

CHAPTER 4

BARKHAUSEN EMISSION FROM PLAIN, WELDED AND CRACKED WELD SPECIMENS OF EN-43A STEEL

4. BARKHAUSEN EMISSION FROM PLAIN, WELDED AND CRACKED WELD SPECIMENS OF EN-43A STEEL.

The joining of materials is an important issue in manufacturing engineering. This can be achieved by methods such as gluing, riveting, screwing or welding. Welding has the advantages that it provides a high strength intimate joint of similar materials. Disadvantages include, the possibility of producing weld defects, sensitivity to cracking and residual stress being left in the weld joint with the possibility of distortion.

In this chapter Barkhausen emission from EN-43A steel is studied. Weld test samples have been studied, formed from EN-43A steel plate. Barkhausen emission and flux leakage have been measured close to the fatigue cracks induced in these welds. Further studies have been undertaken, as the plate surfaces were machined away, using electrical discharge machining and conventional planing of the surface.

Barkhausen emission is known to be very sensitive to material microstructure and the experimental measurement system in use, is discussed in **chapter 1**. The EBE signal will carry information on any change in the material structure. The aim of this work is to

establish how effective BE might be as a technique for the investigation of these changes in engineering materials.

Measurements initially aimed to establish the BE characteristics of EN 43A engineering steel. This clearly had undergone some manufacturing process and for this work, these BE measurements become the base line against which other measurements are compared. Creating a weld provides material of differing metallurgical characteristics which needs to be detectable against the base line of the parent metal. The presence of the weld crack and surface modifications, also need to be detectable.

4.1. EXPERIMENTAL DETAIL.

4.1.1. Specimen Details.

Steel plates, of type EN-43A steel, were used. The steel was manufactured by British Steel, and supplied as rolled plate. EN-43A steel plate has very similar magnetic properties to 50D offshore steel, while being less expensive. The prepared steel plates were obtained from Sonaspection Ltd. The composition of this steel is provided in **table 4.1.1** and the manufactures data sheet is displayed in appendix 3.

Element	C	Si	Mn	P	S	Cr	Mo	Ni
wwt %	0.170	0.153	0.850	0.024	0.009	0.028	0.003	0.022
Element	**Al**	**Co**	**Nb**	**N**	**Sn**	**Ti**	**V**	
wwt %	0.038	0.034	0.003	0.0073	0.005	0.003	0.003	

Table 4.1.1 Composition of EN-43A steel, as supplied by the manufacturer.

Several samples were custom made by Sonaspection Ltd. Amongst the samples prepared was a steel specimen with dimensions 152 mm by 75 mm by 9.5 mm. The 43A steel plate

was machined to size using a circular grinder. This steel plate was labelled specimen'3P'. On one side of the specimen was a manufacture's mark, this is referred to as the back of the plate.

A second specimen of similar dimensions (150 mm by 75 mm by 9.5 mm) was produced (**figure 4.1.1**). This time a perfect TIG weld, running along the width of the specimen, was fabricated at the centre of the plate. One corner of the specimen was labelled '2P'. Two other samples were prepared, which also had TIG weld seams running down along the central width of the sample. These samples were labelled '21A' and '21B'. In the centre of the weld, on both specimens, there was a fine crack 2 mm to 3 mm in depth. The crack was created by low-cycle flexural fatiguing and was located at the central region of the specimens. The weld root and cap on all of these specimens was machined away leaving a smooth finish with no visible sign of the weld.

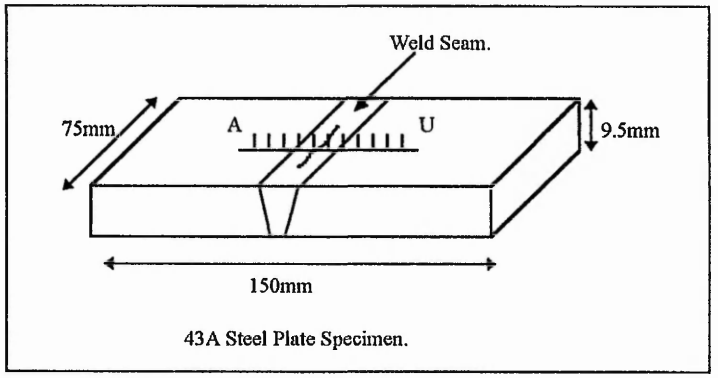


Fig 4.1.1 Diagram of the EN-43A steel plate cracked welded specimen. The plain steel plate and the plain welded plates were of very similar sizes.

4.1.2. Experimentation and Specimen Labelling.

Both acoustic and electromagnetic Barkhausen measurements were carried out on each of the specimens surfaces. The standard Barkhausen measurement system was used, utilising the Griffin and George electromagnetic yoke with a maximum current of 2.5 Amps passing through each coil. The specimens were magnetised using a triangular waveform with a frequency of 0.1Hz. The Hocking pencil probe sensor was employed, which provided better spatial resolution than the original large coil sensor, described earlier in **Chapter 1**.

The EBE measurements were made every 2 mm along a designated region, of length 40mm. This region was in the central part of each specimen, with position 'K' on the centre of the specimens (**figure 4.1.2**). Each position was labelled from 'A' through to 'U'. Position 'A' and 'U' were designated at the 0 mm and 40 mm locations respectively. Location 'K' is positioned on the centre of the weld seam on both the cracked and weld specimens. The width of the weld seam is approximately 10.5 mm. The heat affected zone (HAZ) is located on either side of the weld seam, which is approximately 4 to 5 mm in width. Past the HAZ region, the parent material regained its microstructure.

ABE measurements were taken every 5mm on the same region of the specimen. This allowed only 9 locations to be measured due to the larger sensor dimensions. The measurements were labelled from 'A' through to 'I', 'A' being at 0 mm and 'I' being at 40 mm. In this case the pencil probe was held fixed in position, between the yoke legs, as the steel specimen was moved. This created a condition where the magnetising field strength directly below the sensor was relatively constant.

Barkhausen measurements were taken between six and nine times over a minimum of two experimental runs, to ensure reproducibility in the measurements. The Barkhausen emission envelopes from a given location, e.g. location 'A' are graphically presented as 'AX'. The 'X' denotes that the particular BE envelope is obtained by averaging several (nine or six) repeated results together.

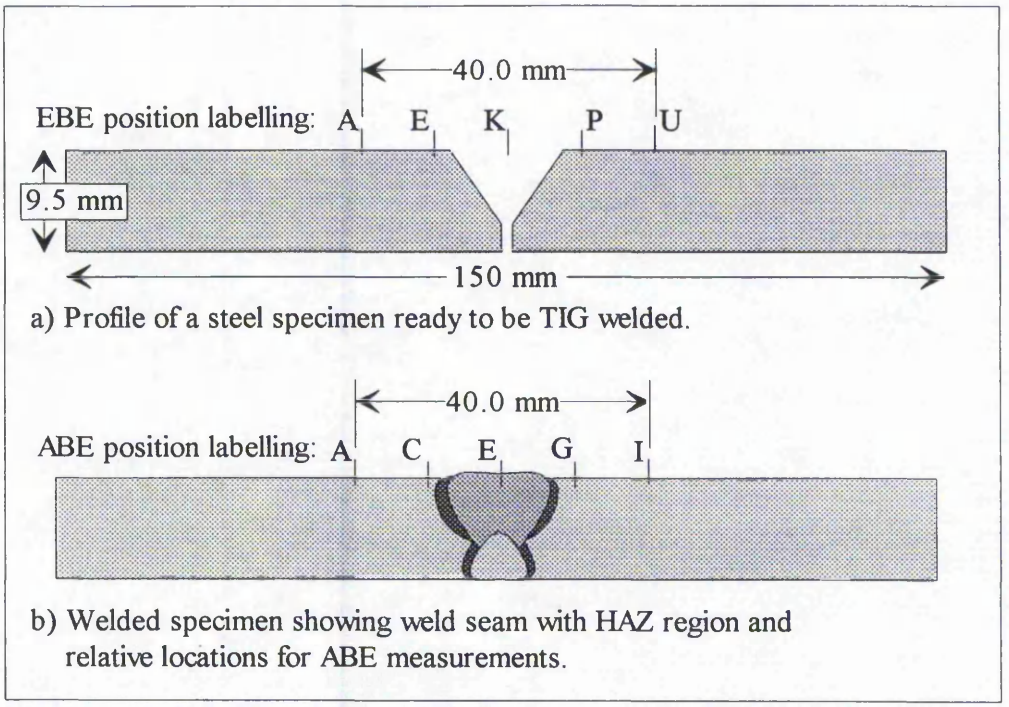


Figure 4.1.2 a). Cross section of key-holed steel specimen. b). Welded steel specimen showing the weld bead. The specimen labelling is on the central region, across a 40 mm length. Location 'E' and 'K' are at the central position of the specimen for ABE and EBE measurements respectively.

4.1.3. TIG Welding and Fatigue Crack Generation.

The specimens used in this study have all been Tungsten Inert Gas (TIG) welded. This welding process belongs to the arc welding family and there are a large number of variations on this technique. The design of a TIG welding system is shown in **figure 4.1.3**.

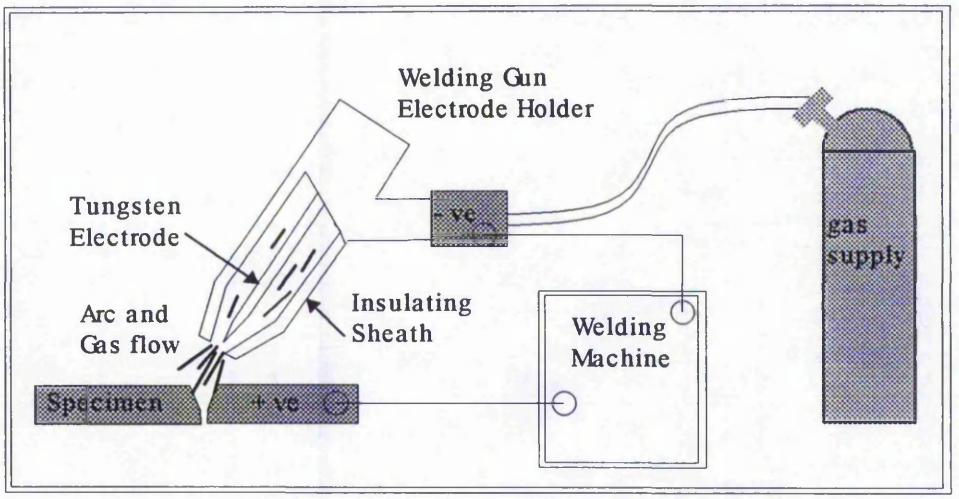


Figure 4.1.3 Schematic diagram of a Tungsten Inert Gas (TIG) welding machine.

An electric arc is set up between the tungsten electrode and the work piece. The magnitude of the electrical current and voltage used in generating the arc depend on the material being welded. The arc reaches very high temperatures and causes the immediate metal to melt and fuse together. The end of the non-consumable tungsten filament is tapered towards a point and is rounded off. This allows the arc to focus with the minimum of electrode wear. The arc and the molten metal are shielded from the external environment by a fast flowing layer of inert gas. The inert gas is blown out through the welding gun and over the welding region. The type of inert gases used vary and include helium and argon. Gases such as CO_2 and O_2 are also used in mixtures. These are used as they are heavier than helium and, therefore, better at shielding. The use of more commonly available gases reduces the cost of the process and certain combinations of gases have been found to allow operation at increased arc voltages **[96]**. The type of gas and gas mixtures used depend on the welding material.

The sample preparation allowed single pass, straight edge butt welding on plates of thicknesses 3-10 mm **[96]**. To obtain complete penetration a funnel shaped cut, created at the centre, was made to pass through the material thickness completely. The penetration width is governed by the width of this funnel shaped cut, which, in turn depends on the travel speed and current. This process is called key-holing and was carried out on all of the specimens used in this research. Low-cycle weld fatigue cracks

were generated by the manufacturers of these specimens. After the crack was established, the weld cap was machined flat in order to eliminate profiles which act as stress raisers.

4.1.4. Machining of the Steel Specimens.

When a crack is formed, depending on size and severity, it is often removed by grinding away the region of material containing the defect. The effect of machining components and structures, can itself, cause problems with the material's surface. All the steel samples including the fatigue crack specimens, 21A and 21B, possessed the same surface finish. They were originally ground using a circular grinder. The grinding generated surface stresses would add to the overall stress profile of the specimens.

Both the plain steel (3P) and welded steel (2P) specimens were subjected to further surface machining processes and the effect of these were studied. The cracked weld specimen 21A was subjected to surface removal by planing. Care was taken, where possible, so as not to cause adverse stresses in the specimen. The surface of cracked weld specimen 21B was altered using the Electro Discharge Machining (EDM) process. The effect of the surface finish is known to affect the Barkhausen emission **[57]** and in this section, the effects of different surface machining will be examined using the two very different machining processes.

4.1.4.1. *Surface planing of the steel specimens.*

The plain, welded and cracked weld (21A) specimens, with their ground surface finish, were machined using a 'shaper' made by Newer of Nottingham, England. This machine has a single point tool. The tool and the work piece are gripped in the machine in such a way that when the appropriate motion is applied by the machine, the tool point generates

the desired shape of the work piece. Shapers are able to generate flat and grooved surfaces in work pieces. The steel tool is reciprocated back and forth and the work piece is fed at right angles to the motion of the tool (**figure 4.1.4**). The forward motion of the tool cuts the specimen while the backward motion lifts the tool off the surface of the specimen and brings it back to the starting position. A steel tool was used to mechanically shave off the surface of the specimen. The tool's sharp angled point machined off thin strips of surface material. The amount of material removed depended on the depth setting of the tool **[97]**.

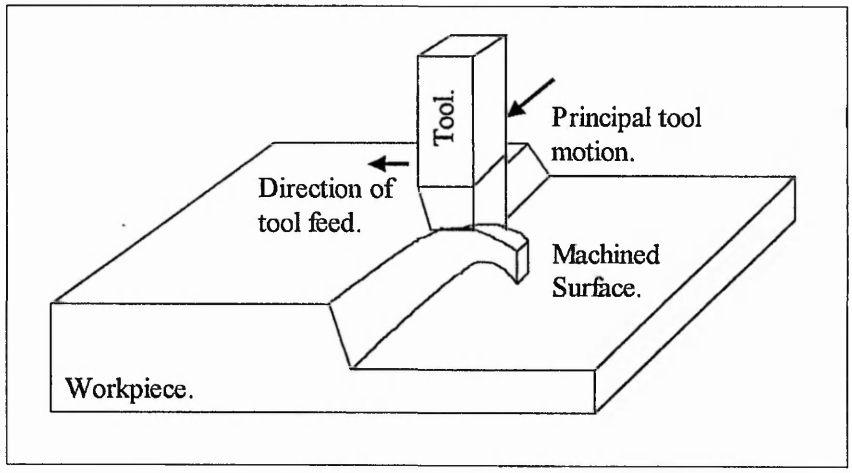


Figure 4.1.4 Shows the principal motion of the shaper's tool tip in removing surface material.

The deeper the setting, the greater the volume of material that was removed by each stroke. This implies that, with a larger depth setting, greater stresses would have been generated within the new surface. For this reason the tool depth, for machining of the specimen, was set very low and the tool was swept back and forth over the entire surface of the specimen. Several thin layers of material was shaved off, in order to remove the desired surface thickness of 0.5 mm. Removal of small volumes of material over several machining runs, helped limit the amount of surface deformation. The steel tool tip was cooled and lubricated using cutting fluid.

The new surface generated on the cracked weld specimen (21A) was labelled '22A'. A surface thickness of 0.5 mm was eventually removed from the '21A' specimen. The planing direction was across the width of the specimen, parallel to the crack length. This helped minimise the formation of a lip over the crack mouth. The formation of a lip would have affected the magnetic leakage field, causing it to reduce in intensity. Since EBE signals are detected from the surface of the specimen, they too would have been affected by the formation of a lip.

4.1.4.2. *Surface machining using Electro Discharge Machining (EDM).*

The Electro Discharge Machine used in this study was made by Charmilles Technologies, Stratford-upon-Avon, England. There are two types of EDM machines: (1) the die-sink type and (2) the wire machine. The EDM machine used in this work was a die-sink type. The process of die-sink EDM machining is indicated in **figure 4.1.5**.

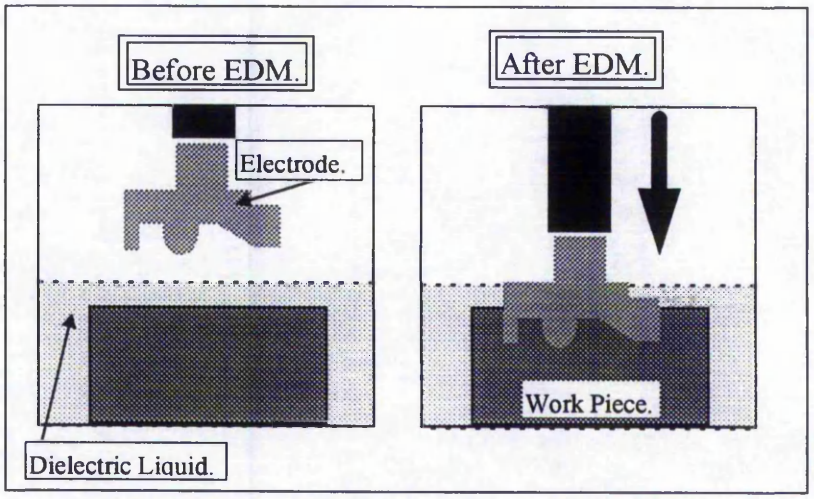


Figure 4.1.5 Die sink EDM machine.

EDM removes material by passing electrical current between a tool and a work piece. In the die-sink machines the work piece is the cathode (-) and the shaping tool is the anode

(+). This electrical discharge occurs through a dielectric fluid between the tool and work piece. The discharge melts, vaporises and removes small amounts of material from the work piece. The dielectric fluid also acts as a coolant and aids the removal of the eroded particles, which are produced as a result of EDM machining. A small gap exists between the work piece and the tool. The work piece and the tool, therefore, do not come into physical contact, so there is no conventional mechanical force exerted upon the material. This significantly reduces the surface stresses generated in work pieces machined using this method and is the reason the technique was chosen as part of this work.

EDM uses a DC voltage (approximately 200 volts) across an average gap of 40μm. As a result, an electric field is generated between the work piece and the tool electrode. At first, due to the insulating properties of the dielectric between the tool and work piece, no current flows. The ultra fine solid impurities suspended in the dielectric are forced to bridge the gap between the tool and the work piece. There is a break-down in the dielectric which leads to the voltage falling to about 25V and the current increases to a set constant value. A plasma channel is created between the two electrodes and around this plasma channel a vapour bubble forms. The surrounding dense dielectric restricts the growth of the plasma channel, concentrating the input energy (governed by VIt) into a small volume. Energy densities of 3 J/mm^2 result which causes the plasma temperature to reach near 40,000°K. At this temperature the work piece is melted and vaporised.

The EDM machine used in this work was under Computer Numerical Control (CNC), so the desired parameters could be directly programmed into the computer and the machine would complete machining without the need for supervision. The EDM process, by controlling the current, voltage, arc time and length, tool finish and flushing time, can create a fine surface finish below 10μm **[98]**.

4.1.4.3. *EDM machined specimens.*

A polished flat copper electrode was used to machine the steel test specimens. The copper electrode's surface measured 50 mm by 50 mm. The EDM machine settings are listed in **table 4.1.2**.

Voltage	Current	spark time	Spark gap	Machining time	Flushing time	Tolerance setting
200 V	8 A	1.6 μs	3.2 μm	0.2 s	0.4 s	5

Table 4.1.2 EDM machine setting parameters.

Both the plain (3P) and welded (2P) specimens' surfaces were machined to a depth of approximately 0.5 mm. A surface thickness of 0.55 mm was removed from the cracked weld specimen (21B) and the new surface generated was labelled as '22B'. The weld seams were not visible on the EDM machined surfaces, although the fatigue crack on surface '22B' was visible and appeared as a very thin dark line. The visible crack on the surface was measured and found to be 26 mm in length and was situated at 20.5 mm from location 'A', moving towards location 'U' (**figure 4.1.2**). The steel specimens' surfaces, which were EDM machined for this study, all showed a surface layer which appeared dull in texture and was referred to as the 'recast white layer'. It is caused by a resolidified layer of molten parent material and is often alloyed with tool material as well as with elements from the broken-down dielectric **[99]**.

4.2. RESULTS AND ANALYSIS OF BARKHAUSEN EMISSION FROM PARENT METAL, WELDED STEEL, CRACKED WELD STEEL AND MACHINED SPECIMENS.

In this section the Barkhausen emission results are presented from the differing specimens; plain steel, welded steel and cracked weld steel. The electromagnetic and acoustic Barkhausen signals, along with their characteristics are briefly discussed. Three signal parameters have been used to quantify the nature of the changing signal envelopes and these are also presented graphically for each specimen. The three signal parameters are the maximum signal voltage (V_{MAX}), time of maximum peak (T_P) and signal energy.

4.2.1. Results from the Plain Steel Specimen.

4.2.1.1. *EBE Results from the plain steel specimen (3P).*

Barkhausen measurements were made across the surface of the plain steel specimen, labelled 3P. The EBE signal envelope shape was consistent and reproducible across the entire region of the steel specimen studied. The EBE signal appeared as a single peak envelope (**figure 4.2.1** to **4.2.4**). The EBE envelope shape exhibited an initial gradual increase which, at **0.7 s** on the envelope, suddenly changed. From this point the signal envelope increased at a greater rate. The envelope's gradient reduced at approximately **0.95 s** only to rapidly increase to a maximum peak at around **1.05 s** in the recording window. The signal then dropped off sharply to zero at around **1.2 s**.

The EBE signal amplitude across the surface of the specimen varied slightly, as seen in **figure 4.2.1** to **4.2.4**. The calculated EBE parameters for each of the locations are provided in **Figure 4.2.5.** The largest 'maximum signal voltage' (V_{MAX}) detected on the EBE envelopes from the plain steel surface (3P) was **0.52 V** on location 'I' and the lowest being **0.46 V** on location 'Q'. This provided an EBE V_{MAX} value range of **0.06 V**.

As the region of material studied was essentially uniform in composition and microstructure, the range of signal amplitude was not expected to change significantly. The presence of a range of maximum signal voltages probably suggested some unevenness in the surface stress distribution on the 'as-received' plain steel specimen.

The time of signal envelope peak from each location on the surface of the specimen fluctuated slightly. The time at which the maximum peak occurred fell between **1.02 s** and **1.05 s**, but a value of **1.04 s** was found to be the average for experimental runs on this steel specimen and is listed in **table 4.2.1**.

Generally signal energies, of the EBE envelopes, varied in a similar manner to the maximum signal voltage. The signal energy range was between **0.051 V^2s** and **0.065 V^2s**, with the average signal energy for the numerous locations on the surface of the specimen being **0.061 V^2s**, **±0.007 V^2s**. The signal energy difference across the specimen was **0.014 V^2s**. This is a reflection of the uneven stress and deformation conditions across the surface of the specimen due to the 'as-received' surface finish. As all the specimens used in this section have the same surface finish, the averaged EBE envelope parameters (listed in **table 4.2.1** along with their percentage errors) can be taken as average characteristic values for the plain EN-43A steel plate.

EN43-A Plain steel specimen (3P).	Maximum Signal amplitude. V_{MAX} (V)	Time of Peak. T_p (s)	Signal Energy. (V^2s)
EBE parameters	0.496 ±0.030	1.039 ±0.015	0.061 ±0.007
% error	6 %	1.4 %	10.7 %

Table 4.2.1 EBE signal envelope parameters from the plain steel specimen (3P) surface are shown. Data from the 40 mm region (locations 'A' through to 'U') were recorded and the average values are shown.

If the trend between signal energy and 'maximum signal voltage' is examined then there does not appear to be an obvious relationship between the two parameters. For positions on the specimen surface from left to right, the signal energy together with the signal voltage decreases. The signal energy decrease, however, does not exactly mimic the maximum voltage decrease from one position to another.

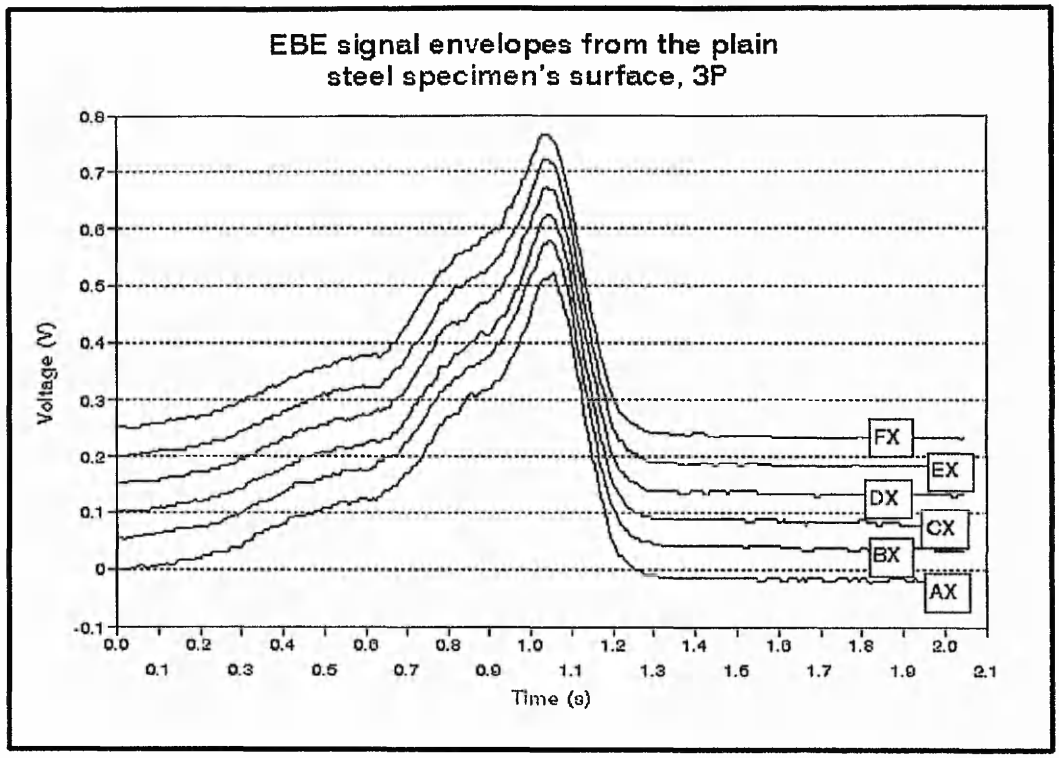


Figure 4.2.1 EBE signal envelopes from locations 'A' to 'F' across the surface of the plain EN-43A steel specimen. Each EBE envelope is the average of a number of signals and this is denoted by 'X'.

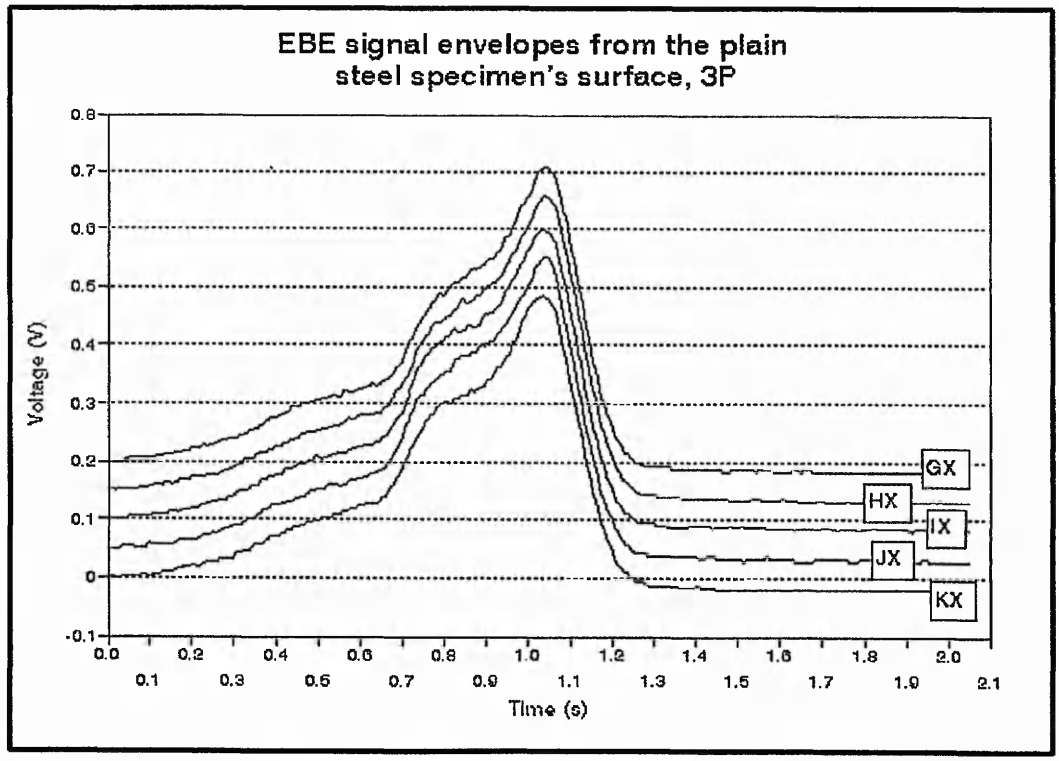


Figure 4.2.2 EBE signal envelopes from locations 'G' to 'K' across the surface of the plain EN-43A steel specimen. Each EBE envelope is the average of a number of signals and this is denoted by 'X'.

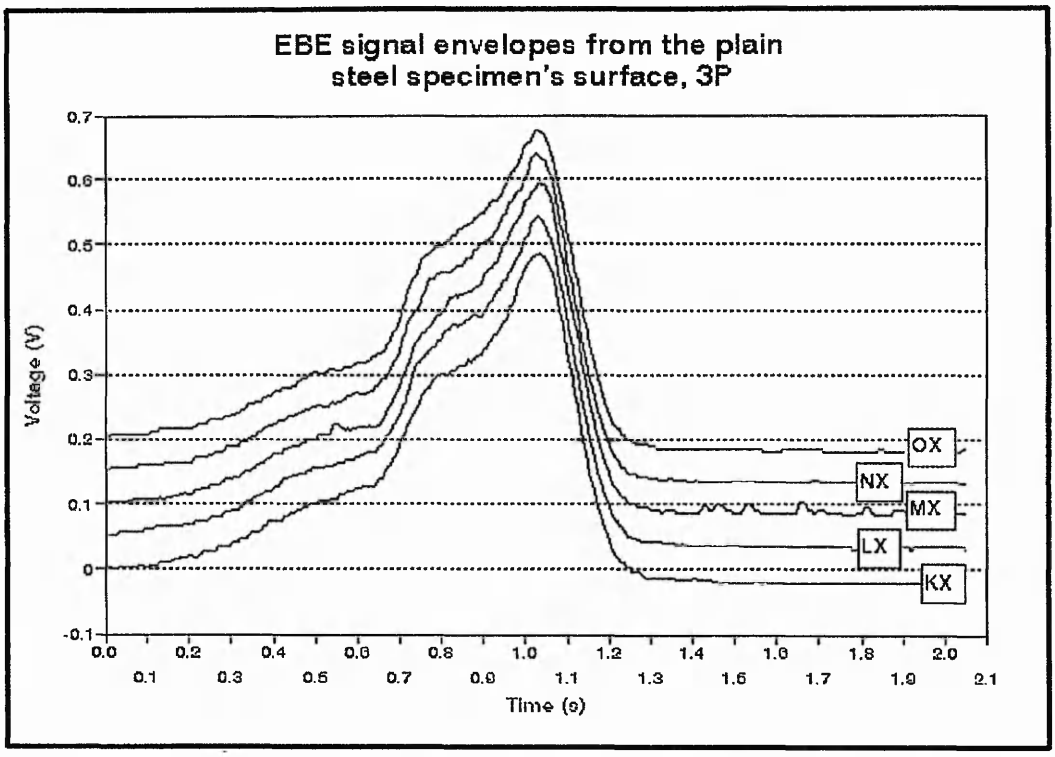


Figure 4.2.3 EBE signal envelopes from locations 'K' to 'O' across the surface of the plain EN-43A steel specimen. Each EBE envelope is the average of a number of signals and this is denoted by 'X'.

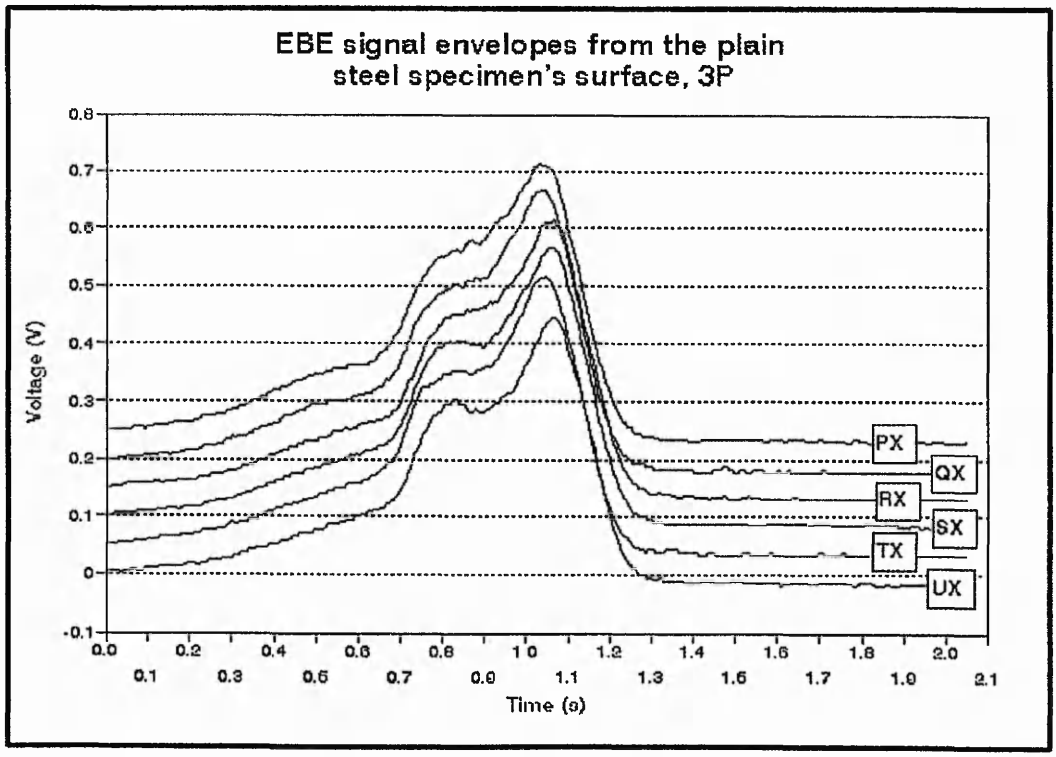


Figure 4.2.4 EBE signal envelopes from locations 'P' to 'U' across the surface of the plain EN-43A steel specimen. Each EBE envelope is the average of a number of signals and this is denoted by 'X'.

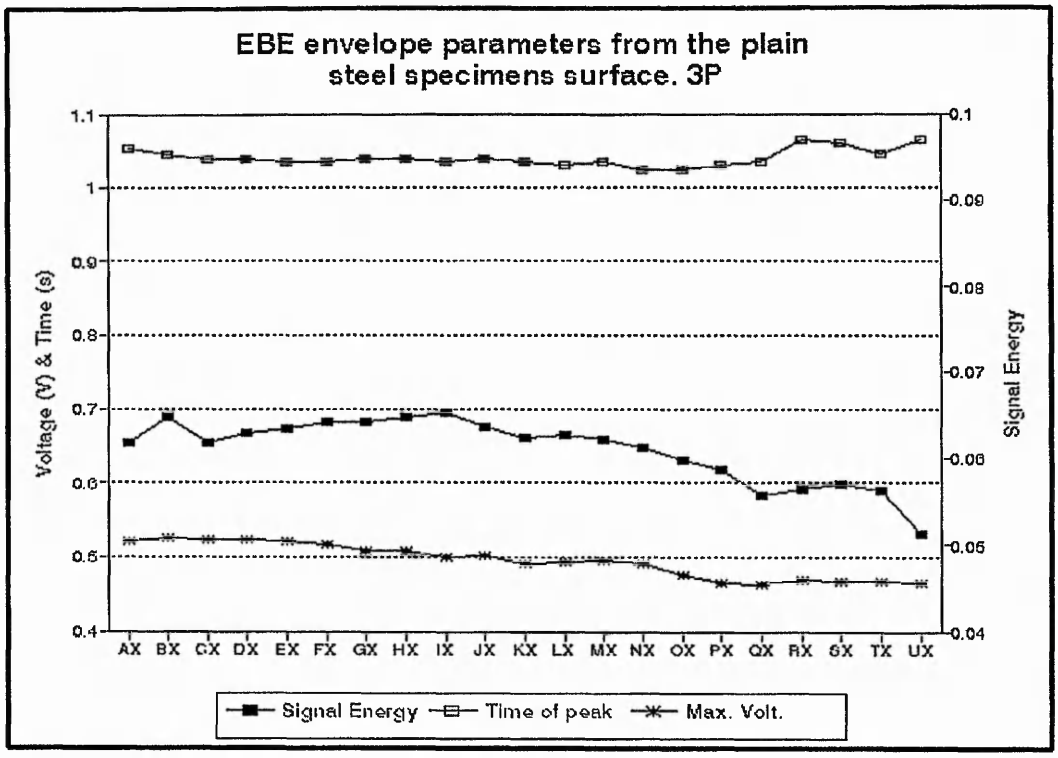


Figure 4.2.5 EBE envelope parameters, signal energy (units V^2s), 'maximum signal voltage' (V_{MAX}) and 'time of peak' (T_P) from the 'as-received' plain EN-43A steel specimens surface. Data taken from **figures 4.2.1** to **4.2.4**.

4.2.1.2. *ABE results from the plain steel specimen (3P).*

The ABE signal shapes were found to be relatively reproducible across the entire central 40mm region of the steel specimen (3P), except for the presence of the spikes on the envelope. The signal envelopes can be seen in **figure 4.2.6** and **4.2.7**. The ABE signal appeared in the form of a double peaked envelope, the first peak being smaller than the second peak. Spikes can also be seen on certain ABE envelopes. The spike peaks mainly appeared near the second peak of the double peak envelopes. Unlike the double peak form of the ABE envelopes, the spikes were not consistently reproducible. In this work they have been considered a part of the ABE envelopes since they influence certain parameters.

The ABE maximum signal voltage (V_{MAX}) varied in amplitude across the surface of the specimen. The maximum signal voltage (second peak of the ABE envelope) varied over a range of values between **0.91 V** to **1.23 V**, as can be seen in **figure 4.2.8**. The largest amplitude presented here was a consequence of a spike peak appearing at the same time as the maximum peak. Excluding the spike peak value found at position 'G' the spread of the signal amplitude was approximately **0.13 V**.

The time of maximum peak (T_P) for ABE signals, from the nine locations, ranged between **1.11 s** and **1.17 s**. This gave a spread of T_P values over **0.06 s**. The presence of a spike was not counted as a maximum voltage unless it occurred upon the maximum peak of the ABE envelope.

The ABE signal energy across the surface of the steel specimen varied between **0.198V^2s** and **0.288 V^2s**, with the majority of the signal energy values lying between **0.20V^2s** and **0.23 V^2s**. The ABE signal energy values for the specimen were expected to be similar, irrespective of surface location, due to the relative uniform structure of the specimen.

As the steel plate specimen was rolled and machined down to size by grinding, the difference in the signal energies and signal amplitude together with the time of peak,

were all a consequence of the specimen preparation process. It should be noted that average signal energy, maximum voltage and time of peak for this specimen are **0.232V^2s (±0.045 V^2s), 0.993 V (±0.167 V), 1.150 s (±0.028 s)** respectively. These ABE envelope parameters are listed in **table 4.2.2** along with their percentage errors. These three values (listed in **table 4.2.2**) can be taken as average and as the characterising values of the plain EN-43A steel plate, but at the same time the variations within the observed results from position to position should not be overlooked. The signal energy may be a more effective parameter of the ABE envelope, in this case, as the effect of sharp spikes are less pronounced on energy compared to the V_{MAX} parameter.

EN-43A Plain steel specimen (3P).	Maximum Signal amplitude. V_{MAX} (V)	Time of Peak. T_p (s)	Signal Energy. (V^2s)
ABE parameters	0.993 ± 0.167	1.150 ±0.028	0.232 ±0.045
% error	17 %	2 %	19 %

Table 4.2.2 ABE signal envelope parameters from the plain steel specimen (3P) are shown. Data from the 40 mm surface region (locations 'A' through to 'I') were recorded and the average values are displayed.

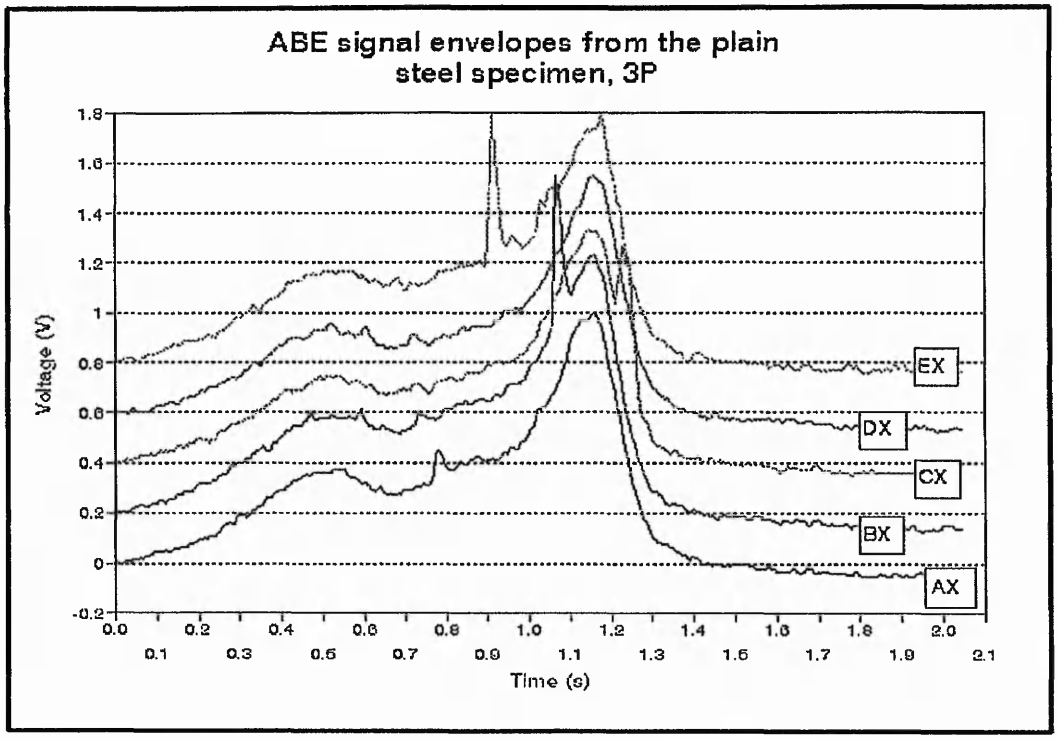


Figure 4.2.6 ABE signal envelopes from locations 'A' to 'E' across the surface of the plain EN-43A steel specimen. Each ABE envelope is the average of a number of signals and this is denoted by 'X'.

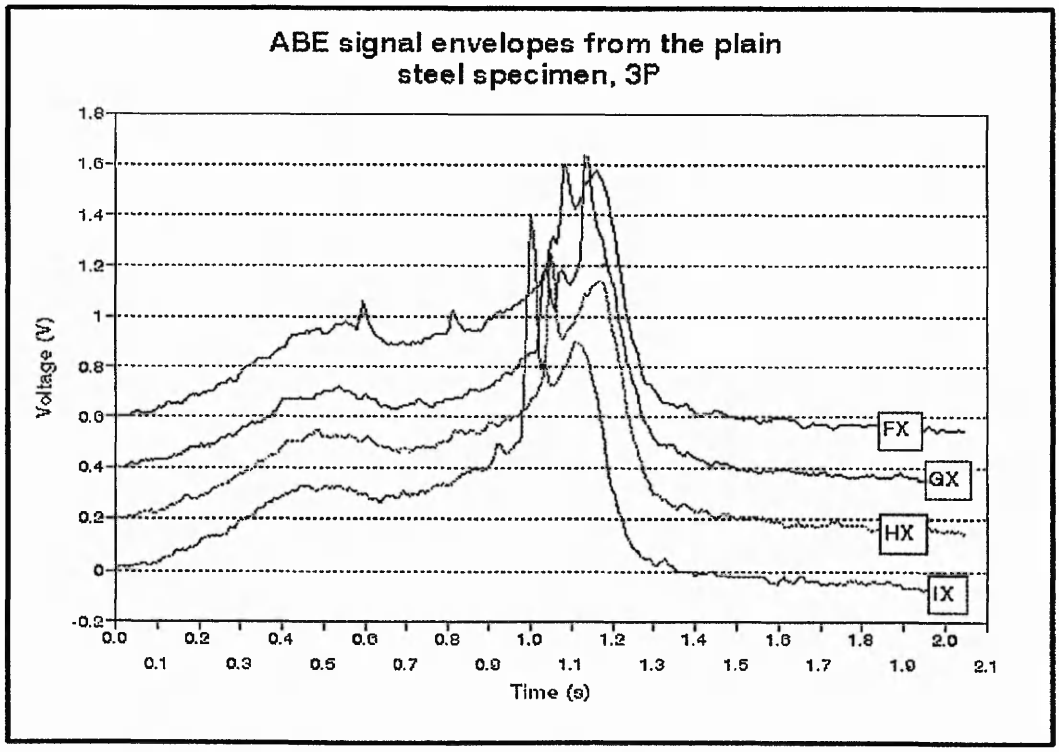


Figure 4.2.7 ABE signal envelopes from locations 'F' to 'I' across the surface of the plain EN-43A steel specimen. Each ABE envelope is the average of a number of signals and this is denoted by 'X'.

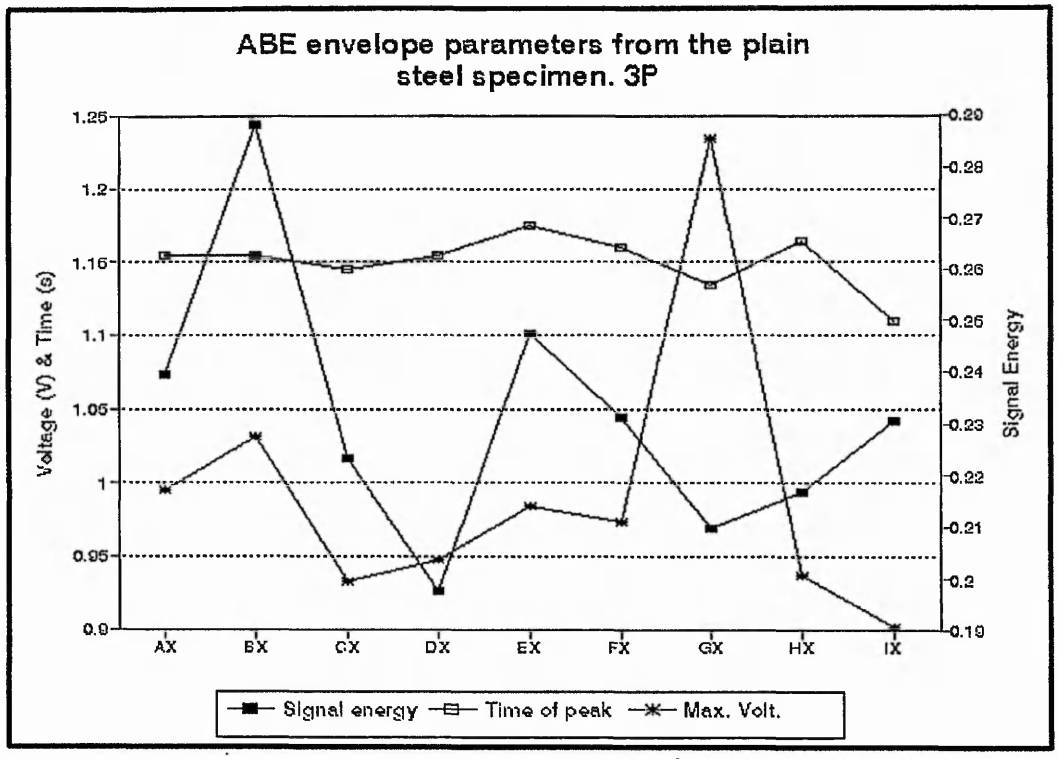


Figure 4.2.8 ABE envelope parameters, signal energy (units V^2s), 'maximum signal voltage' (V_{MAX}) and 'time of peak' (T_P) from the 'as-received' plain EN-43A steel specimens surface. Data taken from **figures 4.2.6** to **4.2.7**.

4.2.2. Results from the Welded Steel Specimen.

4.2.2.1. *EBE results from the welded steel specimen (2P).*

Barkhausen measurements were taken on the welded steel specimen (2P) and the EBE envelopes were found to be reproducible. The EBE envelopes from each location changed shape as the probe was moved across the surface of the specimen. This was due to the change in the microstructure and stress state of the welded specimen. The detected signal envelopes can be seen in **figure 4.2.9** to **4.2.12**. On location 'A' the EBE envelope appeared as a double peak, with the first peak being smaller than the second. As the EBE probe moved towards the centre of the specimen the signal envelopes gradually changed and the first peak began to increase in height while the second peak decreased in height (**figure 4.2.9**). The EBE envelopes changed in shape until there was no second peak left, just a steep downward slope. On the weld region, at the centre of the specimen, the signal envelopes appeared with only the first peak and a plateau was located on the position of the second peak. The same trend was evident as the EBE sensor was moved away from the weld.

The time of the maximum peak (T_P), which was the first peak for the majority of EBE envelopes from this specimen, was used as a parameter to quantify the signal envelopes. The T_P values remained between **0.82 s** close to the edges of the studied region and at **0.75 s** for the weld and affected regions. On the parent material regions (location 'A' and 'U') the second peak became the largest which moved the T_P value close to 1 second. On either side of the weld the EBE envelopes appeared similar in shapes, indicating that the formation of the weld had affected the specimen material properties.

The maximum signal voltage (V_{MAX}) of the EBE envelopes increased as the weld seam was approached (**figure 4.2.13**). The maximum signal voltage was reached at around 8mm on either side from the centre of the weld, on the heat affected zone (HAZ). The V_{MAX} values on both sides differed: the left hand side of the sample exhibited lower amplitudes than the right hand side and this can be seen in **table 4.2.3**. These results

were reproducible even when the specimen was magnetised in a reverse direction and were clearly demonstrated to be due to a specimen material property. A possible explanation could be that the clamp used to hold the specimen in position while the welding was carried out, acted as a heat sink, thus, providing uneven cooling of the specimen. This could be responsible for the asymmetry in the maximum signal voltage across the specimen's surface. The V_{MAX} value at the centre of the weld was **0.60 V ±0.01 V** (location 'K'). The largest V_{MAX} value on either side of the weld seam was recorded as **0.64 V** and **0.68 V** left and right side respectively and is summarised in **table 4.2.3**. The signal amplitude at the edges of the examined region were **0.46 V** and **0.50 V** on position 'A' and 'U' respectively. A spread of maximum signal voltage of **0.21 V** was observed across the three different regions of this specimen.

The signal energy from the EBE envelopes taken across the specimen showed very similar trends to the maximum signal voltage. The signal energy ranged between **0.055V^2s** at the edge of the studied region, to **0.087 V^2s** on the weld centre (location 'K') and a maximum of **0.098 V^2s** on the HAZ region, located approximately 6 mm from weld centre. The three regions provided an energy spread of **0.043 V^2s,** with the HAZ region showing the greatest signal amplitude as well as the largest signal energy. The EBE envelopes from this specimen were larger than the those detected on the plain steel specimen (3P). The change in the microstructure and stress state, due to the welding process, appears to have altered the EBE envelope size and shape.

EN-43A Welded steel specimen (2P). region	location	Maximum amplitude. V_{MAX} (V)	Time of Peak. T_p (s)	Signal Energy. (V^2s)
Parent steel	A	0.46 ±0.01	0.988 ±0.001	0.055±0.002
	U	0.49	0.974	0.067
HAZ region	G	0.64 ±0.01	0.779±0.001	0.093±0.002
	N	0.68	0.768	0.099
Weld seam	J	0.61 ±0.01	0.758 ±0.001	0.087 ±0.002
	K	0.60	0.748	0.088
	L	0.65	0.748	0.094
% error	~	2 %	0.1 %	2 %

Table 4.2.3 EBE envelope parameters from the welded steel specimen (2P) surface. Data from specific material regions ranging from parent material ('A' and 'U'), HAZ region ('G' and 'N') and weld seam ('J', 'K' and 'L') are listed.

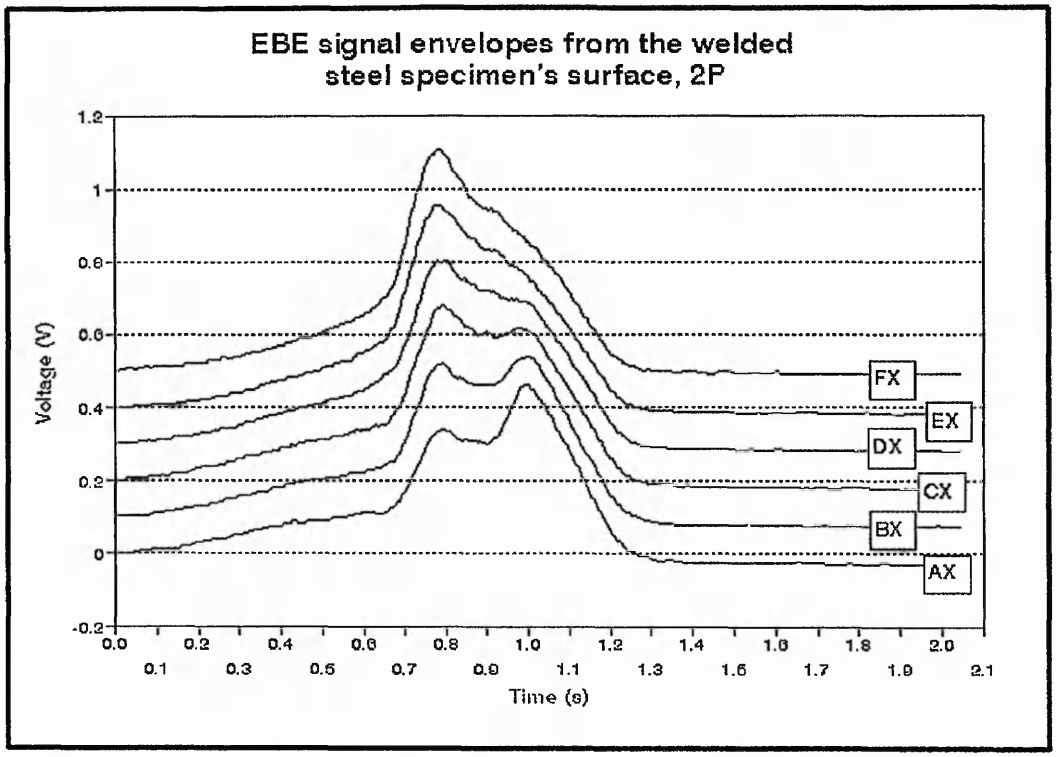


Figure 4.2.9 EBE signal envelopes from locations 'A' to 'F' across the surface of the welded steel specimen. Each EBE envelope is the average of a number of signals and this is denoted by 'X'.

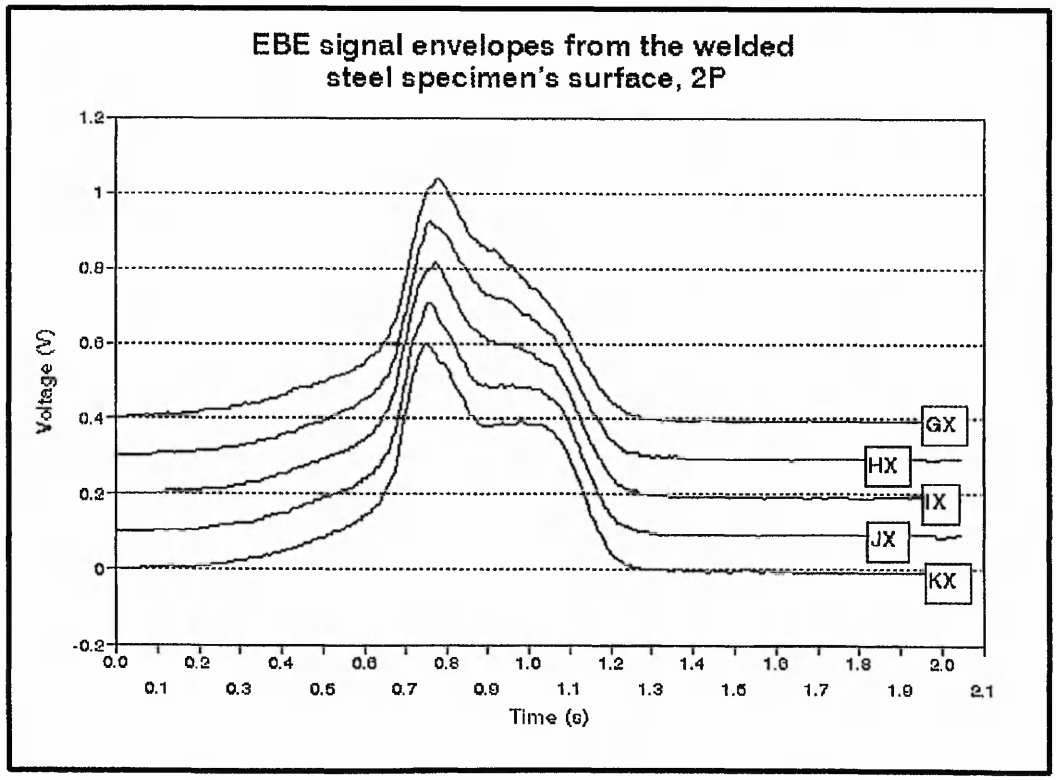


Figure 4.2.10 EBE signal envelopes from locations 'G' to 'K' across the surface of the welded steel specimen. Each EBE envelope is the average of a number of signals and this is denoted by 'X'.

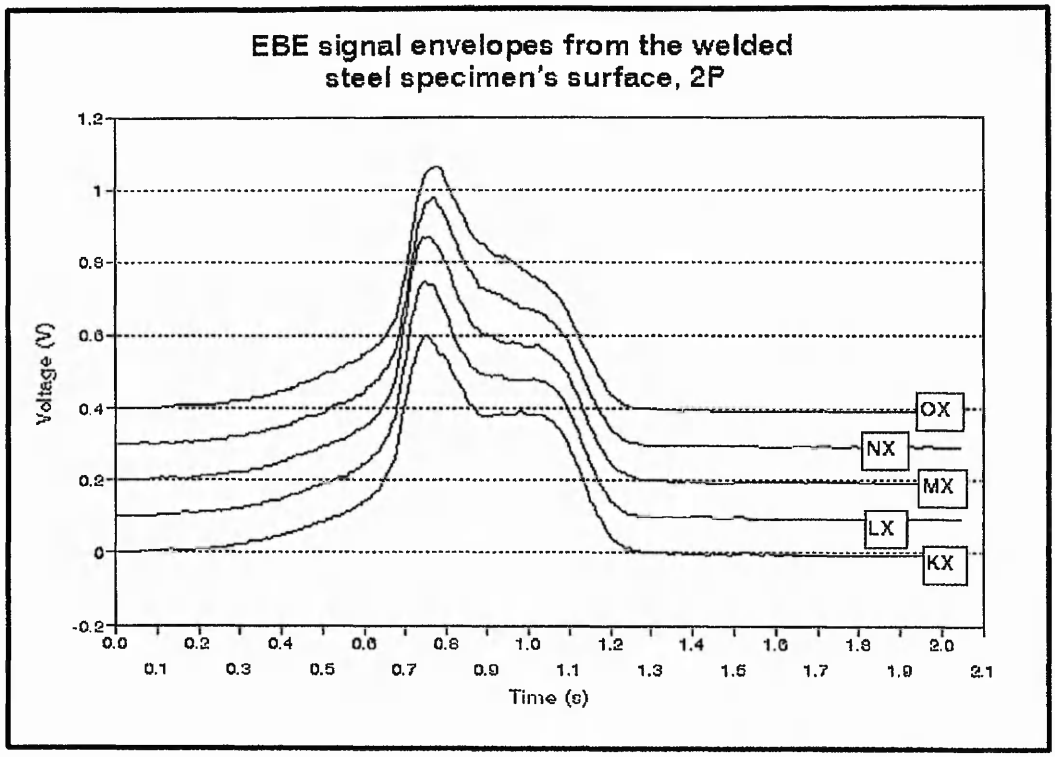


Figure 4.2.11 EBE signal envelopes from locations 'K' to 'O' across the surface of the welded steel specimen. Each EBE envelope is the average of a number of signals and this is denoted by 'X'.

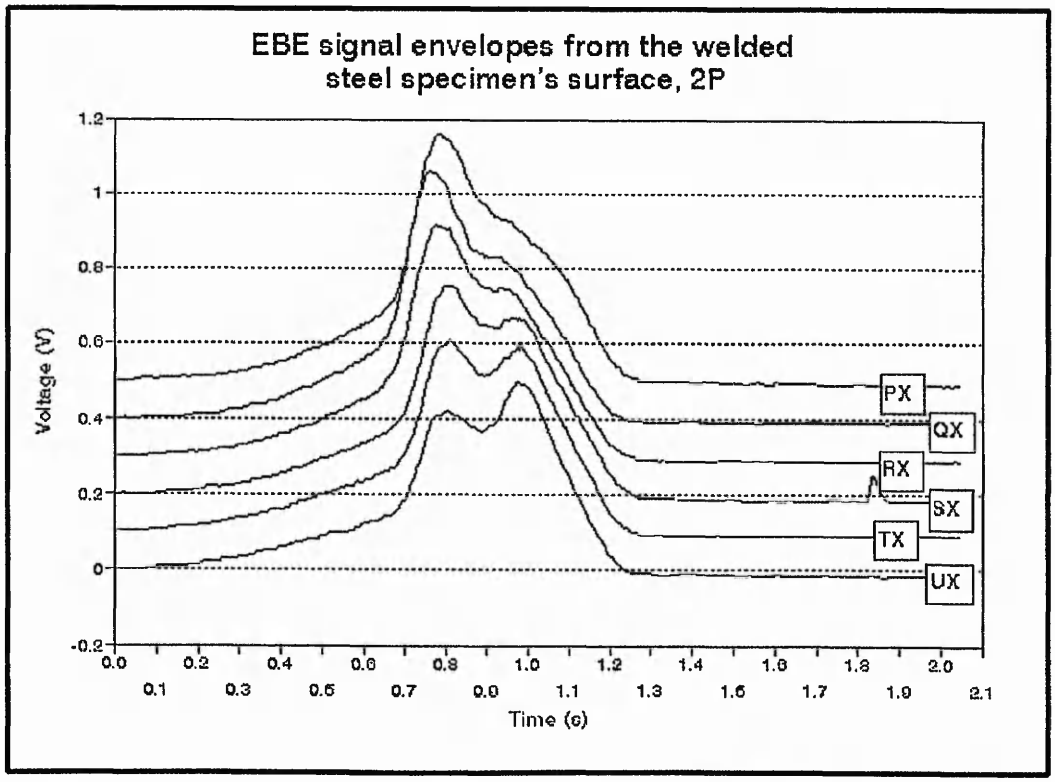


Figure 4.2.12 EBE signal envelopes from locations 'P' to 'U' across the surface of the welded steel specimen. Each EBE envelope is the average of a number of signals and this is denoted by 'X'.

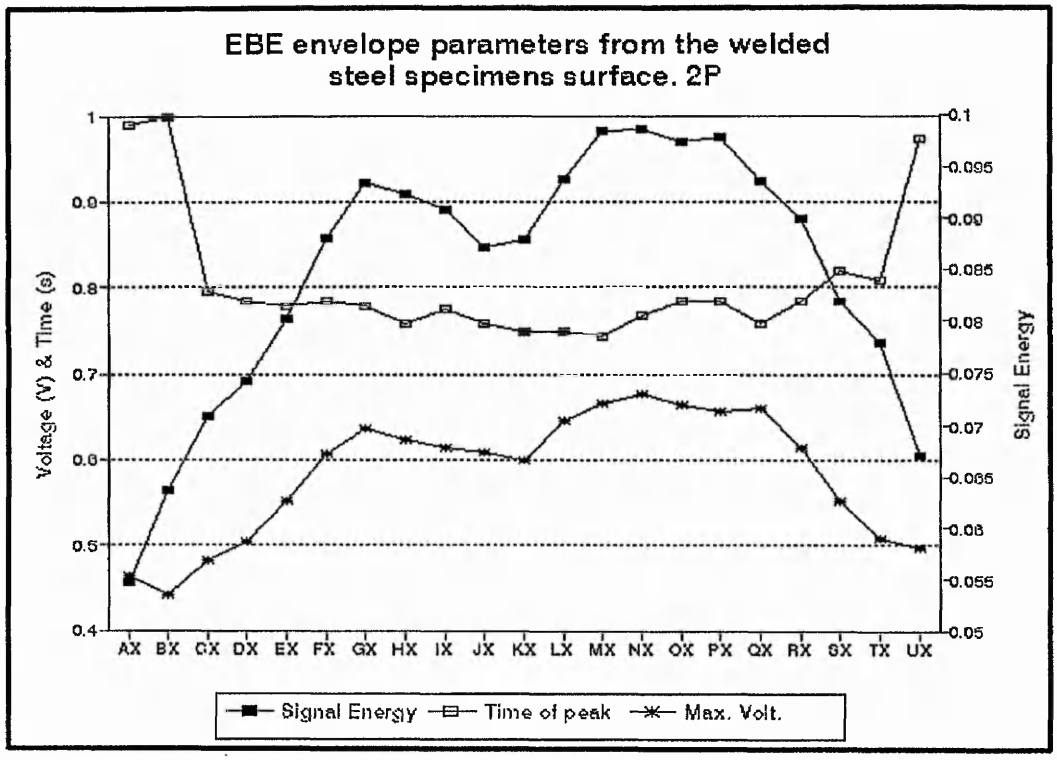


Figure 4.2.13 EBE envelope parameters, signal energy (units V^2s), 'maximum signal voltage' (V_{MAX}) and 'time of peak' (T_P) from the 'as-received' welded steel specimen surface. Location 'A' to 'F' is parent material, 'F' to 'H' is HAZ and the weld seam is approximately 10.5mm in width with the centre being on location 'K'. Data taken from **figures 4.2.9** to **4.2.12**.

4.2.2.2. *ABE results from the welded steel specimen (2P).*

The ABE measurements were taken on the same region as the EBE measurements. The ABE signals from the welded steel specimen (2P) appeared essentially as a double peaked envelope and is shown in **figures 4.2.14** and **4.2.15**. The first peak was smaller than the second and was located between **0.50 s** and **0.55 s**, while the second peak was between **1.13 s** and **1.19 s** on the envelope.

The ABE signal envelopes showed a spike between the first and second peaks. This spike commonly appeared directly after the central dip in the ABE envelope. Occasionally, on repeated measurements, the spike moved away from the central region on the envelope. This lack of reproducibility of the spikes made calculation of the ABE signal energy, time of maximum peak and peak amplitude difficult. However, the ABE signal energies for the welded specimen lay within a range between **0.282 V^2s** to **0.358V^2s**, as shown in **figure 4.2.16**. This gave a signal energy spread of **0.076 V^2s**. The energy spread applies to the transducer positioned on different material types including weld metal, parent steel and finally, the heat affected zone at the weld and steel interface. These three different regions will have differing physical as well as magnetic characteristics, and this will affect the ABE signals in different ways. However, as the ABE is a volume effect, the acoustic emission of the differing material types will combine together, thus, generating a signal envelope from the whole volume of the magnetised specimen, which should be independent of transducer position.

The maximum signal voltage (V_{MAX}), excluding the rogue peaks, ranged between **1.32 V** and **1.72 V**. The spread of the maximum signal voltages was **0.41 V** over the three different material structures and is summarised in **table 4.2.4**. On the weld the maximum signal voltage was recorded at a value of **1.54 V (figure 4.2.16)**, which was lower than ABE voltages from adjoining locations. The presence of the weld appeared to have increased the average V_{MAX}, as well as, the signal energy values compared to the plain steel specimen 3P and this is discussed in **section 4.4**.

EN-43A welded steel specimen (2P).	Maximum Signal amplitude. V_{MAX} (V)	Time of Peak. T_p (s)	Signal Energy. (V^2s)
ABE parameters	1.51 ± 0.21	1.166 ± 0.024	0.322 ± 0.035
% error	13.8 %	2.1 %	10.8 %

Table 4.2.4 ABE signal envelope parameters from the welded steel specimen (2P) surface are shown. Data from the entire 40 mm surface region (locations 'A' through to 'I') were recorded and the average values are shown.

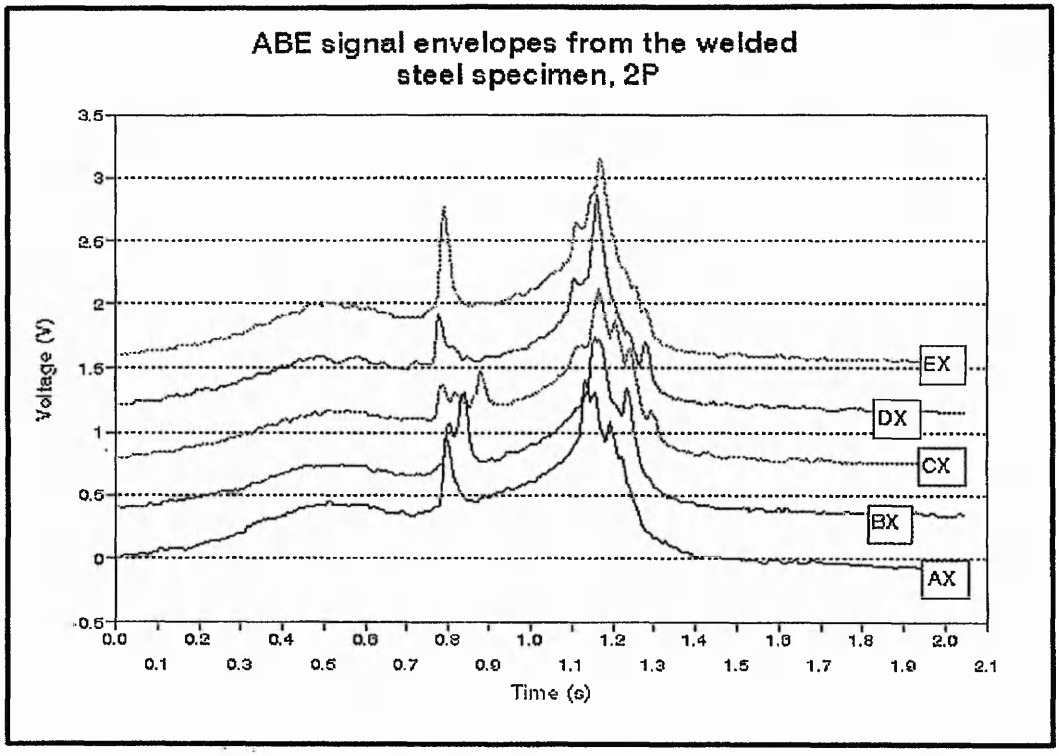


Figure 4.2.14 ABE signal envelopes from locations 'A' to 'E' across the surface of the welded steel specimen. Each ABE envelope is the average of a number of signals and this is denoted by 'X'.

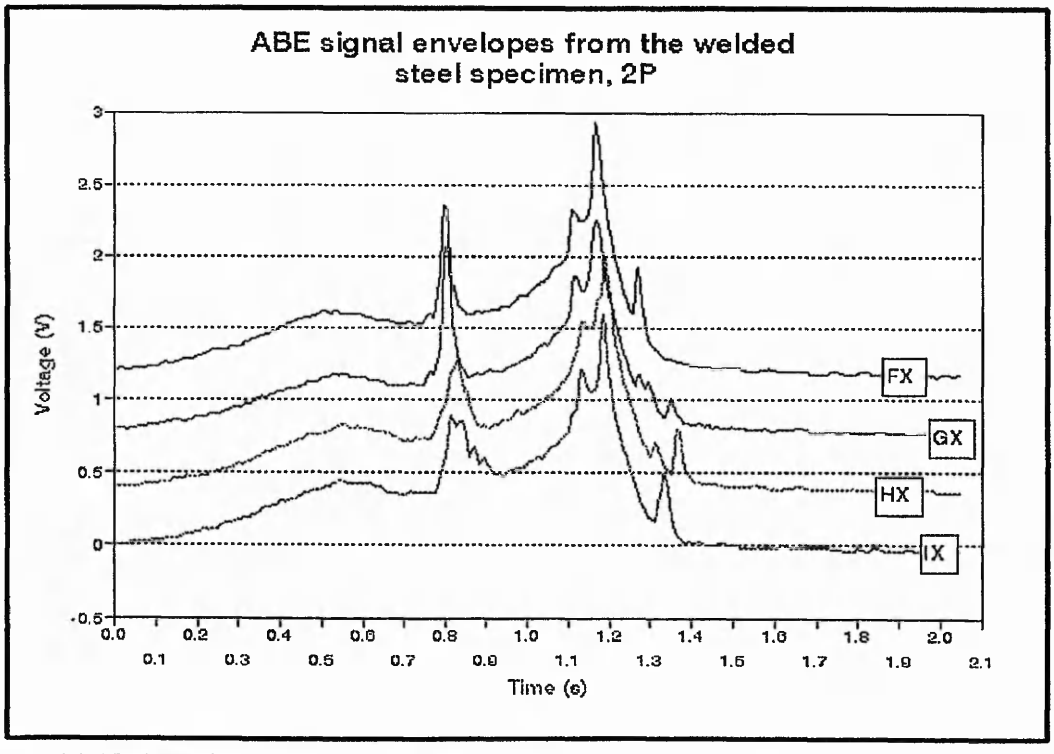


Figure 4.2.15 ABE signal envelopes from locations 'F' to 'G' across the surface of the welded steel specimen. Each ABE envelope is the average of a number of signals and this is denoted by 'X'.

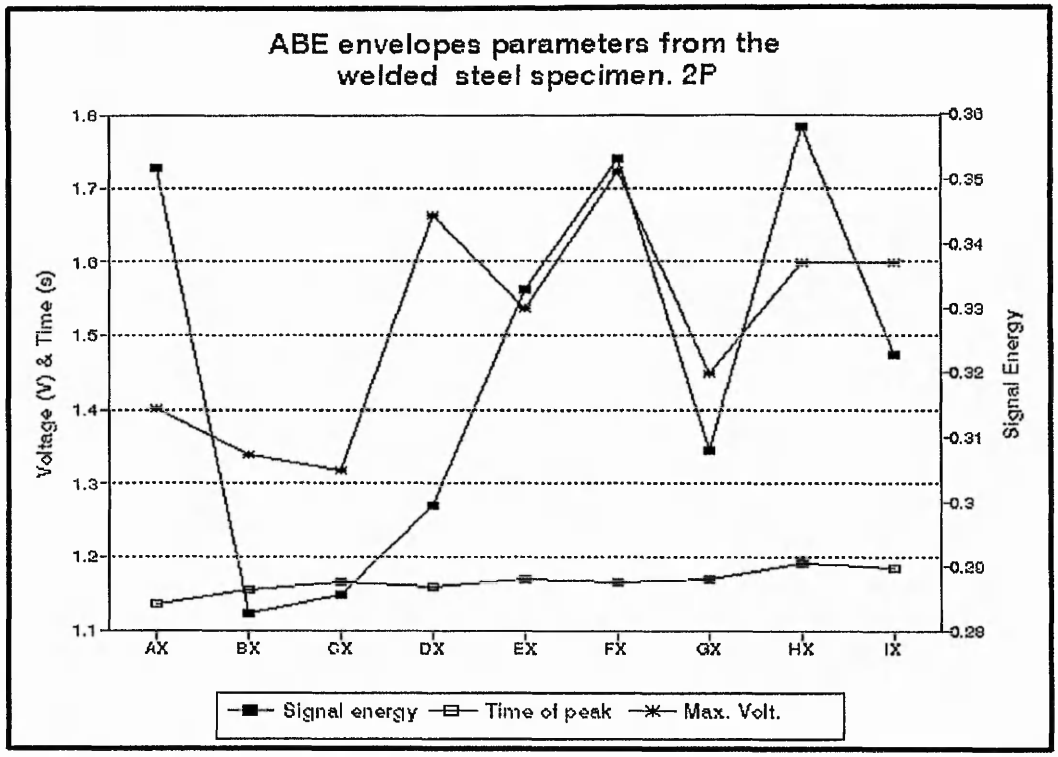


figure 4.2.16 ABE envelope parameters, signal energy (units V^2s), 'maximum signal voltage' (V_{MAX}) and 'time of peak' (T_P) from the 'as-received' welded steel specimens surface. Location 'A' to 'C' is parent material, 'C' to 'D' is HAZ and 'D' to 'F' is the weld seam which is approximately 10.5 mm in width with the centre being on location 'E'. Data taken from **figures 4.2.14** to **4.2.15**.

4.2.3. Results from the Cracked Weld Specimens.

Two welded EN-43A steel plate specimens were prepared by Sonaspection Ltd. The steel specimens contained a fine low-cycle fatigue crack at the centre of the weld. The surface breaking fatigue cracks were approximately 2-3 mm in depth. The surfaces of the specimens were machined using a circular grinder and the weld root and cap removed. The fine crack and weld seam was not visible on either side of each specimen. The top surface of both specimens was divided into 2 mm divisions and each of the 20 locations were marked 'A' to 'U', A=0 mm and U=40 mm. The crack in the specimens was located at around the central region, between positions 'K' and 'L'. The two specimens were labelled 21A and 21B.

4.2.3.1. *The EBE results from cracked weld specimen (21B).*

EBE was measured from a welded steel plate containing a fatigue crack (specimen 21B). The EBE envelopes obtained are shown in **figure 4.2.17** to **4.2.20**. These figures show that the EBE signal envelope changed shape as the transducer traversed across the surface of the specimen. At the edge of the studied region, around locations 'A' and 'U', the Barkhausen signals appeared as double peaked envelopes, with the first peak smaller than the second. As the sensor was moved towards the weld seam the detected EBE signal envelope changed shape. The envelope's maximum peak height decreased as the probe approached the HAZ, weld seam and crack. The smoothed double peaks became jagged and less distinct and the peak shifted to a different position on the envelope. The signal envelope's first peak increased, while the second peak decreased in height as the probe approached the weld seam and crack.

The amplitude of the EBE envelopes tended to decrease as the weld and fatigue crack were approached from both directions. **Figure 4.2.21** summarises this information and shows that the V_{MAX} value was at a minimum around location 'M', at a value of **0.36V**

(**±0.01 V**). The EBE signals with the greatest amplitudes were located at the edges of the studied region (location 'U'), where the maximum amplitude was found to be **0.57V**. This provided an EBE voltage spread of **0.21 V** for the cracked weld specimen 21B.

Time of maximum peak (T_P) also changed as the sensor traversed across the surface of the specimen. For the cracked weld specimen 21B, the change in position of the maximum peak depended on material properties such as microstructure, stress state and specimen history. At the outer edges of the studied regions, locations 'A' and 'U', time of maximum peak was **0.98 s** and **0.99 s** (**±0.01 s**) respectively and is shown in **table 4.2.5**. As the sensor moved towards the cracked weld, the maximum peak occurred earlier on the envelope, around **0.95 s**. The time shift was not large, but it was noticeable.

The signal energy exhibited by the EBE envelopes, from the cracked weld specimen 21B, changed as the sensor was moved across its surface. At the outer edges of the studied region the EBE signal energy values were at a minimum value of **0.053 V^2s** (**±0.002V^2s**). As the probe moved closer to the cracked weld region, the EBE signal energy increased to a maximum at around locations 'H' (**0.072 V^2s**) and 'O' (**0.061 V^2s**), summarised in **table 4.2.5**. As the probe continued towards the defect the EBE signal energy gradually decreased to a minimum of **0.054 V^2s** on location 'L', which was very close to the position of the crack. The overall signal energy spread of the specimen was **0.019 V^2s**. **Table 4.2.5** displays the EBE envelope parameters from each of the material regions on the surface of the cracked weld specimen. The presented data is taken from **figure 4.2.21**.

Cracked weld specimen (21B). region	location	Amplitude. V_{MAX} (V)	Time of Peak. T_p (s)	Signal Energy. (V^2s)
Parent steel	A	0.47 ±0.01	0.98 ±0.01	0.053 ±0.002
	U	0.57	0.99	0.053
HAZ region	H	0.43 ±0.01	0.99 ±0.01	0.072 ±0.002
	O	0.42	0.98	0.061
Cracked weld	L	0.37 ±0.01	0.96 ±0.01	0.054 ±0.002
% error	~	2 %	1 %	3 %

Table 4.2.5 EBE signal envelope parameters from the cracked weld steel specimen 21B. Data from specific material regions ranging from parent material ('A' and 'U'), HAZ region ('H' and 'O') and cracked weld (location 'L').

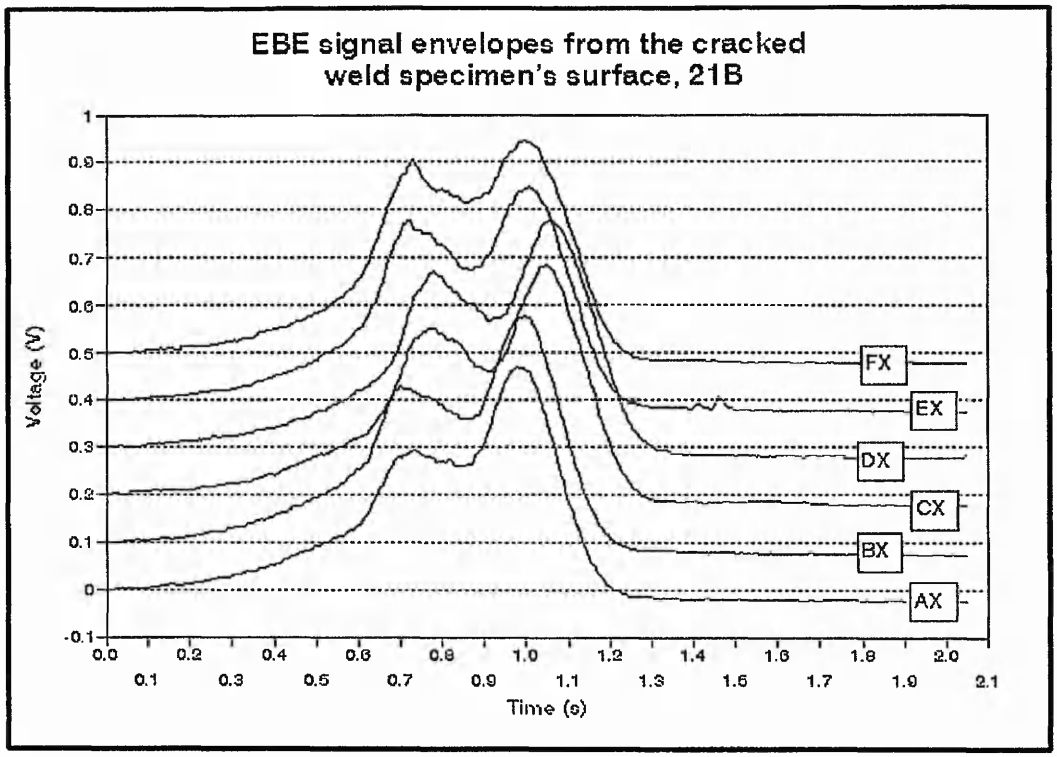


Figure 4.2.17 EBE signal envelopes from locations 'A' to 'F' across the cracked weld specimen's surface. Each EBE envelope is the average of a number of signals and this is denoted by 'X'.

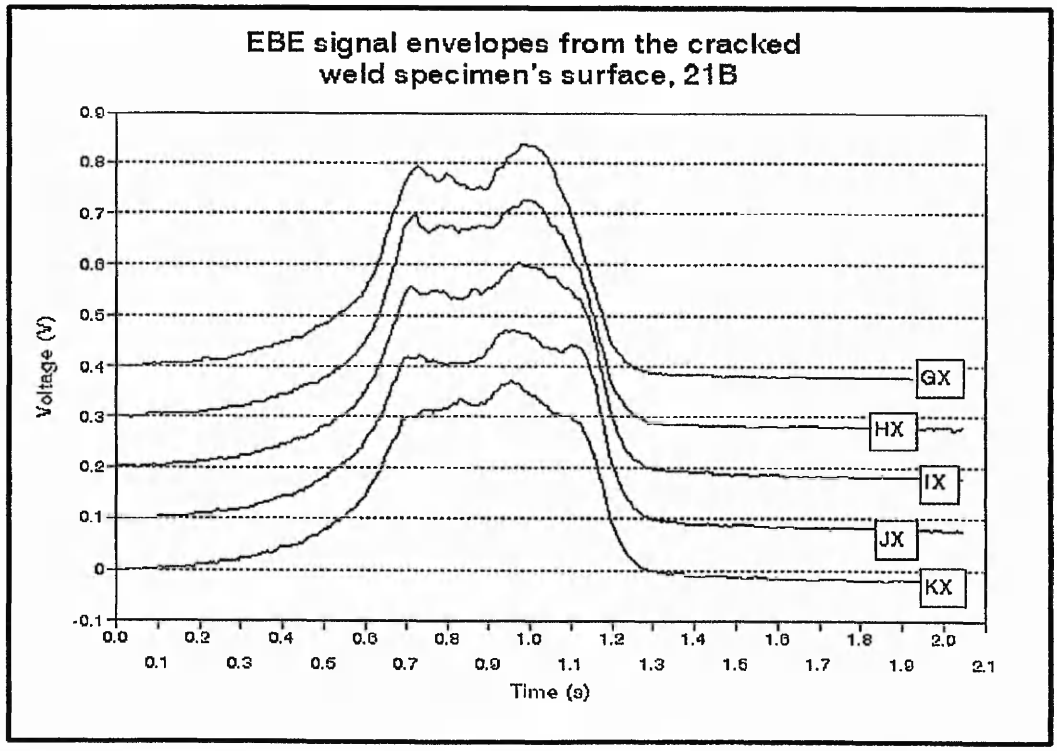


Figure 4.2.18 EBE signal envelopes from locations 'G' to 'K' across the cracked weld specimen's surface. Each EBE envelope is the average of a number of signals and this is denoted by 'X'.

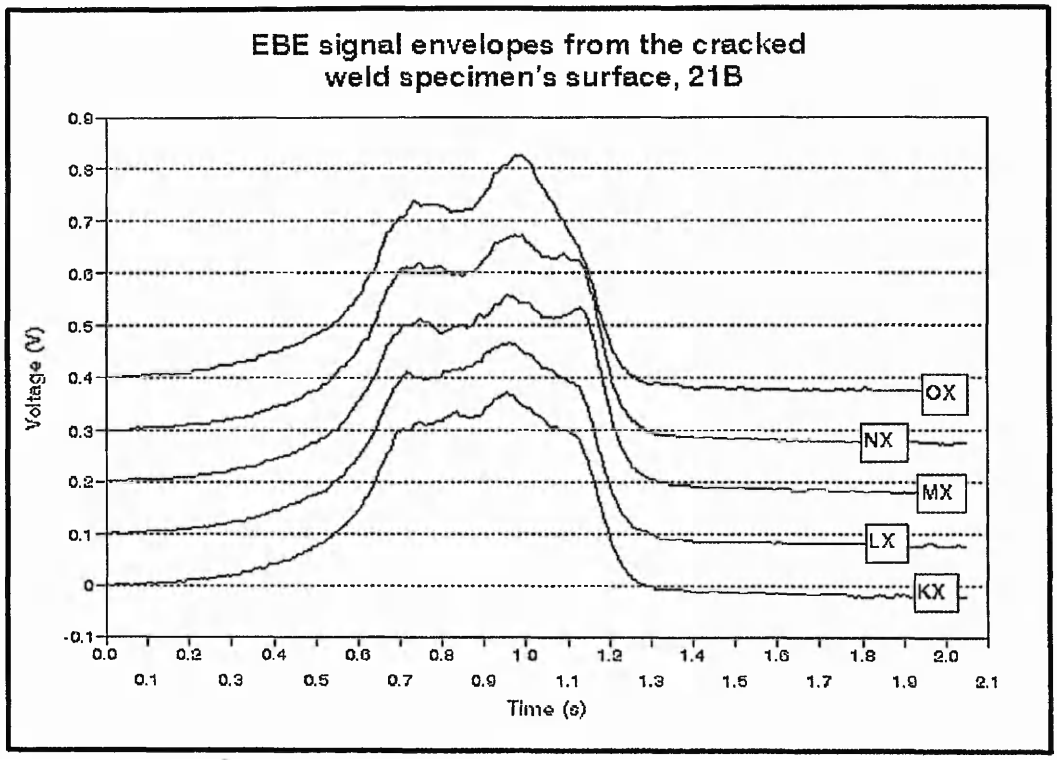


Figure 4.2.19 EBE signal envelopes from locations 'K' to 'O' across the cracked weld specimen's surface Each EBE envelope is the average of a number of signals and this is denoted by 'X'.

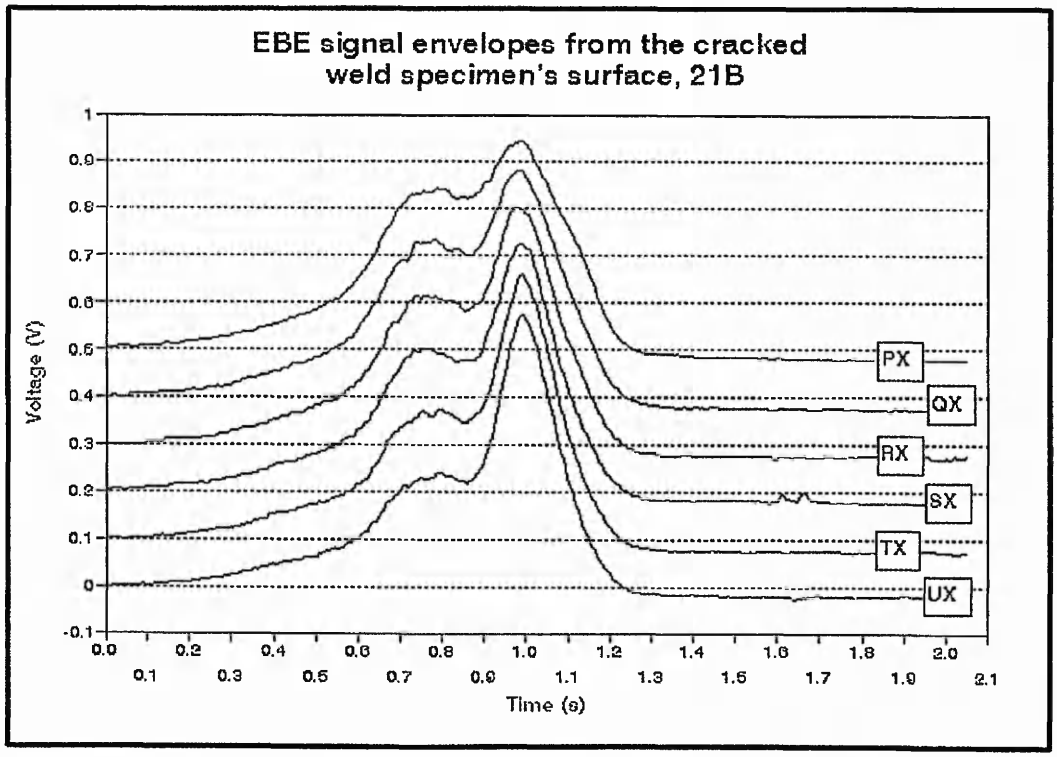


Figure 4.2.20 EBE signal envelopes from locations 'P' to 'U' across the cracked weld specimen's surface. Each EBE envelope is the average of a number of signals and this is denoted by 'X'.

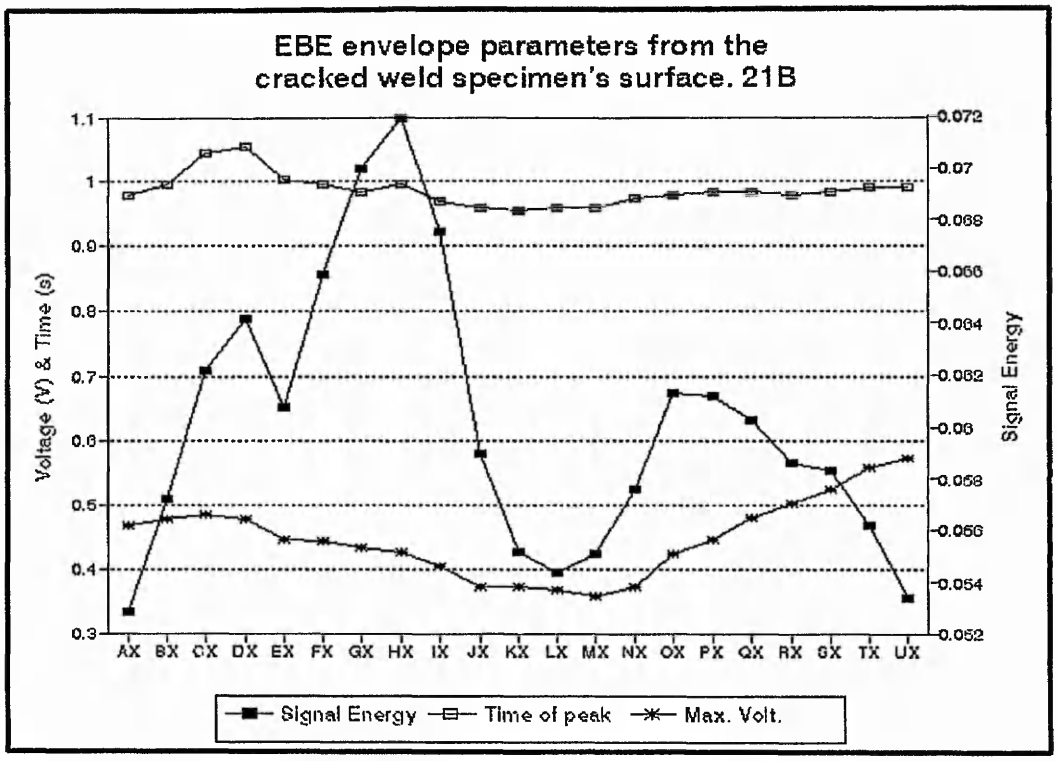


Figure 4.2.21 EBE envelope parameters, signal energy (units V^2s), 'maximum signal voltage' (V_{MAX}) and 'time of peak' (T_P) from the 'as-received' cracked weld steel specimens surface. Location 'A' to 'F' is parent material, 'F' to 'H' is HAZ and the weld seam is approximately 10.5mm in width with the centre being on location 'K'. The crack is positioned close to location 'L'. Data taken from **figures 4.2.17** to **4.2.20**.

4.2.3.2. *The ABE results from cracked weld specimen (21B).*

The ABE signal envelopes from the cracked weld specimen 21B are shown in **figures 4.2.22** and **4.2.23**. The ABE signal appeared, essentially, as a doubled peaked envelope, the first peak being smaller than the second. A number of spikes were observed on the second peak and masked the exact location of this peak. The first peak, in comparison with the second peak, was smooth. On location 'E' the ABE signal was noticeably smaller in magnitude when compared with the envelopes from other locations on the specimen. All of the signals were found to be reproducible.

The ABE envelopes' maximum signal voltage was taken at the point where the largest peak occurred and this data is displayed in **figure 4.2.24**. The largest peak coincided with one of the spikes, which was consistent for all the ABE signals from the cracked specimen 21B. Moving from location 'A' to 'C' the V_{MAX} value increased from **1.82 V** to **2.04 V**. A sudden decrease in signal amplitude was found on location 'E', at this position a signal amplitude of **1.59 V** was recorded. As mentioned before, location 'E' was directly above the weld seam and crack. From location 'F' onwards the V_{MAX} values returned to similar amplitudes to the first half of the specimen. The time at which the maximum signal amplitude occurred, for each of the ABE signals, remained relatively constant. The 'time of maximum peak' was between **1.04 s** and **1.05 s**.

The signal energy calculated from these ABE envelopes showed a similar trend to the maximum voltage peak. The signal energy at location 'E', on the cracked weld, shows a clear energy minimum with a value of **0.219 V^2s**. On the remaining locations, the spread of the signal energies lay between **0.356 V^2s** and **0.444 V^2s**. The presence of the crack appeared to cause this unexpected notable change in the ABE signals and is discussed further in **section 4.4**.

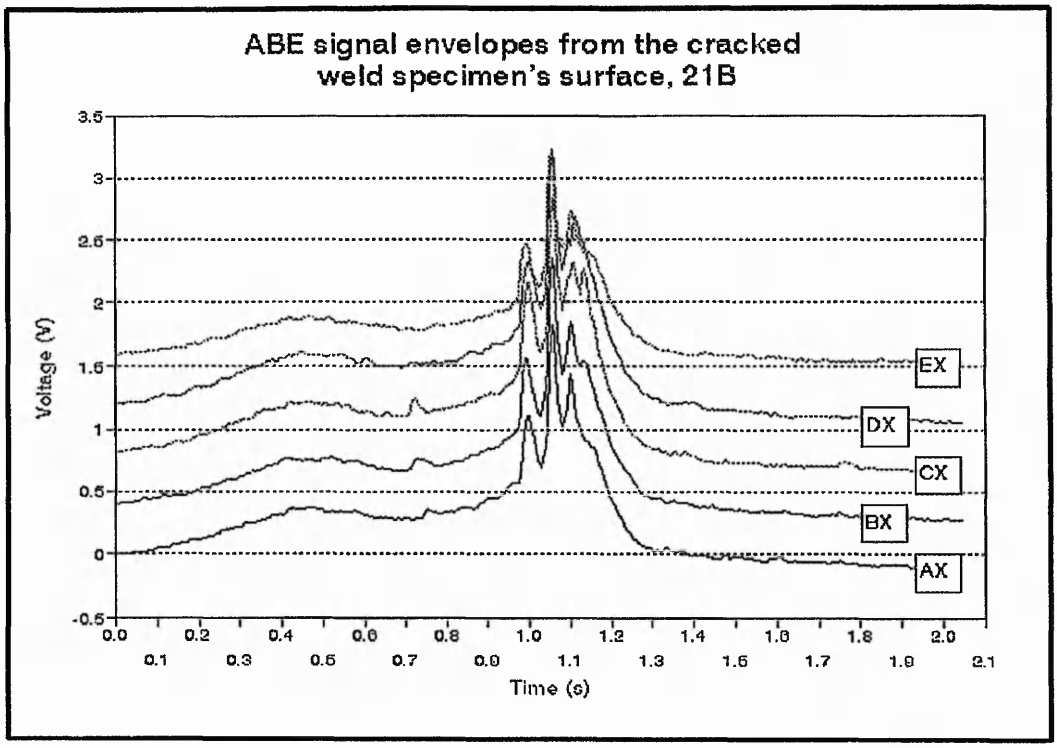


Figure 4.2.22 ABE signal envelopes from locations 'A' to 'E' across the cracked weld specimen's surface. Each ABE envelope is the average of a number of signals and this is denoted by 'X'.

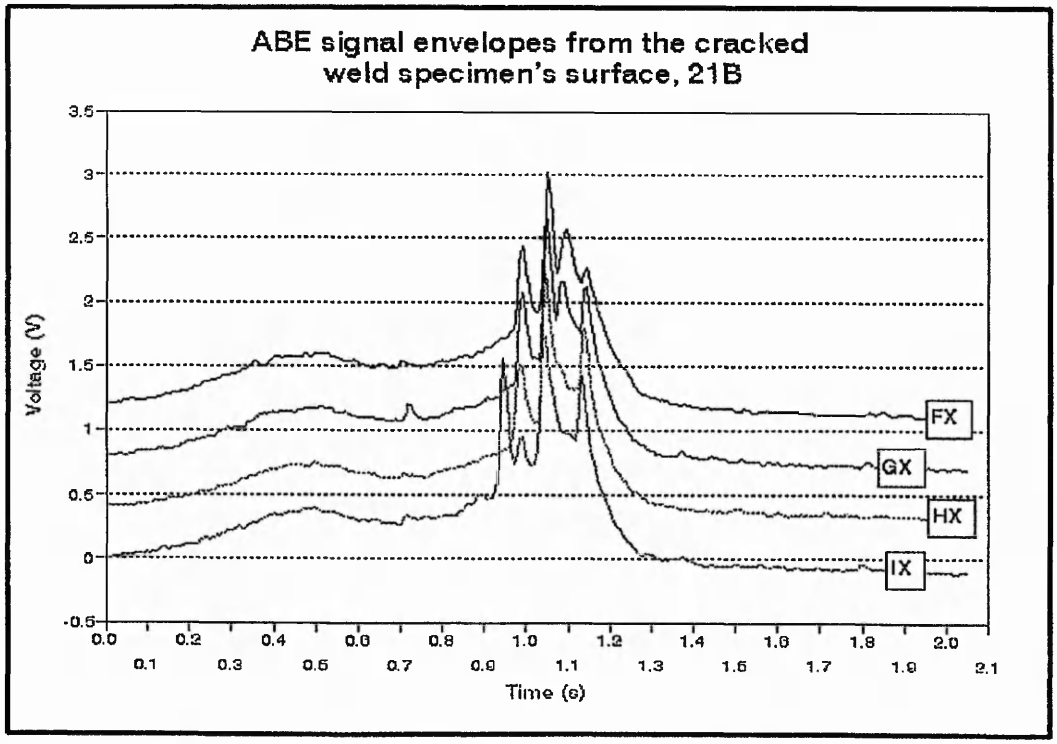


Figure 4.2.23 ABE signal envelopes from locations 'F' to 'I' across the cracked weld specimen's surface. Each ABE envelope is the average of a number of signals and this is denoted by 'X'.

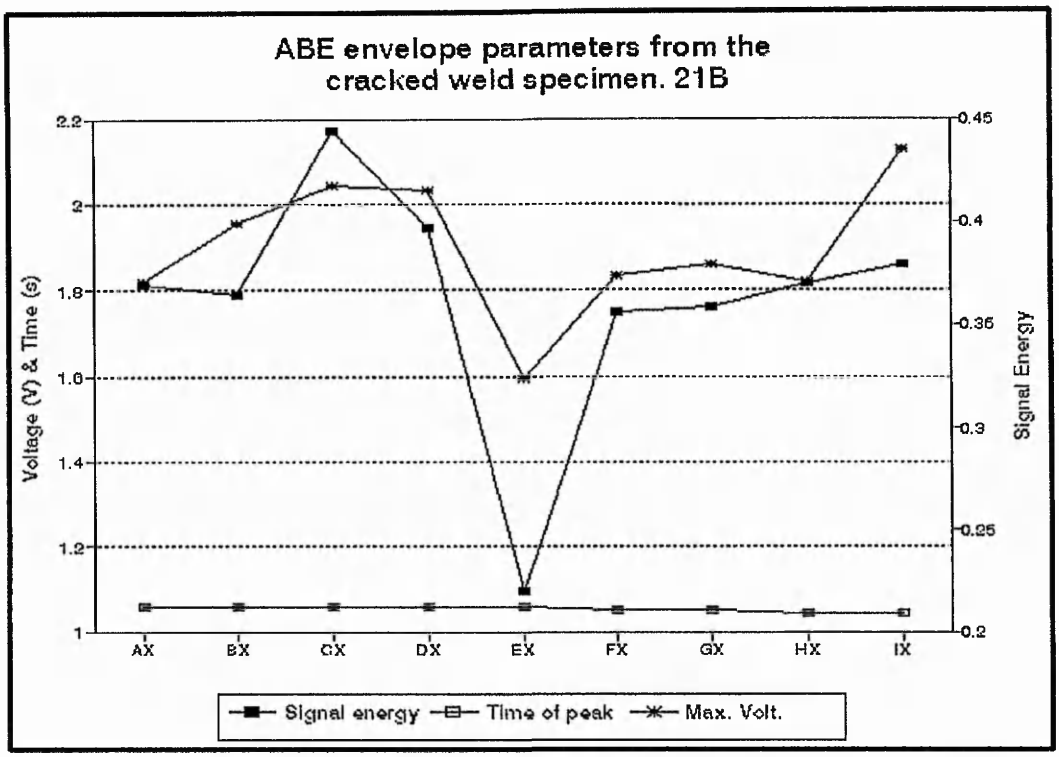


Figure 4.2.24 ABE envelope parameters, signal energy (units V^2s), 'maximum signal voltage' (V_{MAX}) and 'time of peak' (T_P) from the 'as-received' welded steel specimens surface. Location 'A' to 'C' is parent material, 'C' to 'D' is HAZ and 'D' to 'F' is the weld seam which is approximately 10.5 mm in width. The cracked weld centre is situated very close to location 'E'. Data taken from **figures 4.2.22** to **4.2.23**.

4.2.3.3. *The EBE results from the cracked weld specimen (21A).*

The second cracked weld specimen was examined (specimen 21A). As described earlier the EBE measurements were carried out on the central region of the specimen and the EBE envelopes are shown in **figure 4.2.25** to **4.2.28**. Starting at location 'A' on the specimen, the EBE signal appeared as a double peaked envelope, with first peak slightly smaller than the second. As the EBE sensor was moved towards the cracked weld, the EBE envelopes changed shape. The double peaked signal slowly changed to a single peak envelope, with the first peak growing at a greater rate than the second peak. At location 'E', the two peaks were no longer resolved and the resulting single peaked envelope was detected between locations 'E' and 'M'. After location 'M' the EBE envelopes reverted to a double peaked form. As the sensor continued to move across the specimen the second peak increased at a greater rate, eventually leading to a single peaked envelope, where the second peak was the overall maximum. The EBE envelopes from the cracked weld specimen 21A (**figure 4.2.25** to **4.2.28**) appeared different from the detected envelopes from cracked specimen 21B (**figure 4.2.17** to **4.2.20**). Both these cracked weld specimens were prepared in the same way and had similar microstructures and mechanical properties. Although both specimens are nominally the same, the surface condition and crack generation on the 'as-received' material is not closely controlled, leading to the variability in the EBE envelope shape.

The maximum signal voltage (V_{MAX}) for the EBE envelopes changed as the sensor moved to different locations on the surface of the specimen. This data is summarised in **figure 4.2.29**. The V_{MAX} values increased from location 'A' with a value of **0.35 V** to position 'G' with a value of **0.54 V**. From hereon in, the signal amplitude began to fall off to a minimum on location 'N' (**0.42 V**). After this position, the signals from the remaining locations began to steadily increase in amplitude. The spread of signal amplitudes for this specimen was **0.19 V**. The EBE envelope parameters from the various material regions are listed in **table 4.2.6**.

Across the specimen's surface the stress and microstructural features affecting the EBE envelopes changed. This in turn would be expected to change the overall size of each of the EBE peaks on the envelope and ,thus, change the time at which the 'maximum peak' occurred. The largest peak in the double peaked EBE envelope was used to represent the time of maximum peak (T_P). The time of maximum peak was dependent on the transducer location on the specimen. The first peak occurred around **0.84 s** and the second peak occurred just past **1.03 s** on the envelope. The spread of the T_P values detected from across the surface of this specimen was **0.21 s**.

The EBE signal energy steadily increased from **0.042 V^2s** at location 'A', to a maximum of **0.085 V^2s**, at location 'H' on the heat affected zone. From hereon in, the signal amplitude decreased to **0.069 V^2s** at location 'K', very close to the crack. After this minimum, the signal energy of the EBE envelopes began to increase slowly to a second maximum at location 'P', with an energy value of **0.079 V^2s**. From location 'P' to location 'U' the signal energies gradually decreased to a value of **0.062 V^2s**. The signal energy range for this specimen was found to be **0.043 V^2s**.

The asymmetrical EBE parameter profile (**figure4.2.29**) is also reflected in **table 4.2.6**. The EBE energy profiles, observed from both the cracked weld specimens (21B and 21A), show a rise in the magnitude at the weld-HAZ interface. The different material regions within each specimen appear to cause similar trends in the EBE signal energy profile (see **figures 4.2.21** and **4.2.29**). The asymmetry in the signal energy distribution was found on both cracked specimens. It was probably a result of the methods used in the production of the specimen. A possible heat sink used during welding or strain, generated as the plate was low-cycle flexural fatigue during crack induction, may have resulted in the uneven residual stress distribution on either side of the specimen. Therefore, this region would be expected to have affected the EBE amplitude and signal shape. This is discussed further in **section 4.4**.

Cracked weld specimen (21A). region	location	Amplitude. V_{MAX} (V)	Time of Peak. T_p (s)	Signal Energy. (V^2s)
Parent steel	A	0.35 ±0.01	1.00 ±0.01	0.042 ±0.002
	U	0.50	1.05	0.062
HAZ region	H	0.54 ±0.01	0.84 ±0.01	0.085 ±0.002
	O	0.44	1.03	0.076
Cracked weld	K	0.46 ±0.01	0.86 ±0.01	0.069 ±0.002
% error	~	2 %	1 %	3 %

Table 4.2.6 EBE signal envelope parameters from the cracked weld steel specimen (21A) are shown. Data from specific material regions ranging from parent material ('A'), HAZ region ('H') and cracked weld ('K').

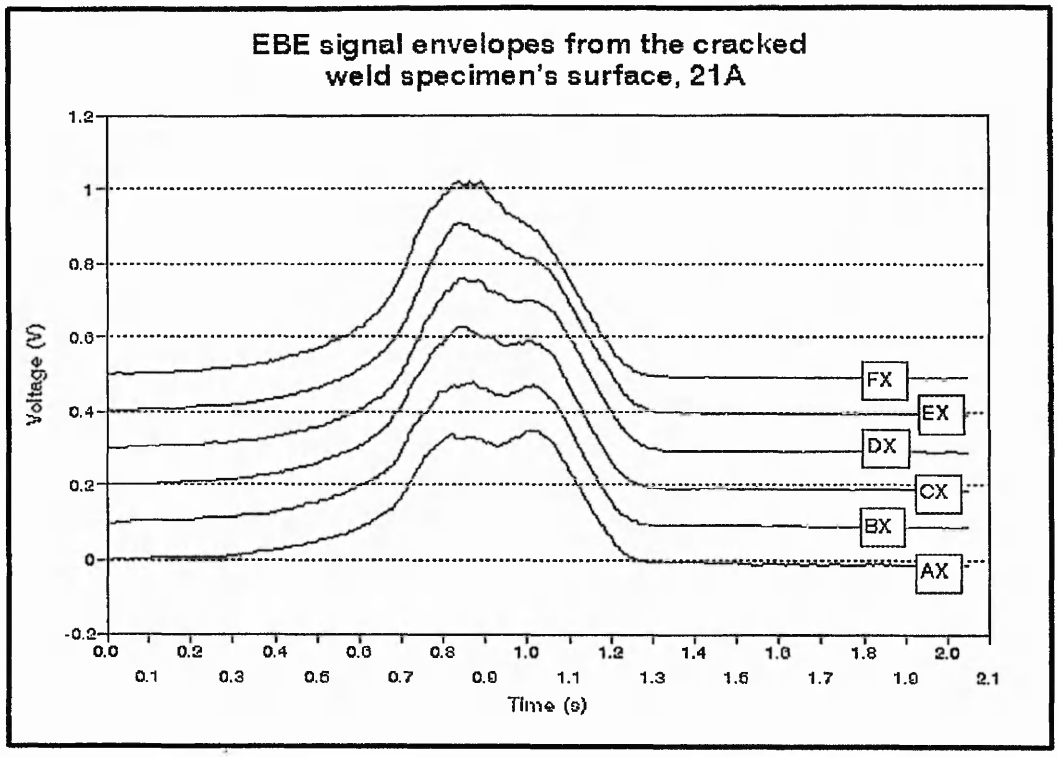


Figure 4.2.25 EBE signal envelopes from locations 'A' to 'F' across the surface of the cracked weld specimen. Each EBE envelope is the average of a number of signals and this is denoted by 'X'.

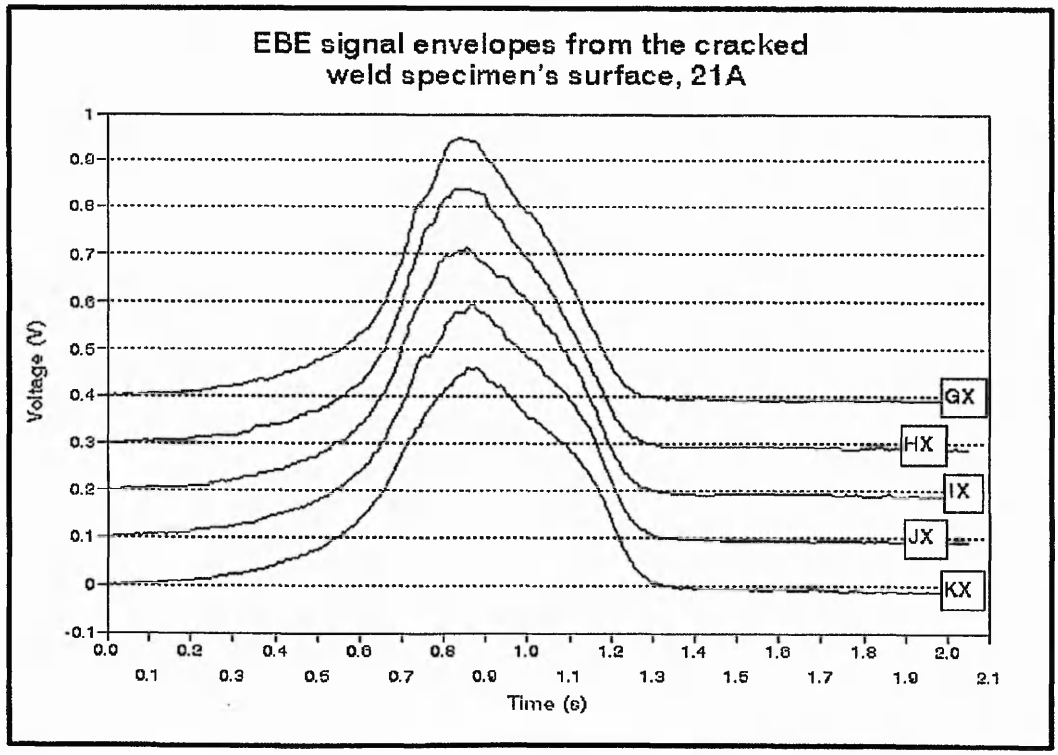


Figure 4.2.26 EBE signal envelopes from locations 'G' to 'K' across the surface of the cracked weld specimen. Each EBE envelope is the average of a number of signals and this is denoted by 'X'.

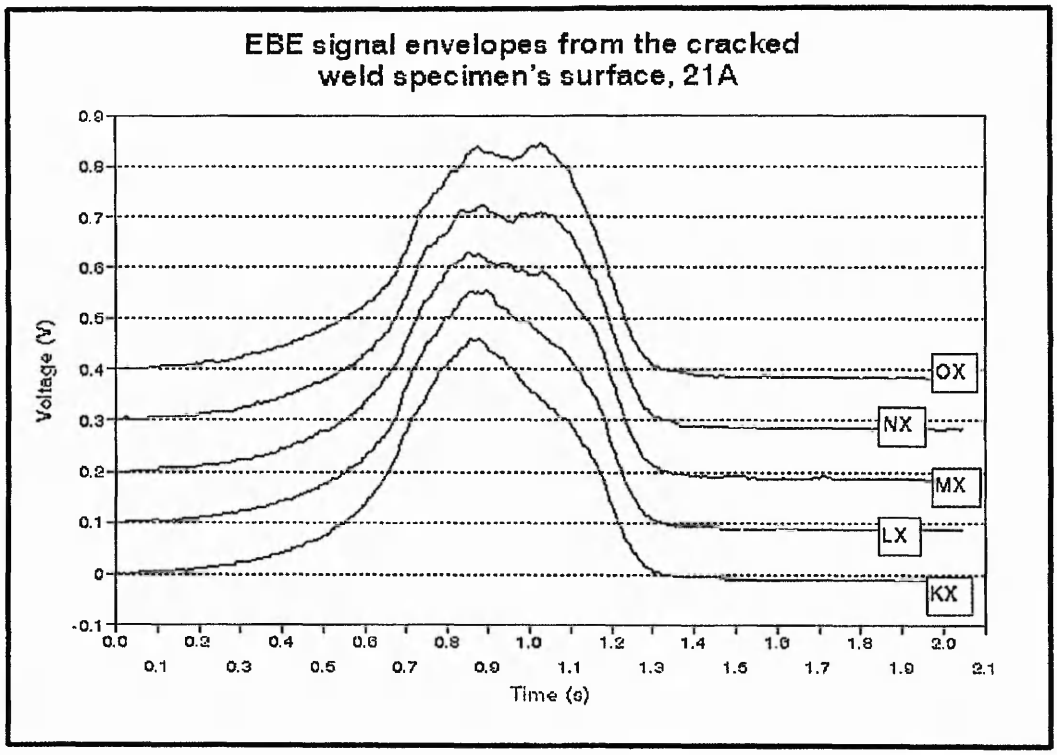


Figure 4.2.27 EBE signal envelopes from locations 'K' to 'O' across the surface of the cracked weld specimen. Each EBE envelope is the average of a number of signals and this is denoted by 'X'.

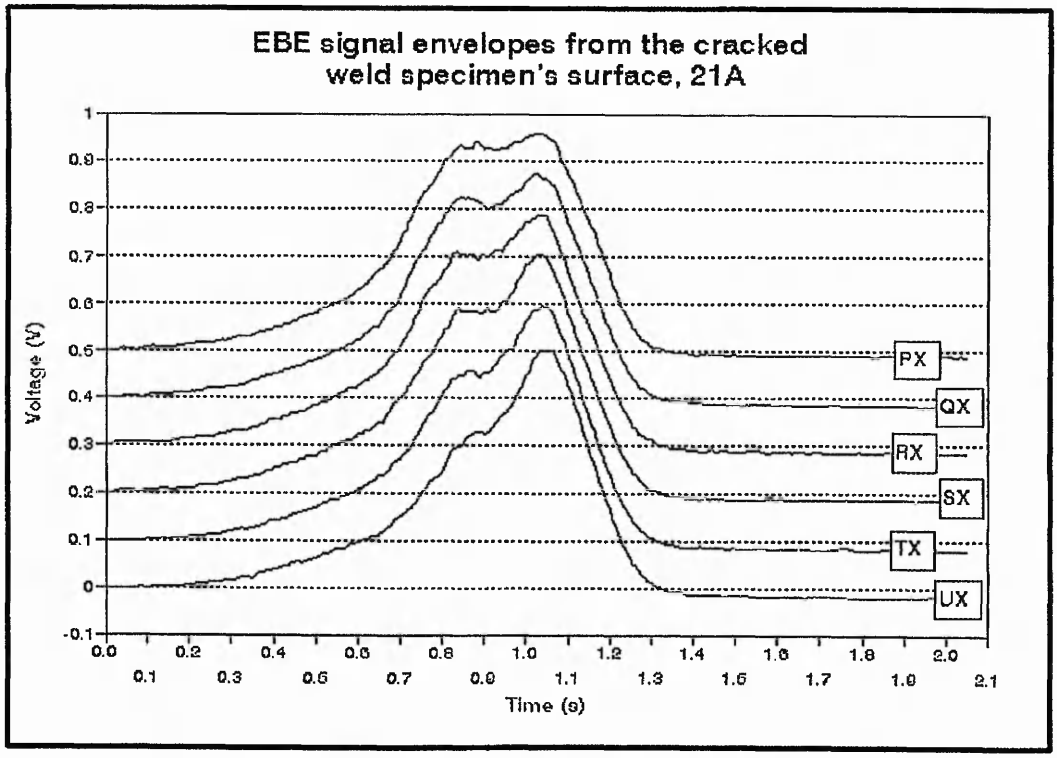


Figure 4.2.28 EBE signal envelopes from locations 'P' to 'U' across the surface of the cracked weld specimen. Each EBE envelope is the average of a number of signals and this is denoted by 'X'.

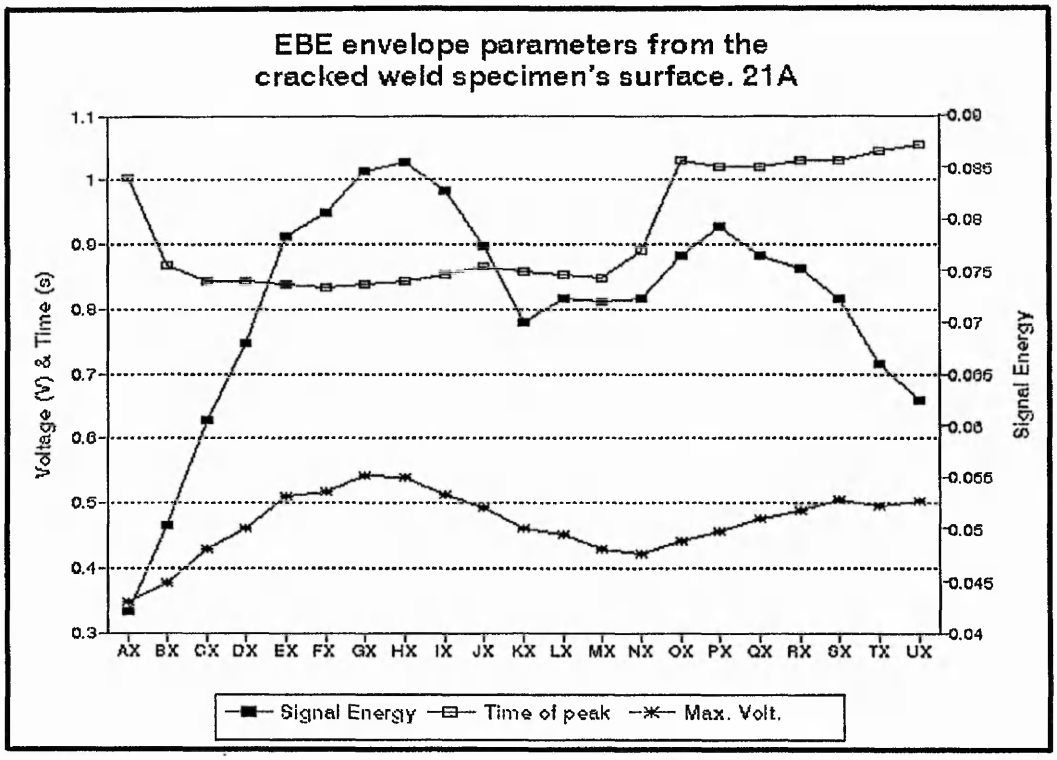


Figure 4.2.29 EBE envelope parameters, signal energy (units V^2s), 'maximum signal voltage' (V_{MAX}) and 'time of peak' (T_P) from the 'as-received' cracked weld steel specimens surface (21A). Location 'A' to 'F' is parent material, 'F' to 'H' is HAZ and the weld seam is approximately 10.5mm in width with the centre being on location 'K'. The crack is positioned very close to location 'K'. Data taken from **figures 4.2.25** to **4.2.28**.

4.2.3.4. *The ABE results from the cracked weld specimen (21A).*

The ABE signal envelopes detected from the cracked weld specimen 21A are shown in **figure 4.2.30** to **4.2.31**. The ABE envelopes from the various locations on the surface of the specimen were similar to those in **section 4.2.3.2**; i.e. wide and double peaked signals. These acoustic signal envelopes, again, had distinctive spikes positioned on the second peak. The spikes provided the signal envelopes with very large maximum signal amplitudes. The position of the signal spikes were fixed and generally reproducible.

Figure 4.2.32 shows the summarised signal parameters of the ABE envelopes across the surface of the cracked weld specimen 21A. From location 'A' through to 'C' the maximum signal voltages remained relatively constant, at a value of **2.4 V**. From location 'C' to location 'E', the maximum signal voltage increased to **2.69 V**. After this maximum, each subsequent location yielded an ABE envelope with a consecutively lower maximum signal voltage. The lowest maximum signal voltage obtained was recorded on locations 'H' and 'I', with voltages of **1.98 V** and **1.96 V** respectively. The maximum ABE voltage spread for this cracked specimen (21A) was **0.73 V**.

The underlying double peaked form of the ABE envelopes was masked by the presence of large sharp spikes clustered on the second peak. The position of the largest spike on the ABE envelopes was consistent and, therefore, the time of maximum signal peak (T_P) remained relatively constant at **1.05 s**. The spread of the times at which maximum signal peak occurred was very small (**±0.01** seconds around the stated value).

The ABE signal energy from the specimen varied, depending on the location of the transducer. Moving across the specimen, from location 'A' to 'D', the signal energies increased from **0.424 V^2s** to **0.497 V^2s**. The largest signal energy was recorded at location 'E', with a value of **0.554 V^2s**, directly above the weld and crack. Location 'F' exhibited a decreased signal energy while location 'G' showed the smallest signal energy at **0.345 V^2s**. After location 'G', locations 'H' and 'I' showed modest increases in signal

energy (**figure 4.2.32**). The ABE signal energy spread was found to be **0.209 V^2s** for the cracked weld specimen 21A.

The ABE signal envelopes from both the cracked weld specimens (21B and 21A) appeared very similar. Both displayed signal envelopes which contained spikes on the position of the second peak. The ABE signal energy parameters from each of the cracked specimens, shown in **figure 4.2.24** and **figure 4.2.32**, displayed very different profiles. The 21B specimen appeared to show a signal energy minimum caused by the crack, while the opposite was found to be true for the 21A specimen. The differences for this may be caused by the relative size of the crack within each steel plate. If a crack within a steel specimen is large enough, it may then be able to decrease the ABE signals reaching a transducer placed above. This is discussed more fully in **section 4.4**.

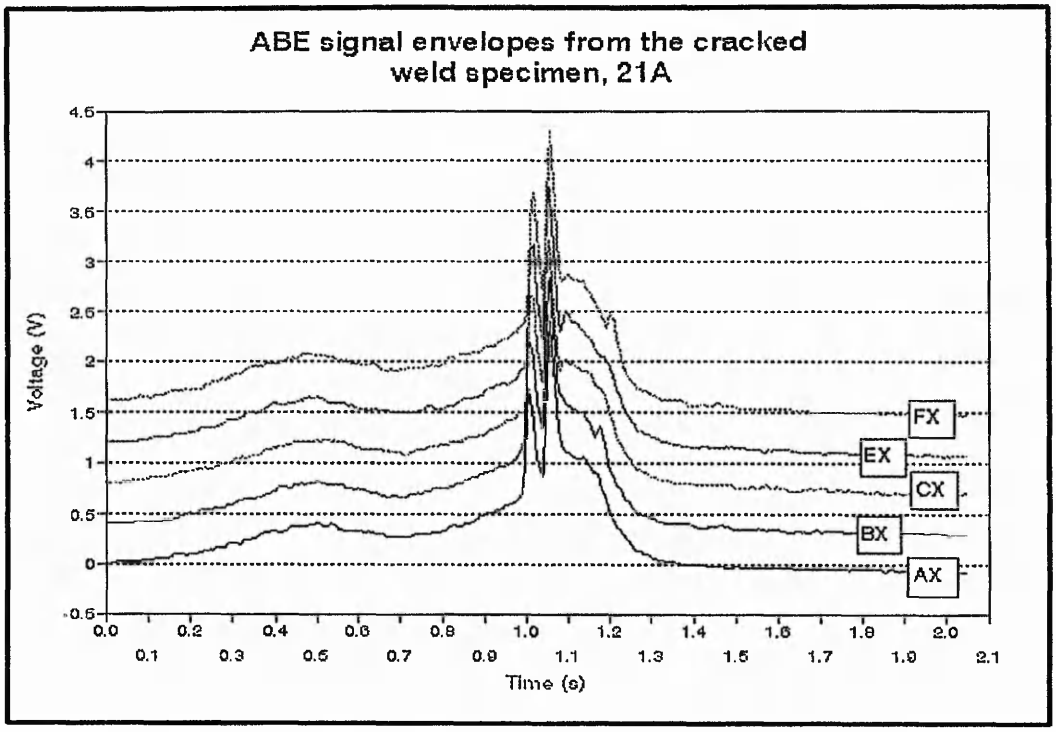


Figure 4.2.30 ABE signal envelopes from locations 'A' to 'E' across the surface of the cracked weld specimen. Each ABE envelope is the average of a number of signals and this is denoted by 'X'.

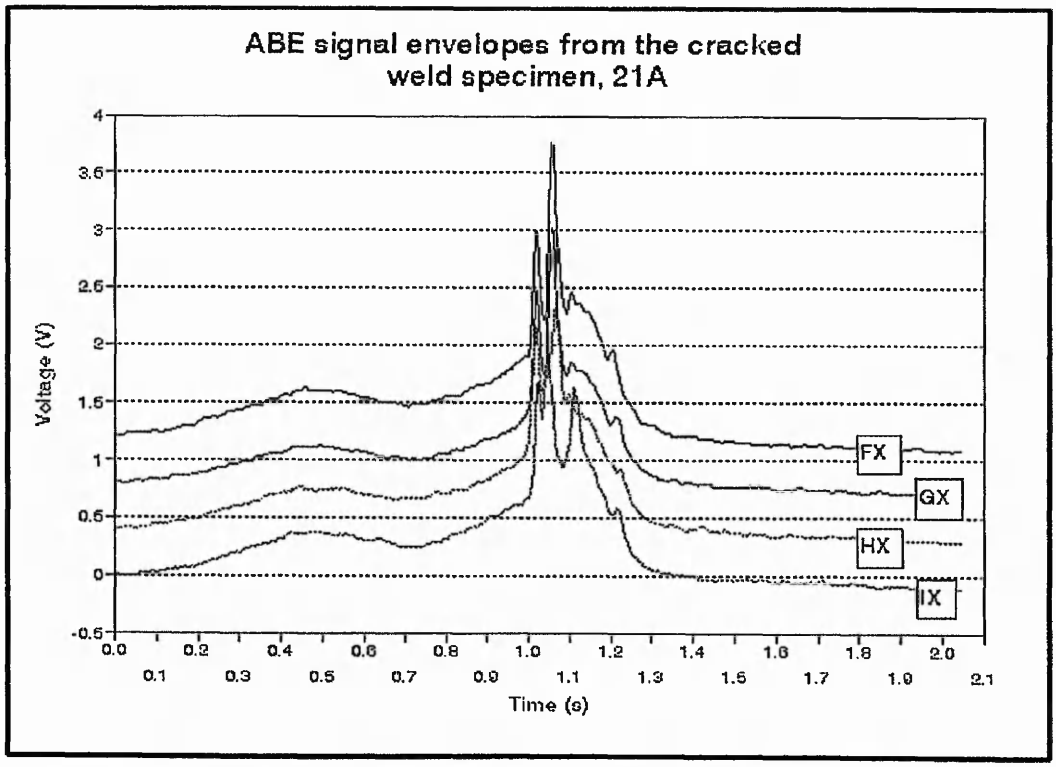


Figure 4.2.31 ABE signal envelopes from locations 'F' to 'I' across the surface of the cracked weld specimen. Each ABE envelope is the average of a number of signals and this is denoted by 'X'.

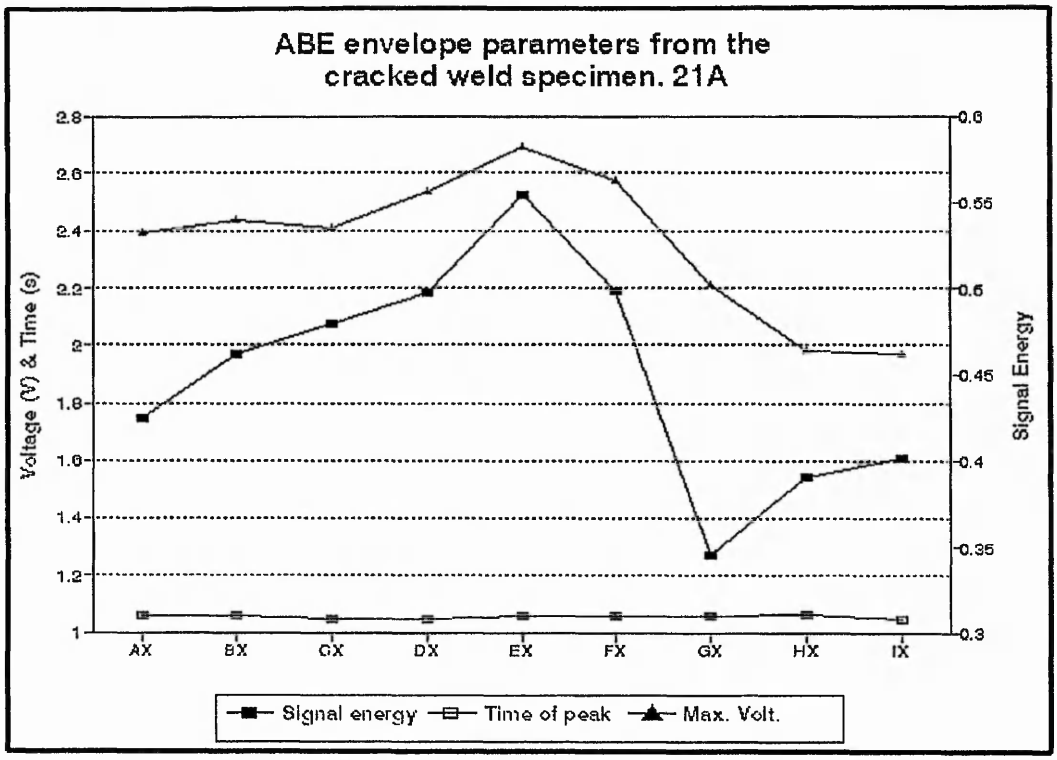


Figure 4.2.32 ABE envelope parameters, signal energy (units V^2s), 'maximum signal voltage' (V_{MAX}) and 'time of peak' (T_P) from the 'as-received' cracked weld steel specimens surface (21A). Location 'A' to 'C' is parent material, 'C' to 'D' is HAZ and 'D' to 'F' is the weld seam which is approximately 10.5 mm in width. The cracked weld centre is situated very close to location 'E'. Data taken from **figures 4.2.30** to **4.2.31**.

4.2.4. Barkhausen Results Following Surface Machining of the Steel Specimens.

The plain steel (3P), welded steel (2P) and cracked weld steel (21B and 21A) specimens had their surfaces subjected to EDM machining and/ or surface planing. Both the plain (3P) and welded (2P) specimens had their surfaces half planed and half EDM machined. The '21B' cracked specimen's surface was EDM machined and the new surface labelled '22B'. A surface thickness of 0.55 mm was removed from the specimen using EDM machining. The '21A' cracked weld specimen's surface was planed and a 0.5 mm thickness was removed. The new surface was labelled '22A'. Acoustic Barkhausen measurements were not conducted on the machined specimens. The machining process was expected to affect only the surface layer of the specimen and, therefore, only EBE measurements were carried out on these specimens. The EBE envelopes were studied and are presented in this section.

4.2.4.1. *The EBE results after planing and EDM machining of the plain steel specimen (3P).*

The surface of the steel specimen 3P was half EDM machined and half planed in order to investigate the effects of machining on EBE signals. The EDM machining was carried out on the left hand side of the specimen, covering locations 'A' to 'K'. The right hand side of the specimen was planed: this covered locations 'K' to 'U'. EBE measurements were carried out on four different locations on both of the machined halves of the specimen. The obtained EBE signals were compared to their corresponding signals from the original surface.

On visual observation the planed steel specimen appeared corrugated. This effect was due to the repeated motion of the cutting tool tip; removing thin strips of material and then traversing across and repeating the motion, until the desired surface thickness was removed. The EBE signals from the planed area (**figure 4.2.33**) appeared similar to the

EBE signals from the cracked weld specimens 21A and 21B surface's parent material regions, as shown in **figure 4.2.17** and **figure 4.2.28**. The EBE envelopes obtained from this planed surface was different from those obtained on the 'as-received' steel specimen surface. On the original 'as-received' plain steel surface (3P) the EBE signals displayed a large amplitude in the first half of the envelope, before the point of maximum peak. The planing of the specimen's surface reduced the amplitude in the first half of the EBE envelope. This change was a direct result of the planing process. As well as the differences between the EBE signals from the 'as-received' and planed surfaces, there are distinct similarities, such as the overall shape of the EBE envelope. Both surfaces displayed a peak in the later part of the envelope. On the planed surface the maximum signal peak was recorded at approximately **1.03 s** on the envelope. After this point the envelope rapidly decreased to zero. **Table 4.2.7** provides the signal parameter of the EBE envelopes detected from the surface of the 'as-received' and machined steel specimen 3P.

On visual inspection the EDM machined surface showed a matt finish. On closer inspection, the surface had a fine granular texture. This texture was caused by the resolidified surface layer due to the dielectric fluid cooling the molten steel back onto the surface. The EBE signal envelopes changed shape as a consequence of the EDM machining. The EBE envelopes obtained from the plain steel specimen are shown in **figure 4.2.33.** The detected signals clearly show that the envelope shape changed dramatically as a result of the EDM machining. These EBE envelopes showed an early peak, from which point, the signal began to drop, gently rising again to expose a less defined second peak. The EBE envelopes' parameters are listed in **table 4.2.7**.

Depending on the surface machining process, the EBE peak appeared at different times on the envelope. The EDM machined surface area generated EBE envelopes with a consistently reproducible 'time of maximum peak' (T_P) of **0.73 s**. EBE signals from the planed surface area possessed similar 'T_P' values to the EBE envelopes from the original 'as-received' surface.

The EBE signal from both the machined areas on the surface of the steel specimen, generated V_{MAX} values which were similar in magnitude. On closer inspection the EBE amplitude from the original 'as-received' surface appeared the largest, with a value of **0.49 V**. The EDM machined surface area displayed the lowest V_{MAX} value at **0.46 V** and can be seen in **table 4.2.7**. The range of values obtain from the EDM machined half of the specimen, overlapped the lower end of the V_{MAX} values obtained from the planed machined surface area.

Each of the machined surface areas showed a range of similar EBE signal energies. The largest average signal energy was found on the original 'as-received' surface, with a value of **0.065 V^2s**, followed by the EDM machined surface and planed surface with energy values of **0.060 V^2s** and **0.055 V^2s** respectively.

Machined steel specimen (3P).	Maximum Signal amplitude. V_{MAX} (V)	Time of Peak. T_p (s)	Signal Energy. (V^2s)
Original surface	0.49 ±0.02	1.052 ±0.003	0.065 ±0.001
% error	3.5 %	0.3 %	1.5 %
EDM surface	0.45 ±0.03	0.733	0.0595 ±0.0040
% error	6.6 %	- %	6.7 %
Planed surface	0.47 ±0.01	1.03 ±0.01	0.0552 ±0.0045
% error	1.7 %	0.5 %	8.1 %

Table 4.2.7 EBE signal data from 'as-received' steel surface, EDM machined surface and planed surface of the plain steel specimen (3P). Four different locations were studied for each of the machined surfaces and the averaged values are shown.

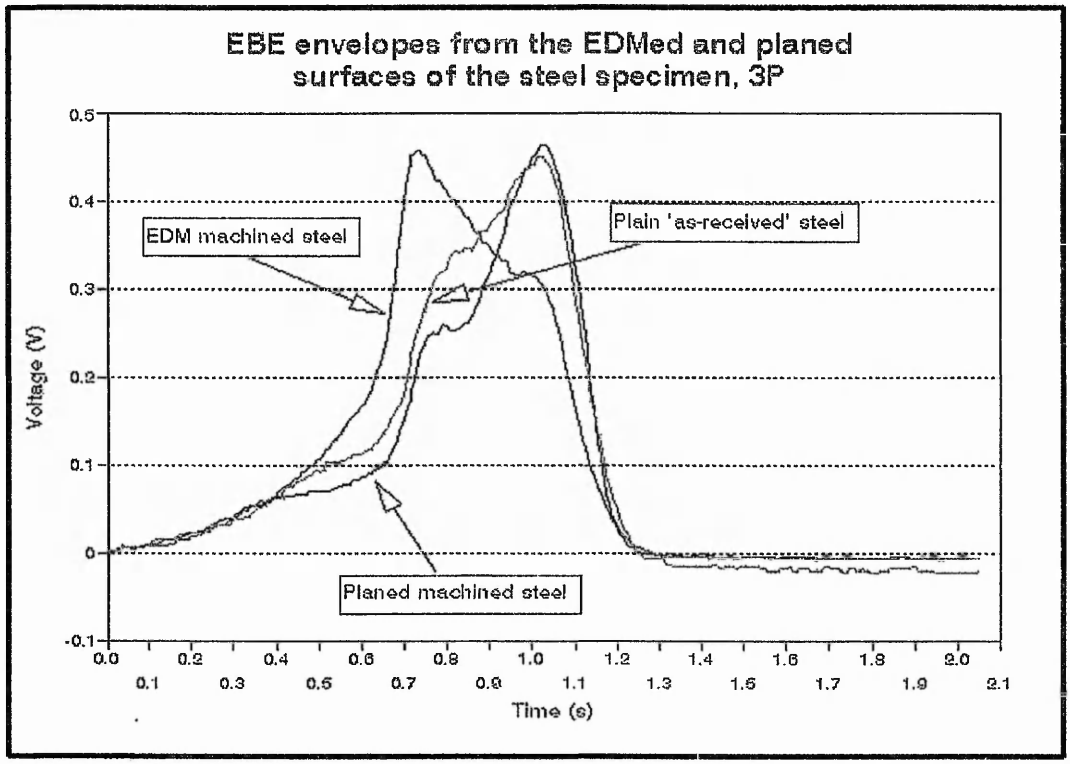


Figure 4.2.33 Averaged EBE signal envelopes from the EN-43A steel surface in three different states. 1) 'as-received' plain steel surface. 2) EDM machined surface. 3) Planed machined surface.

4.2.4.2. *The EBE results after planing and EDM machining of the welded steel specimen (2P).*

The surface of the welded steel specimen (2P) was subjected to planing and EDM machining, similar to the machined steel specimen 3P (**section 4.2.4.1**). Half of the studied region (locations 'A' to 'K') was planed and the second half (locations 'L' and 'U') was EDM machined. **Figures 4.2.34** and **4.2.35** show the EBE envelopes from the EDM machined and planed surface areas respectively. Each graph displays signal envelopes from the parent material, HAZ and weld seam. There was a gradual change in the shape of the EBE envelopes when traversing the three regions.

The EBE envelope from the EDM machined weld seam area was double peaked, with the first peak larger than the second (**figure 4.2.34**). The EBE envelope from the HAZ region (on location 'O') exhibited a very sharp first peak and in the place of the second peak was a plateau. The maximum signal voltage from the HAZ region was very large, having a value of **0.81 V**. Away from the HAZ and weld seam, on the parent material, the EBE envelope appeared with a single peak and was almost triangular in shape.

The EBE signals from the 'as-received' weld specimen (2P) appeared very different from the EBE envelopes detected after the EDM machining. This is noticeable when the EBE envelopes from **figures 4.2.11** and **4.2.12** are compared to the envelopes in **figure 4.2.34**. As a result of EDM machining, the EBE 'maximum signal voltage' (V_{MAX}) increased in magnitude. The time of maximum peak (T_P) occurred at approximately **0.74s** on the envelope. This was very similar to the T_P value from the weld region of the original 'as-received' surface of the welded specimen. **Table 4.2.8** shows the EBE envelope parameters from the planed and EDM machined surface areas.

The EBE signal from the planed surface area of the welded specimen (2P) exhibited very different envelopes from the EDM machined surface area. The EBE envelopes from the parent material, HAZ and weld regions from the planed surface area of the specimen are shown in **figure 4.2.35**. EBE envelopes detected from the original 'as-received' surface

area (before the planing process) can be seen in **figure 4.2.9** to **4.2.10**. Compared to the original 'as-received' weld surface, the EBE signals appear to have been significantly affected by the planing process. For the parent material region, the shape of the EBE envelopes from the planed surface area appeared with a maximum peak of **0.50 V** at **1.1 s** on the envelope. The EBE signal from the HAZ region appeared double peaked, with the first peak being small and the second peak large. A more pronounced double peaked envelope was detected from the weld metal (**0.54 V**). Again, the HAZ region exhibited the maximum signal voltage **(0.59 V)**, although, the planing process depressed the EBE signals. Summarised EBE parameters are shown in **Table 4.2.8**.

EDM surface area, (2P)	Surface location	Amplitude. V_{MAX} (V)	Time of Peak. T_p (s)	Signal Energy. (V^2s)
Parent steel.	U	0.63 ±0.02	0.75 ±0.01	0.098 ±0.002
HAZ.	N	0.74	0.74	0.109
Weld.	L	0.59	0.73	0.093
% error	~	3 %	1 %	2 %
Planed (2P) surface area	**Surface location**	**Amplitude. V_{MAX} (V)**	**Time of Peak. T_p (s)**	**Signal Energy. (V^2s)**
Parent steel.	A	0.50 ±0.02	1.12 ±0.01	0.054 ±0.02
HAZ	H	0.59	1.03	0.078
Weld.	J	0.54	1.03	0.079
% error	~	4 %	1 %	3 %

Table 4.2.8 EBE signal data from the planed and EDM machined surface areas are displayed. The results from the weld, HAZ and parent material locations for the machined 2P specimen are shown.

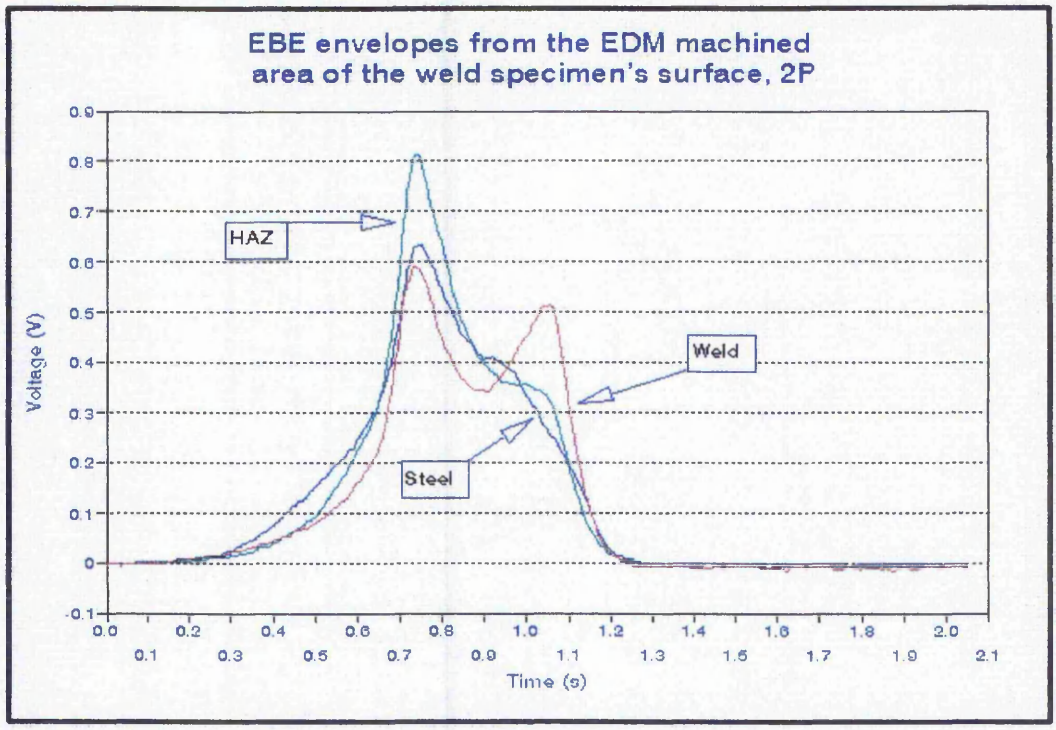


Figure 4.2.34 Averaged EBE signal envelopes from the three different material region (steel, HAZ and weld) across the weld specimen's EDM machined surface.

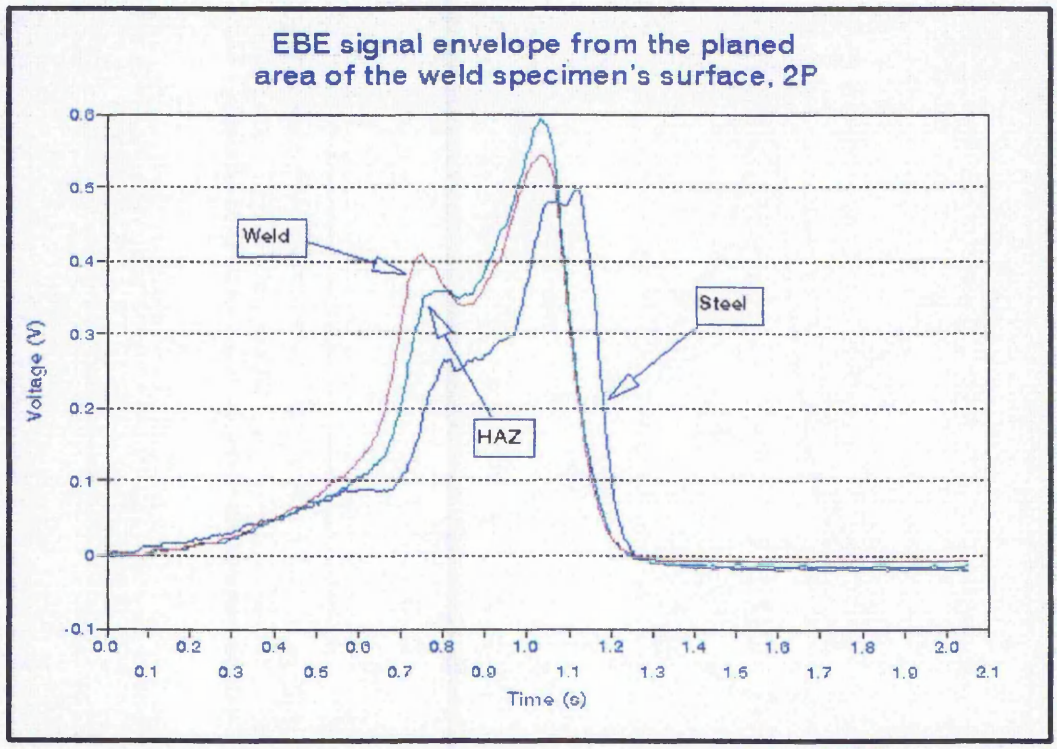


Figure 4.2.35 Averaged EBE signal envelopes from the three different material regions (steel, HAZ and weld) across the weld specimen's planed machined surface.

4.2.4.3. *The EBE results from the cracked weld specimen surface (22B) after EDM machining.*

The EDM machining process removed a 0.55 mm thick surface layer from the cracked weld specimen 21B and the new surface was labelled 22B. **Figures 4.2.36** to **4.2.39** show EBE envelopes from the EDM machined surface 22B from the examined locations, covering weld, HAZ and parent steel.

On the EDM machined surface 22B, furthest away from the cracked weld region, the EBE signal envelope has a double peak. As the weld region was approached the signal amplitude increased and the small second peak decreased and eventually disappeared. Around locations 'H' and 'O', on the HAZ regions, the EBE envelopes appeared almost "triangular" in shape. On the weld seam, the envelope developed a small plateau at the edge. On position 'K' (close to the crack), the plateau became a downward slope. Moving away from position 'K' towards 'U' the EBE envelopes appeared similar, mirroring the first half of the specimen.

The maximum EBE signal voltage was detected over the HAZ region, on locations 'H' and 'O', either side of the weld seam. The magnitude of the 'V_{MAX}' values from both the HAZ regions either side of the weld seam were not the same. This was a result of asymmetric specimen history, probably due to the welding and crack generation processes. For this reason the EBE envelope parameters in **table 4.2.9** are displayed from key specific locations across the specimen surface. The signal amplitudes from the weld seam (locations 'I' to 'N') were smaller than from the HAZ, but larger than the signal amplitudes obtained from the parent material; located around 'A' and 'U'. The specimens 'maximum signal voltage' profile was also reflected in the signal energy profile and are summarised in **figure 4.2.40**. EDM machining has significantly altered the EBE profile of the specimen compared to the 'as-received' specimen and in doing so has created a similar variation of maximum signal voltage and signal energy. The signal parameters for the EDM machined surface (22B) are listed in **table 4.2.9**.

The time of maximum signal peak, T_P, occurred earlier on the envelope as the EBE probe was traversed along the surface of the specimen. Overall, the T_P values indicated that the maximum signal amplitude occurred between **0.65 s** and **0.70 s** on the envelope. Unlike the pre-EDM machined surface the T_P values did not exhibit any clear distinction between the weld material phases. This will be considered further in **section 4.4**.

EDM machined surface (22B).	Location on the surface.	Signal amplitude. V_{MAX} (V)	Time of Peak. T_p (s)	Signal Energy. (V^2s)
Parent steel.	A	0.47 ±0.01	0.69 ±0.01	0.080 ±0.002
	U	0.51	0.66	0.083
HAZ.	H	0.68 ±0.01	0.68 ±0.01	0.137 ±0.002
	O	0.67	0.68	0.113
Cracked weld	L	0.62 ±0.01	0.67 ±0.01	0.105 ±0.002
% error	~	2 %	1.5 %	2 %

Table 4.2.9 EBE signal data from the weld, HAZ and parent material locations for the cracked weld specimen's EDM machined surface 22B. Due to an asymmetric specimen profile, the EBE envelope parameters from specific locations on both sides of the weld are presented.

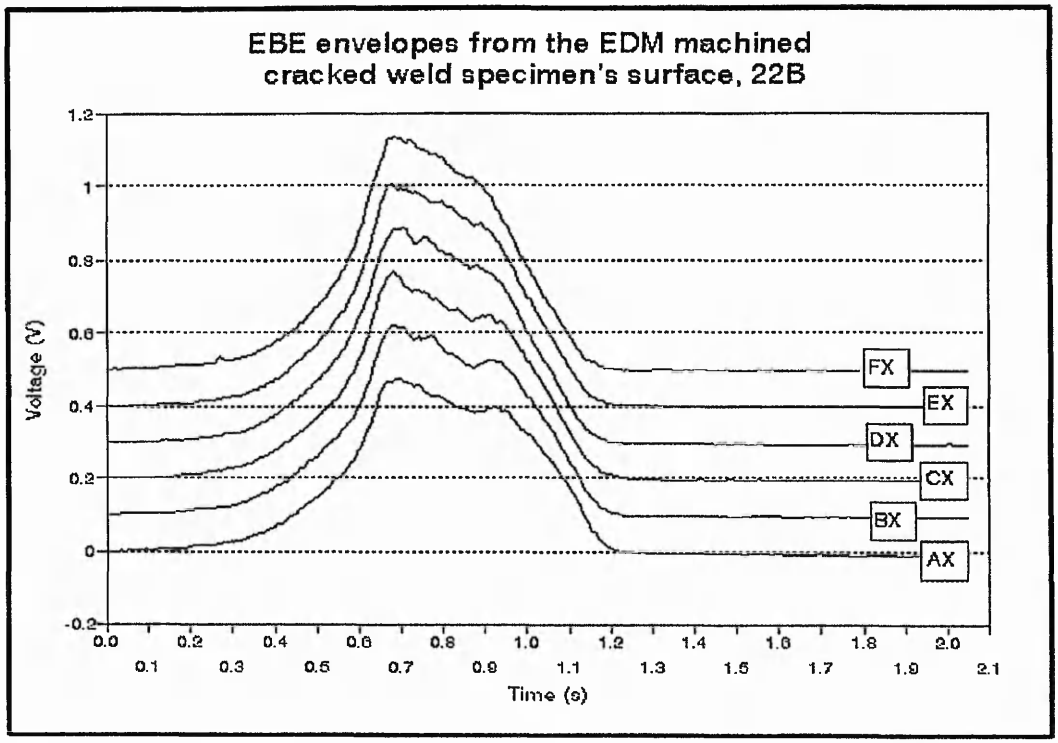


Figure 4.2.36 EBE signal envelopes from locations 'A' to 'F' across the cracked weld specimen's EDM machined surface. Each EBE envelope is the average of a number of signals and this is denoted by 'X'.

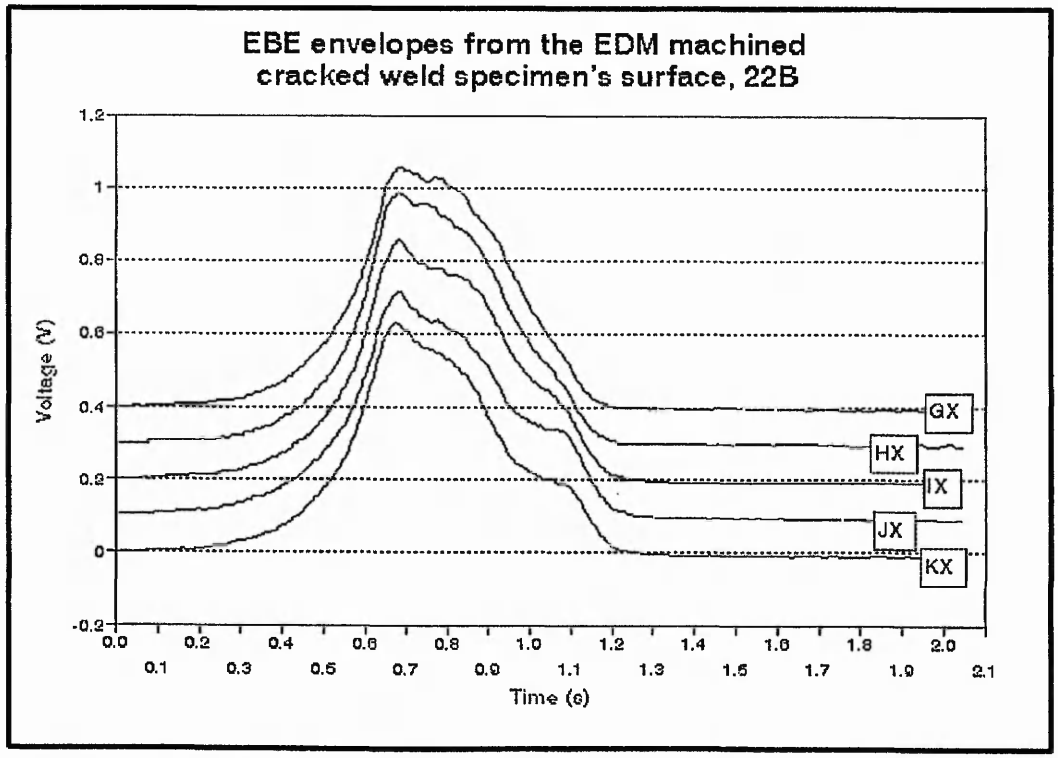


Figure 4.2.37 EBE signal envelopes from locations 'G' to 'H' across the cracked weld specimen's EDM machined surface. Each EBE envelope is the average of a number of signals and this is denoted by 'X'.

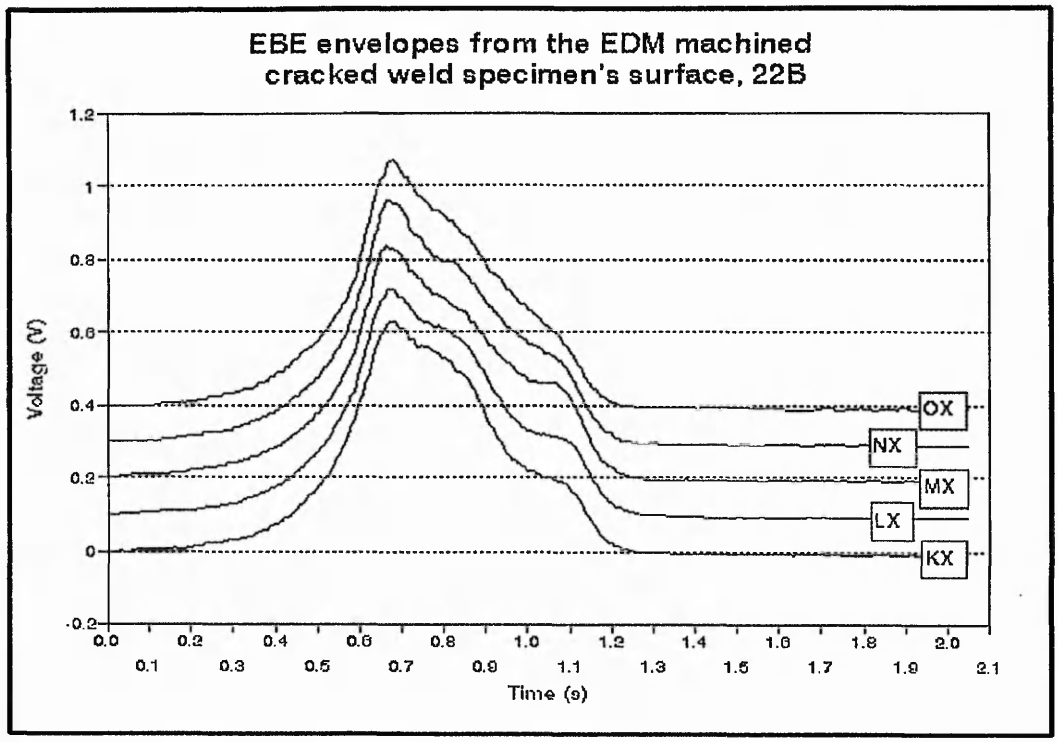


Figure 4.2.38 EBE signal envelopes from locations 'K' to 'O' across the cracked weld specimen's EDM machined surface. Each EBE envelope is the average of a number of signals and this is denoted by 'X'.

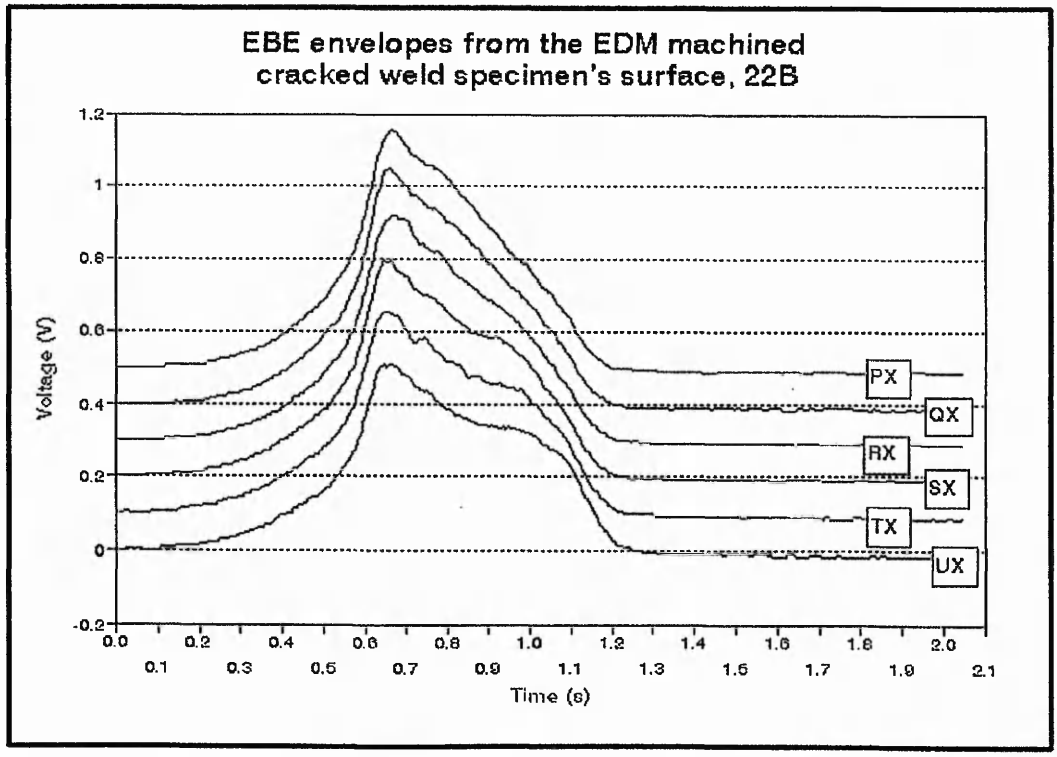


Figure 4.2.39 EBE signal envelopes from locations 'P' to 'U' across the cracked weld specimen's EDM machined surface. Each EBE envelope is the average of a number of signals and this is denoted by 'X'.

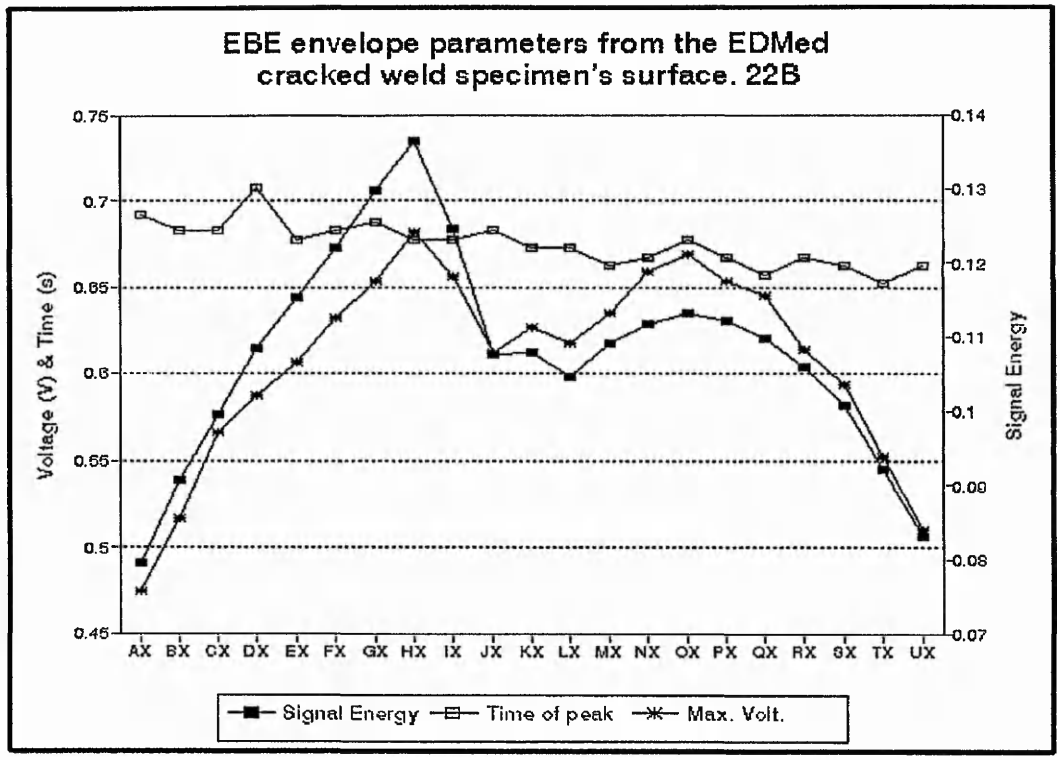


Figure 4.2.40 EBE envelope parameters, signal energy (units V^2s), 'maximum signal voltage' (V_{MAX}) and 'time of peak' (T_P) from the EDM machined cracked weld steel specimens surface (22B). Location 'A' to 'F' is parent material, 'F' to 'H' is HAZ and the weld seam is approximately 10 mm in width with the centre being on location 'K'. The crack is positioned close to location 'L'. Data taken from **figures 4.2.36** to **4.2.39**.

4.2.4.4. *The EBE results from the surface of the cracked weld specimen (22A) after surface planing.*

A thickness of 0.5 mm was carefully planed off the surface of the cracked weld specimen (21A) and the new surface was labelled 22A. The EBE signals are shown in **figure 4.2.41** to **4.2.44**. From the parent material region, of this machined surface (22A), the EBE signal appeared with a single peak, positioned on the right hand side of the envelope. As the EBE probe was moved closer to the weld region, the maximum peak occurred earlier on the envelope and the 'maximum signal voltage' decreased to a minimum on location 'K' (**figure 4.2.45**). The EBE signal shape also changed and the first half of the envelope increased in magnitude as the HAZ region was approached. As the probe was moved closer to the cracked weld, the EBE envelopes became more dome shaped, with a single peak and a decrease in amplitude. The detected EBE signals from across the surface exhibited a symmetry in the envelope shape, about the weld seam. **Table 4.2.10** summarises the EBE envelope parameters from the planed machined cracked weld surface 22A. Again, the EBE envelope parameters are presented from key locations across the specimen surface.

As seen in **figure 4.2.45** the EBE signal energy displayed an increase as the probe was traversed across the cracked weld specimen's planed surface 22A. The increase in signal energy stopped at locations 'H' and 'I', where the HAZ-weld interface existed. After these two locations the signal energy dropped in magnitude to a value of **0.057 V^2s** at location 'K', very close to the crack. Past location 'K', the signal energy returned to values similar to that on location 'H'. After a very small dip on location 'N', the signal energy continued to rise until location 'R' was reached, from where it began to decrease in magnitude. The spread of signal energies for this plane machined surface 22A lay within a range of **0.019 V^2s**.

Plane machined surface (22A)	Location on the surface.	Signal amplitude. V_{MAX} (V)	Time of Peak. T_p (s)	Signal Energy. (V^2s)
Parent steel.	A	0.45 ±0.01	1.01 ±0.01	0.046 ±0.002
	U	0.51	1.05	0.060
HAZ.	H	0.44 ±0.01	0.93 ±0.01	0.062 ±0.002
	O	0.49	1.02	0.064
Cracked weld	K	0.40 ±0.01	0.95 ±0.01	0.057 ±0.002
% error	~	2 %	1 %	3 %

Table 4.2.10 EBE envelope data from the weld, HAZ and parent material locations for the cracked weld specimen's planed surface 22A. Due to an asymmetric specimen profile, the EBE envelope parameters from specific locations on both sides of the weld are presented.

The surface machining changed the V_{MAX} and T_P parameter profiles compared to the 'as-received' surface 21A. The V_{MAX} values from across this planed surface showed a minimum at location 'K', very close to the crack. On the central cracked weld region small changes in the T_P values were recorded. This is displayed in **figure 4.2.45** and can also be seen in **table 4.2.10** above. The surface machining process had altogether changed the Barkhausen envelopes. The planed surface appeared to suppress the EBE envelope parameters as well as, blurring the boundaries between the different material regions. The increased dislocation density and localised residual stresses arising from the planing process are known to decrease EBE activity. This is reflected in the three parameters used to assess the Barkhausen signals. The maximum voltage, time of maximum peak and signal energy have all changed and are discussed later in this chapter.

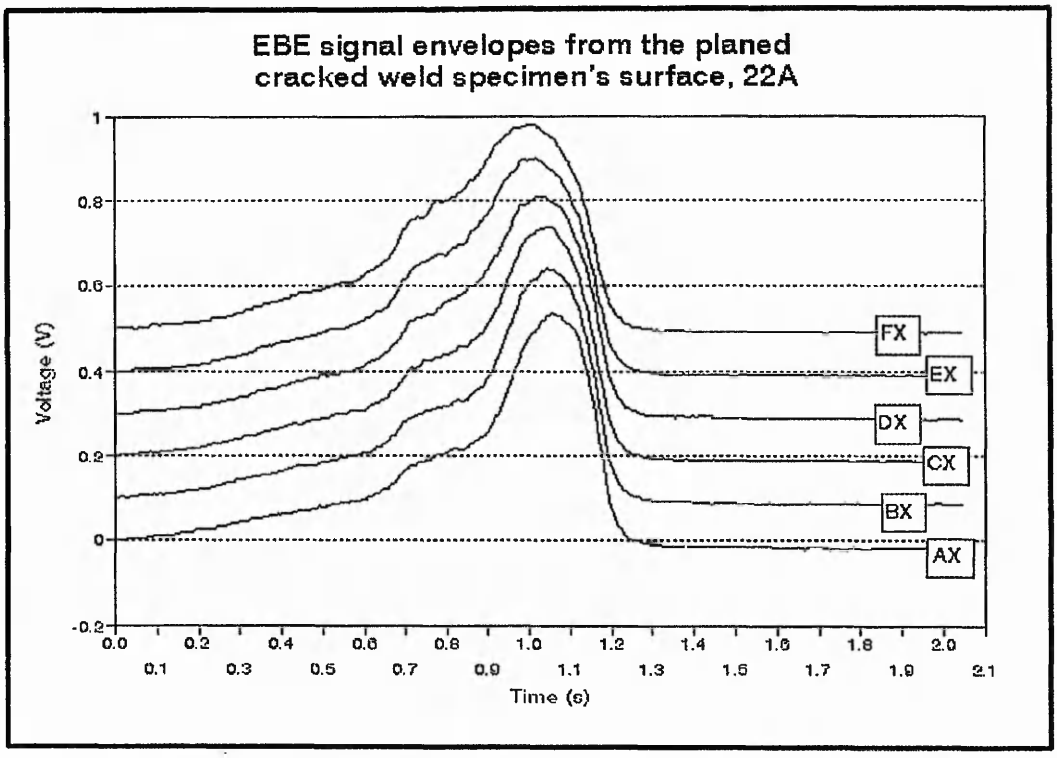


Figure 4.2.41 EBE signal envelopes from locations 'A' to 'F' across the cracked weld specimen's planed surface. Each EBE envelope is the average of a number of signals and this is denoted by 'X'.

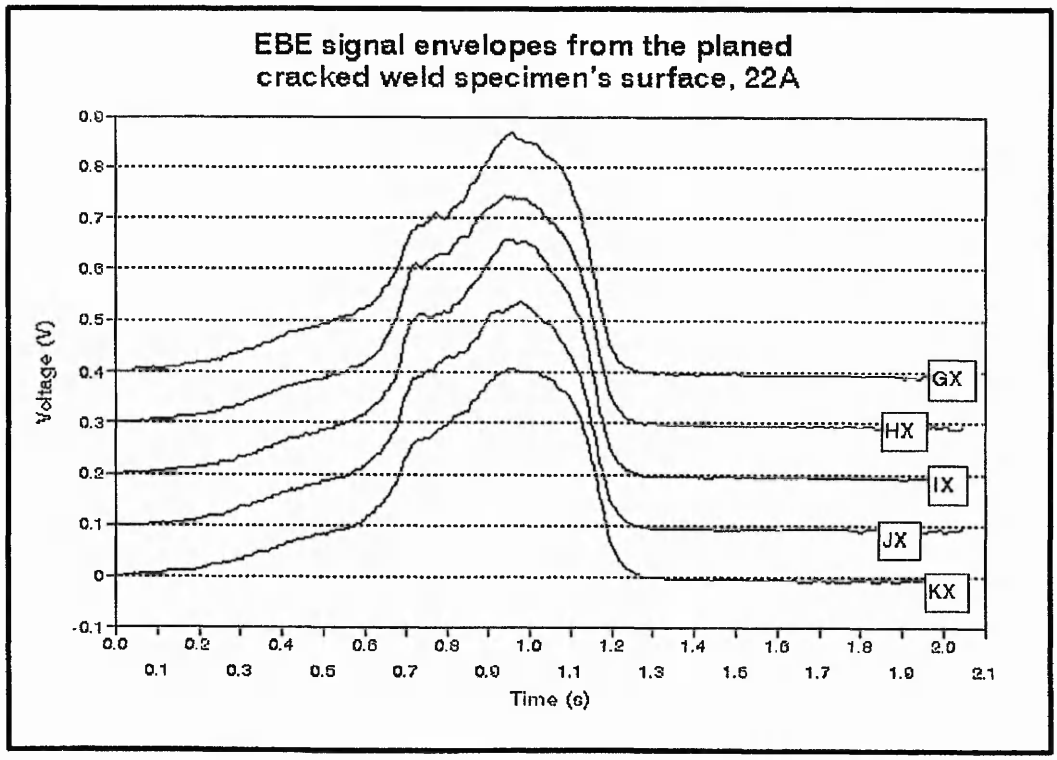


Figure 4.2.42 EBE signal envelopes from locations 'G' to 'K' across the cracked weld specimen's planed surface. Each EBE envelope is the average of a number of signals and this is denoted by 'X'.

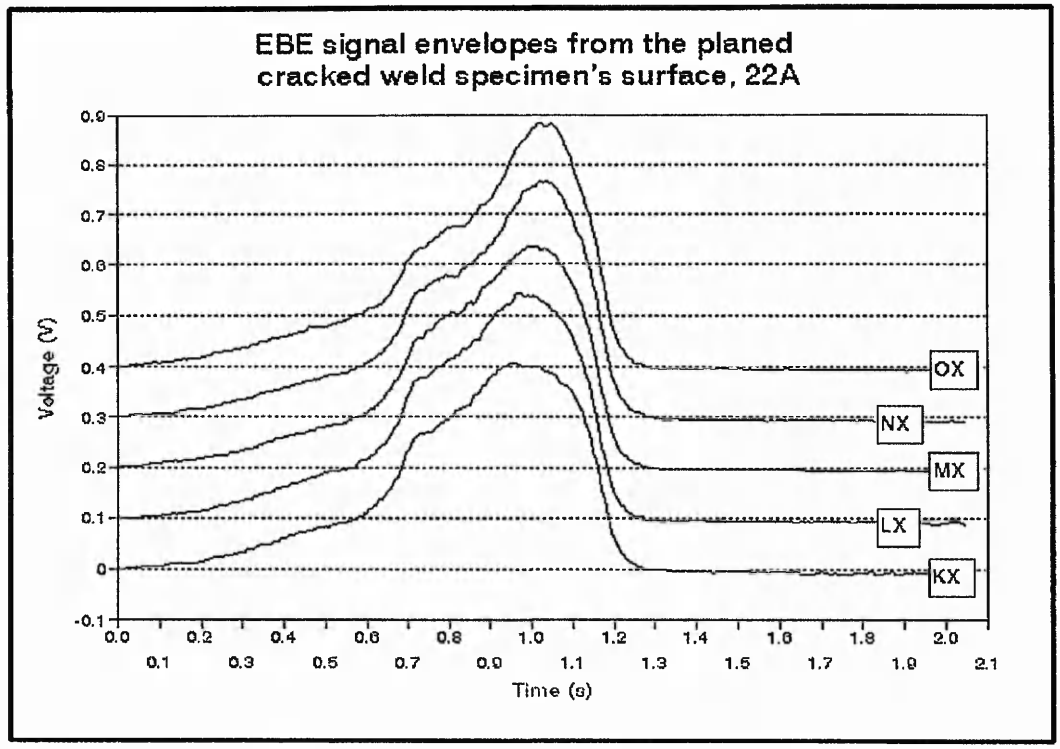


Figure 4.2.43 EBE signal envelopes from locations 'K' to 'O' across the cracked weld specimen's planed surface. Each EBE envelope is the average of a number of signals and this is denoted by 'X'.

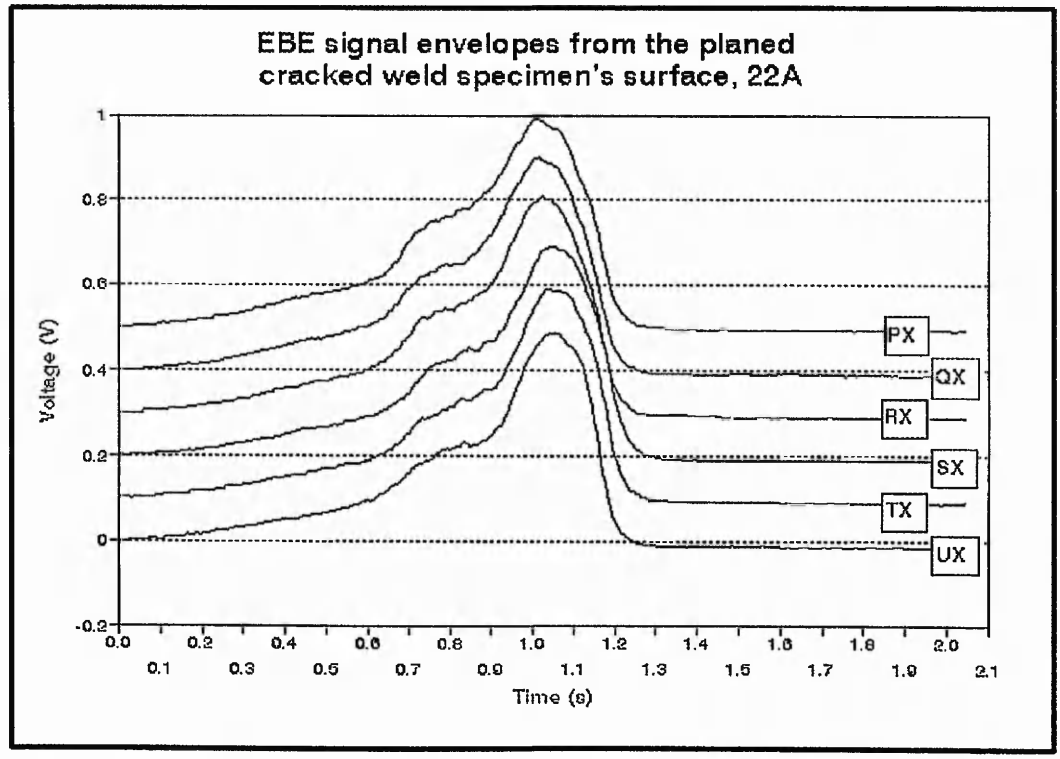


Figure 4.2.44 EBE signal envelopes from locations 'P' to 'U' across the cracked weld specimen's planed surface. Each EBE envelope is the average of a number of signals and this is denoted by 'X'.

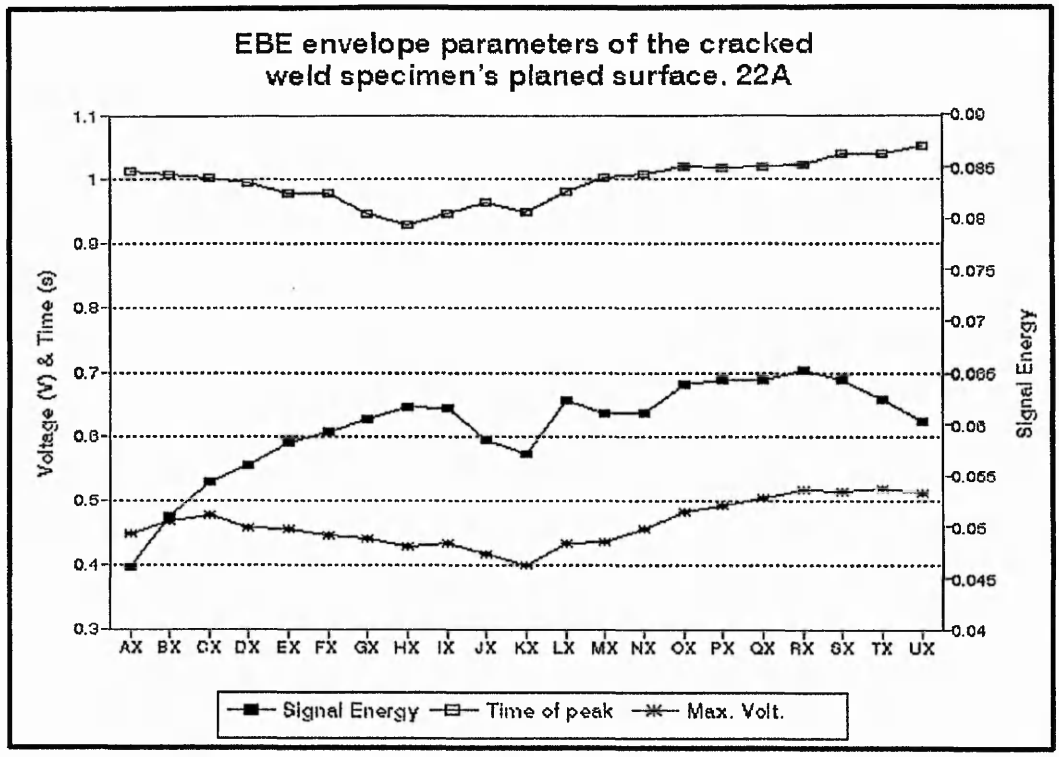


Figure 4.2.45 EBE envelope parameters, signal energy (units V^2s), 'maximum signal voltage' (V_{MAX}) and 'time of peak' (T_P) from the plane machined cracked weld steel specimens surface (22A). Location 'A' to 'F' is parent material, 'F' to 'H' is HAZ and the weld seam is approximately 10 mm in width with the centre being on location 'K'. The crack is positioned very close to location 'K'. Data taken from **figures 4.2.41** to **4.2.44**.

4.3. MAGNETIC LEAKAGE FIELD MEASUREMENTS.

When a material in the demagnetised state is subjected to a saturating magnetic field the magnetic moments are aligned in the direction of the magnetic field. When the applied field is reduced the magnetic domains relax and many return to have their magnetisation in original energetically favourable directions, (the 'easy' directions). This, however, does not apply to all the magnetic domains as some will now have adopted an alternative, favourable direction and may remain in that direction. As a consequence, a net remanent magnetisation is experienced by the material. This is a feature of the hysteresis curve. If the remanent magnetic field is strong enough it can be used for non-destructive evaluation and testing. The magnetic flux caused by the presence of the magnetic field in the material will be sensitive to changes in the material characteristics and the presence of defects. Where there is a change of magnetic permeability in the material, magnetic flux may be concentrated or diverted around that change. This change in the flux pattern can be measured using a detector such as a Hall probe, search coil or the recently developed giant magneto-resistive (GMR) sensor.

4.3.1. GMR Sensors.

The giant magneto-resistance (GMR) effect was discovered in 1988 by French scientists, Baibich et al.. The phenomena of magneto-resistance, (the change in resistance of a conductor when a magnetic field is applied), is well known. Such a phenomenon is to be expected, since applying a magnetic field to a region containing electrons in motion, will cause their trajectories to change due to the Lorentz force. This change in trajectory will cause the change in resistance of the material. The change in resistance experienced by materials within an applied magnetic field is very small; typically a fraction of a percent. For some magnetic materials, such as permalloy, this increase can be as great as 5-6% **[100]**.

The origin of the GMR effect is quite different from classical magneto-resistance. The population of conduction electrons flowing as a current in a magnetised material will exhibit differing mobilities. This varying mobility is a function of the electrons spin direction. The electron spin is designated as either up or down. Depending on the spin direction, one type of electron may suffer more collisions and have a shorter mean-free-path and, therefore, have lower mobility than the other electrons. This means that when electrons flow in a material subjected to an external magnetic field, electrons with an unfavourable spin direction, experience an increased resistance.

The GMR effect is observed in films with thickness of the order of the mean-free-path of an electron. The structure of a GMR sensor consists of a non-magnetic conducting material separating two thin magnetic films. The separator material can be copper and the magnetic film material can be CoFe or NiFeCo. Typical film thicknesses are 150-400 nm **[101]**. The separator material serves to allow the magnetic films to be magnetised in opposite directions while in close proximity. This is seen in **figure 4.3.1**.

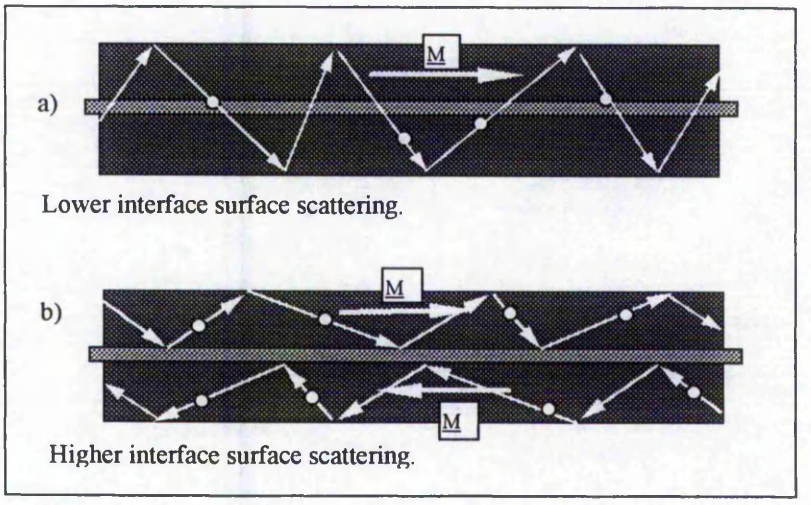


Figure 4.3.1 Black region is the GMR magnetic film and the grey region represents a non magnetic conducting material. a) shows low resistance due to low scattering of electrons at the interfaces. b) shows a increased resistance due to higher scattering of electrons by magnetisation in differing directions.

If the two films are magnetised in the same direction, then those conduction electrons traversing the separator do not suffer collisions and the mean-free-path of electrons are limited only by the physical boundaries of the structure. In this situation the GMR has a low resistance and likewise, if the two magnetic films were magnetised in the differing directions then there would be a high interface scattering, and thus an increase in resistance. These types of structures can show changes in resistance of up to 40%.

Sensors used in this report were produced by Nonvolatile Electronics Inc. . In order to maximise sensitivity of a particular resistor type, a four resistor bridge system was used. Two resistors, acting as references, were shielded with an overlayer of permalloy to screen them from magnetic fields. The same permalloy is used to focus the magnetic field on to the other two resistors, which act as detectors in the bridge circuit. The magnetic characteristics of a GMR shielded bridge device is show in **figure 4.3.2**.

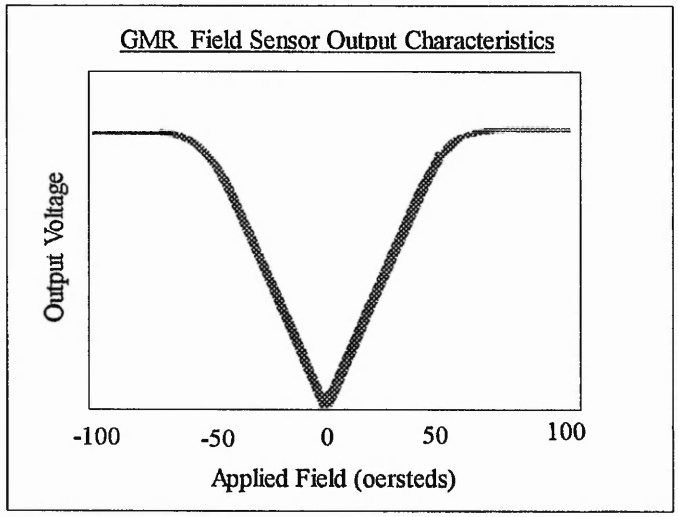


Figure 4.3.2 Shows the response of a GMR sensor to an applied field (1 Oe=79.62 Am^{-1}).

A variety of different GMR sensors are produced by Nonvolatile Electronics Inc. Each type has a different detection range. Careful consideration must be taken when choosing a sensor; the detection range and the saturation field of the sensor must be larger than the field to be measured. It is reported that GMR sensors are very sensitive **[102]**. The aim

of the work here was to see if they can be successfully used to measure the leakage field from surface breaking defects and if they provide any measurement advantages.

4.3.2. Experimental System using the GMR Sensor.

A GMR sensor was used for the detection of remanent magnetic flux from the Barkhausen specimens. An amplifier recommended by NVE electronics was constructed and used. The circuit diagram is shown in **figure 4.3.3**.

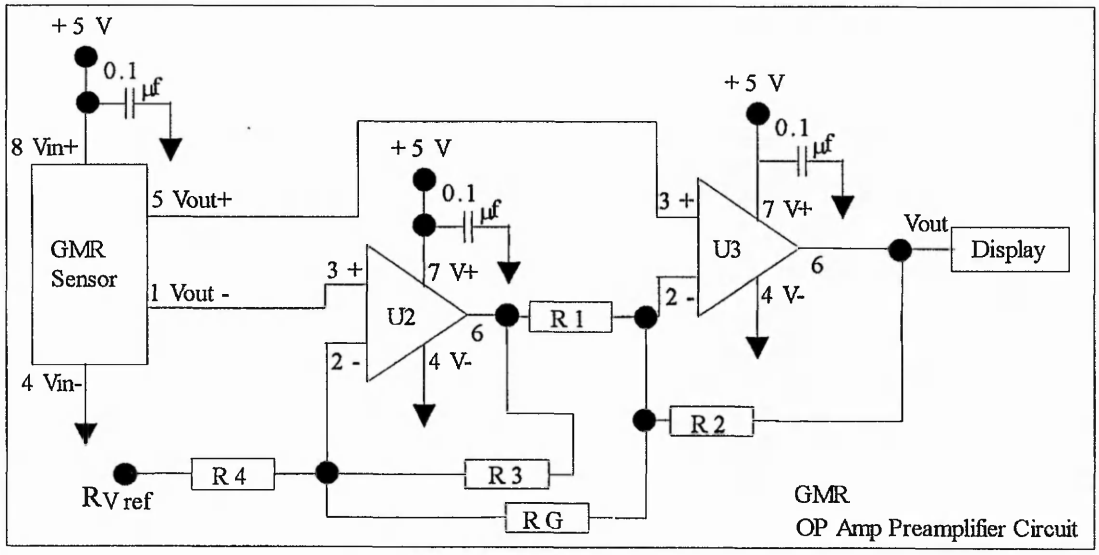


Figure 4.3.3 Two OP preamplifier circuit used for the GMR signal amplification.

The GMR sensor used was the AA004, which can be operated between 0-7962 Am^{-1} and had a linear response to the detected magnetic field within this range. The sensor provided a voltage output which was amplified and recorded using the recommended circuit shown in **figure 4.3.3**. The operating and supply voltage to the GMR was 5V DC, provided by a Farnell power supply. The electronic components used in the circuit were R_3=R_4=RG= 10kΩ, R_1= 500Ω, R_2= 100kΩ and Rv_{ref}=1kΩ. A potentiometer, providing RV_{ref}, was used to change the sensors base line threshold, in turn adjusting the GMR

sensors sensitivity. A Hall sensor and a Gauss meter, model 912, produced by Dowtry RFL Industries Inc., was also used to provide results for comparison with the GMR sensor output. This GMR sensor and equipment were found to be robust, cheap and easy to produce and provided results which were in agreement with the more expensive and delicate Hall probe.

4.3.2.1. *Specimen magnetisation.*

Each of the EN-43A steel specimens were taken around the hysteresis loop to produce a remanent magnetic field. This magnetisation was carried out using the Barkhausen magnetising system, which was set to a magnetising frequency of 0.1 Hz (see **chapter 1**). After magnetisation, the specimens were removed from the magnetic yoke and remanent leakage field measurements were conducted on the surface of the specimens. These measurements were carried out over the same region as the Barkhausen measurements described earlier in this chapter. The measurements, using the GMR sensor were taken every millimetre over the forty millimetre range and this is shown in **figure 4.3.4**.

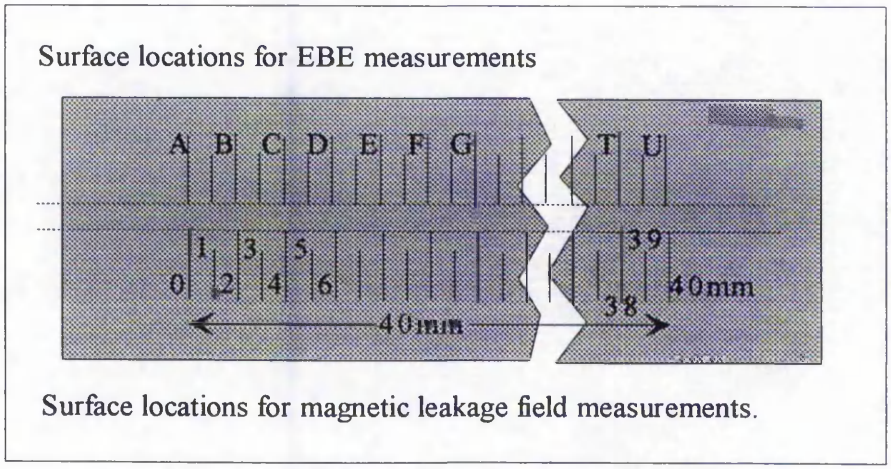


Figure 4.3.4 Central region of the steel plate specimens showing the EBE surface locations and the corresponding positions for magnetic flux leakage measurement. The width of the weld seam (not shown) is approximately 11 mm with it's centre being located on position 'K'.

4.3.3. Results the from GMR Sensor.

The different histories of the specimens affected their magnetic leakage field patterns. Both the GMR sensor and the Hall probe recorded very similar leakage field patterns for each of the specimens studied. This indicated the reliability of the GMR sensor in comparison to the more commonly used Hall probe. Each figure in this section displays the leakage field, from across the surface of a specimen, detected using the Hall probe and the GMR sensor. The leakage field patterns detected by both sensors are plotted on the same graph, allowing an easier comparison. The GMR measurements, for the different specimens, are not comparable as the RV_{ref} setting was changed between each specimen, thus, providing a linear range for the measurement of leakage field.

4.3.3.1. *Leakage field from the plain steel specimen (3P).*

Figure 4.3.5 shows the magnetic leakage field measurements from the plain steel specimen (3P). On the plain steel specimen the remanent magnetic flux on the surface of the sample was found to be relatively constant at around **0.235 mT ±0.01 mT** corresponding to a GMR voltage of **1.3V ±0.1V**. A slight decrease was observed towards the centre of the specimen. The measured field on the surface varied by only **±0.01 mT**. The slight change in the field was attributed to the changes in the 'as-received' surface condition caused by the grinding process.

4.3.3.2. *Leakage field from the welded steel specimen (2P).*

The magnetic field on the surface of the TIG welded specimen is shown in **figure 4.3.6**. The welded steel specimen, again, confirmed the reliability of the GMR sensor when compared to the Hall probe readings. The residual field at the 0 mm position was similar

in magnitude to the plain steel specimen. From the 0 mm to 10 mm position the magnetic leakage field increased from **0.25 mT** to **0.38 mT** (≡ **1.6V** to **2.7V**) and then for the next 20 mm remained constant at around **0.38 mT** (≡**2.7V**). After the 30 mm position the leakage field began to decrease to the value at the 0 mm position. The region of the raised leakage field corresponded to the weld and HAZ regions. The effect of welding lowered the permeability and caused the magnetic field to leak out of the specimen. This region of low permeability extended 8 to 10 mm either side of the weld centre.

Welded steel specimen. (2P)		Magnetic leakage field measurements	
Material region	Surface location	Hall probe (mT)	GMR (V)
Steel	0 mm	0.25 ±0.01	1.6 ±0.1
Weld seam	10 mm	0.38	2.7

Table 4.3.1 Summary of magnetic leakage field (MLF) data from the surface of the welded specimen (2P). Magnetic leakage field data recorded across the weld seam and parent material regions which is also displayed graphically in **figure 4.3.6**.

4.3.3.3. *Leakage field from the cracked weld specimens (21B and 21A).*

Both the cracked specimens were produced in the same way and, therefore, the detected leakage field patterns from both specimens were similar. The GMR and Hall sensors gave similar results and the data is displayed in **figure 4.3.7** and **figure 4.3.8**. At the edge of the examined regions very similar leakage field values were detected on both the cracked specimens. On the cracked weld specimen 21B the flux leakage pattern was distinct and can be seen in **figure 4.3.7**. The leakage field was found to be relatively constant for the first 12mm of the measured range, at around **0.34 mT** (≡**0.6V**). After this position the field increased sharply to a maximum peak at the 21 mm location. The magnitude of the leakage field at this location was **0.76 mT** (≡**4.8V**) and is summarised

in **table 4.3.2**. Past the position of maximum leakage field the measured signals began to decrease, almost mirroring the first half of the specimen.

Figure 4.3.8 shows the leakage field from the cracked weld specimen 21A. The leakage field at the 0 mm position had a magnitude of **0.34 mT** corresponding to a GMR voltage of **1.7 V**. The field values remained relatively stable until the 10 mm location, from where the leakage field began to rise. The leakage field peaked at the 22 mm position. This was very close to the position of the open surface fatigue crack and the leakage field values were at **0.63 mT (≡4.8 V)**. The summarised leakage field data is shown in **table 4.3.2**. The leakage field detected from an open surface crack was clearly much greater than the leakage field from the weld alone (**table 4.3.1**). The leakage field pattern from the crack was a tight sharp peak when compared to the welded specimen (**figure 4.3.6**). The region with the greatest change in permeability on the cracked specimen (the crack itself) was much smaller than the welded region. The increase in the dislocation networks, resulting from the crack generation process, would also lower the permeability of the parent material region. The overall effect of the crack creation accounted for the stronger leakage field at the edge of the examined region of the specimens. These values are similar to the leakage field at the central welded region of the 2P specimen.

Cracked weld specimen.			Magnetic leakage field measurements	
Specimen	Material region	Surface location	Hall probe (mT)	GMR (V)
21B	Steel	0 mm, (A)	0.34 ±0.01	0.6 ±0.1
	HAZ	14 mm, (H)	0.37	1.2
	Weld	22 mm, (L)	0.76	4.8
21A	Steel	0 mm, (A)	0.34 ±0.01	1.7 ±0.1
	HAZ	14 mm, (H)	0.39	2.4
	Weld	20 mm, (K)	0.63	4.8

Table 4.3.2 Summary of magnetic leakage field (MLF) data from the surface of the cracked weld specimens (21B and 21A). The magnetic leakage field data, was recorded across the weld seam, HAZ and parent material regions, is also displayed in **figures 4.3.7** and **4.3.8**.

The leakage field above the open crack, on the cracked weld specimen 21B, was larger than the field from specimen 21A and is shown in **table 4.3.2**. This may imply that the crack defect in specimen 21B was larger than the crack in specimen 21A **[85]**. A way of estimating if this conclusion is correct is by modelling the crack using a slot. A model similar to the Zatsepin-Shcherbinin slot model (equation listed below) was used to aid interpretation of the observed magnetic leakage field data **[53]**.

$$H_x = 2m\left[\frac{(x+p)}{(x+p)^2+(y+h)^2} - \frac{(x-p)}{(x-p)^2+(y+h)^2}\right] \qquad (4.1)$$

Where x and y are positions within a Cartesian co-ordinate system, p is the dipole separation distance (i.e. directly related to slot width) and h is the depth of the dipole from the surface (related to the slot depth). m is the dipole, analogous to the magnetic field strength at the slot. Equation 4.1 has been found to successfully represent leakage

field data from slots with relative accuracy **[53]**. In the use of this model an assumption of a constant field across the slot face is made. This cannot be justified, except perhaps at high levels of applied field. The cracked weld specimens 21B exhibited a magnetic leakage fields which was 17% larger in magnitude compared to the leakage field from the cracked specimen 21A. The magnetic leakage field, calculated using this model (equation 4.1), exhibits a linear response to an increasing slot width. These calculations include a general assumption that the dipole field strength is constant irrespective of slot dimensions. This result may be taken to indicate that specimen 21B possessed a wider crack compared to the specimen 21A. Calculated magnetic leakage field pattern from tight slots are shown **figure 4.3.9**.

4.3.3.4. *Leakage field from the machined cracked weld specimen surfaces (22A and 22B).*

The surface of both the cracked weld specimens 21A and 21B were machined and surface thicknesses of 0.5mm and 0.55mm were removed using the 'shaper' and the EDM machine respectively. **Figure 4.3.10** and **figure 4.3.11** show the magnetic leakage field from both the new surfaces (22B and 22A) of the cracked specimens.

The leakage field, at the edge of the studied region, on the EDM machined surface 22B was measured as **0.25 mT ±0.01 mT (≡1.9 V)** and remained relatively constant between the 0 mm and 12 mm positions. The leakage field then began to increase rapidly to a maximum of **0.55 mT (4.8 V)**, at the 21 mm position (**table 4.3.3**). From this point onwards the field began to decrease, mirroring the first half of the specimen. Finally, the leakage field levelled off at **0.25 mT (1.9 V)** towards the edge. This is shown in **figure 4.3.10**.

The planed surface 22A showed the leakage field, at the outer edges of the studied region, to be at **0.25 mT (2.1 V)** on the left side and **0.24 mT (2.0 V)** on the right side of the crack (see **table 4.3.3**). As the crack was approached from both sides the field

increased rapidly to a maximum on the 22 mm position. The maximum leakage field was found to be **0.44 mT (3.9V)**. The machining of the specimens appeared to have reduced the leakage field from both specimens. This would suggest that the overall permeability of both specimens had increased when the 'as-received' surfaces had been modified by machining.

Machined cracked weld specimen.			Magnetic leakage field measurements	
Specimen	Material region	Surface location	Hall probe (mT)	GMR (V)
EDM machined 22B	Steel	0 mm, (A)	0.25 ±0.01	1.9 ±0.1
	HAZ	14 mm, (H)	0.31	2.4
	Weld	22 mm, (L)	0.55	4.8
Plane machined 22A	Steel	0 mm, (A)	0.25	2.1
	HAZ	14 mm, (H)	0.30	2.6
	Weld	20 mm, (K)	0.44	3.9

Table 4.3.3 Summary of magnetic leakage field data from the machined surfaces (22B and 22A) of the cracked weld specimens. Magnetic leakage field data was recorded from across the weld seam, HAZ and parent material regions and this data is also displayed in **figures 4.3.10** and **4.3.11**.

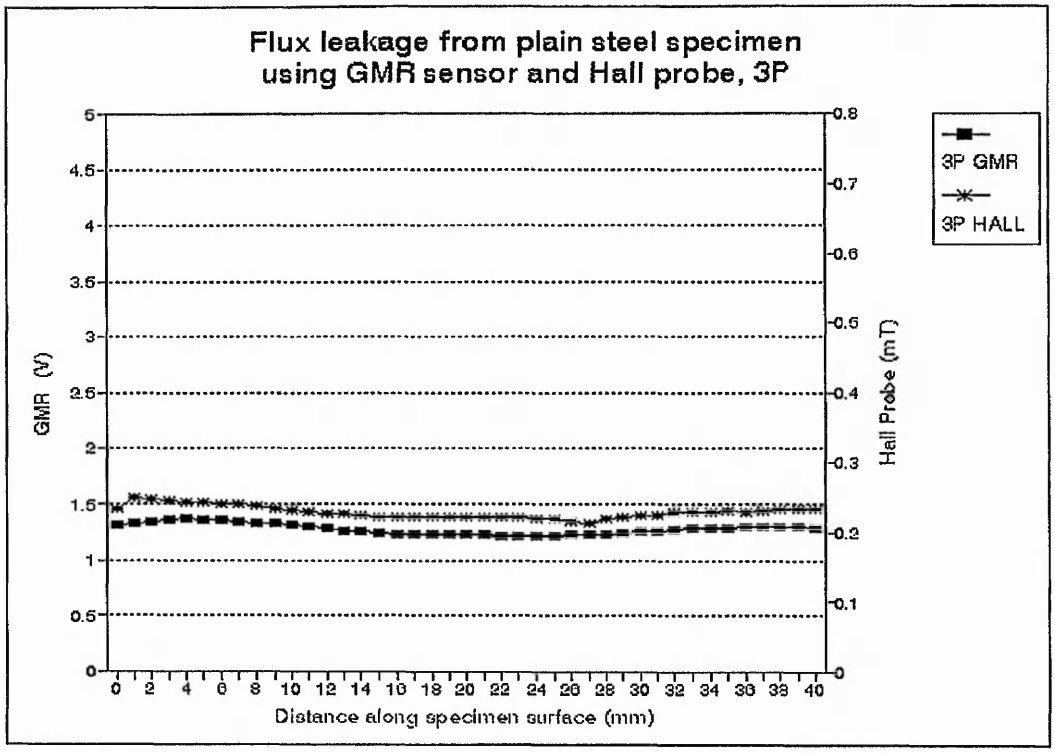


Figure 4.3.5 Magnetic leakage field detected, using a GMR sensor and Hall probe (units milliTesla), on the surface of the plain EN-43A steel specimen (3P).

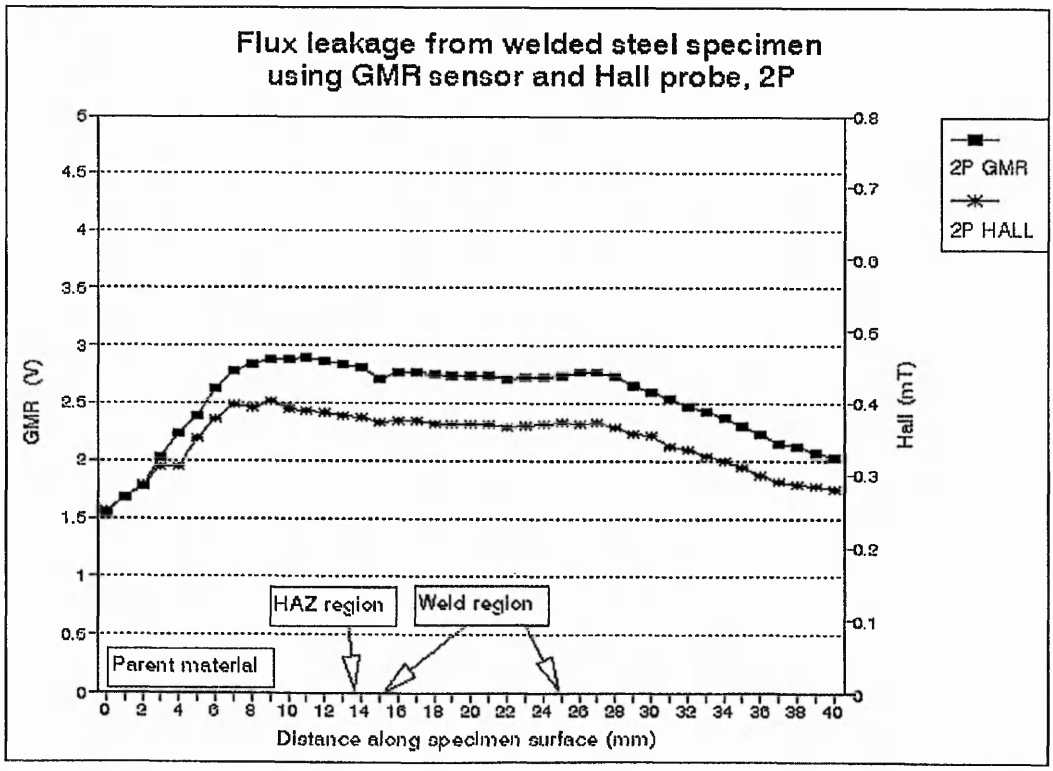


Figure 4.3.6 Magnetic leakage field detected, using a GMR sensor and Hall probe (units milliTesla), on the surface of the welded steel specimen (2P).

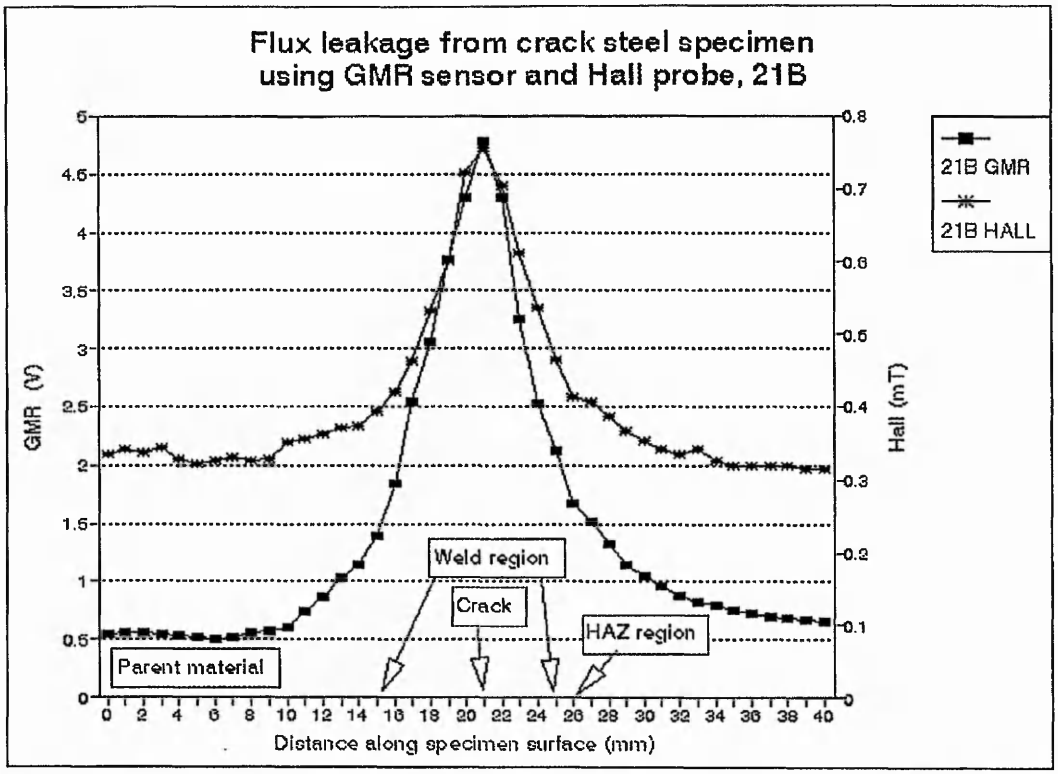


Figure 4.3.7 Magnetic leakage field detected, using a GMR sensor and Hall probe (units milliTesla), on the surface of the cracked weld specimen (21B).

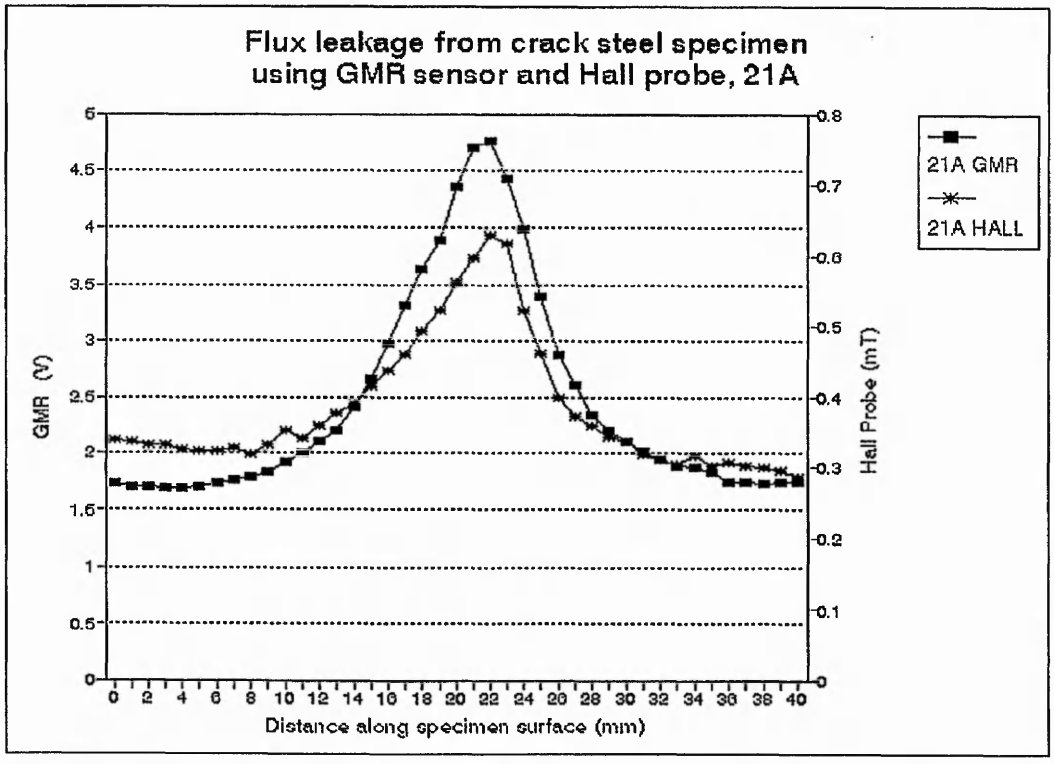


Figure 4.3.8 Magnetic leakage field detected, using a GMR sensor and Hall probe (units milliTesla), on the surface of the cracked weld specimen (21A).

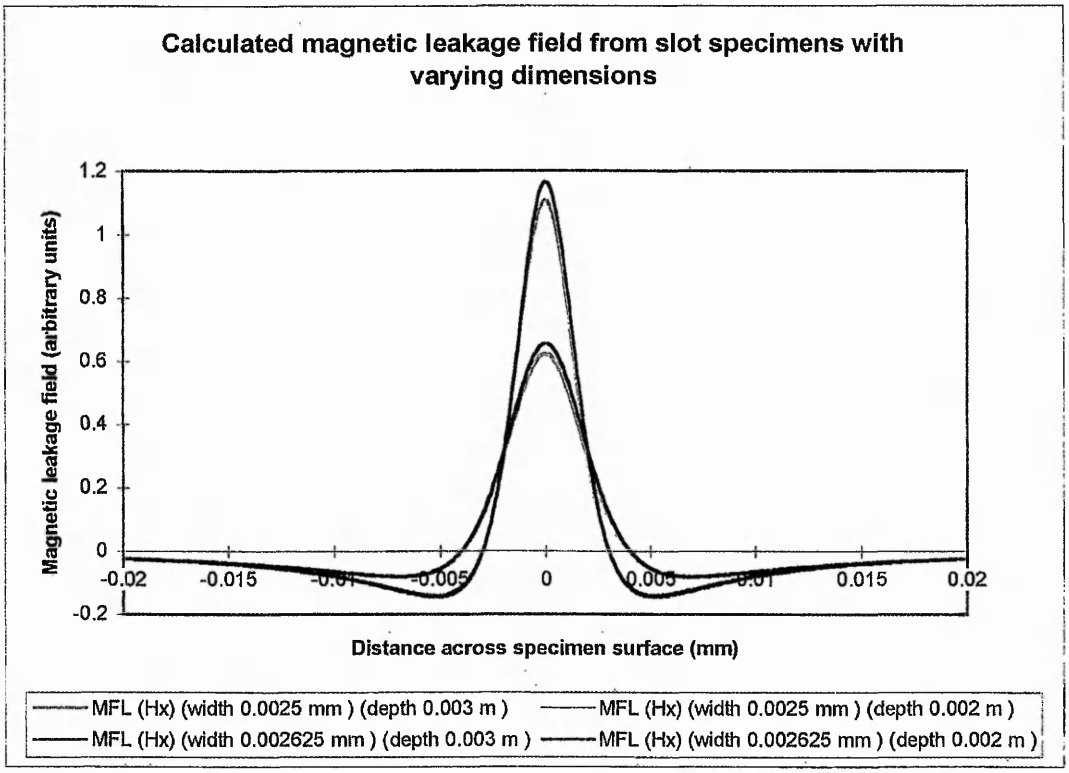


Figure 4.3.9 Calculated magnetic leakage field pattern (**Hx**) from the slot specimen using **equation 4.1**.

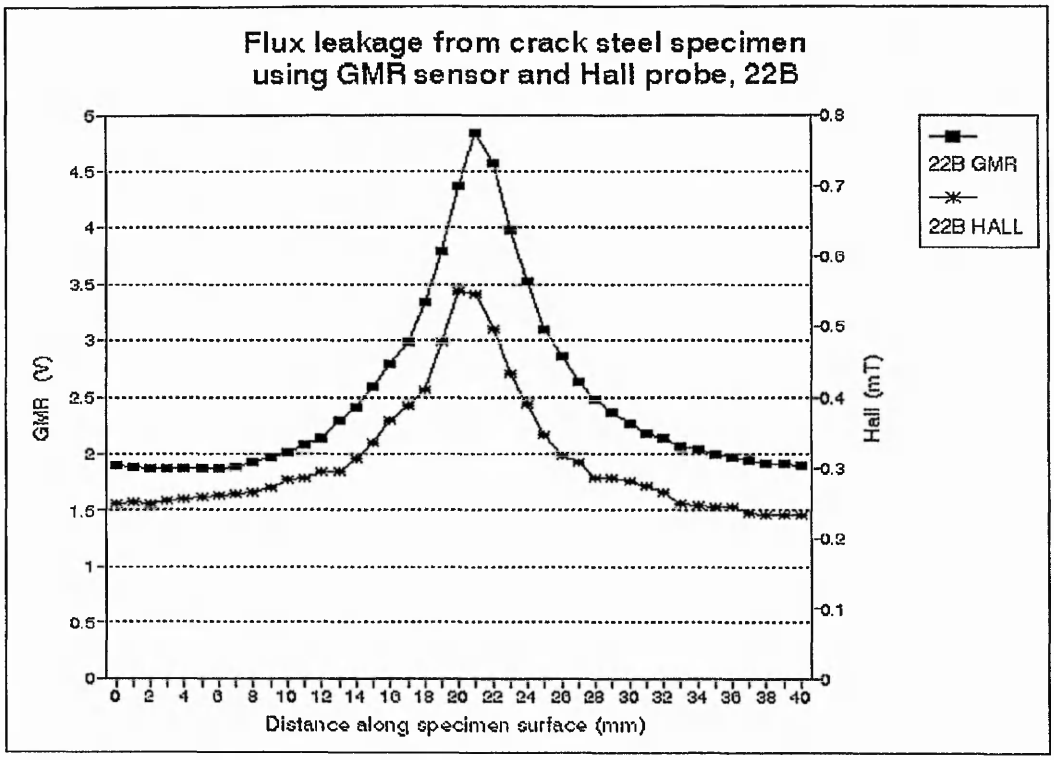


Figure 4.3.9 Magnetic leakage field detected, using a GMR sensor and Hall probe (units milliTesla), on the EDM machined surface (22B) of the cracked weld specimen (21B).

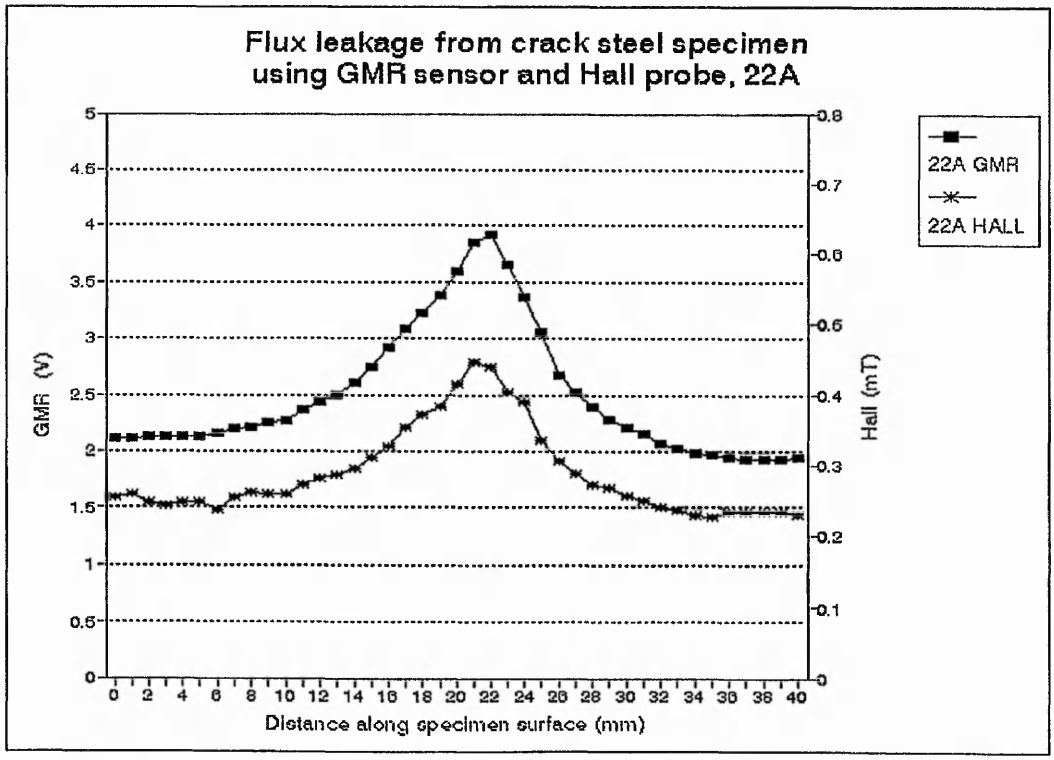


Figure 4.3.10 Magnetic leakage field detected, using a GMR sensor and Hall probe (units milliTesla), on the planed machined surface (22A) of the cracked weld specimen (21A).

4.4. DISCUSSION OF BARKHAUSEN EMISSION FROM PLAIN, WELDED AND CRACKED WELD SPECIMENS OF EN-43A STEEL.

In this section the Barkhausen signal envelopes from the plain steel, welded steel and cracked weld steel specimens and their machined surface are discussed in detail and compared to measurements such as hardness and magnetic leakage field. Optical and scanning electron microscopy were also conducted on these specimens and results from these sources are compared.

4.4.1. The Plain Steel Specimen.

The steel plate, which was rolled and then machined down to size, exhibited a uniform microstructure. The microstructure of a cross section of the specimen, after preparation in 2% Nital, showed a crystalline structure of ferrite and pearlite. Micrographs are shown in **figures 4.4.1** and **4.4.2**. The ferrite appeared white in colour and the pearlite appeared dark in colour. The crystals were elongated in a given direction indicating that the steel plate specimens had been rolled with no heat treatment. The rolling process had physically deformed the shape of the crystals; this would cause an increased residual stress concentration within the crystalline structure. The average size of a ferrite crystal in the bulk of the material was 10μm -15μm thick and approximately 20μm to 35μm in length. The pearlite crystals were thinner and on occasions slightly longer than the ferrite crystals. The crystals appeared significantly thinner at the surface region of the specimen. This would indicate that the surface region was more deformed due to the rolling and machining processes.

Vickers micro-hardness tests, carried out on this specimen using a load of 50g, yielded a hardness value of 200 ±10 VHN. Standard Vickers hardness tests, using a 20kg load, were carried out on the sample's surface and this yielded a hardness value of 160 ±10 VHN. The Vickers micro-hardness indent is carried out over a polished region of one or

two grains and the hardness depends directly on the individual grain type. The standard Vickers hardness test is done over a larger area of material and the effect of the surface damage caused by the machining needs to be taken into consideration. Hardness affects the magnetic coercivity of a material and a near linear relationship exists for pearlitic steels **[46]**. This would imply that if the hardness of a specimen increased then the coercivity would change, leading inevitably, to a change in the Barkhausen envelope.

The magnetic leakage field detected by the GMR sensor showed a relatively constant value across the surface of the specimen, (**figure 4.3.5**). This indicated the magnetic permeability, which closely affects the leakage field, remained uniform across the material. The material microstructure and stress state are factors which also affect permeability and the EBE signal envelopes. These results indicate that the plain steel specimen (3P), was indeed uniform in microstructure and stress state across the studied region.

4.4.1.1. *The EBE signal envelopes from the plain steel specimen (3P).*

In a polycrystalline material, the easy direction of magnetisation varies from one grain to another. Before any kind of magnetic field is applied to steel, the magnetisation vectors within each grain try to align themselves along one of the cubic axes of the crystal, i.e., the <100> direction. This direction is energetically favourable because it reduces the magnetic anisotropy energy. During fabrication of the plain steel plate, the rolling process elongated the grains along a given direction. The rolling direction helped create a net macroscopic easy direction along which 180° domain walls lie. All of the local easy directions combined to form a net macroscopic easy direction which was along the direction of rolling. All of the specimens studied were magnetised along the rolling direction, and hence, the macroscopic easy direction. It is known that the EBE signals and, therefore, the envelopes are generated by the sudden discontinuous changes in the magnetisation of a specimen as the **H** field is increased smoothly. These discontinuous changes arise from the motion of the magnetic domain walls. The EBE envelope is

created from the changes in the potential detected in the sensor coil. Therefore, the EBE maximum signal voltage represents a region in the recording window where the largest number of magnetic 180° domain walls are in motion. In turn this is directly linked to a specific "critical" magnetic field value, experienced by the specimen, at which a large proportion of the domain wall motion takes place.

When the magnetic field is increased through the specimen along the easy direction, the magnetisation process is expected to be completed relatively rapidly. The EBE generation is due to the movement of 180° domain wall and would lead to a single peak envelope. The EBE peak for the plain steel specimen occurred at around **1.04 s**. At this time the applied magnetic field strength, and hence, the magnetisation state of the specimen is such that the significant domain wall pinning energy within this specimen is overcome. The pinning sites within the steel specimens are mainly the grain boundaries, dislocations caused by the rolling process and 'as-received' surface deformation caused by the grinding.

The Barkhausen signal envelopes on the plain steel, specimen 3P, were found to be reproducible across the entire region studied. Typical EBE signal envelope shape from across the studied surface are shown in **figures 4.2.1** to **4.2.4**. The EBE signal parameters gave an average of **0.061 V^2s (± 0.007 V^2s), 1.039 s (±0.015s), 0.496 V (±0.030V)** for signal energy, time of maximum peak and maximum signal voltage respectively. These were taken to be the standard parameter values for plain EN-43A steel plate in the 'as received' condition.

4.4.1.2. *The ABE signal envelopes from the plain steel specimen (3P).*

The ABE signal is generated as a consequence of magnetostriction and the associated volume change that this phenomenon causes when domain walls move in a magnetised specimen. A piezoelectric transducer detects the stress waves generated throughout the specimen. These stress waves are generated when the non-180° domain walls (closure

walls) move through the material due to the increasing magnetic field. Closure domains exist around the edges of the specimen and around defects, such as inclusions, large precipitates and grain boundaries. The closure domains help reduce the magnetostatic energy, but large closure domains are energetically unfavourable because they increase the magnetoelastic energy. The sudden movements of these closure domains causes a change in the strain of the material. This leads to the generation of the stress waves which are detected as the ABE signals.

The doubled peaked ABE signal envelopes were essentially reproducible across the studied region. Spikes appeared on the ABE signals and an example is given in **figure 4.2.6**. Depending on the location on the specimen surface, these spikes occurred at different positions on the signal envelope. For a given sensor attachment the detected ABE envelopes were very reproducible. Only when the sensor had been detached from the steel plate and then repositioned did the rogue peak shift to a new position on the ABE envelope. The lack of stability of these rogue peaks created difficulties in calculating ABE parameters such as signal energy and maximum signal voltage, especially when the rogue peak occurred on the position of the second peak. Clearly, if ABE is to have a role in the characterisation of ferromagnetic materials, then features such as these make utilisation of the technique more difficult. The origin of these peaks is not clear. The uniform composition and stress state of the plain steel specimen, in theory, should not produce significant differences in the detected ABE signals. Therefore, the range of ABE parameter values obtained for this specimen can be taken as a reference. The ABE parametric values for signal energy, time of maximum peak (second peak) and maximum signal voltage from the plain steel specimen were **0.232V^2s (±0.045 V^2s), 1.150 s (±0.028 s)** and **0.993 V (±0.167 V)** respectively.

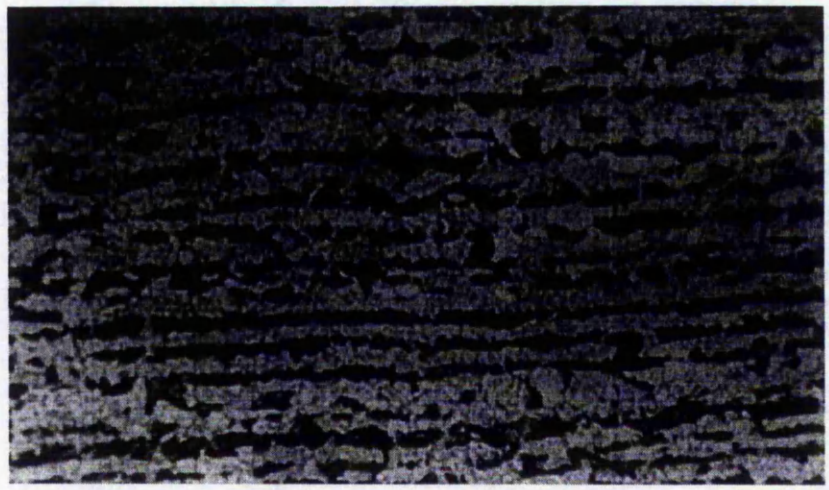


Figure 4.4.1 Microstructure of EN-43A parent steel. Photograph using an optical microscope. The microstructure show definite elongation of microstructure due to rolling process. The light regions are the ferrite and the dark regions are pearlite. Magnification ×400.

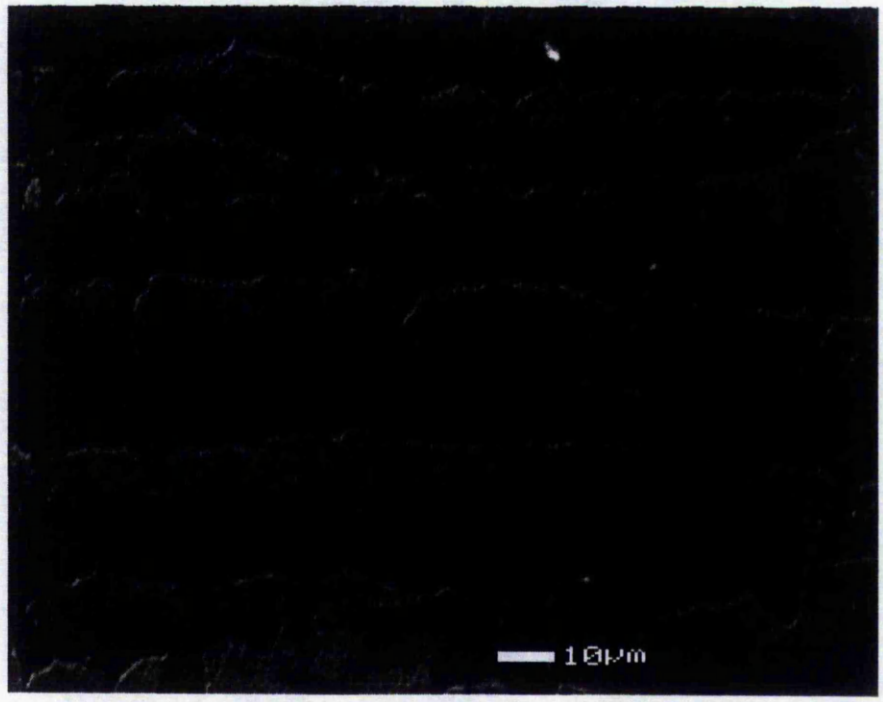


Figure 4.4.2 Scanning Electron Microscope picture of EN-43A steel specimen. The dark region is ferrite and the lighter region is pearlite. Magnification ×2000.

4.4.2. The TIG Welded Steel Specimen.

4.4.2.1. *Microstructure due to welding.*

The heat generated in the steel during welding affects the surrounding areas and changes the microstructure of the parent material. With the exception of electroslag and gas welding, most welding processes allow high rates of cooling and this may lead to insufficient time during the heating phase to homogenise the microstructure. The cooling rates are often rapid, (similar to rates obtained in oil quenching), which can lead to the development of a microstructure that is not found under equilibrium conditions. Under equilibrium conditions in carbon steels two types of transformation occur. Firstly, the transition from austenite (face-centred gamma phase) to ferrite (body-centred alpha phase), which occurs just below 900°C for 0.2% carbon steel. Secondly, the precipitation of carbides, nitrides and other phases whose solubility decreases as the temperature falls. This can lead to precipitation hardening of the steel. Above 900°C the steel is austenitic. As the temperature is reduced slowly (900°C >Temp.>695°C) ferrite containing small amounts of carbon in solid solution is precipitated, leaving austenite grains that become smaller and progressively enriched in carbon as the temperature falls. At 695°C the residual austenite transforms into pearlite (a laminated eutectoid mixture of ferrite and cementite-Fe_3C). These structures, obtained by slow cooling, consist of intermingled grains of ferrite (white) and pearlite (dark/black). Following microstructural analysis, this type of microstructure with the added rolling directionality was found in the parent steel, away from the weld region, (**figure 4.4.1**).

Due to the rapid cooling occurring in the weld, the temperature at which the austenite-to-ferrite change takes place is depressed. As a consequence of the transformation temperature falling, the distance over which the atoms can diffuse is reduced. On slow cooling the atoms can segregate into separate individual grains of austenite. With rapid cooling, carbide precipitates around or within the ferrite, which now appear as needles or plates, rather than equiaxed grains. At even more rapid cooling rates the transformation temperature is depressed to a value where martensite is formed. Martensite, which is

paramagnetic, is formed by a shear movement of the austenite lattice, the carbon being retained in solid solution in a distorted body centred cubic lattice. The lower the transformation temperature the harder the transformation product, especially if the carbon content is higher. The rapid cooling leads to Widmanstatten type structures.

In the Heat Affected Zone (HAZ), the elongated ferrite and pearlite grains changed and became smaller and more equiaxed in shape. This was within a 5 mm region of the weld metal and was caused by the intense heating and cooling, experienced by the steel. Very close to the weld interface large equiaxed grains exist mixed with fine grains and this can be seen if **figure 4.4.3**. The magnetic leakage field measurements (**figure 4.3.6**) indicate that this region, along with the weld, had a lower magnetic permeability compared to the parent steel.

4.4.2.2. *Mechanical properties of weld metal.*

The weld was approximately 10.5 mm in width at the surface of the specimen. The portion of alloying elements lost by oxidation thorough TIG welding would be small **[96]**. Therefore, the material composition was not expected to have changed significantly. TIG welding has a high rate of cooling, which creates microstructure having a fine grain size, along with a high dislocation density (**figure 4.4.5**). The combination of a fine grain size and high dislocation density gives the weld metal its high yield strength. The weld metal consisted of fine ferrite grains with carbides and a phase which appeared to be retained austenite at the grain boundary **[103]**. Another feature of carbon steel weld metal is that it shows no sign of recrystallisation or softening when heated below the critical temperature, probably because of the carbide networks surrounding the ferrite grains. This makes weld metal generally stronger than the parent metal. High yield points and resistance to softening are desirable features as weld joints often experience greater stresses than other parts of a structure.

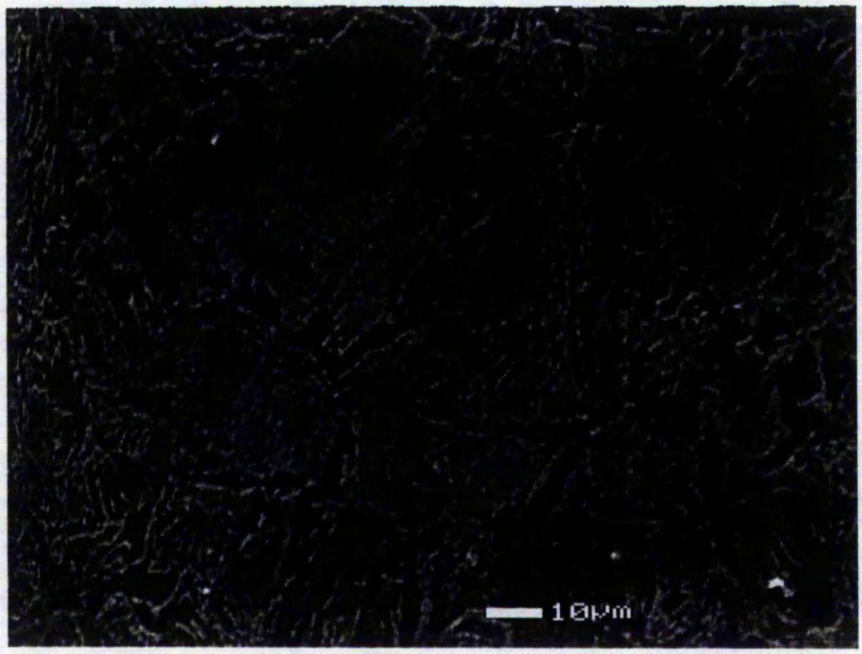


Figure 4.4.3 Scanning electron microscope image showing microstructure with a large grains size existing on the weld and HAZ interface. Magnification ×2000.

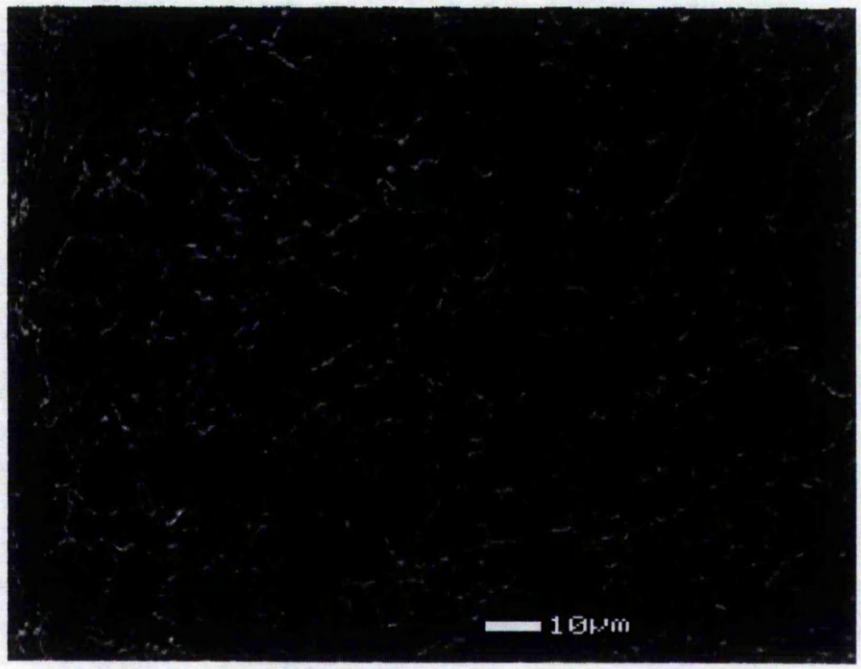


Figure 4.4.4 Scanning electron microscope image showing microstructure with a fine grains size existing on the weld seam. Magnification ×2000.

4.4.2.3. *Residual stress due to welding.*

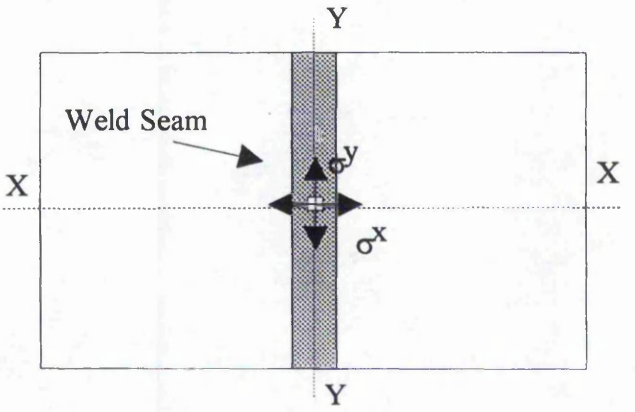
Welding not only changes the local microstructure, it also introduces residual stresses into the steel plate specimen. When the weld cooling is nearly complete the axial stress in the weld zone is characterised by a residual tension, while the HAZ is dominated by residual compression. Shear stresses arise as a result of tensile stress gradient and are a maximum at the transition zone between weld and HAZ **[104]**. Major volume changes associated with the liquid to solid transformation in the weld and the thermal contraction which occurs on cooling from the melting point are the main sources of the residual stress. **Figure 4.4.6.** shows a typical distribution of residual stress in a butt weld. The important stresses are parallel to the weld direction, designated σ_y, and those the transverse to it, designated σ_x.

The longitudinal stress distribution σ_x can be approximated by equation 4.2 below:

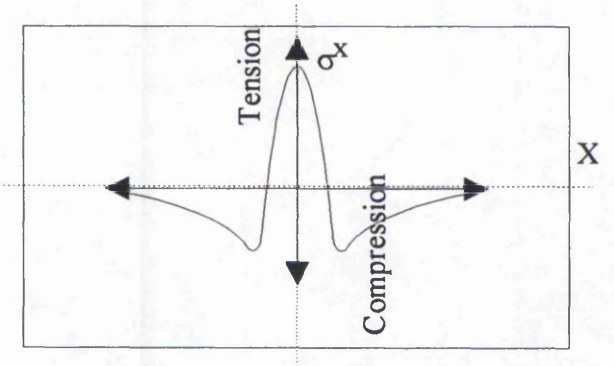
$$\sigma_x(x) = \sigma_m \left\{1 - \left(\frac{x}{b}\right)^2\right\} e^{-\frac{1}{2}\left(\frac{x}{b}\right)^2} \qquad (4.2)$$

The stress distribution is characterised by two parameters. The maximum stress at the weld region σ_m and secondly the width of the tension zone of the residual stress b. In weld metal made of low carbon steel, the maximum residual stress, σ_m, is usually as high as the yield stress of the metal itself **[105]**. Such a high stress state is expected to have significant effect on both acoustic as well as electromagnetic Barkhausen signals.

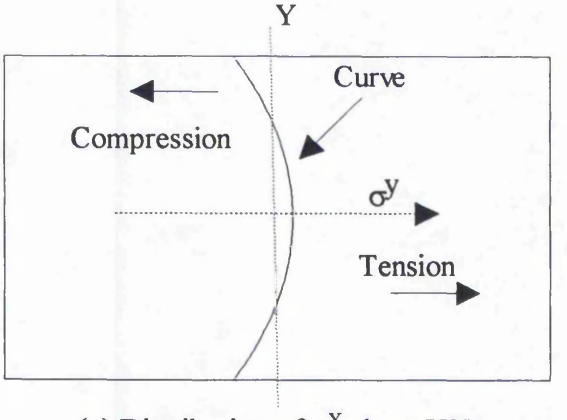
Weld stress profiles.



(a) Butt Weld.



(b) Distribution of σ^X along XX.



(c) Distribution of σ^Y along YY.

Figure 4.4.6 Distribution of the longitudinal residual stresses σ_x and σ_y. Tensile stress of a high magnitude are produced in the region near the weld, which taper off rapidly and become compressive after a distance of several times the width of the weld metal **[105]**.

4.4.2.4. *Leakage field and the effect of material hardness.*

The magnitude of the leakage field, detected by the GMR sensor (**figure 4.3.6**), on the surface of the 2P specimen showed an increase between 10 mm (≡'F') and 28 mm (≡'O') locations. This leakage field indicated a change in the magnetic permeability of the material between these locations. The weld metal and the HAZ were situated between these two locations. The change in microstructure, increased dislocation density coupled with the residual stresses, caused a change in the permeability and, therefore, an increase in the leakage field was observed. The magnetic permeability of the HAZ and weld metal were clearly similar as the leakage field was the same across both these regions. The results show that the region of reduced permeability extended well into the parent material.

Towards the edge of the locations being studied (10 mm away from the weld) the magnetic permeability of the welded specimen returned to similar values to those for the plain steel specimen (3P). The leakage field was measured to be **0.25 mT** to **0.27 mT**. This implied that material at the edge of the studied region was more like the original parent steel. The hardness values at these edge locations was also found to be around 160VHN; this was the same as the hardness of the parent steel.

The Vickers hardness profile across the surface of this welded specimen is shown in **figure 4.4.7**. The graph shows that, on the weld, the hardness of the weld metal was around 240 VHN and it decreased away from the weld. The high dislocation density and small grain size within the weld metal was the main cause for the increased hardness.

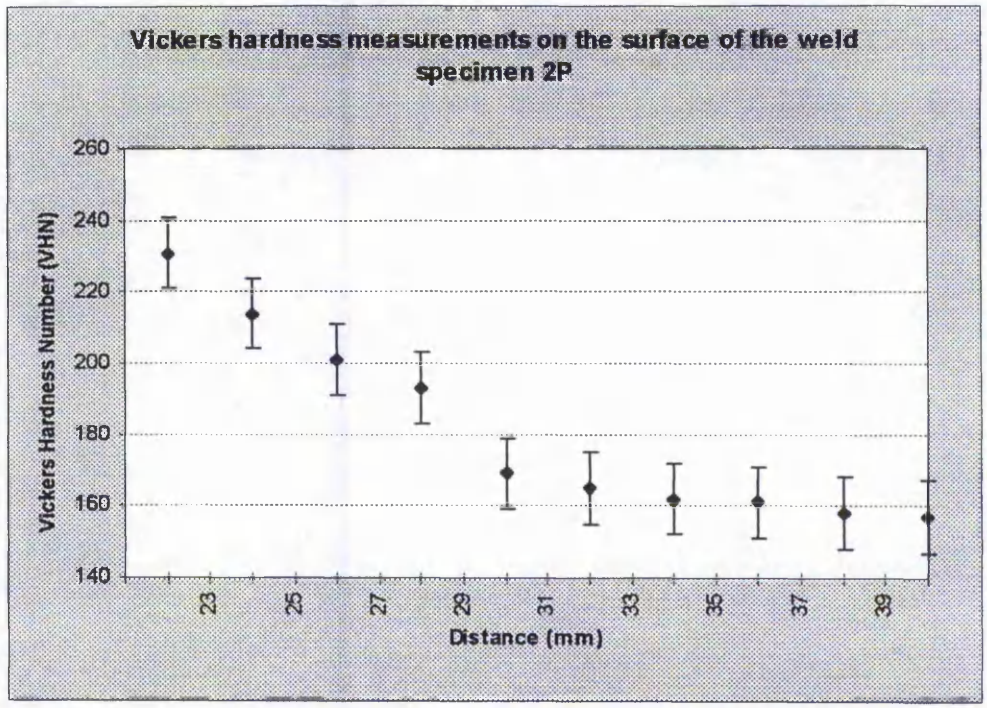


Figure 4.4.7 Vickers hardness profile of the welded specimen across half its surface. A load of 20kg was used for the indentations.

4.4.2.5. *Original 'as-received' surface finish.*

The post weld surface grinding process, which removed the weld root and cap, had some influence on the steel. If the shape of the envelope was controlled solely by the stresses generated by the grinding process, then the effect of welding would be masked and the EBE envelopes would appear very similar to the plain steel (3P) specimen. Also the EBE envelopes from across the entire surface of the specimen would appear the same. However, this was not found to be the case, suggesting that the surface grinding /finishing process, used to remove the weld root and cap, only had a limited effect on the EBE envelope.

4.4.2.6. *The EBE envelopes from the welded steel specimen (2P).*

For a specimen possessing a TIG weld seam, the detected EBE signal envelopes changed form. Signal envelopes from the welded 2P specimen are shown in **figure 4.2.9** to **4.2.12**. At the edge locations A, B, T and U, (away from the weld seam) the EBE signals displayed the lowest 'maximum signal voltages' (**0.497 V**) and signal energy within the studied region (**figure 4.2.13**). The V_{MAX} values at these locations are similar to the V_{MAX} value of **0.496 V** from the plain steel specimen (3P). This also holds true for the signal energy and the time of maximum peak (T_p). At these edge locations (A, B, T and U) the EBE signal appear as double peaked envelopes. As the weld was approached, the first peak increased in height at the expense of the second peak, and eventually became the largest peak. Directly on the weld seam the first EBE peak was the largest and the second peak became flattened, as seen in **figures 4.2.9** to **4.2.12**. As the position of the **maximum peak** changed between the first and second peak, this caused the T_p value to also change.

On locations furthest from the weld seam the EBE envelopes appeared double peaked. The reason for the double peaks are explained in terms of critical field values required to overcome different domain wall pinning energies **[106]**. EBE signals are know to be very sensitive to microstructural features as well as stress **[2][107]**. The pinning sites, thought to have the most significant effect on the EBE envelopes are the grain boundaries and the second phase precipitates. Goodenough has shown on the basis of the energy criterion, that grain boundaries are the preferred sites for reverse domain formation and inclusions would generate only transverse domains. Also Goodenough **[108][109]** & Cullity **[110]** have shown transverse domains around the inclusions act as barriers to moving 180° domain walls and they do not, in general, contribute to flux reversal.

These ideas, that grain boundaries are the preferred sites for reverse domain formation, do not consider the effect of domain wall nucleation as having a significant effect on the EBE signal, even though each of the peaks, from the double peaked EBE envelope occur near to the knee region of the hysteresis loop. It is known that a major contribution to

magnetisation comes from the irreversible motion of 180° domain walls **[111][112]**. This is because domain nucleation is not involved unless ideal saturation is achieved, which is difficult to achieve in practice **[113]**. Even in toroidal shape specimens, where the demagnetisation field is nil, reverse or transverse spikes are formed at defects such as large precipitates, pores and grain boundaries during magnetisation in order to reduce the interface magnetic free pole energy or magnetostatic energy. The reversal of these domains causes flux reversal during cyclic magnetisation. Therefore, the EBE can be considered to be associated with the irreversible movements of already existing reverse domain walls (at grain boundaries) compared with fresh domain nucleation or domain rotation phenomena.

The two most significant pinning sites, grain boundaries and second phase precipitates, are believed to cause the peaks on the EBE envelopes. When the mean critical field, required to overcome the pinning due to the grain boundaries and second phase precipitates, is attained the sudden breakaway of 180° domain walls causes the EBE peak. When the energy required to overcome the two types of pinning sites is significantly different, the EBE signal appears as a double peaked envelope; each peak representing the statistical distribution of domain walls depinning. If the critical field values for the two types of obstacles are close together then the envelope appears with a single peak **[106]** .Work done on a range of steels by Moorthy et al. **[27]** has shown that large precipitates shift the second peak to higher fields. Also increased size distribution of carbide precipitates broadens the second peak width. This model (proposed by Raj **[106]**) has been successful in explaining EBE profiles from several different steels, possessing a range of microstructures, caused by varying heat treatment processes. The notion of 'critical field strength' required to overcome pinning energy is correct, if the magnetisation and the rate of magnetisation used for any comparative study is the same. Otherwise, it must be thought of as the 'critical rate of change of field strength'. This is because the EBE envelope is generated under a dynamic magnetic field and not a static field.

The **parent material region** of the welded specimen (2P) displayed a crystalline structure showing the rolling direction of the plate. The grain size of the parent material

(30 μm × 10 μm) was much larger (on average) than the grains from the HAZ or the weld seam, as shown in **table 4.4.1**. The double peaked EBE envelopes from this region can, thus, be explained, using the model discussed earlier, arising from the critical field required to overcome domain wall pinning at grain boundaries (first peak) and second phase precipitates such as cementite particle (second peak) within the pearlite grains. The effect of residual compressive stress, on the parent material region due to the weld seam, reduces the 180° domain wall population. Therefore, the reduction in the number of 180° domain walls would lead to an overall smaller signal envelope. The larger second peak is caused by the domain walls breaking away from the strongly pinning cementite lamellae **[16]**. The effects of the crystallographic strain (caused by the rolling direction) and the larger mean-free-path of the domain walls (observed in larger grains by Lo et al. **[75]**) should aid EBE generation, but, the effect of these phenomena have been limited in this case by the compressive weld stress.

Material region	Grain size
Plain steel region	30 μm × 10 μm
HAZ region (lager grains)	40 μm × 40 μm
HAZ region (small grains)	<5 μm × 5 μm
Welded region	<1 μm × 2 μm

Table 4.4.1 Crystal grain size; measured using the electron microscope.

The signal envelopes from the weld and HAZ displayed only a single peak in the low field region, around 0.75 seconds on the EBE envelope (**figures 4.2.10** and **4.2.11**). According to the proposed model, this peak was due to pinned domain walls breaking away from grain boundaries. This was backed up by the microscopy images which showed large grains with intermingled finer grains at the HAZ locations and very fine grains in the weld region. The small grains led to an increase in the grain boundary present to cause domain wall pinning, **figure 4.4.8**. In place of the second peak there was a slope present when over the HAZ region and a plateau when over the weld region.

Over these two regions the effect of the second phase precipitates on the EBE envelope was still present, but less significant than the grain boundaries.

In regions with very fine grain structures and very high dislocation concentrations, such as that found in quenched materials, the EBE signals have been reported to decrease **[36]**. It has also been found that under very high tensile stresses, the EBE signal amplitude (V_{MAX}) also decreases **[39][52]** . "No explanation yet exists for this in recent literature"... **[39]**. The residual stress directly at the centre of the weld seam can be close to the yield stress **[105]**. This, along with the very small grain size in the weld region, helped reduce the EBE envelope's V_{MAX} value. Therefore, over the 9 mm weld seam, the central position provided the lowest V_{MAX} value due to the very high tensile stress and fine grain size, (**figure 4.2.13**).

Above the HAZ microstructure region (on locations G, H, I and M, N, O, P) the largest EBE signal voltages were detected, as shown in **figure 4.2.13**. Within the HAZ region there existed large, as well as, small grains. These large grains allowed the domain wall to sweep a greater mean-free-path. As a result, larger EBE signal voltages were recorded from the HAZ locations **[27]**.

The net **EBE signal energy** profile from the welded specimen (2P) showed an increase when compared to the signal energy from the plain steel specimen (3P), (**figures 4.2.5** and **4.2.13**). This was due to the altered microstructure and the new residual stress profile generated on the weld specimen. The surface of the weld seam was in tension, and this tensile force dropped to a compressive force at a distance of several weld widths, (**figure 4.4.6**). In polycrystalline materials which have been rolled, the magnetisation vectors align along the rolling direction. The rolling direction helps create a net macroscopic easy direction, along which 180° domain walls lie. The presence of the residual stress, caused by the application of the weld seam, modifies the easy direction in each grain by inducing a magnetoelastic anisotropy energy in the direction of the stress **[36][32]**. The easy direction is then determined by the minimisation of the magnetocrystalline as well as magnetoelastic energies. For steel, which has a positive magnetostriction, the presence of a residual tensile stress (up to a certain limit) increases

the 180° domain wall population along the direction of the stress **[32]**. Beyond a specific tensile stress the EBE signals have been found to decrease. The specimens studied were all magnetised along the rolling direction, which should have increased the number of 180° domain walls along the easy direction to a maximum.

The weld seam microstructure possessed a smaller grain size and a higher dislocation density due to the rapid weld cooling. This was backed up by the increased hardness observed in the Vickers hardness measurements, leakage field measurements, as well as the SEM and optical microscopy. The high dislocation density in the weld, in addition to the increased grain boundaries acted to limit the domain wall motion. On the weld seam the combination of the very high residual stress and the high density pinning locations, resulted in a net decrease in the EBE signal energy compared to the HAZ region.

Due to the heat treatment, as a result of generating the weld seam, the HAZ microstructure loses its directionality. Some grains grow and while others become finer and more equiaxed compared to the parent material's microstructure. The residual surface stress, caused by the welding, is still tensile over these locations, and thus, helps to maintain an excess population of 180° domain walls. These excess domain walls present in the HAZ were able to move more freely under magnetisation compared to the domain walls in the weld metal. This was due to some grain growth and a reduction in the pinning sites such as dislocation density, which is reflected in the hardness measurements. As a result, the EBE signal energy from these positions were found to be the largest on the specimen. This is also shown in the EBE signal amplitude.

Moving away from the weld and HAZ, the EBE signal energy exhibited a steady decrease. This is accounted for by the residual surface stress becoming compressive. Compressive stress increases the number of closure domains and, therefore, decrease the relative population of 180° domain walls **[1][32]**. This in turn created a smaller EBE signal energy and amplitude. This compressive stress state was not present in the plain steel specimen (3P), and is why the EBE signal energy from the edges of the welded specimen (2P) fell to values below that found on the plain specimen. This was more easily noticeable if locations furthest from the weld were examined.

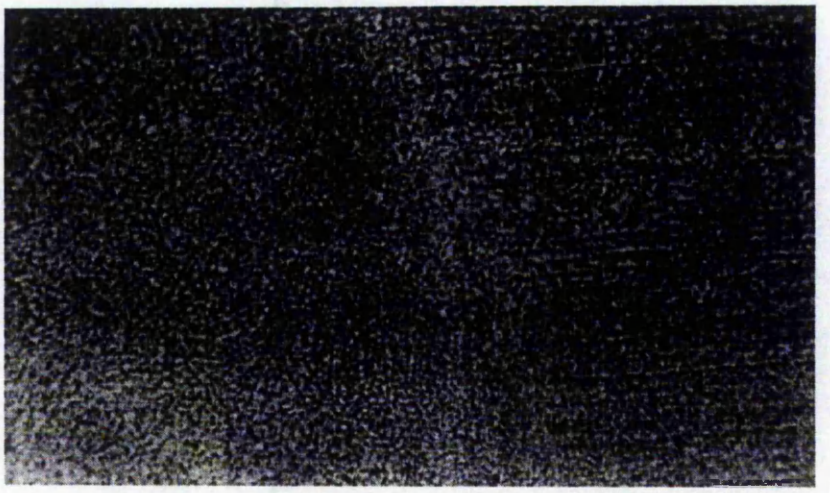


Figure 4.4.8 Optical microscope image of the weld and HAZ interface. Note the overall decrease in grain size within the weld region compared to the parent material. The weld metal is on the left side and the parent steel is on the right side of the image. The rolling direction of the parent material is lost within the weld and HAZ region as a result of the welding process. Magnification ×80.

4.4.2.7. *The ABE envelopes from the welded steel specimen (2P).*

The generation of stress waves due to the impulsive domain wall movements and magnetostrictive changes, causes ABE signals within a specimen. The sweeping magnetic field causes the non-180° domain walls to move impulsively, allowing the expansion of favourably orientated domains. Domain wall motion takes place by the rotation of the magnetisation vector associated with individual atoms, which make up the domain wall. When the magnetisation vector of the atoms inside the domain wall make some angle with the applied field direction, they, under the action of the torque, rotate towards the field direction. As a result of the rotation of the vector inside the domain wall, the centre of the wall is displaced resulting in an increase in the volume of the domain which has its magnetisation parallel to the direction of the applied field. The rotation of the magnetic moments causes a change in the interaction energy which is also a function of bond length **[1]**. The exchange interaction is independent of direction of magnetisation. It, however, does play an important role in the volume magnetostriction. As the domain walls are forced to move, the subsequent rotation of the magnetic moments of individual atoms causes the bond lengths between them to change. This gives rise to changes in the physical dimensions of the material and, thus, generates stress waves which travel through the material. These stress waves are detected as ABE signals. Steels have a low acoustic attenuation, which ensures that the ABE from the whole volume of the magnetised specimen contributes to the overall signal amplitude. Because of this, the effect of differing microstructural regions of material within a specimen is not well distinguished and the signal profile will, therefore, reflect the overall specimen characteristics.

The weld specimen (2P) generated ABE signal envelopes which were reproducible. The process of welding generated the residual stress profile of the plate. ABE is known to be sensitive to stress and this was reflected in the ABE signal energy profile of the specimen, (**figure 4.2.16**). The ABE signal energies detected from the various locations on the weld specimen lay within a range **0.282 V^2s** to **0.358 V^2s**. This signal energy range was higher than the energy range observed for the plain steel specimen (3P) and

was a consequence of the presence of the weld seam. The increased dislocation density, fine grain size and residual surface stress resulting from the weld seam provided an increase in the number of sites for closure domains. These closure domains would be expected to increase the non-180° domain wall activity, thus, resulting in an increased ABE signal envelope.

On the HAZ-weld interface there were large equiaxed grains of pearlite which were visible under SEM and are shown in **figures 4.4.9** and **4.4.10**. These large pearlite grains contain cementite lamellae which strongly pin domain walls. The coarse grain structure also allows the non-180° domain walls to have a greater mean-free-path to sweep across, resulting in stronger ABE signal energies as reported by Jackobovics **[16][91]**. As a result, the ABE maximum signal voltage also increases in amplitude (**figure 4.2.16**) compared to the plain steel specimen (**figure 4.2.8**).



Figure 4.4.9 SEM micrograph of weld and steel interface showing the parent materials microstructure loosing its directionality and producing more equiaxed grains. Magnification ×80.

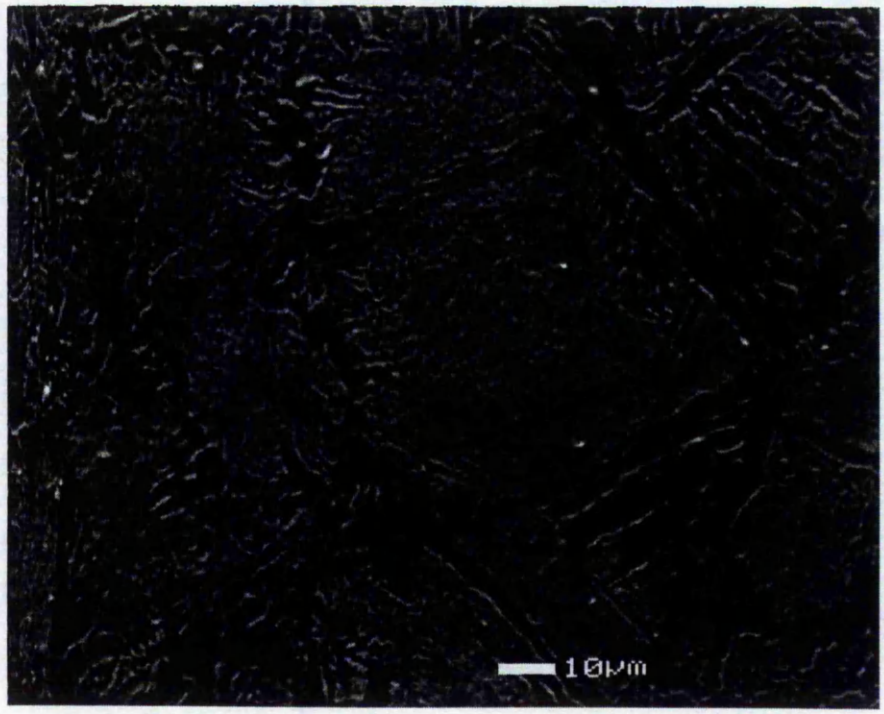


Figure 4.4.10 SEM Micrograph of HAZ structure very close to the weld metal (similar to **figure 4.4.9** with increased magnification). Large grains are present within this region. Magnification ×2000.

4.4.3. The Cracked Weld Steel Specimens.

4.4.3.1. *The EBE results from both the cracked weld specimens (21B and 21A).*

The TIG welded specimens (21B and 21A) both possessed a single surface breaking crack at the centre of the weld seam. The cracks were generated by low-cycle flexural fatigue. On specimen 21B the crack was present 21 mm from the location 'A', in-between locations 'K' and 'L'. On specimen 21A the crack was found to be at 20.5 mm from 'A', closer to the location 'K' than 'L'. The presence of a crack in the welded specimens showed distinct changes in the Barkhausen signal envelopes. This was more noticeable in the EBE envelopes. The two low-cycle fatigued specimen, 21B and 21A, yielded differing EBE signal envelopes despite their very similar histories. **Figures 4.2.17 to 4.2.20** and **4.2.25 to 4.2.28** show this clearly.

On cracked weld specimen 21B the EBE signal envelope on locations 'A' to 'G' appeared double peaked and very similar to the envelopes detected furthest from the weld on the perfect weld specimen 2P. These envelopes suggested that for magnetisation to occur, two distinct pinning energies for domain walls must be overcome. The first peak was thought to be caused by domain wall pinning at the grain boundaries and the second peak was due to precipitates and inclusion. Between locations 'F' through to 'N' the EBE envelopes changed to a broadened single peak with a jagged top. This region was where the weld seam and HAZ were located. Across the studied surface of the specimen the envelopes decreased in amplitude and a minimum was found at location 'M'. From locations 'O' to 'U' the EBE signal reverted to a double peaked envelope, but now the second peak increased while the first peak decreased in height as the distance from the weld seam became larger.

The cracked weld specimen 21A generated differing EBE signal envelopes from the specimen 21B, yet both were made from the same steel and prepared in the same way. The signals from specimen 21A appeared as a double peaked envelope on location 'A'. Moving towards the weld seam, the first peak began to increase at a greater rate

compared to the second peak until, on location 'F', the first peak was no longer resolved. Over this distance the EBE envelope continually increased in magnitude, (**figure 4.2.29**). Between locations 'G' to 'M' the EBE signal consisted of a single peak. Location 'N' showed a minimum in the 'maximum signal voltage' (V_{MAX}) profile. Between locations 'O' through to 'U' the envelopes regained their double peaked form. Furthest from the weld centre, the EBE envelope's first peak reduced in size while the second peak increased. On location 'U' the envelope appeared almost as a single peak.

These changes in the signal envelopes, from the surfaces of both specimens, can be linked to the generation of the crack. The cracks were generated by low-cycle flexural fatiguing and these cracks had changed the overall stress profile of the specimens. The low-cycle fatiguing strained the specimen significantly and, as a result, an increase in the dislocation networks throughout the cracked specimens were expected. The EBE envelopes, from across both the cracked specimens, showed changes when compared to the EBE envelopes from the defect free weld specimen (2P). The EBE signal energy profiles from across the surfaces of both cracked and uncracked specimens are compared in **figure 4.4.11** (data from **figures 4.2.13**, **4.2.21** and **4.2.29**). It is known that, for ferrous materials, the EBE signal energy increases on the application of applied stress up to a limit before the yield point **[36][32]**. This is because increasing stress results in a change in the anisotropy energy along the direction of stress, favouring the generation of the 180° domain wall population **[2]** and the associated EBE and increasing the magnetic permeability **[33]**.

The EBE data in **figure 4.4.11** indicates that the EBE mirrors, to some extent, the residual stress profile for the weld. However, since the microstructure of the weld region differs from the parent metal, the relationship is more complex than might be expected from considering the weld profile from **figure 4.4.6** and shows a minimum at the centre of the weld, when a maximum might be expected.

However, when the weld became cracked (**figure 4.4.11** lower curve) the residual stress at the weld centre was relieved, and overall EBE energy dropped. As both specimens were low-cycle fatigued till crack generation, this would imply that a high level strain

was applied resulting in increased dislocation density within the material. This was supported by the observation of an increased leakage field, away from the crack, on locations 'A', 'B', 'T' and 'U', seen in **figures 4.3.7** and **4.3.8**. (The increased leakage field, at the edge region, was not observed on the welded specimen 2P and was further confirmation of the increased dislocation density on both the cracked specimens).

The increased pinning sites on the surface of the cracked weld specimens reduced the overall V_{MAX} profile and signal energy profile. The signal energy is related to the area of the EBE envelope which in turn reflects domain wall activity across a range of applied magnetic field strengths. If a greater number of domain walls move, especially with a greater mean-free-path, then larger EBE signal energies are obtained. With the presence of the increased dislocation densities, which provided a high pinning site density, the EBE signal energy decreased. This increased pinning limited the domain wall's mean-free-path, thus, leading to a decrease in the maximum signal voltage. It is believed by the author that the acceleration and deceleration of domain walls when crossing a pinning site causes EBE pulses. Sixtus and Tonk **[114]** have shown that domain walls have a finite velocity (= 5 ms^{-1} to 400 ms^{-1}). If the pinning density is very high then the domain walls will experience many sudden pinning and de-pinning movements without achieving terminal velocity due to the applied field. This will lead to the generation of many small Barkhausen pulses leading to a small EBE envelope. However, for very large mean-free-paths , the domain walls would be able to achieve the terminal velocity and, therefore, generate large pulses but less of them; this would lead to a increased EBE envelope. If, however, the pinning site density is in-between the two extremes, then the greater domain wall mean-free-path (allowing large Barkhausen pulses) combined with the dense pinning sites (increase number of Barkhausen pulses) would result in the largest EBE envelopes. This idea explains EBE results following annealing of steels by Moorthy et al. **[95]**.

Each crack was located on the central region of the welded specimen, at location 'K' for specimen 21A and between locations 'K' and 'L' for specimen 21B. The signal energy shows a minimum at locations 'K' and 'L' from cracked specimen 21A and 21B respectively. This minimum was caused by the crack. The presence of the crack, as well

as the increased dislocation density on the surface of the specimen, further reduced the permeability of the cracked location. The leakage field caused a reduction in the intensity of magnetisation at the cracked region. Both these effects led to a signal energy minimum. If the difference in the signal energy between central minimum (at the crack) and the maximum (at the HAZ) are calculated, then it can be seen that a large differential is produced due to the presence of a crack, (see **table 4.4.2**). From the weld specimen (2P) the energy differential between the HAZ and the weld centre was measured as **0.011 V^2s**, whereas both the cracked weld specimens (21B and 21A) displayed higher energy differentials (**0.018 V^2s** and **0.016 V^2s**) indicating the presence of the crack.

Specimen	EBE signal energy maximum. (V^2s)	EBE signal energy minimum. (V^2s) (weld centre)	EBE signal energy differential. (V^2s)
Perfect Weld, 2P	0.098 ±0.0013	0.087 ±0.0013	0.011 ±0.0026
Specimen 21B	0.072 ±0.0013	0.054 ±0.0013	0.018 ±0.0026
Specimen 21A	0.085 ±0.0013	0.069 ±0.0013	0.016 ±0.0026

Table 4.4.2 Shows the differential between the maximum EBE signal energy on the HAZ boundary and minimum EBE signal energy at the weld and weld crack centre.

The weld would be expected to generate a residual stress profile on the surface of the specimens as shown in **figure 4.4.6**. The presence of the crack on the surface, would be expected to change the residual stress profile. In place of the high residual tensile weld stress will be a new stress profile resulting from the crack opening. The EBE V_{MAX} data appeared to indicate that a residual compressive stress concentration existed at locations 'M' and 'N' for the cracked weld specimens 21B and 21A respectively. The crack in each specimen was generated before the weld cap was removed by machining. The edge of the raised weld cap on the parent steel surface, before 'as-received' machining, acted as a stress concentrator and that is the primary reason for its removal, in certain industrial situations. The edge of the weld bead on each of the specimens' surfaces would have been around locations 'M' and 'N', precisely where the minima of the V_{MAX}

profile for each cracked specimen was located, (**figure 4.4.12**). The residual compressive stress (after crack generation) and the loss of the rolling direction's easy axis, due to the heat from the weld, decreased the 180° domain wall population. Both these effects acted to suppress the quantity of 180° domain wall motion, thus, resulting in a smaller EBE signal amplitude.

The time of the maximum peak (T_P) was measured for the largest peak on the EBE envelopes from each of the steel specimens and is shown in **figure 4.4.13**. During the magnetisation change, the domain walls first of all overcome resistance offered by grain boundaries before becoming pinned by the larger second phase precipitates and spike domain walls associated with large inclusions. These two processes occur over a range of field values and when the differing precipitates pinning strengths are widely different the EBE envelope may appear as a double peak envelope **[95]**. The presence of increased dislocation density, caused by low-cycle flexural fatiguing, changes the EBE envelope's shape and thus, the T_P value on the envelope. It is probable that the increased pinning density in the cracked specimens helped merge the double peaks of the EBE envelopes. Compared to the welded specimen (2P) the maximum peak from the cracked weld specimens (21B and 21A) occurred later on the envelope (at a higher applied field), as the increased dislocation density required larger mean fields to overcome the new pinning sites.

On specimen 21B, across the entire studied region, the T_P values occurred between 0.95s to 1.0 s on the envelope. At the weld locations a slight decrease in the T_P value was noticeable, which was small in comparison to the weld (2P) and cracked weld (21A) specimens. From results shown in **figure 4.4.13** it is clear that the presence of high dislocation densities, resulting from the low-cycle flexural fatiguing, forced the maximum signal peaks to occur earlier in the recording window.

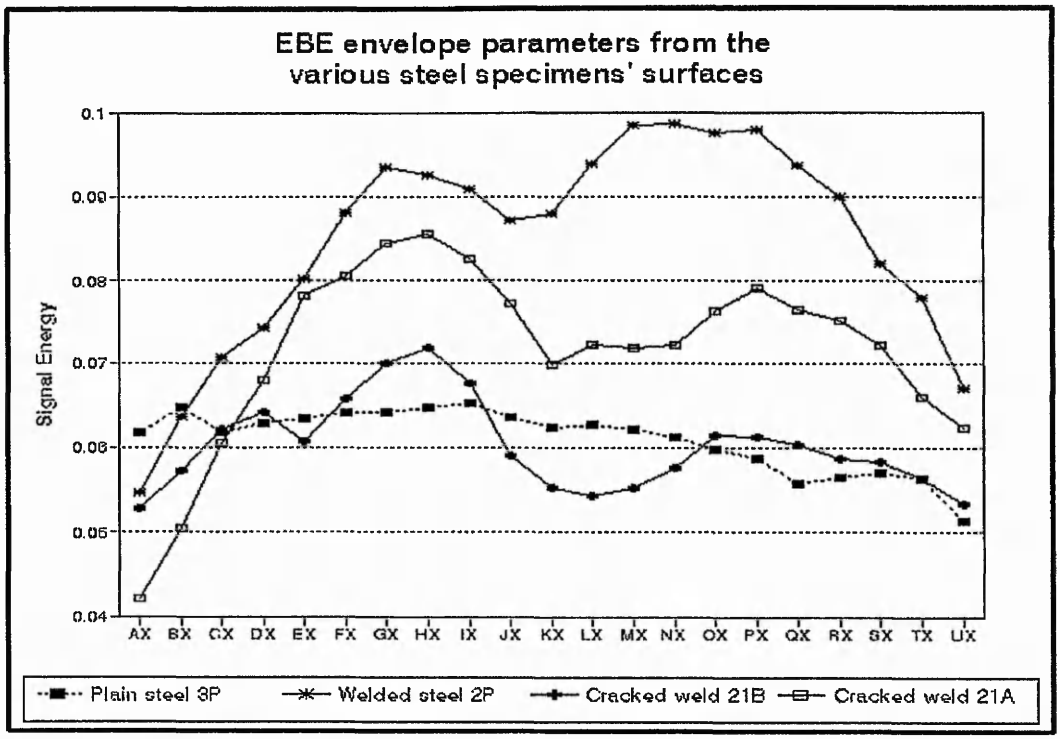


Figure 4.4.11 EBE envelopes signal energy parameter (units V^2s) from the 'as-received' plain steel (3P), welded steel (2P) and cracked weld steel (21B and 21A) specimens. Location 'A' to 'F' is parent material, 'F' to 'H' is HAZ and the weld seam is approximately 10.5 mm in width. The weld centre is situated on location 'K'. The crack is positioned very close to location 'K'.

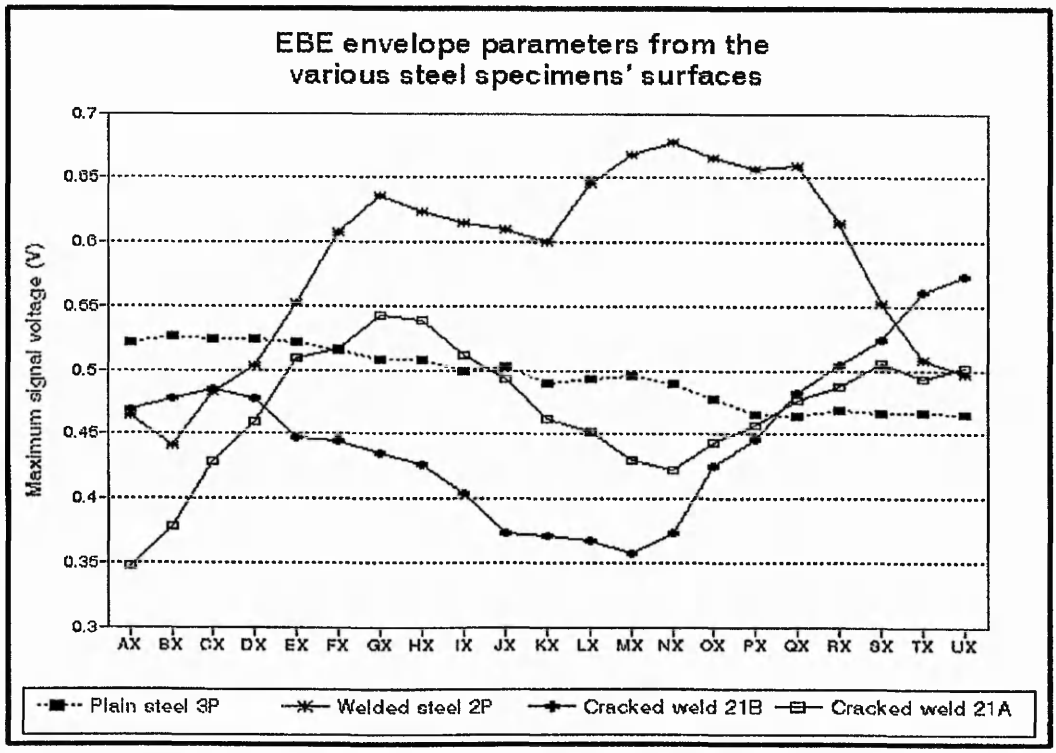


Figure 4.4.12 EBE envelopes 'maximum signal voltage' (V_{MAX}) parameter from the 'as-received' plain steel (3P), welded steel (2P) and cracked weld steel (21B and 21A) specimens.

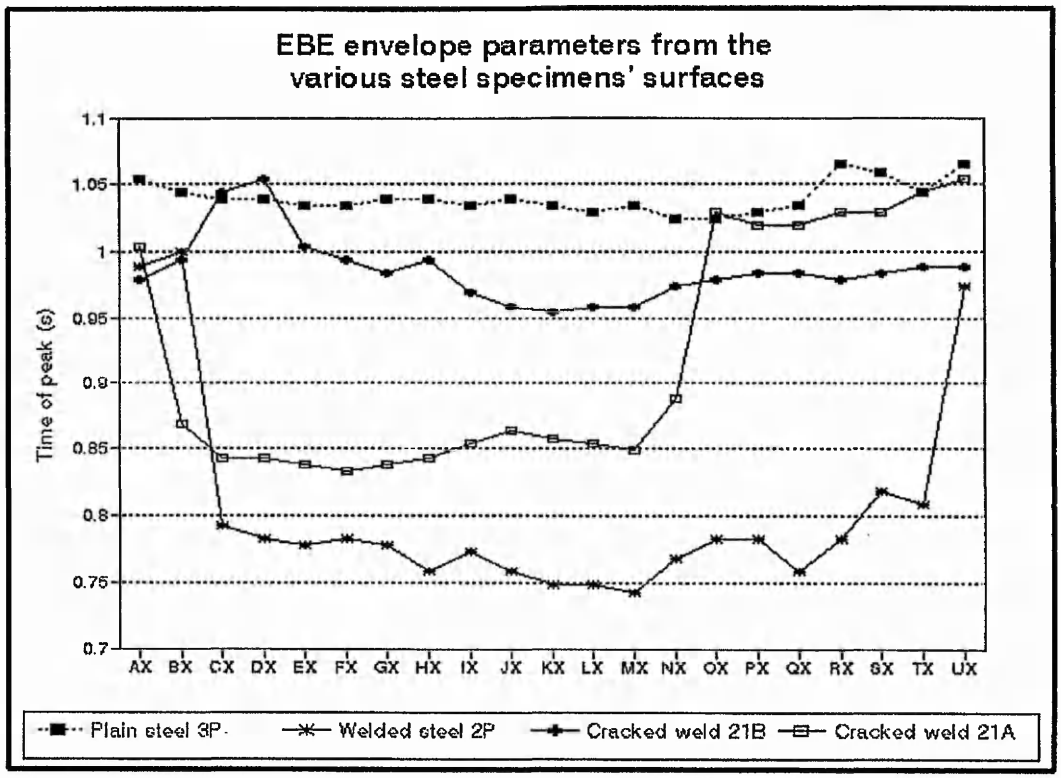


Figure 4.4.13 EBE envelopes 'time of peak' (T_P) parameter from the 'as-received' plain steel (3P), welded steel (2P) and cracked weld steel (21B and 21A) specimens. Location 'A' to 'F' is parent material, 'F' to 'H' is HAZ and the weld seam is approximately 10.5 mm in width. The weld centre is situated on location 'K'. The crack is positioned very close to location 'K'.

4.4.3.2. *The ABE results from both the cracked weld specimens (21B and 21A).*

The ABE envelopes from both the cracked (21A and 21B) specimens appeared double peaked. The first peak was smooth while the second peak was modified by several sharp spikes. The envelopes appeared in this form across the length of the specimen and are shown in **figures 4.2.22 to 4.2.23** and **4.2.30 to 4.2.31**.

The ABE signal energy variation from the cracked weld specimen 21B showed a minimum at the centre of the specimen, directly above the crack. This is shown in **figure 4.4.14**. On locations either side of the crack the ABE signal energy increased. This data suggests that the crack was directly detectable if the ABE signal energies were examined. A similar minimum was also observed for the maximum signal voltage (V_{MAX}) variation (see **figure 4.4.15**). The cracked specimen 21A showed an increased ABE signal energy at the position of the weld and crack: this was the opposite to the energy profile obtained from specimen 21B. The V_{MAX} value from the weld cracked specimen 21A also displayed this trend.

Work carried out on pure nickel in chapter 2.3 suggested that the ABE is a volume effect, with the signal profile providing information about the overall specimen volume and not discrete surface regions, such as the weld or the HAZ. The ABE envelopes provided information from the four different regions i.e. parent steel, weld metal, HAZ and the crack combined together. If the crack occupied a significant fraction of the test plate cross section, then, it would limit a significant amounts of the ABE stress waves from reaching the sensor. The crack would then reduce the detected ABE signal envelope. This possibly explains the very low signal energy from location 'E', directly above the weld and crack on specimen 21B, (**figure 4.4.14**). The magnetic leakage field from the crack on specimen 21B, detected by the Hall probe and GMR sensor, was tighter (sharper) for the two signals detected from the cracked specimens. The leakage field at the crack also possessed the largest amplitude. According to a report by Beissner et al. **[85]** and mathematical slot modelling equations suggested that the cracked weld specimen 21B possessed a wider crack compared to the crack in the 21A specimen.

The creation of the crack by low-cycle flexural fatiguing strained the specimens, probably close to the yield point. This high straining, common in very low-cycle fatiguing, was expected to have greatly increased the dislocation networks across the entire specimen. The increased dislocation networks present in the specimens would be expected to increase the ABE activity, as more non-180° domains are likely to be found at dislocations. As a result of fatiguing, the ABE signal amplitude, as well as the signal energy, increased compared to the welded specimen 2P. The fatiguing process also clearly affected the ABE signal envelopes shape. All of the detected signal envelopes displayed large sharp spikes superimposed on the second peak, while the first peak appeared smooth. As this spiking was present in the ABE signal from both the cracked specimens it was, therefore, assumed that this was generated as a consequence of the fatiguing process.

The average ABE signal energy from the plain steel specimen was **0.232 V^2s** and with weld seam present (2P) it increased to **0.322 V^2s** and is shown in **table 4.4.3**. The two cracked weld specimens 21B and 21A exhibited average energy values of **0.362 V^2s** and **0.450 V^2s** respectively. According to the leakage field measurements the cracked weld plate 21B probably possessed the largest crack. As a result, the ABE signal energy from above the crack location was small and this helped lower the overall signal energy average for the specimen. The averaged V_{MAX} values from the three different states of the steel specimen reflected a similar trend. The observable microstructure of the plain welded and cracked weld specimens appeared to be very similar, with the only difference being the crack. It was, therefore, reasonable to assume that the increased ABE energy may have been caused by the high dislocation densities present within the low-cycle fatigued specimens. The widening of the ABE signal energy spread, accompanied by the overall rise in the average ABE energy, may be useful as an indicator that straining, caused by the flexural fatiguing has occurred, leading to crack formation (see **table 4.4.3**).

The time of maximum ABE peak, T_P, for both the weld cracked specimens showed that the V_{MAX} values occurred earlier on the envelope, (see **figure 4.4.16**). This implied that

the maximum spike (on the cracked specimen) occurred at a lower magnetising field compared to the maximum signal voltage for the welded (2P) and plain steel (3P) specimens. T_P values for the cracked weld specimens' (21B and 21A) corresponded to the maximum spike voltage, which was a characteristic phenomena for both the cracked specimen. This group of spikes, shown in **figures 4.2.22** and **4.2.30**, masked the exact position of the maximum ABE signal amplitude, providing an alternative T_P value. Even though the maximum spikes indicated large ABE events, they, however, were not directly comparable to the maximum ABE events from the welded (2P) and plain steel (3P) specimens. The presence of the large spikes on the second peak may indicate that the specimen has experienced high straining from low-cycle fatigue, which has led to cracking. Due to these spikes, envelope energy may be the most appropriate measure, in this case.

EN-43A Specimen	ABE signal energies. (V^2s)	ABE Maximum signal voltage.(V)	ABE Time of peak. (s)
Plain Steel, 3P	0.232 ± 0.045	0.99 ± 0.17	1.150 ± 0.028
Perfect Weld, 2P	0.322 ± 0.035	1.51 ± 0.21	1.166 ± 0.024
Specimen 21B	0.362 ± 0.081	1.89 ± 0.24	1.051 ± 0.006
Specimen 21A	0.450 ± 0.098	2.36 ± 0.34	1.053 ± 0.004

Table 4.4.3 shows the mean average between the 1) maximum and minimum ABE signal energy, 2) maximum and minimum ABE signal voltages, 3) maximum and minimum time of peak for the plain, welded and cracked weld steel specimens.

The combination of the ABE and EBE signal parameters as previously suggested by Hill et al. **[90]**, along with their Barkhausen envelopes, clearly could be used to show if a crack in the weld seam is present and also indicated the possible strain state of the specimen. An increased strained state, causing dislocation networks within the welded specimen, would lead to increased ABE signal energy and a decrease of EBE signal energy (see **table 4.4.2**) profiles. The EBE signal envelope's V_{MAX} parameter could help locate the point of high residual compressive stress. The EBE signal energy reflected the

combined effects of microstructure and stress state and care must be taken when interpreting these results. Using these parameters, the ABE signals can be used to detect specimens or region on a larger specimen which have undergone high straining due to low-cycle fatiguing and as a result possess high dislocation densities and other domain wall pinning defects.

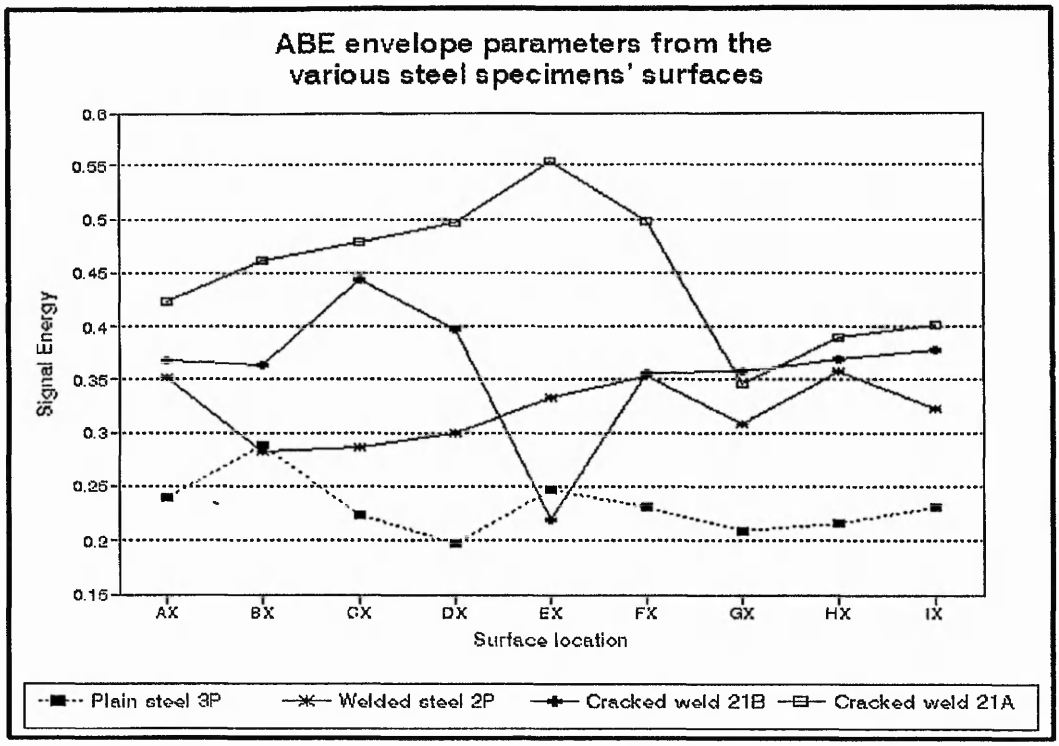


Figure 4.4.14 ABE envelopes signal energy parameter (units V^2s) from the 'as-received' plain steel (3P), welded steel (2P) and cracked weld steel (21B and 21A) specimens. Location 'A' to 'C' is parent material, 'C' to 'D' is HAZ and 'D' to 'F' is the weld seam which is approximately 10.5 mm in width. The crackin specimen (21B and 21A) is situated on location 'E'.

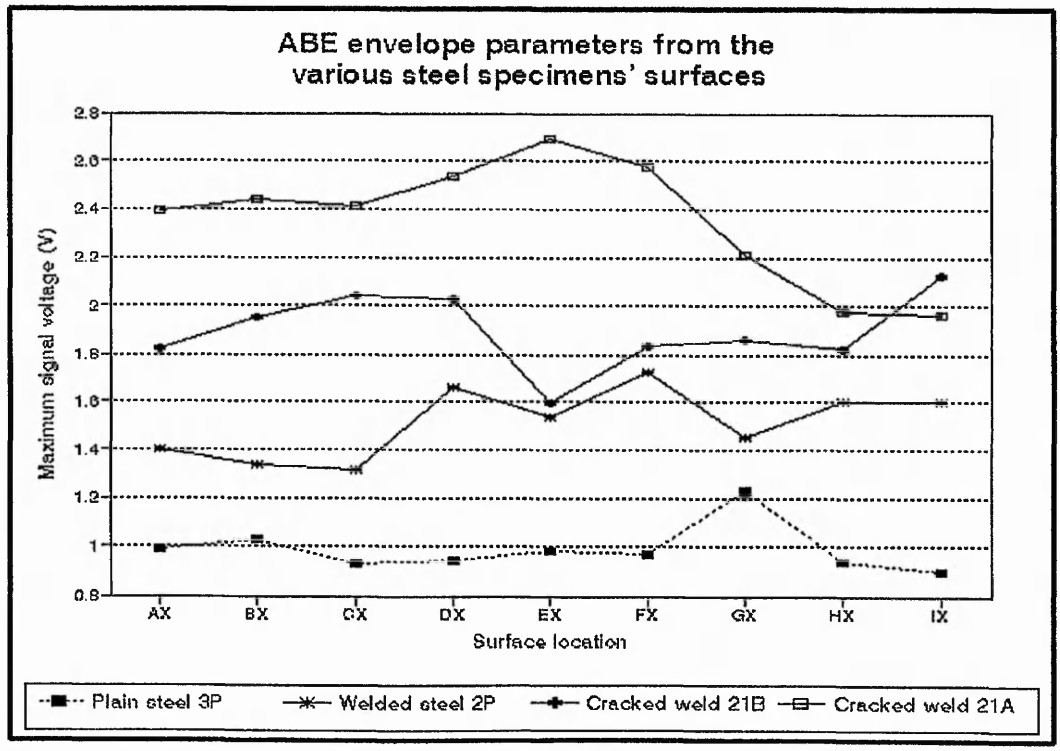


Figure 4.4.15 ABE envelopes 'maximum signal voltage' (V_{MAX}) parameter from the 'as-received' plain steel (3P), welded steel (2P) and cracked weld steel (21B and 21A) specimens.

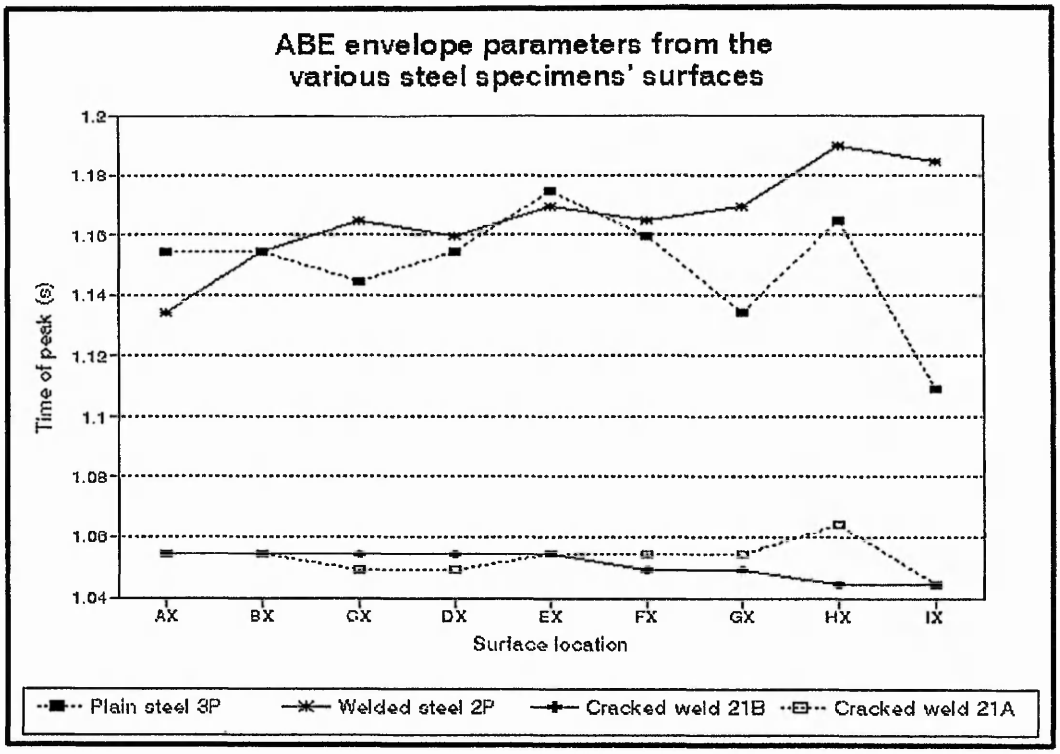


Figure 4.4.16 ABE envelopes 'time of peak' (T_P) parameter from the 'as-received' plain steel (3P), welded steel (2P) and cracked weld steel (21B and 21A) specimens. Location 'A' to 'C' is parent material, 'C' to 'D' is HAZ and 'D' to 'F' is the weld seam which is approximately 10.5 mm in width. The crackin specimen (21B and 21A) is situated on location 'E'.

4.4.4. The Effect of Surface Machining the Steel Specimens.

4.4.4.1. *The effect on EBE of machining the plain steel specimen surface (3P).*

The plain steel specimen, 3P, was subjected to EDM machining, as well as the surface planing processes. Both the machining processes altered the surface characteristics of the specimens. EBE measurements were recorded from each of the specimen's machined surface areas. ABE measurements were not considered as a part of this work, since, ABE is a volume effect and the surface alteration resulting from the machining process would not be expected to affect the ABE signal envelope.

The 'as-received' steel specimen's surface finish was originally generated by machining using a circular grinder. This surface finish was present on all of the specimens used in the study. Mechanical surface machining is known to generate localised heating which can lead to detrimental phases in the surface microstructure. Thermal and mechanical shock can introduce localised surface stresses and dislocation networks. Mechanical machining can reach significantly high surface temperatures where rehardening damage may occur. This can result in phase changes from ferrite to austenite and on rapid cooling this region becomes martensite: a hard brittle phase prone to cracking. These residual mechanical stresses, generated as a result of the original grinding process of the surface, were altered by the planing and EDM machining. Below the machining affected surface layer, the microstructure of the specimen was expected to remain uniform and in the 'as-received' condition. The EBE signal envelopes from the plain steel specimen 3P, showed distinct changes depending on the type of machining process used, as seen in **figure 4.2.33**.

In the EDM machining process, there is no tool-to-work-piece contact and, therefore, no direct mechanical force is applied to the newly created surface. The controlled discrete electrical discharges, between the tool and the specimen submerged in the dielectric medium, removed the material by melting and vaporising the surface layer of the steel specimen. A white recast layer, of thickness 10 μm to 15 μm, is formed by the cooling of

the molten material. The intense heat, generated by each discharge, results in a severe temperature gradient in the machined surface. The dielectric fluid helps cool the surface quickly, thus, developing a residual tensile stress in a very thin surface layer. The residual stress, often sufficient to produce cracking in the recast layer, can be reduced by decreasing the discharge energy **[115]**. Studies carried out on tool steel have found that the surface recast layer possesses a microstructure with small columnar grains, around 5μm in length, at the surface. Below the columnar grains are found interlocked dendritic and plane dendritic crystals **[99]**. The residual tensile stress caused by the rapid cooling of the thin recast layer affects the EBE signal envelopes, but as this layer is very thin (approximately 10μm to 15μm), its effect is not expected to dominate the signal envelope shape. It appears, from the EBE envelope, that the main factor associated with the EDM machining is the altered surface stress characteristics of the steel.

The EDM machining process removed the 'as-received' surface layer containing the deformed surface microstructure, dislocation densities and residual localised surface stresses, arising from the original girding process. The EBE envelopes detected from the EDM machined surface area appeared with a single peak at **0.73 s, (figure 4.2.33)**. The maximum peak on the EBE envelope indicated that domain wall pinning arises mainly at grain boundaries, as opposed to second phase precipitates. The effect of second phase precipitates, however, has not been removed as the EBE signal shows a significant amplitude at the latter region of the envelope, around 1 second on the envelope.

The planing of the 3P steel specimen's surface, mechanically deformed the surface layer. **Figure 4.4.17** shows the deformed crystal grains at the surface of the specimen. The planing process thermally and mechanically stressed the specimen. Tool tip temperatures ranging from 650°C to 900°C have been measured for low carbon steels **[97][116]**. This can lead to microstructural phase changes and may leave martensite (hard, brittle phase) on the surface of the specimen. The physical deformation of the microstructure, caused by the planing process, can also lead to increased 'localised residual deformation stresses' and work hardening. These residual stresses result from the removal, by tearing away the surface layer and can be compressive or tensile in nature.

The EBE envelopes from the 'as-received' surface appeared very similar to the EBE envelopes from the planed surface and are shown in **figure 4.2.33**. Both mechanical machining of the surface generated similar deformation characteristics and also, displayed a maximum signal amplitude around **1.04 s** on the envelope, **table 4.2.7**. The T_P value indicated that the second phase precipitates provided significant domain wall pinning **[95]**. The EBE signals generated by the planing process showed a decreased amplitude, in the first half of the envelope, compared to the EBE envelopes from the original 'as-received' steel surface. The depressed half of the signal, indicated that the grain boundaries provided less resistance to domain wall motion in the planed surface, and that a greater amount of pinning arises from the second phase precipitates.

The shape of the signal envelope can be used to distinguish clearly between the two types of machining processes. The EBE signal energy and V_{MAX} from the EDM surface were similar in magnitude to the energy from the original 'as-received' steel surface. However, as a consequence of the change in envelope shape, the T_P value clearly distinguished the affects of the two machining processes and was the most appropriate measurement parameter in this case.



Figure 4.4.17 Optical microscopy image of the deformation on the surface of a specimen caused by the planing process. The grain structure appears squashed. Magnification ×400.

4.4.4.2. *The effect on EBE of machining the welded steel specimen surface (2P).*

The effect of the weld's thermal history and the resulting changes in the microstructure were acknowledged as causing significant changes in the EBE envelopes. The residual stress profile, in particular, affected the EBE signal envelopes and helped generate a near symmetrical signal energy profile on the welded specimen (2P). The effect of a plain weld seam in a steel specimen with respect to Barkhausen emission has been discussed in **section 4.4.2**.

Machining 0.5 mm thickness off the weld specimen's (2P) surface altered the EBE envelopes significantly. On the surface of the welded specimen, the region subjected to EDM machining covered locations 'K' to 'U'. The EBE envelopes from this region are shown in **figure 4.2.34**. On this EDM machined area, the EBE envelopes from the weld seam appeared double peaked. On the same location, from the original 'as-received' weld seam surface, the EBE envelopes appeared very different, with a large first peak followed by a plateau in place of the second peak, (**figure 4.2.11**). The EBE envelopes, from the EDM machined surface (HAZ and the parent steel region), appeared similar in shape with a sharp peak positioned at **0.74 s** on the envelope. For EBE envelopes from the HAZ regions, in place of the second peak was a slowly reducing signal. The envelopes from the EDM machined parent material region exhibited a very slight rise at the position of the second peak. This was very different from the double peaked signal detected prior to EDM machining, (**figures 4.2.11** to **4.2.12**).

The planed area of the welded specimen (2P) covered locations 'A' to 'K' and the EBE envelopes from this region are shown in **figure 4.2.35**. On location 'A' or 'B' (parent material) the EBE signal appeared as a single peak envelope. The 'time of peak' (T_P) occurred at **1.11 s** on the envelope. The EBE envelope, detected from the planed weld specimen (2P) surface, was similar to those obtained from the planed steel specimen (3P) which are shown in **figure 4.2.33**. Location 'H', on the HAZ region, exhibited an EBE envelope with a plateau followed by a single peak. On the weld, locations 'J' and 'K', the EBE signal envelope's plateau increased in height and became a peak.

For the two different machining processes, the EBE envelopes appeared distinctively different. After surface removal, both the HAZ regions exhibited the largest signal amplitudes at **0.81 V** and **0.59 V** for the EDM and planed machined surface areas respectively, (**table 4.2.8**). The EDM machining of the welded (2P) specimen's HAZ regions increased the V_{MAX} value by 20%, while the planing process suppressed it by 7%.

The EBE envelopes V_{MAX} value, from the parent material region within the EDM machined area, was **0.64 V**. The parent material within the planed machined region exhibited a V_{MAX} value of **0.50 V**. The maximum signal voltage values from the parent material region of the machined areas, when compared to the original 'as-received' surface, showed that the planing process had little effect on the V_{MAX} value, compared to the EDM machining. The planing process showed an increase of 7% while the EDM machining exhibited an increase of 28% in the V_{MAX} parameter. This showed that the 2P welded specimens surface was altered far more by the EDM machining than the planing process.

Irrespective of the machining processes the weld seam exhibited doubled peaked envelopes, as half of the welded 2P specimen was first EDM machined and then the other half was planed. The interface between the two different machined surfaces lay on the centre of the weld seam and, as a result, the effect of planing up to the EDM machined region affected the EBE signal from this location. At the machined interface on the weld seam the EBE signals appeared doubled peaked. The EDM machined side possessed a large first peak (**0.59 V**), while on the planed side the second peak was the largest (**0.54 V**), (**figures 4.2.34** and **4.2.35**).

The EDM machining removed the 'as-received' welded specimen's surface layer which contained distorted microstructure, localised residual stresses and dislocation densities resulting from mechanical and thermal shock **[58][59]**. In their place, the EDM machining introduced a heat affected zone below the recast layer. The extreme heat generated by the electrical discharges thermally stressed a thin surface layer of the material. The resolidified layer, with its fine dendritic and columnar crystal grain

structure **[99]**, was approximately 5 to 10 μm in thickness. As a result of EDM machining the domain wall pinning occurred most probably at the grain boundaries and this led to a single peaked envelope. As a consequence, the T_P value occurred earlier on the EBE envelope at **0.74 s**.

The 'as-received' welded specimen's stress profile (**figure 4.4.6**) was symmetrical about the weld seam, the surface finish was uniform and this affected the detected EBE envelopes. As well as the weld stress profile, the EBE envelopes were also influenced by microstructure i.e. grain size, dislocation network density, easy direction due to rolling, etc. The planing process generated a surface very similar to the 'as-received' surface condition and, therefore, did not greatly change the EBE envelope shape from the parent material region. The deformation associated with general mechanical machining was also found within the planed surface. The planed machining introduced mechanical and thermal shock, which resulted in dislocation density, high 'localised residual stresses' and possibly even microstructural phase changes being generated within the surface layer. The EBE envelopes from the planed surface area appear smaller in magnitude compared to the envelopes from the 'as-received' original welded specimen. The EBE signal peak occurred late on the envelope around **1.03 s** to **1.11s**, indicating that the majority of domain wall pinning was due to dislocations and second phase pinning resulting from the mechanically and thermally shocked crystalline structure.

The maximum signal amplitude from both machined surface areas were influenced by the weld's residual stress profile which now, due to differing surface machining, was more complex than the form shown in **figure 4.4.6**. The EDM machining increased the EBE signal energy, while the planing process overall suppressed the energy (**table 4.2.8**). This was also reflected in the V_{MAX} values of the weld specimen's machined surface areas. The increased signal energy was a result of the larger peaked envelopes, which occurred as a consequence of the EDM machining. The large first peak suggested that a large number of domain walls broke away from grain boundaries. Also a greater domain wall mean-free-path existed, as there were expected to be a lower dislocation density within the surface layer of the EDM machined area. Both of these factors helped generate large EBE signal energies. For the planed region, with its increased localised residual

compressive stresses and dislocation densities, the number of 180° domain wall were reduced and their mean-free-path was limited. This led to smaller signal envelopes, and thus, a reduction in the EBE signal energy.

4.4.4.3. *The effect on EBE of machining the cracked weld specimens' surfaces (22B and 22A).*

The effect of machining the surfaces of the two cracked specimens by various methods completely altered their EBE signal envelopes. The cracked weld specimen 21B was EDM machined. A surface thickness of 0.55 mm was removed and the new surface was labelled 22B. The specimen 21A was planed and a 0.5 mm layer was machined away. The new surface was labelled 22A. The effect of machining the two specimens completely altered their surface characteristics, but, the overall bulk properties of the specimens were not expected to change, as only a thin layer of material was removed. Therefore, only the EBE measurements were taken in this study.

The EDM machined surface (22B), exhibited EBE envelopes, which were larger than the signal envelopes from the original cracked surface 21B. **Figures 4.2.36** to **4.2.39** and **4.2.17** to **4.2.20**, show the respective signal envelopes. The EBE envelopes, from the parent material region of the EDM machined surface, appeared wide and slightly double peaked. As the weld was approached, the envelopes steadily increased in amplitude. Unlike the EBE envelopes from the EDM machined weld specimen 2P, the cracked specimen's (22B) envelopes did not possess a sharp peak. Instead , the EBE signal peaks remained wide at the top portion of the envelopes. The large envelope size increased the signal energy for the specimen. On the welded region, the EBE signals appeared with a step on the second half of the envelope. This step was detected only in the envelopes from the EDM machined weld seam and crack region. The EBE envelopes from the HAZ region were more triangular in shape.

The low-cycle flexural fatiguing of the specimen, used to generate the crack, probably strained the specimen close the yield point **[105][39]**. The high strains led to increased dislocation networks throughout the volume of the specimen. This was reflected in the ABE measurements from the original cracked specimen. The recast surface layer created by EDM machining contained fine crystal grains, similar to the EDM machined weld specimen 2P. The EDM machining removed the original 'as-received' surface finish

containing the localised residual stresses and dislocation densities. As there was no tool-to-work-piece contact, the new surface was expected to contain lower mechanical defect concentrations. As a result, domain wall pinning would now arise mainly from the grain boundaries, second phase precipitates and dislocation densities which remained below the EDM machined surface layer but within the EBE detection range. The residual weld stresses, decreased and modified by the presence of the crack, probably aided the creation of large EBE signals from certain regions on the EDM machined surface.

The EBE signal energy profiles from the 'as-received' (21B) and EDM machined (22B) cracked weld surfaces appeared in a similar form, both showing the largest signal energy on the HAZ regions, (**figure 4.4.18**). The signal energy from the HAZ region (location 'H') for the 'as-received' and EDM machined surfaces were **0.072 V^2s** and **0.137 V^2s** respectively. This represented a signal energy increase of 90%, due to the EDM machining. When the EBE energy profiles of both of the surface states are viewed together it becomes evident that the EDM machining process greatly increased the energy profile, (**figure 4.4.18**). The removal of the 'as-received' surface layer increased the signal energy profile of the specimen. The EDM machining helped remove dislocation networks, localised residual surface stresses and work hardened microstructure present in the original 'as-received' surface layer. Increase in grain size, in different specimens **[87][24]** and by heat treatment of a single specimen, up to an optimum size **[111][38]** has been reported to increase the magnitude of the EBE envelopes. A larger domain wall mean-free-path **[95][112]** due to increased pearlite spacing **[16]** also generated larger EBE envelopes and, therefore, a larger signal energy. Increase in the relative number of 180° domain walls **[36][49]** resulting from the application of tensile stresses, are all known to account for the increased EBE signal energy. In the case of the EDM machined surface (22B), the increased signal energy arose from the reduction in 'localised residual surface deformation stresses' and dislocation networks. Also, the microstructure across the specimen had, to an extent, been relieved of the original weld stress profile leaving the net easy direction aligned along the rolling direction. As the magnetisation direction was along the rolling direction too, the detected EBE envelopes were expected to be at a maximum **[35]**.

Figure 4.4.19 shows the EBE V_{MAX} profile for the 'as-received' (21B) and EDM machined (22B) cracked weld surfaces. Stress concentration due to the crack generation process, and localised residual stresses resulting from the 'as received' surface finishing, led to the V_{MAX} exhibiting a minimum on location 'M' (at the edge of the, now removed, weld bead). Without generating any significant new stresses the removal of the 0.55 mm original surface layer, which contained the 'as-received' machining defects, increased the V_{MAX} profile. The V_{MAX} profile from the EDM machined surface (22B) appeared similar in shape to the signal energy profile, (see **figure 4.2.40**). The large V_{MAX} values were now generated by the easier domain wall motion through the (reduced pinning network and the residual weld's stress profile) microstructure of the material.

The T_P parameter's profile, shown in **figure 4.4.20**, might be explained by the fact that domain wall pinning mainly arose from grain boundaries and less at second phase precipitates and dislocation networks **[95]**. Although dislocation networks on the surface layer were now present in a reduced quantity, they still affected EBE signal envelopes. This was deduced from the larger EBE peaks which implied a reduction from the very high dislocation density and overall pinning sites, therefore, allowing an optimum domain wall mean-free-path.

The planing process generated a surface where the detected EBE envelopes possessed a single peak, situated on the latter part of the envelope (**figures 4.2.41** to **4.2.44**). The EBE signals from the planed surface (22A) were very different when compared to the envelopes from the original 'as-received' cracked weld surface (21A). On the parent material, the EBE signals also displayed an initial slope, positioned between **0.7 s and 0.85 s** on the envelope. This slope became smaller due to the signal peak increasing in width, as the HAZ and cracked weld were approached. The EBE envelopes from the HAZ and weld regions possessed wide peaks, implying that pinning strengths were spread over a range of values **[95]**. The top part of the signal envelope was the widest on location 'K'.

The EBE signal energy profiles from the 'as-received' and planed cracked weld surfaces are shown in **figure 4.4.21**. The planed cracked specimen's surface (22A) exhibited a

lower signal energy profile, when compared to the 'as-received' surface (21A). It appeared that the planing process actively suppressed the EBE energy profile from the machined specimen's surface. If, for example, the signal energy from the HAZ region (location 'H') is considered, then it appears to have decreased from **0.085 V^2s** to **0.062V^2s** due to the planing process. The V_{MAX} profile (**figure 4.4.22**), from across the planed machined surface (22A), showed a minimum at location 'K' (**0.399 V**), very close to the crack. When the V_{MAX} profiles from the 'as-received' (21A) and planed (22A) surfaces are viewed together (**figure 4.4.22**), they clearly show that the range of V_{MAX} values remained within a similar magnitude, unlike the EDM machined cracked weld specimen 22B (**figure 4.4.19**). The physical deformation of the surface layer, caused by the planing process is seen in **figure 4.4.17** and was expected to be similar in character to the 'as-received' surface. The grains at the surface appear to have been squashed as they were torn from the bulk material, this process generated temperatures of 650°C to 900°C **[116]**, leading to localised thermal as well as mechanical stressing. This also probably led to the formation of martensite on the surface of the specimen. The planing process led to an increased pinning density, which limited the 180° domain walls' mean-free-path and in turn reduced the EBE signal voltage and signal energy **[27][95]**. The reduced magnetisation intensity due to the field perturbation around the crack further reduced the signal energy **[13]**.

The 'time of peak' showed that, for the parent material region on the planed cracked weld specimen's surface (22A), the EBE peak occurred at time values between **1 s** and **1.05 s** on the envelope (**figure 4.4.23**). However, the HAZ and weld locations exhibited peaks that were earlier (in between **0.929 s** and **0.982 s**) on the envelope compared to the parent material. The T_P profile from the planed surface, in comparison to the 'as-received' specimen 21A, showed that the maximum signal peak generally occurred later on the EBE signal envelope.

The EBE signal envelopes from the planed cracked weld surface 22A (**figures 4.2.41** to **4.2.44)** appeared very different, when compared to the signals from the EDM machined surface (**figures 4.2.36** to **4.2.39**). The EBE signals from the EDM machined surface exhibited a peak earlier on the envelope, compared to the planed surface. Both

machining processes: EDM and planing, altered the specimen's surface characteristics and, as such, had a different effect on the Barkhausen emission. The non-contact EDM machining, relieved localised residual surface stresses and high dislocation networks. This aided domain wall motion. The mechanical and thermal shock resulting from the planing process deformed the surface microstructure and increased dislocation networks and localised residual surface stress and, therefore, pinning sites. As a result, a larger applied field was required to overcome the domain wall pinning. The distance over which the domain walls were free to move was also reduced, thus, lowering EBE signal amplitudes.

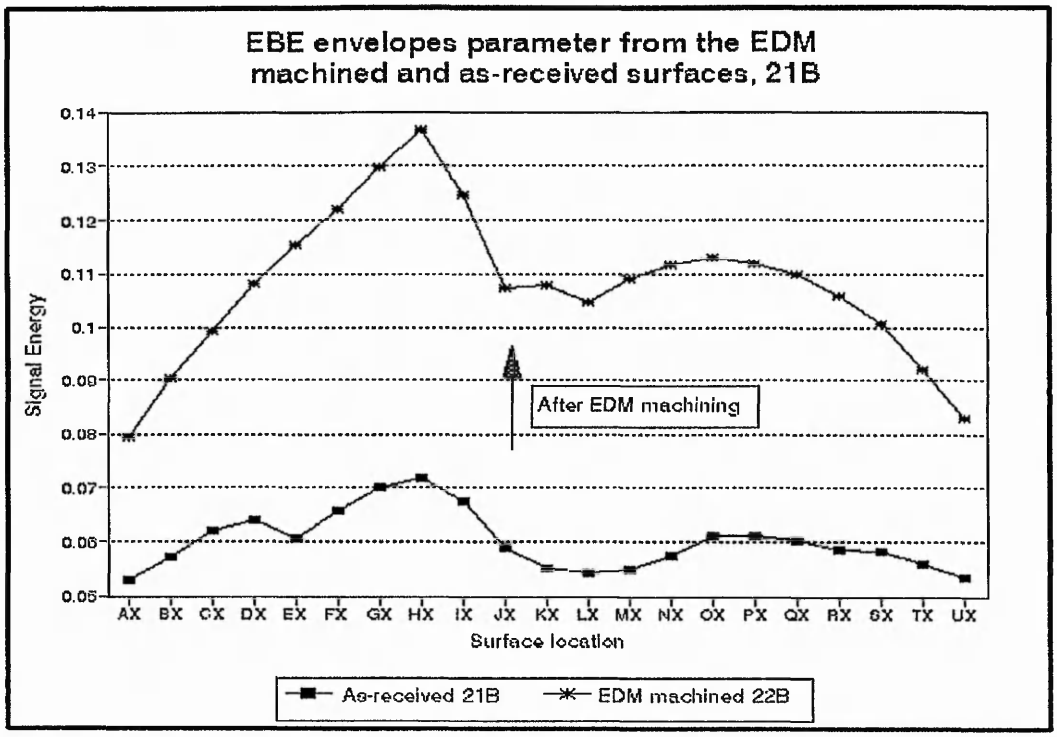


Figure 4.4.18 EBE envelopes signal energy (units V^2s) parameter from the 'as-received' (21B) and EDM machined surface (22B) of the cracked weld steel specimen. Location 'A' to 'F' is parent material, 'F' to 'H' is HAZ and the weld seam is approximately 10.5mm in width. The weld centre is situated on location 'K'. The crack is positioned very close to location 'L'.

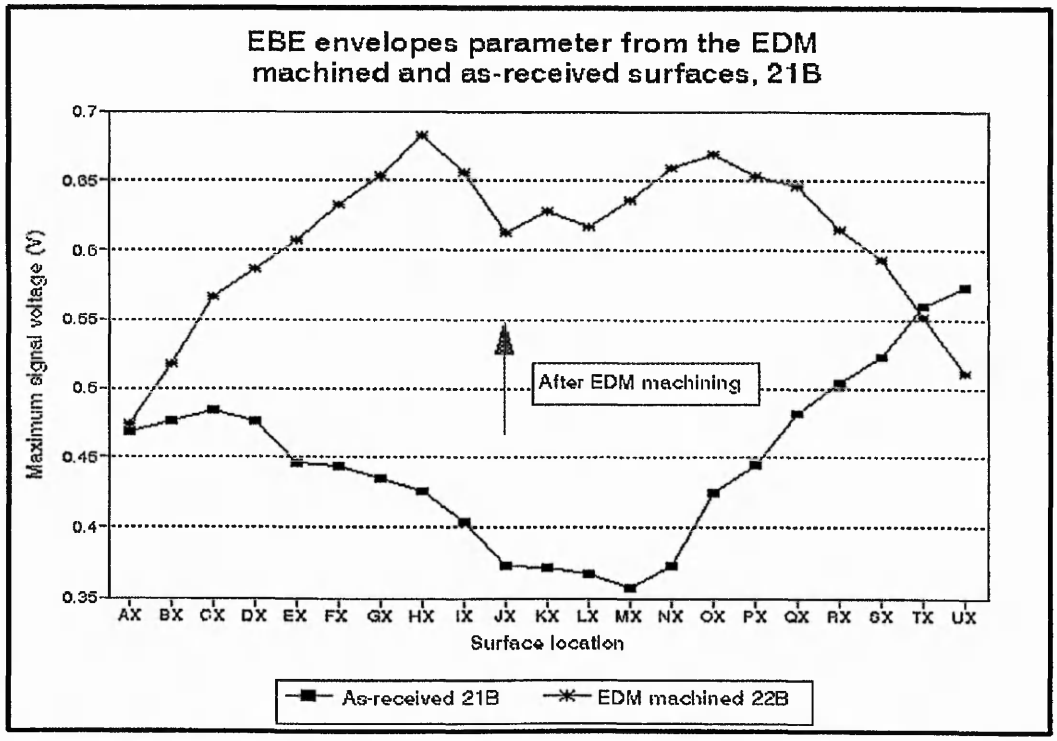


Figure 4.4.19 EBE envelopes 'maximum signal voltage' (V_{MAX}) parameter from the 'as-received' (21B) and EDM machined surface (22B) of the cracked weld steel specimen.

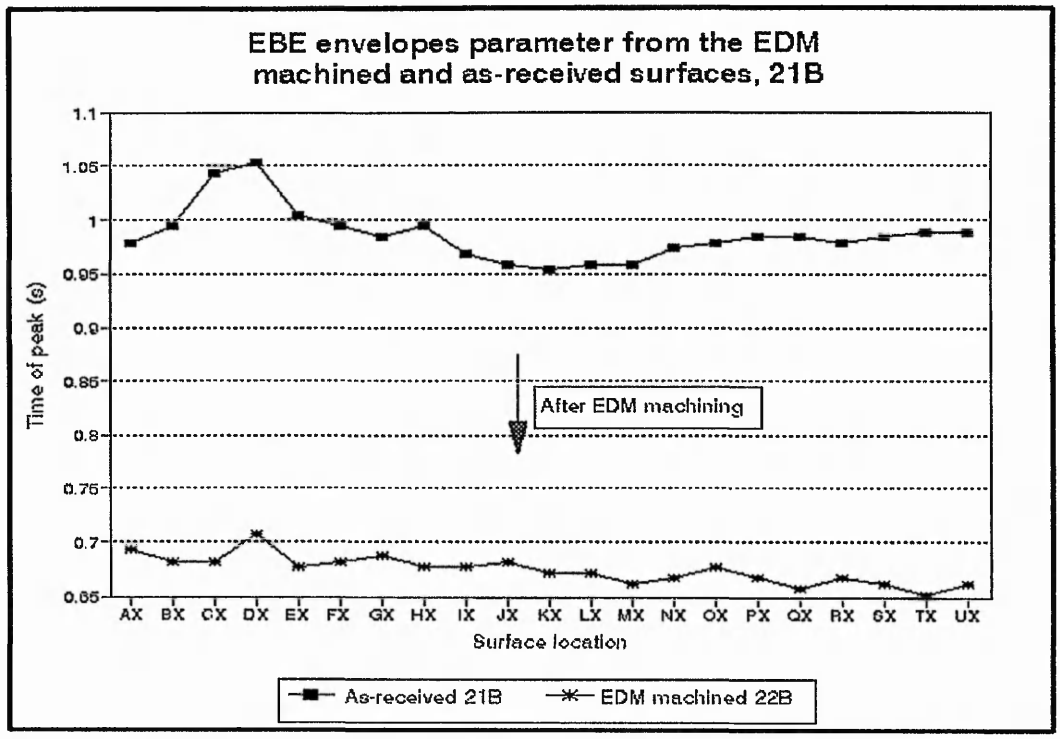


Figure 4.4.20 EBE envelopes 'time of peak' (T_P) parameter from the 'as-received' (21B) and EDM machined surface (22B) of the cracked weld steel specimen.

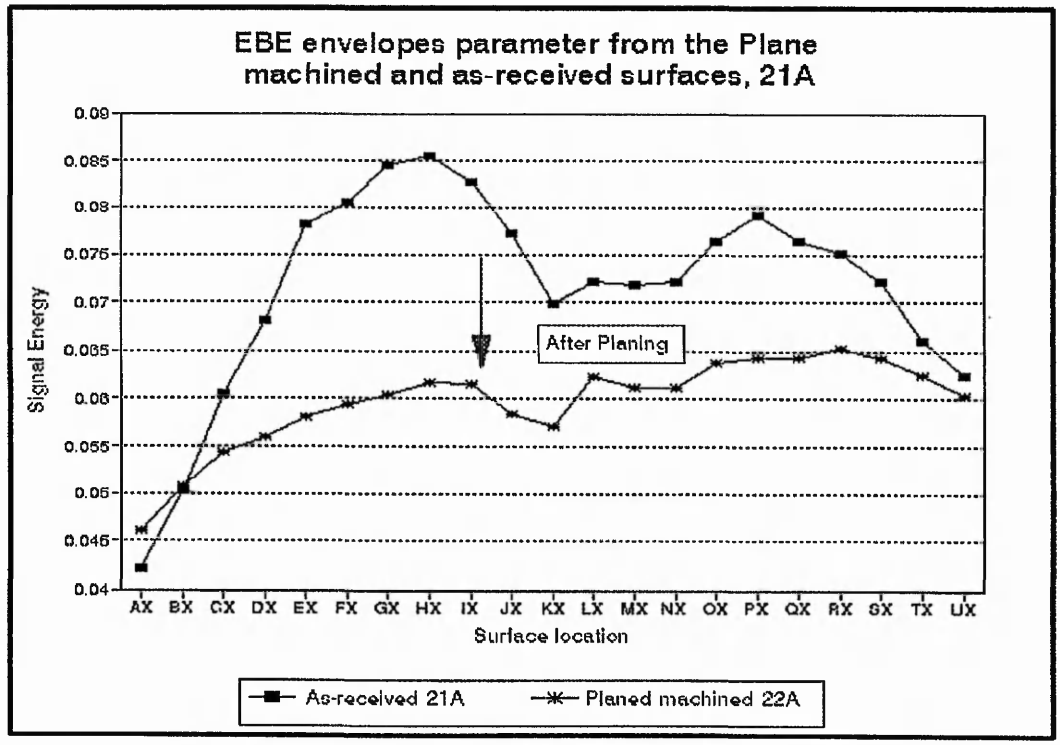


Figure 4.4.21 EBE envelopes signal energy parameter (units V^2s) from the 'as-received' (21A) and plane machined surface (22A) of the cracked weld steel specimen. Location 'A' to 'F' is parent material, 'F' to 'H' is HAZ and the weld seam is approximately 10.5mm in width. The weld centre is situated on location 'K'. The crack is positioned very close to location 'K'.

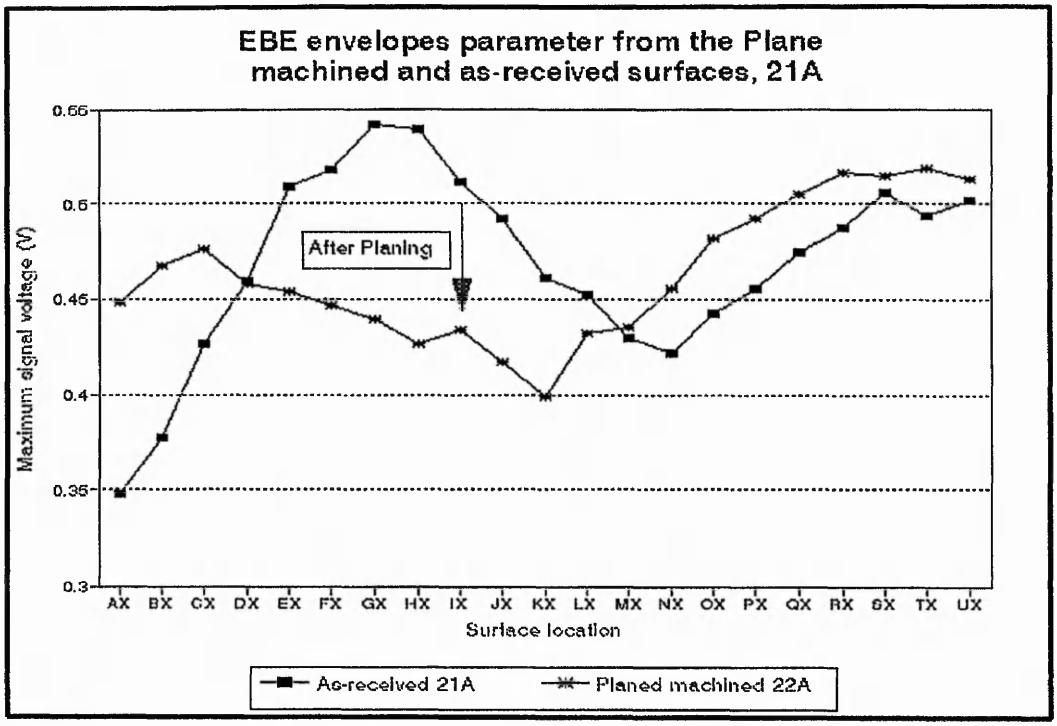


Figure 4.4.22 EBE envelopes 'maximum signal voltage' (V_{MAX}) parameter from the 'as-received' (21A) and EDM machined surface (22A) of the cracked weld steel specimen. Location 'A' to 'F' is parent material, 'F' to 'H' is HAZ and the weld seam is approximately 10.5mm in width. The weld centre is situated on location 'K'. The crack is positioned very close to location 'K'.

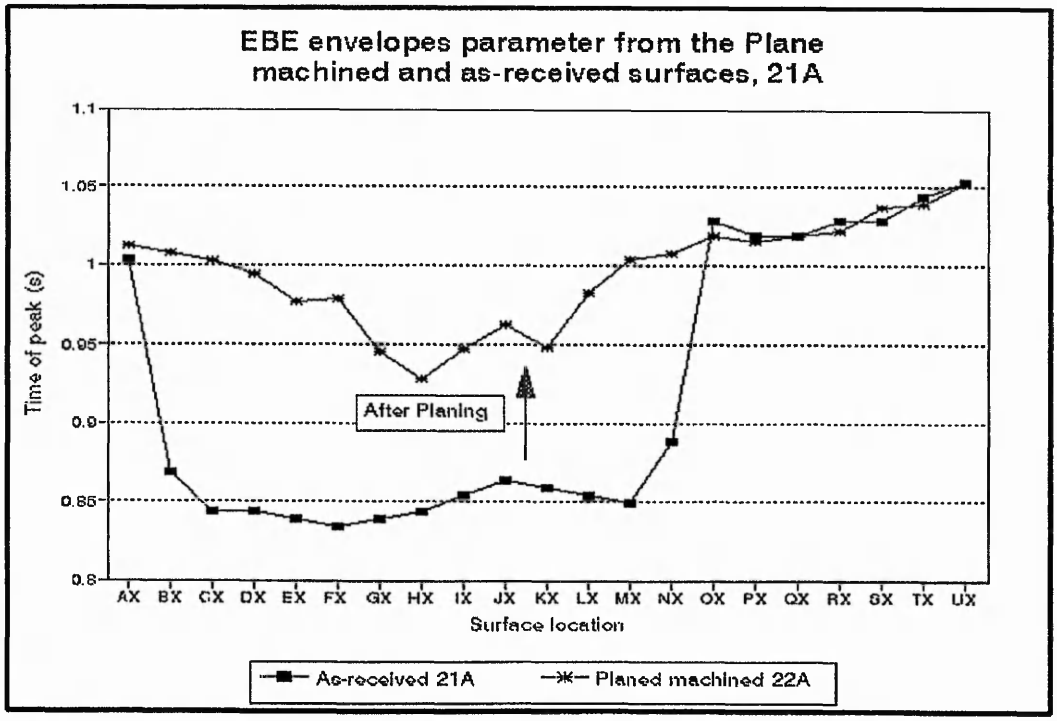


Figure 4.4.23 EBE envelopes 'time of peak' (T_P) parameter from the 'as-received' (21A) and EDM machined surface (22A) of the cracked weld steel specimen.

CHAPTER 5

REDUCTION OF THE CRACK DEPTH BY MACHINING AND THE EFFECT ON BARKHAUSEN EMISSION

5. REDUCTION OF THE CRACK DEPTH BY MACHINING AND THE EFFECT ON BARKHAUSEN EMISSION.

When small defects such as cracks are detected in large engineering structures they are often removed by grinding away the defective region: this stops the further growth of the crack. Weld seams, by their nature, are often found in highly stressed regions where cracks are likely to occur. The detection of cracks is very important if prevention of catastrophic failure is to be achieved. It is known that Barkhausen emission is a very sensitive technique, which responds to changes in stress and microstructure. If a correlation between the crack depth and Barkhausen emission exists, then it could prove to be useful in crack analysis.

The cracked weld specimens examined in **chapter 4**, were studied further. Consecutive layers of surface material were removed by machining and the effect on the Barkhausen emission was studied. Defects are known to change the local permeability of a material and it was expected that the size of the defect (crack depth) may have a direct effect on the Barkhausen emission. The Barkhausen signal envelopes were measured from the two cracked weld samples. The defect size was reduced by progressively machining away the surface of the specimens. This not only reduced the size of the defect, but also reduced

the thickness of the specimen as well. Two different machining processes were utilised: the first was a conventional mechanical machining method (using a shaper) and the second involved electrical discharge machining using an EDM machine. Unlike mechanical machining, in the EDM process, there is no tool-to-work-piece contact and, therefore, the EDM machining process generates no mechanical stresses between the tool and the work piece and this was the primary reason for its use.

5.1. EXPERIMENTAL AND SPECIMEN DETAILS.

The two cracked weld specimens, 21A and 21B, discussed in **chapter 4** were studied. Each specimen was reduced in thickness by planing and EDM machining. Each machining process progressively removed thin layers of surface material and the effect of this on the Barkhausen emission and magnetic leakage field are examined. Both the cracked weld specimens contained a fine fatigue crack, approximately 5μm in width (see **figures 5.1.1** and **5.1.2**). This crack was positioned on the centre of the TIG weld seam. The preparation of the TIG weld involved the creation of a "V" shaped groove, known as the key and this is shown in **figure 5.1.3**.

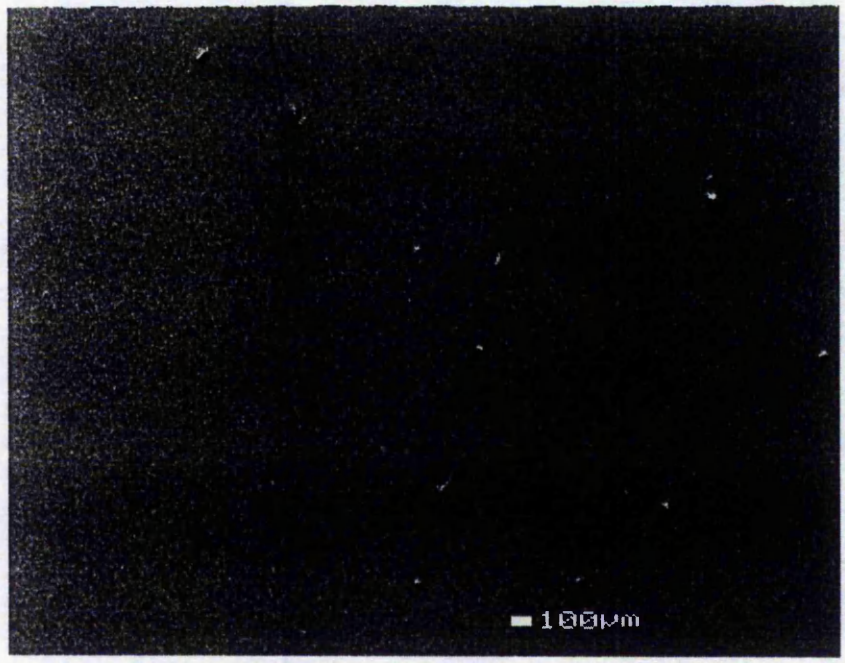


Figure 5.1.1 SEM image of crack in the centre of the weld metal. Magnification ×80.

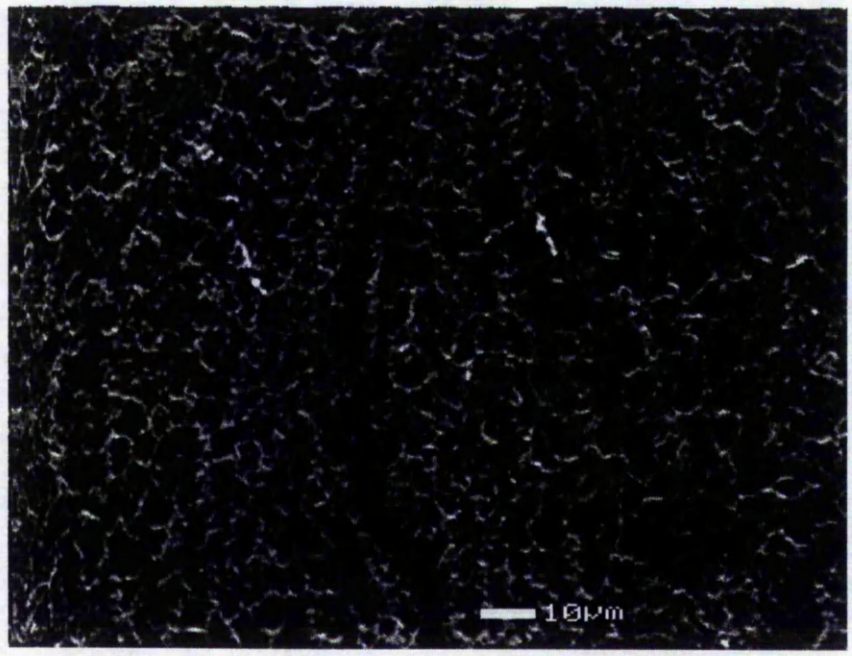


Figure 5.1.2 SEM image of crack in the centre of the weld metal at a higher magnification showing the crack width to be approximately 5 µm. Magnification ×2000.

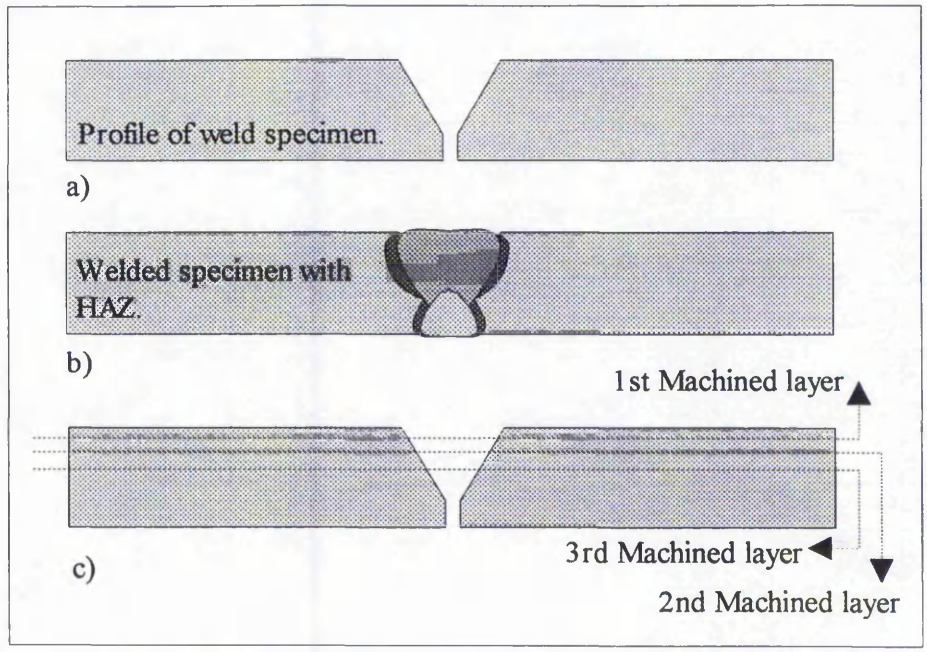


Figure 5.1.3 Welded EN-43A steel specimen. a) shows the specimen profile before welding. b) shows the weld beads present in the seam. c) shows the surface machining process and how the welded surface regions reduce in size.

The TIG welding was carried out within this groove. **Figure 5.1.3(b)** shows the weld bead pattern found on the cross-section of a cracked weld specimen. The weld metal was contained inside the groove. The surface machining reduced the thickness of the specimen and, therefore, also decreased the size of the mouth of the weld. **Figure 5.1.3(c)** shows the way in which the removal of subsequent surface layers, by machining, reduces the size of the weld mouth. The size of the mouth of the weld on subsequent machining, is shown in **table 5.1.1**. As the size of the funnel mouth decreased the effective weld material region exposed to the EBE sensor decreased. Between each machining the new surface of the specimen was cleaned using acetone. This removed any residual dielectric, cutting fluid and loose debris from the surface of the specimen, depending on the machining process.

The different surface layers removed by planing and EDM machining are listed in **table 5.1.1**. The initial EDM machined surface was labelled 22B and was discussed in **chapter 4**. On further surface EDM machining each new subsequent surface was labelled 23B,

24B, 25B and so on. The cracked weld specimen 21A was planed and the new surfaces were labelled 22A, 23A, 24A and so forth, as seen in **table 5.1.1**.

Planed machined surface.	Removed surface layer. (mm)	Width of weld mouth dimensions. (mm)	EDM machined surface.	Removed surface layer. (mm)	Width of weld mouth dimensions. (mm)
21A	-	10.66	21B	-	10.66
22A	0.5	10.08	22B	0.55	10.03
23A	0.47	9.54	23B	0.82	9.08
24A	0.54	8.92	24B	0.24	8.81
25A	0.52	8.32	25B	0.47	8.27
26A	0.67	7.54	26B	0.37	7.85
27A	0.42	7.06	27B	0.38	7.41
28A	0.51	6.19	-	-	-

Table 5.1.1 Thickness of material removed from the cracked weld specimen surface by each subsequent planing and EDM machining processes.

5.1.1. Specimen Labelling Using the BE Sensor.

BE positions on the surface of the specimen were labelled as in **chapter 4** and this is also shown in **figure 5.1.4**. A 40 mm region on the central section of the specimen was subdivided into 2 mm spacings. These 2 mm divisions were labelled 'A' through to 'U'. On each subsequent machining, the new surface was marked in the same way. The studied region remained on the same central position of the specimen. On locations 'A' through to 'U', the EBE signal envelopes were recorded. On the same 40 mm region magnetic leakage field (MLF) measurements were carried out every 1 mm, using both the GMR and Hall probe sensors. ABE measurements were recorded every 5 mm across the 40 mm region. The locations were labelled 'A' through to 'I' and this is also

described in **chapter 4**. The standard Barkhausen system described in **chapter 1** was used along with the pencil probe sensor for EBE measurements.

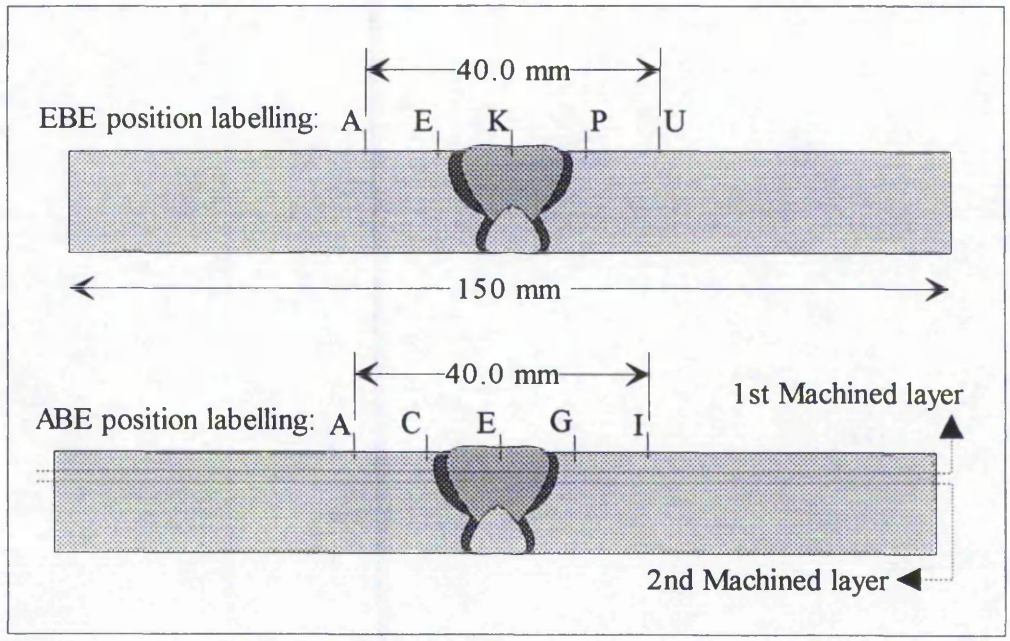


Figure 5.1.4 ABE and EBE transducer positions on the surface of the cracked weld steel specimens. The transducer positions were maintained fixed after the removal of subsequent surface layers.

5.2. RESULTS AND ANALYSIS OF BARKHAUSEN EMISSION FROM THE CRACKED WELD SPECIMENS.

The machining processes were carried out on the surface of the cracked specimens. Between each surface machining, both acoustic and electromagnetic Barkhausen measurements were recorded and the results are displayed in this section. All the figures in this section display EBE signal envelopes detected from locations 'F' through to 'P' on each of the machined surfaces. These locations cover the crack, weld and HAZ regions on the specimens' surface. Selected EBE signal envelopes from the parent material region are also displayed (locations 'A' and 'U'). The EBE signal envelope parameters from across the whole of the studied region are considered and presented. ABE signals from the different machined surfaces are shown and envelopes from selected locations ('A', 'C', 'E', 'G' and 'I') are displayed in the graphs. The ABE signal parameters are considered from every location across the entire studied region.

5.2.1. Crack Depth Reduction by Planing of the Cracked Weld Specimen.

5.2.1.1. *EBE Results from the planed cracked weld specimen 21A for different thicknesses.*

In this section the effects of progressive machining are discussed with respect to relative specimen thickness and crack depth. The EBE signal envelopes from the planed surfaces are considered. Initially, a thickness of 0.5 mm was planed off the surface of the cracked weld specimen 21A and the new surface was labelled as 22A. The planing of the cracked weld specimen's surface changed the form of the detected EBE signal envelopes. The detected envelopes from the initial planed surface (22A) are shown in **figures 5.2.1** and **5.2.2**. The EBE signal envelope shape also changed as the weld seam was approached. Away from the weld, on locations 'A' and 'U', the EBE envelopes possessed a well defined peak which occurred at around 1.1 s on the envelope. The EBE signal amplitude

was low on the first half of the envelope. EBE envelopes detected on the weld displayed an increase in amplitude in the first half of the envelope. On the second half of the envelope the peak decreased in amplitude. The EBE signal parameters from this planed surface are summarised in **figure 5.2.3**.

After further planing a surface thickness of 0.47 mm was removed (total 0.97 mm) and the new surface was labelled 23A. The EBE envelopes from surface 23A are shown in **figures 5.2.4** and **5.2.5**. The signal envelopes from the weld and HAZ region possessed a jagged top with a maximum signal amplitude occurring at approximately 1 second on the envelope. EBE signal envelopes from location 'A' and 'U' displayed a double peaked envelope. The first peak was smaller and the second peak larger. On location 'A' the first peak was not well defined. The manner in which the envelope parameters changed across the specimen, between the parent material and the weld metal, can be seen in **figure 5.2.6**.

On removal of a further 0.54 mm of surface material the detected EBE envelopes changed form compared to the surface 23A. Surface 24A displayed EBE signal envelopes which appeared similar to envelopes detected from surface 22A; a single peak featuring on the latter part of the EBE envelope. The EBE envelopes from surface 24A are shown in **figures 5.2.7** and **5.2.8**. On the weld region, the envelopes appeared as a single domed peak and toward the edge region (location 'U'), the signal split into a doubled peak envelope. For locations on the weld, crack and HAZ regions, the 'time of peak' occurred slightly earlier on the envelope at a time of **0.9 s**, when compared to the envelopes from the parent material occurring at **0.97 seconds**. The first half of the envelopes also increased in amplitude slightly as the welded region was approached. The summarised EBE envelope parameters are shown in **figure 5.2.9**.

Removal of a further 0.52 mm (total thickness loss 2.03 mm) showed a change in the amplitude of the detected EBE envelopes. On surface 25A the EBE signals on location 'H' through to 'M' displayed envelopes which were jagged and similar in shape to the envelopes from the 23A's weld region. These signals are shown in **figures 5.2.10** and **5.2.11**. The EBE envelopes, from the 25A surface's weld region, exhibited a maximum

peak at around 0.9 s on the envelope. Away from the weld region the EBE envelopes appeared double peaked, with the first peak smaller and the second peak larger. As the weld region was approached from the edge locations, the first half of the envelopes increased in height. Moving from location 'A' towards the weld, the maximum EBE peak appeared to decrease. A decrease in signal amplitude was also displayed from location 'U' toward the weld. The location 'A' also exhibited the largest signal envelope at approximately 0.7 V and this is seen in **figure 5.2.12** which summarises the envelope data.

Surface 26A, created by planing off a further 0.67 mm in thickness, displayed EBE envelopes which were similar to the previous surface (25A). These signal envelopes are shown in **figures 5.2.13** and **5.2.14**. On the 26A planed surface, the weld metal and HAZ regions exhibited EBE envelopes which featured a single peak around 0.87 seconds on the envelope. The maximum peak was around the central region of the envelope. The EBE envelopes from the edge of the studied region displayed a double peaked form, with the maximum peak occurring at around 1.05 s on the envelope. This is summarised in **figure 5.2.15**. The largest signals were also detected around location 'A', as for the previous surface.

Surface 27A exhibited EBE signal envelopes from the weld region, which were similar to the previous surface and are shown in **figures 5.2.16** and **5.2.17**. However, from location 'K' toward 'U' the EBE envelopes displayed a maximum peak on the edge of the central region of the envelope. This caused the 'time of peak' to shift to a later time in the signal envelope and mask the characteristic early 'time of peak' associated with the machined weld region. The EBE envelopes were largest at around location 'A'. These signals decreased in amplitude and remained relatively constant over the weld and HAZ regions. The EBE signal parameters associated with the surface 27A are shown in **figure 5.2.18**.

On further machining of the surface to create surface 28A the visible crack, present on the previous surface, was removed. Surface 28A exhibited EBE envelopes from the weld and HAZ regions which were similar to the envelopes from surface 26A. The EBE envelopes from the 28A surface are displayed in **figures 5.2.19** and **5.2.20**. Locations

'A' to 'G' exhibited a rapidly decreasing signal envelope amplitude. The EBE envelope from the edge of the studied region showed a double peaked form, with the maximum peak occurring late in the signal envelope. The time of peak, for the EBE envelopes from across this surface, showed that the T_p occurred earlier on the locations 'H' and 'N'. The maximum signal amplitude was found to be larger on the left side of the specimen compared to the right side of the specimen and envelope data is shown in **figure 5.2.21**.

On the planing of the 'as-received' cracked weld specimen's surface, the overall signal energy profile of the machined surface decreased. This planing led to an asymmetric EBE signal energy profile being recorded: the right hand side of the specimen exhibited a larger signal energy. The envelopes parameters of the EBE signals, from specific locations, on the different machined surfaces, are displayed in **appendix 4a**. Surface 23A displayed a signal energy profile which gradually decreased from locations 'A' through to 'U'. A small sharp dip, in the otherwise steadily decreasing energy profile, was noticeable on location 'K' very close to the crack. On surface 24A, the signal energy displayed an increase on the weld locations, while at the end regions the signal energy was found to be lower. Further machining (surface 25A) displayed a steady signal energy. Also, there was an overall energy profile increase. The weld and HAZ regions were not distinguishable using the EBE signal energy profile from surface 25A. The different material regions were not distinguishable using the energy profile from the 24A and 25A surfaces.

On the 26A surface the signal energy profile showed a steady decrease in the magnitude, whilst moving from location 'A' through to 'U'. The central region, containing the weld seam, crack and HAZ, was evident from the signal energy increase. A small drop in the magnitude of the signal energy was noticeable on location 'K', very close to the crack. Surface 27A displayed an EBE energy profile which steadily decreased in magnitude from location 'A' through to 'U'. The effect of the weld was not clearly visible in the energy profile. However, a small dip at location 'K' was noticeable. On surface 28A the energy profile, once again, displayed a gradual decrease from location 'A' to 'U'. The effect of the weld and HAZ was noticeable and caused the signal energy to increase in magnitude. As the planed specimen was progressively reduced in thickness, the overall

EBE energy profile from each of the specimen's surfaces increased. This phenomenon was a result of the specimen's thickness being reduced. The increasing reluctance of the specimen increased the magnetic flux on the surface of the specimen which was detected by the EBE sensor.

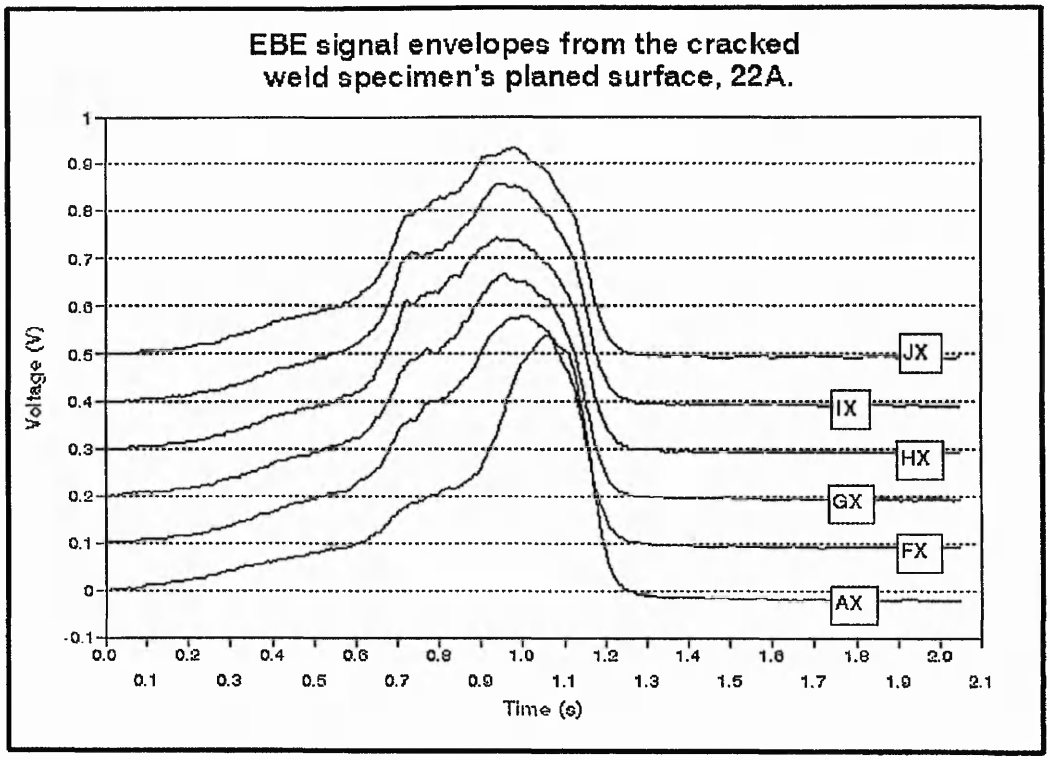


Figure 5.2.1 EBE signal envelopes from the cracked weld specimen's plane machined surface 22A. Location on the parent steel ('A'), HAZ ('H') and weld seam ('J') are displayed.

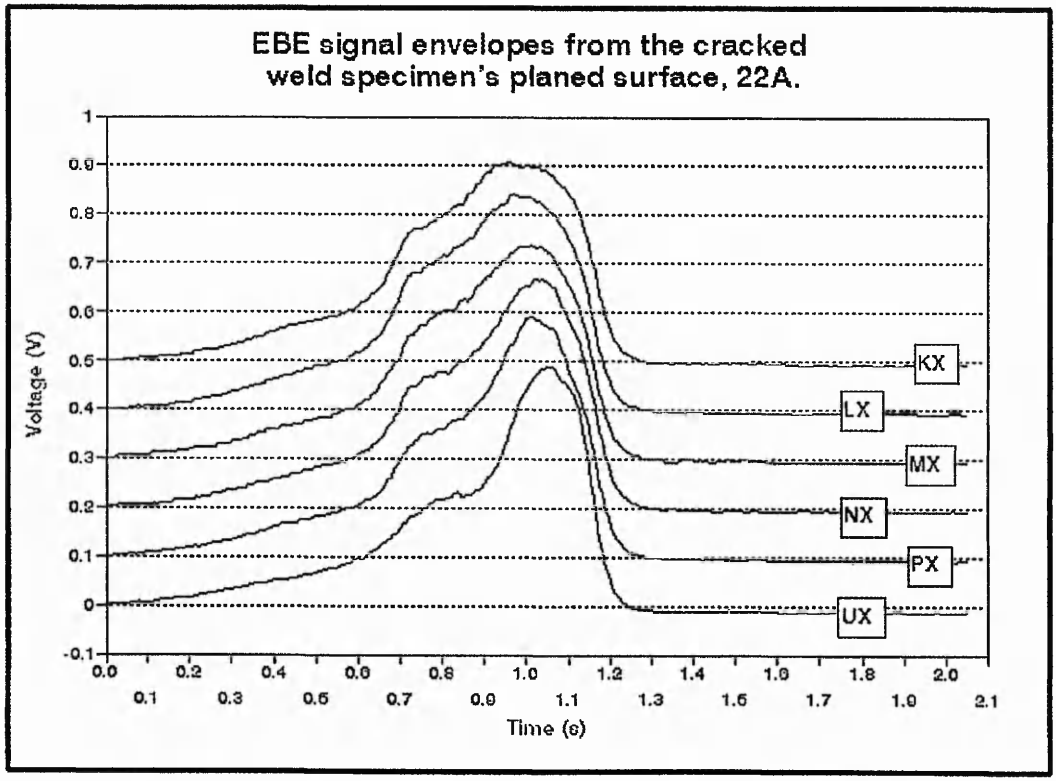


Figure 5.2.2 EBE signal envelopes from the cracked weld specimen's plane machined surface 22A. Location on the parent steel ('U'), HAZ ('N') and cracked weld seam ('K') are displayed.

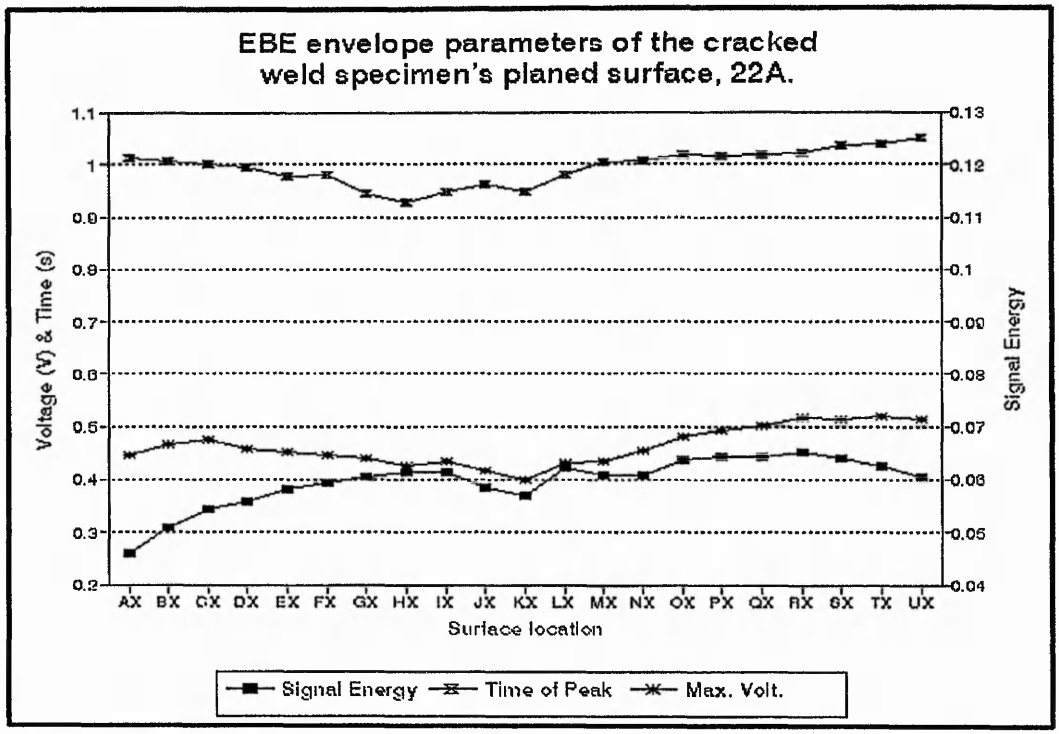


Figure 5.2.3 The EBE envelope's signal energy (units V^2s), time of peak (T_P) and maximum signal voltage (V_{MAX}) parameter profiles from the planed surface 22A are displayed.

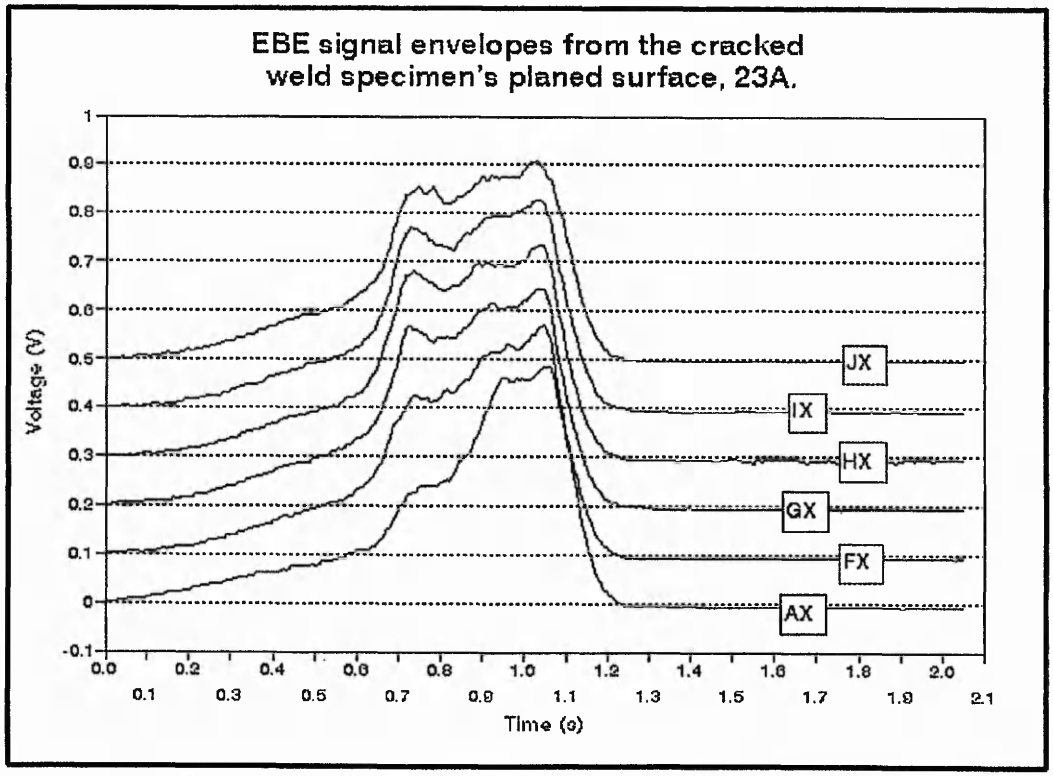


Figure 5.2.4 EBE signal envelopes from the cracked weld specimen's plane machined surface 23A. Location on the parent steel ('A'), HAZ ('H') and weld seam ('J') are displayed.

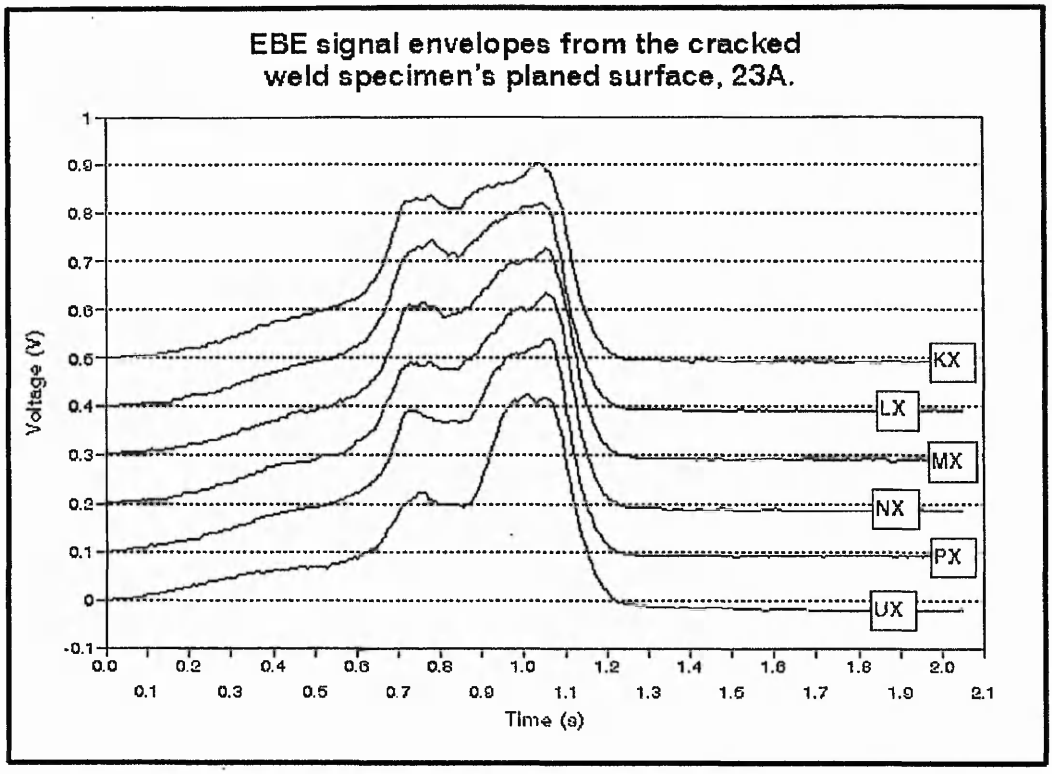


Figure 5.2.5 EBE signal envelopes from the cracked weld specimen's plane machined surface 23A. Location on the parent steel ('U'), HAZ ('N') and cracked weld seam ('K') are displayed.

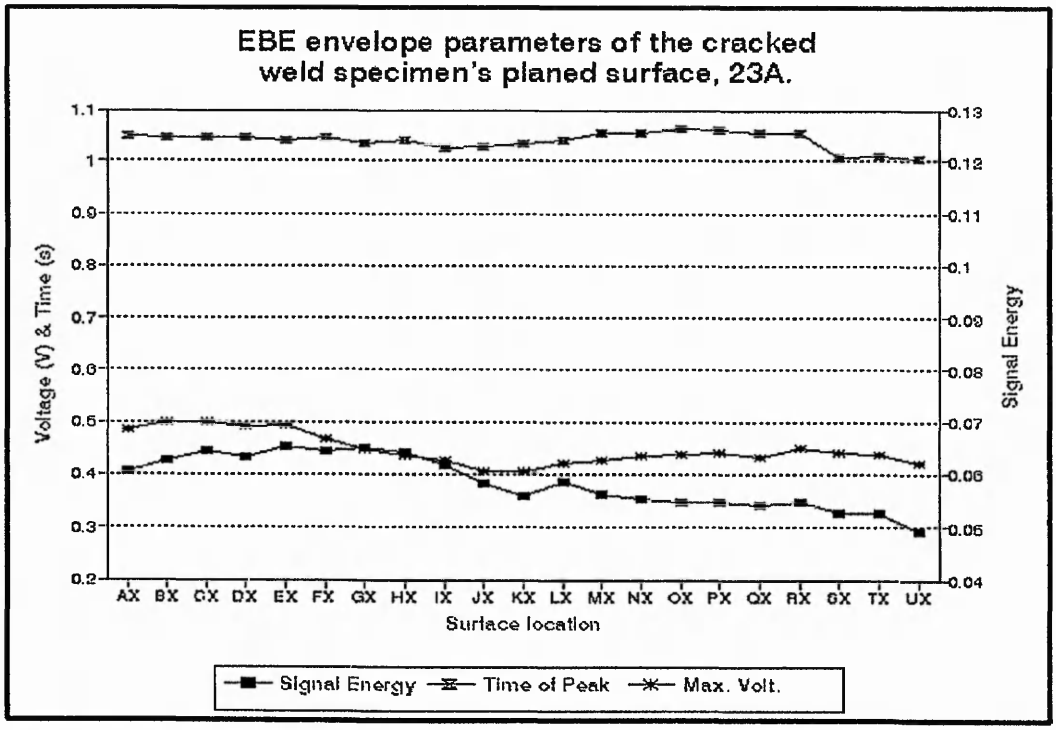


Figure 5.2.6 The EBE envelope's signal energy (units V^2s), time of peak (T_P) and maximum signal voltage (V_{MAX}) parameter profiles from the planed surface 23A are displayed.

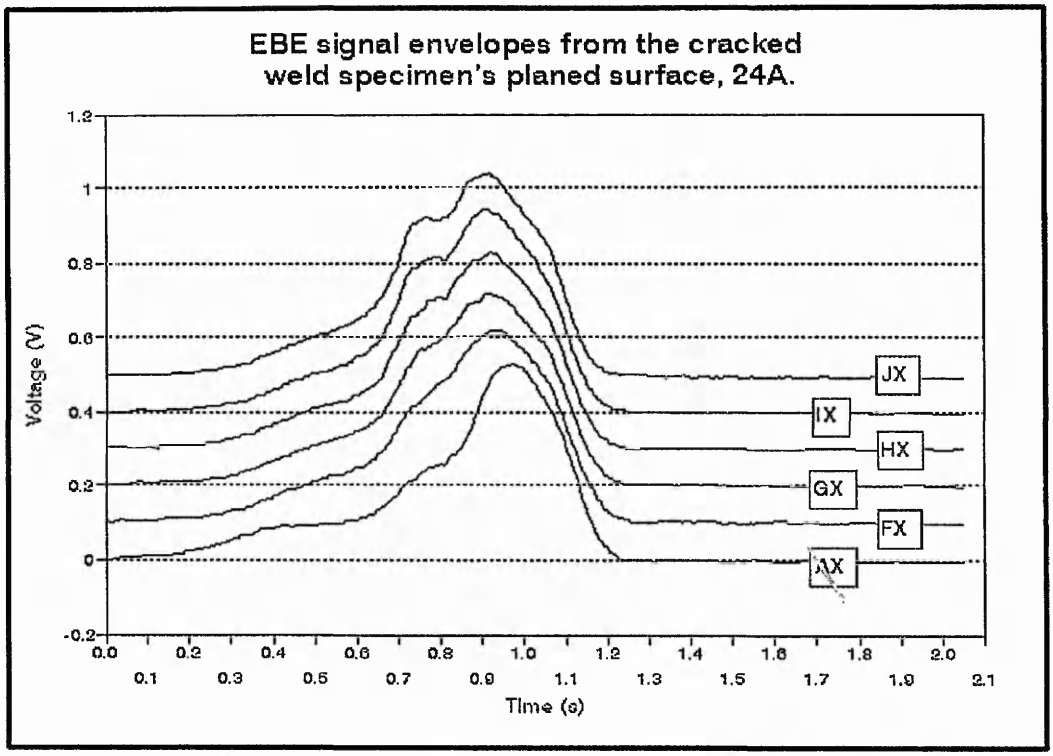


Figure 5.2.7 EBE signal envelopes from the cracked weld specimen's plane machined surface 24A. Location on the parent steel ('A'), HAZ ('H') and weld seam ('J') are displayed.

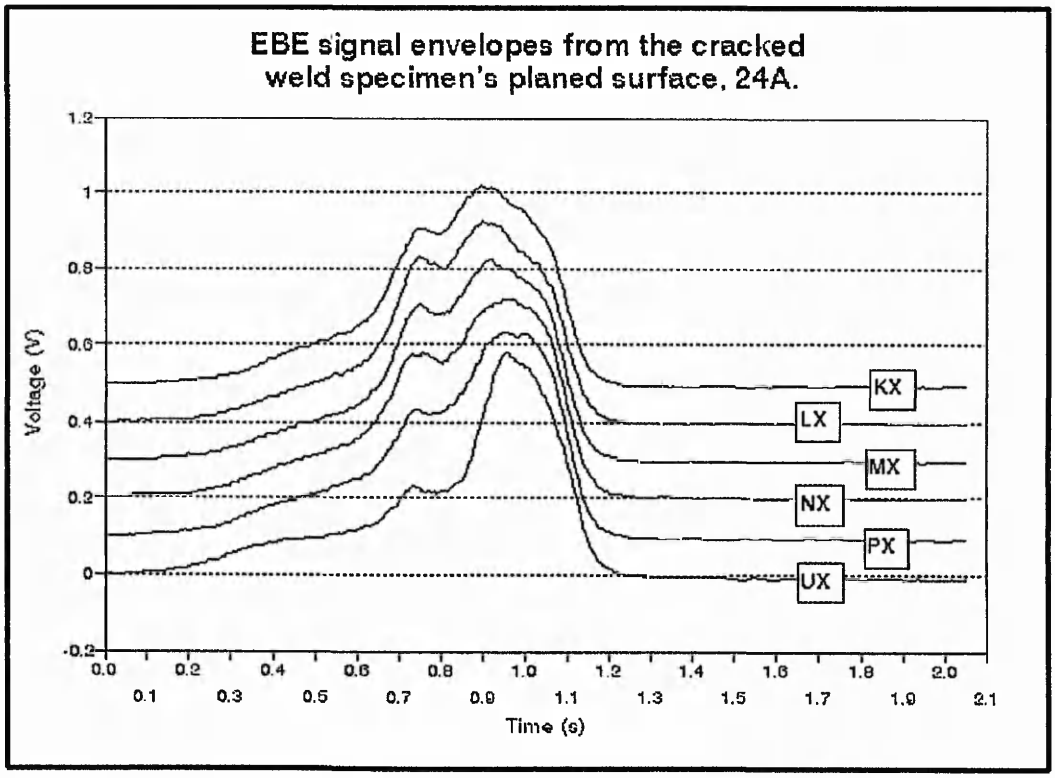


Figure 5.2.8 EBE signal envelopes from the cracked weld specimen's plane machined surface 24A. Location on the parent steel ('U'), HAZ ('N') and cracked weld seam ('K') are displayed.

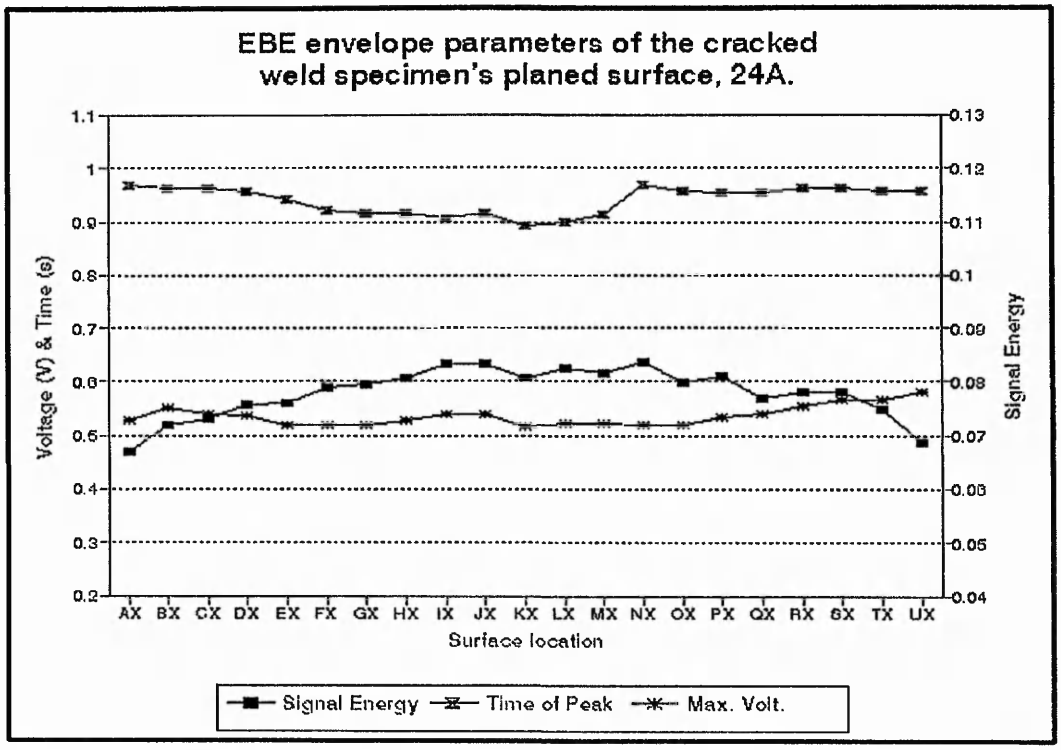


Figure 5.2.9 The EBE envelope's signal energy (units V^2s), time of peak (T_P) and maximum signal voltage (V_{MAX}) parameter profiles from the planed surface 24A are displayed.

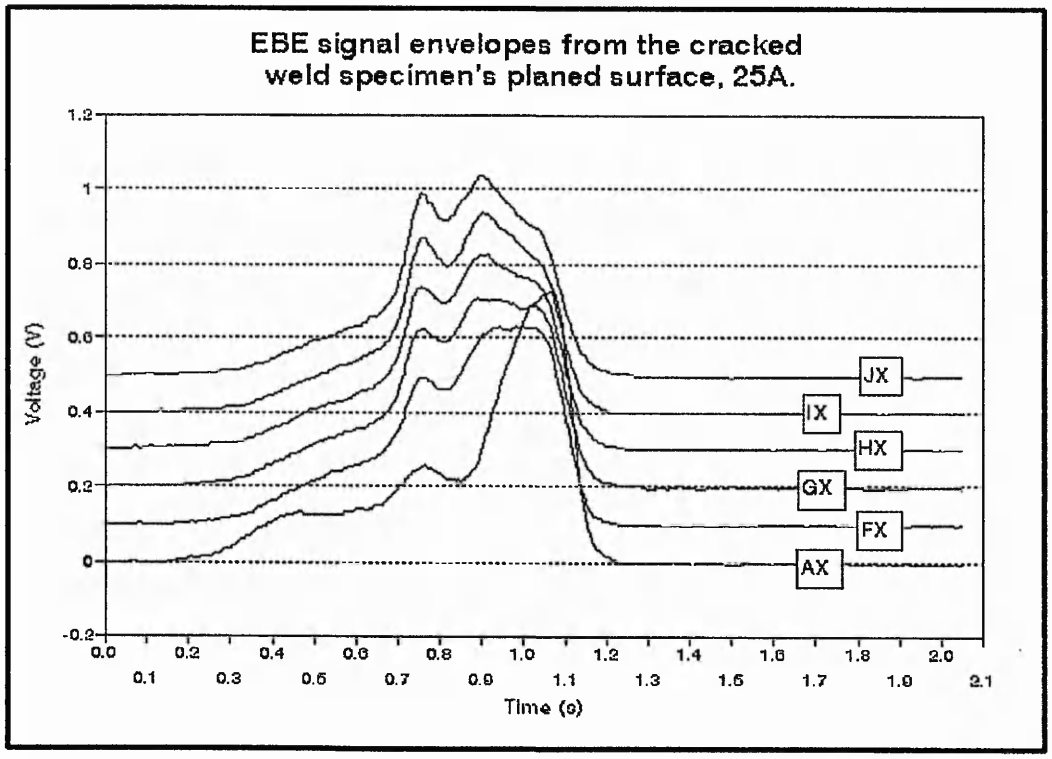


Figure 5.2.10 EBE signal envelopes from the cracked weld specimen's plane machined surface 25A. Location on the parent steel ('A'), HAZ ('H') and weld seam ('J') are displayed.

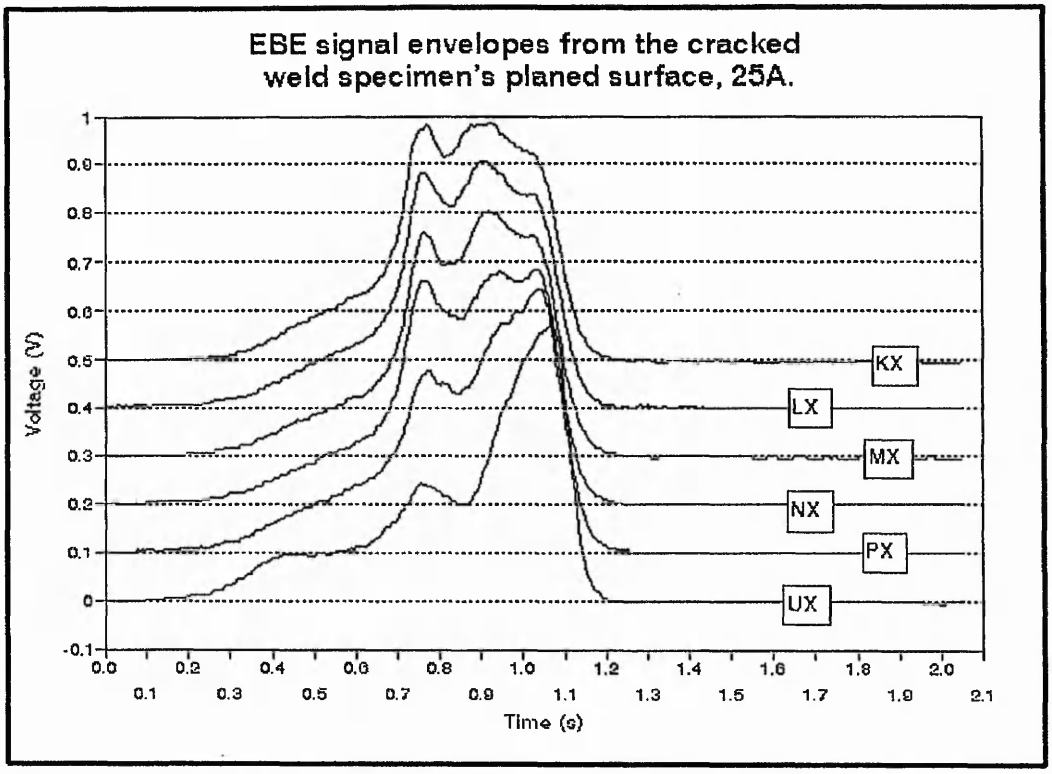


Figure 5.2.11 EBE signal envelopes from the cracked weld specimen's plane machined surface 25A. Location on the parent steel ('U'), HAZ ('N') and cracked weld seam ('K') are displayed.

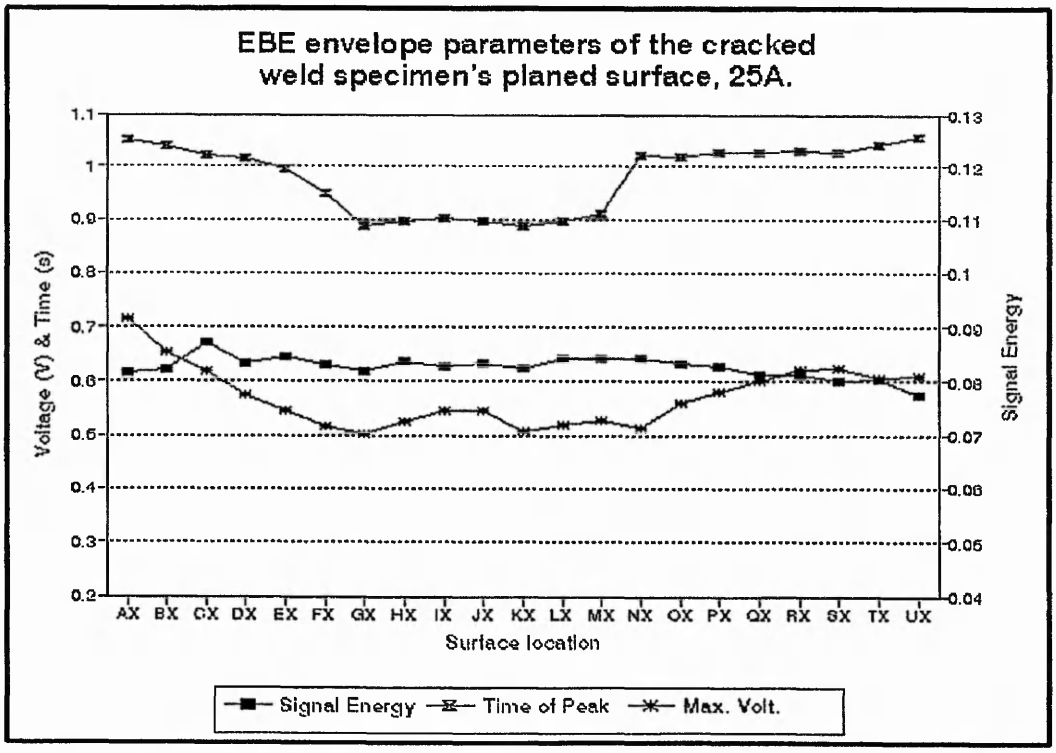


Figure 5.2.12 The EBE envelope's 'signal energy' (units V^2s), 'time of peak' (T_P) and 'maximum signal voltage' (V_{MAX}) parameter profiles from the planed surface 25A are displayed.

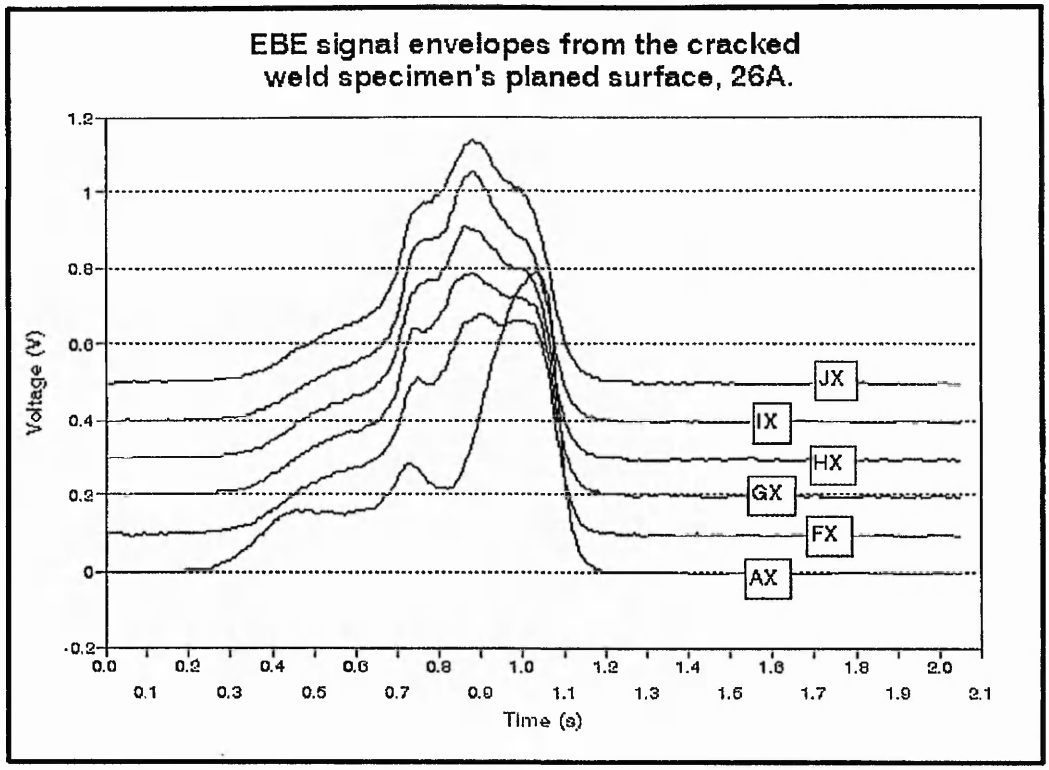


Figure 5.2.13 EBE signal envelopes from the cracked weld specimen's plane machined surface 26A. Location on the parent steel ('A'), HAZ ('H') and weld seam ('J') are displayed.

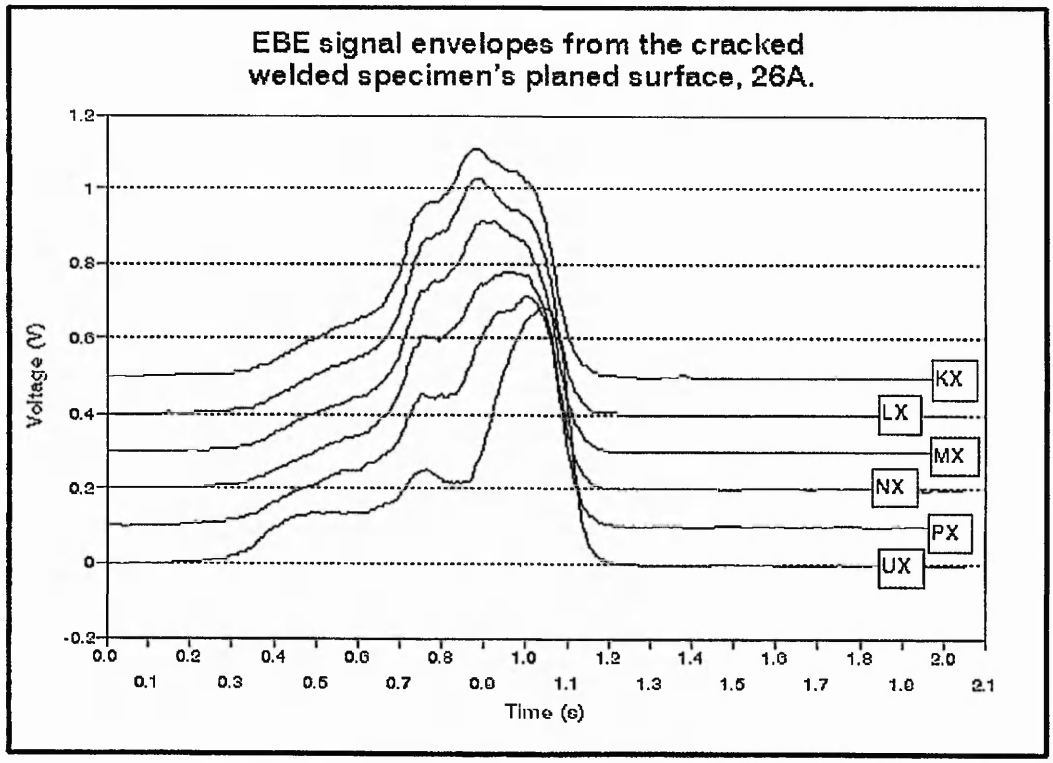


Figure 5.2.14 EBE signal envelopes from the cracked weld specimen's plane machined surface 26A. Location on the parent steel ('U'), HAZ ('N') and cracked weld seam ('K') are displayed.

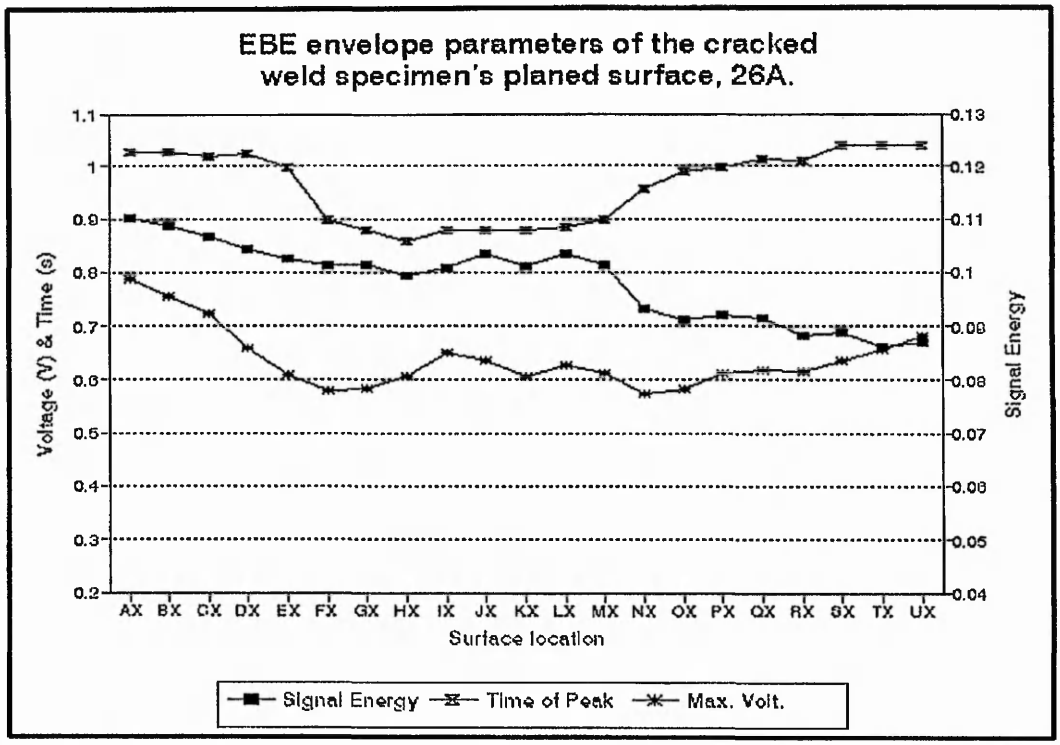


Figure 5.2.15 The EBE envelope's 'signal energy' (units V^2s), 'time of peak' (T_P) and 'maximum signal voltage' (V_{MAX}) parameter profiles from the planed surface 26A are displayed.

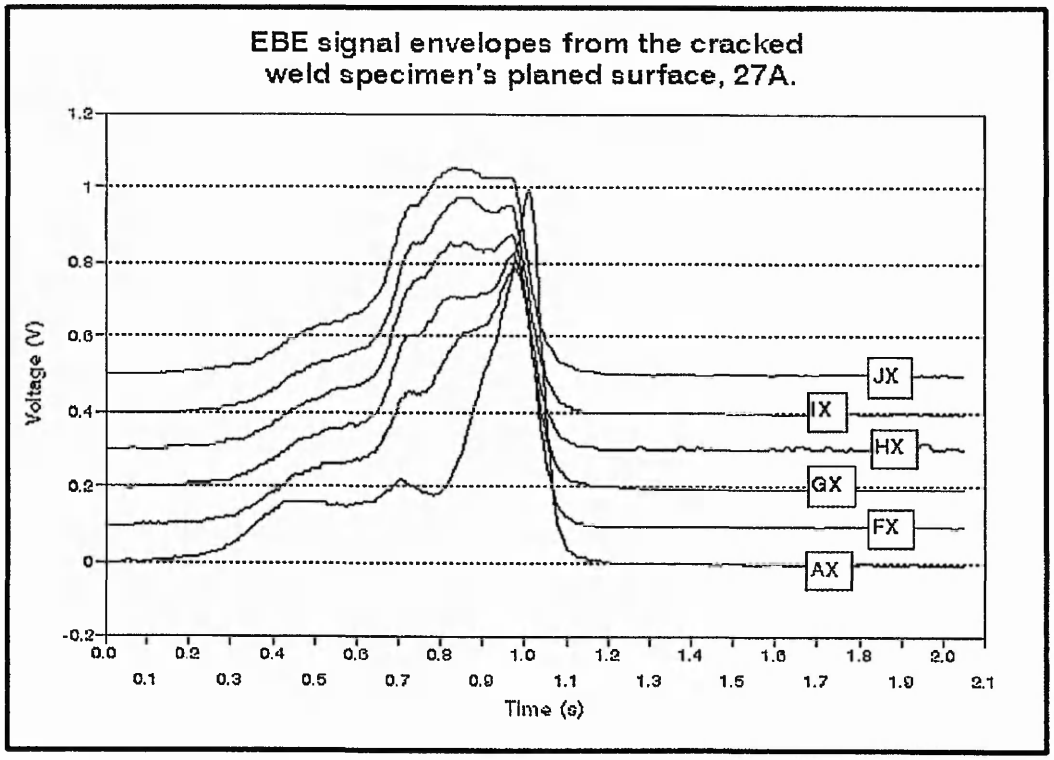


Figure 5.2.16 EBE signal envelopes from the cracked weld specimen's plane machined surface 27A. Location on the parent steel ('A'), HAZ ('H') and weld seam ('J') are displayed.

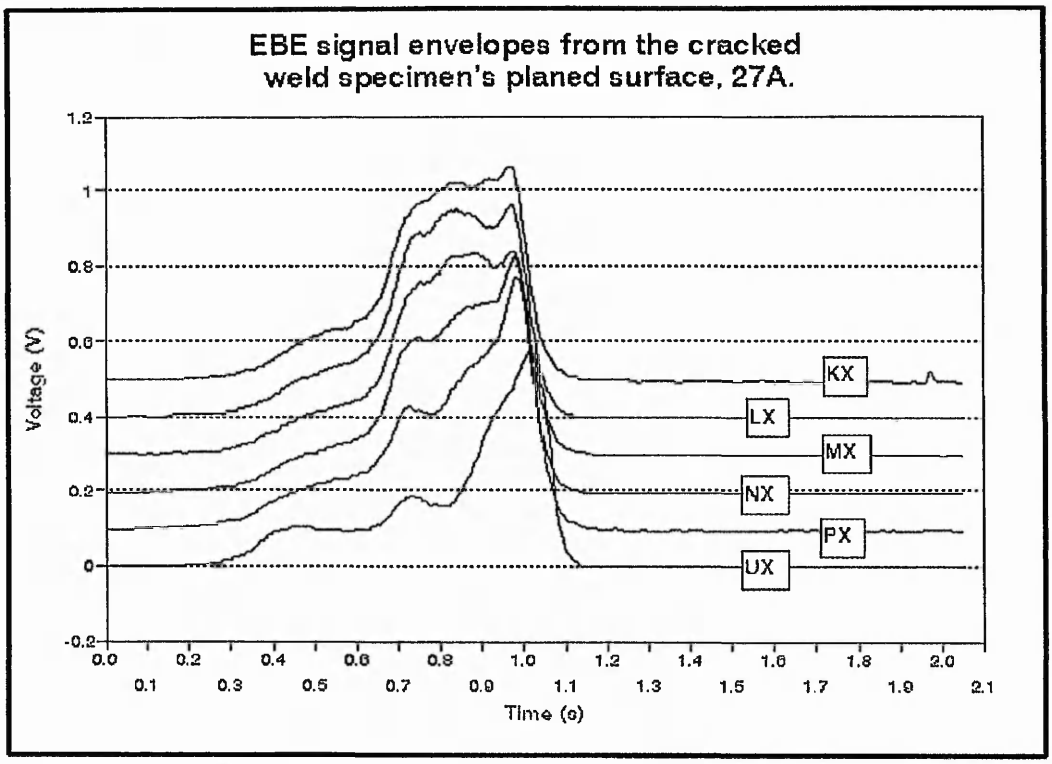


Figure 5.2.17 EBE signal envelopes from the cracked weld specimen's plane machined surface 27A. Location on the parent steel ('U'), HAZ ('N') and cracked weld seam ('K') are displayed.

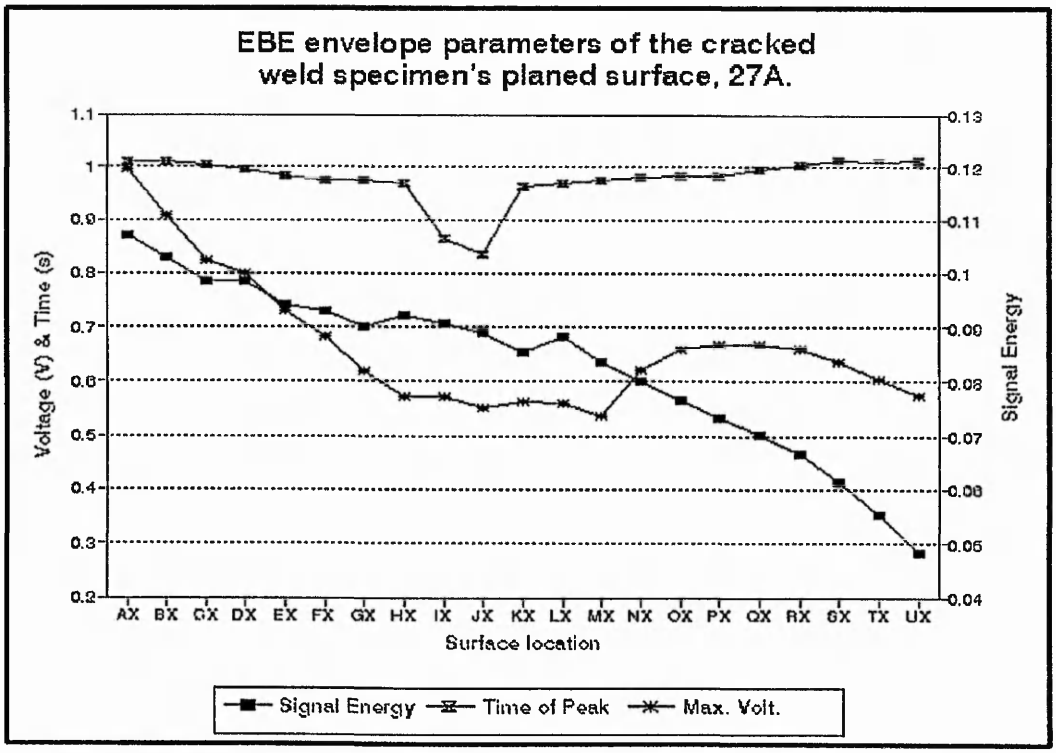


Figure 5.2.18 The EBE envelope's 'signal energy' (units V^2s), 'time of peak' (T_P) and 'maximum signal voltage' (V_{MAX}) parameter profiles from the planed surface 27A are displayed.

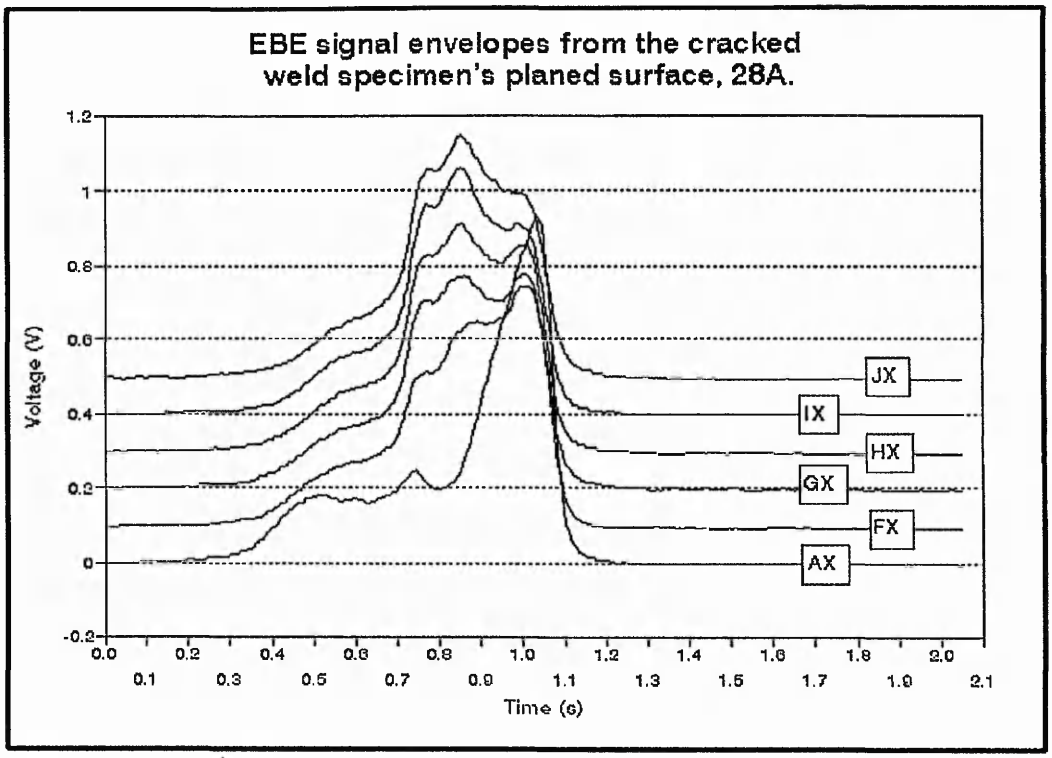


Figure 5.2.19 EBE signal envelopes from the cracked weld specimen's plane machined surface 28A. Location on the parent steel ('A'), HAZ ('H') and weld seam ('J') are displayed.

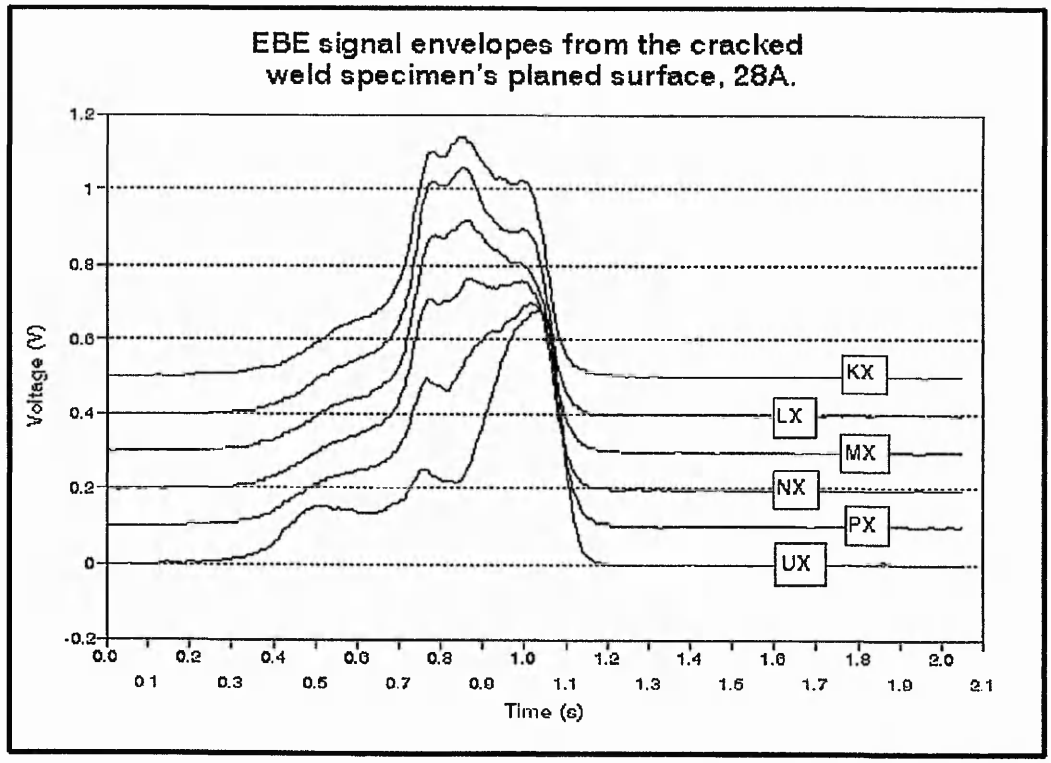


Figure 5.2.20 EBE signal envelopes from the cracked weld specimen's plane machined surface 28A. Location on the parent steel ('U'), HAZ ('N') and cracked weld seam ('K') are displayed.

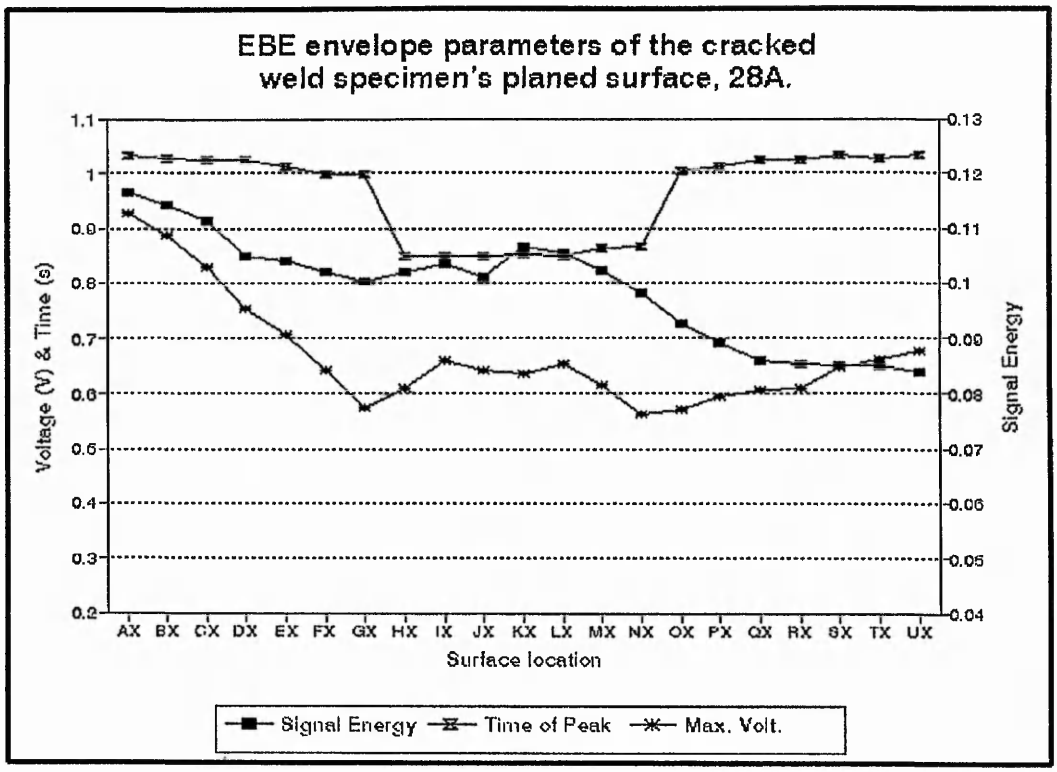


Figure 5.2.21 The EBE envelope's 'signal energy' (units V^2s), 'time of peak' (T_P) and 'maximum signal voltage' (V_{MAX}) parameter profiles from the planed surface 28A are displayed.

5.2.1.2. *ABE Results from the planed cracked weld specimen 21A for different thicknesses.*

The planing of the 'as-received' cracked weld specimen surface significantly altered the detected ABE envelopes and this is displayed in **figure 5.2.22**. The ABE signals, from the planed surface 22A, displayed the conventional doubled peaked signal. From the majority of surface locations the central dip on the envelopes possessed small jagged spikes. As ABE is a volume effect, the presence of the different phases (weld, HAZ and parent steel) within the specimen were not expected to independently affect the ABE signal. Therefore, the average signal parameters could be considered as being characteristic of the specimen as a whole, including its microstructural and macrostructural properties and size. The time of maximum peak, T_P, occurred around **1.11 s** on the envelope. The 'maximum signal voltage' (V_{MAX}) covered a range from **1.17V** to **1.45 V**. The removal of the surface layer caused a decrease in the maximum signal amplitude. This was mainly due to the loss of the large spike signals which were found on the original 'as-received' surface (21A). On further planing (surface 23A) the majority of the ABE envelopes appeared smooth and double peaked and the time of maximum peak, T_P, occurred between **1.09 s** and **1.15 s** on the envelope. These envelopes are shown in **figure 5.2.23**.

On subsequent machining the new surfaces, 24A through to 28A, all exhibited double peaked ABE signals. The **figures 5.2.24** to **5.2.27** show the ABE envelopes from the respective surfaces. Surface 24A displayed a few locations which showed small spikes on the central region of the ABE envelopes, otherwise, most location displayed a smooth signal envelope. ABE data from surface 25A was lost due to computer software failure and, hence, cannot be considered. Surface 26A displayed a spike at the base of the ABE envelope's second peak. ABE signals from the 27A and 28A planed surfaces displayed smooth double peaked envelopes. The ABE envelope parameters from these signals are displayed in **table 5.2.1**.

The ABE envelope parameters from the plane machined surfaces exhibited T_P values which were relatively constant, at around **1.12 s** from the first three planed surfaces. Surface 26A,27A and 28A exhibited an averaged T_P value of **1.07 s**. The ABE 'maximum signal voltage' value detected from the various surface showed an increasing trend. This was similarly reflected in the signal energy values from each of the machined surfaces and this is discussed in greater detail in **section 5.4**.

Surface.	Average T_P (s)	T_P Range (s)	Average V_{MAX} (V)	V_{MAX} Range (V)
22A	1.11	1.10- 1.12	1.31	1.17- 1.45
23A	1.13	1.09- 1.15	1.45	1.36- 1.55
24A	1.13	1.11- 1.17	1.44	1.27- 1.52
25A	-	-	-	-
26A	1.08	1.07- 1.09	1.73	1.49- 1.92
27A	1.07	1.05- 1.10	1.77	1.67- 1.86
28A	1.08	1.06- 1.10	1.64	1.47- 1.81

Surface.	Average Signal Energy (V^2s)	Signal Energy Range (V^2s)
22A	0.344	0.231- 0.478
23A	0.371	0.265- 0.464
24A	0.340	0.247- 0.436
25A	-	-
26A	0.414	0.332-0.523
27A	0.466	0.361-0.526
28A	0.361	0.236-0.458

Table 5.2.1 ABE signal data from the planed machined cracked weld specimen (21A), showing 'time of peak' (T_P), 'maximum signal voltage' (V_{MAX}) and signal energy obtained from the various surface layers.

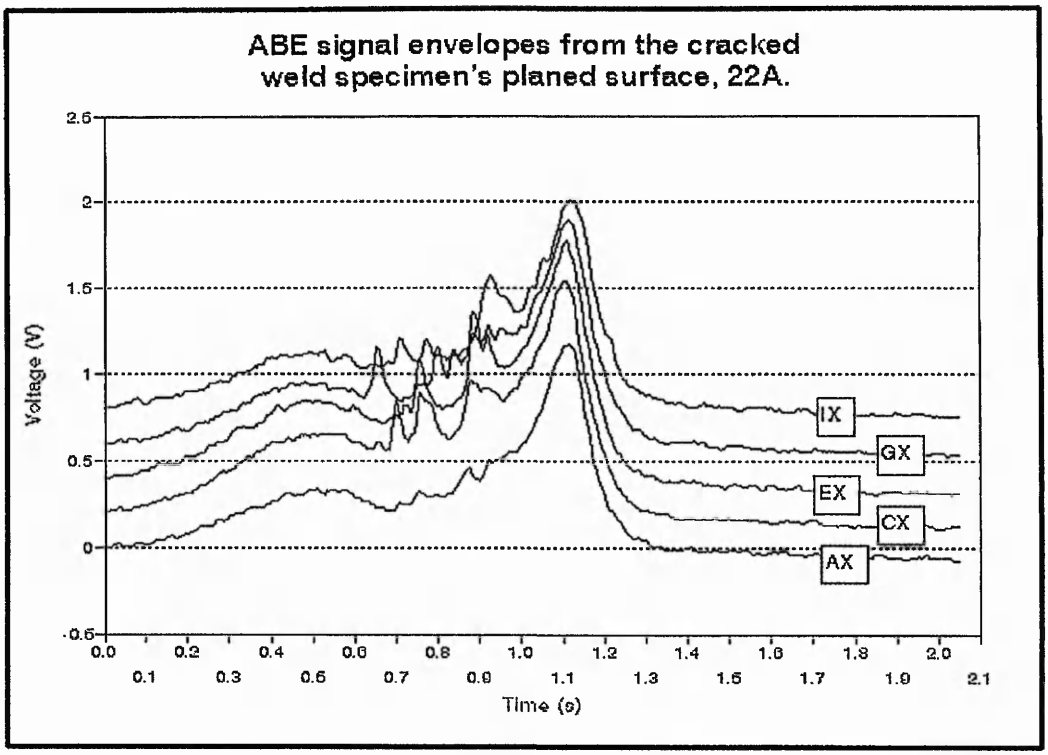


Figure 5.2.22 ABE signal envelopes from the cracked weld specimen's planed machined surface 22A. Locations 'A' and 'I' are from parent material regions and location 'E' is from the cracked weld region.

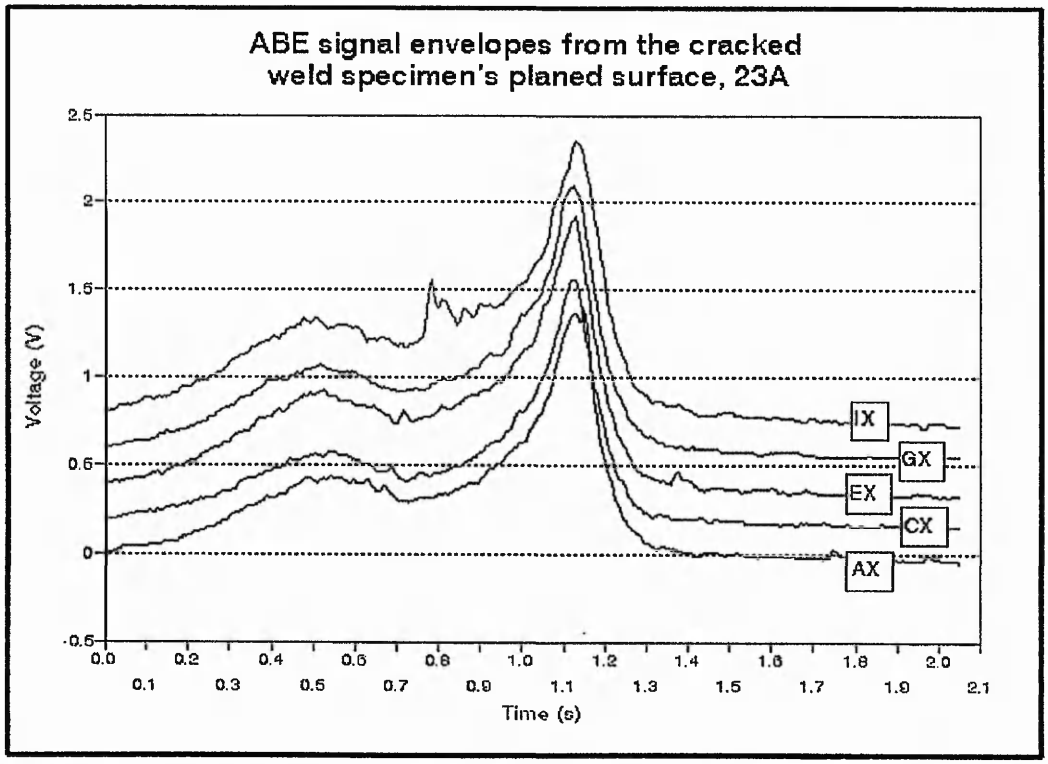


Figure 5.2.23 ABE signal envelopes from the cracked weld specimen's planed machined surface 23A. Locations 'A' and 'I' are from parent material regions and location 'E' is from the cracked weld region.

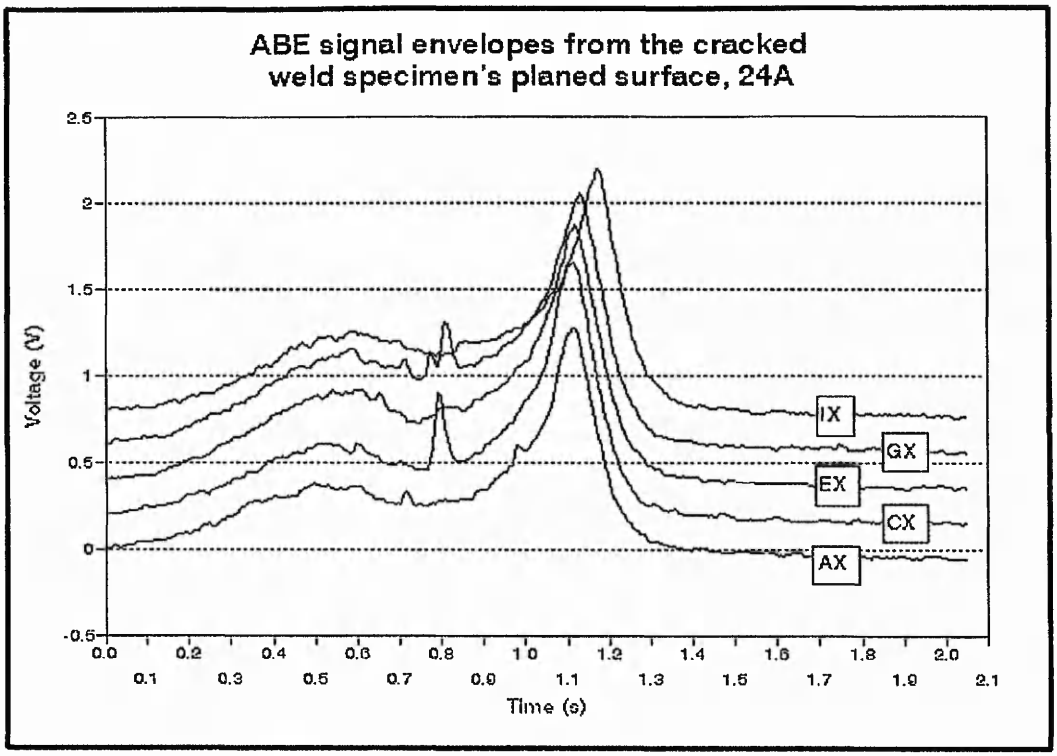


Figure 5.2.24 ABE signal envelopes from the cracked weld specimen's planed machined surface 24A. Locations 'A' and 'I' are from parent material regions and location 'E' is from the cracked weld region.

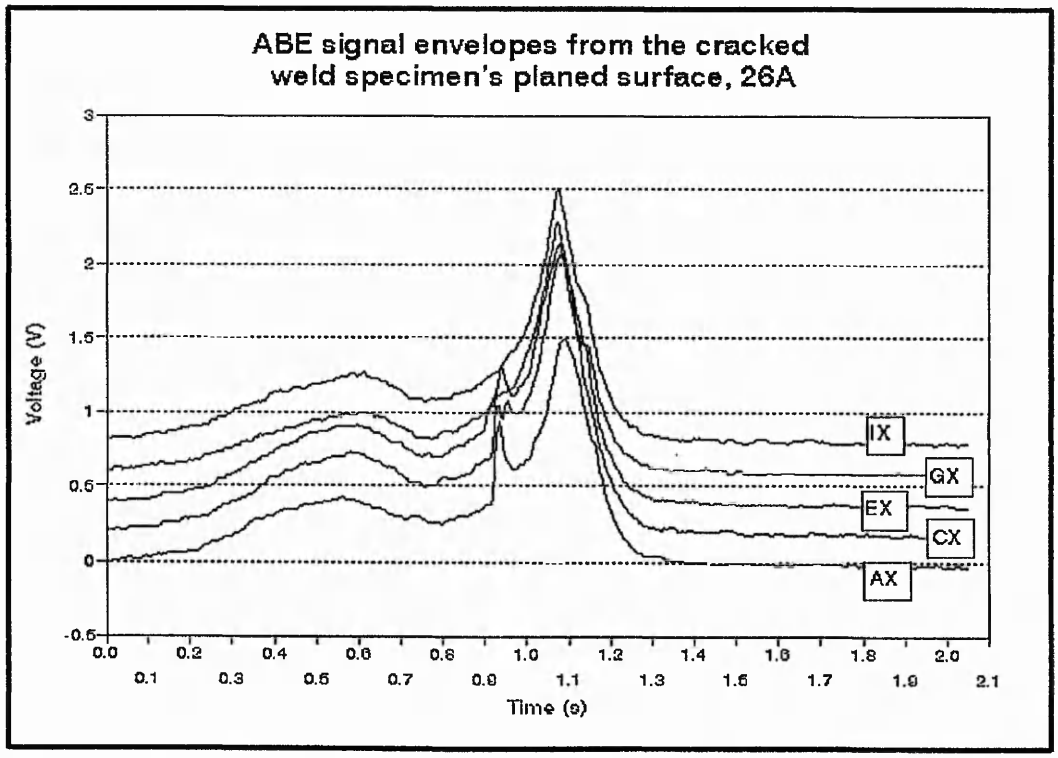


Figure 5.2.25 ABE signal envelopes from the cracked weld specimen's planed machined surface 26A. Locations 'A' and 'I' are from parent material regions and location 'E' is from the cracked weld region.

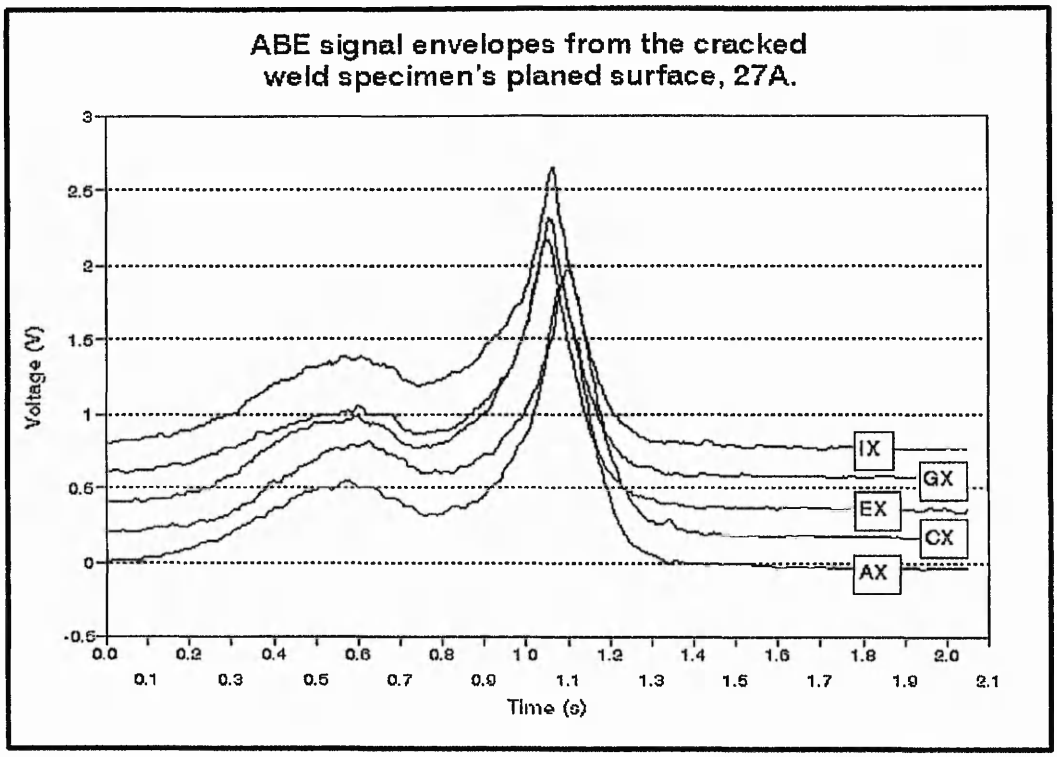


Figure 5.2.26 ABE signal envelopes from the cracked weld specimen's planed machined surface 27A. Locations 'A' and 'I' are from parent material regions and location 'E' is from the cracked weld region.

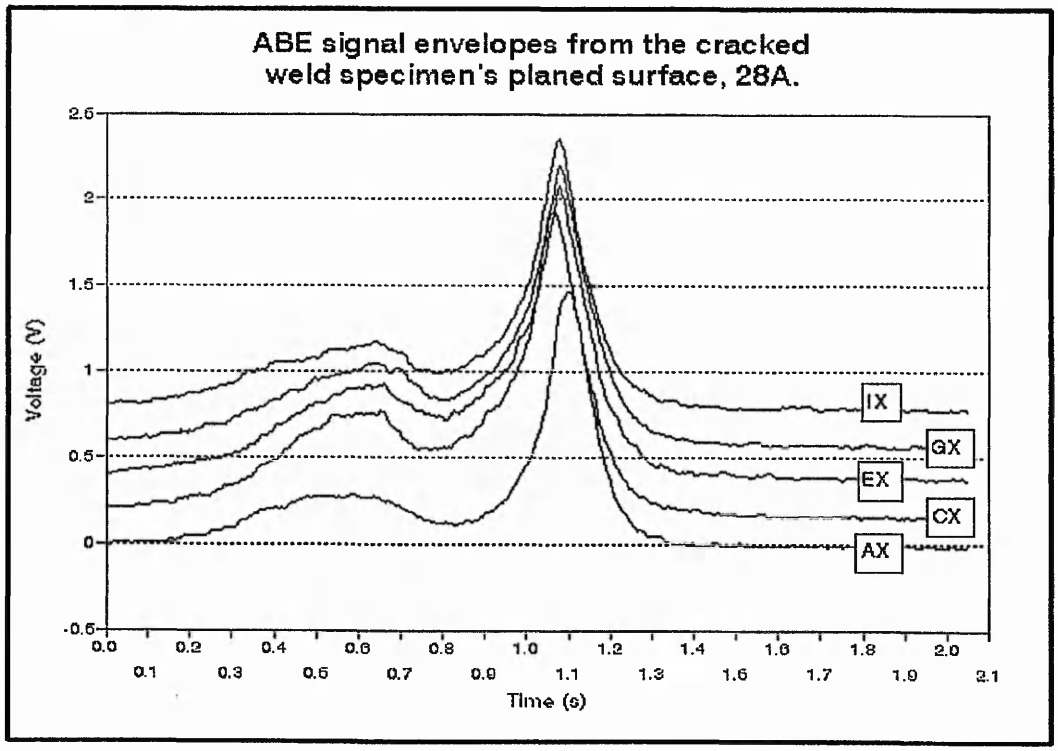


Figure 5.2.27 ABE signal envelopes from the cracked weld specimen's planed machined surface 28A. Locations 'A' and 'I' are from parent material regions and location 'E' is from the cracked weld region.

5.2.2. Crack Depth Reduction by EDM machining of the Cracked Weld Specimen.

5.2.2.1. *EBE Results from the EDM machined cracked weld specimen 21B for different thicknesses.*

The cracked weld specimen (21B) was EDM machined and the new surface was labelled 22B. The EDM machining removed 0.55 mm from the thickness of the 'as-received' cracked welded specimen. The EBE signal envelopes from this machined surface 22B are shown in **figures 5.2.28** and **5.2.29**. The EBE envelopes displayed a smooth rapid rise to an early maximum peak and then decreased to a flat central region before steadily falling off to zero. In contrast, the 'as-received' cracked weld surface displayed a signal peak late in the envelope (around 1.0 s for the parent material). On the weld and HAZ regions the peak moved to earlier times in the recording window. The EDM machining of the surface also increased the overall EBE signal amplitude. The summarised signal envelope parameters from the EDM machined surface 22B are shown in **figure 5.2.30**. The signal amplitude from the parent material region was the smallest and on location 'A' the signal displayed a small second peak. On the weld region, the steady decrease in signal amplitude on the right hand side of the envelopes changed. Instead of decreasing smoothly, the signal envelope becomes a plateau at the position of the weld material or crack. This occurred around 1.0 s on the envelope.

On further removal of 0.82 mm by EDM machining, the new surface (23B) exhibited signal envelopes similar to the envelops from the 22B surface (see **figures 5.2.31** and **5.2.32**). All the signals displayed a 'time of peak' around **0.7 s** on the envelope. The EBE envelope parameters are shown in **figure 5.2.33**. The parent steel, at locations 'A' and 'U', displayed the smallest signal amplitude, while location 'H', on the HAZ region, exhibited the largest signal amplitude at a value of 0.72 V. Close to the crack, on location 'K', the envelope shape displayed a change in the rate of decrease of the signal envelope similar to that noted on surface 22B. This position on the cracked weld surface also exhibited an energy minimum.

Surface 24B was created by machining off a total of 1.85 mm from the surface of the cracked weld specimen. The new surface displayed unusually low, broad EBE envelopes on both locations 'A' and 'U'. The EBE signal envelopes from surface 24B are shown in **figures 5.2.34** and **5.2.35**. The envelopes from positions 'A' and 'U' showed a sharp peak around **1.10 s** on the EBE envelope. The weld, crack and HAZ regions all displayed the characteristic early signal peak found on the previous EDM machined surface. The envelope parameters from surface 24B are shown in **figure 5.2.36**. The change in the EBE signal's rate of decrease at the edge of the envelope, on location 'K', was very small. The maximum signal voltage of **0.82 V** was exhibited on location 'I'. This was on the HAZ-parent material interface.

The EDM machined surface 25B displayed EBE envelopes which were essentially the same as the EBE envelopes from the previous surfaces and are shown in **figures 5.2.37** and **5.2.38**. **Figure 5.2.39** displays the EBE parameters. As with the previous EDM machined surfaces, the signal amplitude increased as the HAZ, weld and crack regions were approached. Away from the weld region, on location 'U', the EBE envelope displayed a sharp peak on the latter part of the envelope at around **1.07 s**. This caused the T_P and V_{MAX} values to occur later in the envelope and increase in magnitude respectively.

On surface 26B, the location furthest from the weld region displayed envelopes which again appeared double peaked. On the HAZ and weld region the EBE envelopes have a single peak, around **0.7 s** on the envelope. On further machining, the new surface 27B, displayed very similar envelopes to surface 26B. The EBE envelopes from both of these surfaces are shown in **figures 5.2.40**, **5.2.41** and **5.2.43**, **5.2.44** respectively. The signal envelope parameters, from these two surfaces, are shown in **figures 5.2.42** to **5.2.45** respectively. On the EDM machined surface 26B the crack mouth became blocked by resolidified material. On surface 27B the crack mouth was completely covered over by resolidified material. There was a faint imprint of the crack presence although it was difficult to be certain if this was the crack or merely the EDM tool imprint of the crack.

On the parent steel metal the EBE envelopes were doubled peaked, while the EBE envelopes from the HAZ, weld and cracked regions the envelopes were single peaked.

The maximum signal voltage and signal energy, both followed very similar trends for each of the EDM machined surfaces. The signal energy was found to be a maximum on the HAZ-parent material interface. The summarised EBE envelope parameters, from specific material regions, on the different machined surfaces are displayed in **appendix 4b**. The TIG weld was carried out within a 'funnel shaped' key. As progressive EDM machining reduced the thickness of the specimen, the size of the exposed weld mouth decreased, (see **figure 5.1.3**). This caused a shift in the relative position of the HAZ-weld and HAZ-parent material interface. This effect can be seen in the signal energy profile from each subsequent machined surface and is discussed later in **section 5.4**.

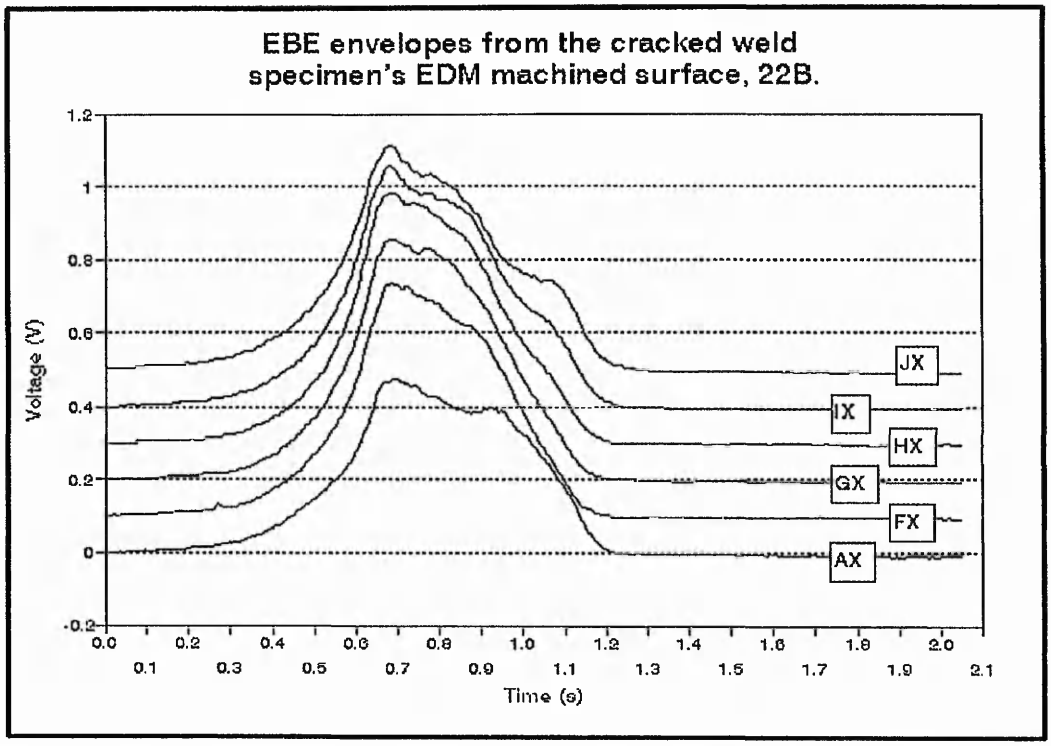


Figure 5.2.28 EBE signal envelopes from the cracked weld specimen's EDM machined surface 22B. Envelopes from locations on the parent steel ('A'), HAZ ('H') and weld seam ('J')are displayed.

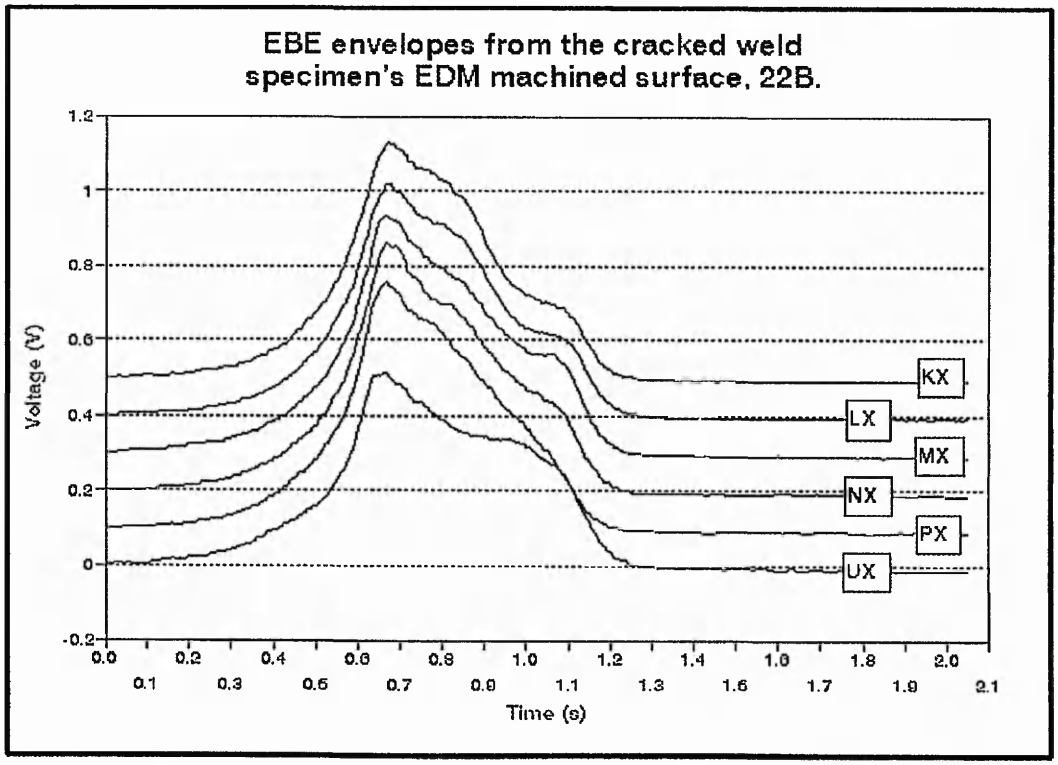


Figure 5.2.29 EBE signal envelopes from the cracked weld specimen's EDM machined surface 22B. Envelopes from locations on the parent steel ('U'), HAZ ('N') and cracked weld seam ('K')are displayed.

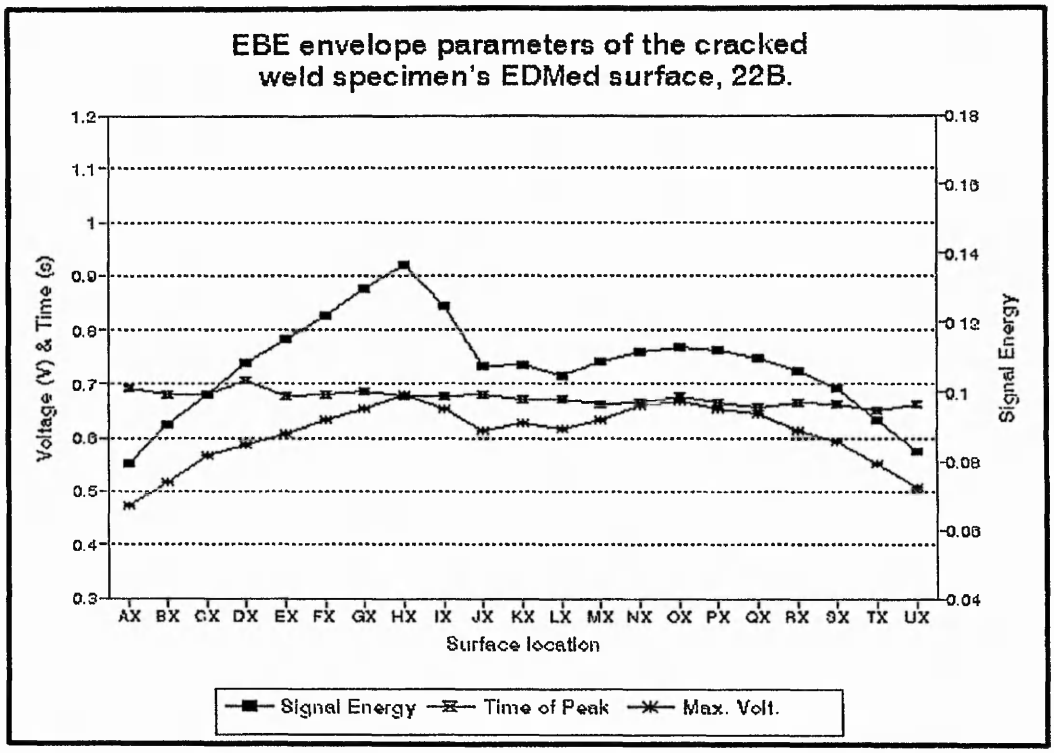


Figure 5.2.30 The EBE envelope's signal energy (units V^2s), time of peak (T_P) and maximum signal voltage (V_{MAX}) parameter profiles from the EDM machined surface 22B are displayed.

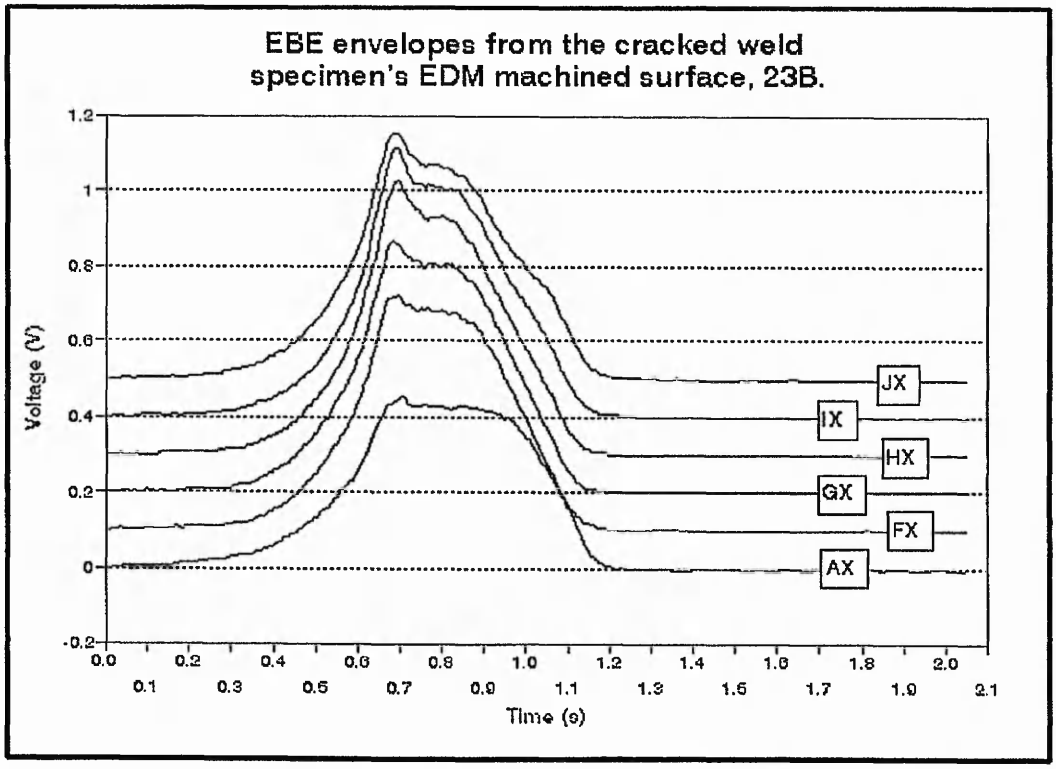


Figure 5.2.31 EBE signal envelopes from the cracked weld specimen's EDM machined surface 23B. Envelopes from locations on the parent steel ('A'), HAZ ('H') and weld seam ('J')are displayed.

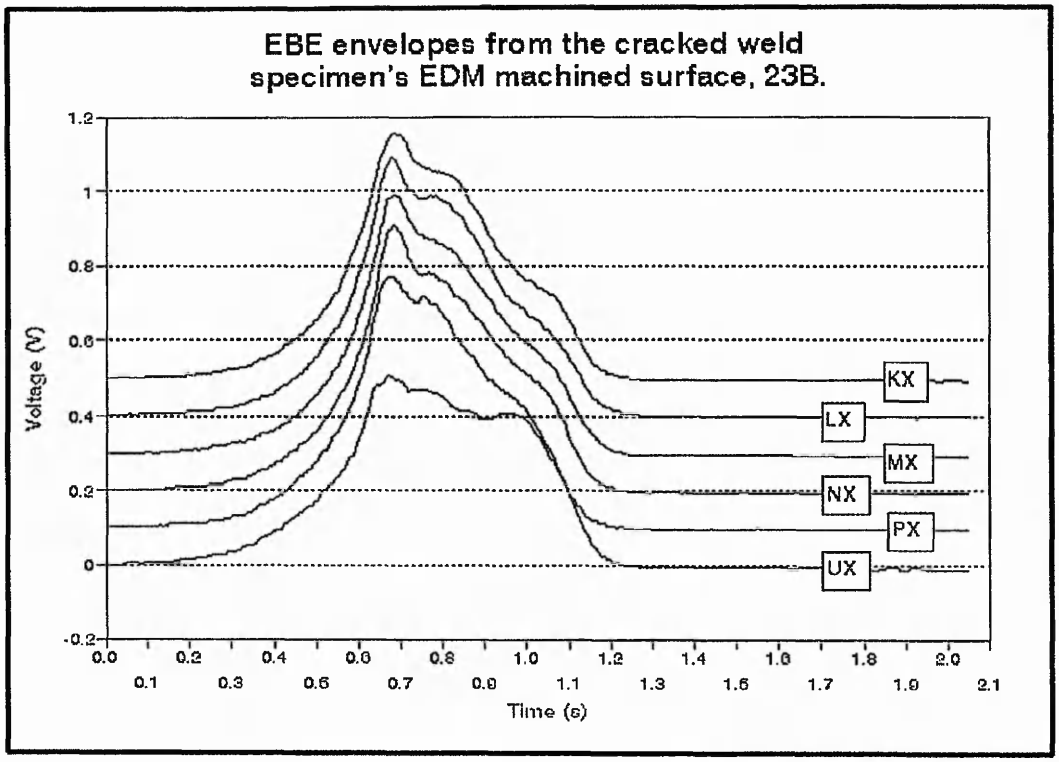


Figure 5.2.32 EBE signal envelopes from the cracked weld specimen's EDM machined surface 23B. Envelopes from locations on the parent steel ('U'), HAZ ('N') and cracked weld seam ('K')are displayed.

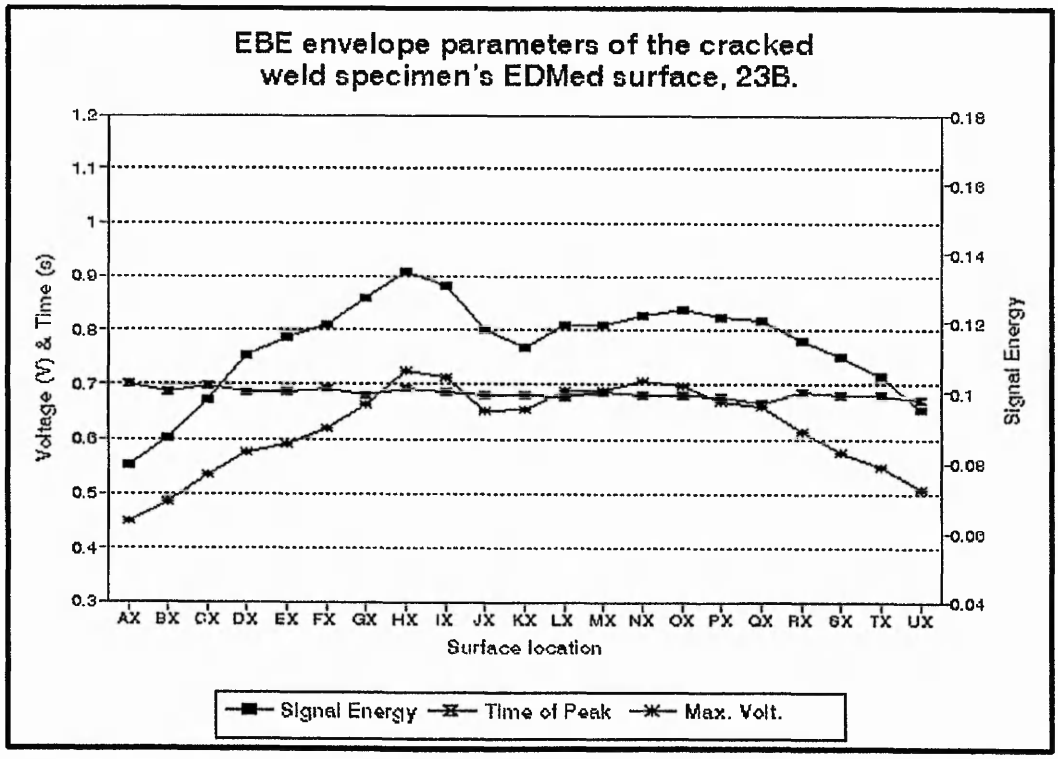


Figure 5.2.33 The EBE envelope's signal energy (units V^2s), time of peak (T_P) and maximum signal voltage (V_{MAX}) parameter profiles from the EDM machined surface 23B are displayed.

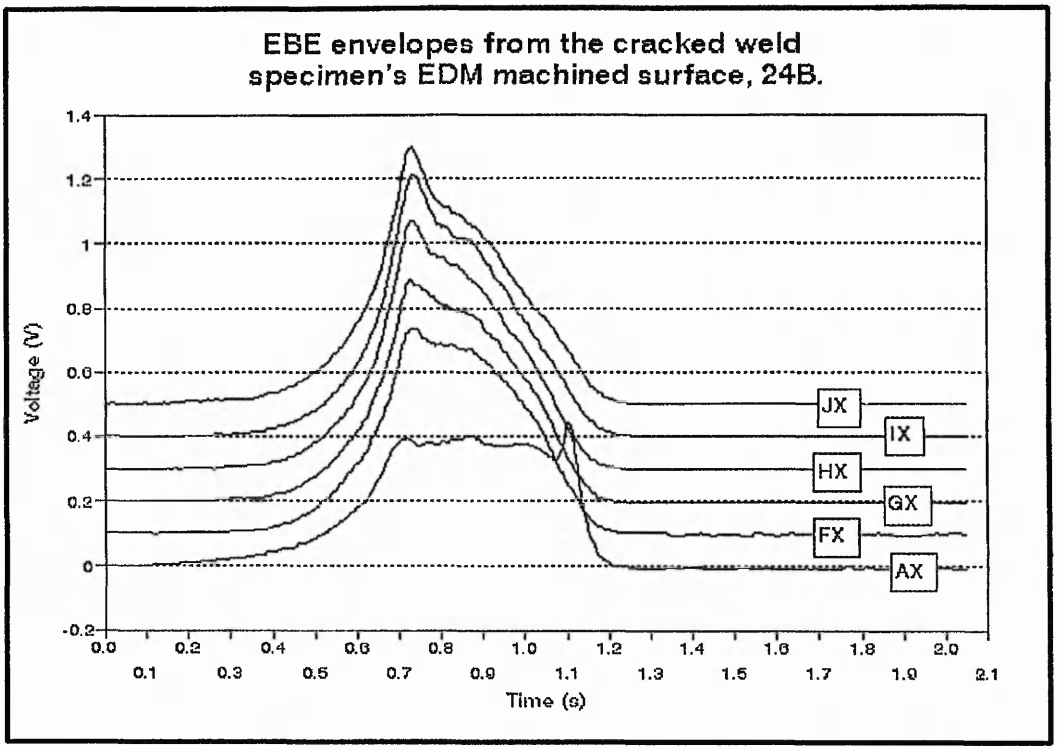


Figure 5.2.34 EBE signal envelopes from the cracked weld specimen's EDM machined surface 24B. Envelopes from locations on the parent steel ('A'), HAZ ('H') and weld seam ('J')are displayed.

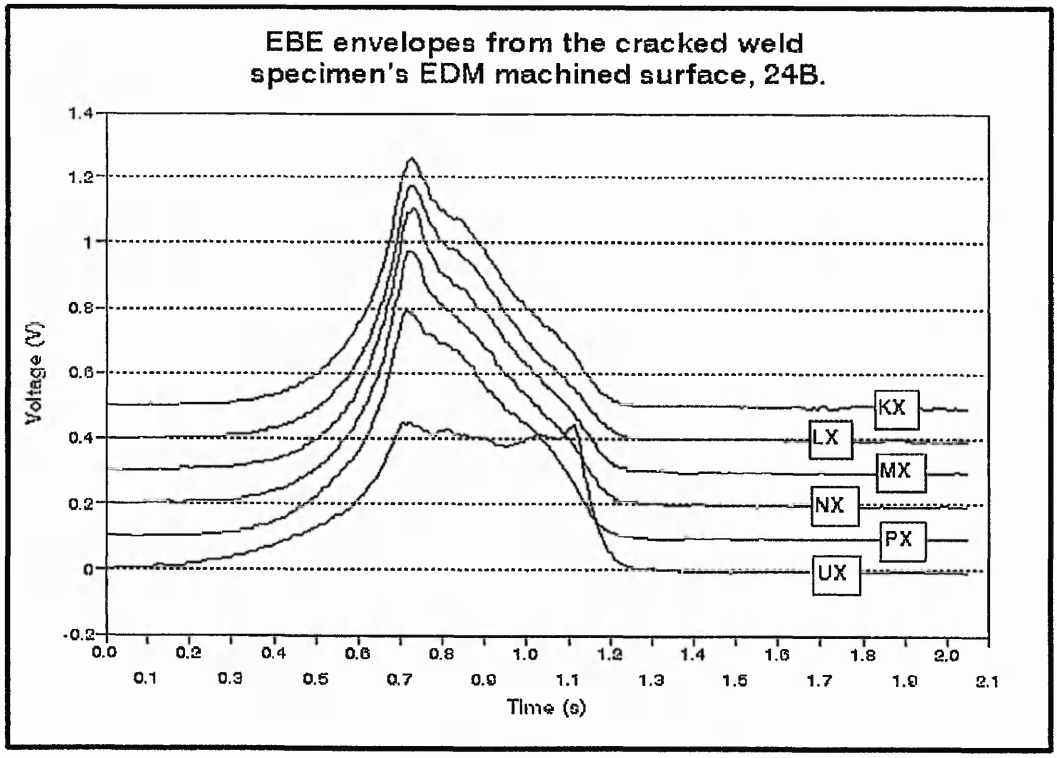


Figure 5.2.35 EBE signal envelopes from the cracked weld specimen's EDM machined surface 24B. Envelopes from locations on the parent steel ('U'), HAZ ('N') and cracked weld seam ('K')are displayed.

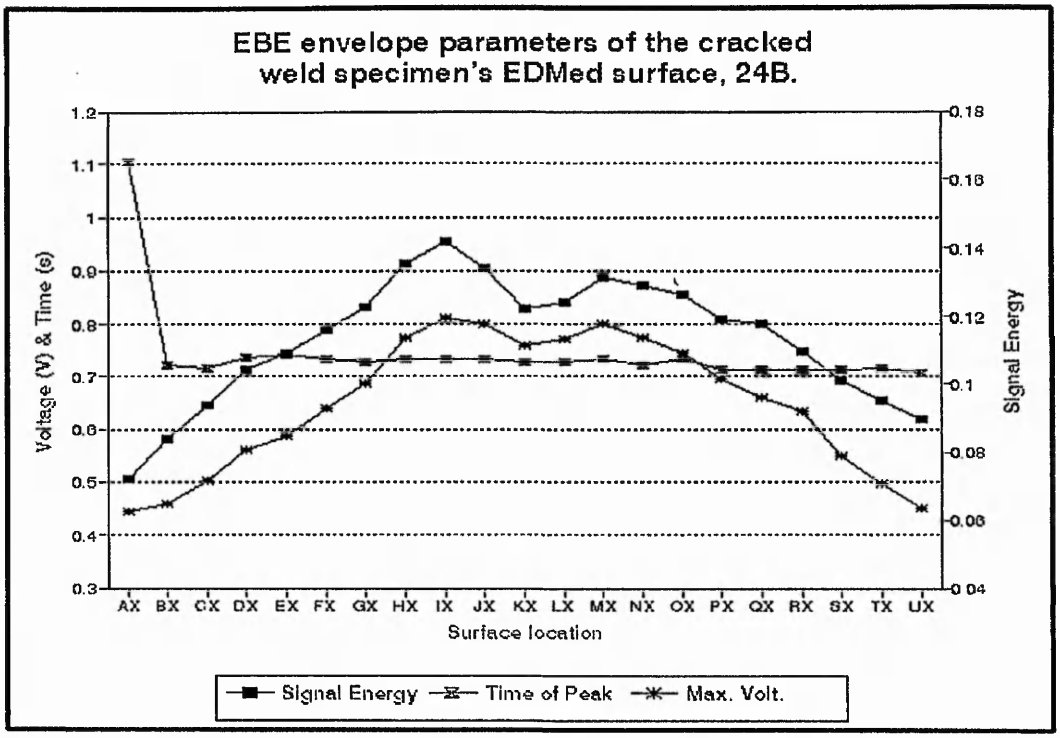


Figure 5.2.36 The EBE envelope's signal energy (units V^2s), time of peak (T_P) and maximum signal voltage (V_{MAX}) parameter profiles from the EDM machined surface 24B are displayed.

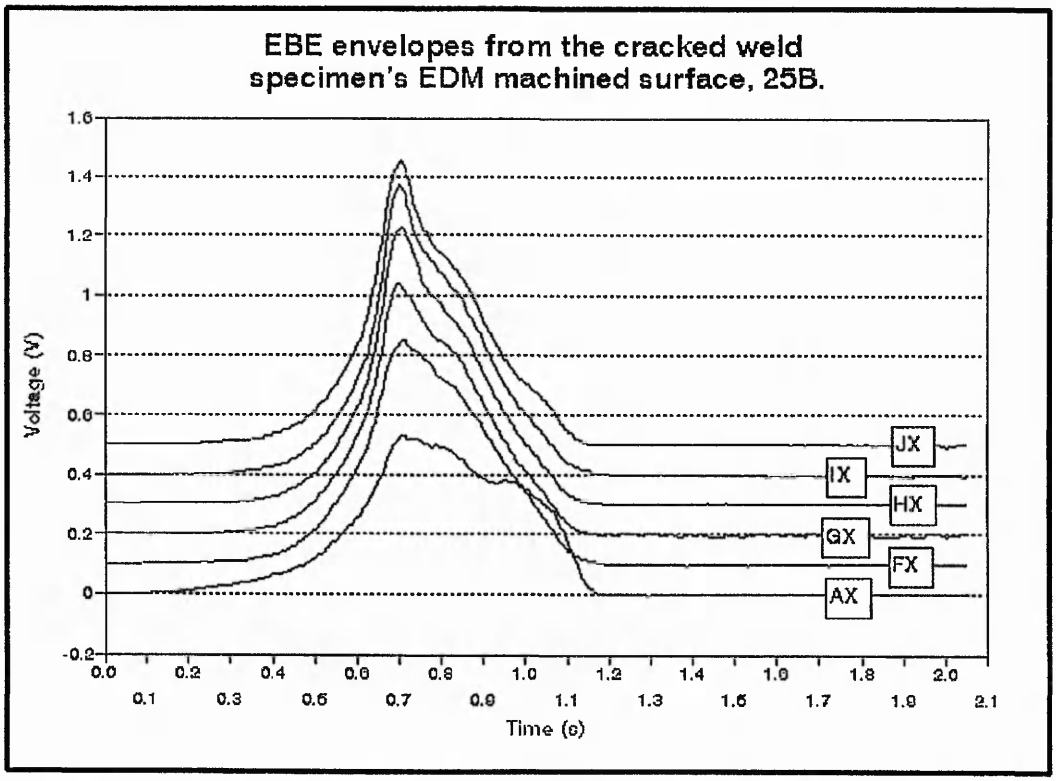


Figure 5.2.37 EBE signal envelopes from the cracked weld specimen's EDM machined surface 25B. Envelopes from locations on the parent steel ('A'), HAZ ('H') and weld seam ('J')are displayed.

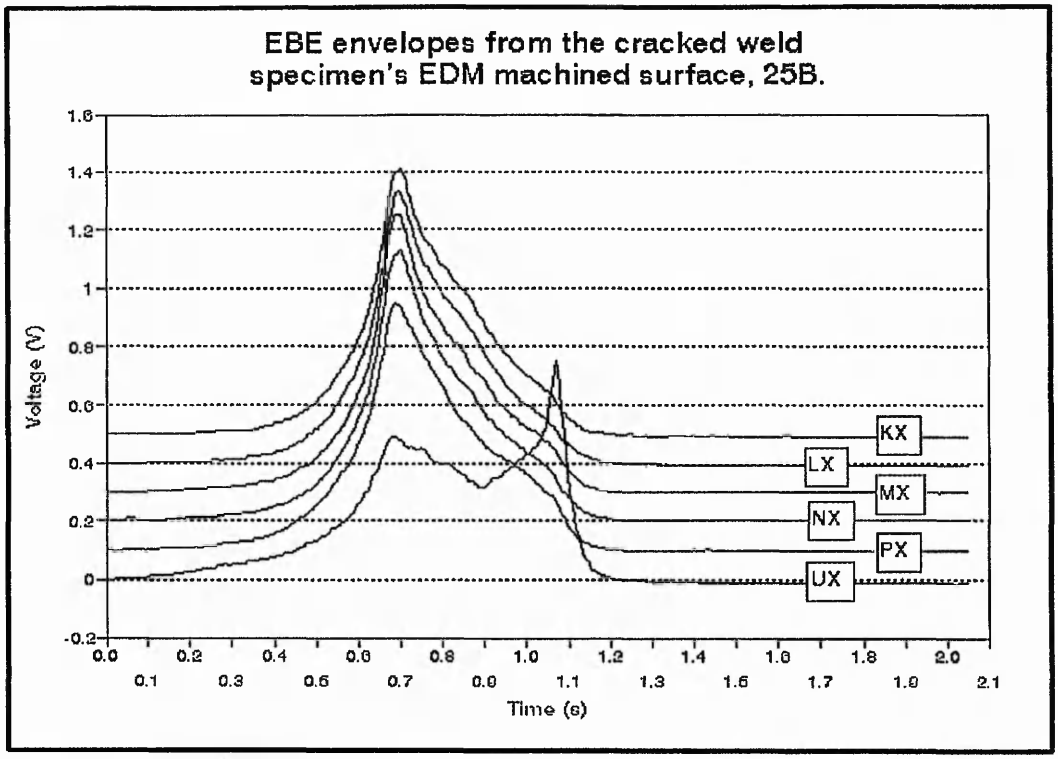


Figure 5.2.38 EBE signal envelopes from the cracked weld specimen's EDM machined surface 25B. Envelopes from locations on the parent steel ('U'), HAZ ('N') and cracked weld seam ('K')are displayed.

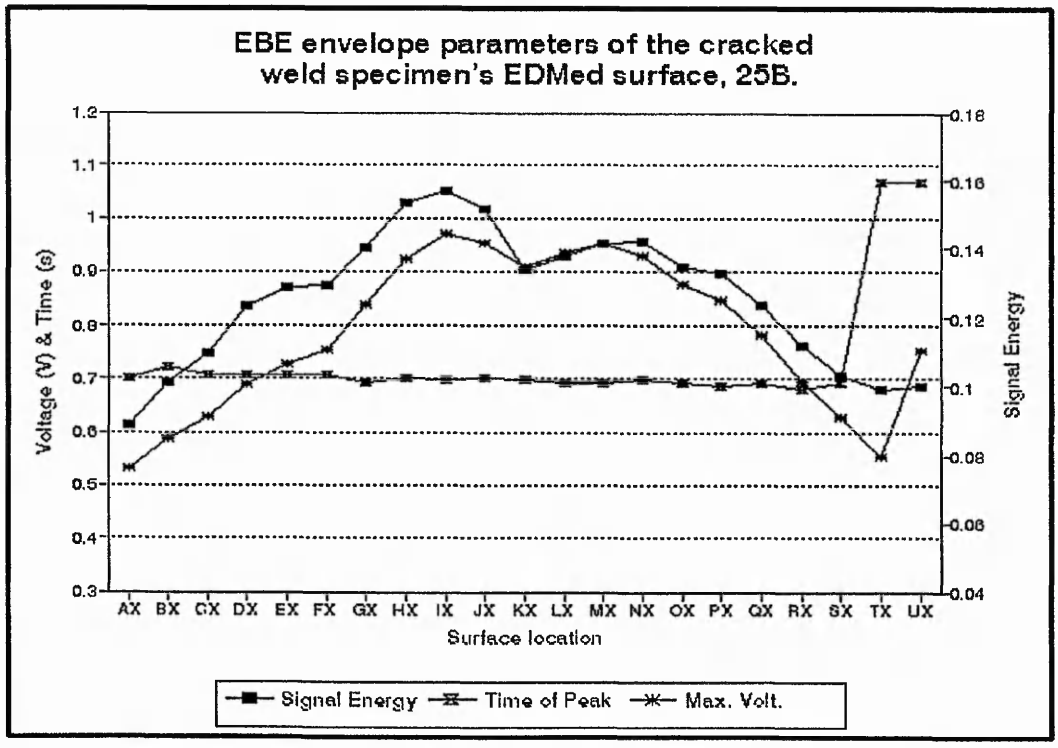


Figure 5.2.39 The EBE envelope's signal energy (units V^2s), time of peak (T_P) and maximum signal voltage (V_{MAX}) parameter profiles from the EDM machined surface 25B are displayed.

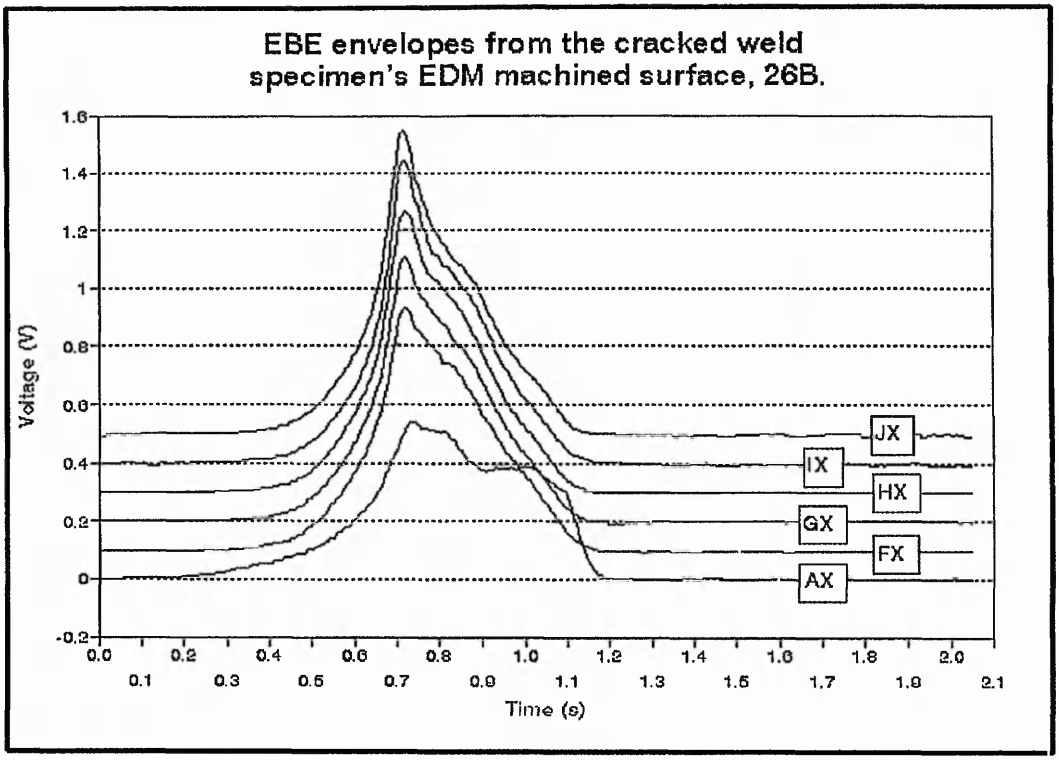


Figure 5.2.40 EBE signal envelopes from the cracked weld specimen's EDM machined surface 26B. Envelopes from locations on the parent steel ('A'), HAZ ('H') and weld seam ('J')are displayed.

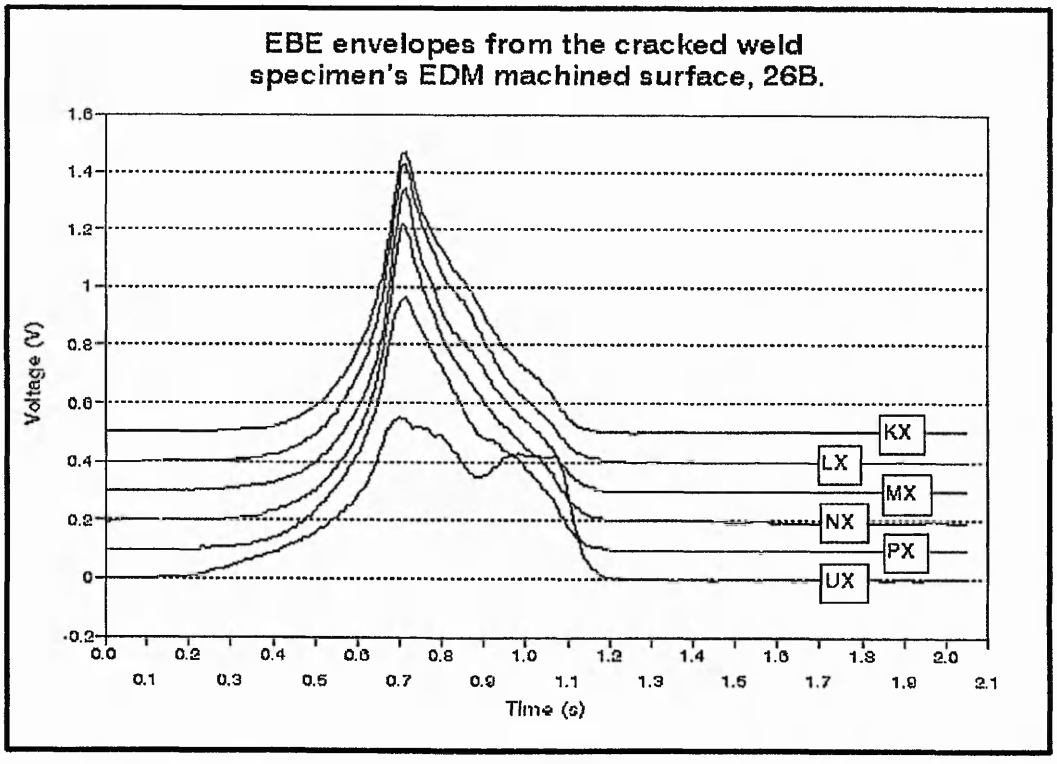


Figure 5.2.41 EBE signal envelopes from the cracked weld specimen's EDM machined surface 26B. Envelopes from locations on the parent steel ('U'), HAZ ('N') and cracked weld seam ('K')are displayed.

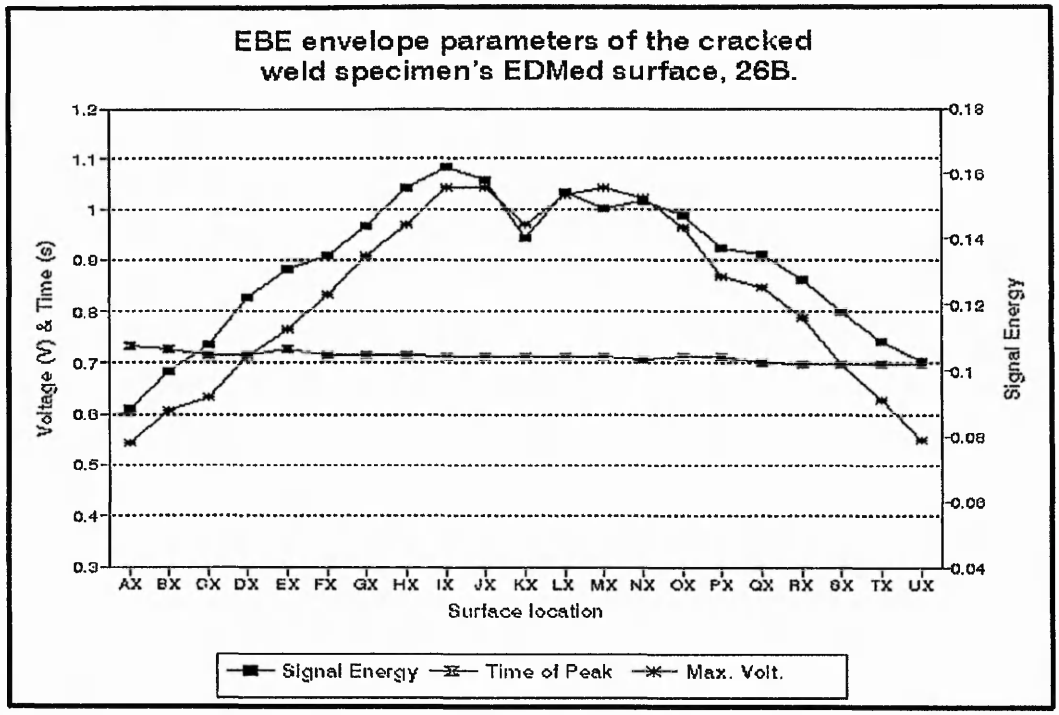


Figure 5.2.42 The EBE envelope's signal energy (units V^2s), time of peak (T_P) and maximum signal voltage (V_{MAX}) parameter profiles from the EDM machined surface 26B are displayed.

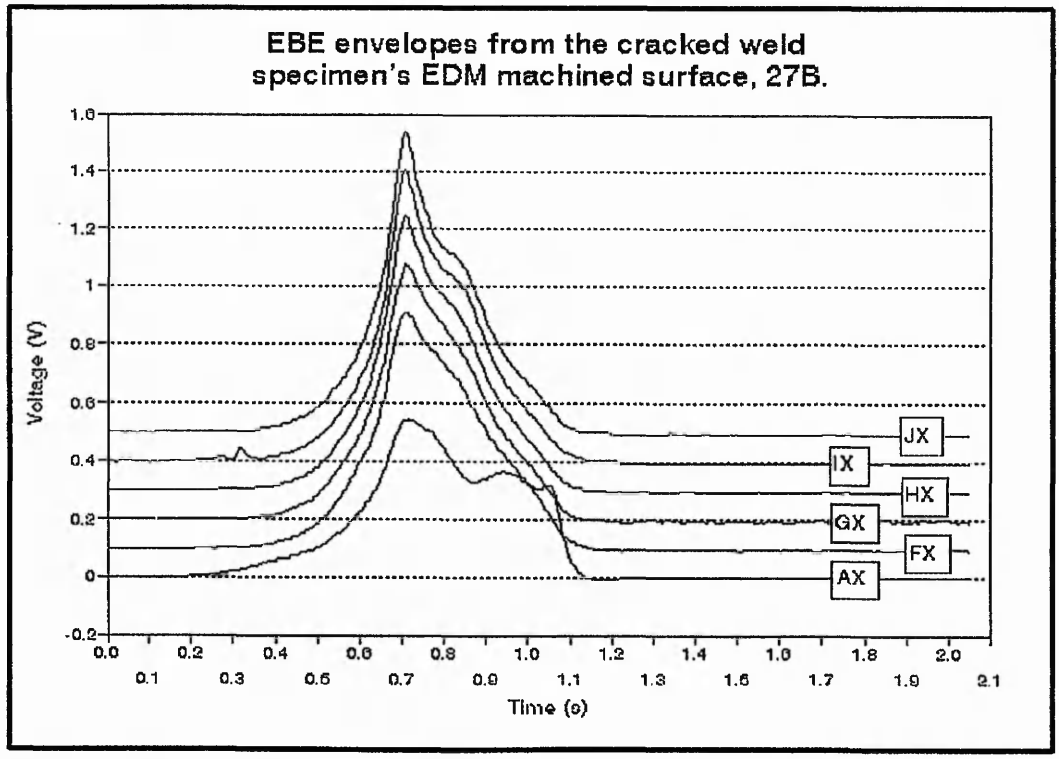


Figure 5.2.43 EBE signal envelopes from the cracked weld specimen's EDM machined surface 27B. Envelopes from locations on the parent steel ('A'), HAZ ('H') and weld seam ('J')are displayed.

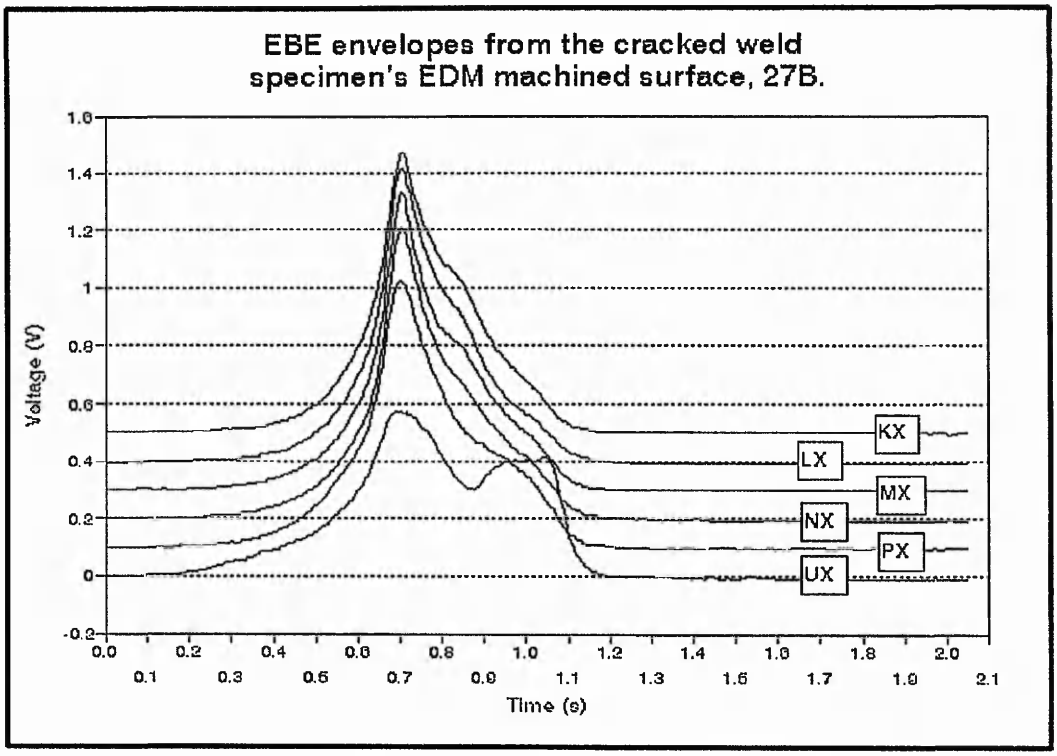


Figure 5.2.44 EBE signal envelopes from the cracked weld specimen's EDM machined surface 27B. Envelopes from locations on the parent steel ('U'), HAZ ('N') and cracked weld seam ('K')are displayed.

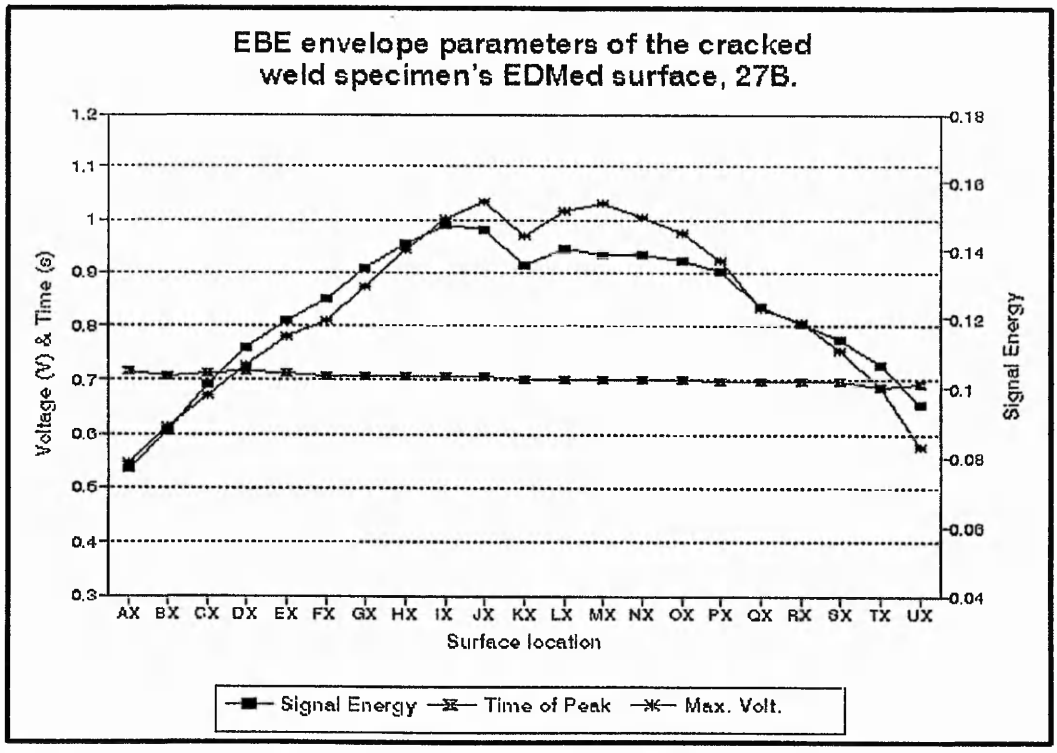


Figure 5.2.45 The EBE envelope's signal energy (units V^2s), time of peak (T_P) and maximum signal voltage (V_{MAX}) parameter profiles from the EDM machined surface 27B are displayed.

5.2.2.2. *ABE Results from the EDM machined cracked weld specimen 21B for different thicknesses.*

The 'as-received' cracked weld surface (21B) was EDM machined and the new surface generated was labelled 22B. The ABE signal envelopes detected from the cracked weld specimens EDM machined surfaces are considered in this section. The ABE signal envelopes from the machined surface 22B are shown in **figure 5.2.46**. The ABE envelope appeared as a double peaked envelope, with a first peak which was smaller than the second. The second peak had a single large spike, with several other small spikes present on the second peak. On the 22B surface, the spikes on the ABE envelope were taken as the maximum signal amplitude.

On further machining (surface 23B) the ABE signals appeared as spike free double peaked envelopes, as shown in **figure 5.2.47**. As there were no spikes covering the maximum peak the V_{MAX} was taken as the second peak. However, on further machining, surface 24B exhibited ABE signals which contained spikes on the latter part of the envelope again. The ABE envelopes from the 24B surface are shown in **figure 5.2.48**. The spikes recorded on this surface were greatly reduced in number compared to the 22B surface. On the majority of locations, it was possible to differentiate the spikes from the maximum second peak of the ABE envelope. In such cases the maximum second peak was used for the T_P and V_{MAX} parameters. These parameters are displayed in **table 5.2.2**.

On machining of the surface 24B, the ABE signals from the new surface (25B) displayed a double peaked form, the second peak being larger than the first. These ABE envelopes are shown in **figure 5.2.49**. On location 'E' the ABE signal displayed a spike after the maximum second peak. The spike was smaller than the second peak itself. Also, location 'F' provided the largest envelope detected from any of the EDM machined surfaces studied. On the remaining positions the ABE envelopes resumed their normal size.

Surfaces 26B and 27B, both displayed ABE envelopes which were doubled peaked and similar to the ABE envelope from the previous surfaces. The envelopes are shown in **figures 5.2.50** and **5.2.51**. The ABE signals from location 'E' displayed a low envelope on each of the EDM machined surfaces from the cracked weld specimen (21B). The ABE signal parameters from each of the EDM machined surfaces are listed in **table 5.2.2** and discussed in detail in **section 5.4**.

Surface.	Averaged T_P (s)	T_P Range (s)	Averaged V_{MAX} (V)	V_{MAX} Range (V)
22B	1.16	1.12- 1.19	1.74	1.32- 2.16
23B	1.13	1.11- 1.13	1.28	1.12- 1.39
24B	1.13	1.11- 1.14	1.53	1.23- 2.03
25B	1.10	1.10- 1.10	1.48	1.39- 1.64
26B	1.12	1.10- 1.14	1.55	1.39- 1.71
27B	1.08	1.08- 1.09	1.58	1.43- 1.76

Surface.	Averaged Signal Energy (V^2s)	Signal Energy Range (V^2s)
22B	0.285	0.239- 0.347
23B	0.269	0.212- 0.317
24B	0.344	0.269- 0.441
25B	0.335	0.266- 0.534
26B	0.380	0.311- 0.442
27B	0.325	0.285- 0.430

Table 5.2.2 ABE signal data from the EDM machined cracked weld specimen (21B), showing 'time of peak' (T_P), 'maximum signal voltage' (V_{MAX}) and signal energy obtained from the various surface layers.

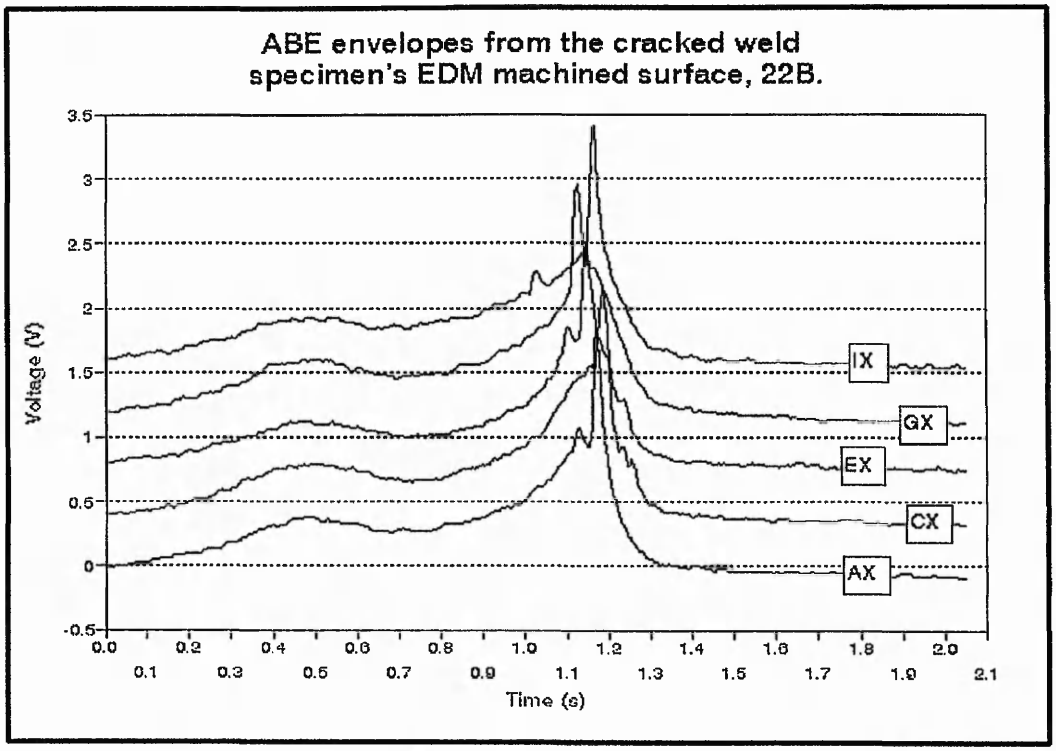


Figure 5.2.46 ABE signal envelopes from the cracked weld specimen's EDM machined surface 22B. Envelopes 'A' and 'I' are from the parent material regions and envelope 'E' is from the cracked weld region.

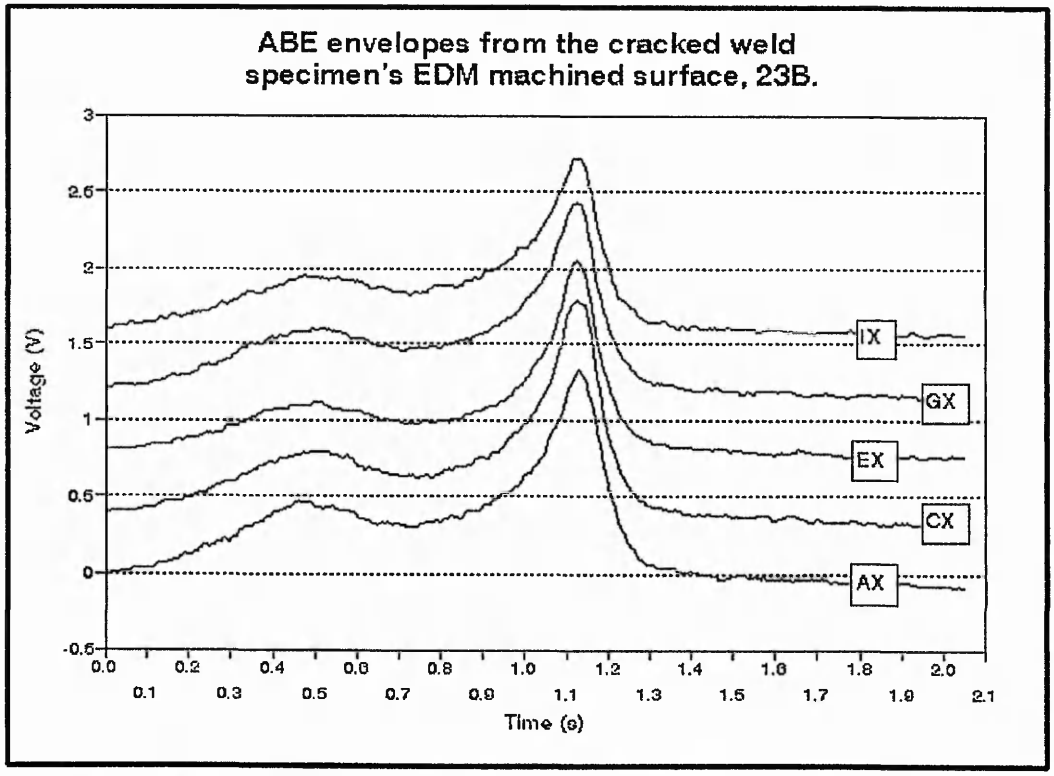


Figure 5.2.47 ABE signal envelopes from the cracked weld specimen's EDM machined surface 23B. Envelopes 'A' and 'I' are from the parent material regions and envelope 'E' is from the cracked weld region.

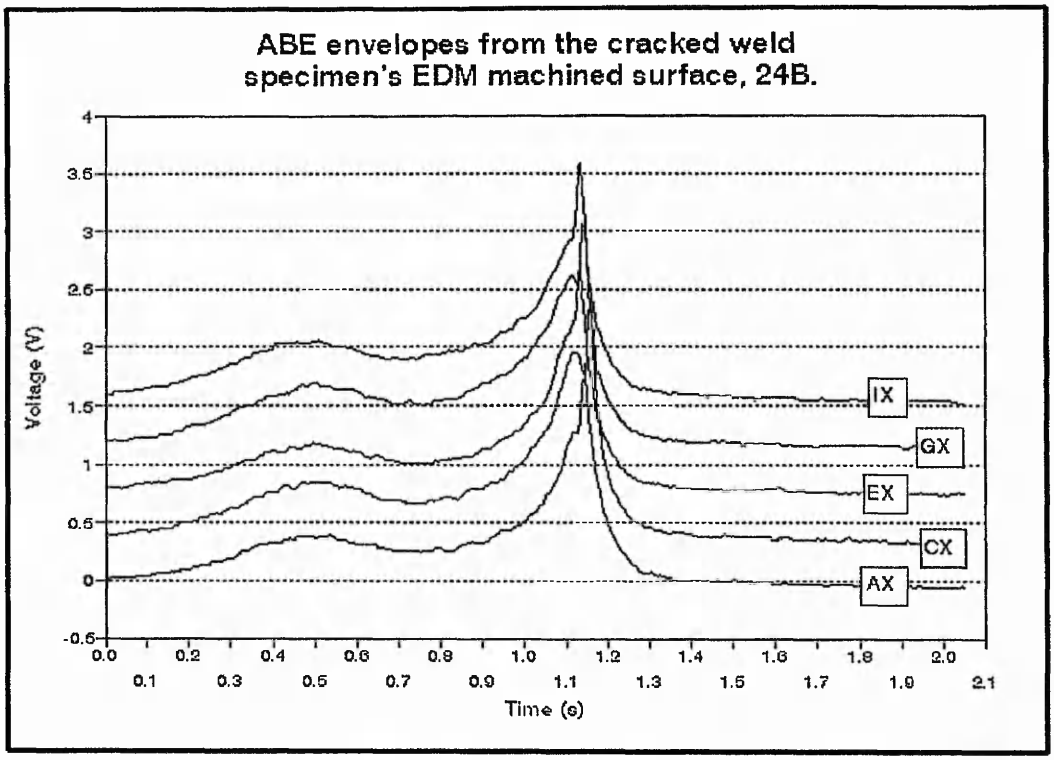


Figure 5.2.48 ABE signal envelopes from the cracked weld specimen's EDM machined surface 24B. Envelopes 'A' and 'I' are from the parent material regions and envelope 'E' is from the cracked weld region.

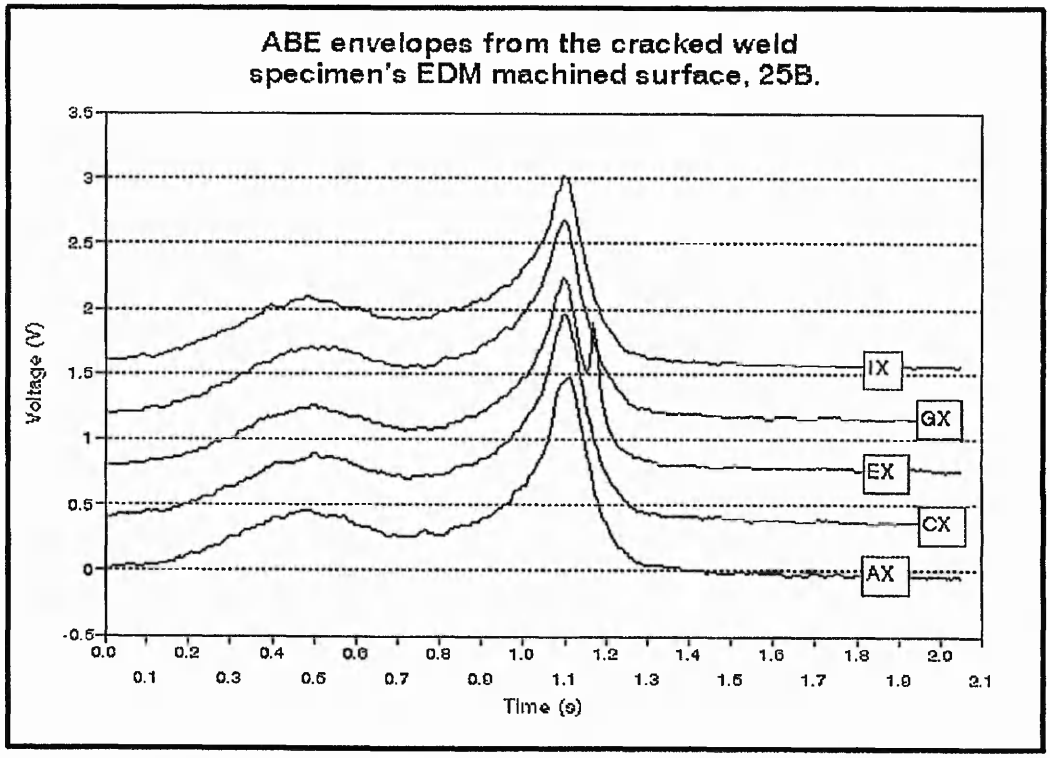


Figure 5.2.49 ABE signal envelopes from the cracked weld specimen's EDM machined surface 25B. Envelopes 'A' and 'I' are from the parent material regions and envelope 'E' is from the cracked weld region.

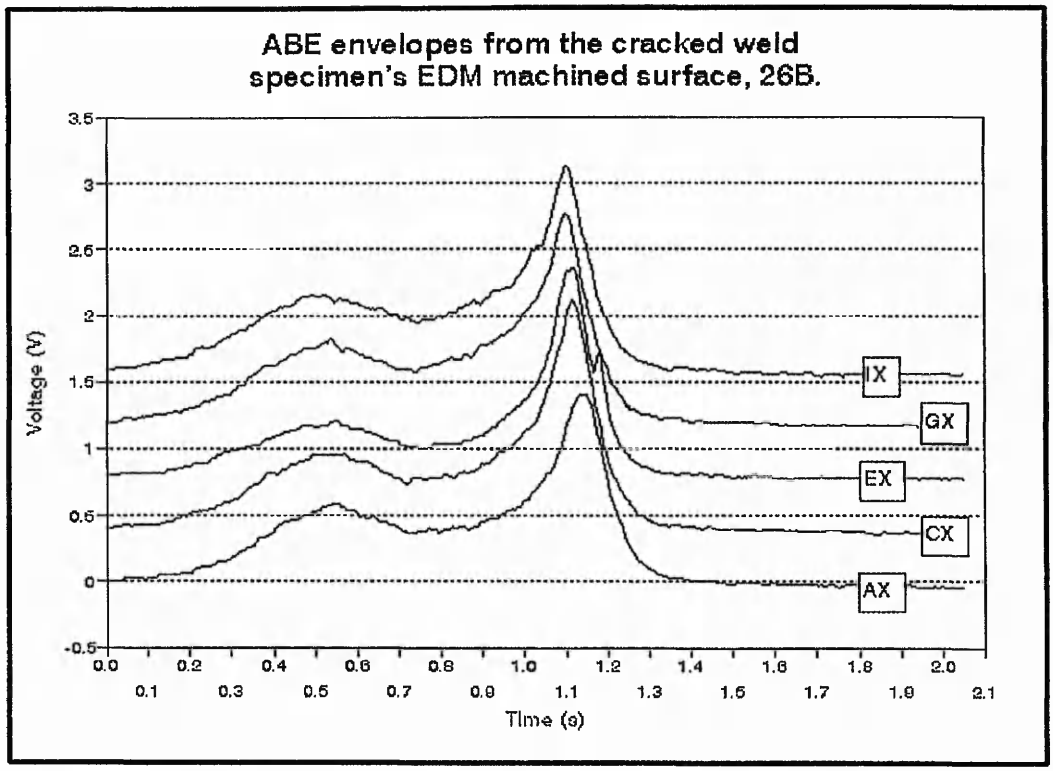


Figure 5.2.50 ABE signal envelopes from the cracked weld specimen's EDM machined surface 26B. Envelopes 'A' and 'I' are from the parent material regions and envelope 'E' is from the cracked weld region.

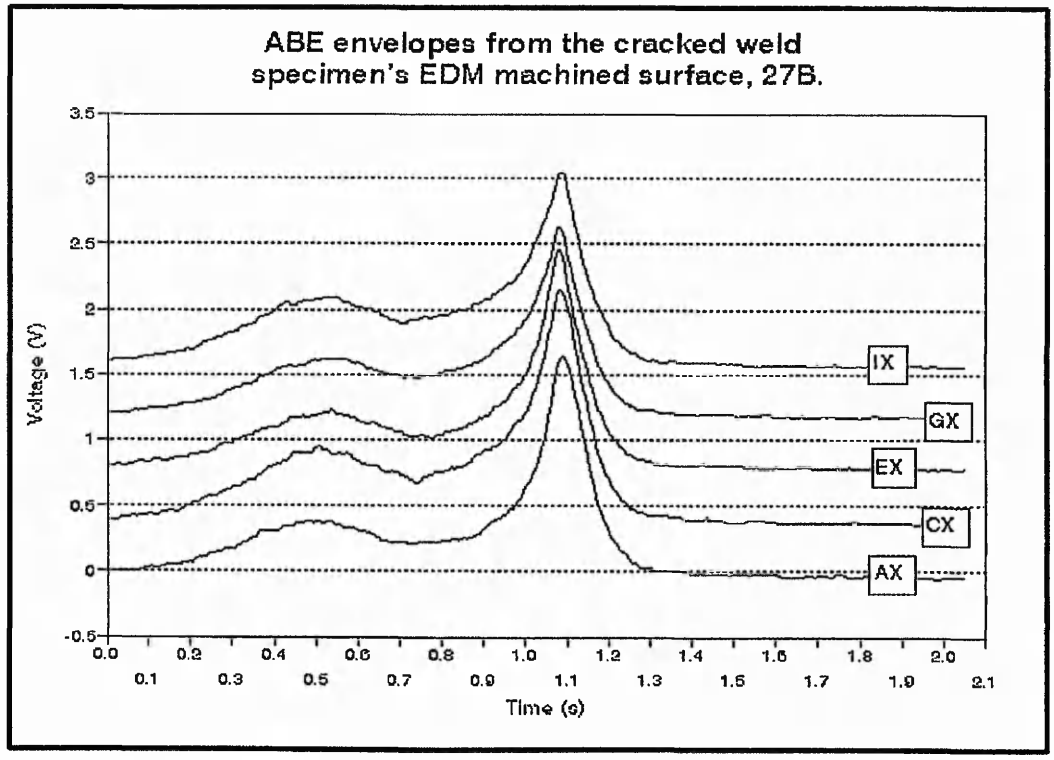


Figure 5.2.51 ABE signal envelopes from the cracked weld specimen's EDM machined surface 27B. Envelopes 'A' and 'I' are from the parent material regions and envelope 'E' is from the cracked weld region.

5.3. MAGNETIC LEAKAGE FIELD FROM THE MACHINED CRACKED WELD STEEL SPECIMENS' SURFACES.

The GMR sensor and the Hall probe, described in **section 4.3**, were used to measure the leakage field on the machined surfaces of both the cracked weld specimens, 21A and 21B. Both specimens were magnetised using the standard Barkhausen system and the remanent leakage field was measured on each of the subsequent machined surfaces.

Reduction of the crack depth, by machining away the top surface layer of the specimen, was expected to affect the leakage field pattern. The reduction in the specimen volume and change in the permeability due to the surface machining was expected to have some effect on the magnetic leakage field profiles. The effective reduction in the crack depth by surface machining was expected to be detectable in the leakage field profile. Both specimens' surfaces, between locations 'A' and 'U', were subdivided into millimetre spacing. Remanent leakage field measurements were recorded every millimetre across the studied region as is described in **section 4.3**.

5.3.1. Magnetic Leakage Field Patterns from the Planed Cracked Weld Specimen's Surfaces.

The magnetic leakage field (MLF) patterns detected on the plane machined surfaces of the cracked weld specimen 21A are shown in **figures 5.3.1** to **5.3.3**. Results from the planed machined surface (22A) were considered and discussed in **section 4.3**, however, they will again be considered in this section to give a more complete overview of the effect of crack depth and specimen thickness reduction.

On the planing of the 'as-received' surface, the leakage field pattern detected by the GMR and Hall probe sensors appeared very similar. Surface 22A was created by planing 0.5 mm from the thickness of the 'as-received' specimen. The magnetic leakage field

pattern from this planed surface (22A) is shown in **figure 5.3.1** and summarised in **table 5.3.1**. On the edge of the detected region, furthest from the weld, HAZ and cracked region, the leakage field appeared constant at around **0.24 mT (±0.01 mT)** or **2.0V (±0.1 V)**. As the sensor approached the cracked weld region, the leakage field increased in magnitude to a value of **0.45 mT or 3.9 V**. On further planing a thickness of 0.47 mm was removed (total 0.97 mm), and the new surface (23A) displayed an increased leakage field pattern compared to surface 22A, (see **figure 5.3.1**). At locations 0 mm and 40 mm the leakage field was recorded as **0.41 mT** or **1.1 V**. The GMR sensor showed a gradual increase in the leakage field, which began from the edge of the studied region. Traversing towards the central region on the surface, the rate at which the leakage field increased changed rapidly at the 10 mm and 30 mm locations. A maximum leakage field (**0.70 mT** or **4.3 V**) was detected on the 21 mm location, directly above the visible crack.

On planed surface 24A the leakage field appeared more spread when compared to the leakage field pattern from surface 22A (**figure 5.3.2**). The leakage field pattern from the parent material region, the 0 mm and 40 mm positions, (**0.34 mT** or **1.7 V**) appeared to gradually increase as the sensors were moved closer to the cracked region. The maximum leakage field was detected on the 21 mm location, at a value of **0.55 mT** or **3.94 V** (see **table 5.3.1**). On the surface 25A the leakage field measurements were lost due to computer failure. However, surface 26A, with the total crack depth reduced by 2.70 mm, showed a leakage pattern (**figure 5.3.2**) which appeared to possess a plateau between the 16 mm and 22 mm positions. The field was found to steadily increase as the weld region was approached. On 10 mm and 26 mm locations, the leakage field began to sharply increase and reach a maximum value of **0.60 mT** or **3.0 V**, on the central region of the specimen. The lack of a sharp leakage field profile may be accounted for by the presence of a lip, resulting from the planing process, covering the crack mouth.

The leakage field from the planed surfaces 27A and 28A, shown in **figure 5.3.3**, displayed field patterns which were similar to that found on the planed machined surface 24A. The magnetic leakage field on the parent material region of surface 27A, at 0 mm and 40 mm locations, exhibited a field strength of **0.49 mT** or **0.5 V**. The maximum leakage field was detected above the 22 mm position and found to be **0.82mT** or **4.19 V**

for the 27A surface. Leakage field from surface 28A is also shown in **figure 5.3.3**. The surface 28A displayed no visible signs of the crack. A remanent field pattern from this surface showed a maximum on the 22 mm location, with a field value of **0.88mT** or **4.8V**. Furthest away from the weld, on 0 mm and 40 mm locations, the leakage field was detected at a value of **0.48 mT** or **0.7 V**. Using the Hall probe sensor an increased rate of change in the leakage field profile was noticeable on the 12 mm and 30 mm locations. These two locations were very close to the HAZ and metal interface.

Planed machined surface and thickness removal.		Magnetic leakage field measurements from the parent material region.		Magnetic leakage field measurements from the crack location.	
Surface label.	Machined layer.	Hall probe (mT)	GMR (V)	Hall probe (mT)	GMR (V)
22A	0.5 mm	0.24 ±0.01	2.0 ±0.1	0.45 ±0.01	3.8 ±0.1
23A	0.47 mm	0.41	1.1	0.70	4.3
24A	0.54 mm	0.33	1.7	0.55	3.9
25A	0.52 mm	-	-	-	-
26A	0.67 mm	0.39	0.7	0.60	3.0
27A	0.42 mm	0.49	0.5	0.82	4.2
28A	0.51 mm	0.48	0.7	0.88	4.8

Table 5.3.1 Summary of magnetic leakage field data from the various planed surfaces of the cracked weld specimen (21A). Magnetic leakage field data recorded above the crack and on the parent material locations are displayed. The specimen thickness removed between each machining process is also listed from **table 5.1.1**.

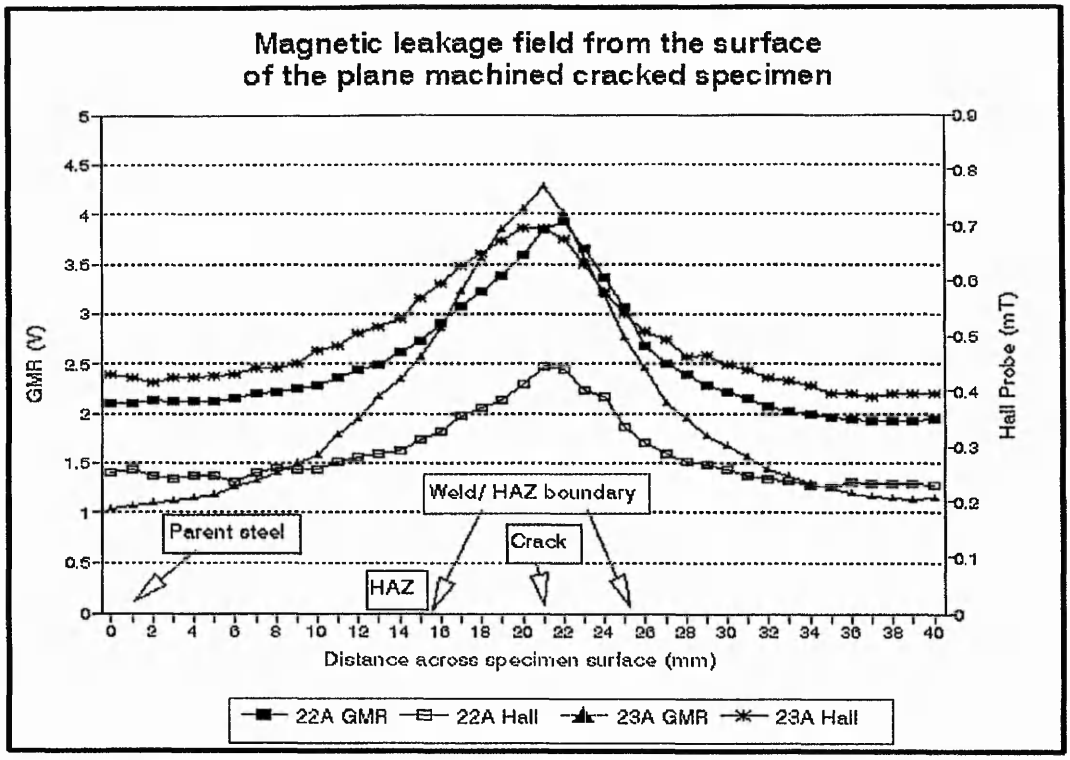


Figure 5.3.1 Magnetic leakage field from the cracked weld specimen's planed surfaces 22A and 23A. Leakage field detected using GMR sensor (units voltage) and Hall probe (units milliTesla).

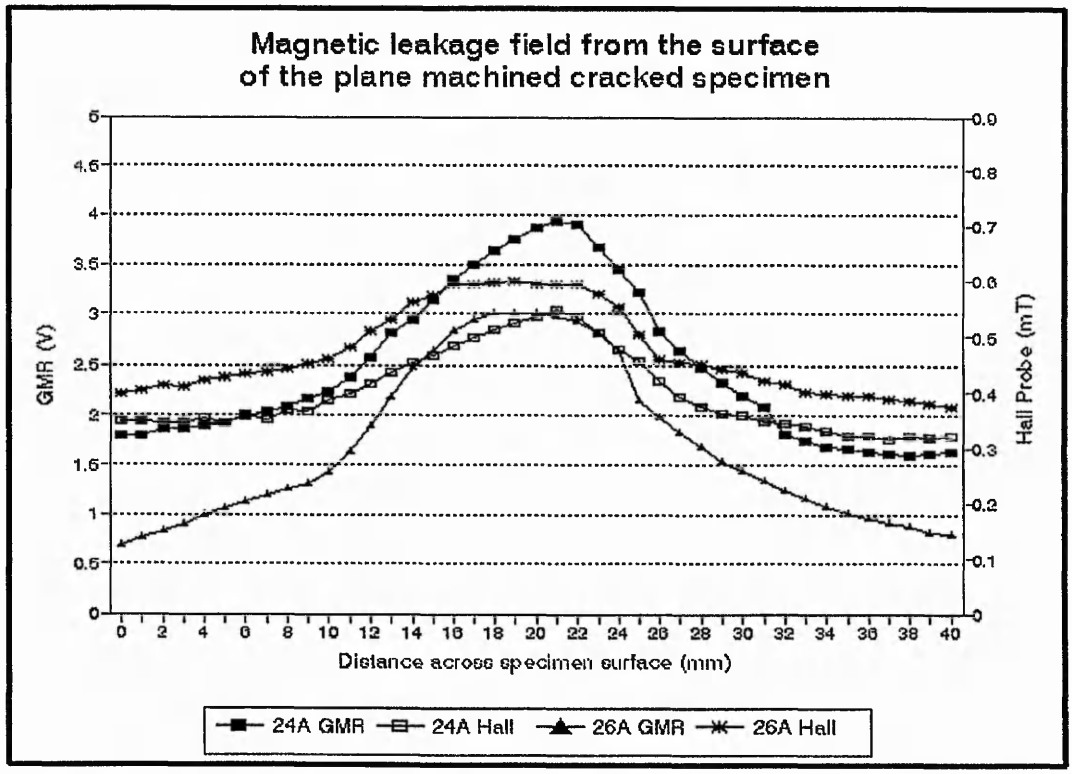


Figure 5.3.2 Magnetic leakage field from the cracked weld specimen's planed surfaces 24A and 26A. Leakage field detected using GMR sensor (units voltage) and Hall probe (units milliTesla).

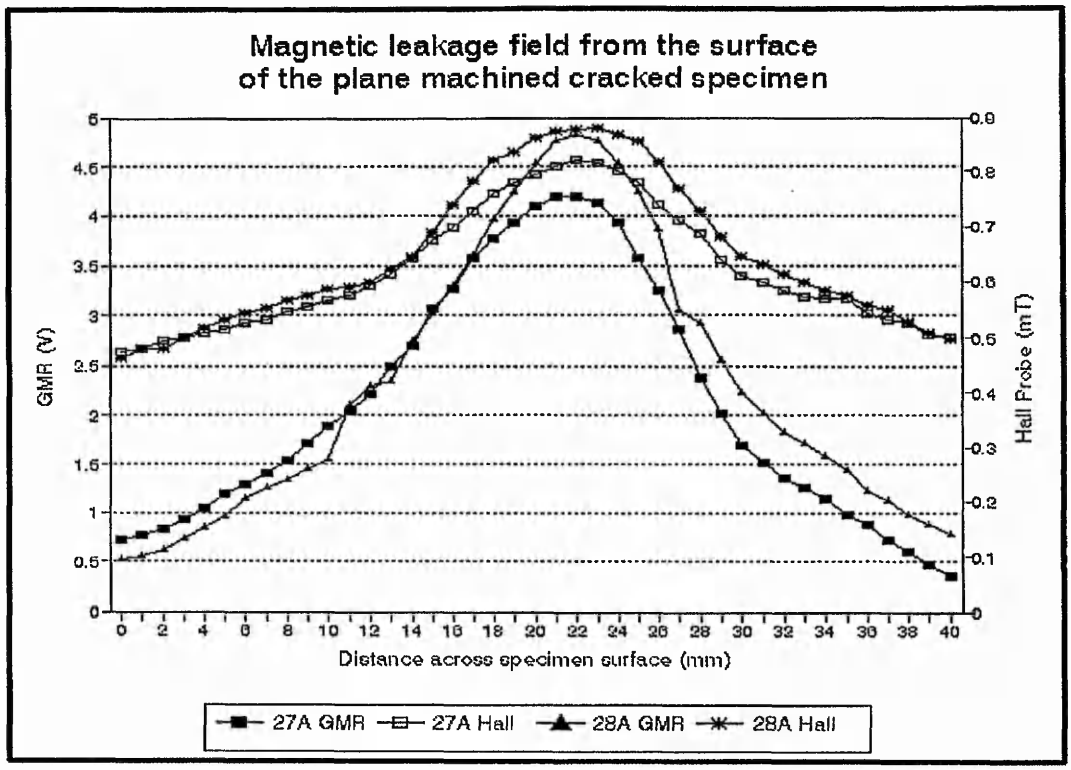


Figure 5.3.3 Magnetic leakage field from the cracked weld specimen's planed surfaces 27A and 28A. Leakage field detected using GMR sensor (units voltage) and Hall probe (units milliTesla).

5.3.2. Magnetic Leakage Field Patterns from the EDM Machined Cracked Weld Specimens Surfaces.

On visual inspections the EDM machined surfaces possessed a matt finish. This texture was consistently reproduced on each of the EDM machined surfaces. The magnetic leakage field detected on the EDM machined surface 22B is shown in **figure 5.3.4** and has also been discussed in **section 4.3**. A crack depth and surface thickness of 0.55 mm were removed using EDM machining. Furthest away from the cracked weld region, at locations 0 mm and 40 mm, the leakage field of **0.24 mT (±0.01 mT)** or **1.9 V (±0.1 V)** was recorded. Above the surface crack a leakage field of **0.55 mT** or **4.4 V** was recorded. A summary of the leakage field from each of the EDM machined surfaces is provided in **table 5.3.2**. Surface 23B was created by the removal of a total thickness of 1.37 mm from the 'as-received' surface. The magnetic leakage field from the new surface (23B) displayed a leakage field value of **0.46 mT** or **0.4 V** on the parent material region at the 0 mm and 40 mm locations. The leakage field on the location of the surface crack (21 mm location) exhibited the largest field at a value of **0.88mT** or **4.6 V**.

On further removal of 0.24 mm thickness a new surface was generated and labelled 24B. **Figure 5.3.5** shows the leakage field pattern detected using both the GMR and Hall probe sensors on surfaces **24B** and **25B**. The leakage field from surface 24B was very similar to the field from surface 23B. The surface removal, in this case, altered the magnetic leakage field pattern very slightly. Above the crack mouth, surface 24B displayed the largest leakage field, with a value of **0.89 mT** or **4.7 V**. Surface 25B was generated by EDM machining a further 0.47 mm off (total thickness of 2.08 mm) the thickness of the cracked specimen. The leakage field (also shown in **figure 5.3.5**) on the parent material region, at positions 0 mm and 40 mm, displayed a field value of approximately **0.48 mT** or **0.8 V**. On the 22 mm location, very close to the crack mouth, the leakage field was found to be a maximum, with a value of **0.84 mT** or **4.6 V**.

Removal of a further 0.37 mm surface layer generated surface 26B. On surface 26B an overall decrease in the magnitude leakage field was recorded and is shown in **figure**

5.3.6 (summarised in **table 5.3.2**). The crack mouth was partially covered with resolidified material, though the position of the crack could still be seen. A leakage field value of **0.40 mT** or **1.0 V** was recorded at the edges of the studied region. Above the surface crack, a leakage field value of **0.66 mT** or **3.8 V** was recorded. Removal of a further of 0.38 mm from surface 26B generated a new surface which was labelled 27B. The crack mouth was now totally covered by the resolidified layer and the leakage field from this new surface is shown in **figure 5.3.6**. The field value from the crack mouth was measured to be **0.67 mT** or **3.3 V**. The shape of the magnetic leakage field pattern became wider as the machined specimen's thickness decreased. The width of the magnetic leakage field signal remained relatively constant for each of the EDM machined surfaces. The increased reluctance due to the reduced specimen thickness led to an increasing leakage field on the surface above the parent material.

EDM machined surface and specimen thickness removal.		Magnetic leakage field measurements from the parent material region.		Magnetic leakage field measurements from the crack location.	
Surface labelling	Machined layer.(mm)	Hall probe (mT)	GMR (V)	Hall probe (mT)	GMR (V)
22B	0.55 mm	0.24 ±0.01	1.9 ±0.1	0.55 ±0.01	4.4 ±0.1
23B	0.82 mm	0.47	0.3	0.88	4.7
24B	0.24 mm	0.48	0.5	0.89	4.7
25B	0.47 mm	0.48	0.9	0.84	4.6
26B	0.37 mm	0.40	1.0	0.66	3.8
27B	0.38 mm	0.42	0.6	0.67	3.3

Table 5.3.2 Summary of magnetic leakage field data from the various EDM machined surfaces of the cracked weld specimen (21B). Magnetic leakage field data recorded above the crack and on the parent material locations are displayed. The specimen thickness removed between each machining process is also listed from **table 5.1.1**.

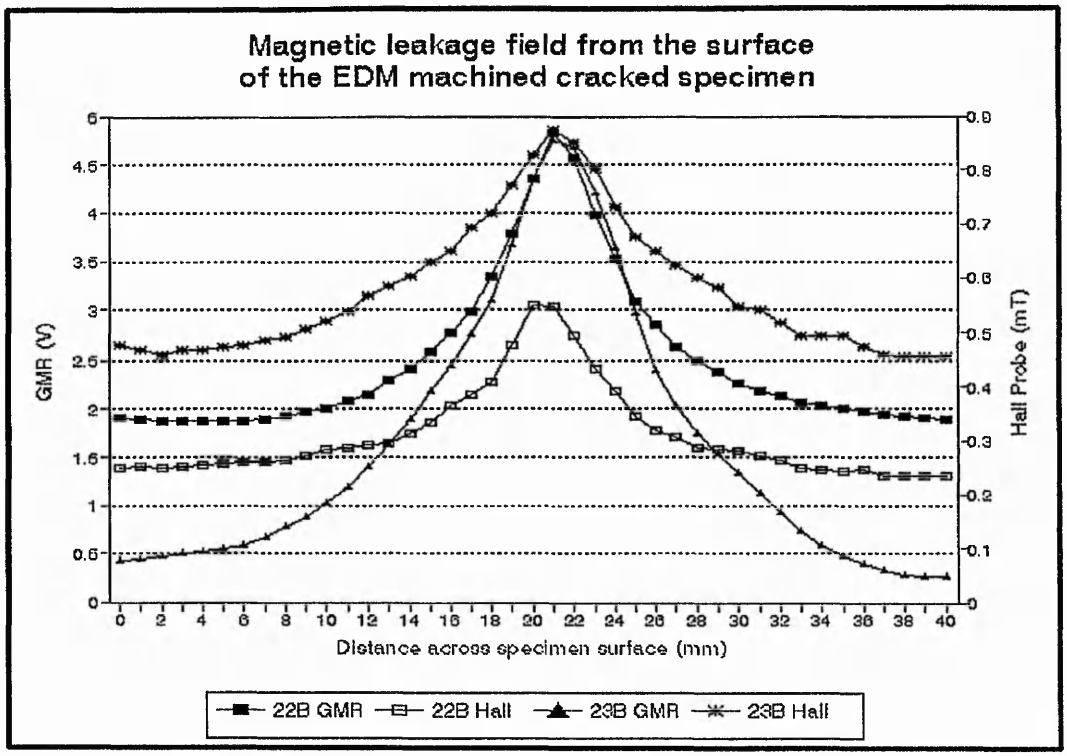


Figure 5.3.4 Magnetic leakage field from the cracked weld specimen's EDM machined surfaces 22B and 23B. Leakage field detected using GMR sensor (units voltage) and Hall probe (units milliTesla).

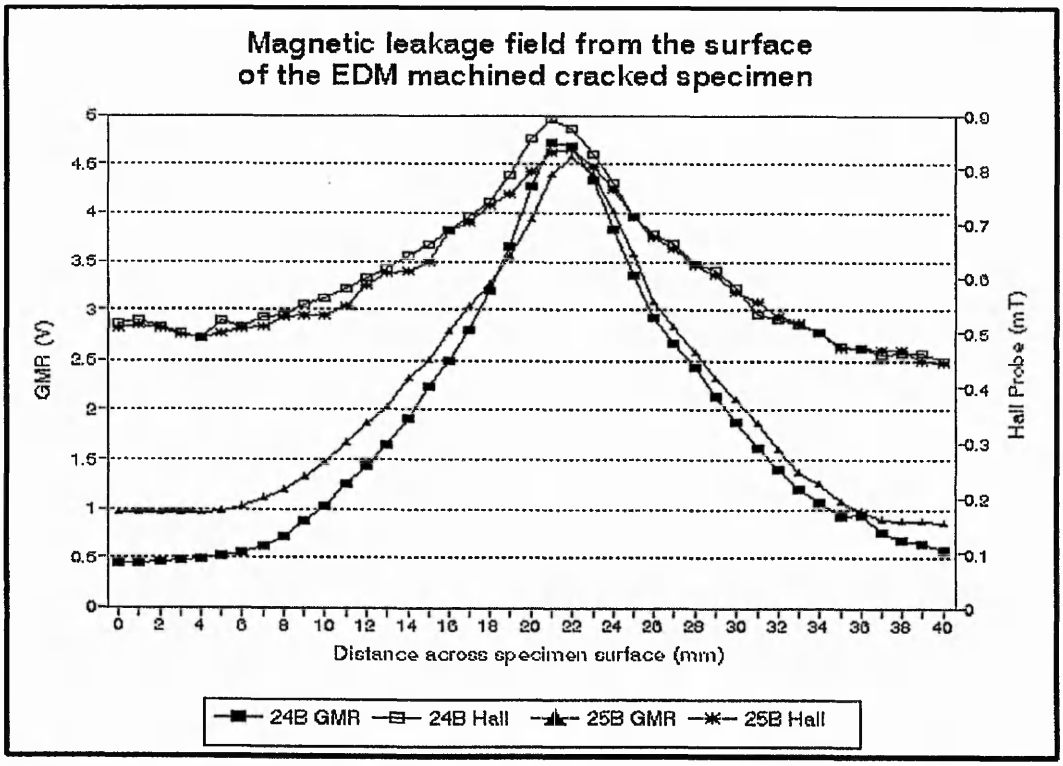


Figure 5.3.5 Magnetic leakage field from the cracked weld specimen's EDM machined surfaces 24B and 25B. Leakage field detected using GMR sensor (units voltage) and Hall probe (units milliTesla).

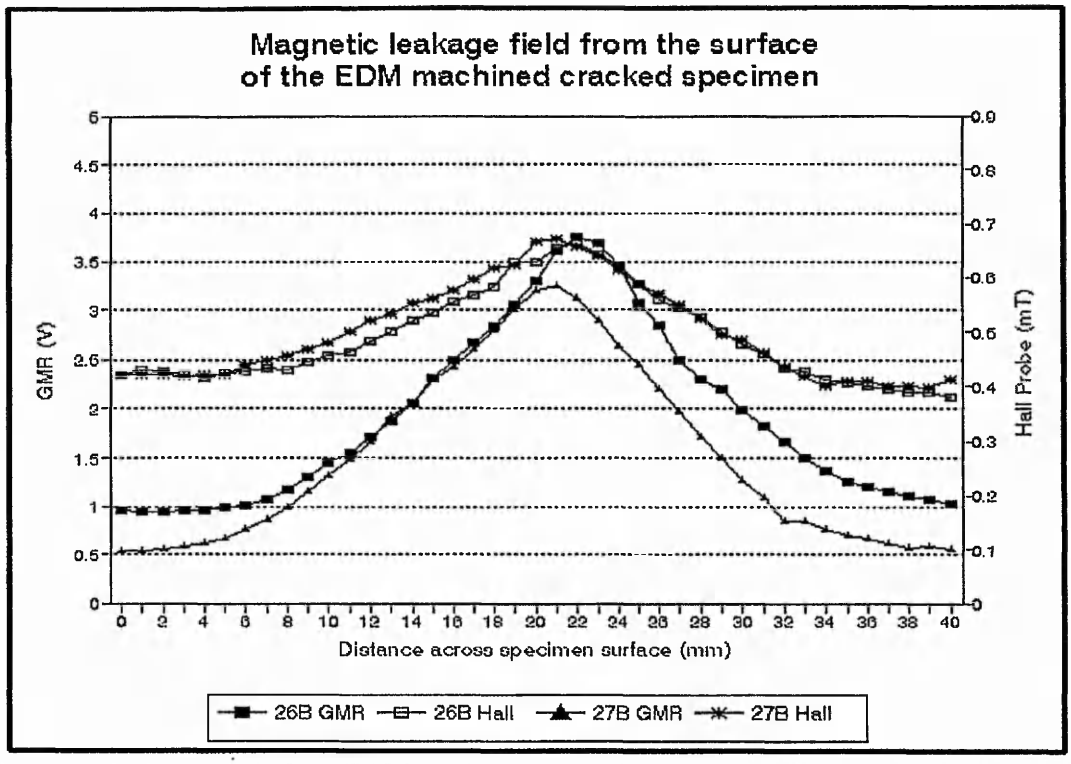


Figure 5.3.6 Magnetic leakage field from the cracked weld specimen's EDM machined surfaces 26B and 27B. Leakage field detected using GMR sensor (units voltage) and Hall probe (units milliTesla).

The leakage field from the crack regions (A) and parent material (B) on each of the machined specimens are shown in **figures 5.3.7** and **5.3.8**. **Figures 5.3.9** and **5.3.10** show that reduction of the crack depth (by machining the thickness of the specimen), affects the leakage field in different ways depending on the machining technique. The planed surfaces exhibited a trend where there was an overall increase in the leakage field and the EDM machined surfaces appeared to show a net decrease in the magnitude of the leakage field with a decreasing specimen thickness. These trends are highlighted by the dashed lines in **figures 5.3.9** and **5.3.10**.

The reduction in the crack depth and specimen thickness caused the net magnetic leakage field (A-B), due to the presence of the cracked weld, to change between each of the machined surfaces (**figures 5.3.9** and **5.3.10**). The reluctance of the machined specimens increased with decreasing specimen thickness and is also shown in **figures 5.3.9** and **5.3.10**. These reluctance values were calculated using magnetic permeability data for a similar steel. The planed machined surfaces displayed a trend where the leakage field directly above the crack increased in magnitude as the thickness of the specimen was reduced. The EDM machined surfaces displayed a similar rising trend. However, these surfaces displayed a greater increase in the leakage field on the parent material region. EDM machining between the 22B and 23B caused a large rise in the magnitude of the leakage field. After several surface machining processes the leakage field above the crack began to decrease. The measurements of the machined surfaces' leakage field, from the parent material (location 'A'), also displayed similar trends to the measurements above the crack, only this time the leakage field values were smaller.

Both machining processes reduced the thickness of the specimens as well as the crack depth. The reduction in specimen thickness by planing was expected to result in a proportional increase in the effect of the machined surface layer. This machined layer was relatively thin, since it was on the surface of the specimen, the effect on the leakage field was expected to be significant. The planing process generated a surface high in dislocation density and localised residual stresses, which reduced the permeability of the

surface, thus, resulting in an increased leakage field, (see **figure 5.3.9**). The reluctance values for the differing specimen thicknesses were calculated using **equation 5.1**.

$$R = \frac{L}{(A\mu_r\mu_0)} \qquad (5.1)$$

'R' is the reluctance, 'L' and 'A' are the length and the cross-sectional area of the specimen and μ_r μ_0 are the relative permeability of the test material and free space respectively. The calculated reluctance values for the planed specimen's surface are displayed in **figure 5.3.9**. The reluctance values, for the decreasing specimen thickness, show a similar trend to the magnetic leakage field values (A-B) from the cracked weld seam.

The calculated reluctance values for each of the machined specimens, as expected, showed an increase with decreasing specimen thickness, (see **figure 5.3.10**). However, the net magnetic leakage field from the EDM machined cracked weld specimen surfaces showed a general decrease. This was opposite to what might be expected if the change in reluctance of the specimen was the sole cause of the leakage field. The EDM machining removed the surface layer without the creation of any new mechanical stresses. This machining left a thin residual surface layer approximately 5μm to 10μm in thickness **[99]**. This surface layer alone, is expected to be too thin to significantly affect the leakage field. As further EDM machining was carried out the thickness of 'as-received' surface material, containing the residual stress and dislocation densities, decreased. Progressive EDM machining removed the 'as-received' low permeability surface region created by the original (grinding) machining process. After several EDM machining runs the crack mouth slowly became covered by resolidified molten material, which helped further decrease the leakage field magnitude.

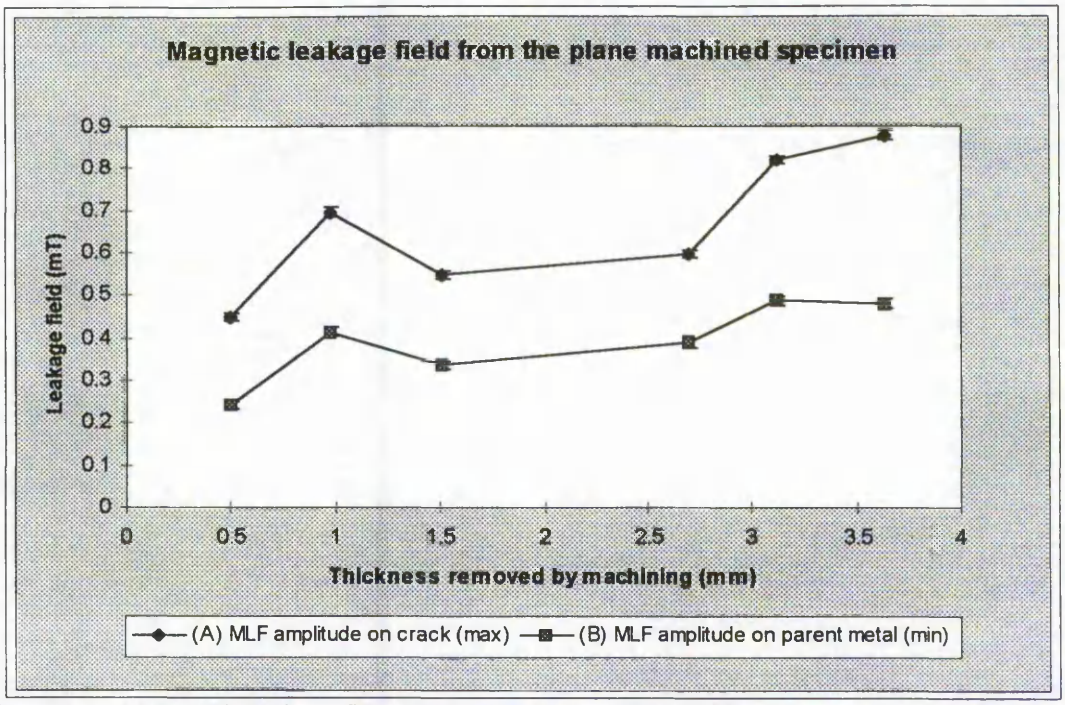


Figure 5.3.7 Magnetic leakage field (MLF) from the cracked weld specimens planed surfaces. The magnitude of the leakage field from the crack locations (A) and parent material (B) are shown. Y-axis in milli-Tesla and error bar for data ±0.01 mT.

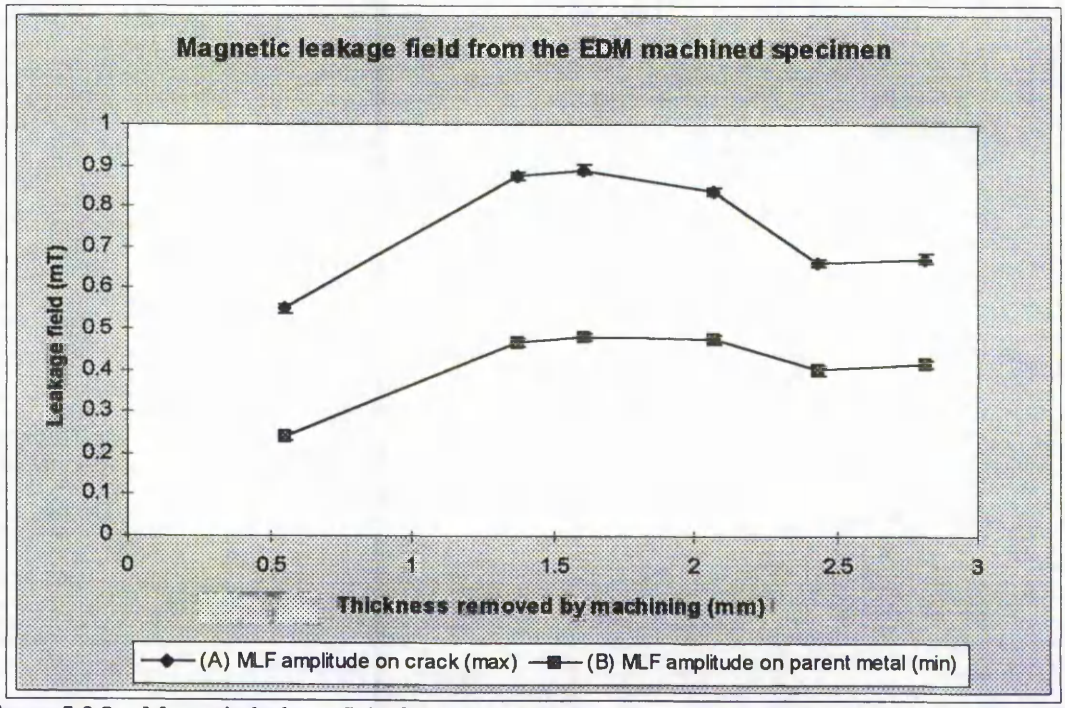


Figure 5.3.8 Magnetic leakage field from the cracked weld specimens EDM machined surfaces. The magnitude of the leakage field from the crack locations (A) and parent material (B) are shown. Y-axis in milli-Tesla and error bar for data ±0.01 mT.

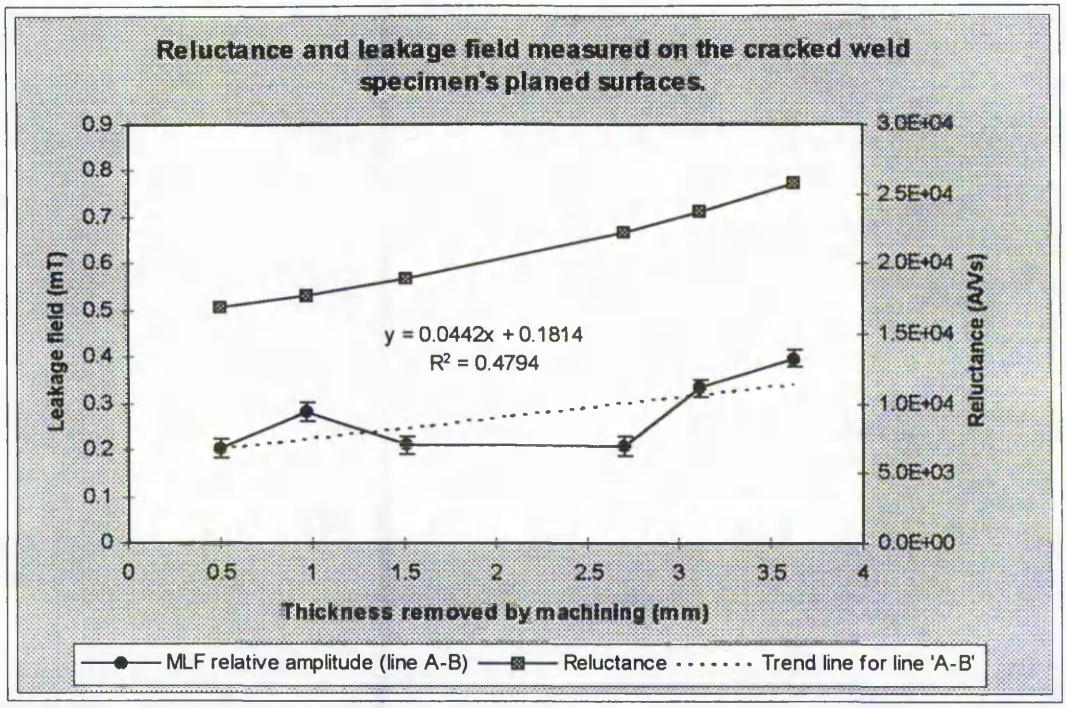


Figure 5.3.9 Magnetic leakage field and calculated reluctance values of the cracked weld specimen's planed surfaces. The magnitude of the leakage field due to the presence of the cracked weld seam (line A-B) is shown (data from **figure 5.3.7**). The trend line shows an increasing relationship between the leakage field and decreasing crack depth. Leakage field measured in milli-Tesla (error bar for data ±0.02 mT) and reluctance in (A/Vs).

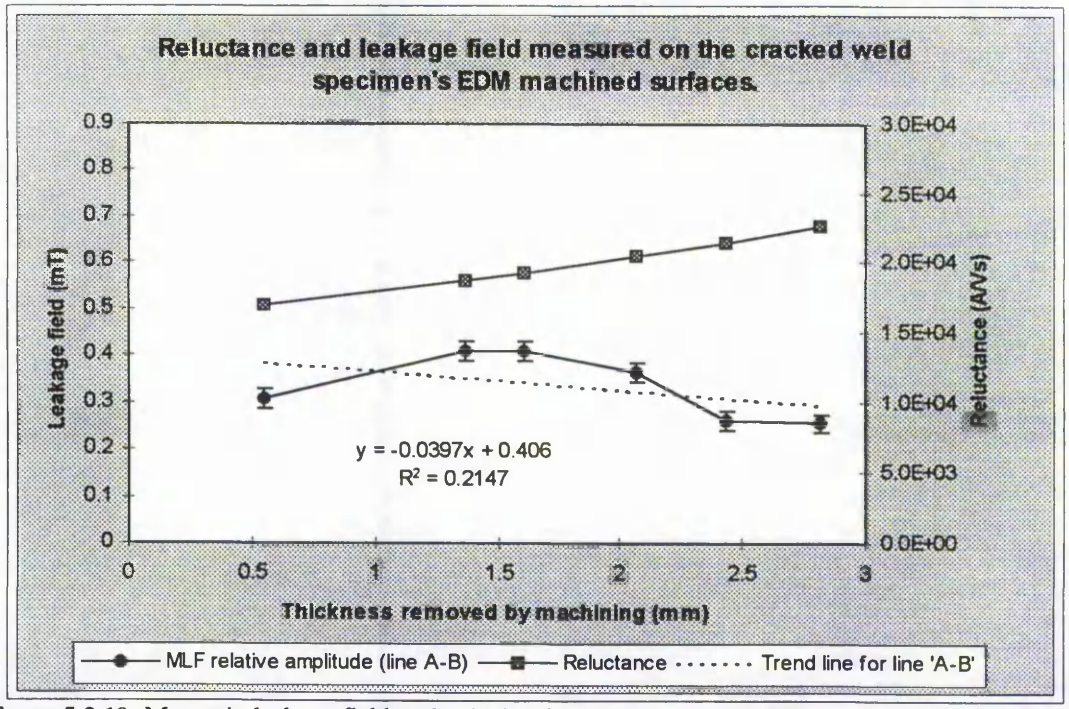


Figure 5.3.10 Magnetic leakage field and calculated reluctance values of the cracked weld specimen's EDM machined surfaces. The magnitude of the leakage field due to the presence of the cracked weld seam (line A-B) is shown (data from **figure 5.3.8**). The trend line shows an decreasing relationship between the leakage field and decreasing crack depth. Leakage field measured in milli-Tesla (error bar for data ±0.02 mT) and reluctance in (A/Vs).

5.4. DISCUSSION OF THE BARKHAUSEN EMISSION RESULTS FROM THE VARIOUS MACHINED SURFACES.

The effect of reduced crack depth on the Barkhausen emission was investigated. Cracked weld specimens 21A and 21B were planed and EDM machined respectively and their detected Barkhausen envelopes are shown in **section 5.2**. Both Planing and EDM machining removed layers of material from each of the cracked weld specimen surfaces in differing ways. Machining the surfaces resulted in the reduction in the thickness of the specimen and thus, an overall reduction in the crack depth. On the surfaces of both the specimens, after the initial machining process, the crack became visible and appeared as a very fine line on the central region of the weld, between locations 'K' and 'L'.

5.4.1. EBE Signal Envelopes from the Machined Cracked Weld Specimens.

The EBE signals from the planed and EDM machined surfaces appeared very different. The planed surfaces generated EBE signal envelopes which were both smooth and domed shaped (22A, 24A) or more often jagged (irregular) flat topped envelopes (23A, 25A, 26A, 27A, 28A) over the cracked weld region. The shape of the envelopes from these planed surfaces were affected by the machining process itself, which varied between each machining. EDM proved to be a more consistent machining technique. This was evident from the detected EBE envelopes. The EBE envelopes, from successively EDM machined surfaces, appeared with the maximum peak on the left side of the envelope. This was found for all the EDM machined surfaces. Away from the cracked weld region, the EBE envelopes were smaller in amplitude. As the specimen's thickness was further reduced, the position of the maximum signal amplitude, on the parent steel region (location 'A' and 'U'), shifted to a position later on the envelope.

As both types of machining reduced the thickness of the specimens, the width of weld mouth changed. This was a consequence of the "V" shape of the weld, (see **figure 5.1.3**

and **table 5.1.1**). As a result, the distance between the weld-HAZ interface and locations 'A' and 'U' changed with each machining.

The EBE envelopes are shown along with their respective Barkhausen envelope parameters in **section 5.2**. The effect of reducing crack depth, by planing off surface layers, changed the EBE profile of the specimens. On the planed machined surface (22A) the time of peak (T_P) occurred after 1 s on the parent material region, while T_P values occurred earlier as the cracked weld was approached (**figures 5.4.1** and **5.4.2**). On further machining (surface 23A) the T_P value, between the parent material and the crack was found to be similar. However, on close inspection the T_P value was found to occur slightly earlier over the cracked weld region. Surfaces 25A, 26A and 28A showed sharp changes in EBE envelope shape between the weld affected region and the parent material region. From the HAZ region on surface 27A, the peak on the latter edge of the envelopes appeared larger than expected (see **figure 5.2.17**) and, hence, was recorded as the T_P value. This forced the T_P values to occur later in the envelope. If the T_P parameter alone is considered, then on surface 27A an illusion that a HAZ region (associated with the occurrence of early T_P values on a plane machined surfaces) does not exist, is found. For each of the subsequent machined surfaces of the planed specimen, the T_P value on the parent material (location 'A') was found to be between 1 s and 1.05 s. Surface 24A exhibited T_P values which occurred earlier and were probably caused by the machining process.

The EDM machining generated the recast white layer surface which appeared dull in appearance compared to the non-EDM machined side of the specimen. The EBE envelopes from the various EDM machined surfaces exhibited T_P values earlier on the signal envelopes, around 0.7 seconds (see **figures 5.4.3** and **5.4.4**). The different material regions (HAZ, weld and crack) which lay beneath the recast layer were indistinguishable using the 'time of peak' alone.

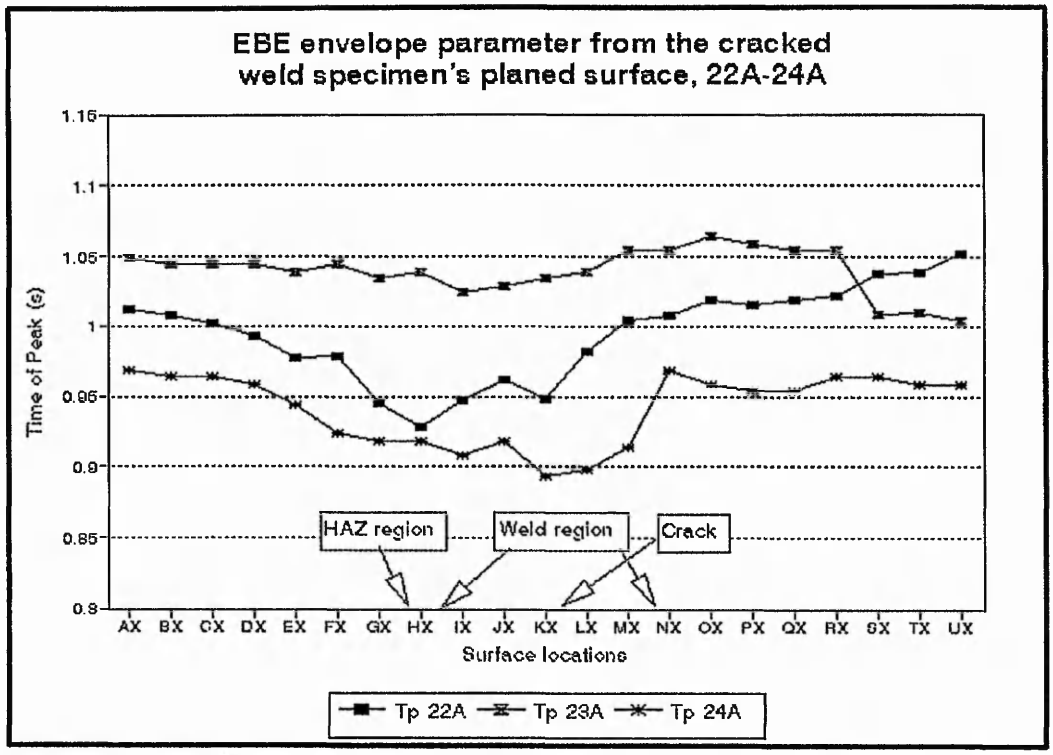


Figure 5.4.1 'Time of Peak' (T_P) profile from the cracked weld specimen's planed surfaces 22A, 23A and 24A. The crack is positioned close to location 'K'.

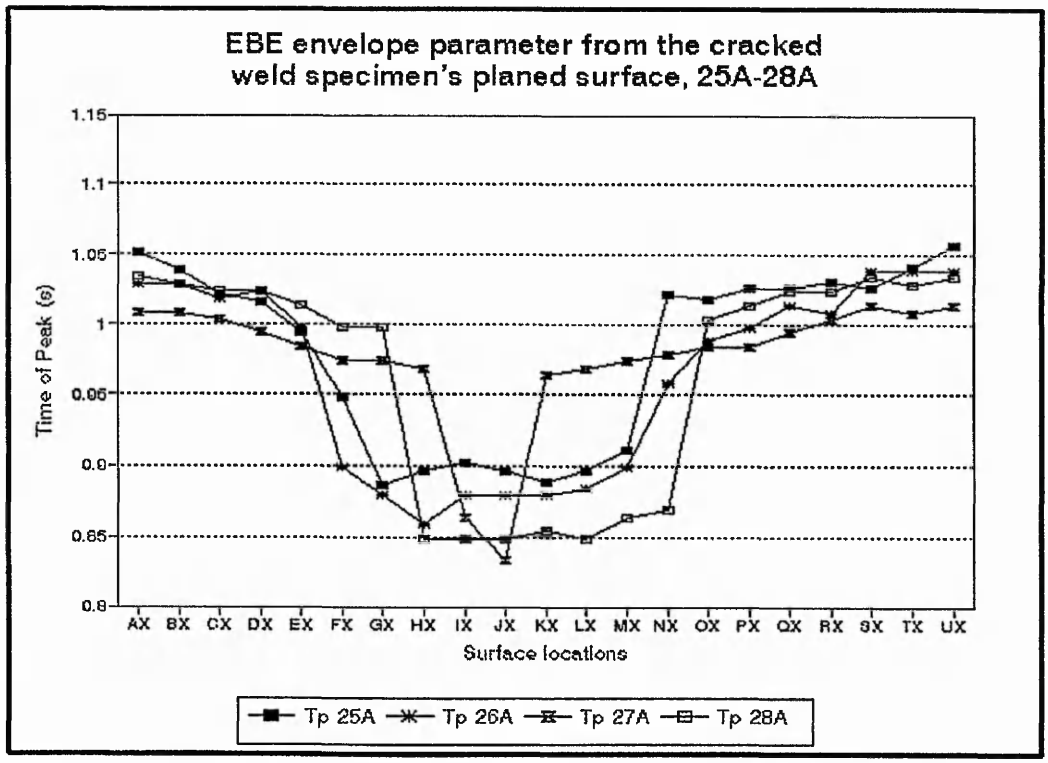


Figure 5.4.2 'Time of Peak' (T_P) profile from the cracked weld specimen's planed surfaces 25A, 26A, 27A and 28A. The crack is positioned close to location 'K'.

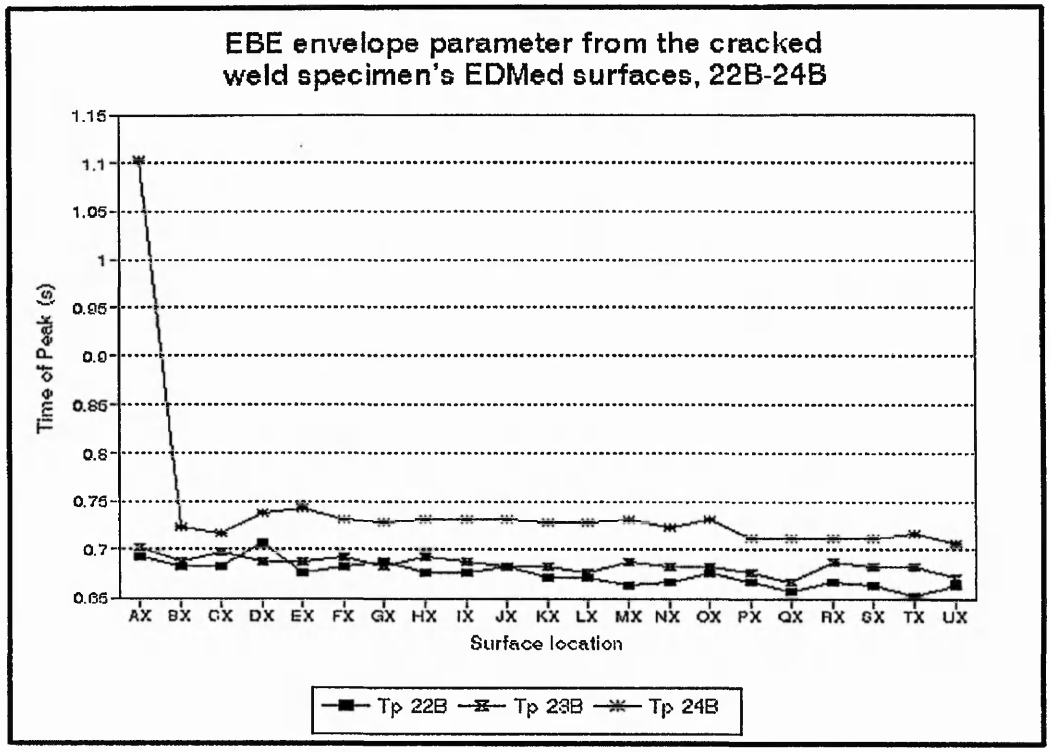


Figure 5.4.3 'Time of Peak' (T_P) profile from the cracked weld specimen's EDM machined surfaces 22B, 23B and 24B. The crack is positioned close to location 'K'.

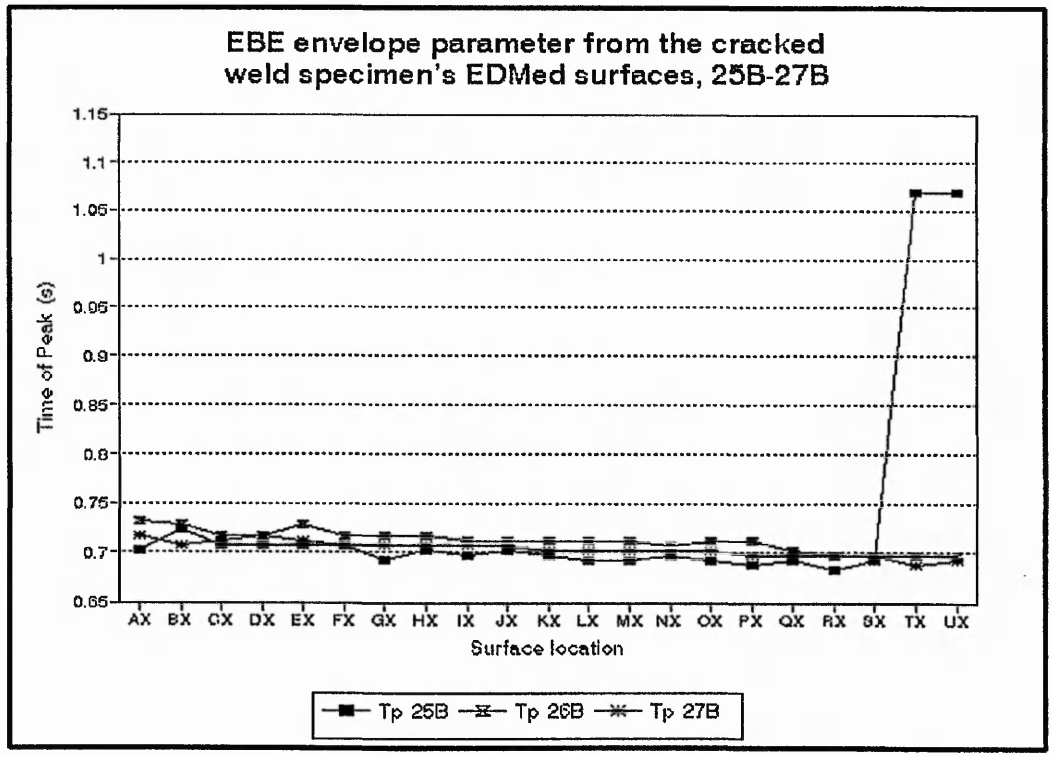


Figure 5.4.4 'Time of Peak' (T_P) profile from the cracked weld specimen's EDM machined surfaces 25B, 26B and 27B. The crack is positioned close to location 'K'.

The **EBE envelope** 'time of peak' (T_P) parameter shows distinct differences for the differently machined specimen surfaces. On the planed machined surface, the T_P value occurred, on the parent material (location 'A'), around **1 s** on the envelope and remained similar for subsequent planed surfaces. The T_P value from very close to the crack (location 'K') always occurred earlier compared to the parent material region (location 'A'). **Figures 5.4.5** and **5.4.6** display the T_P values from the two different types of machined surfaces. For the planed machined specimen the difference between the T_P values from the parent material and cracked weld regions, from the different surfaces, lay between **0.02 s** and **0.19 s** (±0.04 s). On the EDM machined surfaces the difference between the T_P value from the crack and the parent material was very small and lay between **0.01 s** and **0.025 s** (±0.04 s). **Figure 5.4.6** shows that on every EDM machined surface the averaged T_P value from the cracked weld region always occurred slightly earlier than on the parent material locations. Also, the T_P values on the EDM machined surfaces appeared around **0.7 s** on the envelope. This was ≈**0.3 s** earlier compared to the T_P values from the planed specimen's surfaces. On the planed specimen, the large variation between the T_P values, from the crack and parent material region, was due to the significant localised residual stress and dislocation networks present as a result of mechanically tearing away thin layers of surface material. The EDM process, however, generated a surface more consistent in texture and with more uniform residual stress profile, which led to the T_P values being more consistent when compared to the values from the planed machined surfaces.

As the T_P values were measured at the maximum peak on the Barkhausen envelope, its position was directly affected by the domain wall mobility involved in the magnetisation process. The type of pinning sites which generated the largest peak on the parent material region appears to be dislocations and second phase precipitates **[78]**. As the welded region on the planed specimen was approached the T_P values shifted earlier on the envelope. This was a result of the increased residual stress (due to welding) and dislocation networks within the weld region, (**figures 5.4.1** and **5.4.2**). Also, localised residual stress and dislocation networks resulting from the planing process, helped merge the two peaks together, as well as, causing the peak to occur later on the envelope compared to a plain welded specimen 2P, as discussed in **section 4.4.2**.

The thickness of the EDM machined recast layer was ~5 to 10 microns in depth. The EBE envelopes are detected from a surface depth of approximately 1.0 mm **[56]**. Therefore, it can be concluded that the recast layer (though has a significant effect on the EBE envelope due to being closest to the sensor) is not the sole cause of the T_P value occurring earlier on the envelope and remaining relatively stable. The removal of the 'as-received' surface containing the machining defects, caused a new surface layer to became present within the EBE detection range. The removal of the 'as-received' machined surface layer reduced the pinning concentration, such as dislocation networks, localised microstructural deformation and changed the residual stress profile. The introduction of the new stress profile of the recast layer combined with the cracked weld stress profile was expected to generate a new complex stress state on the specimen surface. The effect of reducing the specimen thickness and crack depth by consecutive EDM machining processes did not appear to have a significant effect on the T_P values of the EBE envelopes. The T_P values remained constant at around **0.7 s**. The EDM machining technique itself, however, does significantly change the T_P value as can be seen when compared to the planed surface.

The EDM machined surfaces displayed a single peak appearing early on the EBE envelope (in the low applied field region). Moorthy et al. **[27]** claimed grain boundary pinning causes an early peak in steel. The EDM machined surface recast layer, has been reported by Lim et al. **[99]**, to be composed of a very fine microstructure. In certain tool steels the interface between the recast layer and the parent specimen exhibited fine dendritic grain, while the top surface exhibited columnar grains. The EBE signal shape indicated that 'stronger pinning' sites exists on the parent material region as the envelopes were flat toped and almost double peaked. The T_P values over the cracked weld region always occurred slightly earlier on the envelope, at a lower magnetising field. The early peak indicated that domain walls were pinned at grain boundary sites and the sudden breakaway of large numbers of domain walls causes the initial large EBE peak. The pinning resulting from grain boundary (first peak) at low fields and at precipitates (for the second peak) at higher fields was seen in the EBE envelope from the parent material region (e.g. **figure 5.2.35)**.

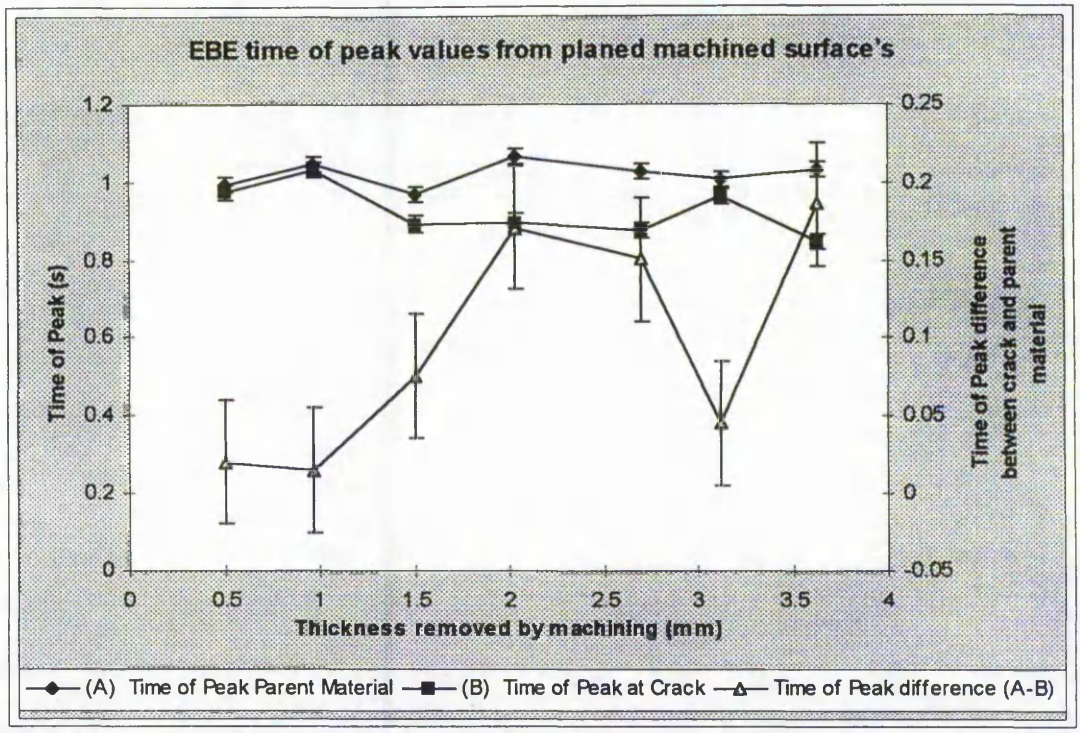


Figure 5.4.5 Time of peak (T_P) on the EBE envelopes from the planed machined surfaces. The T_P values from the parent material (line A) and the crack (line B) are exhibited for each machined surface. The difference between the T_P values from these two regions are also shown. Error bars for T_P values are ±0.02 s and ±0.04 s for the difference values.

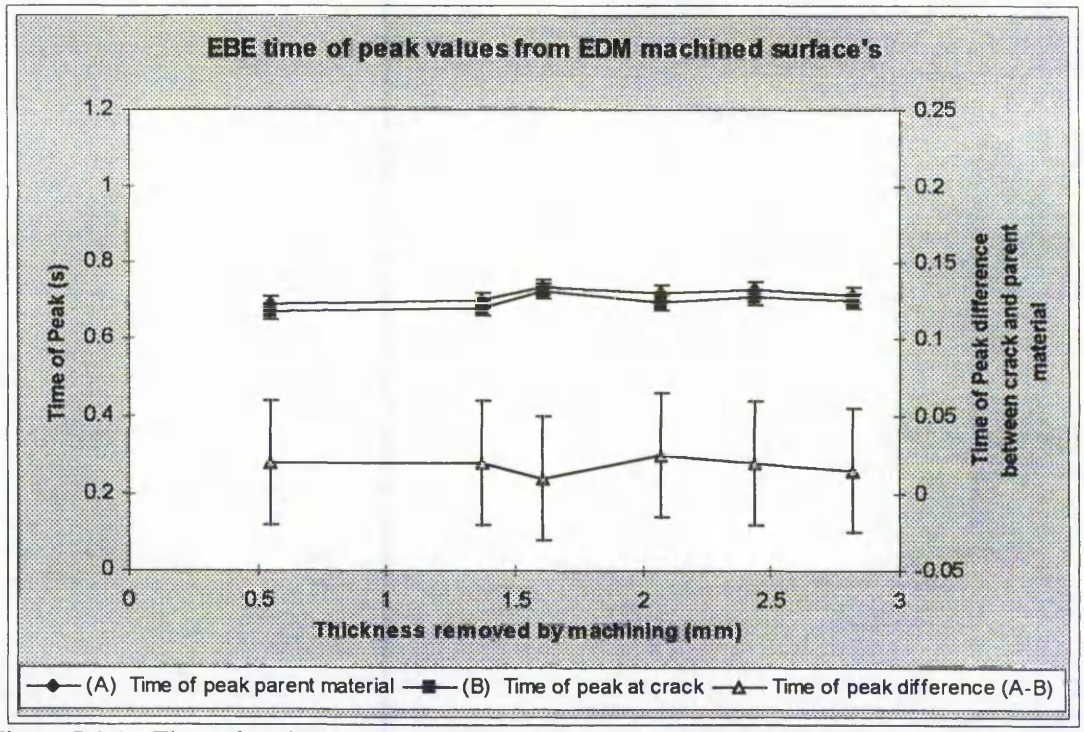


Figure 5.4.6 Time of peak (T_P) on the EBE envelopes from the EDM machined surfaces. The T_P values from the parent material (line A) and the crack (line B) are exhibited for each machined surface. The difference between the T_P values from these two regions are also shown. Error bars for T_P values are ±0.02 s and ±0.04 s for the difference values.

Figure 5.4.7 shows the maximum signal voltage (V_{MAX}) profile, for the planed surfaces 22A and 23A, indicated by a minimum very close to the crack. Planed surface 24A displayed a V_{MAX} profile which was relatively flat with an overall increase in magnitude compared to surfaces 22A and 23A. Consecutively planed surfaces 25A, 26A, 27A and 28A showed an increase in V_{MAX} values over locations 'A' to 'F', for each subsequent machining (**figure 5.4.8**). The parent material, between locations 'P' and 'U', showed that the V_{MAX} remained relatively constant for the numerous planed surfaces (**figures 5.4.7** and **5.4.8**). Over the central region of a specific machined surface, the V_{MAX} values displayed a decrease at the HAZ and parent material interface region, located around positions 'G' and 'N'. A small increase in the V_{MAX} value was generally detected over the welded region, followed by a small decrease on location 'K'. Location 'K' was very close to the crack- which was always situated between positions 'K' and 'L'. This pattern was also noticeable on surfaces 25A, 26A and 28A.

Each of the EDM machined surfaces displayed similar EBE V_{MAX} and signal energy profiles. The V_{MAX} profiles (**figures 5.4.9** and **5.4.10**) from any particular EDM machined surface showed that the EBE signal amplitudes on either side of the crack were very similar. Each EDM machined surface showed a small increase in the EBE signal amplitude (V_{MAX}) over the parent material region, though the largest increase in amplitude took place over the central weld, HAZ and cracked regions. On location 'A' the V_{MAX} value remained relatively constant, between values of **0.45 V** to **0.55 V** (**±0.01V**) for the various EDM machined surfaces. The decreasing specimen thickness and its resulting reduction of the exposed weld mouth can be seen in the V_{MAX} and signal energy profiles. The location from which the largest V_{MAX} occurred (weld-HAZ interface) shifted closer to the crack location upon subsequent machining. This can be clearly seen in **figures 5.4.9** and **5.4.10**.

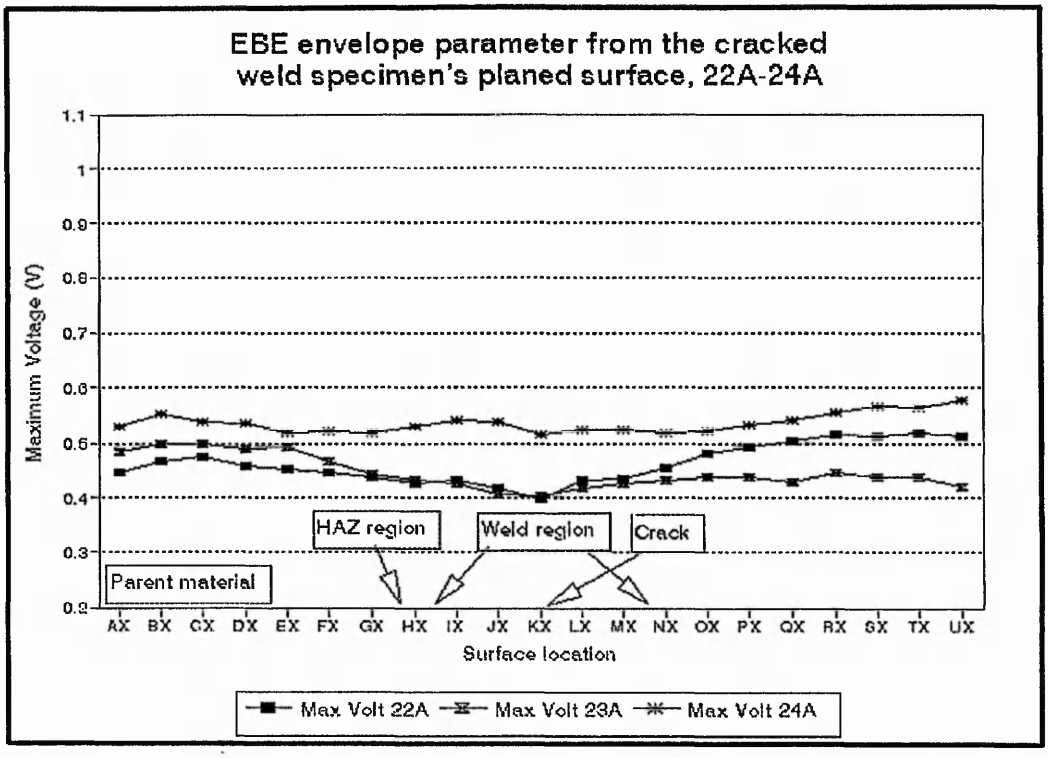


Figure 5.4.7 'Maximum signal voltage' (V_{MAX}) profile from the cracked weld specimen's planed surfaces 22A, 23A and 24A. The crack is positioned close to location 'K'.

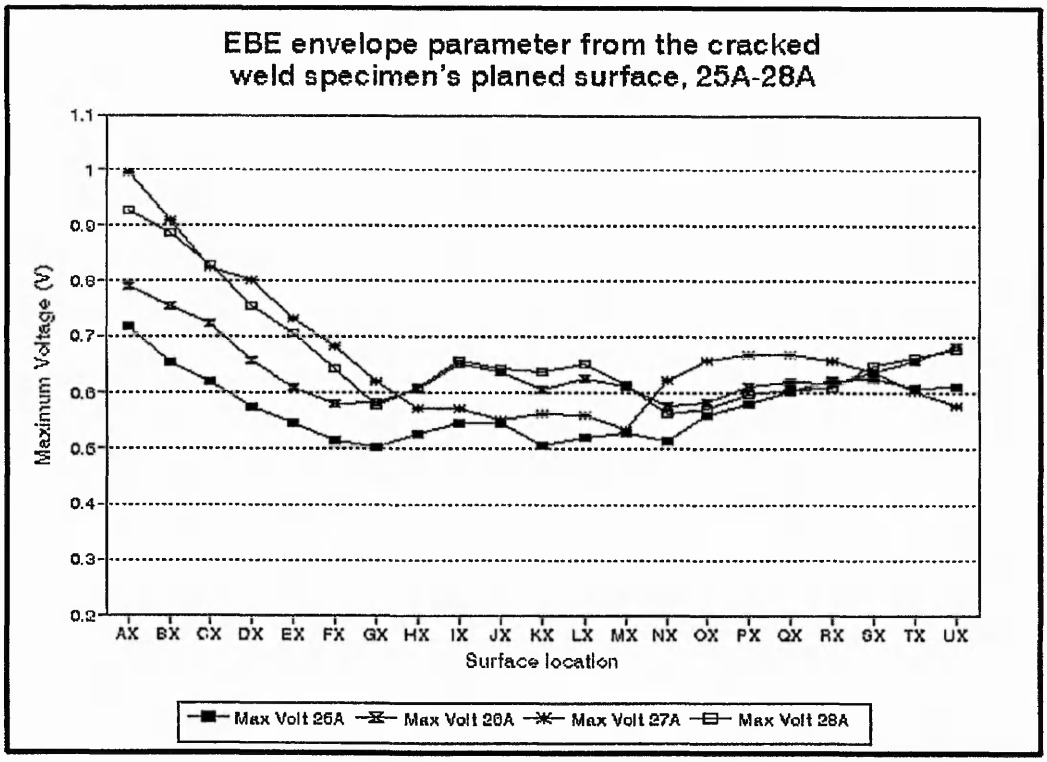


Figure 5.4.8 'Maximum signal voltage' (V_{MAX}) profile from the cracked weld specimen's planed surfaces 25A, 26A, 27A and 28A. The crack is positioned close to location 'K'.

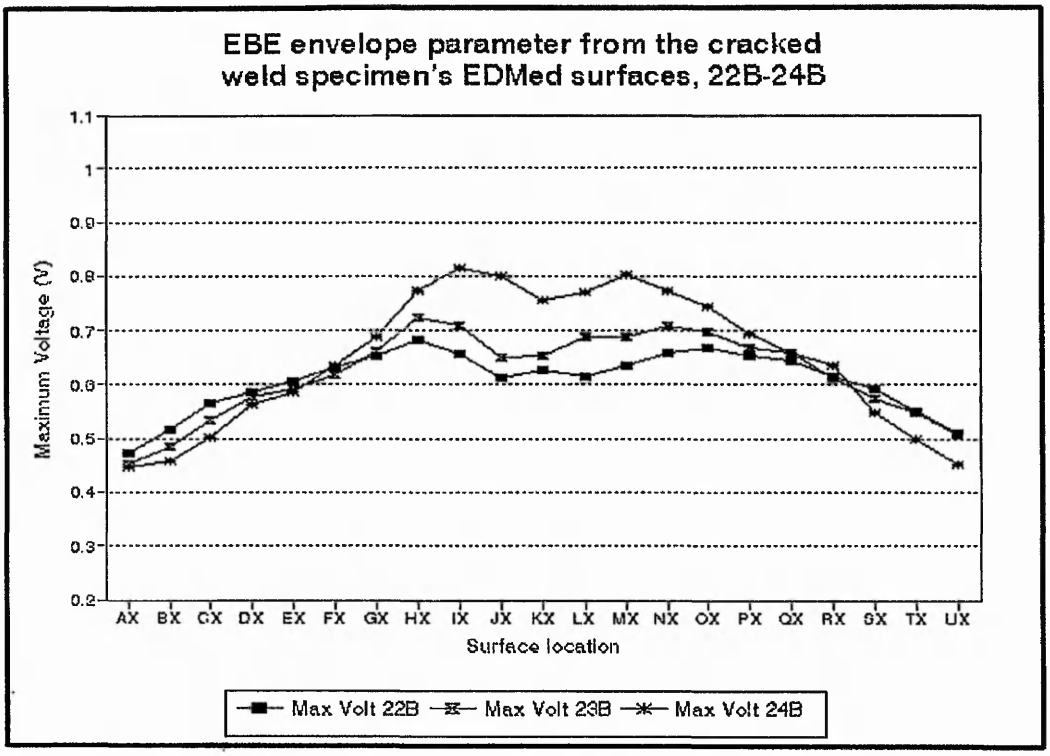


Figure 5.4.9 'Maximum signal voltage' (V_{MAX}) profile from the cracked weld specimen's EDM machined surfaces 22B, 23B and 24B. The crack is positioned close to location 'K'.

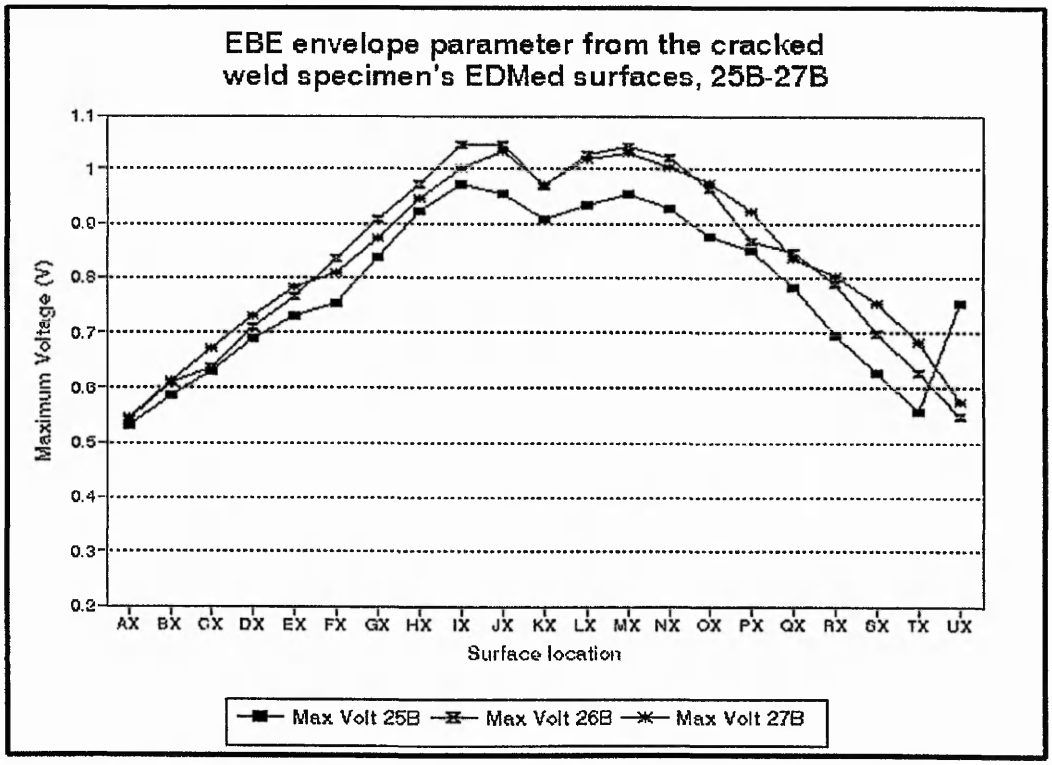


Figure 5.4.10 'Maximum signal voltage' (V_{MAX}) profile from the cracked weld specimen's EDM machined surfaces 25B, 26B and 27B. The crack is positioned close to location 'K'.

In both **planed and EDM machined** specimens, the detected EBE envelopes were found to change as a result of the crack depth and sample thickness reduction. The maximum EBE signal voltage (V_{MAX}) parameter from each of the machined surfaces is displayed in **figures 5.4.11** and **5.4.12**.

For each machined specimen, the V_{MAX} values from the three different material regions- HAZ, cracked weld and parent material- showed slight differences. The results show that as the specimen thickness was reduced by planing, the V_{MAX} values from across the parent material region (location 'A') increased in magnitude. The V_{MAX} values from the HAZ and crack regions also increased, but at a slower rate (see **figure 5.4.11**). Surface 24A appeared to show that the planing process blurred the boundary between each of the different material regions. The V_{MAX} from all three regions were similar in magnitude and this led to an increased difficulty in interpreting the EBE V_{MAX} data from the planed specimen.

Figure 5.4.12 shows the V_{MAX} parameter from the EDM machined surfaces. The V_{MAX} on the parent material region remained relatively constant upon subsequent EDM machining and then eventually increased slightly. The V_{MAX} values, from the HAZ and cracked regions, significantly increased in magnitude. The size of the maximum signal voltage (V_{MAX}) increases when greater numbers of domain walls move simultaneously or the domain walls have an optimum mean-free-path to sweep across before encountering impediments **[39][27]**. Also, as the specimen thickness was reduced, the flux leakage on the surface increased (**figures 5.3.7** and **5.3.8**) and was detected by the pencil probe sensor. The increasing flux leakage helped increase the overall size of the EBE envelope, leading to an increased V_{MAX} value.

When the difference between the V_{MAX} values on the parent material and cracked weld region was considered (**figures 5.4.11** and **5.4.12**), the two machining processes exhibited differing trends. Both the consecutive planing and EDM machining processes exhibited an increasing disparity between the V_{MAX} values from the parent material and the cracked region. For the planed specimen this increasing disparity in the V_{MAX} parameter was positive, while the EDM machined surfaces displayed a negatively

increasing disparity. The planing blurred the boundary between the different material regions and as only location 'A' was used for the parent material region, this led to a larger than normal increase in difference between the crack and parent material region. EDM machining generated a consistent surface finish and the disparity between the V_{MAX} from the cracked weld and parent material region was probably due to the decrease in crack size.

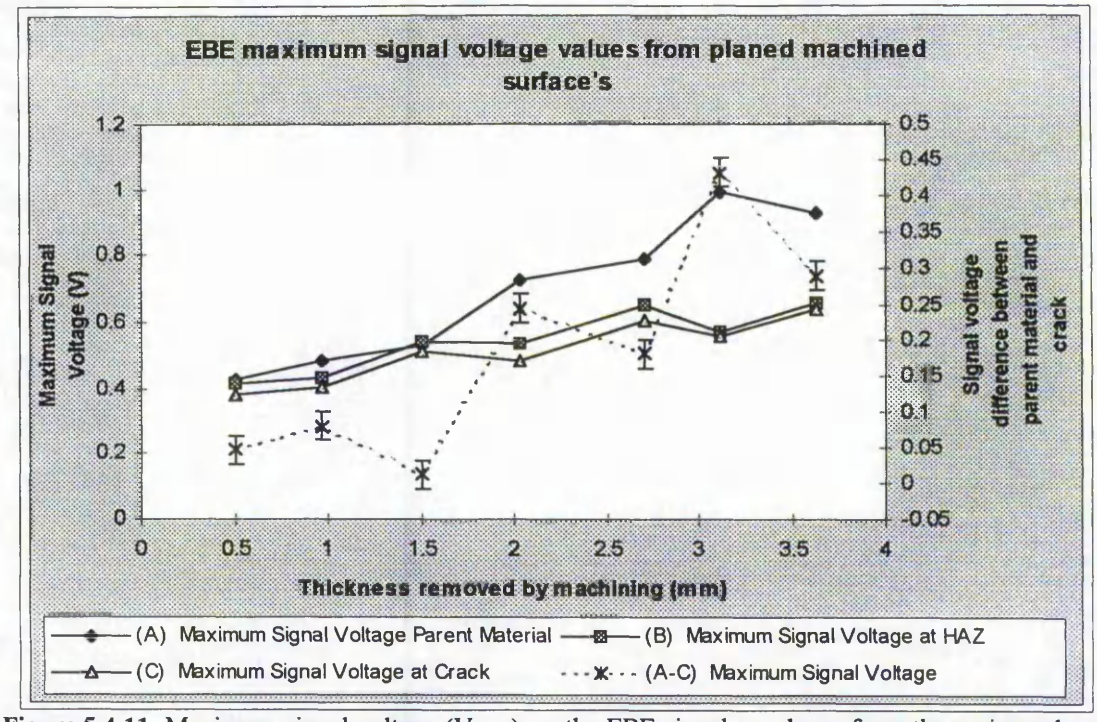


Figure 5.4.11 Maximum signal voltage (V_{MAX}) on the EBE signal envelopes from the various planed machined surfaces. The V_{MAX} values from the three material regions; parent material (line A), HAZ region (line B) and on the crack (line C) are exhibited for each machined surfaces. The difference between the V_{MAX} from the parent material and the crack are shown in the dashed line. Error bars for V_{MAX} difference values was are ±0.04 V.

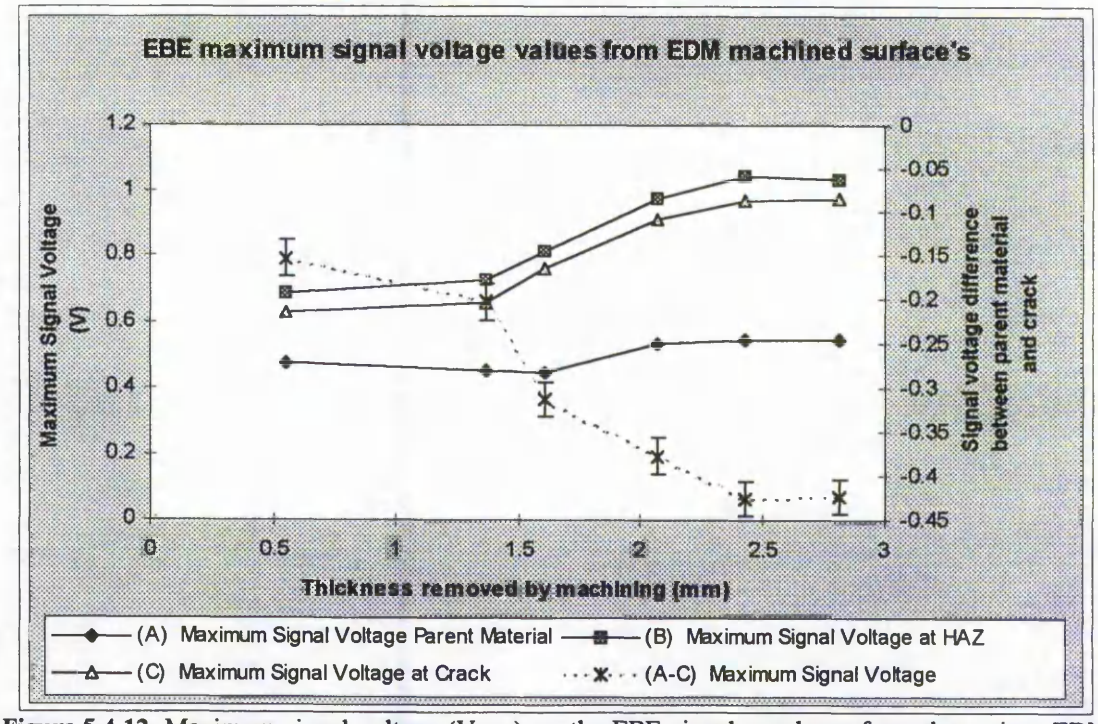


Figure 5.4.12 Maximum signal voltage (V_{MAX}) on the EBE signal envelopes from the various EDM machined surfaces. The V_{MAX} values from the three material regions; parent material (line A), HAZ region (line B) and on the crack (line C) are exhibited for each machined surfaces. The difference between the V_{MAX} from the parent material and the crack are shown in the dashed line. Error bars for V_{MAX} difference values was are ±0.04 V.

The **energy profile** from certain plane machined surfaces failed to show effectively the position of the crack on the weld metal. Planed surfaces 22A and 23A (**figure 5.4.13**) indicated an energy minimum on location 'K', close to the crack. Surface 24A exhibited an overall increase in the energy profile compared to the previous surfaces, but with no clear indication of the HAZ or cracked weld region. On each subsequent machined surfaces the overall energy profile increased. Planed surface 25A showed no signs of the different material (crack, weld or HAZ) regions. Surface 27A (**figure 5.4.14**) displayed a low EBE signal energy on the right side of the specimen, between locations 'L' and 'U'. This was thought to be caused by the residual surface deformation stresses due to the planing process. The EBE signal energy values from the various planed surfaces failed to clearly show the material characteristics due to a complex residual stress profile.

The EDM machined specimen's signal energy profile was asymmetrical about the cracked location, (see **figures 5.4.15** and **5.4.16**). The left side of the specimen (location 'H' or 'I') exhibited the maximum signal energy. On the right hand side of the specimen (covering location 'K' to 'U') on the HAZ-metal interface the maximum signal energy values were smaller than the corresponding left side. As the overall specimen thickness and crack depth was reduced, the magnitude of the signal energy profile increased. The increase in signal energy values, on the parent material, was small compared to the planed machined specimen. The magnitude of the signal energy recorded on the HAZ and cracked weld regions were larger than that found on the planed specimen. The maximum signal energy values from each EDM machined surface was located on the weld-HAZ interface. Location 'K' and 'L' displayed an energy minimum, which was also the location of the crack within the weld seam. On the EDM machined surface, the signal energy values were able to distinguish between the different material regions within the cracked weld specimen.

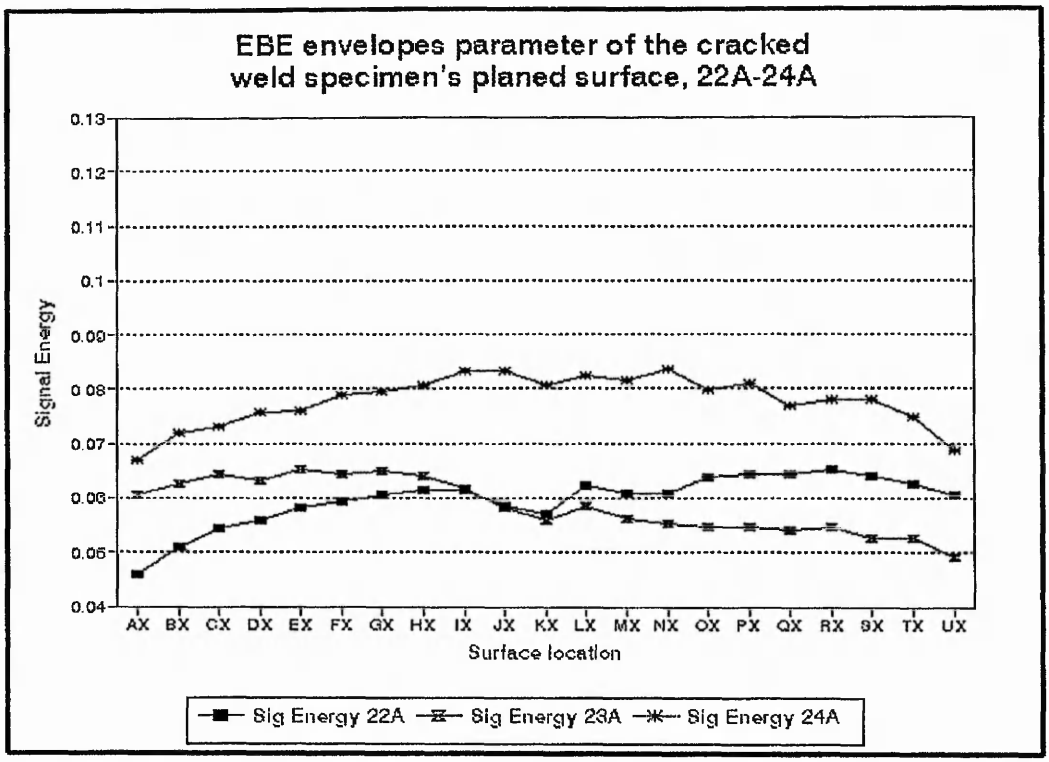


Figure 5.4.13 Signal energy (units V^2s) profiles from the cracked weld specimen's planed surfaces 22A, 23A and 24A. The crack is positioned close to location 'K'.

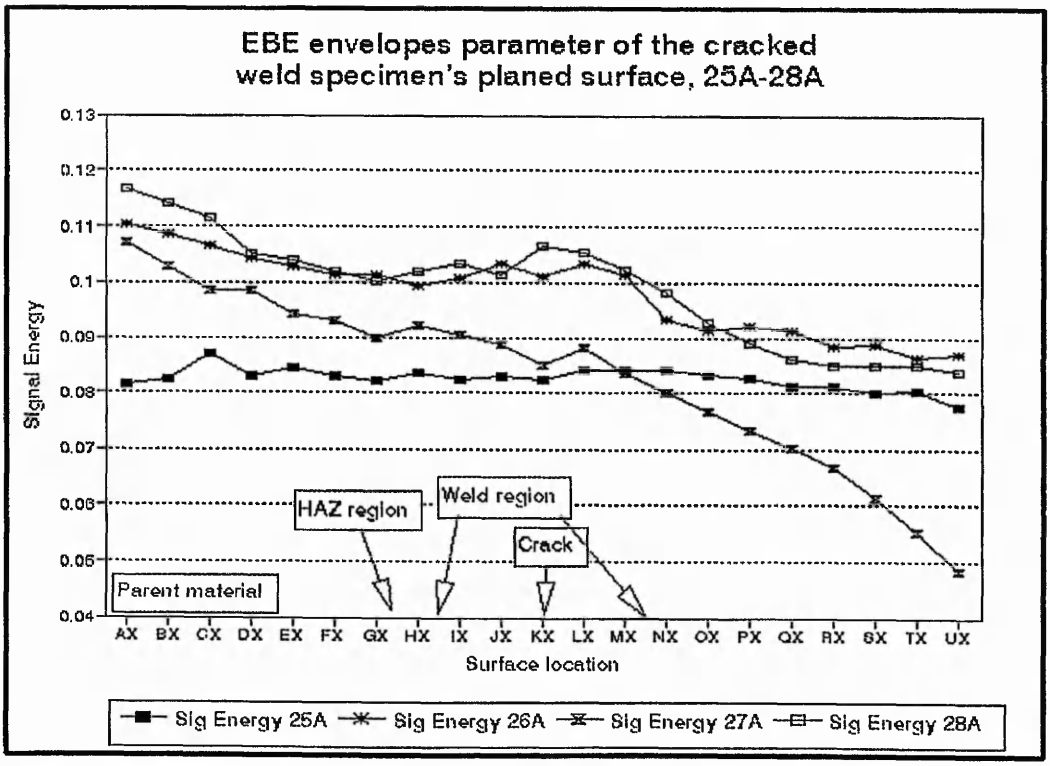


Figure 5.4.14 Signal energy (units V^2s) profile from the cracked weld specimen's planed surfaces 25A, 26A, 27A and 28A. The crack is positioned close to location 'K'.

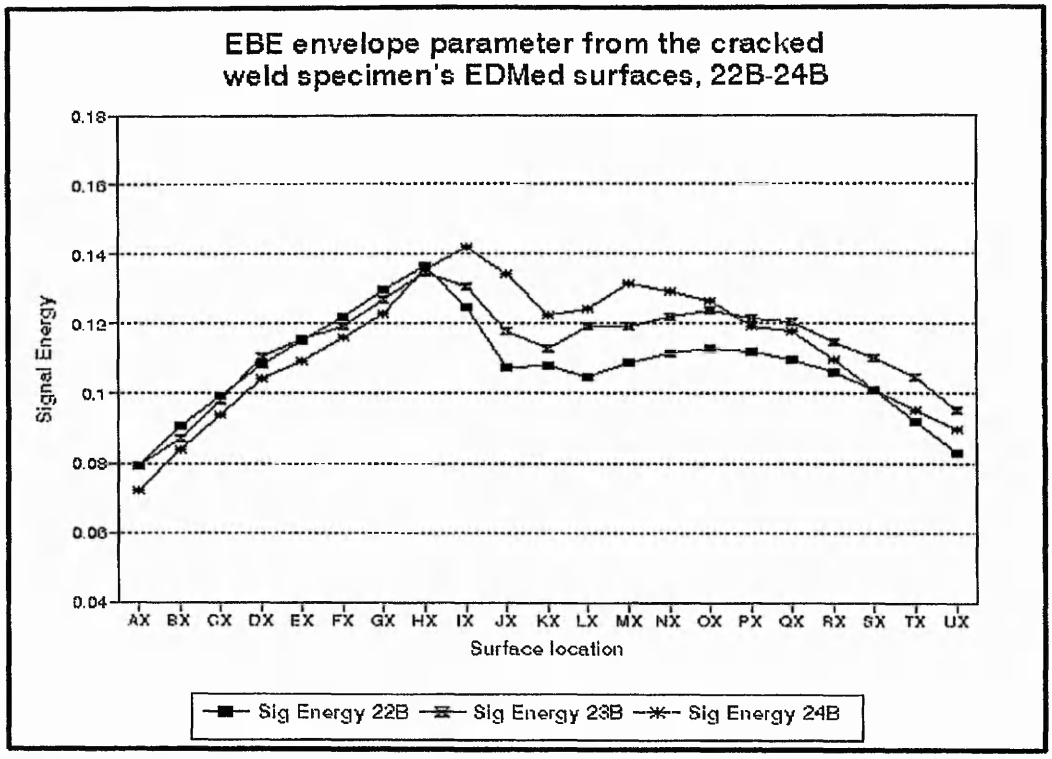


Figure 5.4.15 Signal energy (units V^2s) profile from the cracked weld specimen's EDM machined surfaces 22B, 23B and 24B. The crack is positioned close to location 'K'.

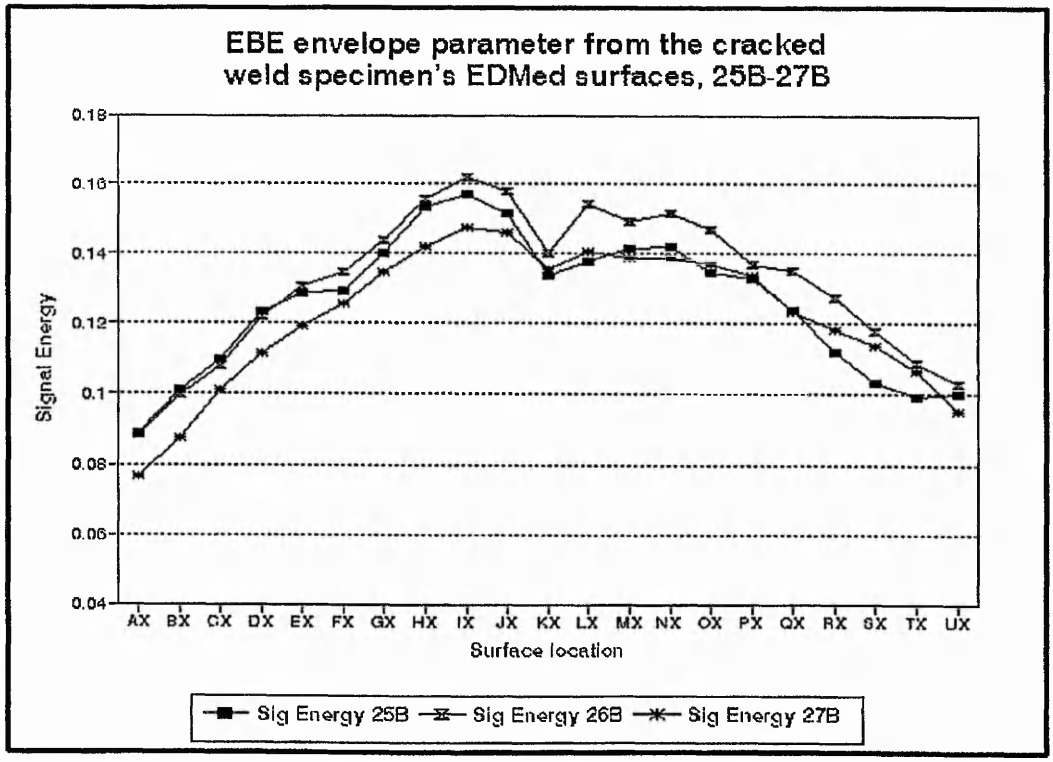


Figure 5.4.16 Signal energy (units V^2s) profile from the cracked weld specimen's EDM machined surfaces 25B, 26B and 27B. The crack is positioned close to location 'K'.

Figure 5.4.17 shows the EBE signal energy, from the various surfaces of the planed specimen, which exhibited a general increase in magnitude with decreasing crack depth and specimen thickness. The planing process generated high residual surface deformation as a result of the tool tip tearing off the surface material **[116]**. The localised stresses and dislocation density act as pinning sites and also help reduce the magnetic permeability of the surface. Proportionally, the thickness of the low permeability surface, increased with the reduction in specimen thickness. This increased the leakage field detected on the surfaces of the planed specimen and is shown in **figure 5.3.7**. On the parent material region (location 'A') the signal energy increased by a large amount compared to the EDM machined parent material region. This is shown in **figures 5.4.17** and **5.4.18**. This indicated a relative increase in the domain wall activity on the parent material region on the planed specimen. The EBE pencil probe's hemispherical tip provided a small point of contact with the specimen's surface. As the specimen thickness was reduced, the leakage field on the surface increased due to an increased magnetic reluctance of the specimen, (see **figure 5.3.10**). This may also account for the increased magnitude of the EBE signal energy from the parent material region (location 'A') on the subsequent planed surfaces.

The signal energy from the EDM machined surfaces generally was larger compared to the planed surfaces, (**figure 5.4.18**). As EDM machining involved no mechanical contact between the tool and work-piece there were no significant residual mechanical stresses generated by the surface removal process. The overall signal energy profile of the specimen increased as the thickness and crack depth were reduced. The EBE energy profile due to the removal of the first 1.5 mm thickness displayed little change. Further machining exhibited an increase in the energy profile. As noted before, the reduced density of pinning sites, present on the specimen surface after EDM machining, allowed an optimum mean-free-path for the domain walls to sweep, thus, generating larger EBE envelopes and signal energy (**section 4.4.3**). The steady signal energy profile from the machining of the first 1.5 mm surface thickness (**figure 5.4.18**) was probably caused by the residual stress and dislocation density present within the 'as-received' surface resulting from the grinding and welding processes. The EDM machining removed the high stress and dislocation densities contained within the 'as-received' surface. After the surface layer, containing these pinning sites, was removed, the signal energy began to

increase as the domain walls were able to move with greater ease over a larger volume. As the EDM machining generated consistently reproducible surfaces, the variation in the EBE signal energy between each machining process (seen in **figure 5.4.18**) was considered to be due to the reduction in crack depth and specimen thickness. The width of the cracked weld region, with its lower magnetic permeability, decreased in size as the crack depth was reduced. This was also reflected in the magnitude of the magnetic leakage field pattern and can be seen in **figure 5.3.8**. The decrease in the crack size was expected to increase the magnetisation intensity around the weld seam, which in turn was expected to enhance EBE. This is reflected in the increasing EBE signal energy from the crack location as the crack depth was reduced.

The EBE signal energy profiles from each of the machined surfaces (**figures 5.4.13** to **5.4.16**) were further examined and it was found that the magnitude of the signal energy value from the different material locations changed in relation to each other. The difference between the signal energy from the parent material, HAZ region and cracked weld locations from each of the machined specimens are displayed in **figure 5.4.19** and **5.4.20**. The EBE energy value of the parent material was measured at location 'A'. The HAZ region energy was measured at the maximum energy value close to the crack, located between positions 'F' and 'J'. The EBE signal energy from the crack was measured as the energy minimum on locations 'K' or 'L'.

On the planed machined specimen surfaces, the difference between the signal energy from the parent material (A) and the cracked location (C) appeared to show a general increase as the specimen thickness and crack depth were reduced, (**figure 5.4.19**). This trend was encouraged by the large EBE energy values recorded on the parent material region. As the specimen thickness and crack depth were reduced, the energy differences between the 'parent material- crack' (line A-C) remained relatively constant. The 'HAZ region- crack' (line B-C) showed a general increase with decreasing specimen thickness.

EDM machining generated reproducible surface structure and texture. This was confirmed by the EBE envelope shape reproducibility between different machined surfaces (**figure 5.2.28 to 5.2.44**). As the specimen thickness was reduced, the energy

difference between the parent material and the crack locations exhibited a decrease, (**figure 5.4.20**). The EBE energy from the crack location increased at a greater rate compared with the surrounding material, (**figure 5.4.18**). As the machining reduced the crack depth, this led to a general decrease in the signal energy difference between the HAZ region and crack location. **Figure 5.4.20** shows the effect of the specimen thickness and crack depth being reduced. The energy differences between the 'parent material- crack' (line A-C) and the 'HAZ region- crack' (line B-C) decreased, though at slightly differing rates. This was a result of the central dip in the EBE signal energy profile, from the EDM machined surfaces, becoming smaller with subsequent machining. This can be seen graphically in **figures 5.4.15** and **5.4.16**.

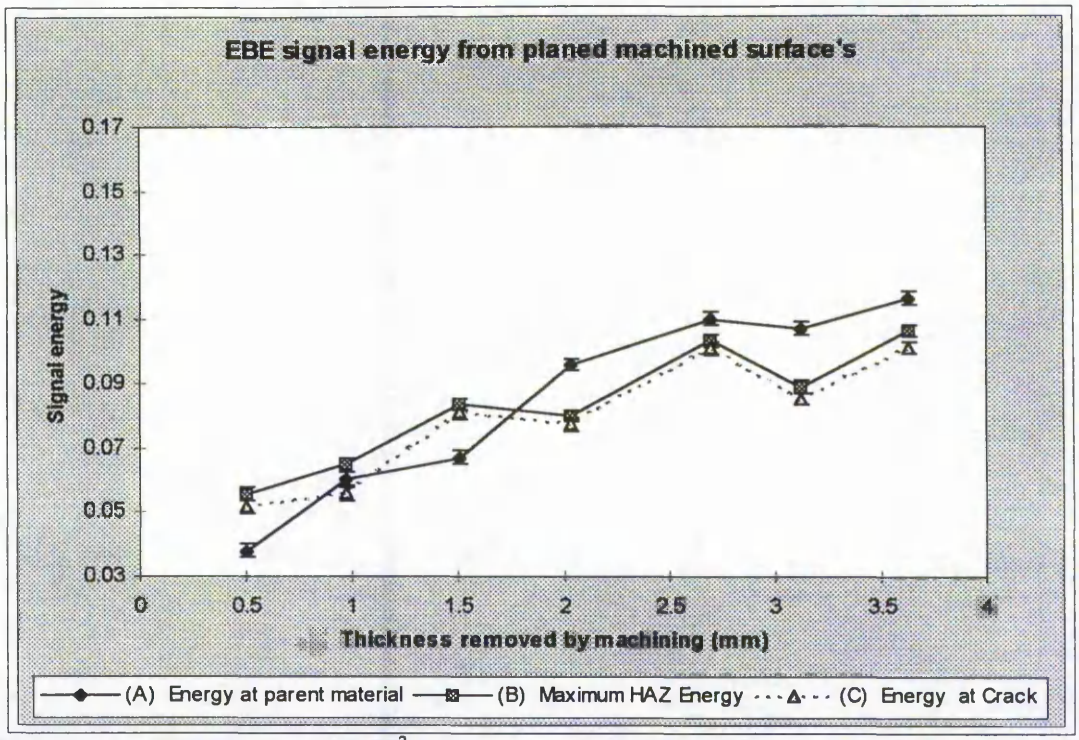


Figure 5.4.17 EBE Signal energy (V^2s) from the cracked weld specimen's various planed machined surfaces. The signal energy values from the different material regions; parent material (line A), HAZ region (line B) and crack (line C) are exhibited for each machined surface. Error bars for signal energy values are ± 0.002 V^2s.

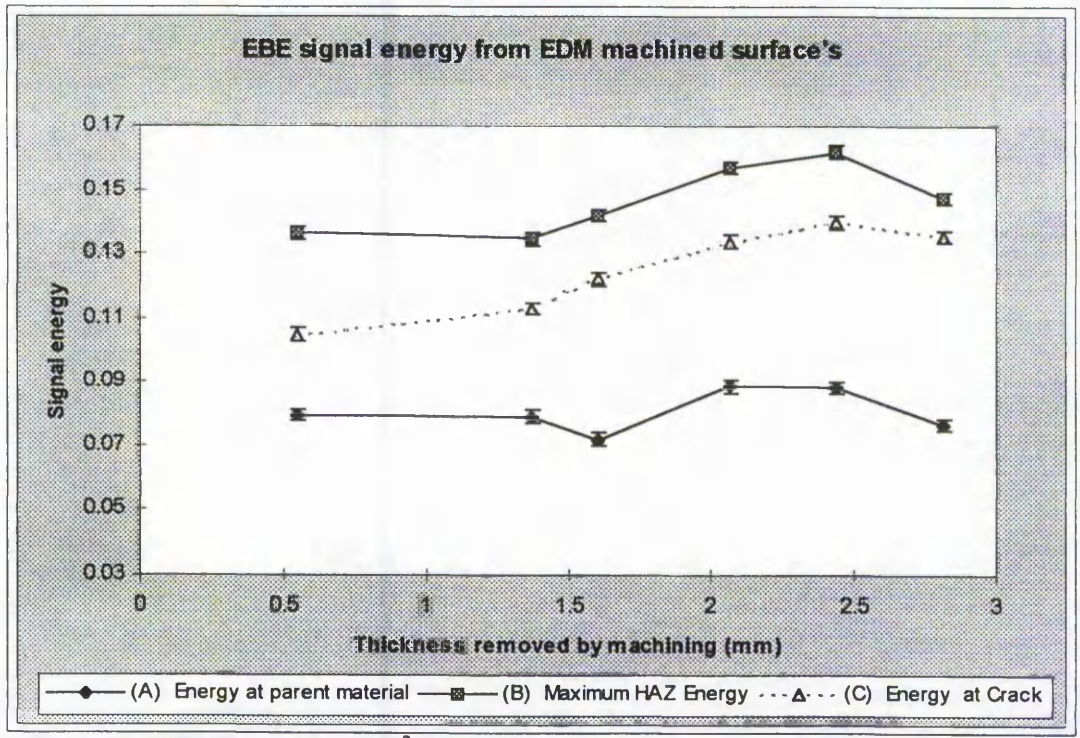


Figure 5.4.18 EBE Signal energy (V^2s) from the cracked weld specimen's various EDM machined surfaces. The signal energy values from the different material regions; parent material (line A), HAZ region (line B) and crack (line C) are exhibited for each machined surface. Error bars for signal energy values are ± 0.002 V^2s.

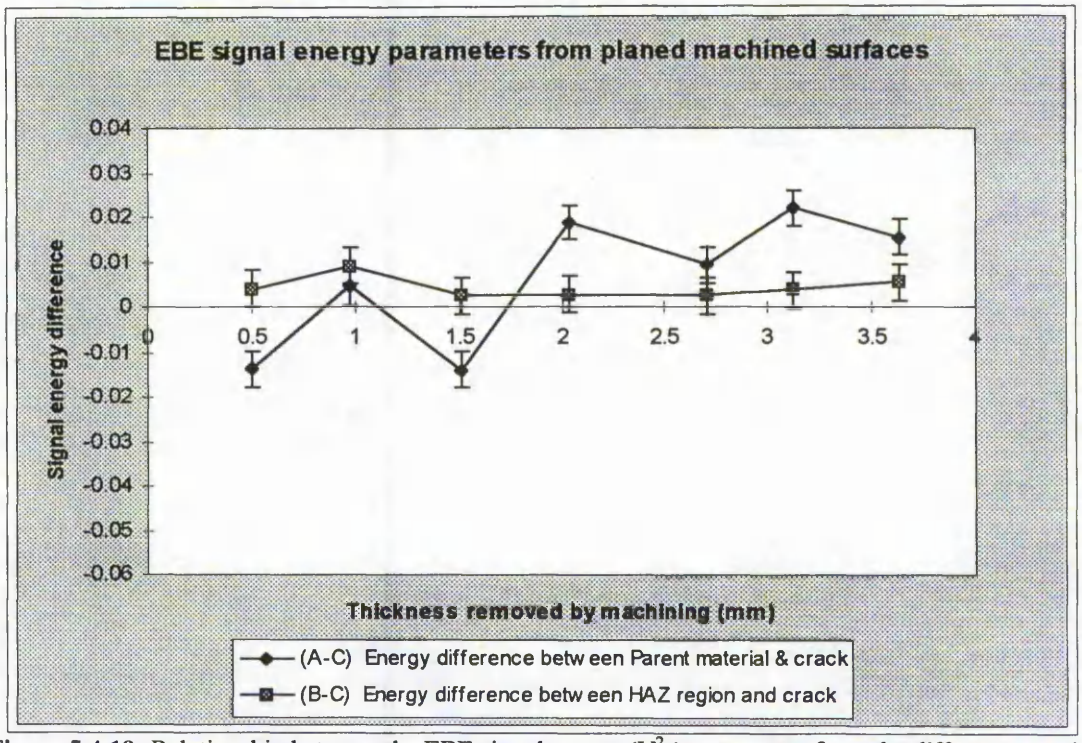


Figure 5.4.19 Relationship between the EBE signal energy (V^2s) parameters from the different material regions on the planed machined surfaces shown in **figure 5.4.17**. Error bars for signal energy difference values are ±0.004 V^2s.

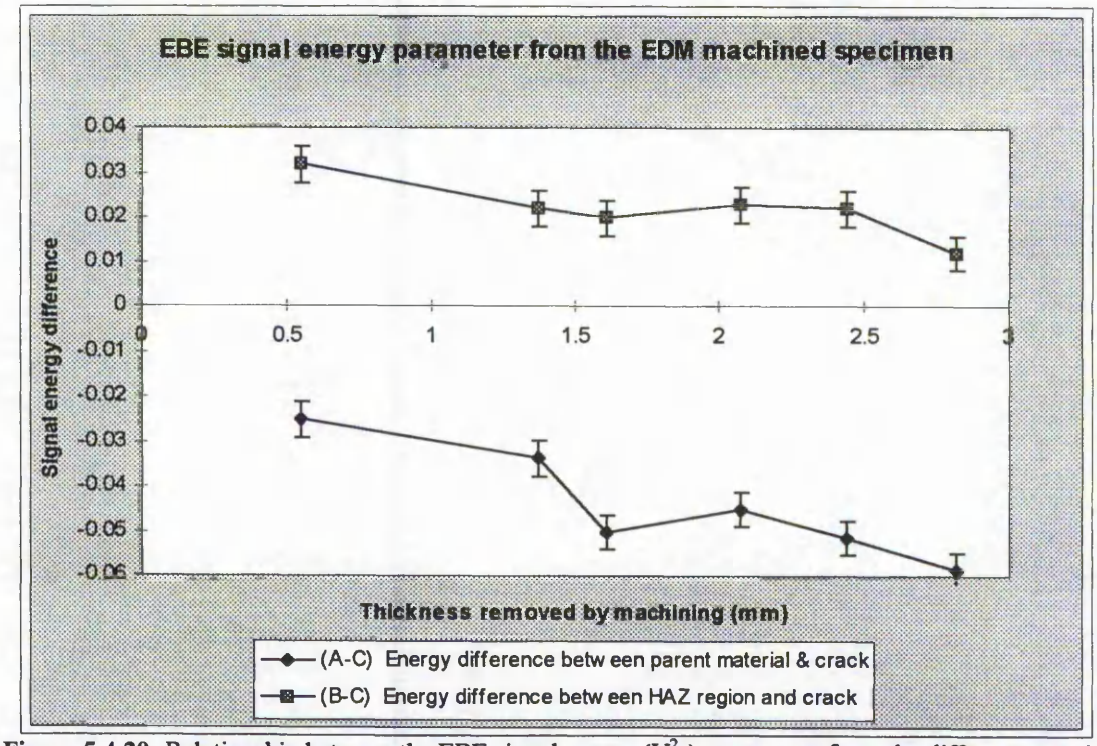


Figure 5.4.20 Relationship between the EBE signal energy (V^2s) parameters from the different material regions on the EDM machined surfaces shown in **figure 5.4.18**. Error bars for signal energy difference values are ±0.004 V^2s.

EBE **signal envelopes**, being sensitive to surface conditions, were able to detect changes resulting from the machining processes. The planed specimen surfaces yielded EBE envelopes which, by their shape and size, reflected the material type i.e. weld or parent material. A combination of the EBE envelopes T_P and V_{MAX} values may be used to characterise the machined surfaces. Analysis of the EBE envelope parameters, especially T_P values, effectively showed the weld affected region. Generally, on the planed surfaces 25A to 28A the changes in the V_{MAX} profile highlighted the transition point between the weld and parent material. The signal energy parameter was not very effective in distinguishing between material phases in the planed specimen. The signal envelopes from the EDM machined surfaces showed consistent T_P values irrespective of the material type and were generally incapable of distinguishing the different regions within the welded specimen. This was due to the complex microstructure and stress profile present within by the recast layer. However, the V_{MAX} parameter was able to distinguish changes in the material's structure resulting from a weld. The V_{MAX} parameter exhibited large values on the 'HAZ-weld' interface with a decrease on the crack location. The changes in the material structure, within the weld region, combined with the presence of the crack helped lower the magnitude of the V_{MAX} values. Away from the weld the parent material region showed lower V_{MAX} values. Similar trends were found with the signal energy parameter. Each machining technique generated EBE envelopes which were slightly different. By noting the characteristics of an EBE envelope it was possible to distinguish the type of machining used, as well as, the location on the material from where the EBE envelopes was detected. Successful interpretation of the data and application of this method is dependent on prior knowledge of the technique and its capabilities.

5.4.2. ABE Signal Envelopes from the Machined Cracked Weld Specimens.

The ABE signal envelopes detected from the machined cracked weld specimens appeared, essentially, double peaked in shape. The planed surface (22A) exhibited ABE envelopes, some of which possessed spikes and minor peaks on the central region of the specimen. Further planing greatly reduced the presence of such spikes and minor peaks. Surfaces 27A and 28A exhibited smooth envelopes, completely free of spikes. The EDM machined surface (22B) displayed large spikes which were situated on the position of the large second peak. This led to a large signal voltage (V_{MAX}) being recorded for this particular EDM machined surface. Surface 23B displayed smooth double peaked ABE envelopes. Surface 24B, again, exhibited the sharp spikes situated on the position of the maximum peak. These spikes were smaller than the ones detected on surface 22B. On further machining the ABE envelopes, in nearly all cases, were found to be spike free. Occasionally, certain positions, such as surface 25B; location 'E' (**figure 5.2.49**), exhibited small spikes after the maximum second peak. On further machining the detected ABE envelopes appeared smooth, without the presence of any spikes.

The ABE envelope Time of Peak (T_P) and maximum signal voltage (V_{MAX}) were measured at the position of the largest peak, which was usually the second peak. When the position of the maximum second peak was disguised by a spike, the spike itself was used to measure the T_P and V_{MAX} values. For the planed and EDM machined surfaces, each exhibited a relatively stable time of peak, (**figure 5.4.21** to **5.4.24**). The time of peak for different locations on each surface varied by 0.05 s. The averaged T_P value from each of the planed and EDM machined surfaces also lay within 0.05 seconds spread.

As the crack depth and surface thickness were reduced the ABE envelopes from both of the machined surfaces changed slightly. The T_P values from the planed specimen increased for the first three machined surfaces, then decreased on surface 26A and remained at this new level for each of the subsequent planed surfaces, (see **figure 5.4.25**). The EDM machined surfaces displayed T_P values which gradually decreased as more machining was carried out, (see **figure 5.4.26**). Surface 25B displayed a very small

spread of T_P values, while surface 22B exhibited a much larger T_P spread due to the presence of the spikes masking the exact location of the maximum second peak.

The maximum signal voltage (V_{MAX}) detected on each of the planed machined surfaces was relatively consistent and lay within a **0.4 V** spread **(figures 5.4.27** and **5.4.28)**. However, this stability was not found on the EDM machined surfaces. The EDM machined surfaces, 22B and 24B, both exhibited large spikes on the position of the second peak. These spikes caused the V_{MAX} values to vary greatly: by **0.9 V** on surface 24B, (see **figures 5.4.29** and **5.4.30**). With the exception of surfaces 22B and 24B, the V_{MAX} values for the ABE envelopes from a given EDM machined surface fell within a **0.2 V** to **0.4 V** range. This was the same as for the planed machined specimen's surface. The machining process, when carefully carried out, is know to affect only the surface of the specimens, (**section 2.4**). The ABE is a volume effect and any stresses generated by the machining process are restricted to a relatively thin surface layer. The ABE signals, therefore, are not expected to be affected by the changes in surface stresses. The different material regions: parent material, HAZ and cracked region, were not distinguishable from the V_{MAX} parameter. This was expected as small volumes of material, such as the HAZ regions, were not expected to have a significant effect on the overall bulk of the ABE signal envelope.

The 'maximum signal voltage' from each of the planed machined surfaces displayed a gradual trend where the reduction in the crack depth and surface thickness increased the overall V_{MAX} values detected from each planed surfaces, (**figure 5.4.31**). The EDM machining generated two surfaces, 22B and 24B, which exhibited large spikes directly on the second peak of the ABE envelopes. This forced the V_{MAX} values to have a larger spread compared to other EDM machined surfaces. The general trend where V_{MAX} increased with decreasing specimen thickness can also be seen on the EDM machined surfaces, if the spiked signal generating surfaces are ignored, (see **figure 5.4.32**).

ABE signal energy from the planed machined surfaces are shown in **figure 5.4.33** and **5.4.34**. The ABE signal energy from the various locations on the planed surface 22A

exhibited a signal energy spread between **0.23** to **0.48 V^2s**. For the rest of the planed surfaces (23A to 28A) the magnitude of the signal energy spread remained very similar.

ABE signal energy from the EDM machined surfaces are displayed in **figure 5.4.35** and **5.4.36**. The EDM machined surfaces displayed an interesting phenomena which was not evident on the planed machined surfaces. It appeared that location 'E', directly on the cracked region, exhibited a smaller signal energy than its neighbouring locations. This was evident on all surfaces except 25B. Surface 25B exhibited a spike on the ABE envelope detected above the crack, on location 'E' and, therefore, failed to display the reduced ABE signal energy on this position. As the EDM machining process reduced the crack depth and specimen thickness the ABE signal energy from the crack location 'E' generally increased in magnitude. A possible explanation could be that the presence of the 'as-received' large crack provided a greater masking of the ABE signal, while the reduction in the crack depth caused the masking effect to decrease. For the final few machining runs, the crack mouth became covered by resolidified material and this would be expected to also increase the detected ABE signals. The spread of the signal energy from the EDM machined surfaces was very similar, between **0.25 V^2s** and **0.45V^2s**, with a clear exception of surface 25B. Surface 25B exhibited an abnormally large ABE signal envelope on location 'F', which led to the large signal energy.

The signal energy spread from each of the planed machined surfaces exhibited a relatively wide range of energy values (**figure 5.4.37**). The overall trend appeared to show an increase in the ABE signal energy with reduced specimen thickness. The EDM machined surfaces exhibited signal energy ranges which were smaller than for the planned surfaces (**figure 5.4.38**). However, surfaces such as 25B, which exhibited an anomalous signal on location 'F' showed a large signal energy spread. The overall trend showed that, as with the planed specimen, the reduction in thickness by EDM machining caused the signal energy to gradually increase.

The double peaked form of the ABE envelope was also observed throughout both types of machined surfaces. Both EDM and planing processes generated very different machined surfaces, yet the ABE envelope from both specimens were very similar. This

alone indicated that ABE signals, unlike EBE signals, are not just a surface effect. The ABE signals are generated as a consequence of magnetostriction and the resulting volume change that this phenomena causes within a magnetised specimen. The volume change, which causes stress waves, arises due to the non-180° domain walls (closure walls) moving through the specimen. These stress waves are generated when the closure domain walls move through the material due to the sweeping magnetic field. The sudden movements of these closure domain walls cause a change in the strain of the material; this leads to the generation of the stress waves which are detected by the piezoelectric transducer as the ABE signals. The double peaked form of the ABE envelope can, therefore, be thought of as originating due to two large burst of stress waves during the magnetisation process. These large bursts occur when a large number of closure walls move or when closure walls move over a relatively large distance before being stopped **[91]**.

The ABE envelopes from the cracked weld specimen were doubled peaked, with a few exceptions. Occasionally spikes appeared on the latter half of the envelopes. Planed surface 22A exhibited spikes at the central region of the ABE envelopes, whereas the EDM machined surface (22B) exhibited spikes at the position of the second peak. In **chapter 4**, it can be seen that ABE envelopes from the original 'as-received' specimens displayed spikes. On the 'as-received' surfaces, the spikes were attributed to the overall residual stress left by the welding process on the specimens, (see **figure 4.4.6**). The residual stress profile placed certain parts of the overall specimen under compression while other parts were in tension. The presence of these forces on the specimen were thought to affect the magnetostrictive volume changes during magnetisation, therefore, resulting in the sudden spikes on the ABE envelopes. The ABE envelopes from the machined specimen surfaces 26B, 27B and 28B, did not exhibit spiked envelopes. This indicated that the EDM machining process, by removing a volume of surface material, significantly reduced the residual welding stress profile, thus, limiting the ABE spikes. This phenomenon may be used to asses the residual stress state of a weld specimen.

The three different material regions (parent steel, HAZ region and the cracked weld) within the specimens were generally indistinguishable from ABE measurements. This was

because ABE originated from the magnetised volume of the specimen. The low acoustic attenuation of steel ensured that the ABE signals were detected from the entire magnetised specimen. As a result, the planed specimen's ABE signal energy did not show any clear indication of the cracked region. However, the EDM machined specimen exhibited a decreased ABE energy above the cracked region on majority of the machined surfaces. Surface 25B did not exhibit the distinctive drop in ABE energy on the cracked location, (**figure 5.4.35**). This was attributed to the large ABE envelope from location 'F' which masked this effect. The magnetic leakage field measurements, indicated that the crack on the EDM machined specimen was larger than the crack on the planed specimen (discussed in **section 4.3**). This implied that the crack size was sufficient to possibly cause masking of the ABE signal from part of the specimen volume. This resulted in a decreased ABE signal energy above the crack.

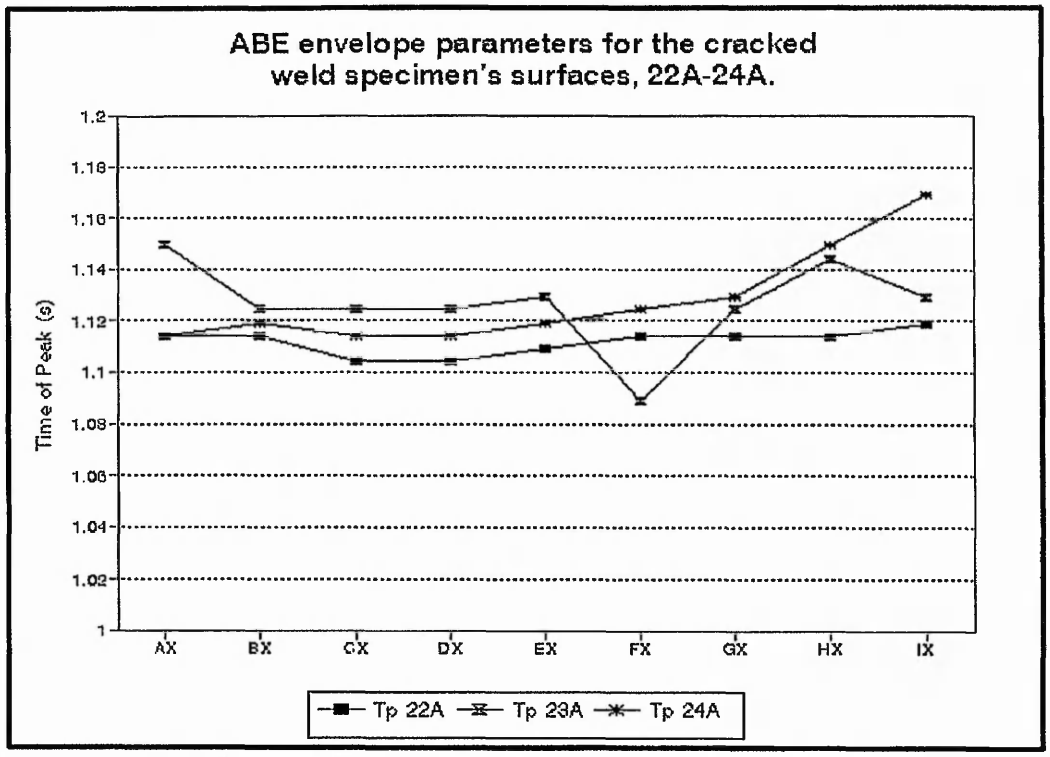


Figure 5.4.21 Time of peak (T_P) profile from the cracked weld specimens planed machined surfaces 22A, 23A and 24A. Location 'A' to 'C' is parent material, 'C' to 'D' is HAZ and between 'D' and 'F' is the weld seam which is approximately 10.5 mm in width (The weld width decreases with the reduction in the specimen width). The crack on the weld centre is situated very close to location 'E'.

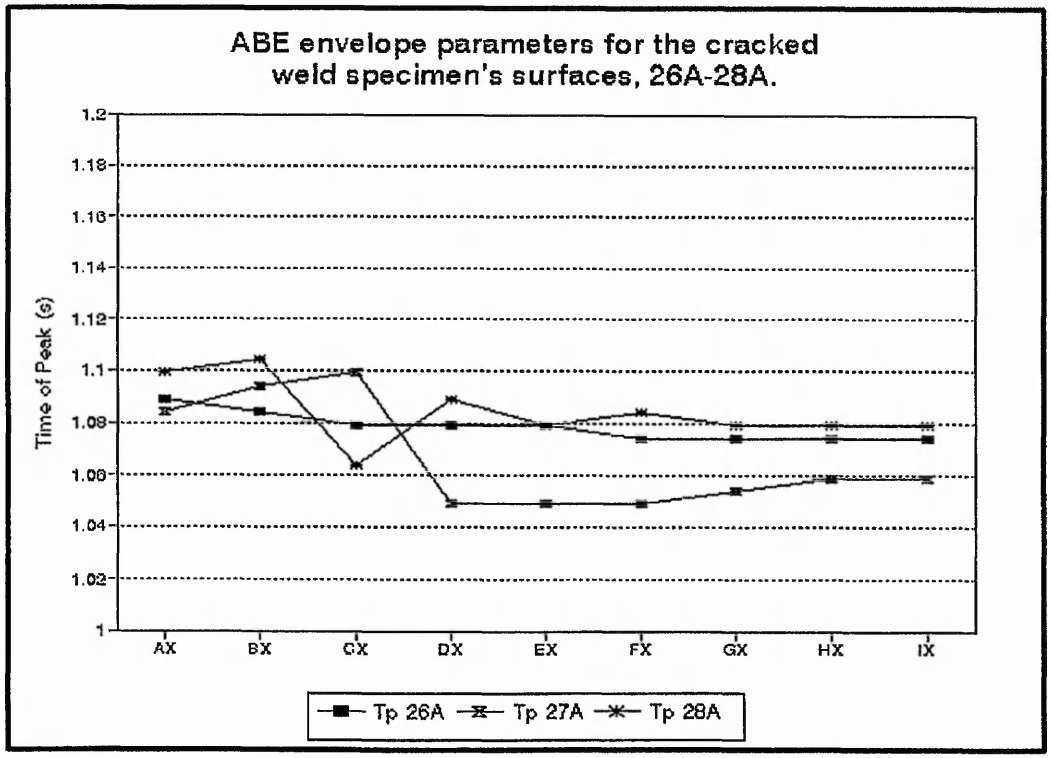


Figure 5.4.22 Time of peak (T_P) profile from the cracked weld specimens planed machined surfaces 26A, 27A and 28A. Cracked weld region is located on position 'E'.

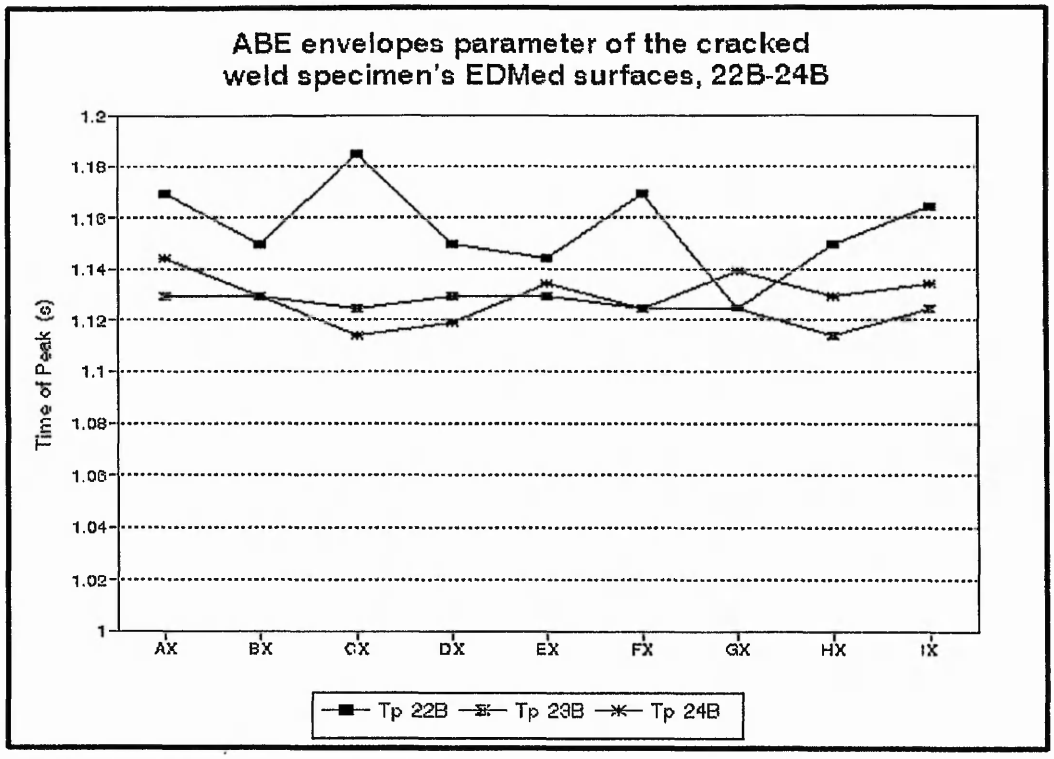


Figure 5.4.23 Time of peak (T_P) profile from the cracked weld specimens EDM machined surfaces 22B, 23B and 24B. Cracked weld region is located on position 'E'.

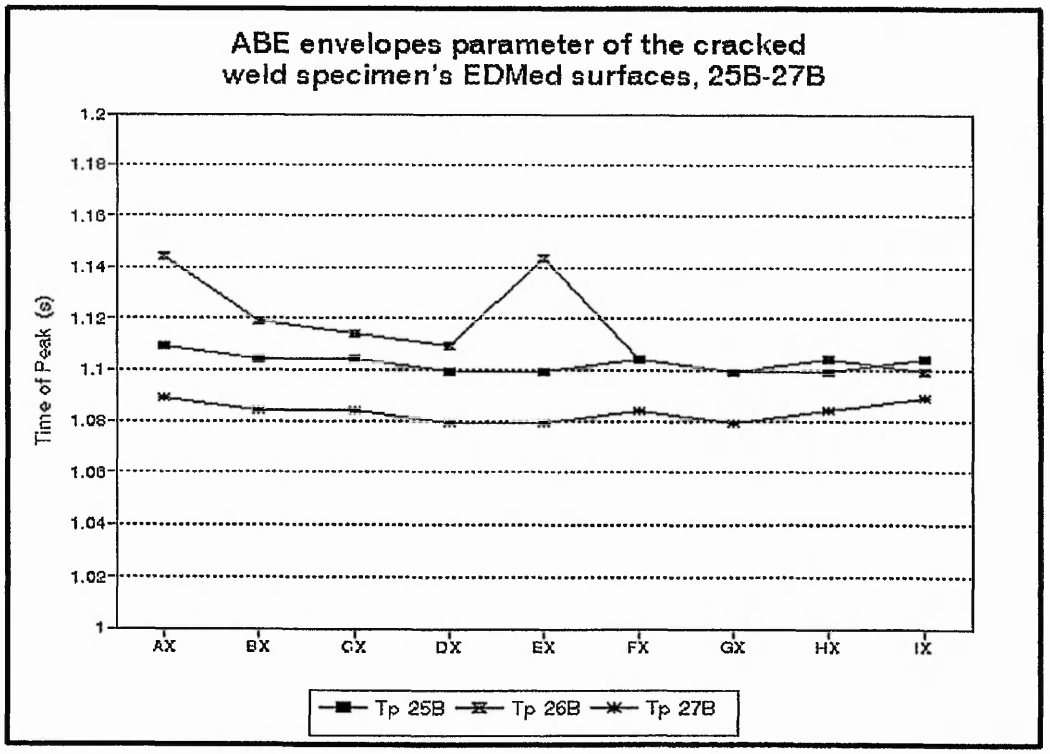


Figure 5.4.24 Time of peak (T_P) profile from the cracked weld specimens EDM machined surfaces 25B, 26B and 27B. Cracked weld region is located on position 'E'.

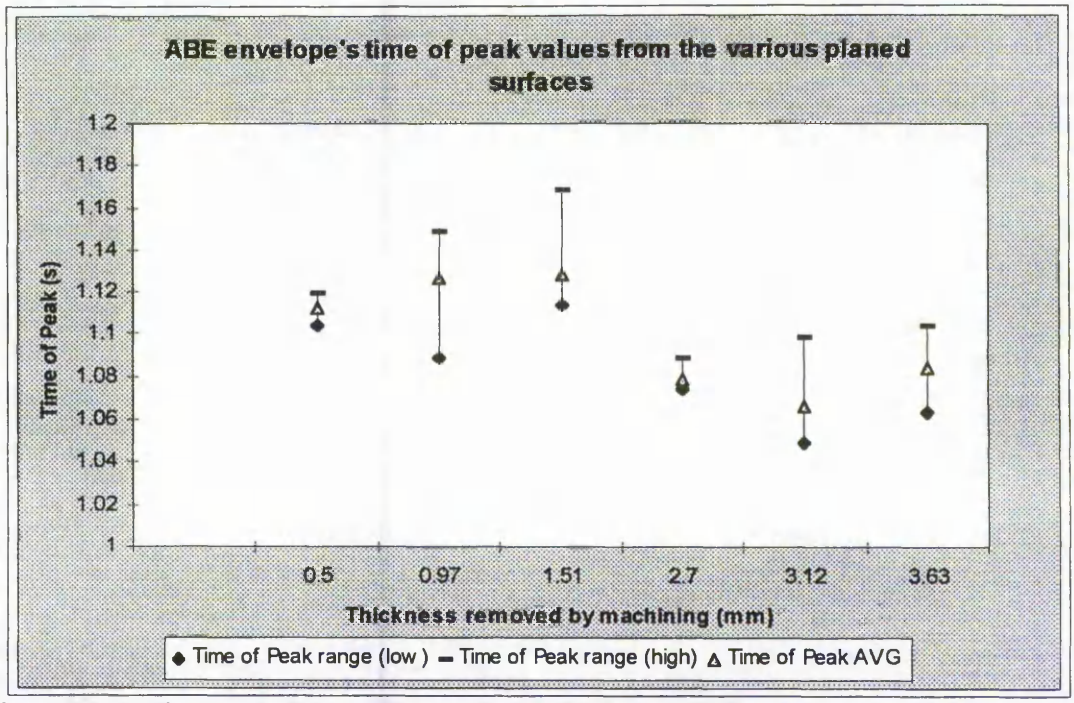


Figure 5.4.25 The spread of the ABE time of peak (T_P) from the different locations across the various planed machined surfaces of the cracked weld specimen.

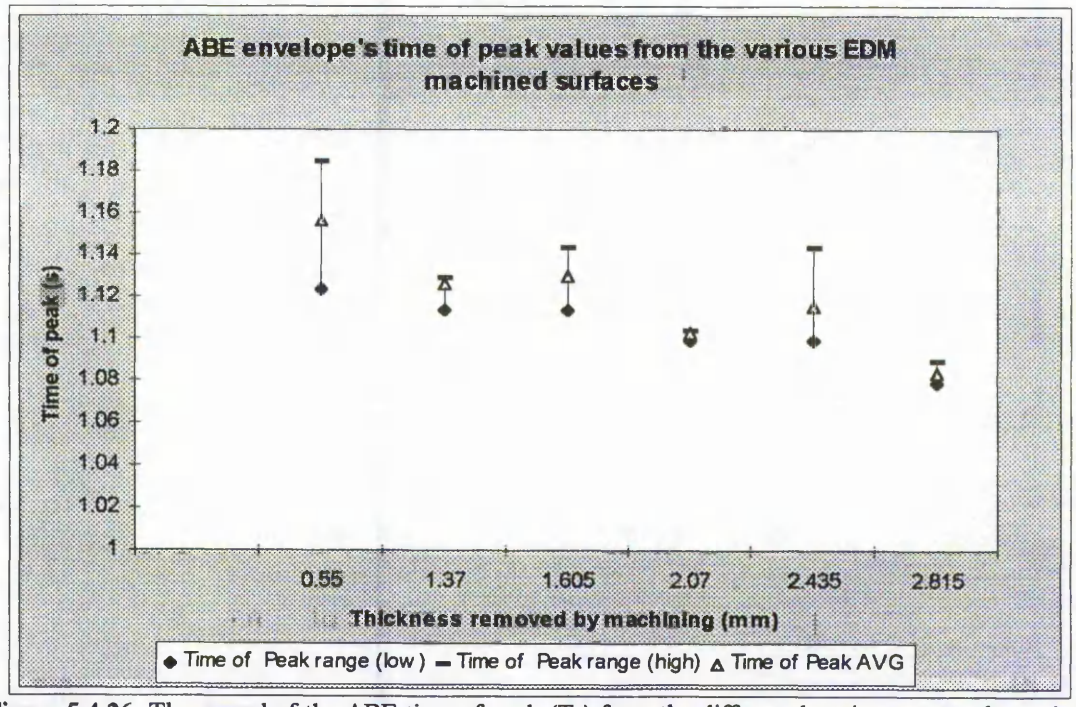


Figure 5.4.26 The spread of the ABE time of peak (T_P) from the different locations across the various EDM machined surfaces of the cracked weld specimen.

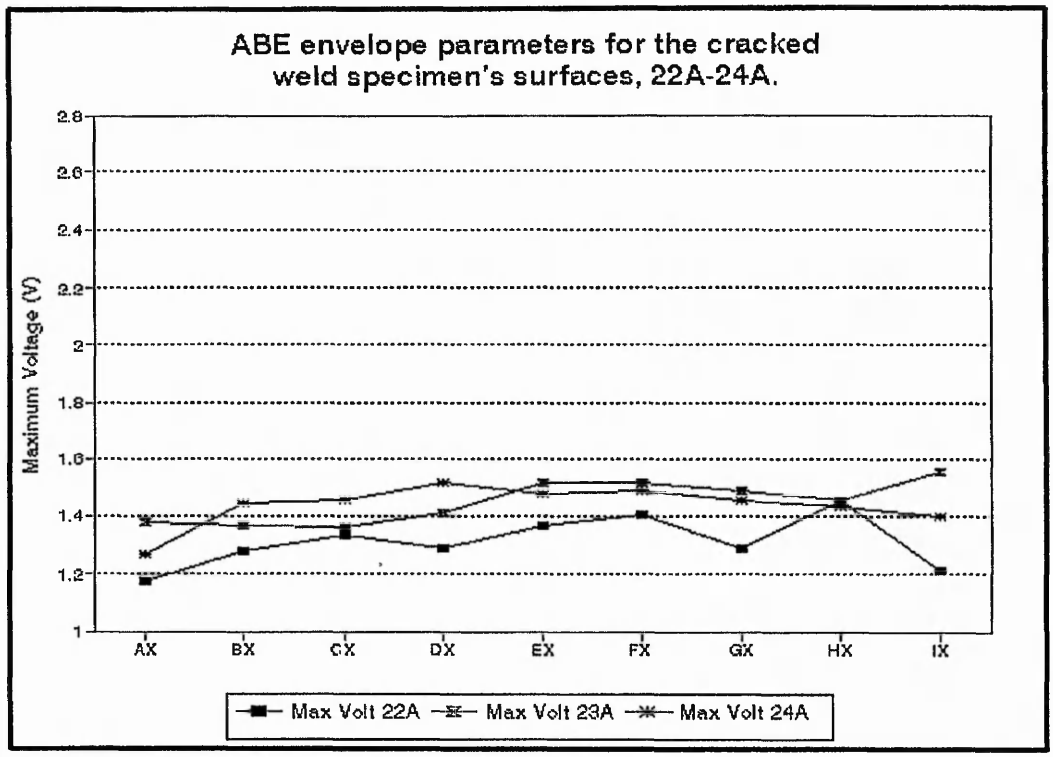


Figure 5.4.27 Maximum signal voltage (V_{MAX}) profile from the cracked weld specimens planed machined surfaces 22A, 23A and 24A. Location 'A' to 'C' is parent material, 'C' to 'D' is HAZ and between 'D' and 'F' is the weld seam which is approximately 10.5 mm in width (The weld width decreases with the reduction in the specimen width). The crack on the weld centre is situated very close to location 'E'.

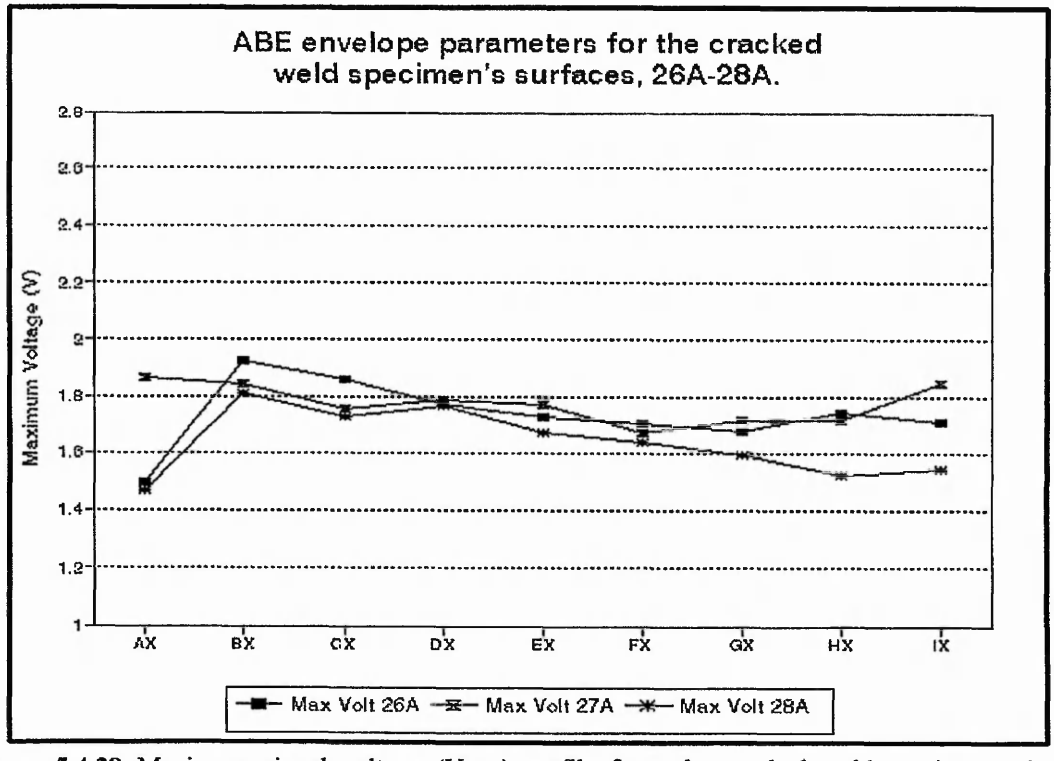


Figure 5.4.28 Maximum signal voltage (V_{MAX}) profile from the cracked weld specimens planed machined surfaces 26A, 27A and 28A. Cracked weld region is located on position 'E'.

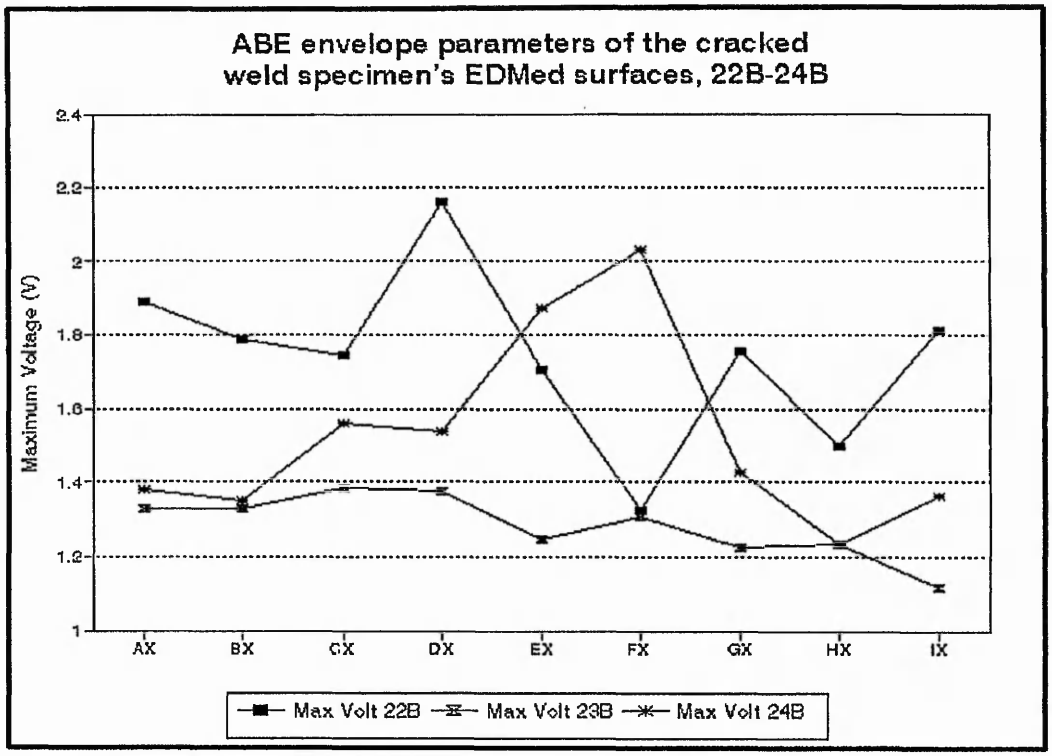


Figure 5.4.29 Maximum signal voltage (V_{MAX}) profile from the cracked weld specimens EDM machined surfaces 22B, 23B and 24B. Cracked weld region is located on position 'E'.

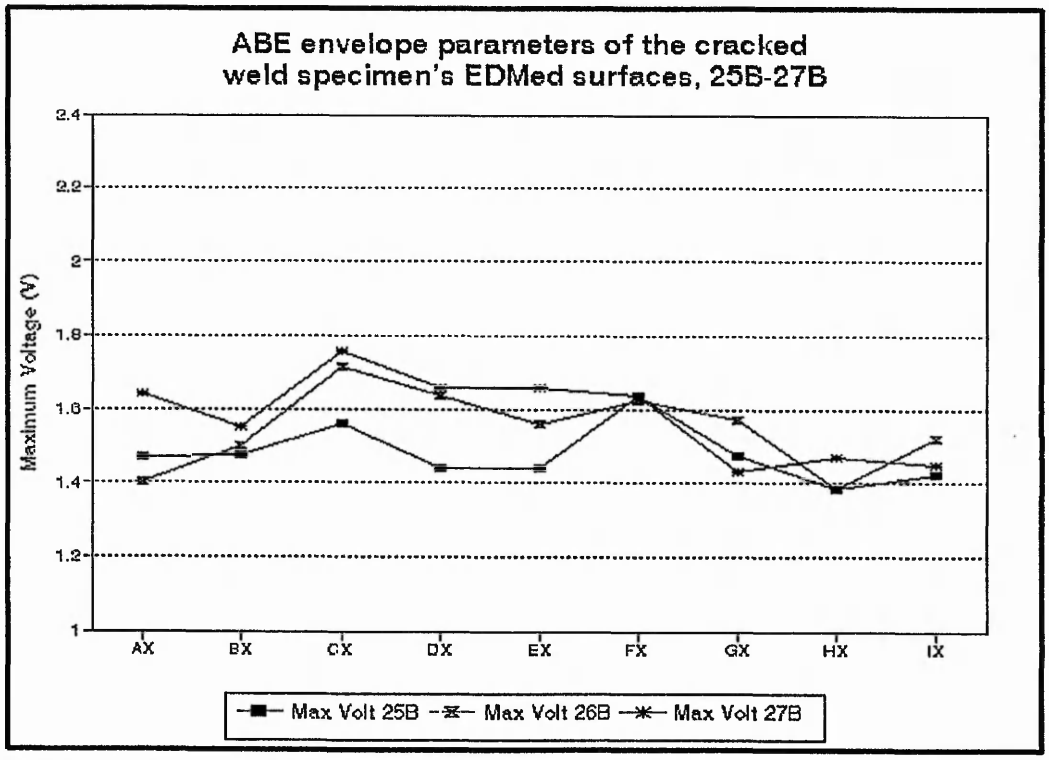


Figure 5.4.30 Maximum signal voltage (V_{MAX}) profile from the cracked weld specimens EDM machined surfaces 25B, 26B and 27B. Cracked weld region is located on position 'E'.

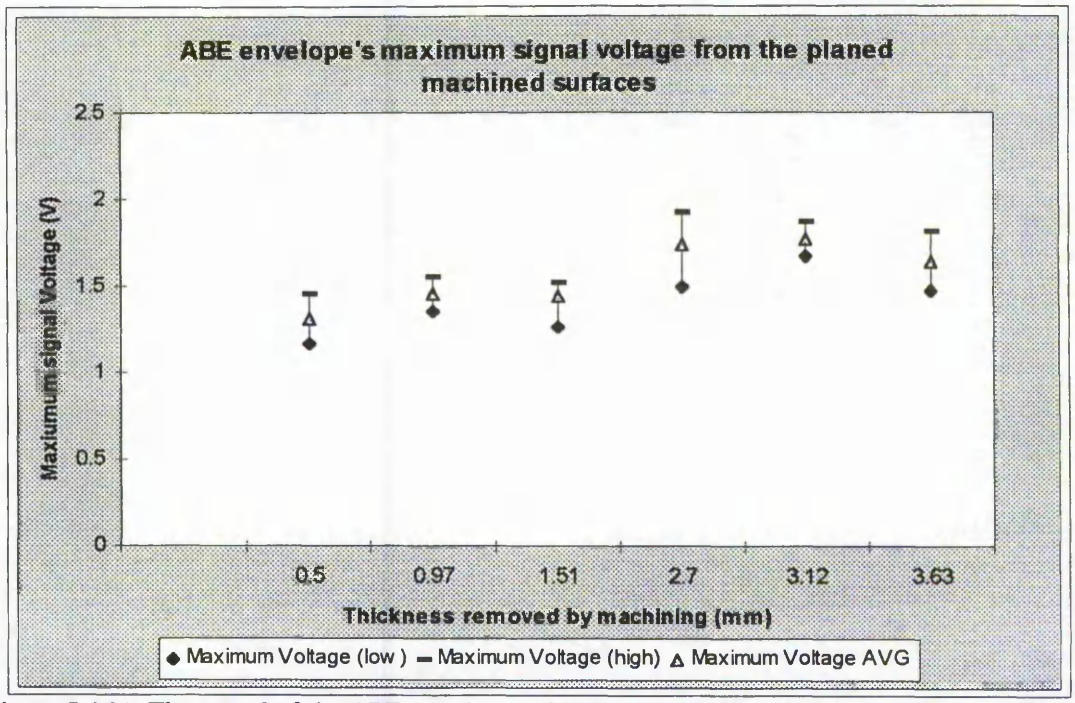


Figure 5.4.31 The spread of the ABE 'maximum signal voltages' (V_{MAX}) from the different locations across the various planed machined surfaces of the cracked weld specimen.

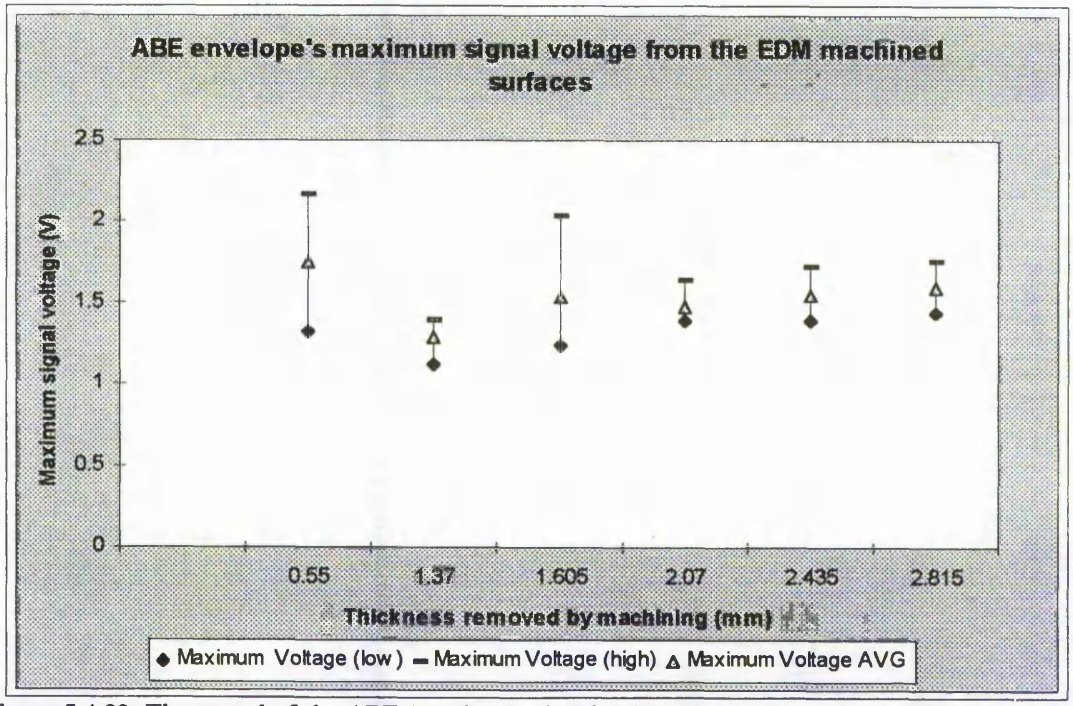


Figure 5.4.32 The spread of the ABE 'maximum signal voltages' (V_{MAX}) from the different locations across the various EDM machined surfaces of the cracked weld specimen.

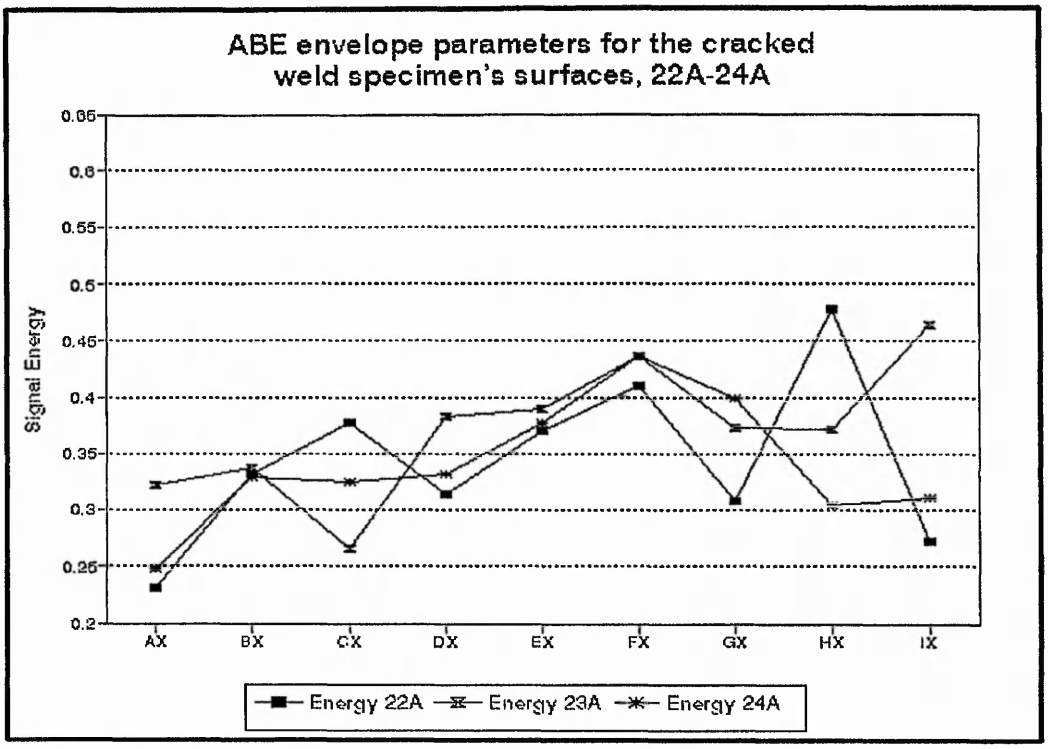


Figure 5.4.33 Signal enregy (units V^2s) profile from the cracked weld specimens planed machined surfaces 22A, 23A and 24A. Location 'A' to 'C' is parent material, 'C' to 'D' is HAZ and between 'D' and 'F' is the weld seam which is approximately 10.5 mm in width (The weld width decreases with the reduction in the specimen width). The crack on the weld centre is situated very close to location 'E'.

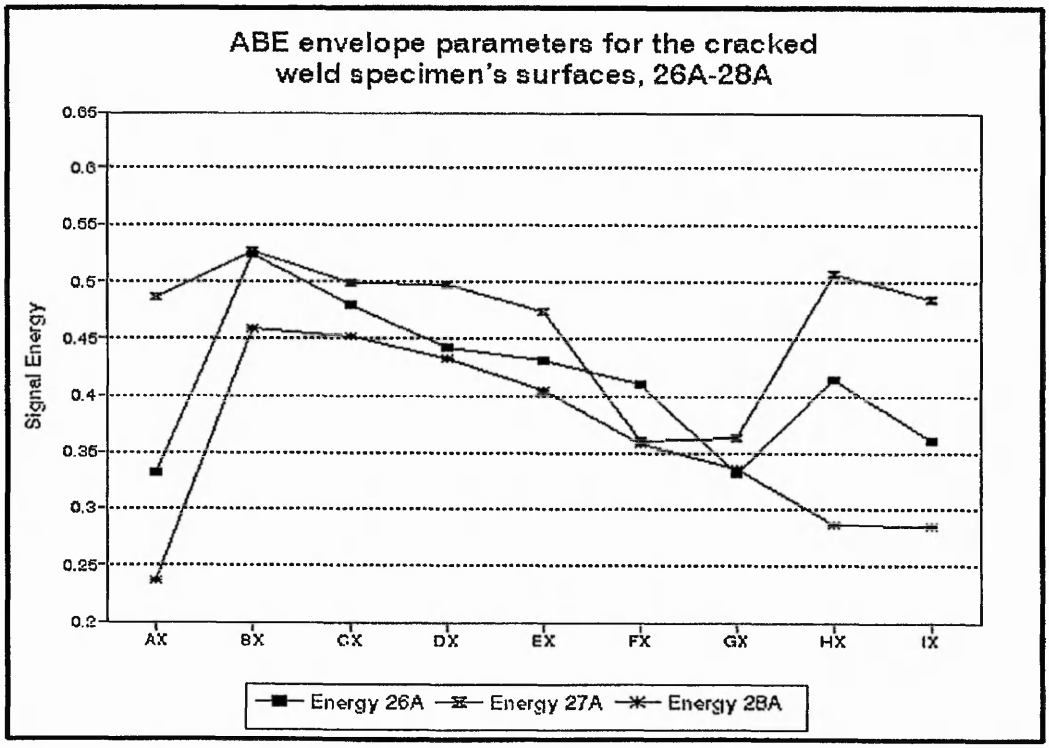


Figure 5.4.34 Signal enregy (units V^2s) profile from the cracked weld specimens planed machined surfaces 26A, 27A and 28A. Cracked weld region is located on position 'E'.

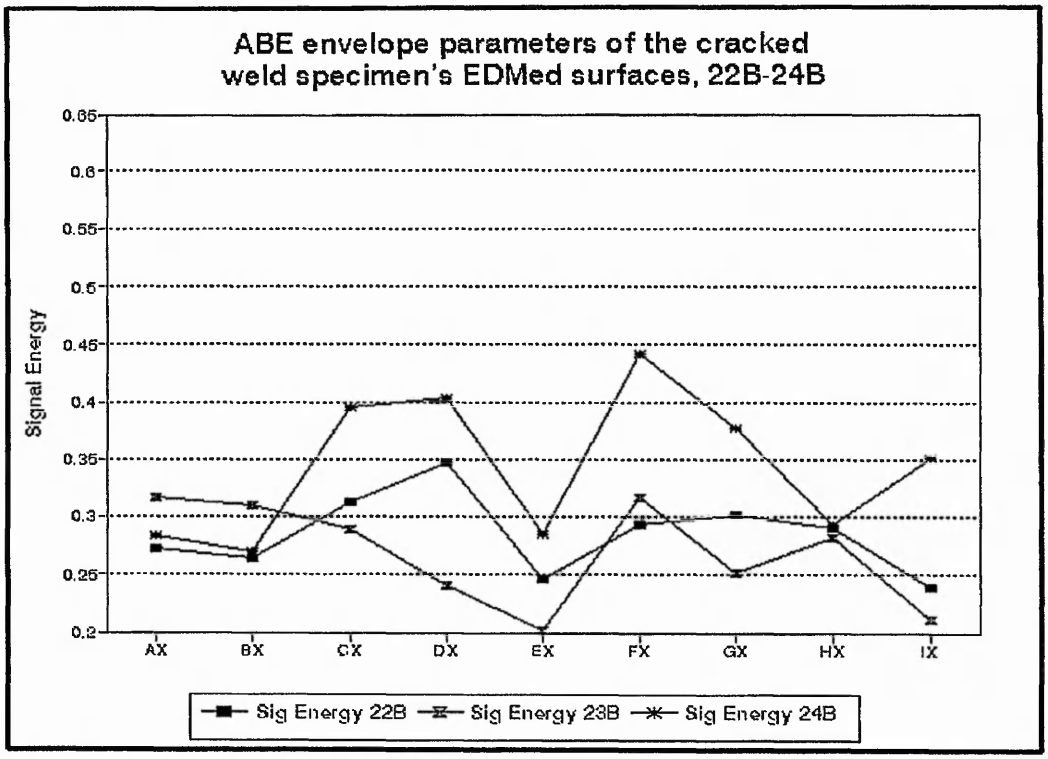


Figure 5.4.35 Signal enregy (units V^2s) profile from the cracked weld specimens EDM machined surfaces 22B, 23B and 24B. Cracked weld region is located on position 'E'.

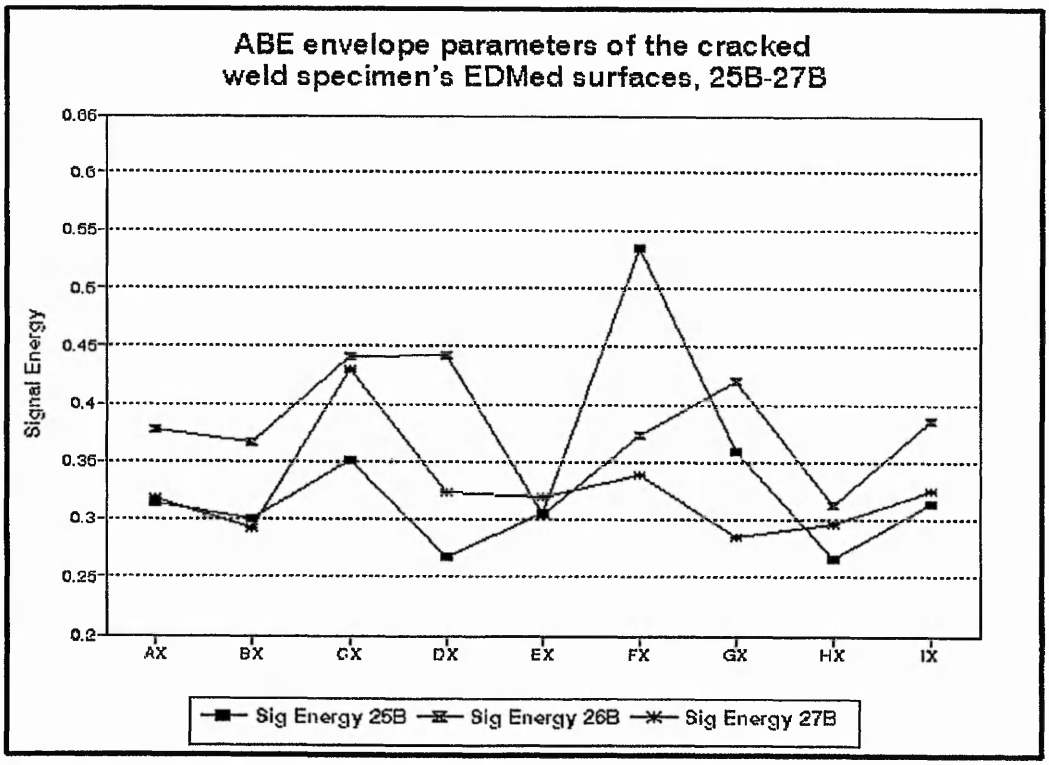


Figure 5.4.36 Signal enregy (units V^2s) profile from the cracked weld specimens EDM machined surfaces 25B, 26B and 27B. Cracked weld region is located on position 'E'.

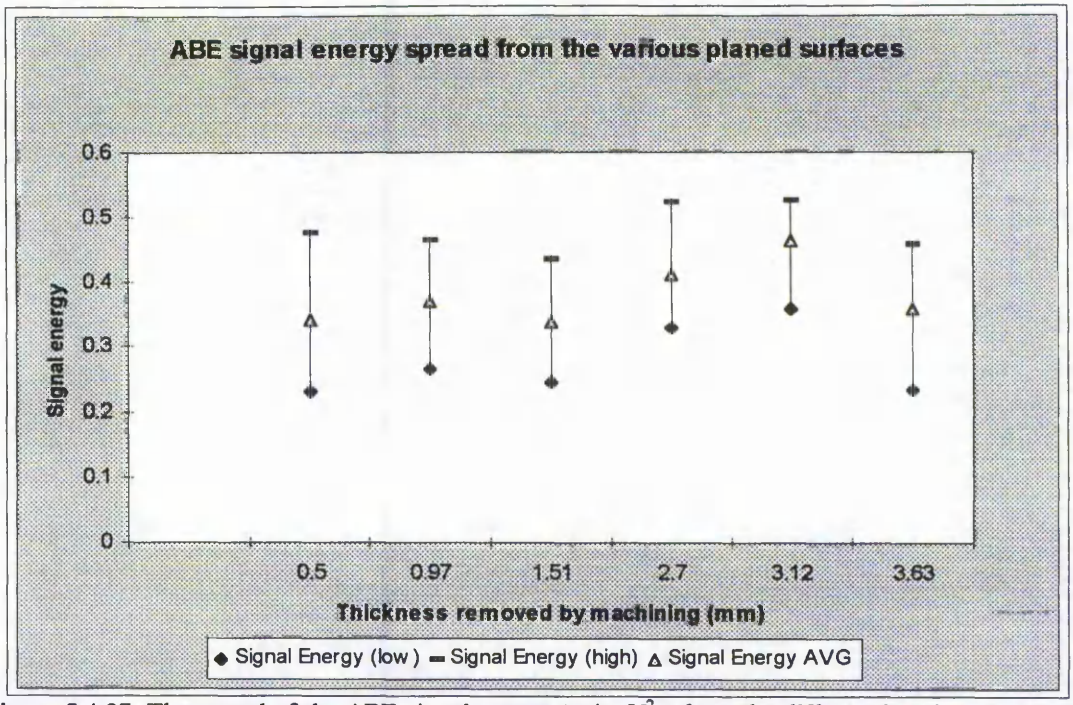


Figure 5.4.37 The spread of the ABE signal energy (units V^2s) from the different locations across the various planed machined surfaces of the cracked weld specimen.

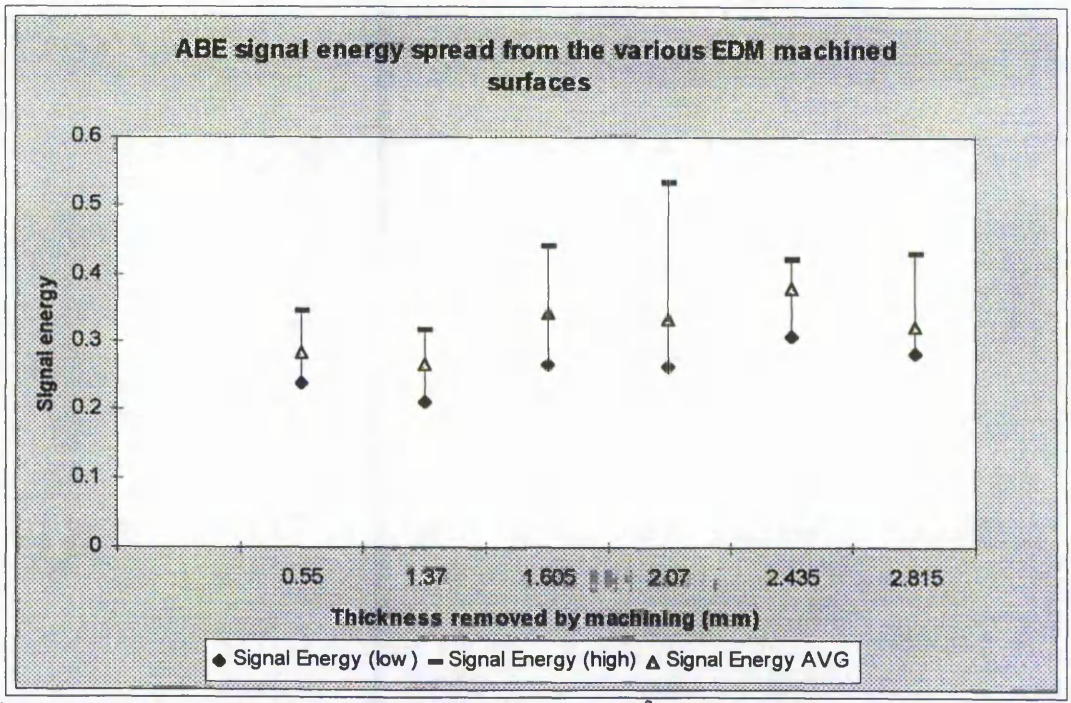


Figure 5.4.38 The spread of the ABE signal energy (units V^2s) from the different locations across the various EDM machined surfaces of the cracked weld specimen.

END *of* CHAPTER

PART 3

Conclusion and Further Work.

Conclusion

6

6. Conclusion.

Barkhausen emission is heavily influenced by stress and microstructural properties of the specimen under consideration. In the early section of this thesis it was found that the distribution of magnetic field for the specimen would affect the EBE signal. Optimum reproducible results were expected from the central portion (50 mm in length) of a magnetised specimen. EBE 'maximum signal voltage' (V_{MAX}) values were affected by non-uniform magnetisation, as seen in chapter 2 of this thesis. The change in the EBE envelopes V_{MAX} values were found to be similar to the x-component of the FE modelled magnetic flux on the surface of the specimen. A discrepancy between the V_{MAX} values and the **Bx** component of the magnetic induction exists as EBE envelopes are also influenced by material microstructure, composition and stress state. It was also shown that the ABE envelopes from a high purity nickel specimen were related to the specimen volume, whereas, the EBE was a surface effect and not influenced by the specimen volume changes. Upon surface alteration of a nickel specimen, the EBE envelope parameters were found to be sensitive to the condition of the surface. 'Time of peak' (T_P), 'V_{MAX}', signal energy and envelope shape changed depending on the surface condition.

Work on Barkhausen emission from around an idealised surface defect, showed that a sufficiently large defect (modelled by a slot) altered the EBE envelopes, which clearly indicated its location. The use of a high resolution sensor, yielded EBE envelopes which were detected from a small region of material. For the initial study it was found that using an optimum sized EBE sensor the shape of the envelopes, may be able to indicate the location of a slot type defect. Combining an optimum sized sensor and magnetisation rate, it was also found that the exact position of the defects could be located.

The combination of 'sensor size' and 'magnetisation rate' was successfully applied to the detection of a tight fatigue crack. The EBE envelopes detected from the surface of a cracked steel specimen (OLI 95F) showed little overall change in shape. However, the EBE envelope parameters, such as V_{MAX} and signal energy, clearly showed that above the crack location there was a decrease in magnitude. On either side of the crack, due to the plastically deformed regions, large signal energy values were recorded. The T_P values, from across the fatigue cracked surface, occurred earlier compared to regions away from the crack. ABE signals from the fatigue cracked specimen were shown to be of a general form: doubled peaked, with the second peak being larger than the first. The ABE envelope parameters were not expected to yield information regarding the location of the crack, although changes in the state of the material's bulk properties is known to affect the ABE envelope and may be used as an indicator of damage arising from stress.

Work on the 'as-received' EN-43A steel plates showed that the changes in stress and microstructural state resulting from specimen history were clearly detectable using Barkhausen emission. Due to the relatively uniform microstructure and the stress state of the plain steel plate the averaged EBE parameters could be used as calibration (T_P=1.039 ±0.015 s, V_{MAX}= 0.496 ±0.030 V, signal energy =0.061 ±0.007 V^2s). The ABE envelopes were known to be affected by the volume of the magnetised specimen, (section 2.3). The ABE envelopes were found to be generally reproducible across the surface of the specimen with parameters of T_P=1.150 ±0.028 s, V_{MAX}= 0.993 ±0.167 V, signal energy =0.232 ±0.045 V^2s. These values for the ABE and EBE parameters were used as reference values for the 'as-received' plain EN-43A steel plate specimen.

It has been found that the EBE envelopes, detected from the TIG welded steel plate (2P), changed form compared to the plain steel plate specimen (3P). However, the ABE envelopes remain of a similar form to the plain steel plate. Both the plain and welded specimens' sizes were very similar and the composition of the parent material was identical; the only difference being the presence of the weld and the resulting changes in the microstructure and residual stress profile around the weld seam. The changes in the EBE envelopes shape and parameters were attributed to the welding process and the presence of the weld seam. It was found that, with a weld seam present, the EBE envelope parameters, V_{MAX} and signal energy values, increased significantly and the T_P values were found to occur earlier in the envelope. For the welded plate specimen the EBE envelopes could be used to successfully detect the differing material regions within the specimen. The ABE envelope parameters from the welded steel specimen were also found to change compared to the plain steel specimen. It is known that the presence of residual stress has a significant influence on the ABE signals. Compared to the ABE signal energy and V_{MAX} values from the plain steel specimen, the welded specimen exhibited an increase. Combining the observed envelope shape and its respective BE parameters it is possible to clearly distinguish between a welded and plain EN-43A steel specimen.

A low-cycle flexural fatigue crack present within a weld seam was found to lower the overall signal energy and V_{MAX} parameter profile. However, T_P parameter profiles were shown to occur even later in the envelope compared to the plain welded steel specimens. As well as affecting the BE parameters, the tight fatigue cracks, as expected, exhibited the largest magnetic leakage field (MLF) over the cracked region. On the plain steel specimen (3P) the MLF was approximately **0.23 mT**; similar to the MLF from the parent material region of the welded (2P) specimen. It appeared that the weld seam had decreased the permeability of the material, thus, causing an increased leakage field at the centre of the specimen. The presence of the fatigue crack, which created large leakage field values, changed the permeability of the local parent material (at the edge of the studied region on locations 'A' and 'U'). On the parent material region leakage field values of approximately **0.3 mT** were recorded. Under optical microscopy it was found

that the visible microstructure, of the parent material region on all specimens was very similar. This indicated that the change in permeability, most probably, resulted from an increase in dislocation networks throughout the fatigue cracked specimens.

The change in material microstructure within a steel specimen, resulting from welding and crack generation, has been found to be clearly measurable using Barkhausen emission. The presence of the weld seam was shown to increase the overall V_{MAX} and signal energy profiles (**figures 4.4.14** to **4.4.16**). This increase in the ABE envelopes' parameters was accredited to the complex residual stress profile as well as the large grains found in the HAZ region resulting from the welding process. The generation of a crack, by low-cycle flexural fatiguing, increased the ABE signal energy profile of both the 'cracked weld specimens' compared to the perfect weld seam (2P). Both the cracked weld plates displayed ABE envelopes which possessed a cluster of spikes in place of the large second peak. This increased the V_{MAX} profiles. The signal energy profile, however, appeared to indicate the location of the crack on the plate 21B. According to the MLF measurements, combined with calculated MLF results, a larger crack was predicted to exist in specimen 21B compared to the cracked steel specimen 21A. The crack on the specimen 21B may have been of sufficient size to cause significant acoustic screening of the ABE signal above the crack location. The averaged ABE envelope parameters from each of the steel specimens (displayed in **table 4.4.3**) show that the presence of the crack-free weld seam (2P) caused a rise in the average V_{MAX} and signal energy values. A further rise in both the averaged V_{MAX} and signal energy values were recorded for both of the cracked weld specimens (21A and 21B). This may be used to monitor and indicate the severity of the damage suffered by an engineering material.

Changes arising due to the effects of machining the surface of the steel specimens were found to be detectable using Barkhausen emission. Electrical (EDM) and mechanical (planing) machining were studied and both were found to alter the steel specimen surface characteristics. Mechanical machining (planing) carried out on the plane steel specimen was found to reduce the first half of the Barkhausen envelope. The EDM machining significantly altered the EBE envelopes detected from the steel specimen. The envelopes

appeared as a reflection of the signal from the plane machined surface. This led to the T_P value occurring early in the envelope.

The weld specimen's machined surface exhibited distinctly different types of EBE envelopes. The planed surface exhibited envelopes which possessed higher T_P values compared to the EDM machined surface. However, the EDM machined surface area showed larger V_{MAX} values compared to the planed surface. The HAZ, irrespective of machining processes, exhibited the largest V_{MAX} and signal energy parameters. The cracked weld specimens machined surfaces exhibited different responses depending on the machining process. The planing process was found to suppress the EBE signals, whereas, the EDM machining increased the EBE signals and this was reflected in the signal energy parameter. The type of machining process used on these specimens and the changes arising from the different machining techniques, could clearly be distinguished by considering the shapes of the detected EBE envelopes. On each plate specimen the different material regions can be deduced from the Barkhausen emission profile. On the planed surface, the T_P values (by occurring earlier compared to the parent material region) were able to identify the change in the material structure due to the crack generation process. On the EDM machined surface, the T_P values were found to be insensitive to the material below the recast layer. However, the V_{MAX} and signal energy values were able to yield information on the changed material structure beneath the recast layer. This was found to be very useful in determining crack and weld locations. The differences between the two types of machining processes used on the steel specimens were clearly visible in the Barkhausen signal envelopes. This raises the possibility of using BE as a quality control technique for surface machining.

Crack removal by repeated surface machining was carried out and the effect on the Barkhausen emission studied. It was noted that the reduction in specimen thickness reduced the specimen cross section for the magnetic flux. This led to an increased magnetic leakage field on the surface of both of the cracked weld specimens. When the net magnetic leakage field above the crack was measured, the planed specimen exhibited an increase in magnitude with decreasing specimen thickness (helped by the increased dislocation densities, caused by the planing process). However, the same could not be

said for the EDM machined specimen. It was found that the EDM machined surfaces (on subsequent machined surfaces) also showed an increasing leakage field, although, the net leakage field from the crack was found to decrease with decreasing specimen thickness.

As the specimen thickness was reduced by EDM machining the EBE signal energy profiles from each of the machined surfaces (22B-27B) exhibited a gradual increase. The signal energy on the parent material region was found to change the least, whereas, the EBE energy from the weld region increased by the greatest amount. The signal energy from the crack mouth (location 'K'), after each subsequent machining process, also exhibited an increase. When the signal energy parameters from each of the surfaces are compared (**figures 5.4.15** and **5.4.16**) it can be seen that the dip in the signal energy, resulting from the crack, decreased. This led to the signal energy values between the HAZ and cracked weld regions becoming more closely matched. This observation may be a result of the decrease in crack size and further research needs to be carried out in order to fully understand this effect.

The ABE envelopes from both of the cracked weld specimens exhibited certain trends. On the original cracked weld, subjected to surface planing and EDM machining, the ABE signals displayed the presence of spikes on the envelopes. No explanation exists for the cause of the cluster of spikes, which mainly occurred close to the second peak on the ABE envelopes. As both the cracked weld specimens showed similarly clustered spike, it may suggest that the low-cycle fatiguing, involved in the crack generation process, led to the formation of a complex residual stress profile which resulted in the formation of the spikes. On subsequent machining the spikes disappeared. It is believed that the machining process, by removing the highly stressed surface material, eliminated the occurrence of the spike peaks. The welded specimen (2P) showed smaller spikes distributed across the ABE envelopes. Again, this may have been a result of the weld stress profile present within the specimen. Further work on welded and low-cycle fatigued materials may yield the to true nature of these spikes.

The Barkhausen technique has been found to be responsive to varying surface conditions. Stress and changes in surface microstructure all play a role in influencing the

shape and size of the EBE envelopes. The technique is at its most powerful when used with some prior knowledge of material microstructure and history. Calibrating a test material using BE and then, during service-life, monitoring changes arising from service conditions shows promise. Changes in material characteristics and microstructure due to in-service conditions and possible generation of fatigue cracks may all be detected using EBE. Away from an in-service condition, the EBE can also be used as an microstructural analysis technique. The sensitivity of EBE to microstructural changes within a specimen has been shown to makes this a possibility. This would provide an economical and time saving aid to techniques such as x-ray diffraction. ABE being a volume effect and highly sensitive to the presence of stress can be used to monitor the stress state of in-service structural components. Once again, by calibrating the component in early service-life, the changes in the ABE signal energy level as well as the presence of spikes can all be used to indicate important changes within the bulk material.

The Barkhausen emission, as with all non-destructive testing and evaluation techniques, has limitations and certain features which must be known and understood in order to effectively use this technique. The magnetisation and detection systems need to be standardised, at least for certain applications where measurements and results need to be recorded and compared for later use. A 'U-shaped' electromagnetic yoke has been found to be the most practical and suitable. The rate of change of the magnetic field, as has been shown, is very important for signal integrity. The BE transducers need to be used within a region of uniform magnetisation, if comparable results are to be achieved. If these limiting parameters are not accepted and followed, then often meaningless conclusions may be drawn from the detected Barkhausen emissions. The EBE, due to eddy current dampening, is limited to being a surface analysis technique. This limitation allows the study of microstructure and stress state of localised surface regions, which is not possible with other portable non-destructive analysis techniques. With prior knowledge, about both the detection system and test material, Barkhausen emission's simplest and most effective use may be as a laboratory or field microscopy technique.

Interpretation of the Barkhausen technique (ABE and EBE) depends on successfully understanding the effects of varying microstructure and stress state on the BE response.

This thesis has found distinct changes in the ABE and EBE signals from steel specimens resulting from welding processes. The presence of a crack defect within the weld seam was found to be reflected in the Barkhausen emission. The technique is most effective when prior knowledge about the test specimen and its initial Barkhausen response is known. Then, by analysing the changes within the detected Barkhausen signals, effective and meaningful conclusions can be made.

6.1. FUTURE WORK.

Barkhausen emission, as has been shown in this thesis, is capable of detecting changes within test materials. In particular, changes in microstructure and stress state are detectable as are the effects surface breaking defects. Continued work should focus on applying this method in an industrial non-destructive testing (NDT) and evaluation setting. Suggested work should focus on this ultimate goal and a few ideas for future work are presented which might establish the full acceptance of this technique as a non-destructive evaluation method.

- Barkhausen measurements on other types of defects such as inclusions and subsurface cracks need to be studied and their effects clearly understood.
- Measurements from materials with differing microstructures and the understanding of the causes of BE envelope size and shape.
- Conduct systematic study of many other various types of structural and off-shore steel specimens. Measurements should be carried out on different specimens; plain, specimens containing a weld seam and defective cracked weld specimens.
- Barkhausen responses from the various ferromagnetic materials and their defects need to be compiled and catalogued. A library of this information digitally stored in a database to be used as a reference.
- Carry out in-situ measurements on actual weld seams and plain steels within various structures. An in-depth comparative study between specimens within the laboratory and industrial setting would enhance the understanding and acceptance and, therefore, increase the use of this technique, within the NDE field.

END *of* SECTION

ACKNOWLEDGEMENTS

I would first of all like to thank my supervisors Dr. Roger Hill of The Nottingham Trent University for his guidance and for taking me to Hawaii. I would also like to thank Lewis Morgan of British Gas Research Plc., for providing me with samples and helpful ideas.

It was helpful having access to the mechanical engineering department of NTU and the availability of their equipment. I would also like to acknowledge the help from the technicians within the physics department; Peter, Steve, Nick and a big 'thank you' to Larry for machining my samples, promptly, on request.

There are many people who have helped me on technical matters and I thank them very much. I single out for special thanks Simon Forsyth. The completion of this thesis would not have been possible without the invaluable help from Gayle Acors.

The writing up of this work would not have been possible without the loan of equipment from by brother Shaek-ur-Rahman Choudhury and from my friend Naheim Akbar.

REFERENCES

[1] Chikazumi S.
Physics of Magnetism.
John Wiley and Sons, NY. Inc. (1964).

[2] Jiles D. C.
Introduction to Magnetism and Magnetic Materials.
Chapman and Hall. (1991).

[3] Barkhausen H.
Earth Noises and Noises Due to Change of Magnetisation of Iron.
Physikalische Zeitschrift., Vol. 29, (1919), pp 401-403.

[4] Bitter F.
Experiments on the Nature of Ferromagnetism.
Physical Review., Vol. 41, (1932), pp 507-515.

[5] Lord A. E. Jr.
Physical Acoustics Vol. 6, eds Mason W. P. and Thurston R.N.,
Academic Press, New York, (1975), pp 290

[6] Mackersie J., Hill R. and Cowking A.
Model for Acoustic and Electromagnetic Barkhausen Emission.
Non-destructive Testing., Vol. 2 :ed J Boogaard and GM Van Dijk.
Elsevier: Amsterdam 1989.

[7] Dhar A., Atherton D. L.
Flux-density Dependence of Magnetoacoustic Emission in Pipeline Steel.
Journal of Applied Physics., Vol. 72, No. 2, (1992), pp 601-606.

[8] Guyot M. and Cagan V.
The Acoustic Emission along the Hysteresis Loop of Various Ferro and Ferrimagnets.
Journal of Magnetism and Magnetic Materials., Vol. 101, (1991), pp 256-262.

[9] Guyot M., Cagan V.
Magneto Acoustic Emission (invited).
Journal of Applied Physics., Vol. 73, No. 10, (1993), pp 5348 -5353.

[10] Biorci G. and Pescati D.
Frequency Spectrum of Barkhausen Noise.
Journal of Applied Physics., Vol. 28, No. 7, (1957), pp 777-780.

[11] Grundle A., Deimel P., Rode B. and Daniel H.
Three Dimensional Measurements of Barkhausen Effect.
Physica, 86-88B, (1977), pp 1379-1380.

[12] Saynajakangas S.
A New Surface Transducer for Generating and Detecting Magnetic Field Transients in Ferromagnetics.
IEEE Transactions on Magnetics., Vol. MAG 10, No. 1, (1974), pp 44-50.

[13] Thomas W. Krause and Atherton D. L.
High resolution Barkhausen noise measurements.
NDT & E International., Vol. 27, No. 4, (1994), pp 201-207.

[14] Buque C., Trschler W. and Holste C.
Analysis of Local Variation of Internal Stresses n Cyclically Deformed Nickel Crystal by Barkhausen Noise Measurements.
Materials Science and Engineering., A215, (1996), pp 168-174.

[15] Vengrinovich V.and Zolotarev S.
Ferromagnetic Surface Layer Testing with Depth Resolution Using Priori Knowledge.
Materials Science Forum., Vols. 210-213, (1996), pp 25-30.

[16] Lo C. C. H., Jackubovics J. P. and Scruby C. B.
Monitoring the Microstructure of Pearlitic Steels by Magnetoacoustic Emission.
Journal of Applied Physics., Vol. 81, Part 8, (1997), pp 4069-4071.

[17] Hill R. and El-Dardiry S. M. A.
Variables in the Use and Design of Acoustic Emission Transducers.
Ultrasonics., (January 1981), pp 9-16.

[18] Sundstorm O. and Torronen K.
The Use of Barkhausen Noise Analysis in Non-Destructive Testing.
Materials Evaluation., Vol. 37, (1979), pp 51-56.

[19] Mikheev M. N. and Grakunov E. S.
Relationship of Magnetic Properties of the Structural Condition of a Substance- The Physical Basis of Magnetic Structure Analysis.
Soviet Journal of NDT., Vol. 17, No. 8, (1981), pp 579-592.

[20] Ranjan R., Jiles D C. and Rastogi P. K.
Magnetic Properties of Decarburized Steels:-An Investigation of the Effect of Grain Size and Carbon Content.
IEEE Transactions on Magnetics., Vol. MAG 23, No. 3, (1987), pp 1869-1876.

[21] Ishihara M., Sakamoto T. and Minami H.
Non Destructive Characterisation of Materials. (eds) Ruud C O. Bussiere J. F. and Green R. E. jr.
Plenum Press., NY. (1991), pp 277.

[22] Ranjan R., Jiles D. C., Buck O. and Thompson R. B.
Grain Size Measurements Using Magnetic and Acoustic Barkhausen Noise.
Journal of Applied Physics., Vol. 61, No. 8, (1987), pp 3199-3201.

[23] Hill R., Geng R. S., Cowking A. and Mackersie J. W.
The Effect of Nickel Hardness and Grain Size on Acoustic and Electromagnetic Barkhausen Emission.
NDT & E International., Vol. 24, No. 4, (1991), pp 179-186.

[24] Tiitto S.
On the Influence of Microstructure on Magnetisation Transitions in Steel.
Acta Polytechnica Scandinavica., Applied Physics Series, No 119, Helsinki, (1977).

[25] Kameda J. and Ranjan R.
Nondestructive Evaluation of Steels Using Acoustic and Magnetic Barkhausen Signals. Parts I & II.
Acta Metall., Vol. 35, No. 7, (1987), pp 1515-1526 & pp 1527-1531.

[26] Raj B., Bhattacharaya D. K. and Jayakumar T.
Magnetic Hysteresis Loop Parameters and Barkhausen Noise for Microstructural Characterisation of Steels.
Metals Materials and Processes., Vol. 7, No. 1, (1995), pp 19-28.

[27] Moorthy V., Vaidyanathan S., Jayakumar T. and Raj B.
On the Influence of Tempered Microstructures on Magnetic Barkhausen Emission in Ferritic Steels.
Philosophical Magazine A., Vol. 77, No. 6, (1998), pp 1499-1514.

[28] Atherton D. L. and Jiles D. C.
Effects of Stress on Magnetisation.
NDT International., Vol. 19, No. 1, (1986), pp 15-19.

[29] Pasley R. L.
Barkhausen effect - An indication of stress.
Materials Evaluation., Vol. 28, (1970), pp 157-161.

[30] Karjalainen L. P., Moilanen M. and Rautioaho R.
Influence of tensile and cyclic loading upon Barkhausen noise in a mild steel.
Materials Evaluation., Vol. 37, (1979), pp 45-51.

[31] Ruuskanen P. and Kettunen P.
Two ferromagnetic methods for the evaluation of the fatigue limit in polycrystalline iron.
NDT International., Vol. 13, (1980), pp 105-108.

[32] Krause T. W., Makar j. M. and Atherton D. L.
Investigation of the Magnetic Field and Stress Dependence of 180° Domain Wall Motion in Pipeline Steel Using Magnetic Barkhausen Noise.
Journal of Magnetism and Magnetic Materials., Vol. 137, (1994), pp 25-34.

[33] Krause T. W., Pattanyus A. and Atherton D. L.
Investigation of Strain Dependent Magnetic Barkhausen Noise in Steel.
IEEE Transactions on Magnetics., Vol. 31, No. 6, (1995), pp 3376-3378.

[34] Clapham L., Krause T. W., Olsen H., Ma B., Atherton D. L., Clark P. and Holden T. M.
Characterisation of Texture and Residual Stress in a Section of 610 mm Pipeline Steel.
NDT & E International., Vol. 28, No. 2,(1995), pp 73-82.

[35] Krause T. W., Pulfer N., Weyman P. and Atherton D. L.
Magnetic Barkhausen Noise: Stress Dependent Mechanisms in Steel.
IEEE Transactions on Magnetics., Vol. 32, No. 5, (1996), pp 4764-4766.

[36] Mandal K., Dufour D., Sabet-Sharghi R., Sijgers B.,Micke D., Krause T. W., Clapham L. and Atherton D.L.
Detection of Stress Concentrations Around a Defect by Magnetic Barkhausen Noise Measurements.
Journal of Applied Physics., Vol. 11, (1996), pp 6391-6395.

[37] Buttle D. J., Dalzell W., Scruby C. B. and Langman R. A.
Comparison of three Magnetic Techniques for Biaxial Stress Measurement.
Materials Physics and Metallurgy Division, Harwell Laboratory, Oxford. December 1989.

[38] Scruby C. B., Buttle D. J., Briggs G. A. D. and Jakubovics J. P.
The Monitoring of Stress and Microstructure by Magnetoacoustic Emission
Materials Physics and Metallurgy Division, Harwell Laboratory, Oxford. October 1987.

[39] Makar J. M. and Tanner B. K.
The Effect of Stress Approaching and Exceeding the Yield Point on the Magnetic Properties of High Strength Pearlitic Steels.
NDT & E International., Vol. 31, No. 2, (1998), pp 117-127.

[40] Scherpereel D. E., Kazmerski and Allen C. W.
The Magnetoelastic Interaction of Dislocations and Ferromagnetic Domain Walls in Iron and Nickel.
Metallurgical Transactions., Vol. 1, (1970), pp 517-524.

[41] Buttle D.J., Briggs G. A. D., Jakubovics J. P., Little E. A. and Scruby C. B.
Magneto-Acoustic and Barkhausen Emission in Ferromagnetic Materials.
Department of Metallurgy and Science of Materials, University of Oxford. August 1985.

[42] Ranjan R., Buck O. and Thompsom R. B.
A Study on the Effect of Dislocation on the Magnetic Properties of Nickel Using Magnetic NDE Methods.
Journal of Applied Physics., Vol. 61., No. 8, (1987), pp 3196-3198.

[43] Gao Z., Chen Z. J., Jiles D. C. and Biner S.
Variation of Coercivity of Ferromagnetic Material During Cyclic Stressing.
IEEE Transactions on Magnetics., Vol. 30, No. 6, (1994), pp 4593-4595.

[44] Roderic K. Stanley
Present State of Magnetic Nondestructive Testing Techniques.
Materials Evaluation., (September1991), pp 1169-1172.

[45] Jiles D. C.
Review of Magnetic Methods for Nondestructive Evaluation.
NDT International., Vol. 21, No. 5, (1988), pp 311-319.

[46] Bhattacharya D. K.
Characterisation of Microstructure in Steel by Magnetic Techniques-An Overview.
Transactions of the Indian Institute of Metals., Vol. 48, No. 6, (1995), pp 495-509.

[47] Maylin M.G. and Squire P.T.
The Effect of Stress on Induction, Differential Permeability and the Barkhausen Count in a Ferromagnet.
IEEE Transactions on Magnetics., Vol. 29, No. 6, (1993), pp 3499-3501.

[48] Steinberg A. P., Hagemaier D. J., Barton J. R. and Williams R. D.
Determining Crack Depth in a High Strength Steel Cylinder Using Magnetic Perturbation.
Materials Evaluation., Vol. 40, (1982), pp 288-293.

[49] Krause T. W., Mandal K., Hauge C., Weyman P., Sijgers B. and Atherton D. L.
Correlation Between Magnetic Flux Leakage and Magnetic Barkhausen Noise: Sterss Dependence in Pipeline Steel.
Journal of Magnetism and Magnetic Materials., Vol. 169, (1997), pp 207-219.

[50] Krause T. W., Little R. W., Barnes R., Donaldson R. M., Ma B., Atherton D. L.
Effects of Stress Concentration on Magnetic Flux Leakage Signals from Blind-Hole Defects in Stresses Pipline Steel.
Research in Nondestructive Evaluation., Vol. 8, (1996), pp 83-100.

[51] Mandal K., Corey A., Loukas M. E., Weyman P., Eichenberger J. and Atherton D. L.
The Effect of Defect Depth and Bending Stress on Magnetic Barkhausen Noise and Flux Leakage Signals.
Journal of Physics D: Applied Physics., Vol. 30, (1997), pp 1976-1983.

[52] Mandal K., Dufour D., Krause T. W. and Atherton D. L.
Investigation of Magnetic Flux Leakage and Magnetic Barkhausen Noise Signals from Pipeline Steel.
Journal of Physics D: Applied Physics., Vol. 30, (1997), pp 962-973.

[53] Don E. Bray and Roderick K. Stanley.
Nondestructive Evaluation. -A tool in design, manufacturing and service.
McGraw-Hill Inc., (1989).

[54] Pautz J. F and Abend K.
Automated Magnetic Particle Inspection.
Materials Evaluation., (September 1996), pp 1004-1008.

[55] Negley M. A. and Jiles D. C.
Imaging Surface Conditions of Ferromagnetic Steel Using Barkhausen Technique.
IEEE Transactions on Magnetics., Vol. 30, No. 6, (1994), pp 4509-4511.

[56] Jiles D. C. and Souominen L.
Effects of Stress on Barkhausen Effect Emissions: Model Prediction and Comparison with X-Ray Diffraction Studies.
IEEE Transactions on Magnetics., Vol. 30, No. 6, (1994), pp 4924-4926.

[57] Parakka A. P., Jiles D. C., Gupta H. and Jalics S.
Effect of Surface Condition on Barkhausen Emissions from Steel.
Journal of Physics., Vol. 79, Part 8, (1996), pp 6045-6046.

[58] Parakka A. P., Jiles D. C., Gupta H. and Zang M.
Barkhausen Effect in Steel and its Dependence on Surface Condition.
Journal of Physics., Vol. 81, Part 8, (1997), pp 5085-5086.

[59] Gupta H., Zhang M. and Parakka A. P.
Barkhausen Effect in Ground Steels.
Acta Materialia., Vol. 45, No. 5, (1997), pp 1917-1921.

[60] Gauthier J., Krause T. W. and Atherton D. L.
Measurement of Residual Stress in Steel Using the Magnetic Barkhausen Noise Technique.
NDT & E International., Vol. 31, No. 1, (1998), pp 23-31.

[61] Sipahi L. B.
Effects of Creep Damage, Shot Peening and Case Hardening on Magnetic Barkhausen Noise Analysis.
IEEE Transactions on Magnetics., Vol. 30, No. 6, (1994), pp 4830-4832.

[62] Yu. C. C., Quin C-D. and Ng D. H. L.
Nondestructive Inspection of Fractured Nickel Bar by Barkhausen and Magnetoacoustic Emission.
Journal of Physics., Vol. 79, Part 8, (1996), pp4750-4752.

[63] Yu. C. C. and Ng D. H. L.
Determination of the Rolling Direction of Electrolytic Zinc-Coated Steel Plate by Barkhausen Emission.
IEEE Transactions on Magnetics., Vol. 32, No. 5, (1996), pp 4917-4919.

[64] Ng D. H. L., Yu. C. C., Li A. S. K. and Lo C. C. H.
Measurement of Barkhausen Emission and Magnetoacoustic Emission from a Fractured Steel Bar.
IEEE Transactions on Magnetics., Vol. 31, No. 6, (1995), pp 3394-3396.

[65] Kameda J.
Characterisation of Tempered Martensite Microstructure and Embrittlement by Acoustic and Magnetic Barkhausen Signal Measurement.
Scripta Metallurgica., Vol. 22, (1988), pp 1487-1492.

[66] Tomita Y., Hashimoto K. and Osawa N.
Nondestructive Estimation of Fatigue Damage for Steel by Barkhausen Noise Analysis.
NDT & E International., Vol.29, No. 5, (1996), pp 275-280.

[67] Lang M. A., Altpeter I. and Dobmann G.
Early Detection of Hydrogen-Induced Stress Corrosion Cracking Using Micromagnetic Test Methods.
Materials Science Forum., Vol. 210-213, (1996), pp 1-8.

[68] Lo C. C. H., Tang F., Shi Y., Jiles D. C. and Biner S. B.
Monitoring Fatigue Damage in Materials Using Magnetic Measurement Techniques.
Journal of Applied Physics., Vol. 85, No. 8, (1999), pp 4595-4597.

[69] Ginsztler J., Meszaros I., Hidasi B. and Devenyi L.
Magnetic Testing Methods of High-Temperature Steels.
International Journal of Pressure Vessels and Piping., Vol. 59, (1994), pp 271-273.

[70] Sipahi L. B., Govindaraju M. R. and Jiles D. C.
Monitoring Neutron Embrittlement in Nuclear Pressure Vessel Steels Using Micromagnetic Barkhausen Emissions.
Journal of Applied Physics., Vol. 75, Part 10, (1994), pp 6981-6983.

[71] Blaszkiewicz M.
The Development of Nondestructive Evaluation (NDE) for Monitoring the Embrittlement in Nuclear Reactor Pressure Vessels.
Materials Science Forum., Vol. 210-213, (1996), pp 9-16.

[72] Park D. G., Hong J. H., Jang K. S., Jung M. M. and Kim G. M.
The Changes of the Structural, Magnetic and Mechanical Properties in Reactor Pressure Vessel Steel Neutron Irradiated at 70°C.
Journal of the Korean Physical Society., Vol. 34, No. 5, (1999), pp 434-438.

[73] Mandal K., Loukas M. E., Corey A. and Atherton D. L.
Magnetic Barkhausen Noise Indications of Stress Concentrations near Pits of Various Depths.
Journal of Magnetism and Magnetic Materials., Vol. 175, (1997), pp 255-262.

[74] Mandal K., Dufour D. and Atherton D. L.
Use of Magnetic Barkhausen Noise and Magnetic Flux Leakage Signals for Analysis of Defects in Pipeline Steel.
IEEE Transactions on Magnetics., Vol. 35, No. 3, (1999), pp 2007-2017.

[75] Lo C. C. H., Jakubovics J. P. and Scruby C. B.
Non-Destructive Evaluation of Spheroidizied Steel Using Magnetoacoustic and Barkhausen Emission.
IEEE Transaction on Magnetics., Vol. 33, No. 5, (1997), pp 4035-4037.

[76] Lo C. C. H. and Scruby C. B.
Study of Magnetisation Processes and the Generation of Magnetoacoustic and Barkhausen Emission in Ferritic/ Pearlitic Steel.
Journal of Applied Physics., Vol. 85, No.8, (1999), pp 5193-5195.

[77] Rodriguez P. and Raj B.
Development of In-service Inspection Techniques for Nuclear Power Plants in India.
International Journal of Pressure Vessel and Piping., Vol.73, (1998), pp 59-68.

[78] Vaidyanathan S., Moorthy V., Jayakumar T. and Raj B.
Evaluation of Carburization Depth in Service Exposed Ferritic Steel Using Magnetic Barkhausen Noise Analysis.
Materials Evaluation., Vol. 56, (1998), pp 449-452.

[79] Moorthy V., Vaidyanathan S., Jayakumar T., Raj B. and Kashyap B. P.
Effect of Tensile Deformation on Micromagnetic Parameters in 0.2% Carbon Steel and 2.25Cr-1Mo Steel.
Acta Materialia., Vol. 47, No. 6, (1999), pp 1869-1878.

[80] Jeong H. T., Park D. G., Hong J. H., Ahn Y. S. and Kim G. M.
The Effect of Microstructural Changes on Magnetic Barkhausen Noise in Mn-Mo-Ni Pressure Vessel Steel.
Journal of the Korean Physical Society., Vol. 34, No. 5, (1999), pp 429-433.

[81] Park D. G., Jeong H. T. and Hong J. H.
A Study on the Radiation Damage and Recovery of Neutron Irradiated Vessel Steel Using Magnetic Barkhausen Noise.
Journal of Applied Physics., Vol. 85, No.8, (1999), pp 5726-5728.

[82] Park D. G., Ok C. I., Jeong H. T., Kuk I. H. and Hong J. H.
Nondestructive Evaluation of Irradiation Effects in RPV Steel Using Barkhausen Noise and Magnetoacoustic Emission Signals.
Journal of Magnetism and Magnetic Materials., Vol. 196, (1999), pp 382-384.

[83] Saynajakangas S.
A Non-Destructive Electromagnetic Method for Structural Studies of Ferrous Alloys.
Acta Polytechnica Scandinavica., Electrical Engineering Series No. 33, (1973).

[84] Mackersie J. W.
A Study of Acoustic and Electromagnetic Barkhausen Emission.
Ph.D., (1989), CNAA.

[84] R.E. Beissner, G.A. Matzkanin, C.M. Teller.
NDE Application of magnetic leakage filed methods. State of the Art Survey.
Southwest Research Institute, San Antonio, Texas, January 1980.

[85] Non-destructive Testing Handbook. (second edition).
Magnetic Particle Testing., Volume 6.
American Society for Non-destructive Testing. (1989).

[86] Tiitto S., Saynajakangas S. and Rulka R.
High Frequency Investigation of Magnetic Noise Characteristics.
IEEE Transactions on Magnetics., Vol. MAG 12, No 4, (1976) pp 406-410.

[88] Spasojevic D., Bukvic S., Milosevic S. and Stanley H. E.
Barkhausen noise: Elementary signals, power laws and scaling relations.
Physical Review E., Vol. 54, No. 3, (1996), pp 2531-2546.

[89] Ramesh A., Govindaraju M. R., Jiles D. C. and Biner S.B.
Magnetic Property Variations in Nickel Caused by Non-Magnetic Inclusions.
IEEE Transactions on Magnetics., Vol.32, No 5, (1996) pp 4836-4838.

[90] Hill R., Geng R. S. and Cowking A.
Acoustic and Electromagnetic Barkhausen Emission from Iron and Steel: Application of the Technique to Weld Quality Assessment and NDE.
British Journal of Non-destructive Testing.,Vol. 35, No. 5, (1993), pp 225-231.

[91] Beale A. D., Jackubovics J. P., Hetherington M. G., Scruby C. B., Lewis B. A. and Davies K. J.
TEM studies of domains and micromagnetic processes in structural steels.
Journal of Magnetism and Magnetic Materials., Vol. 104, Part 1, (1992), pp 365-367.

[92] Bhattacharya D. K. and Vaidyanathan S.
Effect of the Demagnetisation Factor on the Barkhausen Noise Signal.
Journal of Magnetism and Magnetic Materials., Vol. 166, (1997), pp 111-116.

[93] Petrofes N. F. and Gadalla A. M.
Processing Aspects of Shaping Advanced Materials by Electrical Discharge Machining.
Adv. Materials and Manufacturing Processes., 3 (1), (1988), pp 127-153.

[94] Suresh S.
Fatigue of Materials, Cambridge Solid State Science Series,
Cambridge University Press., (1991), pp 135+ and 197+.

[95] Moorthy V., Vaidyanathan S., Jayakumar T. and Raj B.
Microstructural Characterisation of Quenched and Tempered 0.2% Carbon Steel using Barkhausen Noise Analysis.
Journal of Magnetism and Magnetic Materials., Vol. 171, (1997), pp 179-189.

[96] Cornu J.
Advanced Welding Systems, TIG and Related Processes.
(English Editor: John Weston), IFS (publications) Ltd., U. K., 1985.

[97] Boothroyd G.
Fundamentals of Metal Machining.
Edward Arnold (Publishers) Ltd., London, 1965.

[98] Soni S. J. and Chakraverti G.
Study of Surfaces and Accuracies Produced During EDM of High Carbon High Chromium Die Steel with Rotating Electrodes.
Indian Journal of Engineering and Materials Sciences., Vol. 1, (June 1994), pp 127-134.

[99] Lim L. C., Lee L. C., Wong Y. S. and Lu H. H.
Solidification Microstructure of Electrodischarge Machined Surfaces of Tool Steels.
Materials Science and Technology., Vol. 7, (March 1991), pp 239-247.

[100] White R. L.
Giant Magnetoresistance Materials and their Potential as Read Head Sensors.
IEEE Transaction on Magnetics., Vol. 30, No. 2, (1994), pp 346-352.

[101] Neale R.
Taming the Giant MagnetoResistance (GMR) Effect.
Electronic Engineering., (April 1996), pp 36-40.

[102] Popovic R. S., Flanagan J. A. and Besse P. A.
The Future of Magnetic Sensors.
Sensors and Actuators A., Vol. 56, (1996), pp 39-55.

[103] Lancaster J. F.
The Metallurgy of Welding Brazing and Soldering.
George Allen and Unwin Ltd., London, 1970.

[104] Brandon D. and Kaplan W. D.
Joining Processes, An Introduction.
John Wiely and sons, N. Y., 1997, pp181-218.

[105] Masubuchi K.
Analysis of Weld Structures.
International Series on material Science and Technology,
Vol. 33, Pergamon Press, N. Y, 1980.

[106] Raj B.
Fresh Insight into Microstructure, Deformation & Processes Using Nondestructive Methodologies.
Transaction of the Indian Institute of Metals., Vol. 50, Part 2-3, (1997), pp 119-146.

[107] Baldev R. and Moorthy V.
Non-Destructive Testing Methods for Assessment of Creep and Fatigue Damage.
Transactions of the Indian Institute of Metals., Vol. 49, Part 4, (1996), pp 277-302.

[108] Goodenough J. B.
A Theory of Domain Creation and Coercive Force in Polycrystalline Ferromagnetics.
Physical Review., Vol. 95, No. 4, (1954), pp 917-933.

[109] Bates L. F. and Martin D. H.
Ferromagnetic Domain Nucleation in Silicon Iron
Proceedings of the Physical Society., Vol. 69, (1955), pp 145-152.

[110] Cullity B. D.
Introduction to Magnetic Materials.
Reading, Massachusetts: Addison-Wesley, (1972), p.292.

[111] Moorthy V., Vaidyanathan S., Laha K., Jayakumar T., Rao Bhanu S. and Raj B.
Evaluation of Microstructure in 2.25Cr-1Mo and 9Cr-1Mo Steel Weldments using Magnetic Barkhausen Noise.
Materials Science and Engineering A., Vol. 231, Part 1-2, (1997), pp 98-104.

[112] Moorthy V., Vaidyanathan S., Jayakumar T. and Raj B.
Evaluation of Post-Weld Heat Treatment in 2.25Cr-1Mo Steel Tube Sheet Welded Joints using Magnetic Barkhausen Noise Measurements.
Materials Science and Technology., Vol. 13, (July 1997), pp 614-617.

[113] Tebbel. R. S. & Craik D.
Magnetic Materials.
John Wiley and sons., London and New York, (1969), pp369.

[114] Brailsford F.
Physical principles of magnetism.
Van Nostrad company Ltd., London, (1966), pp 184+

[115] Abu Zeid O. A.
On the Effect of Electrodischarge Machining Parametres on the Fatigue Life of AISI D6 Tool Steel.
Journal of Materials Processing., Vol. 68, (1997), pp 27-32.

[116] Trent E. M.
Metal Cutting,
Butterworth Heinemann., England, 1991.

APPENDIX 1.A

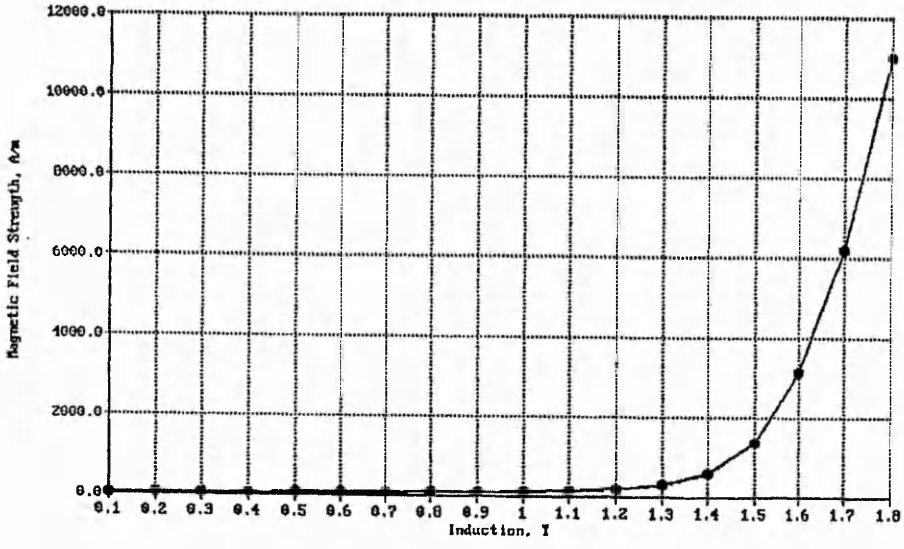
B - H Data for SiFe electromagnetic yoke

Sankey Laminations Ltd.

BANKFIELD WORKS
Greenway Road, Bilston, West Midlands WV14 0TJ
Tel: (0902) 401140 Telex: 339927 SANBAN G
Facsimile: (0902) 494418 (General)
(0902) 409710 (Sales)

PEAK MAGNETIC FIELD STRENGTH vs PEAK MAGNETIC FLUX DENSITY-Typical Curve

Grade:	Scotsil 330
Code:	S3335
Thickness:	0.35mm
Conventional Density:	7.65 kg/dm³
Frequency:	50 Hz
Test Method:	BS 6404: part 2 Epstein strips



Registered in London
under No. 472505
Registered Office:
Bankfield Works, Bilston WV14 0TJ

Appendix 1.A B vs H Data for SiFe electromagnetic yoke, supplied by manufacturer.

APPENDIX 1.B

B - H Data from sample OLI-95D

Magnetic field H kA/m	Magnetic flux density B Tesla	Magnetic field H kA/m	Magnetic flux density B Tesla
0.043185	0.00722	3.626270	1.526015
0.085665	0.016078	4.204461	1.565158
0.324774	0.082364	4.963401	1.606658
0.482118	0.158694	5.907751	1.645739
0.571693	0.225448	7.014961	1.683487
0.629856	0.281212	8.605198	1.727529
0.680067	0.338960	10.335699	1.765506
0.716380	0.385669	12.617999	1.808473
0.753788	0.430916	15.260903	1.849475
0.791947	0.481031	18.455702	1.889475
0.818761	0.518711	22.396606	1.929583
0.857878	0.569137	24.054506	1.943507
0.897110	.0619661		
0.922732	0.652862		
0.962600	0.700828		
1.005370	0.749027		
1.057510	0.804839		
1.087000	0.834128		
1.149270	0.891948		
1.197610	0.933567		
1.263510	0.983697		
1.322510	1.025528		
1.376250	1.058699		
1.465320	1.109327		
1.561830	1.154921		
1.651210	1.192679		
1.742390	1.226716		
1.931740	1.285777		
2.060890	1.318376		
2.262270	1.361070		
2.537340	1.408521		
2.798050	1.444443		
3.183751	1.487089		

Appendix 1.B Data supplied by British Gas Plc.

APPENDIX 2.A

Referred to in Chapter 2.1
ANSYS Transient Loading Data.

```
Transient Load Data.
!
!
!applying loads etc..
!
Antype,tran
trnopt,full
!initial condition
lsel,s,,,11,14
nsll,s,1
d,all,az,0
lsel,all
timint,off
time,1e-6
kbc,1
esel,s,mat,,4
bfe,all,js,3,1.79104
esel,s,mat,,5
bfe,all,js,3,-1.79104
alls
lswrite
!transient portion
timint,on
deltim,0.5
kbc,0
time,2.5
esel,s,mat,,4
bfe,all,js,3,4477612
esel,s,mat,,5
bfe,all,js,3,-4477612
alls
lswrite
!load down to -2.5 amps
deltim,0.5
kbc,0
time,7.5
esel,s,mat,,4
bfe,all,js,3,-4477612
esel,s,mat,,5
```

```
bfe,all,js,3,4477612
alls
lswrite
!ramp back to zero
deltim,0.5
kbc,0
time,10
esel,s,mat,,4
bfe,all,js,3,0
esel,s,mat,,5
bfe,all,js,3,0
alls
lswrite
save
!end
```

APPENDIX 2.B

Referred to in Chapter 2.1
Data File of "slot1x.dat;1"

```
INPUT DATA FOR 2-D TRANSIENT MODEL OF MAGNETIC TEST YOKE
/TITLE, 2-D Magnetic Improved Yoke & Slot Model.
!
! Set-up
!
ET,1,13
mp,murx,1,1
tb,bh,2
tbpt,,46.3,0.3
,,55.3,0.4
,,61.8,0.5
,,69.5,0.4
,,78,0.7
,,88,0.8
,,101.8,0.9
,,119.5,1.0
,,148.3,1.1
,,197.5,1.2
,,302.8,1.3
,,603.8,1.4
,,1512.5,1.5
,,3457.5,1.6
,,6153,1.7
,,11025,1.8
tb,bh,3
tbpt,,482.1,0.159
,,680,0.339
,,753.7,0.431
,,818.7,0.518
,,897.1,0.619
,,962.6,0.7
,,1057.5,0.805
,,1197.6,0.934
,,1376,1.058
,,1561,1.15
,,1742,1.227
,,2060,1.318
,,2798,1.444
,,3626,1.526
,,4963,1.607
```

```
,,7014,1.683
,,12617,1.808
,,18455,1.889
,,22396,1.929
,,24054,1.945
mp,murx,4,1
,murx,5,1
,murx,6,1
!
! Model
!
! Define Keypoints
K,1,.025,.012
K,2,.125,.012
KGEN,2,1,2,1,,.1,,0
KGEN,2,1,2,1,,.1115,,0
K,7,.0125,.0385
K,8,.0125,.1055
KGEN,2,7,8,1,.01,,,0
KGEN,2,7,8,1,.0125,,,0
KGEN,2,7,8,1,.0375,,,0
KGEN,2,7,8,1,.04,,,0
KGEN,2,7,8,1,.05,,,0
KGEN,2,7,8,1,.075,,,0
KGEN,2,7,8,1,.085,,,0
KGEN,2,7,8,1,.0875,,,0
KGEN,2,7,8,1,.1125,,,0
KGEN,2,7,8,1,.115,,,0
KGEN,2,7,8,1,.125,,,0
K,31,.05,.037
K,32,.1,.037
KGEN,2,31,32,1,,.075,,0
K,35,0,0
K,36,.15,0
K,37,0,.16
K,38,.15,.16
KGEN,2,1,2,1,,.1005,,0
!new K points to help messing and kgen
K,41,0.0697,0.1165
K,42,0.07,0.1165
KGEN,2,41,42,1,,.007,,0
K,45,0.06,.1145
K,46,0.08,.1145
KGEN,2,45,46,1,,0.019,,0
KGEN,2,45,46,1,,0.0455,,0
KGEN,2,45,46,1,,0.009,,0
!
! Define Lines
L,1,2
```

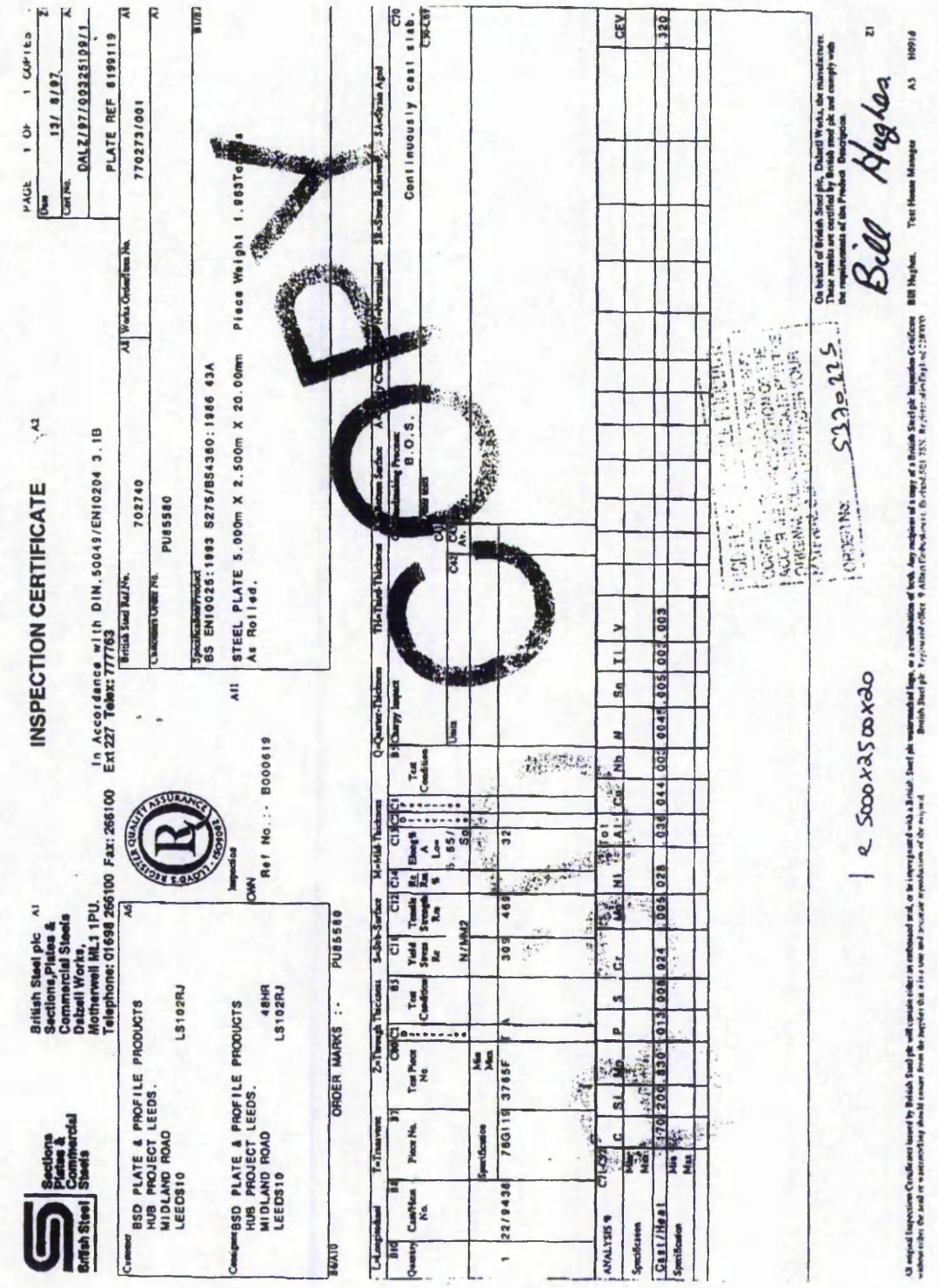
```
L,2,25
L,25,26
L,26,4
!L,4,6          Line from static no airgap
L,6,40
!L,6,5          Line 6 from air gap
L,5,51
L,5,39
!L,5,3          line from no airgap
L,3,12
L,12,11
L,11,1
L,35,36
L,36,38
!L,38,37        line 13 from airgap
L,37,49
L,37,35
L,12,3
L,10,8
L,10,12
L,8,7
L,7,9
L,9,11
L,10,9
L,3,33
L,33,34
L,34,4
L,33,14
L,14,13
L,13,31
L,31,32
L,32,23
L,23,24
L,24,34
L,14,16
L,16,15
L,15,13
L,16,18
L,18,17
L,17,15
L,20,22
L,22,24
L,22,21
L,21,23
L,21,19
L,19,20
L,25,27
L,27,29
L,29,30
```

```
L,30,28
L,28,26
L,28,27
L,1,35
L,2,36
L,31,1
L,32,2
L,37,5
L,38,6
!L points for air gap
L,40,4
L,39,3
L,39,40
!Lines for air crack
L,51,45
L,45,46
L,46,52
L,52,44
L,44,43
L,43,51
L,41,42
L,42,44
L,41,43
L,52,6
L,51,47
L,47,48
L,48,52
L,47,49
L,48,50
L,49,50
L,50,38
!
! Define Areas
AL,P44A,    4
    15    17    18    20
AL,P44A,    4
    34    32    36    35
AL,P44A,    4
    37    42    41    39
AL,P44A,    4
    46    48    44    45
AL,P44A,    4
    27    51     1    52
AL,P44A,    8
     7    57     5    67    60    59    58     6
AL,P44A,    4
    16    20    19     9
AL,P44A,    4
    31    25    33    32
```

```
AL,P44A,    4
   38    39    40    29
AL,P44A,    4
   47     3    43    48
AL,P44A,   16
   22    24    31    34    35    36    33    26    27    28
   40    41    42    37    38    30
AL,P44A,    4
   49    11    50     1
AL,P44A,    5
   13    53     6    68    71
AL,P44A,    8
   21     8     9    10    51    26    25    24
AL,P44A,    8
   29    28    52     2     3     4    23    30
AL,P44A,   12
   53    14    49    10    19    18    17    15    16     8
   56     7
AL,P44A,   12
   54     5    55     4    47    46    45    44    43     2
   50    12
AL,P44A,    6
   22    21    56    57    55    23
AL,P44A,    4
   73    71    69    72
AL,P44A,    5
   54    67    70    72    74
AL,P44A,    6
   68    69    70    61    62    63
AL,P44A,    8
   58    59    60    61    65    64    66    63
AL,P44A,    4
   64    65    62    66
!
! Mesh
AATT,1,1,1
ESIZE,.005
AMESH,7
AMESH,8
AMESH,9
AMESH,10
AMESH,11
AMESH,12
AMESH,16
AMESH,17
ESIZE,.003
AMESH,13
AMESH,20
ESIZE,.001
```

```
AMESH,18
ESIZE,.0003
AMESH,21
ESIZE,0.0001
AMESH,23
ESIZE,.0008
AMESH,19
! Mesh - Core
AATT,2,1,1
ESIZE,.003
AMESH,5
AMESH,14
AMESH,15
! Mesh - NICKEL now for slot
AATT,3,1,1
ESIZE,.003
AMESH,6
ESIZE,.0003
AMESH,22
! Mesh - Coils+
AATT,4,1,1
ESIZE,.003
AMESH,1
AMESH,4
! Mesh - Coils-
AATT,5,1,1
ESIZE,.003
AMESH,2
AMESH,3
!
save
!End of Model Data
```

APPENDIX 3.A



INSPECTION CERTIFICATE

British Steel plc
Sections, Plates & Commercial Steels
Dalzell Works,
Motherwell ML1 1PU.
Telephone: 01698 266100 Fax: 266100

In Accordance with DIN.50049/EN10204 3.1B
Ext 227 Telex: 777763

PLATE REF 8199119

Customer: BSD PLATE & PROFILE PRODUCTS
HUB PROJECT LEEDS.
MIDLAND ROAD
LEEDS10
LS102RJ

Consignee: BSD PLATE & PROFILE PRODUCTS
HUB PROJECT LEEDS.
MIDLAND ROAD
LEEDS10
LS102RJ

British Steel Ref/No. 702740
Customers Order No. PU85580
Specification/Product: BS EN10025:1993 S275/BS4360:1986 43A
STEEL PLATE 5.000m X 2.500m X 20.00mm
As Rolled.
Piece Weight 1.883Tonnes
Continuously cast slab.
B.O.S.

Cert No. DALZ/97/0932510971
Date 13/ 8/97

ORDER MARKS :- PU85580

Bid Quantity 1
Cast/Heat No. 22/94436
Piece No. 76G119
Test Piece No. 3765F

ANALYSIS %

	C	Si	Mn	P	S	Cr	Ni	Al	Cu	Nb	N	Sn	Ti	V	CEV
Specification Max															
Cast/Heat Min	170	200	830	013	008	024	005	028	036	014	002	0045	005	002	003	320
Specification Min															

Yield Stress Re N/MM2: 309
Tensile Strength Rm N/MM2: 468
Elong. Lo = 5.65√So %: 32

Bill Hughes
Test House Manager

On behalf of British Steel plc, Dalzell Works, the manufacturer. Their results are certified by British Steel plc and comply with the requirements of the Product Description.

1 @ 5000x2500x20

SPECIMEN

Appendix 3.A Technical data sheet for EN-43A steel plate sample, supplied by manufacturer.

APPENDIX 4.A

Plane Machined Surface	Envelope Parameter	Parent Material (Location A)	HAZ (Location H)	Cracked Weld (Location K)	±
22A	T_P	1.01 ±0.01	0.93 ±0.01	0.95 ±0.01	2 %
	V_{MAX}	0.44 ±0.01	0.44 ±0.01	0.40 ±0.01	1 %
	Energy	0.046 ±0.002	0.062 ±0.002	0.057 ±0.002	3 %
23A	T_P	1.05	1.04	1.03	
	V_{MAX}	0.48	0.43	0.04	
	Energy	0.061	0.064	0.056	
24A	T_P	0.97	0.92	0.89	
	V_{MAX}	0.53	0.53	0.52	
	Energy	0.067	0.081	0.081	
25A	T_P	1.07	0.91	0.90	
	V_{MAX}	0.73	0.53	0.48	
	Energy	0.096	0.083	0.077	
26A	T_P	1.03	0.86	0.86	
	V_{MAX}	0.79	0.61	0.61	
	Energy	0.110	0.099	0.101	
27A	T_P	1.01	0.97	0.96	
	V_{MAX}	0.99	0.68	0.56	
	Energy	0.107	0.093	0.085	
28A	T_P	1.03	0.85	0.85	
	V_{MAX}	0.93	0.61	0.64	
	Energy	0.117	0.102	0.107	

Appendix 4.A EBE signal data from the weld, HAZ and parent material locations for the cracked weld specimen's plane machined surfaces. The EBE envelope parameters from specific locations on one sides of the weld are presented.

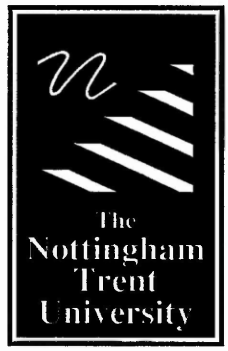
APPENDIX 4.B

EDM Machined Surface	EBE Envelope Parameter	Parent Material (Location A)	HAZ (Location B)	Cracked Weld (Location L*/K)	±
22B	T_P	0.69 ±0.01	0.68 ±0.01	0.67 ±0.01 *	1.5 %
	V_{MAX}	0.47 ±0.01	0.68 ±0.01	0.62 ±0.01 *	2 %
	Energy	0.080 ±0.002	0.137 ±0.002	0.105 ±0.002 *	2 %
23B	T_P	0.70	0.69	0.68	
	V_{MAX}	0.45	0.72	0.65	
	Energy	0.079	0.135	0.113	
24B	T_P	1.10	0.73	0.73	
	V_{MAX}	0.45	0.77	0.76	
	Energy	0.072	0.136	0.122	
25B	T_P	0.70	0.69	0.70	
	V_{MAX}	0.53	0.92	0.91	
	Energy	0.089	0.153	0.134	
26B	T_P	0.73	0.73	0.71	
	V_{MAX}	0.54	0.97	0.97	
	Energy	0.088	0.155	0.140	
27B	T_P	0.72	0.71	0.70	
	V_{MAX}	0.55	0.95	0.97	
	Energy	0.077	0.142	0.135	

Appendix 4.B EBE signal data from the weld, HAZ and parent material locations for the cracked weld specimen's EDM machined surfaces. The EBE envelope parameters from specific locations on one sides of the weld are presented.

" …D'oh!!!"

-Homer J. Simpson



Libraries &
Learning
Resources

The Boots Library: 0115 848 6343
Clifton Campus Library: 0115 848 6612
Brackenhurst Library: 01636 817049